

AMIDATE COMPLEXES OF THE GROUP 4 METALS:
SYNTHESIS, REACTIVITY, AND HYDROAMINATION CATALYSIS

by

ROBERT KENNETH THOMSON

B.Sc. (Honours), University of British Columbia, 2002

A THESIS SUBMITTED IN PARTIAL FULFILLMENT OF
THE REQUIREMENTS FOR THE DEGREE OF

DOCTOR OF PHILOSOPHY

in

THE FACULTY OF GRADUATE STUDIES

(Chemistry)

THE UNIVERSITY OF BRITISH COLUMBIA

January 2008

© Robert Kenneth Thomson, 2008

ABSTRACT

A series of bidentate amidate ligands with variable groups R' and R'' abbreviated by $[\text{R}''(\text{NO})\text{R}']$ and adamantyl substituted tetradentate amidate ligands abbreviated by $\text{Ad}[\text{O}_2\text{N}_2]$ were utilized as ancillaries for Ti, Zr, and Hf. Protonolysis routes into homoleptic amidate complexes, tris(amidate) mono(amido), bis(amidate) bis(amido), and bis(amidate) dibenzyl complexes are high yielding when performed with tetrakis(amido) and tetrabenzyl group 4 starting materials. Many of these complexes have been characterized in both the solid-state and in the solution phase, where in the latter case these complexes are fluxional and undergo exchange processes.

Multiple geometric isomers are possible with the mixed N,O chelate provided by the amidate ligands, and geometric isomerization of bis(amidate) bis(amido) complexes has been examined through X-ray crystallographic and density functional theory (DFT) calculations. Isomerization is dictated largely by the steric bulk present at the N of the amidate ligands, and is proposed to proceed through a κ^2 - κ^1 - κ^2 ligand isomerization mechanism, which is supported by crystallographic evidence of κ^1 -bound amidate ligands. The amidate ligand system binds to these metals in a largely electrostatic fashion, with poor orbital overlap, generating highly electrophilic metal centers.

The bis(amidate) dibenzyl complexes of Zr and Hf are reactive towards insertion, abstraction, and protonolysis. Insertion of isocyanides into the Zr-C bonds of $[\text{DMP}(\text{NO})^{\text{tBu}}]_2\text{Zr}(\text{CH}_2\text{Ph})_2$ results in the formation of η^2 -iminoacyl complexes, which can either undergo thermally induced C=C coupling to generate an enediamido complex (aryl isocyanides), or rearrange to generate a bis(amidate) bis(vinylamido) complex (alkyl isocyanides). Benzyl abstraction to generate cationic Zr bis(amidate) benzyl complexes is also possible through reaction with $[\text{Ph}_3\text{C}][\text{B}(\text{C}_6\text{F}_5)_4]$ or $\text{B}(\text{C}_6\text{F}_5)_3$.

Terminal imido complexes with novel pyramidal geometries are generated through protonolysis of bis(amidate) bis(amido) Ti and Zr complexes with primary aryl amines. DFT calculations demonstrate the existence of a $\text{Zr}\equiv\text{N}$ triple bond for these complexes. Dimeric imido complexes have been characterized in the solid state, but are not maintained in solution. Cycloaddition reactions of the terminal Zr imido complexes with C=O bonds result in the formation of proposed oxo complexes and organic

metathesis products. Catalytic aminoalkene cyclohydroamination has also been realized with these complexes, generating N-heterocyclic products.

A series of kinetic and labeling studies support an imido-cycloaddition mechanism for catalytic cyclohydroamination of primary aminoalkenes with neutral bis(amidate) Ti and Zr precatalysts. The intermediate Ti imido complex, κ^2 - $[\text{DIPP}(\text{NO})^{\text{tBu}}]_2\text{-}\kappa^1\text{-}[\text{DIPP}(\text{NO})^{\text{tBu}}]\text{Ti}=\text{NCH}_2\text{CPh}_2\text{CH}_2\text{CH}=\text{CH}_2(\text{NHMe}_2)$, has been isolated and characterized in the solid-state and in solution. Amine stabilized imido complexes of this type are invoked as the resting state for the catalytic reaction, and solution phase data support a chair-like geometry, where the alkene is coordinated to the metal center. A diastereoselectivity study supports this proposed solution structure. Eyring and Arrhenius parameters, as well as isolation of a 7-coordinate model imido complex, support a seven-coordinate transition state for the rate-determining metallacycle protonolysis reaction.

In contrast, *secondary* aminoalkene hydroamination catalysis with cationic Zr benzyl complexes is proposed to proceed through a σ -bond insertion mechanism. Proton loss from cationic Zr amido complexes to generate imido species is proposed with *primary* aminoalkenes, and the resultant neutral imido complexes can catalyze the cyclization of these substrates by the aforementioned imido-cycloaddition mechanism. The ability of the amidate ligand system to promote both mechanisms is unique in the field of alkene hydroamination catalysis.

1.5.3.4	Amidates as Ancillary Ligands for Group 4 Metals.....	20
1.6	Scope of Thesis.....	21
1.7	References.....	24
CHAPTER TWO: COORDINATION CHEMISTRY OF GROUP 4 AMIDATE COMPLEXES.....		33
2.1	Introduction.....	33
2.2	Homoleptic Amidate Complexes.....	36
2.2.1	Introduction.....	36
2.2.2	Results and Discussion.....	36
2.2.3	Summary.....	44
2.3	Amidate Amido Complexes.....	45
2.3.1	Introduction.....	45
2.3.2	Results and Discussion.....	46
2.3.2.1	Tris(amidate) Mono(amido) Complexes of Zr.....	46
2.3.2.2	Bis(amidate) Bis(amido) Complexes of Ti and Zr.....	49
2.3.2.3	Insertion Reactivity of Amido Ligands.....	60
2.3.3	Summary.....	62
2.4	Geometric Isomerization of Amido Complexes.....	62
2.4.1	Introduction.....	62
2.4.2	Results and Discussion.....	63
2.4.2.1	Structural Studies.....	63
2.4.2.2	Electronic Structure Analysis.....	72
2.4.3	Summary.....	77
2.5	Conclusions.....	79
2.6	Experimental.....	80
2.6.1	General Considerations.....	80
2.6.2	Starting Materials and Reagents.....	82
2.6.3	Synthesis.....	83
2.7	References.....	98

CHAPTER 3: SYNTHESIS, STRUCTURE, AND REACTIVITY OF ZR AND HF		
AMIDATE BENZYL COMPLEXES.....		104
3.1	Introduction.....	104
3.2	Synthesis and Characterization of Dibenzyl Complexes.....	108
3.2.1	Introduction.....	108
3.2.2	Results and Discussion.....	109
3.2.2.1	Bidentate Amidate Dibenzyl Complexes.....	109
3.2.2.2	Tethered Tetradentate Amidate Dibenzyl Complexes.....	117
3.2.3	Summary.....	120
3.3	Insertion Reactions of Isocyanides with $[\text{DMP}(\text{NO})^{\text{iBu}}]_2\text{Zr}(\text{CH}_2\text{Ph})_2$ (3.9).....	121
3.3.1	Introduction.....	121
3.3.2	Results and Discussion.....	121
3.3.3	Summary.....	132
3.4	Hydrolysis of Dibenzyl Complex $[\text{DMP}(\text{NO})^{\text{Ph}}]_2\text{Hf}(\text{CH}_2\text{Ph})_2(\text{THF})$ (3.6).....	132
3.4.1	Introduction.....	132
3.4.2	Results and Discussion.....	135
3.4.3	Summary.....	140
3.5	Abstraction Reactivity of Bis(amidate) Dibenzyl Complexes.....	140
3.5.1	Introduction.....	140
3.5.2	Results and Discussion.....	141
3.5.3	Summary.....	143
3.6	Conclusions.....	144
3.7	Experimental.....	145
3.7.1	General Considerations.....	145
3.7.2	Starting Materials and Reagents.....	145
3.7.3	Synthesis.....	146
3.8	References.....	155

CHAPTER 4: SYNTHESIS, STRUCTURE, AND REACTIVITY OF AMIDATE SUPPORTED IMIDO COMPLEXES.....		162
4.1	Introduction.....	162
4.2	Synthesis and Structure of Terminal Imido Complexes.....	171
4.2.1	Introduction.....	171
4.2.2	Results and Discussion.....	173
4.2.2.1	Synthesis and Structure of Amido Anilido Complex.....	173
4.2.2.2	Synthesis and Structure of a Pentagonal Pyramidal Imido Complex.....	177
4.2.2.3	Electronic Structure of Pentagonal Pyramidal Imido Complex 4.25	182
4.2.2.4	Ligand Lability Investigations.....	185
4.2.3	Summary.....	186
4.3	Synthesis and Structure of a Seven-Coordinate Imido Complex.....	187
4.3.1	Introduction.....	187
4.3.2	Results and Discussion.....	187
4.3.3	Summary.....	191
4.4	Structural Characterization of Dimeric Zr Imido Complexes.....	192
4.4.1	Introduction.....	192
4.4.2	Results and Discussion.....	193
4.4.3	Summary.....	199
4.5	Cycloaddition Reactivity with Terminal Imido Complexes.....	200
4.5.1	Introduction.....	200
4.5.2	Results and Discussion.....	201
4.5.2.1	Development of Spectroscopically Simpler Imido Complexes.....	201
4.5.2.2	Cycloaddition of C=O Bonds.....	204
4.5.3	Summary.....	206
4.6	Catalytic Hydroamination of Aminoalkenes.....	207
4.6.1	Introduction.....	207

4.6.2	Results and Discussion.....	207
4.6.3	Summary.....	209
4.7	Conclusions.....	210
4.8	Experimental.....	211
4.8.1	General Considerations.....	211
4.8.2	Starting Materials and Reagents.....	211
4.8.3	Synthesis.....	211
4.9	References.....	222
CHAPTER 5: CATALYTIC HYDROAMINATION MECHANISTIC STUDIES.....		230
5.1	Introduction.....	230
5.1.1	General Introduction.....	230
5.1.2	Late Transition Metal Catalyst Mechanisms.....	234
5.1.3	Rare-Earth Metal Catalyst Mechanism.....	238
5.1.4	Group 4 Catalyst Mechanism.....	240
5.2	Alkyne Hydroamination.....	242
5.2.1	Introduction.....	242
5.2.2	Results and Discussion.....	244
5.2.3	Summary.....	246
5.3	Alkene Hydroamination.....	247
5.3.1	Introduction.....	247
5.3.1.1	Cationic Group 4 Catalysts.....	247
5.3.1.2	Neutral Group 4 Catalysts.....	250
5.3.2	Results and Discussion.....	252
5.3.2.1	Imido Precatalyst Kinetic Analysis.....	252
5.3.2.2	Bis(amido) Precatalyst Kinetic Analysis.....	258
5.3.2.3	Substrate Scope and Reaction Optimization.....	262
5.3.2.4	Protonolysis Transition State Studies.....	264
5.3.2.5	Stoichiometric Experiments.....	267
5.3.2.6	Diastereoselectivity.....	276

5.3.3	Summary of Neutral Catalyst Studies.....	277
5.4	Cationic Alkene Hydroamination Investigations.....	278
5.4.1	Introduction.....	278
5.4.2	Results and Discussion.....	279
5.4.3	Summary of Cationic Catalyst Systems.....	283
5.5	Conclusions.....	284
5.6	Experimental.....	285
5.6.1	General Considerations.....	285
5.6.2	Starting Materials and Reagents.....	286
5.6.3	Kinetic Investigations.....	286
5.6.4	Synthesis.....	288
5.7	References.....	291
CHAPTER 6: CONCLUDING REMARKS AND FUTURE DIRECTIONS.....		297
6.1	Summary and Conclusions.....	297
6.2	Future Work.....	299
6.2.1	Insertion Reactivity of Alkyl Complexes.....	299
6.2.2	Fluorinated Amidate Ligands for Enhanced Reactivity...	300
6.2.3	Phosphinidene Complexes.....	302
6.2.4	Further Catalytic Hydroamination Mechanistic Investigations.....	303
6.3	References.....	307
APPENDIX A: X-RAY CRYSTALLOGRAPHIC DATA.....		309
APPENDIX B: COMPUTATIONAL DETAILS.....		324
B1	Bis(amidate) bis(amido) DFT calculations.....	324
B2	Bis(amidate) imido DFT calculations.....	331
B3	References.....	332

LIST OF TABLES

Table 2.1:	Selected Bond Distances (Å) and Angles (°) for $[\text{DMP}(\text{NO})^{\text{Ph}}]_4\text{Hf}$, 2.8	38
Table 2.2:	Selected Bond Distances (Å) and Angles (°) for $[\text{DMP}(\text{NO})^{\text{tBu}}]_4\text{Zr}$, 2.9	40
Table 2.3:	Selected Bond Distances (Å) and Angles (°) for $^{\text{Ad}}[\text{O}_2\text{N}_2]_2\text{Zr}$, 2.10	43
Table 2.4:	Selected Bond Distances (Å) and Angles (°) for $[\text{DIPP}(\text{NO})^{\text{Ph}}]_3\text{ZrNHPh}$, 2.14	49
Table 2.5:	Selected Bond Distances (Å) and Angles (°) for $[\text{tBu}(\text{NO})^{\text{Ph}}]_2\text{Zr}(\text{NEt}_2)_2$, 2.15	51
Table 2.6:	Selected Bond Distances (Å) and Angles (°) for $[\text{tBu}(\text{NO})^{\text{Ph}}]_2\text{Ti}(\text{NEt}_2)_2$, 2.16	52
Table 2.7:	Selected Bond Distances (Å) and Angles (°) for $[\text{DMP}(\text{NO})^{\text{tBu}}]_2\text{Zr}(\text{NMe}_2)_2$, 2.18	55
Table 2.8:	Selected Bond Distances (Å) and Angles (°) for $\kappa^2\text{-}[\text{DMP}(\text{NO})^{\text{tBu}}]\text{-}$ $\kappa^1\text{-}[\text{DMP}(\text{NO})^{\text{tBu}}]\text{Zr}(\text{NMe}_2)_2(\text{Py})$, 2.19	58
Table 2.9:	Selected Bond Distances (Å) and Angles (°) for $[\text{DMP}(\text{NO})^{\text{Ph}}]_2\text{Ti}(\text{NEt}_2)_2$, 2.23	68
Table 2.10:	Selected Bond Distances (Å) and Angles (°) for $[\text{DIPP}(\text{NO})^{\text{Ph}}]_2\text{Ti}(\text{NEt}_2)_2$, 2.24	71
Table 2.11:	Theoretical and Experimental λ_{max} Values for 2.16 , 2.23 , and 2.24	75
Table 3.1:	Selected Bond Distances (Å) and Angles (°) for $[\text{DMP}(\text{NO})^{\text{Ph}}]_2\text{Hf}(\text{CH}_2\text{Ph})_2(\text{THF})$, 3.6	111
Table 3.2:	Selected Bond Distances (Å) and Angles (°) for $[\text{DMP}(\text{NO})^{\text{tBu}}]_2\text{Zr}(\text{CH}_2\text{Ph})_2$, 3.9	115
Table 3.3:	Selected Bond Distances (Å) and Angles (°) for $^{\text{Ad}}[\text{O}_2\text{N}_2]\text{Zr}(\text{CH}_2\text{Ph})_2(\text{THF})$, 3.14	119
Table 3.4:	Selected Bond Distances (Å) and Angles (°) for $[\text{DMP}(\text{NO})^{\text{tBu}}]_2\text{Zr}(\eta^2\text{-2,6-Me}_2\text{C}_6\text{H}_3\text{N=CCH}_2\text{Ph})_2$, 3.16	125
Table 3.5:	Selected Bond Distances (Å) and Angles (°) for $[\text{DMP}(\text{NO})^{\text{tBu}}]_2\text{Zr}(\eta^4\text{-ArNC}(\text{CH}_2\text{Ph})=\text{C}(\text{CH}_2\text{Ph})\text{NAr})$, 3.17 (Ar = 2,6-Me ₂ C ₆ H ₃).....	128
Table 3.6:	Selected Bond Distances (Å) and Angles (°) for $\{[\text{DMP}(\text{NO})^{\text{Ph}}]_2\text{Hf}(\mu\text{-O})\}_4$, 3.21	139
Table 4.1:	Selected Bond Distances (Å) and Angles (°) for $[\text{DIPP}(\text{NO})^{\text{Ph}}]_2\text{Zr}(\text{NH-2,6-Me}_2\text{C}_6\text{H}_3)(\text{NMe}_2)$, 4.17	176

Table 4.2:	Selected Bond Distances (Å) and Angles (°) for [^{DIPP} (NO) ^{Ph}] ₂ Zr=N(2,6-Me ₂ C ₆ H ₃)(TPPO), 4.25	181
Table 4.3:	Selected Bond Distances (Å) and Angles (°) for [^{DMP} (NO) ^{tBu}] ₂ Zr=N(2,6-Me ₂ C ₆ H ₃)(TPPO)(Py), 4.27	190
Table 4.4:	Selected Bond Distances (Å) and Angles (°) for [^{DIPP} (NO) ^{Ph}] ₂ Zr(μ-N(2,6-Me ₂ C ₆ H ₃)) ₂ Zr[^{DIPP} (NO) ^{Ph}] ₂ , 4.31	195
Table 4.5:	Selected Bond Distances (Å) and Angles (°) for [^{DMP} (NO) ^{tBu}] ₂ Zr(μ-N(2,6-Me ₂ C ₆ H ₃)) ₂ Zr[^{DMP} (NO) ^{tBu}]NH(2,6-Me ₂ C ₆ H ₃), 4.33	198
Table 4.6:	Unoptimized alkene hydroamination results with precatalyst 4.25	209
Table 5.1:	Effect of electronic modification of amidate ligands on alkyne cyclohydroamination efficiency.....	245
Table 5.2:	Comparison of bond distances for bis(amidate) bis(amido) complex 5.9 and fluorinated variant 5.10	245
Table 5.3:	Optimized hydroamination results with precatalytic complex 5.36	264
Table 5.4:	Selected Bond Distances (Å) and Angles (°) for κ ² -[^{DIPP} (NO) ^{tBu}]- κ ¹ -[^{DIPP} (NO) ^{tBu}]Ti=NCH ₂ CPh ₂ CH ₂ CH=CH ₂ (NHMe ₂), 5.49·HNMe₂	272
Table A2.1:	Crystallographic Data and Refinement Details for [^{DMP} (NO) ^{Ph}] ₄ Hf, 2.8	309
Table A2.2:	Crystallographic Data and Refinement Details for [^{DMP} (NO) ^{tBu}] ₄ Zr, 2.9	309
Table A2.3:	Crystallographic Data and Refinement Details for ^{Ad} [O ₂ N ₂] ₂ Zr, 2.10	310
Table A2.4:	Selected Bond Distances (Å) and Angles (°) for ^{Ad} [O ₂ N ₂] ₂ Hf, 2.11	311
Table A2.5:	Crystallographic Data and Refinement Details for ^{Ad} [O ₂ N ₂] ₂ Hf, 2.11	311
Table A2.6:	Crystallographic Data and Refinement Details for [^{DIPP} (NO) ^{Ph}] ₃ ZrNHPh, 2.14	312
Table A2.7:	Crystallographic Data and Refinement Details for [^{tBu} (NO) ^{Ph}] ₂ Zr(NEt ₂) ₂ , 2.15	312
Table A2.8:	Crystallographic Data and Refinement Details for [^{tBu} (NO) ^{Ph}] ₂ Ti(NEt ₂) ₂ , 2.16	313
Table A2.9:	Selected Bond Distances (Å) and Angles (°) for [^{tBu} (NO) ^{Ph}] ₂ Ti(NMe ₂) ₂ , 2.17	314
Table A2.10:	Crystallographic Data and Refinement Details for [^{tBu} (NO) ^{Ph}] ₂ Ti(NMe ₂) ₂ , 2.17	314

Table A2.11:	Crystallographic Data and Refinement Details for [^{DMP} (NO) ^{tBu}] ₂ Zr(NMe ₂) ₂ , 2.18	315
Table A2.12:	Crystallographic Data and Refinement Details for κ^2 -[^{DMP} (NO) ^{tBu}]- κ^1 -[^{DMP} (NO) ^{tBu}]Zr(NMe ₂) ₂ (Py), 2.19	315
Table A2.13:	Crystallographic Data and Refinement Details for [^{DMP} (NO) ^{Ph}] ₂ Ti(NEt ₂) ₂ , 2.23	316
Table A3.1:	Crystallographic Data and Refinement Details for [^{DMP} (NO) ^{Ph}] ₂ Hf(CH ₂ Ph) ₂ (THF), 3.6	316
Table A3.2:	Crystallographic Data and Refinement Details for [^{DMP} (NO) ^{Ph}] ₂ Zr(CH ₂ Ph) ₂ , 3.9	317
Table A3.3:	Crystallographic Data and Refinement Details for ^{Ad} [O ₂ N ₂]Zr(CH ₂ Ph) ₂ (THF), 3.14	317
Table A3.4:	Selected Bond Distances (Å) and Angles (°) for ^{Ad} [O ₂ N ₂]Hf(CH ₂ Ph) ₂ (THF), 3.15	318
Table A3.5:	Crystallographic Data and Refinement Details for ^{Ad} [O ₂ N ₂]Hf(CH ₂ Ph) ₂ (THF), 3.15	319
Table A3.6:	Crystallographic Data and Refinement Details for [^{DMP} (NO) ^{tBu}] ₂ Zr(η^2 -2,6-Me ₂ C ₆ H ₃ N=CCH ₂ Ph) ₂ , 3.16	319
Table A3.7:	Crystallographic Data and Refinement Details for [^{DMP} (NO) ^{tBu}] ₂ Zr(η^4 -ArNC(CH ₂ Ph)=C(CH ₂ Ph)NAr), 3.17 (Ar = 2,6-Me ₂ C ₆ H ₃).....	320
Table A3.8:	Crystallographic Data and Refinement Details for {[^{DMP} (NO) ^{Ph}] ₂ Hf(μ -O)} ₄ , 3.21	320
Table A4.1:	Crystallographic Data and Refinement Details for [^{DIPP} (NO) ^{Ph}] ₂ Zr(NH-2,6-Me ₂ C ₆ H ₃)(NMe ₂), 4.17	321
Table A4.2:	Crystallographic Data and Refinement Details for [^{DIPP} (NO) ^{Ph}] ₂ Zr=N(2,6-Me ₂ C ₆ H ₃)(TPPO), 4.25	321
Table A4.3:	Crystallographic Data and Refinement Details for [^{DMP} (NO) ^{tBu}] ₂ Zr=N(2,6-Me ₂ C ₆ H ₃)(TPPO)(Py), 4.27	322
Table A4.4:	Crystallographic Data and Refinement Details for [^{DIPP} (NO) ^{Ph}] ₂ Zr(μ -N(2,6-Me ₂ C ₆ H ₃)) ₂ Zr[^{DIPP} (NO) ^{Ph}] ₂ , 4.31	322
Table A4.5:	Crystallographic Data and Refinement Details for [^{DMP} (NO) ^{tBu}] ₂ Zr(μ -N(2,6-Me ₂ C ₆ H ₃)) ₂ Zr[^{DMP} (NO) ^{tBu}]NH(2,6-Me ₂ C ₆ H ₃), 4.33	323
Table A5.1:	Crystallographic Data and Refinement Details for κ^2 -[^{DIPP} (NO) ^{tBu}]- κ^1 -[^{DIPP} (NO) ^{tBu}]Ti=NCH ₂ CPh ₂ CH ₂ CH=CH ₂ (NHMe ₂), 5.49·HNMe₂	323

Table B2.1:	Experimental and Calculated Bond Lengths (Å) and Angles (°) for 2.16	325
Table B2.2:	Experimental and Calculated Bond Lengths (Å) and Angles (°) for 2.23	326
Table B2.3:	Experimental and Calculated Bond Lengths (Å) and Angles (°) for 2.24	327
Table B2.4:	Energetic Ordering of Geometric Isomers.....	328

LIST OF FIGURES

Figure 1.1:	Constrained geometry catalyst (CGC).....	4
Figure 1.2:	Selected early metal complexes with amido ancillary ligands.....	5
Figure 1.3:	Selected aryloxy complexes and hydroamination regioselectivity.....	6
Figure 1.4:	Living olefin polymerization phenoxyimine catalysts.....	7
Figure 1.5:	Amidinate ligand and selected amidinate complexes.....	9
Figure 1.6:	Guanidinate resonance structures and selected metal complexes.....	10
Figure 1.7:	Carboxylate ligand framework and bimetallic paddlewheel complex.....	11
Figure 1.8:	Coordination modes of amidate ligands.....	14
Figure 1.9:	N-bound κ^1 -amidate complexes.....	14
Figure 1.10:	Ti complex with κ^2 -O-bound and bidentate κ^1 -amidate ligands.....	15
Figure 1.11:	Selected bridging bimetallic amidate complexes.....	16
Figure 1.12:	Selected amidate complexes for bioinorganic studies.....	17
Figure 1.13:	Amidate bridged Mo complex with Mo-Mo bonds (some <i>para</i> -anisyl units omitted for clarity).....	18
Figure 1.14:	Bis(amidate) bis(amido) Ti complex.....	21
Figure 2.1:	ORTEP depiction (ellipsoids at 30% probability) of solid-state molecular structure of $[\text{DMP}(\text{NO})^{\text{Ph}}]_4\text{Hf}$, 2.8 (hydrogens and non- <i>ipso</i> phenyl carbons omitted for clarity).....	38
Figure 2.2:	View of $[\text{DMP}(\text{NO})^{\text{Ph}}]_4\text{Hf}$ (2.8) down C_2 axis of symmetry (left), and view of dodecahedral core structure (right).....	39
Figure 2.3:	ORTEP depiction (ellipsoids at 30% probability) of solid-state molecular structure of $[\text{DMP}(\text{NO})^{\text{tBu}}]_4\text{Zr}$, 2.9 (hydrogens omitted for clarity).....	40
Figure 2.4:	ORTEP depiction (ellipsoids at 30% probability) of solid-state molecular structure of $^{\text{Ad}}[\text{O}_2\text{N}_2]_2\text{Zr}$, 2.10 (hydrogens omitted for clarity).....	42
Figure 2.5:	ORTEP depiction (ellipsoids at 30% probability) of core structure of $^{\text{Ad}}[\text{O}_2\text{N}_2]_2\text{Zr}$, 2.10 (hydrogens and adamantyl groups omitted for clarity).....	42
Figure 2.6:	ORTEP depiction (ellipsoids at 30% probability) of solid-state molecular structure of $[\text{DIPP}(\text{NO})^{\text{Ph}}]_3\text{ZrNHPH}$, 2.14 (non- <i>ipso</i> phenyl carbons and hydrogens omitted).....	48

Figure 2.7:	ORTEP depiction (ellipsoids at 30% probability) of solid-state molecular structure of $[\text{tBu}(\text{NO})^{\text{Ph}}]_2\text{Zr}(\text{NEt}_2)_2$, 2.15 (hydrogens omitted for clarity).....	50
Figure 2.8:	ORTEP depiction (ellipsoids at 30% probability) of solid-state molecular structure of $[\text{tBu}(\text{NO})^{\text{Ph}}]_2\text{Ti}(\text{NEt}_2)_2$, 2.16 (hydrogens omitted for clarity).....	52
Figure 2.9:	Tautomers of amidate ligand.....	53
Figure 2.10:	ORTEP depiction (ellipsoids at 30% probability) of solid-state molecular structure of $[\text{DMP}(\text{NO})^{\text{tBu}}]_2\text{Zr}(\text{NMe}_2)_2$, 2.18 (hydrogens omitted).....	54
Figure 2.11:	ORTEP depiction (ellipsoids at 30% probability) of solid-state molecular structure of $\kappa^2\text{-}[\text{DMP}(\text{NO})^{\text{tBu}}]\text{-}\kappa^1\text{-}[\text{DMP}(\text{NO})^{\text{tBu}}]\text{Zr}(\text{NMe}_2)_2(\text{Py})$, 2.19 (hydrogens omitted for clarity).....	57
Figure 2.12:	Extended structure of 2.19 in the solid-state (A), and viewed down crystallographic C_2 screw axis (B) (C = gray, H = green, Zr = purple, N = blue, O = red; hydrogen bonds = dashed red and blue lines).....	59
Figure 2.13:	Possible geometric isomers of bis(amidate) Ti complexes.....	63
Figure 2.14:	Relative energetic ordering of geometric isomers of 2.16 (Ti = white, N = blue, O = red, C = gray).....	65
Figure 2.15:	ORTEP depiction (ellipsoids at 30% probability) of solid-state molecular structure of $[\text{DMP}(\text{NO})^{\text{Ph}}]_2\text{Ti}(\text{NEt}_2)_2$, 2.23 (hydrogens omitted for clarity).....	67
Figure 2.16:	Relative energetic ordering of geometric isomers of 2.23 (Ti = white, N = blue, O = red, C = gray).....	69
Figure 2.17:	ORTEP depiction (ellipsoids at 30% probability) of solid-state molecular structure of $[\text{DIPP}(\text{NO})^{\text{Ph}}]_2\text{Ti}(\text{NEt}_2)_2$, 2.24 (hydrogens omitted for clarity).....	71
Figure 2.18:	Relative energetic ordering of geometric isomers of 2.24 (Ti = white, N = blue, O = red, C = gray).....	72
Figure 2.19:	Frontier bonding orbitals of ground state isomer of 2.16 (Ti = white, N = blue, O = red, C = gray).....	73
Figure 2.20:	Amido σ -bonding orbital of ground state isomer of 2.16 (Ti = white, N = blue, O = red, C = gray).....	74
Figure 2.21:	Frontier non-bonding orbital of ground state isomer of 2.16 (Ti = white, N = blue, O = red, C = gray).....	74
Figure 2.22:	Amidate bonding interactions of ground state isomer of 2.16 (Ti = white, N = blue, O = red, C = gray).....	75
Figure 2.23:	Experimental UV/vis absorption spectrum of 2.16	76

Figure 2.24:	Calculated UV/vis absorption spectrum of 2.16	77
Figure 3.1:	Hapticities of benzyl ligands.....	109
Figure 3.2:	ORTEP depiction (ellipsoids at 30% probability) of solid-state molecular structure of $[\text{DMP}(\text{NO})^{\text{Ph}}]_2\text{Hf}(\text{CH}_2\text{Ph})_2(\text{THF})$, 3.6 (hydrogens omitted).....	111
Figure 3.3:	Stacked plot ^1H NMR spectra showing THF exchange on $[\text{DMP}(\text{NO})^{\text{Ph}}]_2\text{Hf}(\text{CH}_2\text{Ph})_2(\text{THF})$, 3.6	113
Figure 3.4:	ORTEP depiction (ellipsoids at 30% probability) of solid-state molecular structure of $[\text{DMP}(\text{NO})^{\text{tBu}}]_2\text{Zr}(\text{CH}_2\text{Ph})_2$, 3.9 (hydrogens omitted for clarity).....	114
Figure 3.5:	ORTEP depiction (ellipsoids at 30% probability) of solid-state molecular structure of $^{\text{Ad}}[\text{O}_2\text{N}_2]\text{Zr}(\text{CH}_2\text{Ph})_2(\text{THF})$, 3.9 (hydrogens omitted).....	119
Figure 3.6:	Common geometric isomers of bis(η^2 -iminoacyl) complexes.....	123
Figure 3.7:	ORTEP depiction (ellipsoids at 30% probability) of solid-state molecular structure of $[\text{DMP}(\text{NO})^{\text{tBu}}]_2\text{Zr}(\eta^2\text{-}2,6\text{-Me}_2\text{C}_6\text{H}_3\text{N}=\text{CCH}_2\text{Ph})_2$, 3.16 (hydrogens omitted for clarity).....	124
Figure 3.8:	ORTEP depiction (ellipsoids at 30% probability) of simplified structure of 3.16 viewed down the C_2 axis of symmetry (amidate substituents and hydrogens omitted for clarity).....	125
Figure 3.9:	ORTEP depictions (ellipsoids at 30% probability) of $[\text{DMP}(\text{NO})^{\text{tBu}}]_2\text{Zr}(\eta^4\text{-ArNC}(\text{CH}_2\text{Ph})=\text{C}(\text{CH}_2\text{Ph})\text{NAr})$, 3.17 (Ar = 2,6-Me ₂ C ₆ H ₃) (A – hydrogens omitted, B – hydrogens and amidate substituents omitted).....	127
Figure 3.10:	ORTEP depiction (ellipsoids at 30% probability) of solid-state molecular structure of $\{[\text{DMP}(\text{NO})^{\text{Ph}}]_2\text{Hf}(\mu\text{-O})\}_4$, 3.21 (hydrogens omitted).....	137
Figure 3.11:	ORTEP depiction (ellipsoids at 30% probability) of core solid-state molecular structure of $\{[\text{DMP}(\text{NO})^{\text{Ph}}]_2\text{Hf}(\mu\text{-O})\}_4$, 3.21 (hydrogens and amidate substituents omitted).....	139
Figure 3.12:	Proposed structure of 3.24 in solution.....	143
Figure 4.1:	Grubbs and Schrock olefin metathesis catalysts.....	164
Figure 4.2:	New Ti imido polymerization catalysts.....	165
Figure 4.3:	The first group 4 imido complexes.....	167
Figure 4.4:	ORTEP depiction (ellipsoids at 30% probability) of solid-state molecular structure of $[\text{DIPP}(\text{NO})^{\text{Ph}}]_2\text{Zr}(\text{NH-}2,6\text{-Me}_2\text{C}_6\text{H}_3)(\text{NMe}_2)$, 4.17 (non-N-H hydrogens omitted).....	175

Figure 4.5:	Five-coordinate bis(guanidinate) imido complex and guanidinate resonance forms.....	177
Figure 4.6:	ORTEP depiction (ellipsoids at 30% probability) of solid-state molecular structure of $[\text{DIPP}(\text{NO})^{\text{Ph}}]_2\text{Zr}=\text{N}(2,6\text{-Me}_2\text{C}_6\text{H}_3)(\text{TPPO})$, 4.25 (hydrogens omitted for clarity).....	180
Figure 4.7:	ORTEP depiction (ellipsoids at 30% probability) of bottom view of solid-state molecular structure of $[\text{DIPP}(\text{NO})^{\text{Ph}}]_2\text{Zr}=\text{N}(2,6\text{-Me}_2\text{C}_6\text{H}_3)(\text{TPPO})$, 4.25 (hydrogens omitted for clarity).....	181
Figure 4.8:	HOMO of $[\text{DIPP}(\text{NO})^{\text{Ph}}]_2\text{Zr}=\text{N}(2,6\text{-Me}_2\text{C}_6\text{H}_3)(\text{TPPO})$, 4.25	183
Figure 4.9:	HOMO-1 of $[\text{DIPP}(\text{NO})^{\text{Ph}}]_2\text{Zr}=\text{N}(2,6\text{-Me}_2\text{C}_6\text{H}_3)(\text{TPPO})$, 4.25	183
Figure 4.10:	HOMO-59 of $[\text{DIPP}(\text{NO})^{\text{Ph}}]_2\text{Zr}=\text{N}(2,6\text{-Me}_2\text{C}_6\text{H}_3)(\text{TPPO})$, 4.25	184
Figure 4.11:	Space-filling models of 4.25 (imido ligand = purple balls, amidate ligands = green balls, TPPO ligand = gray balls).....	185
Figure 4.12:	ORTEP depiction (ellipsoids at 30% probability) of solid-state molecular structure of $[\text{DMP}(\text{NO})^{\text{tBu}}]_2\text{Zr}=\text{N}(2,6\text{-Me}_2\text{C}_6\text{H}_3)(\text{TPPO})(\text{Py})$, 4.27 (non- <i>ipso</i> phenyl carbons and hydrogens omitted for clarity).....	189
Figure 4.13:	Space-filling models of 4.27 with pyridine removed (imido ligand = purple balls, amidate ligands = green balls, TPPO ligand = gray balls).....	191
Figure 4.14:	ORTEP depiction (ellipsoids at 30% probability) of solid-state molecular structure of $[\text{DIPP}(\text{NO})^{\text{Ph}}]_2\text{Zr}(\mu\text{-N}(2,6\text{-Me}_2\text{C}_6\text{H}_3))_2\text{Zr}[\text{DIPP}(\text{NO})^{\text{Ph}}]_2$, 4.31 (hydrogens omitted).....	194
Figure 4.15:	ORTEP depiction (ellipsoids at 30% probability) of core molecular structure of $[\text{DIPP}(\text{NO})^{\text{Ph}}]_2\text{Zr}(\mu\text{-N}(2,6\text{-Me}_2\text{C}_6\text{H}_3))_2\text{Zr}[\text{DIPP}(\text{NO})^{\text{Ph}}]_2$, 4.31 (bond distances in Å).....	195
Figure 4.16:	ORTEP depiction (ellipsoids at 30% probability) of solid-state molecular structure of $[\text{DMP}(\text{NO})^{\text{tBu}}]_2\text{Zr}(\mu\text{-N}(2,6\text{-Me}_2\text{C}_6\text{H}_3))_2\text{Zr}[\text{DMP}(\text{NO})^{\text{tBu}}]\text{-NH}(2,6\text{-Me}_2\text{C}_6\text{H}_3)$, 4.33 (non-N-H hydrogens omitted).....	197
Figure 4.17:	Metallacycles relevant to catalytic hydroamination.....	200
Figure 5.1:	Structures of alkaloid natural products.....	231
Figure 5.2:	Biologically active N-heterocycles synthesized via hydroamination.....	239
Figure 5.3:	Selected group 4 alkyne hydroamination catalysts.....	243
Figure 5.4:	Cationic precatalysts for alkene hydroamination.....	248
Figure 5.5:	Selected neutral Ti and Zr alkene hydroamination precatalysts.....	251
Figure 5.6:	Amidate Ti and Zr aminoalkene cyclohydroamination precatalysts.....	252

Figure 5.7:	Time-resolved 300 MHz ¹ H NMR spectra showing consumption of substrate (olefinic signals (*) at δ 4.96 and 5.44).....	253
Figure 5.8:	Natural log of [5.32] vs. time plot showing first-order substrate dependence.....	254
Figure 5.9:	Ln [5.32'] vs. time plot for 4 different catalyst loadings showing first-order substrate dependence over a wide range of catalyst loadings.....	256
Figure 5.10:	Plot of k _{obs} vs. [catalyst] (5.31) showing first-order catalyst dependence.....	257
Figure 5.11:	Kinetic profile comparison of Zr amido 5.29 vs. imido 5.31 for cyclization of aminoalkene 5.32 ([5.32] vs. time).....	259
Figure 5.12:	Kinetic profile comparison of Zr imido 5.31 and amido 5.29 + TPPO for cyclization of aminoalkene 5.32 ([5.32] vs. time).....	260
Figure 5.13:	Kinetic isotope effect experiment showing small primary kinetic isotope effect for cyclization of aminoalkene 5.32 (Ln [5.32'] vs. time).....	262
Figure 5.14:	ORTEP depiction of solid-state molecular structure of 7-coordinate imido (A) and proposed protonolysis transition state (B).....	265
Figure 5.15:	Eyring plot for cyclization of substrate 5.32 between 90 and 117 °C using amido precatalyst 5.36.....	266
Figure 5.16:	Arrhenius plot for cyclization of substrate 5.32 between 90 and 117 °C using amido precatalyst 5.36.....	267
Figure 5.17:	400 MHz ¹ H NMR spectrum of Zr mixed amido complex 5.47.....	268
Figure 5.18:	400 MHz ¹ H NMR spectrum of Ti imido complex 5.49.....	270
Figure 5.19:	ORTEP depiction of solid-state molecular structure (ellipsoids at 30% probability) of κ ² -[^{DIPP} (NO) ^{tBu}]-κ ¹ -[^{DIPP} (NO) ^{tBu}]Ti=NCH ₂ CPh ₂ CH ₂ CH=CH ₂ (NHMe ₂), 5.49·HNMe ₂ (non-N-H hydrogens omitted for clarity).....	272
Figure 5.20:	ORTEP depiction of core structure of 5.49·HNMe ₂ (hydrogen atoms and amidate/dimethylamine substituents removed for clarity).....	273
Figure 5.21:	Ln [substrate] vs. time for Ti imido 5.49 and Ti bis(amido) 5.48 showing similar rates and first-order substrate consumption.....	275
Figure 5.22:	Rationalization of diastereoselectivity of cyclization.....	276
Figure 5.23:	[5.34] vs. time plot for cationic Zr precatalyst 5.51 showing zero-order substrate dependence and product inhibition.....	281
Figure 6.1:	ORTEP depiction (ellipsoids at 30% probability) of solid-state molecular structure of [^{DIPP} (NO) ^{Ph-p-CF₃}] ₂ Zr(NMe ₂) ₂ , 6.4 (hydrogens omitted).....	301

Figure A1:	ORTEP depiction (ellipsoids at 30% probability) of core solid-state molecular structure of $^{Ad}[O_2N_2]_2Hf$, 2.11 (hydrogens and adamantyl groups omitted for clarity).....	310
Figure A2:	ORTEP depiction (ellipsoids at 30% probability) of solid-state molecular structure of $[^{tBu}(NO)^{Ph}]_2Ti(NMe_2)_2$, 2.17 (hydrogens omitted for clarity).....	313
Figure A3:	ORTEP depiction (ellipsoids at 30% probability) of solid-state molecular structure of $^{Ad}[O_2N_2]Hf(CH_2Ph)_2(THF)$, 3.15 (hydrogens omitted for clarity).....	318
Figure B1:	Experimental UV/vis spectrum of 2.23	329
Figure B2:	Experimental UV/vis spectrum of 2.24	329
Figure B3:	Calculated UV/vis spectrum of 2.23	330
Figure B4:	Calculated UV/vis spectrum of 2.24	330

LIST OF ABBREVIATIONS

2D	2-Dimensional
Å	Angstrom
Ad	Adamantyl
Anal.	Analysis
atm	Atmosphere
Ar	Aryl
BBI	Broadband inverse
Bn	Benzyl
br	Broad
°C	Degrees Celsius
CGC	Constrained geometry catalyst
Calcd.	Calculated
cat.	Catalytic
CCD	Charge-coupled device
cm	Centimeter
cm ⁻¹	Wavenumber
CI	Chemical impact
COSY	Correlation spectroscopy
Cp	Cyclopentadienyl
Cp*	Pentamethylcyclopentadienyl
Cy	Cyclohexyl
d	Doublet
d ⁿ	Number of d-electrons
DCC	Dicyclohexylcarbodiimide
DD	Dodecahedron
d.e.	Diastereomeric excess
DFT	Density functional theory
DIPP	2,6-Diisopropylphenyl

DME	Dimethoxyethane
DMP	2,6-Dimethylphenyl
E	Element
E	Energy
e ⁻	Electron
E _a	Activation energy
EI	Electron impact
Eq.	Equation
Equiv	Equivalent
Et	Ethyl
e.u.	Entropy units
eV	Electron volts
Fig.	Figure
FT	Fourier-transform
g	Gas
g	Gram
G	Gibbs free energy
ΔG^\ddagger	Activation energy
GC	Gas chromatography
GPC	Gel permeation chromatography
h	Hours
ΔH^\ddagger	Enthalpy of activation
HMQC	Heteronuclear multiquantum correlation
HOMO	Highest occupied molecular orbital
HSAB	Hard-soft acid-base
Hz	Hertz, s ⁻¹
ⁱ Pr	Isopropyl
IR	Infrared
<i>J</i>	Coupling constant
k	Rate constant
K	Equilibrium constant

K	Kelvin
kcal	Kilocalorie
KIE	Kinetic isotope effect
kJ	Kilojoule
L	Ligand
LMCT	Ligand-to-metal charge transfer
LUMO	Lowest unoccupied molecular orbital
m	Multiplet
<i>m</i>	<i>Meta</i>
M	Metal
M	Molar
MALDI	Matrix assisted laser desorption ionization
MAO	Methylalumoxane
max	Maximum
Me	Methyl
Mg	Milligram
MHz	Megahertz
min	Minute
mL	Millilitre
μL	Microlitre
mm	Millimeter
MOCVD	Metal-organic chemical vapour deposition
mol	Mole
mmol	Millimole
MS	Mass spectrometry
m/z	Mass-to-charge ratio
NA	Natural abundance
ⁿ Bu	<i>n</i> -butyl
n	Number (integer)
NOE	Nuclear overhauser effect
NOESY	Nuclear overhauser effect spectroscopy

NMR	Nuclear magnetic resonance
nm	Nanometer
<i>o</i>	<i>Ortho</i>
obs	Observed
ORTEP	Oakridge Thermal Ellipsoid Program
OTf	Triflate, trifluoromethylsulfonate
<i>p</i>	<i>Para</i>
Ph	Phenyl
Py	Pyridine
R	Organic group
RCM	Ring closing metathesis
ROMP	Ring-opening metathesis polymerization
r.t.	Room temperature
$[\text{R}''(\text{NO})\text{R}']$	$\text{R}''\text{-N}(\text{CO})\text{R}'$ amidate anion (R'' = variable group on N, R' = variable group on carbonyl)
$[\text{R}(\text{O}_2\text{N}_2)]$	$\text{R}(\text{CO})\text{NCH}_2\text{CMe}_2\text{CH}_2\text{N}(\text{CO})\text{R}$ bis(amidate) dianion (R = variable group on carbonyl)
s	Second
s	Singlet
ΔS^\ddagger	Entropy of activation
SAP	Square antiprismatic geometry
sept	Septet
t	Triplet
^t Bu	<i>Tert</i> -butyl
tacn	Triazacyclononane
TC	Coalescence temperature
THF	Tetrahydrofuran
TM	Trademark
TMS	Trimethylsilane
TMS	Trimethylsilyl
TON	Turnover number
TPPO	Triphenylphosphine oxide

UBC	University of British Columbia
TTP	<i>p</i> -Tolyl-NC(CH ₃)CHC(CH ₃)N- <i>p</i> -tolyl
UV	Ultraviolet
Vis.	Visible
w	Wide
xs	Excess
©	Copyright
°	Degree
δ	<i>Delta</i> , chemical shift
Δ	<i>Delta</i> , change in
Δ	<i>Delta</i> , elevated temperature
λ	<i>Lambda</i> , wavelength
κ	<i>Kappa</i> , denticity
μ	<i>Mu</i> , bridging
η	<i>Eta</i> , hapticity

FOREWORD

The uniting theme within this dissertation is the development and utility of the amidate ligand set for group 4 metals. This thesis covers the topics of coordination chemistry and organometallic chemistry of group 4 amidate complexes, as well as imido chemistry and hydroamination catalysis. This is a manuscript based thesis and each chapter is meant to be a stand-alone document. As such, there are some instances of repetition between chapters, and certain compounds are utilized in more than one chapter. Compound numbering is consistent within each chapter; however, in cases where a compound is used in multiple chapters, the compound number from its first appearance may also be given in subsequent chapters for reference purposes.

The work presented in this dissertation represents a new project within the Schafer research group. A literature review of each area of investigation is provided at the beginning of each chapter, and is meant to be a resource for future researchers in the Schafer group. Subsections within each chapter are divided into introduction, results and discussion, and summary sections, to clearly separate background material from experimental results. Each experimental chapter ends with a detailed conclusions section, and as such, Chapter 6 provides only an overall summary and conclusion, without many of the details present in Chapters 2-5.

X-ray crystallographic data and refinement details for all crystallographically characterized compounds are presented in Appendix A. Appendix B contains details regarding the theoretical (DFT) calculations performed during the course of this work.

ACKNOWLEDGEMENTS

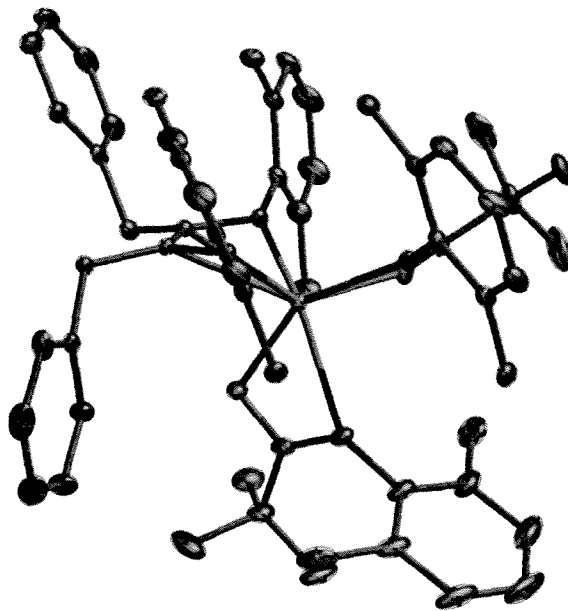
I would like to first thank my research supervisor, Dr. Laurel Schafer, for her incredible support, encouragement, and guidance during the course of this research. The exploration of new ideas was strongly encouraged by Laurel, and this cultivated an atmosphere of independent thought and creativity within the research group. Working as a member of the Schafer research group has been an extremely rewarding experience. I have enjoyed my time with each and every member to come through the group. In particular, I would like to thank Ali, Louisa, Jason, Mark, Rashidat, Dave and Courtney for many engaging discussions about chemistry, life, and everything in between. I would also like to thank Jason Bexrud and Dr. Federico Zahariev for our fruitful scientific collaborations.

I am grateful to Dr. Mike Fryzuk and Dr. Michael Shaver for their encouragement and support during my graduate work, and for getting me interested in chemical research in the first place. I would also like to thank Dr. Jennifer Love, Dr. Brian James, and Dr. Pierre Kennepohl for many fruitful discussions and assistance in technical areas.

The support staff in the UBC chemistry department has been instrumental in moving the research presented within this thesis forward. I would especially like to thank Ken Love and Brian Snapkauskas for their expertise and assistance with glovebox related issues, and Brian Ditchburn for always quickly repairing my J-Young NMR tubes and Schlenk lines. NMR spectroscopy was utilized extensively in this thesis, and I must thank Dr. Nick Burlinson, Zorana Danilovic, and Dr. Maria Ezhova for their expertise and assistance with some of the more complicated experiments presented in this work. X-ray crystallography was instrumental to the success of this project, and I would like to thank Dr. Brian Patrick for his numerous crystallography lessons, and for teaching me how to collect, process, and solve crystallographic data.

Finally, I would like to thank my parents for supporting me in all senses of the word during all of my academic endeavors. Without their endless love and support, this thesis could never have been written. I must also thank Shiva Shoai, she has been a bastion of strength when I have needed it most, and has always pushed me to succeed and be a better person. I dedicate this work to them.

CHAPTER 1



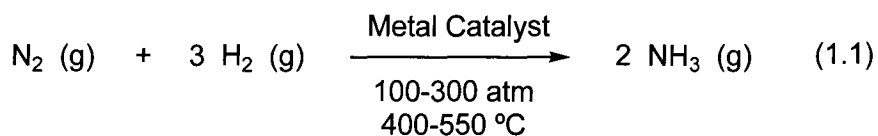
Amidates as New Modular Ligands for Group 4 Metals

1.1 Ligand Driven Reactivity of Early Transition Metals

There are a number of unique properties of transition metals that give them the capacity to facilitate novel transformations otherwise not possible by standard organic synthesis. Transition metals, having *d*-orbitals available for bonding, are capable of adopting expanded coordination numbers of 4 through 9 and higher.¹⁻⁸ In addition, many metal complexes are known to have multiple stable oxidation states, which can facilitate interactions with a variety of different reagents.

Metals facilitate reactivity by bringing reagents together in a such a way that they have the appropriate energy and orientation to allow for their combination. While reaction geometry is important to allow for successful chemical transformations, in many cases the thermodynamic requirements of the reaction are a larger obstacle to overcome. In particular, reactions that require the cleavage of very strong bonds typically require metals. One of the best examples of this is in the cleavage and functionalization of dinitrogen.

The N₂ molecule has an extremely strong N≡N triple bond. The ability to utilize N₂ from the atmosphere as a source of nitrogen in the formation of new N-E bonds (E = C, H, O, etc.) represents one of the biggest challenges for synthetic chemistry.⁹ One of the most important industrially synthesized molecules is ammonia, which is generated on a massive scale every year.^{10, 11} The Haber-Bosch process has been developed to produce ammonia from nitrogen and hydrogen as shown in Eq. 1.1.⁹⁻¹¹ This process utilizes heterogeneous metal catalysts, typically containing iron or ruthenium.^{12, 13} The gases are passed at high temperatures and pressures over an activated catalyst surface, where they are physisorbed and chemisorbed onto the surface. The adsorbed N and H atoms form new N-H bonds on the surface of the metal catalyst, and NH₃ is subsequently eliminated as a gas.

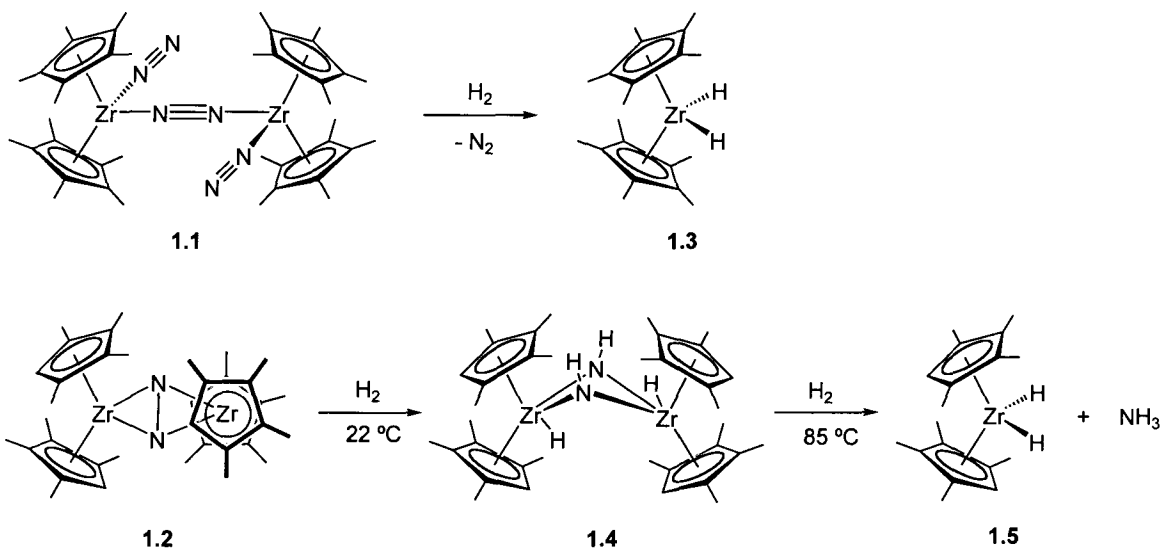


Heterogeneous catalysis is prevalent in other industrial processes such as ethylene polymerization, where stereocontrol is not an issue. In fact, the vast majority of polyethylene is produced with highly effective heterogeneous Ziegler-Natta catalysts, which are mixtures of titanium chloro complexes and aluminum alkyls.¹⁴⁻¹⁸ The development of homogeneous catalysts has enabled polymerization of α -olefins, which can generate polymers of a particular tacticity.¹⁹⁻²³ For example, the symmetry of cationic Ti and Zr complexes influences the tacticity of the polymer produced, and therefore the physical properties of the material generated.²³

With these homogeneous polymerization catalysts, the ligands play two important roles. First, the ligands solubilize the metal centers so that the catalyst and reactants are

in the same phase. Second, the ancillary ligands determine the symmetry of the overall complex, which dictates the nature of the products formed. In the case of propylene polymerization, this involves the tacticity of the polypropylene generated.^{22, 24-30} While the factors determining reactivity at metal centers are complex, in general, the ancillary ligands control steric access to the metal through the presence of groups that can be varied in size. Additionally, the relative electronic properties of the metal center can be modulated by the ancillary ligand.

An excellent example of how small changes to the ancillary ligand result in large changes in observed reactivity is shown in Scheme 1.1. The complex $(\eta^5\text{-C}_5\text{Me}_5)_2\text{ZrCl}_2$ has long been known to generate the end-on bound bridging dinitrogen complex $[(\eta^5\text{-C}_5\text{Me}_5)_2\text{Zr}(\eta^1\text{-N}_2)]_2(\mu\text{-}\eta^1\text{:}\eta^1\text{-N}_2)$ (**1.1**) upon reduction with Na/Hg amalgam in the presence of N_2 .^{31, 32} Chirik and coworkers have recently shown that a very similar complex $(\eta^5\text{-C}_5\text{Me}_4\text{H})_2\text{ZrCl}_2$, when reduced under the same conditions, generates the side-on bound bridging dinitrogen complex $[(\eta^5\text{-C}_5\text{Me}_4\text{H})_2\text{Zr}]_2(\mu\text{-}\eta^2\text{:}\eta^2\text{-N}_2)$ (**1.2**).³³ This difference in binding geometry of the N_2 is critical to the resulting reactivity displayed by these complexes.



Scheme 1.1

While the end-on bound complex **1.1** reacts with H_2 and simply eliminates N_2 , generating the dihydrido complex **1.3**,^{31, 32} the side-on bound complex **1.2** adds H_2 to the

bound N_2 ligand, generating bridging hydrazido ligands, as shown in **1.4**.³³ This complex can react further with H_2 to generate NH_3 and the dihydrido complex **1.5**.³³ By changing the ancillary ligand by one methyl group a dramatic change in reactivity is observed,³³⁻³⁶ allowing for the functionalization of dinitrogen, an extremely challenging, and rarely observed reaction.³⁷⁻⁴⁴ While cyclopentadienyl (Cp) derived ligands have been heavily exploited in organometallic chemistry, it is relatively difficult to modify the substitution of these ligands in comparison to other systems.

1.2 Non-Cyclopentadienyl Ligand Systems for Early Transition Metals

While metallocenes offer rich stoichiometric and catalytic chemistry, the difficulties and limitations associated with modifying these ancillary ligands resulted in an explosion of interest in the study of non-metallocene complexes, mainly for the development of new polymerization catalysts.⁴⁵⁻⁴⁹ In particular, early transition metal complexes were heavily studied, and several important classes of ligands were found to act as excellent stabilizing groups for these metals.

Due to the hard, highly electrophilic nature of early transition metals, the most successful ligand designs for these metals incorporate hard donors, such as N and O. One important success in this area was the development of the constrained geometry catalysts (CGC) **1.6**, shown in Fig. 1.1, which incorporate a Cp ligand, and a hard amido ligand that are tethered together.⁵⁰⁻⁵³ This combination effectively stabilizes the highly electrophilic metal center, and ties the ligand back, opening a “reactivity pocket” in which polymerization catalysis can occur.⁵⁰

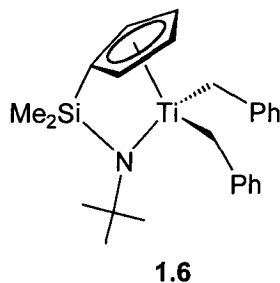


Figure 1.1 Constrained geometry catalyst (CGC)

The success of the CGC ligand spurred the development of a wide variety of amido ligands for early transition metals.^{45, 54} Many permutations of the amido ligand have been developed, including monodentate, bidentate, tridentate, and tetradentate motifs.^{45, 54-56} While it is impossible to introduce this entire area, a few notable examples are shown in Fig. 1.2.

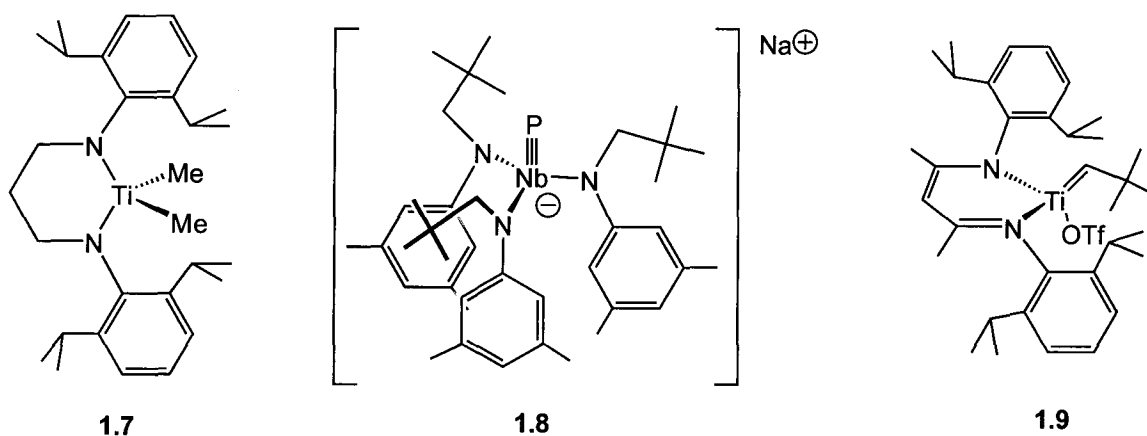


Figure 1.2 Selected early metal complexes with amido ancillary ligands

In 1996, McConville and coworkers discovered the first catalyst capable of living polymerization of α -olefins.^{57, 58} Complex **1.7**, once activated with $B(C_6F_5)_3$, was capable of polymerizing 1-hexene, 1-octene, and 1-decene in a living manner, with polydispersities of nearly 1.00. This new diamide ligand essentially eliminated chain-termination processes, and opened new avenues to access block copolymers with extended aliphatic side groups. The mixed aryl-alkyl amido ligand developed by Cummins and coworkers has allowed access to a plethora of metal-element multiple bonds, including oxo ($M=O$),⁵⁹ nitride ($M\equiv N$),^{43, 60} and phosphide ($M\equiv P$) (**1.8**) complexes,⁶¹ which are accessed through reduction chemistry. The steric protection afforded by these monodentate amido ligands, and their electron rich nature, allows for the stabilization of low-valent, low-coordinate trigonal planar metal species, which are extremely reactive toward normally inert molecules like N_2 and P_4 .^{62, 63} A third important ligand system which has been developed is the bidentate β -diketiminato, or NacNac, ligand architecture. This ligand system has been widely exploited by numerous research groups for a wide variety of applications.^{64, 65} In particular, Mindiola and coworkers have

had great success stabilizing reactive alkylidene ($M=CHR$) (**1.9**),^{66, 67} imido ($M=NR$),⁶⁸⁻⁷⁰ and phosphinidene ($M=PR$)⁶⁶ complexes with NacNac ligands on group 4 and 5 metals.⁷¹

Oxygen-based ligands have also proven to be successful ancillary groups for early transition metals. In particular, aryloxy ligands have been used to great success by Rothwell and coworkers for group 4 organometallic chemistry,⁷²⁻⁷⁷ especially in the synthesis and reactivity of η^2 -iminoacyl complexes like **1.10** (Fig 1.3).⁷⁸⁻⁸¹ Rothwell also first reported that the aryloxy ligand system is capable of facilitating the catalytic hydroamination of alkynes.⁸² Recently, Beller and coworkers have elaborated on this work demonstrating that the substitution at the 2- and 6- positions of the aryl rings in **1.11** dictates the regioselectivity of the hydroamination reaction.^{83, 84} When $R = \textit{tert}$ -butyl, the predominant product formed from the hydroamination of octyne with aryl amines and aliphatic amines is the Markovnikov product.⁸³ However, when $R = \textit{isopropyl}$, the regioselectivity reverses to favor the *anti*-Markovnikov product.⁸⁴

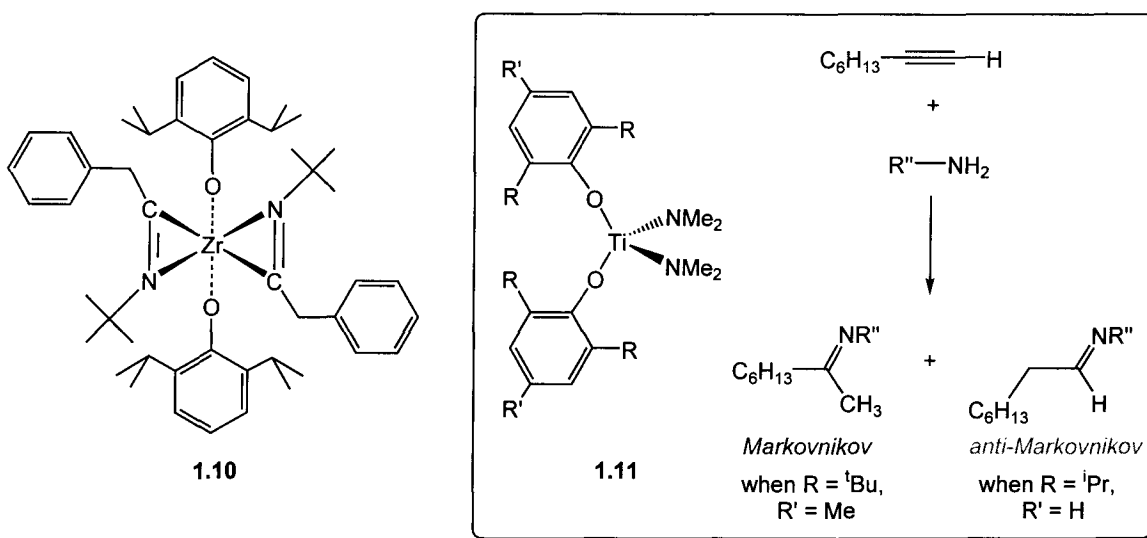


Figure 1.3 Selected aryloxy complexes and hydroamination regioselectivity

Since both nitrogen and oxygen donors proved to be highly effective for the formation of stable, but reactive early transition metal complexes, the combination of these donors would logically generate similarly stable complexes capable of promoting novel reactivity. One particular mixed N,O chelating ligand that has been extremely successful is the phenoxyimine ligand. The most prevalent use of this ligand type has

been in the generation of exceptionally reactive olefin polymerization catalysts.⁸⁵⁻⁸⁷ Coates and coworkers have shown **1.12** (Fig. 1.4) to be a living catalyst for the polymerization of propylene.^{88, 89} A closely related complex **1.13**, was also shown to produce polyethylene in a living manner by Fujita and coworkers at Mitsui.^{90, 91}

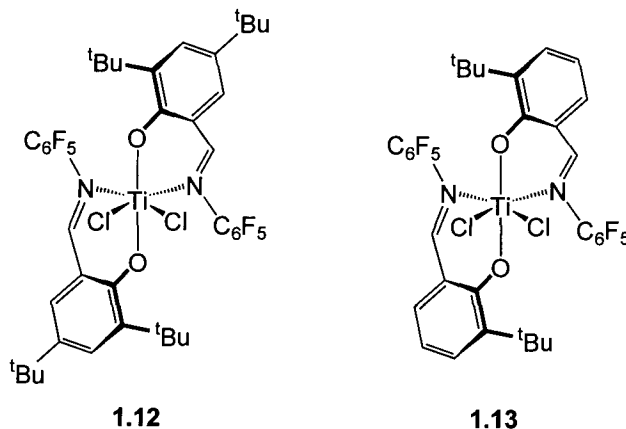


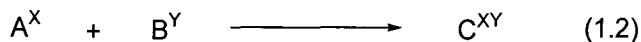
Figure 1.4 Living olefin polymerization phenoxyimine catalysts

While these complexes demonstrate how different ligand systems can promote varied reactivity, and small differences within a class of ligands can lead to divergent reactivity, systematic investigation of structure-activity relationships with metal complexes can only be effectively accomplished with modular ligand systems.

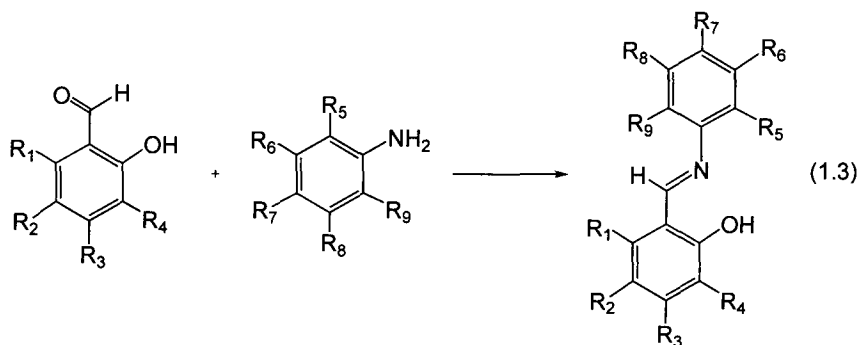
1.3 Modular Ligand Systems

Modular ligands are generated by combining simple modifiable building blocks, where variations in the final ligand are brought about by simply changing the nature of the building blocks in the synthesis. A generic scheme for such a synthesis is illustrated in Eq. 1.2, where A^X is one reagent in the synthesis, with side groups X_1 through X_n , where these substituted groups are either present in the commercially available starting material, or are installed by simple synthetic routes. Likewise, B^Y is a second reagent with similarly variable side groups Y_1 through Y_n . The number of components involved in the synthesis of the proligand can vary, but ideally all reagents should be combined in a single-pot reaction, resulting in an easily isolated and purified proligand C^{XY} . This type

of synthesis readily lends itself to combinatorial methods, where libraries of systematically varied proligands can be generated rapidly for use in the synthesis of catalyst candidates for various reactions.⁹²⁻⁹⁴



The simplest possible modular ligands are alkoxide or aryloxide ligands, where the monoanionic ligands are derived from alcohols (ROH), of which numerous examples are known and commercially available. Similarly, monoanionic amido ligands are very simple modular ligands, derived from primary (NH₂R) or secondary (NHRR') amines, where the amines are typically either commercially available, or are easily synthesized in a few steps. The phenoxyimine ligands shown in Fig. 1.4 are an excellent example of a highly variable modular ligand architecture. Synthesis of the phenolimine proligand is accomplished in a single step, through Schiff base condensation of substituted salicylaldehydes and substituted anilines, as shown in Eq. 1.3.⁹⁵ Combinatorial methods have been applied to this ligand system to generate heteroligated bis(phenoxyimine) catalysts for olefin polymerization, which exhibit high activity, and excellent tacticity selectivity.⁹⁶



Most bidentate ligand systems generate 5- or 6-membered metallacycles upon coordination to the metal center, where the phenoxyimine ligand set is a prime example. Several modular nitrogen-based bidentate ligand systems have been exploited, which form 4-membered metallacycles when coordinated to metal centers, and these show novel reactivity and interesting coordination chemistry.

1.4 Four-Membered Chelate Systems

Amidinate ligands are monoanionic bidentate donors, which are derived from organic amidines. While amidinate ligands have been widely utilized for many metals,^{97, 98} they have been most heavily exploited for groups 4 and 5 metal chemistry.⁹⁷⁻¹⁰³ These modular ligands can be easily varied at the R and R' positions (Fig. 1.5), and the resulting ligand offers substantial steric protection, while also satisfying the metal center's electronic requirements by donating four electrons in a σ -fashion. While an additional lone pair of electrons is available for π -donation to the metal center, these electrons are generally thought to delocalize into the backbone of the amidinate ligand, and are essentially uninvolved in bonding to the metal center.^{97, 104}

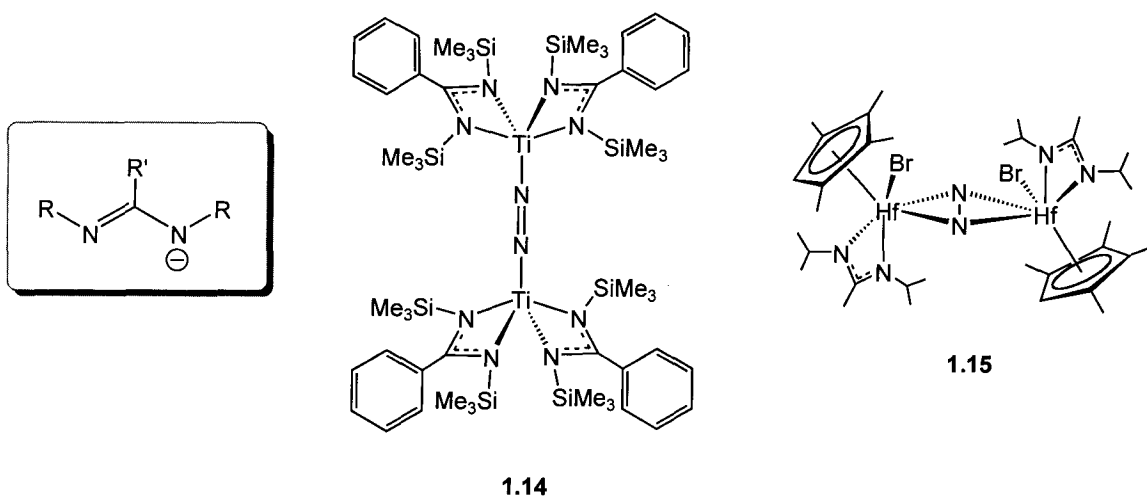


Figure 1.5 Amidinate ligand and selected amidinate complexes

While amidinate complexes have been applied to many types of reactivity, including olefin polymerization,¹⁰⁵⁻¹⁰⁷ one of the most interesting areas of study has been in the activation of N_2 . Bis(amidinate) dichloro complexes were shown by Arnold and coworkers to generate end-on bound μ -dinitrogen complexes upon reduction with Na/Hg amalgam (**1.14**, Fig. 1.5).¹⁰⁸⁻¹¹⁰ Likewise, Sita and coworkers have utilized mixed cyclopentadienyl amidinate complexes for a wide range of reactivity, but have recently found that these species generate dinitrogen complexes, which exhibit side-on N_2 binding (**1.15**), and undergo reaction with H_2 , alkyl halides, and silanes.^{41, 42}

Another well studied ligand motif that generates 4-membered metallacycles when bound to metals are the guanidates, or deprotonated guanidines.¹¹¹ These ligands are closely related to amidates, where guanidates bear an additional amine group in the backbone of the ligand, as illustrated in Fig. 1.6. As with the amidates, these ligands can be modified sterically and electronically at both of the side groups (R), as well as the backbone amine group (R'). The Arnold,^{112, 113} Bergman,^{112, 113} and Richeson¹¹⁴⁻¹¹⁹ groups have invested considerable effort in generating novel group 4 complexes supported by guanidinate ancillary ligands. Dinitrogen complexes supported by guanidinate ligands have been isolated (**1.16**), and are quite stable, due in large part to the electron rich nature of the guanidinate ligands.¹¹² The source of this stability is also featured in Fig 1.6, where resonance structure **B** illustrates how the amine group in the ligand backbone can effectively provide additional electron donation to the metal center.¹¹²

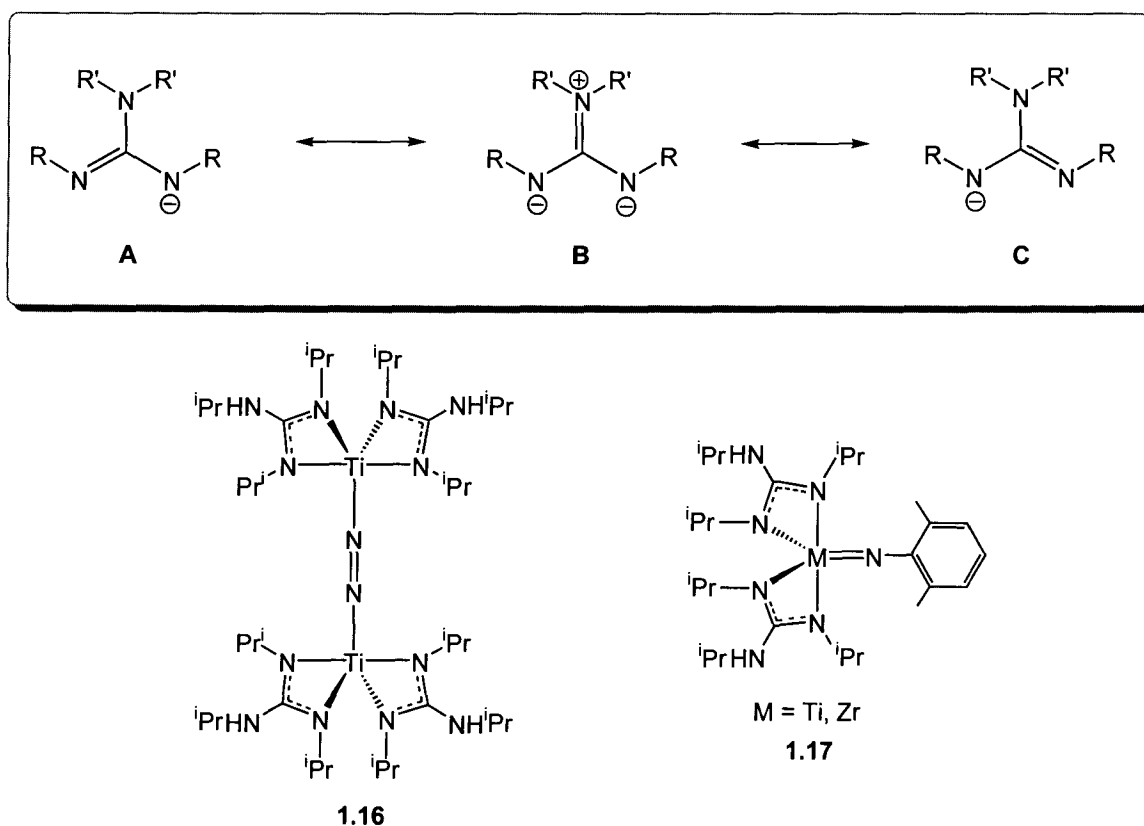


Figure 1.6 Guanidinate resonance structures and selected metal complexes

Novel 5-coordinate imido complexes of group 4 metals have also been characterized with guanidinate ancillary ligands (**1.17**).^{115, 116} These low-coordinate complexes are stabilized by the aforementioned electron rich nature of the guanidinate ligands, as well as the steric protection afforded by the substituents on the two nitrogens coordinated to the metal center. These imido complexes have been isolated for both Ti and Zr,^{115, 116} and the Ti complexes show modest activity towards alkynes in catalytic hydroamination.¹¹⁶ It is also interesting to note that the imido complexes (**1.17**) can be accessed by a novel and rare rearrangement reaction with arylisocyanides,^{115, 120} suggesting that the guanidinate ligands are able to promote unique modes of reactivity. The mechanism for this interesting reaction will be revisited in Chapter 3.

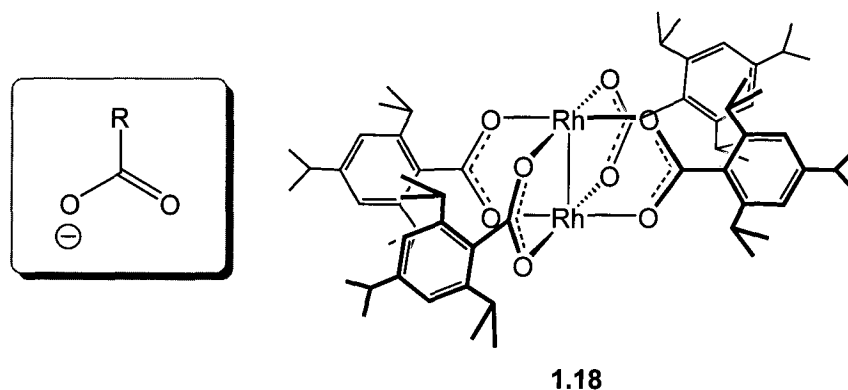


Figure 1.7 Carboxylate ligand framework and bimetallic paddlewheel complex

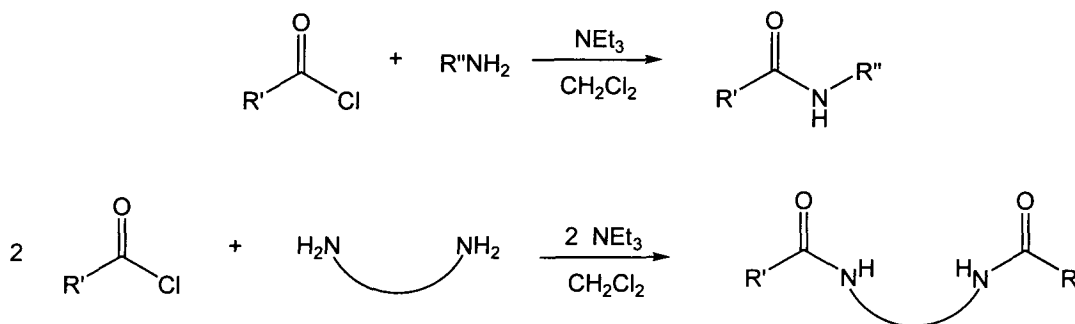
While the carboxylate ligands shown in Fig. 1.7 are inherently less variable than the amidinate and guanidinate ligands, they have nonetheless proven successful as structurally rigid bridging ligands for bimetallic transition metal complexes.¹²¹⁻¹²³ These ligands have been instrumental in the quest to understand metal-metal bonding (**1.18** in Fig. 1.7), and bond orders greater than 3.¹²⁴⁻¹²⁸ Extension of carboxylate based paddlewheel complexes as core units for supramolecular chemistry has also been very fruitful, with supramolecular arrays of various shapes and sizes being successfully isolated.¹²³ The interesting magnetic properties of these materials may prove important in the development of new nanodevices for future applications.¹²³ While carboxylate ligands are excellent bridging ligands, their application to monomeric metal complexes has not been widely explored.

Despite the fact that the structurally related amidinate, guanidinate, and carboxylate ligands have been widely investigated, their mixed N,O chelating congeners, the amidates, have not been extensively studied. Considering the success seen with the mixed N,O chelating phenoxyimine ligands, described in sections 1.2 and 1.3, it was hypothesized that amidate ligands, possessing a similar N,O chelate, would offer unique reactivity. Additionally, the 4-membered chelates generated upon coordination of amidinate and guanidinate ligands to metal centers result in novel structures and reactivity. Thus, the 4-membered chelates formed upon coordination of amidate ligands would likewise be expected to generate interesting coordination complexes, possibly displaying novel and unexpected reactivity.

1.5 Amidate Ligands

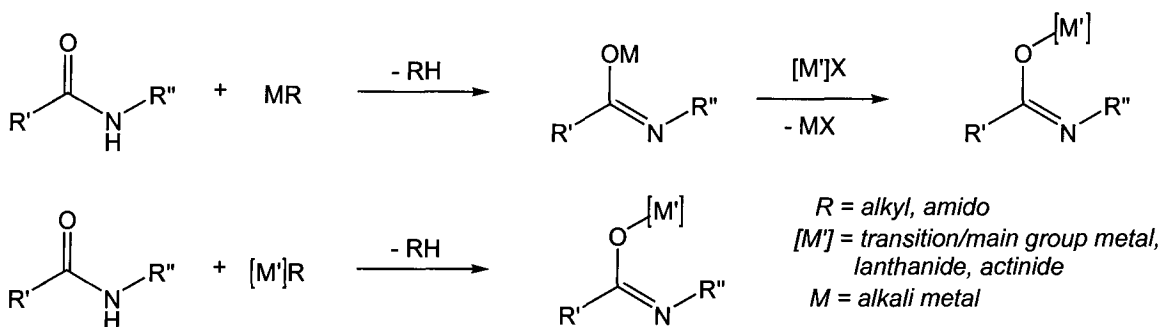
1.5.1 Synthetic Methodology

Amidate ligands are deprotonated organic amides, which in turn can be synthesized in a single step by combination of acyl chlorides with primary amines as illustrated in Scheme 1.2.⁹⁵ By incorporation of a diamine in the synthesis, tethered bis(amide) proligands can also be generated through the same procedure. Due to the wide range of commercially available acyl chlorides and amines/diamines, the amidate ligand system is highly modular. This makes this ligand system ideally suited for the study of structure-activity relationships in catalytic and stoichiometric reactivity of metal complexes bearing these ligands.



Scheme 1.2

These proligands can be complexed to metals through two main routes, illustrated in Scheme 1.3. Addition of an alkali metal base to organic amides results in deprotonation of the amide to generate the alkali salt of the amidate ligand.¹²⁹ Transmetalation can then be performed with a metal halide starting material, resulting in the desired amidate complex.¹²⁹ Conversely, the pK_a of an amide proton is approximately 15, making the amide proton acidic enough to participate in protonolysis reactions with metal amido or alkyl starting materials.⁹⁵ Installation of the amidate ligand is accompanied by the formation of amine or alkane byproducts, which are volatile and easily removed. While the syntheses presented in Scheme 1.3 are the most widely utilized routes into amidate complexes, select amidate complexes have also been generated through the insertion of isocyanates ($RN=C=O$) into the metal-carbon bonds of metal alkyl complexes.¹³⁰⁻¹³²



Scheme 1.3

1.5.2 Binding Motifs

Scheme 1.3 highlights an important feature of the amidate ligand set. There are several distinct modes of coordination that amidate ligands can adopt when bound to metal centers. These binding motifs are summarized in Fig. 1.8. While the metal complexes illustrated in Scheme 1.3 are bound in a monodentate fashion through the oxygen donor (**A**), the amidate ligands can also coordinate through the nitrogen in a monodentate fashion (**B**). Furthermore, it is also possible for both donors to coordinate to metal centers at the same time. This can result in chelation to a single metal in a κ^2 -fashion (**C**), or bimetallic species can be generated, where the amidate ligand acts as a

bridge between two metal centers, with the nitrogen donor coordinated to one metal, and the oxygen donor coordinated to the other metal (**D**).

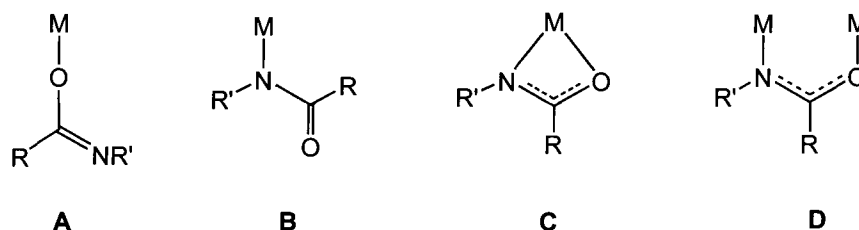


Figure 1.8 Coordination modes of amidate ligands

While numerous amidate complexes have been isolated exhibiting these four coordination modes, in the interest of brevity, select examples will be given here. A recent microreview on amidate complexes has additional references for each of these coordination modes.¹³³ In general, amidate ligands bind in a monodentate fashion (**A** and **B**) to metal centers that are coordinatively saturated, and can not accommodate both donors in the coordination sphere.¹³⁴ The choice of N vs. O donation fits largely with the principles of hard-soft acid-base (HSAB) theory, where soft metals are bound through the N donor, and hard metals are bound through the O donor.¹³⁵ For example, the Pt complexes **1.19**¹³⁶ and **1.20**,¹³⁷ and the Co complex **1.21**¹³⁴ have all been characterized as N-bound amidate species, in keeping with the soft nature of these metals (Fig. 1.9).

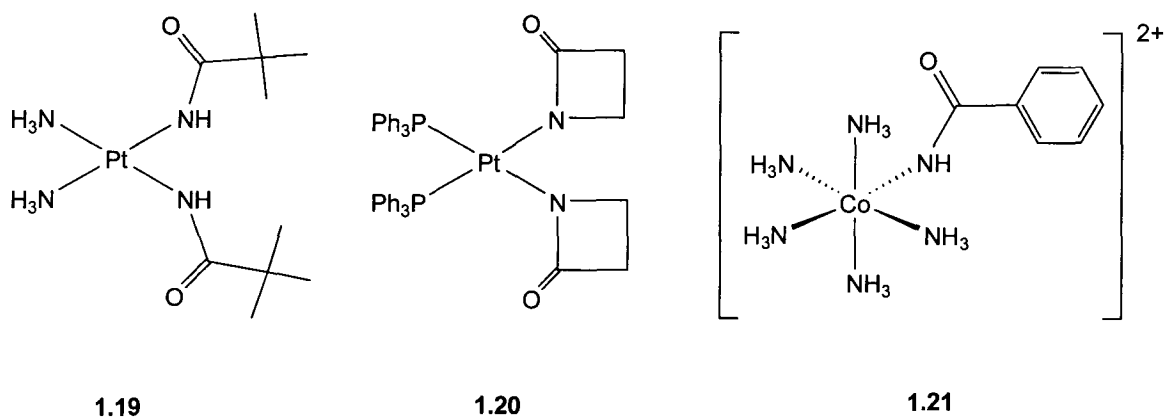


Figure 1.9 N-bound κ^1 -amidate complexes

In contrast, harder metal centers like Ti tend to bind monodentate amidate ligands through the oxygen donor.^{135, 138} One such complex (**1.22**) has been characterized by Stahl and coworkers, where one of the amidate ligands is bound in a κ^1 -fashion to the metal center through the hard oxygen donor.^{135, 138} This complex is illustrated in Fig. 1.10, and also features two bidentate chelating amidate ligands (coordination mode C, Fig. 1.8). While the donation of N vs. O is dictated largely by thermodynamics, the propensity of κ^2 -amidate ligands to bridge between metal centers or chelate to a single metal center is controlled mainly by steric bulk. Steric properties of both the amidate ligand, and the metal center are important, as too much bulk at a small metal center will prevent chelation from occurring. In contrast, too little steric bulk at a larger metal center may promote bridging interactions.

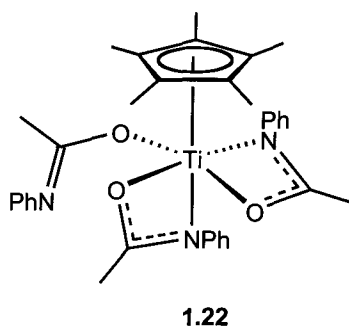


Figure 1.10 Ti complex with κ^1 -O-bound and bidentate κ^2 -amidate ligands

In Fig. 1.11, selected complexes are shown that illustrate how amidate ligands can bridge between metal centers. The aluminum complexes **1.23** and **1.24** indicate that even with relatively bulky substituents on the N donors of the amidate ligands, bridging interactions can still occur.¹³⁹ This can be rationalized by the lack of steric bulk provided by the methyl ligands in **1.23** and **1.24**. In addition to illustrating bridging interactions, **1.23** also demonstrates that the oxygen donor of the amidate ligand can be part of a bidentate chelate, and bridge to a second metal center at the same time. Complex **1.25** is a so-called lantern-type complex,¹⁴⁰ which is structurally related to the paddlewheel complexes described in section 1.4. With this general knowledge in hand, the following section will highlight some areas where amidate ligands have proven useful in both structural studies and reactivity investigations.

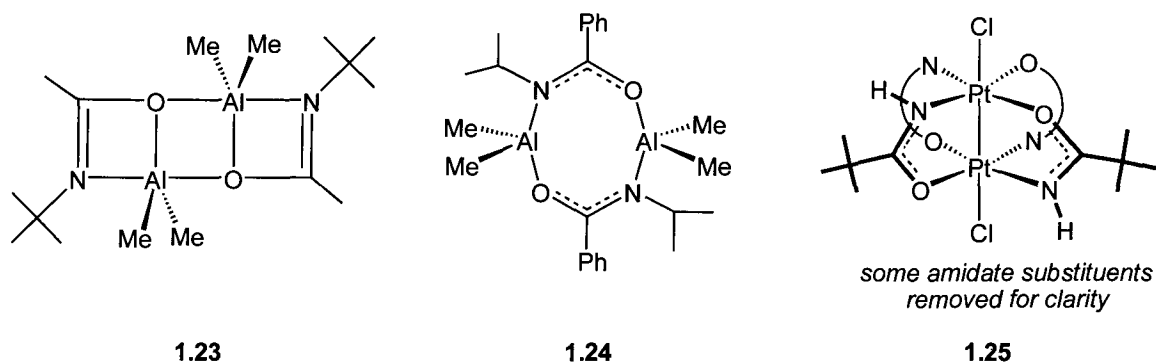


Figure 1.11 Selected bridging bimetallic amidate complexes

1.5.3 Selected Applications of Amidate Ligands

1.5.3.1 Biological Models

Amidate ligands have an important tie to biological chemistry and bioinorganic chemistry, as they are derived from organic amides, which are the building blocks of peptides and proteins. This makes these ligands important models for the study of interactions between transition metals and peptide units in metalloenzymes.¹⁴¹ As such, amidate ligands have been utilized in the investigation of biological models of peptide-metal interactions in bio-inorganic chemistry.¹⁴² While this is a large field, a few select model complexes are given in Fig. 1.12. Vanadium is an essential element,¹⁴³⁻¹⁴⁵ and is known to be a key component of two vanadium-dependent enzymes, the nitrogenases,^{146, 147} and the haloperoxidases.^{148, 149} In biological systems, vanadium is known to exist as the vanadyl unit ($V=O$)²⁺.¹⁴⁵ Model systems, like **1.26**¹⁵⁰ and **1.27**,¹⁵¹ have been developed to study protein-metal interactions to better understand the role of vanadium in metalloenzymes like the nitrogenases^{146, 147} and haloperoxidases.^{148, 149} Another biologically important metal is nickel, which is present in Ni/Fe hydrogenases.^{152, 153} Models have been developed for these species in an effort to determine the redox properties of the hydrogenases.¹⁵² Amidate ligands, like the sulfide terminated bis(amidate) ligand in **1.28**, have proven useful in this area.¹⁵⁴

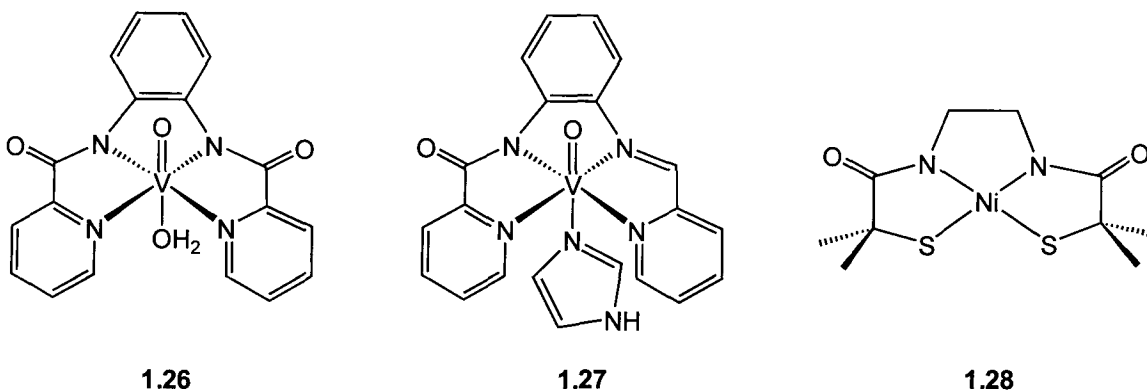


Figure 1.12 Selected amidate complexes for bioinorganic studies

1.5.3.2 Amidates as Structural Units

Bimetallic complexes exhibiting metal-metal bonds are interesting targets for materials applications and supramolecular architectures.¹²³ The dirhodium carboxylate complex (**1.18**), shown in Fig. 1.7, illustrates how carboxylate ligands can effectively act as bridging units for late transition metals.¹²¹ Amidate ligands can also bridge metals in the same fashion, as shown by Cotton and coworkers in Fig. 1.13, where the bis(amidate) ligand links two Mo₂ units, with each Mo₂ unit bridged by one N,O unit of the bis(amidate) ligand.¹⁵⁵ The remaining ligands utilized to generate the paddlewheel structures around each Mo₂ group are formamidinate ligands, substituted with *para*-anisyl groups. It was found that subtle changes to the substituents on the N donors of the bis(amidate) ligand could be used to fine tune the redox potential of the Mo₂ unit.¹⁵⁵ Bridging carboxylate ligands like that found in **1.18** have been utilized to generate a wide range of supramolecular species, having diverse sizes and shapes.¹²³ Bis(amidate) ligands, like the one bridging the Mo₂ units in **1.29**, have the potential to generate similar supramolecular complexes, which may have novel electronic properties vs. the known carboxylate species.

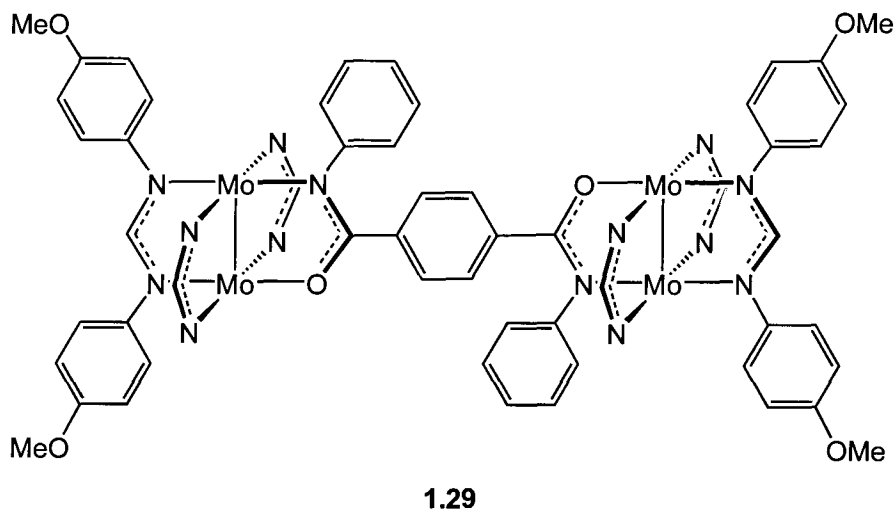


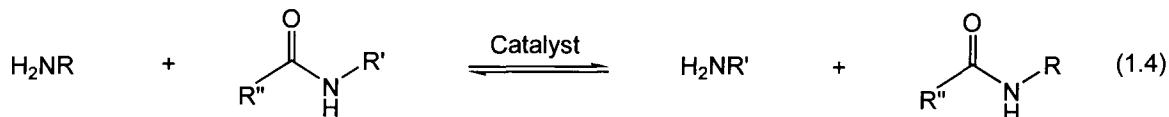
Figure 1.13 Amidate bridged Mo complex with Mo-Mo bonds (some para-anisyl units omitted for clarity)

1.5.3.3 Amidates as Reactive Intermediates

While sections 1.5.3.1 and 1.5.3.2 have illustrated how amidate ligands can be successfully applied in a structural capacity, this section will shed light on some catalytic processes that involve amidate species as intermediates.

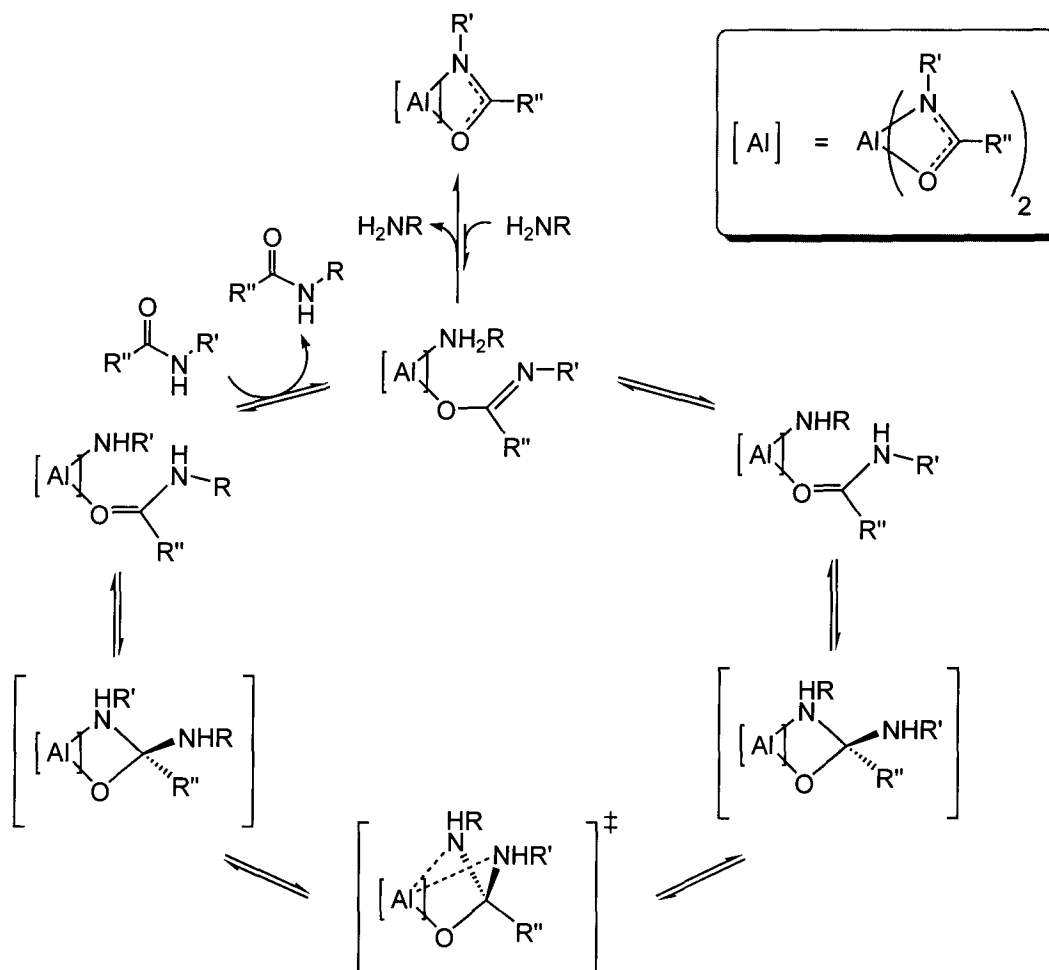
1.5.3.3.1 Intermediates in Transamidation Reactivity

Transamidation is a process which exchanges the nitrogen substituent of an organic amide through reaction of primary amines with amides, as illustrated in Eq. 1.4.¹⁵⁶ Recently, Stahl and coworkers have reported that a variety of metals facilitate this transformation.¹⁵⁶ In particular, Ti^{135, 138} and Al¹⁵⁷ complexes are highly effective for this process when the amide substituents are not very large.¹⁵⁶ Tris(amidate) aluminum complexes are believed to be the resting state for Al catalyzed transamidation.¹⁵⁷

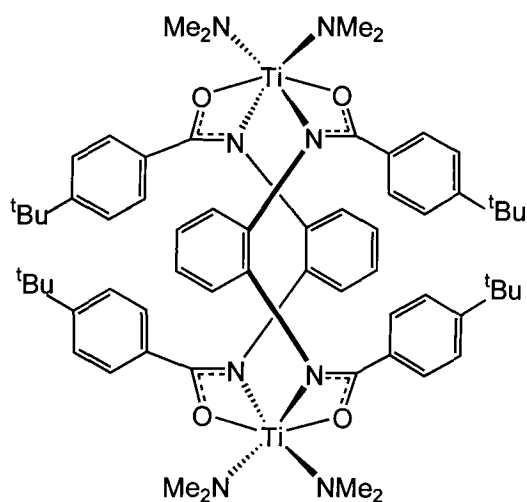


The ability of the amidate ligands to bind in a κ^1 -motif to the metal center allows for coordination of the primary amine, which can then transfer a proton to the κ^1 -amidate ligand, generating a neutral amide, as shown in Scheme 1.4.¹⁵⁷ Subsequent nucleophilic

attack of the amido ligand on the coordinated organic amide generates a tetrahedral intermediate. Exchange of the coordinated nitrogen groups in this intermediate results in a new tetrahedral intermediate, which can collapse to generate an amido complex with a coordinated neutral amide.¹⁵⁷ Exchange of the new organic amide for an incoming one closes the catalytic cycle. A similar mechanism has been proposed for Ti-based catalysts.¹³⁸ Due to the ability of Ti imido complexes to form upon reaction with primary amines, amidine formation has also been observed as a side product for these species.¹³⁸ This results from cycloaddition of organic amides with the imido fragment, generating Ti oxo complexes, and liberating the amidine in the process.



protonolysis methodology presented in Scheme 1.3 allowed for the isolation of a bis(amidate) bis(amido) complex (**1.32**) in modest yield (33 %).¹²⁹ Solid-state molecular structure characterization indicated that **1.32** was dimeric in nature, where the amidate ligands bridged the two Ti centers, as illustrated in Fig 1.14. Clearly, successful implementation of amidate ancillary ligands for group 4 metals is possible, as demonstrated by complexes **1.22** and **1.32**.^{129, 135, 138} However, careful choice of steric bulk in the amidate ligand is critical in the selective formation of mononuclear species. Additionally, bis(amidate) ligands must be designed with careful consideration of the geometric constraints imposed by the tethering unit if mononuclear complexes are to be isolated.



1.32

Figure 1.14 Bis(amidate) bis(amido) Ti complex

1.6 Scope of Thesis

This introduction has shown how ligand design can influence the reactivity of transition metal complexes. In particular, dinitrogen activation, olefin polymerization, and alkyne hydroamination were selected as illustrative examples of how different ligand systems can facilitate various types of useful reactivity. It was also noted that small changes to individual ligand types can lead to large changes in reactivity, making ligand

tuning an important area of investigation. Evolution of new ligand architectures in the post-metallocene era has been fruitful, and many new non-Cp ligands have been developed for early transition metals. Nitrogen and oxygen donors have been especially successful for the group 4 metals, and several examples of these ligands were discussed. Novel structures and reactivity have been observed for group 4 amidinate and guanidinate complexes in which these ligands bind the metals in a bidentate fashion, forming 4-membered chelates. Structurally related amidate ligands, which feature an N,O chelating motif, have not been widely studied in conjunction with group 4 metals, and are the subject of this dissertation.

The fundamental coordination chemistry of amidate ligands is explored in Chapter 2, where homoleptic amidate complexes, tris(amidate) mono(amido), and bis(amidate) bis(amido) complexes of the group 4 metals are studied. Static solid-state molecular structures and dynamic solution phase behavior of these complexes is discussed, with an emphasis on the factors controlling the fluxionality of these species. Theoretical (density functional) studies explore the interconversion between the different possible geometric isomers. Preliminary protonolysis and insertion reactivity with the bis(amidate) bis(amido) complexes is also addressed.

Chapter 3 details the synthesis and reactivity of organometallic complexes supported by amidate ligands. Fluxional processes of these species are described, and the influence of the amidate ligands on the hapticity of benzyl ligands is discussed. Insertion of isocyanides into the Zr-C bonds of the alkyl complexes is explored, and both solid and solution phase behavior of the resulting complexes are evaluated. Products of hydrolysis and alkyl abstraction reactions are also presented.

Catalytic hydroamination is an important area of investigation, and the Schafer research group has made important contributions to this area in recent years. Chapter 4 describes the synthesis, characterization, and behavior of amidate supported imido complexes, which are believed to be key intermediates in catalytic hydroamination. The unique solid-state molecular structures observed for these imido complexes are mirrored by their reactivity, where catalytic cyclohydroamination of alkenes is described for the first time using group 4 imido complexes. This novel reactivity is supported by the unique electronic structure observed for these terminal imido species.

Chapter 5 explores the mechanism of catalytic cyclohydroamination of alkenes through a variety of kinetic studies, and the isolation of intermediates in the catalytic cycle. These studies demonstrate the importance of imido species in the catalytic hydroamination of primary aminoalkenes. The cationic benzyl complexes discussed in Chapter 3 are also examined as precatalysts for cyclohydroamination of secondary aminoalkenes. Control experiments and preliminary kinetic investigations suggest a contrasting mechanism for these complexes, involving σ -bond insertion, rather than cycloaddition of imido species. The overall utility of amidate ligands for group 4 metal chemistry is summarized in Chapter 6, with a brief description of future areas of investigation.

The work presented in this dissertation represents the initiation of a new research program focused on the development of a modular ligand system, and the exploitation of the reactivity of complexes bearing these ligands. The fundamental studies presented herein are meant to guide future studies in the areas of hydroamination catalysis and small molecule activation with amidate complexes.

1.7 References

1. Willey, G. R.; Woodman, T. J.; Fisher, M. *Transition Met. Chem.* **1998**, *23*, 467.
2. Kaiser, V.; Ebinal, S.; Menzel, F.; Stumpp, E., *Z. Anorg. Allg. Chem.* **1997**, *623*, 449.
3. Morozov, I. V.; Fedorova, A. A.; Palamarchuk, D. V.; Troyanov, S. I. *Russ. Chem. Bull.* **2005**, *54*, 93.
4. Tikhomirov, G. A.; Znamenkov, K. O.; Morozov, I. V.; Kemnitz, E.; Troyanov, S. I. *Z. Anorg. Allg. Chem.* **2002**, *628*, 269.
5. Moore, P. *Inorg. React. Mech.* **1981**, *7*, 245.
6. Drew, M. G. B. *Coord. Chem. Rev.* **1977**, *24*, 179.
7. Burgess, J. *Inorg. React. Mech.* **1972**, *2*, 140.
8. Muetterties, E. L.; Wright, C. M. *Quart. Rev., Chem. Soc.* **1967**, *21*, 109.
9. Postgate, J. *Nitrogen fixation*. Cambridge Press: Cambridge, **1998**.
10. Appl, M. *Ammonia*. Wiley-VCH: Weinheim, **1999**.
11. Schlogl, R. *Angew. Chem. Int. Ed.* **2003**, *42*, 2004.
12. Szmigiela, D.; Bielawa, H.; Kurtz, M.; Hinrichsen, O.; Muhler, M.; Rarog, W.; Jodzis, S.; Kowalczyk, Z.; Znak, L.; Zielinski, J. *J. Catal.* **2002**, *205*, 205.
13. Bielawa, H.; Hinrichsen, O.; Birkner, A.; Muhler, M. *Angew. Chem. Int. Ed.* **2001**, *40*, 1061.
14. Natta, G.; Pino, P.; Mazzanti, G.; Giannini, U. *J. Am. Chem. Soc.* **1957**, *79*, 2975.
15. Breslow, D. S.; Newburg, N. R. *J. Am. Chem. Soc.* **1959**, *81*, 81.
16. Breslow, D. S.; Newburg, N. R. *J. Am. Chem. Soc.* **1957**, *79*, 5072.
17. Sinn, H.; Kaminsky, W. *Adv. Organomet. Chem.* **1980**, *18*, 99.
18. Sinn, H.; Kaminsky, W.; Vollmer, H. J.; Woldt, R. *Angew. Chem.* **1980**, *92*, 396.
19. Coates, G. W. *Dalton Trans.* **2002**, 467.
20. Kaminsky, W. *Catal. Today* **2000**, *62*, 23.
21. Kaminsky, W.; Kuelper, K.; Brintzinger, H. H.; Wild, F. R. W. P. *Angew. Chem.* **1985**, *97*, 507.

22. Chien, J. C. W.; Llinas, G. H.; Rausch, M. D.; Lin, G. Y.; Winter, H. H.; Atwood, J. L.; Bott, S. G. *J. Am. Chem. Soc.* **1991**, *113*, 8569.
23. Coates, G. W. *Chem. Rev.* **2000**, *100*, 1223.
24. Spaleck, W.; Aulbach, M.; Bachmann, B.; Kueber, F.; Winter, A. *Macromol. Symp.* **1995**, *89*, 237.
25. Spaleck, W.; Kueber, F.; Winter, A.; Rohrmann, J.; Bachmann, B.; Antberg, M.; Dolle, V.; Paulus, E. F. *Organometallics* **1994**, *13*, 954.
26. Spaleck, W.; Antberg, M.; Rohrmann, J.; Winter, A.; Bachmann, B.; Kiprof, P.; Behm, J.; Herrmann, W. A. *Angew. Chem. Int. Ed.* **1992**, *31*, 1347.
27. Herzog, T. A.; Zubris, D. L.; Bercaw, J. E. *J. Am. Chem. Soc.* **1996**, *118*, 11988.
28. Miyake, S.; Bercaw, J. E. *J. Mol. Catal. A: Chem.* **1998**, *128*, 29.
29. Veghini, D.; Day, M. W.; Bercaw, J. E. *Inorg. Chim. Acta* **1998**, *280*, 226.
30. Veghini, D.; Henling, L. M.; Burkhardt, T. J.; Bercaw, J. E. *J. Am. Chem. Soc.* **1999**, *121*, 564.
31. Manriquez, J. M.; Bercaw, J. E. *J. Am. Chem. Soc.* **1974**, *96*, 6229.
32. Sanner, R. D.; Manriquez, J. M.; Marsh, R. E.; Bercaw, J. E. *J. Am. Chem. Soc.* **1976**, *98*, 8351.
33. Pool, J. A.; Lobkovsky, E.; Chirik, P. J. *Nature* **2004**, *427*, 527.
34. Pool, J. A.; Chirik, P. J. *Can. J. Chem.* **2005**, *83*, 286.
35. Bernskoetter, W. H.; Pool, J. A.; Lobkovsky, E.; Chirik, P. J. *J. Am. Chem. Soc.* **2005**, *127*, 7901.
36. Bernskoetter, W. H.; Olmos, A. V.; Pool, J. A.; Lobkovsky, E.; Chirik, P. J. *J. Am. Chem. Soc.* **2006**, *128*, 10696.
37. Fryzuk, M. D.; Love, J. B.; Rettig, S. J.; Young, V. G. *Science* **1997**, *275*, 1445.
38. Morello, L.; Love, J. B.; Patrick, B. O.; Fryzuk, M. D. *J. Am. Chem. Soc.* **2004**, *126*, 9480.
39. Spencer, L. P.; MacKay, B. A.; Patrick, B. O.; Fryzuk, M. D. *Proc. Natl. Acad. Sci. U. S. A.* **2006**, *103*, 17094.
40. MacKay, B. A.; Munha, R. F.; Fryzuk, M. D. *J. Am. Chem. Soc.* **2006**, *128*, 9472.

41. Hirotsu, M.; Fontaine, P. P.; Epshteyn, A.; Zavalij, P. Y.; Sita, L. R. *J. Am. Chem. Soc.* **2007**, *129*, 9284.
42. Hirotsu, M.; Fontaine, P. P.; Zavalij, P. Y.; Sita, L. R. *J. Am. Chem. Soc.* **2007**, *129*, 12690.
43. Figueroa, J. S.; Piro, N. A.; Clough, C. R.; Cummins, C. C. *J. Am. Chem. Soc.* **2006**, *128*, 940.
44. Kozak, C. M.; Mountford, P. *Angew. Chem. Int. Ed.* **2004**, *43*, 1186.
45. Britovsek, G. J. P.; Gibson, V. C.; Wass, D. F. *Angew. Chem. Int. Ed.* **1999**, *38*, 428.
46. Gibson, V. C.; Spitzmesser, S. K. *Chem. Rev.* **2003**, *103*, 283.
47. Owen, C. T.; Bolton, P. D.; Cowley, A. R.; Mountford, P. *Organometallics* **2007**, *26*, 83.
48. Bolton, P. D.; Mountford, P. *Adv. Synth. Catal.* **2005**, *347*, 355.
49. Adams, N.; Arts, H. J.; Bolton, P. D.; Cowell, D.; Dubberley, S. R.; Friederichs, N.; Grant, C. M.; Kranenburg, M.; Sealey, A. J.; Wang, B.; Wilson, P. J.; Cowley, A. R.; Mountford, P.; Schroeder, M. *Chem. Commun.* **2004**, 434.
50. Chen, Y.-X.; Marks, T. J. *Organometallics* **1997**, *16*, 3649.
51. Shapiro, P. J.; Bunel, E.; Schaefer, W. P.; Bercaw, J. E. *Organometallics* **1990**, *9*, 867.
52. Woo, T. K.; Margl, P. M.; Lohrenz, J. C. W.; Bloechl, P. E.; Ziegler, T. *J. Am. Chem. Soc.* **1996**, *118*, 13021.
53. Chen, Y.-X.; Stern, C. L.; Yang, S.; Marks, T. J. *J. Am. Chem. Soc.* **1996**, *118*, 12451.
54. Kempe, R. *Angew. Chem. Int. Ed.* **2000**, *39*, 468.
55. Curtis, N. F. *Comp. Coord. Chem. II* **2004**, *1*, 447.
56. Guerin, F.; McConville, D. H.; Vittal, J. J.; Yap, G. A. P. *Organometallics* **1998**, *17*, 5172.
57. Scollard, J. D.; McConville, D. H. *J. Am. Chem. Soc.* **1996**, *118*, 10008.
58. Scollard, J. D.; McConville, D. H.; Payne, N. C.; Vittal, J. J. *Macromolecules* **1996**, *29*, 5241.
59. Mendiratta, A.; Figueroa, J. S.; Cummins, C. C. *Chem. Commun.* **2005**, 3403.

60. Clough, C. R.; Greco, J. B.; Figueroa, J. S.; Diaconescu, P. L.; Davis, W. M.; Cummins, C. C. *J. Am. Chem. Soc.* **2004**, *126*, 7742.
61. Figueroa, J. S.; Cummins, C. C. *J. Am. Chem. Soc.* **2004**, *126*, 13916.
62. Laplaza, C. E.; Cummins, C. C. *Science* **1995**, *268*, 861.
63. Piro, N. A.; Figueroa, J. S.; McKellar, J. T.; Cummins, C. C. *Science* **2006**, *313*, 1276.
64. Bourget-Merle, L.; Lappert, M. F.; Severn, J. R. *Chem. Rev.* **2002**, *102*, 3031.
65. Qian, B.; Scanlon, W. J.; Smith, M. R., III; Motry, D. H. *Organometallics* **1999**, *18*, 1693.
66. Basuli, F.; Tomaszewski, J.; Huffman, J. C.; Mindiola, D. J. *J. Am. Chem. Soc.* **2003**, *125*, 10170.
67. Basuli, F.; Bailey, B. C.; Watson, L. A.; Tomaszewski, J.; Huffman, J. C.; Mindiola, D. J. *Organometallics* **2005**, *24*, 1886.
68. Kilgore, U. J.; Basuli, F.; Huffman, J. C.; Mindiola, D. J. *Inorg. Chem.* **2006**, *45*, 487.
69. Basuli, F.; Kilgore, U. J.; Brown, D.; Huffman, J. C.; Mindiola, D. J. *Organometallics* **2004**, *23*, 6166.
70. Bailey, B. C.; Basuli, F.; Huffman, J. C.; Mindiola, D. J. *Organometallics* **2006**, *25*, 2725.
71. Mindiola, D. J. *Acc. Chem. Res.* **2006**, *39*, 813.
72. Rothwell, I. P. *Acc. Chem. Res.* **1988**, *21*, 153.
73. Himes, R. A.; Fanwick, P. E.; Rothwell, I. P. *Chem. Commun.* **2003**, 18.
74. Eade, G. F.; Fanwick, P. E.; Rothwell, I. P. *Dalton Trans.* **2003**, 1061.
75. Lentz, M. R.; Vilardo, J. S.; Lockwood, M. A.; Fanwick, P. E.; Rothwell, I. P. *Organometallics* **2004**, *23*, 329.
76. Phomphrai, K.; Fenwick, A. E.; Sharma, S.; Fanwick, P. E.; Caruthers, J. M.; Delgass, W. N.; Abu-Omar, M. M.; Rothwell, I. P. *Organometallics* **2006**, *25*, 214.
77. Hill, J. E.; Fanwick, P. E.; Rothwell, I. P. *Inorg. Chem.* **1989**, *28*, 3602.
78. Durfee, L. D.; Rothwell, I. P. *Chem. Rev.* **1988**, *88*, 1059.

79. Latesky, S. L.; McMullen, A. K.; Niccolai, G. P.; Rothwell, I. P.; Huffman, J. C. *Organometallics* **1985**, *4*, 902.
80. Thorn, M. G.; Lee, J.; Fanwick, P. E.; Rothwell, I. P. *Dalton Trans.* **2002**, 3398.
81. McMullen, A. K.; Rothwell, I. P.; Huffman, J. C. *J. Am. Chem. Soc.* **1985**, *107*, 1072.
82. Hill, J. E.; Profflet, R. D.; Fanwick, P. E.; Rothwell, I. P. *Angew. Chem. Int. Ed.* **1990**, *29*, 664.
83. Khedkar, V.; Tillack, A.; Beller, M. *Org. Lett.* **2003**, *5*, 4767.
84. Tillack, A.; Jiao, H.; Castro, I. G.; Hartung, C. G.; Beller, M. *Chem.--Eur. J.* **2004**, *10*, 2409.
85. Mitani, M.; Saito, J.; Ishii, S.-I.; Nakayama, Y.; Makio, H.; Matsukawa, N.; Matsui, S.; Mohri, J.-I.; Furuyama, R.; Terao, H.; Bando, H.; Tanaka, H.; Fujita, T. *Chem. Rec.* **2004**, *4*, 137.
86. Lamberti, M.; Mazzeo, M.; Pappalardo, D.; Zambelli, A.; Pellecchia, C. *Macromol. Symp.* **2004**, *213*, 235.
87. Makio, H.; Kashiwa, N.; Fujita, T. *Adv. Synth. Catal.* **2002**, *344*, 477.
88. Tian, J.; Coates, G. W. *Angew. Chem. Int. Ed.* **2000**, *39*, 3626.
89. Tian, J.; Hustad, P. D.; Coates, G. W. *J. Am. Chem. Soc.* **2001**, *123*, 5134.
90. Saito, J.; Mitani, M.; Mohri, J.-I.; Yoshida, Y.; Matsui, S.; Ishii, S.-I.; Kojoh, S.-I.; Kashiwa, N.; Fujita, T. *Angew. Chem. Int. Ed.* **2001**, *40*, 2918.
91. Saito, J.; Mitani, M.; Mohri, J.-I.; Ishii, S.-I.; Yoshida, Y.; Matsugi, T.; Kojoh, S.-I.; Kashiwa, N.; Fujita, T. *Chem. Lett.* **2001**, 576.
92. Dominguez, J. M. *Comb. Chem. Tech.* **2005**, 369.
93. Schunk, S. A.; Busch, O.; Demuth, D. G.; Gerlach, O.; Haas, A.; Klein, J.; Zech, T. *Surf. Nanomol. Catal.* **2006**, 373.
94. Woo, S. I.; Kim, K. W.; Cho, H. Y.; Oh, K. S.; Jeon, M. K.; Tarte, N. H.; Kim, T. S.; Mahmood, A. *QSAR Comb. Sci.* **2005**, *24*, 138.
95. Smith, M. B.; March, J. *March's Advanced Organic Chemistry: Reactions, Mechanisms, and Structure.* 5th ed.; Wiley: Toronto, **2001**.
96. Mason, A. F.; Coates, G. W. *J. Am. Chem. Soc.* **2004**, *126*, 10798.

97. Kissounko, D. A.; Zabalov, M. V.; Brusova, G. P.; Lemenovskii, D. A. *Russ. Chem. Rev.* **2006**, *75*, 351.
98. Stewart, P. J.; Blake, A. J.; Mountford, P. *Organometallics* **1998**, *17*, 3271.
99. Stewart, P. J.; Blake, A. J.; Mountford, P. *J. Organomet. Chem.* **1998**, *564*, 209.
100. Guiducci, A. E.; Boyd, C. L.; Mountford, P. *Organometallics* **2006**, *25*, 1167.
101. Keaton, R. J.; Koterwas, L. A.; Fettingner, J. C.; Sita, L. R. *J. Am. Chem. Soc.* **2002**, *124*, 5932.
102. Stewart, P. J.; Blake, A. J.; Mountford, P. *Inorg. Chem.* **1997**, *36*, 3616.
103. Kissounko, D. A.; Epshteyn, A.; Fettingner, J. C.; Sita, L. R. *Organometallics* **2006**, *25*, 1076.
104. Hagadorn, J. R.; Arnold, J. *Organometallics* **1994**, *13*, 4670.
105. Baugh, L. S.; Sissano, J. A. *J. Polym. Sci., Part A: Polym. Chem.* **2002**, *40*, 1633.
106. Talarico, G.; Budzelaar, P. H. M. *Organometallics* **2000**, *19*, 5691.
107. Littke, A.; Sleiman, N.; Bensimon, C.; Richeson, D. S.; Yap, G. P. A.; Brown, S. *J. Organometallics* **1998**, *17*, 446.
108. Hagadorn, J. R.; Arnold, J. *J. Am. Chem. Soc.* **1996**, *118*, 893.
109. Hagadorn, J. R.; Arnold, J. *Inorg. Chem.* **1997**, *36*, 2928.
110. Hagadorn, J. R.; Arnold, J. *Organometallics* **1998**, *17*, 1355.
111. Bailey, P. J.; Pace, S. *Coord. Chem. Rev.* **2001**, *214*, 91.
112. Mullins, S. M.; Duncan, A. P.; Bergman, R. G.; Arnold, J. *Inorg. Chem.* **2001**, *40*, 6952.
113. Duncan, A. P.; Mullins, S. M.; Arnold, J.; Bergman, R. G. *Organometallics* **2001**, *20*, 1808.
114. Wood, D.; Yap, G. P. A.; Richeson, D. S. *Inorg. Chem.* **1999**, *38*, 5788.
115. Ong, T.-G.; Wood, D.; Yap, G. P. A.; Richeson, D. S. *Organometallics* **2002**, *21*, 1.
116. Ong, T.-G.; Yap, G. P. A.; Richeson, D. S. *Organometallics* **2002**, *21*, 2839.
117. Bazinet, P.; Wood, D.; Yap, G. P. A.; Richeson, D. S. *Inorg. Chem.* **2003**, *42*, 6225.
118. Ong, T.-G.; Yap, G. P. A.; Richeson, D. S. *Chem. Commun.* **2003**, 2612.

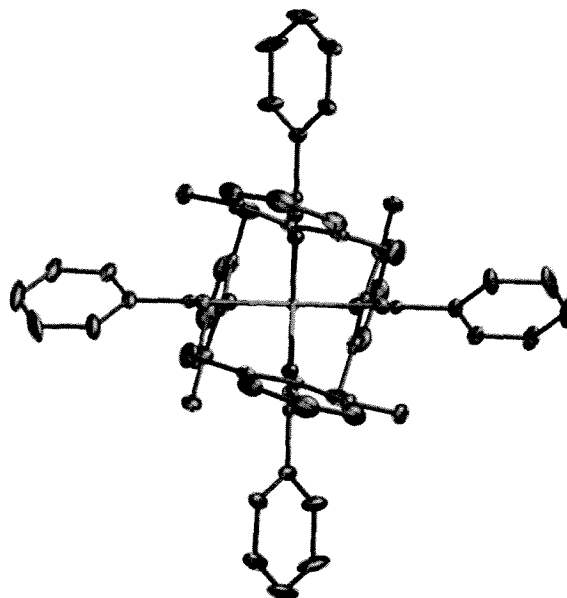
119. Ong, T.-G.; Yap, G. P. A.; Richeson, D. S. *Organometallics* **2003**, *22*, 387.
120. Scott, M. J.; Lippard, S. J. *Organometallics* **1997**, *16*, 5857.
121. Cotton, F. A.; Hillard, E. A.; Murillo, C. A. *J. Am. Chem. Soc.* **2002**, *124*, 5658.
122. Cotton, F. A.; Daniels, L. M.; Lin, C.; Murillo, C. A. *J. Am. Chem. Soc.* **1999**, *121*, 4538.
123. Cotton, F. A.; Lin, C.; Murillo, C. A. *Acc. Chem. Res.* **2001**, *34*, 759.
124. Cotton, F. A. *Multiple Bonds between Metal Atoms*. 3rd ed.; Springer Verlag: New York, **2005**, 35.
125. Cotton, F. A. *Multiple Bonds between Metal Atoms*. 3rd ed.; Springer Verlag: New York, **2005**, 69.
126. Cotton, F. A.; Nocera, D. G. *Acc. Chem. Res.* **2000**, *33*, 483.
127. Cotton, F. A. *Acc. Chem. Res.* **1978**, *11*, 225.
128. Chisholm, M. H.; Cotton, F. A. *Acc. Chem. Res.* **1978**, *11*, 356.
129. Giesbrecht, G. R.; Shafir, A.; Arnold, J. *Inorg. Chem.* **2001**, *40*, 6069.
130. Braunstein, P.; Nobel, D. *Chem. Rev.* **1989**, *89*, 1927.
131. Zhou, X.-G.; Zhang, L.-B.; Zhu, M.; Cai, R.-F.; Weng, L.-H.; Huang, Z.-X.; Wu, Q.-J. *Organometallics* **2001**, *20*, 5700.
132. Gambarotta, S.; Strologo, S.; Floriani, C.; Chiesi-Villa, A.; Guastini, C. *Inorg. Chem.* **1985**, *24*, 654.
133. Lee, A. V.; Schafer, L. L. *Eur. J. Inorg. Chem.* **2007**, 2243.
134. Fairlie, D. P.; Angus, P. M.; Fenn, M. D.; Jackson, W. G. *Inorg. Chem.* **1991**, *30*, 1564.
135. Kissounko, D. A.; Guzei, I. A.; Gellman, S. H.; Stahl, S. S. *Organometallics* **2005**, *24*, 5208.
136. Chen, W.; Matsumoto, K. *Inorg. Chim. Acta* **2003**, *342*, 88.
137. Henderson, W.; Sabat, M. *Polyhedron* **1997**, *16*, 1663.
138. Kissounko, D. A.; Hoerter, J. M.; Guzei, I. A.; Cui, Q.; Gellman, S. H.; Stahl, S. S. *J. Am. Chem. Soc.* **2007**, *129*, 1776.
139. Huang, B.-H.; Yu, T.-L.; Huang, Y.-L.; Ko, B.-T.; Lin, C.-C. *Inorg. Chem.* **2002**, *41*, 2987.

140. Dolmella, A.; Intini, F. P.; Pacifico, C.; Padovano, G.; Natile, G. *Polyhedron* **2002**, *21*, 275.
141. Berreau, L. M. *Eur. J. Inorg. Chem.* **2006**, 273.
142. Mylonas, M.; Krezel, A.; Plakatouras, J. C.; Hadjiliadis, N.; Bal, W. *J. Mol. Liq.* **2005**, *118*, 119.
143. Smith, M. J.; Kim, D.; Horenstein, B.; Nakanishi, K.; Kustin, K. *Acc. Chem. Res.* **1991**, *24*, 117.
144. Taylor, S. W.; Kammerer, B.; Bayer, E. *Chem. Rev.* **1997**, *97*, 333.
145. Rehder, D. *Coord. Chem. Rev.* **1999**, *182*, 297.
146. Harvey, I.; Arber, J. M.; Eady, R. R.; Smith, B. E.; Garner, C. D.; Hasnain, S. S. *Biochem. J.* **1990**, *266*, 929.
147. Chen, J.; Christiansen, J.; Tittsworth, R. C.; Hales, B. J.; George, S. J.; Coucouvanis, D.; Cramer, S. P. *J. Am. Chem. Soc.* **1993**, *115*, 5509.
148. Van Schijndel, J. W.; Barnett, P.; Roelse, J.; Vollenbroek, E. G.; Wever, R. *Eur. J. Biochem.* **1994**, *225*, 151.
149. Macedo-Ribeiro, S.; Hemrika, W.; Renirie, R.; Wever, R.; Messerschmidt, A. *J. Biol. Inorg. Chem.* **1999**, *4*, 209.
150. Vlahos, A. T.; Tolis, E. I.; Raptopoulou, C. P.; Tsohos, A.; Sigalas, M. P.; Terzis, A.; Kabanos, T. A. *Inorg. Chem.* **2000**, *39*, 2977.
151. Tolis, E. J.; Soulti, K. D.; Kabanos, T. A.; Raptopoulou, C. P.; Terzis, A.; Deligiannakis, Y. *Chem. Commun.* **2000**, 601.
152. Cammack, R. *Adv. Inorg. Chem.* **1988**, *32*, 297.
153. Cammack, R.; Fernandez, V. M.; Schneider, K. *The Bioinorganic Chemistry of Nickel*. VCH: New York, **1988**.
154. Kruger, H. J.; Peng, G.; Holm, R. H. *Inorg. Chem.* **1991**, *30*, 734.
155. Cotton, F. A.; Daniels, L. M.; Donahue, J. P.; Liu, C. Y.; Murillo, C. A. *Inorg. Chem.* **2002**, *41*, 1354.
156. Eldred, S. E.; Stone, D. A.; Gellman, S. H.; Stahl, S. S. *J. Am. Chem. Soc.* **2003**, *125*, 3422.
157. Hoerter, J. M.; Otte, K. M.; Gellman, S. H.; Stahl, S. S. *J. Am. Chem. Soc.* **2006**, *128*, 5177.

Chapter 1: Amidates as New Modular Ligands for Group 4 Metals

158. Fujita, K.-I.; Yamashita, M.; Puschmann, F.; Martinez Alvarez-Falcon, M.; Incarvito, C. D.; Hartwig, J. F. *J. Am. Chem. Soc.* **2006**, *128*, 9044.
159. Ikawa, T.; Barder, T. E.; Biscoe, M. R.; Buchwald, S. L. *J. Am. Chem. Soc.* **2007**, *129*, 13001.

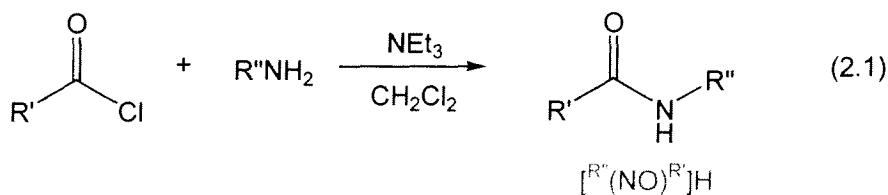
CHAPTER 2



Coordination Chemistry of Group 4 Amidate Complexes

2.1 Introduction

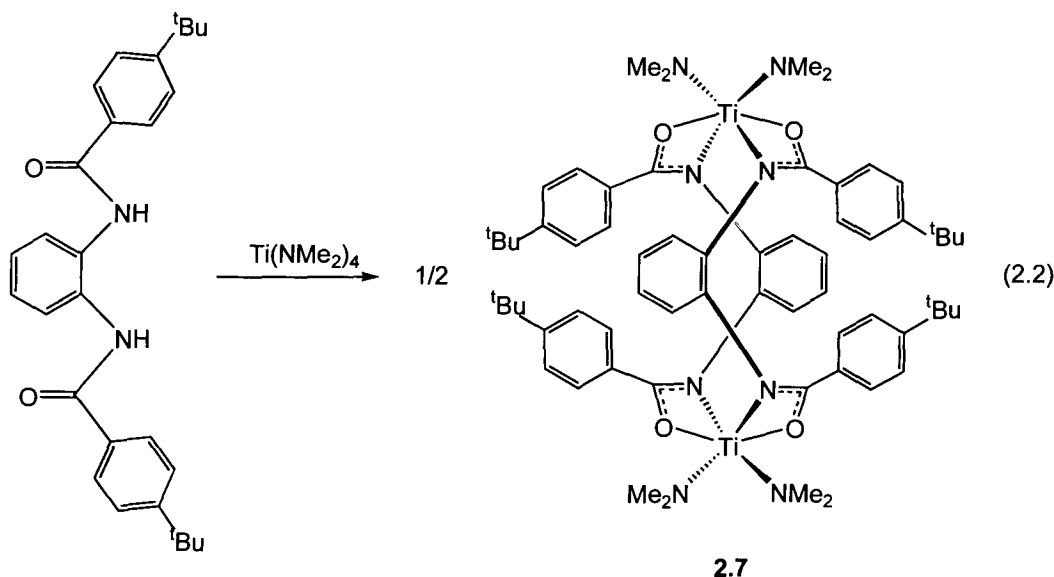
The utility of amidate ligands has been well documented for many transition and main group metals.¹⁻³⁰ Amidates, or deprotonated amides, are an easily accessed ligand motif, which can be derived from the reaction of an acyl chloride and a primary amine. A general synthetic scheme for the synthesis of organic amide proligands is shown in Eq. 2.1, where the R' and R'' groups of the resulting organic amide are easily modified by choosing the appropriate acyl chloride and amine starting materials.



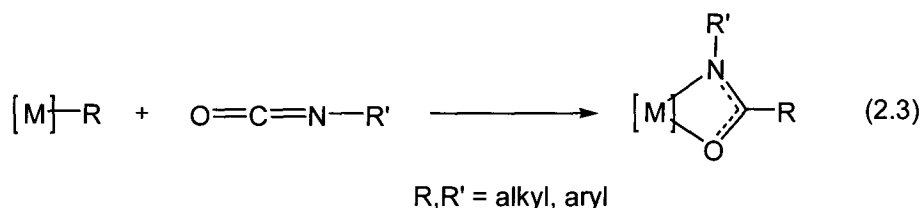
© Reproduced in part with permission from Thomson, R. K.; Zahariev, F. E.; Zhang, Z.; Patrick, B. O.; Wang, Y. A.; Schafer, L. L. *Inorg. Chem.* **2005**, *44*, 8680. Copyright 2005 American Chemical Society.

The key proligands that were utilized for metal chemistry in this project are $[\text{tBu}(\text{NO})^{\text{Ph}}]\text{H}$ (**2.1**), $[\text{DIPP}(\text{NO})^{\text{Ph}}]\text{H}$ (**2.2**), $[\text{DMP}(\text{NO})^{\text{Ph}}]\text{H}$ (**2.3**), $[\text{DMP}(\text{NO})^{\text{tBu}}]\text{H}$ (**2.4**), $[\text{DIPP}(\text{NO})^{\text{tBu}}]\text{H}$ (**2.5**), and $^{\text{Ad}}[\text{O}_2\text{N}_2]\text{H}_2$ (**2.6**). The abbreviated notation used throughout this thesis for these (pro)ligands is shown in Eq. 2.1, where R' denotes the substituent on the nitrogen on the amidate ligand, and R denotes the substituent on the carbonyl of the amidate ligand. In the case of the $[\text{O}_2\text{N}_2]$ tethered bis(amides), the variable R group is in the carbonyl position.

Although extensively utilized with late transition metals as a structural ligand for generation of multinuclear metal complexes, amidate ligands have not been widely studied with group 4 metals.³⁰⁻³⁸ A single report in 2001 detailed the synthesis and characterization of Ti complexes bearing a phenylene bridged bis(amidate) ligand.³⁹ It was found that salt metathesis for this ligand was problematic, and ill-defined metal complexes were formed through this process. A protonolysis methodology was found to yield clean amido metal complexes; however, the species generated were not monometallic in nature, but rather bimetallic with the amidate ligands bridging between the two Ti centers (Eq. 2.2).³⁹ The importance of incorporation of steric bulk into the amidate ligand proximal to the metal center was quite apparent from this early communication.



Amidate ligation can also be observed with some metal complexes upon insertion of isocyanates into metal alkyl bonds.^{40, 41} The general formation of such species is outlined in Eq. 2.3. Although there is precedent for this reaction with group 4 metals as well, metal complexes formed through this reaction do not always have bidentate bound amidate ligands.⁴²



Amidate complexes have also been postulated and observed as reactive intermediates in certain metal-mediated or metal-catalyzed organic transformations.^{28, 43-45} The most important of these processes being catalytic transamidation, where a secondary organic amide R^1CONHR^2 reacts with a primary amine H_2NR^3 resulting in the formation of a new amide R^1CONHR^3 (Eq. 2.4).⁴³



While amidate ligands offer great potential as modular ancillary ligands for transition metals, the fundamental understanding of these ligands and their interactions with metal centers is very limited, particularly for early transition metals. This chapter will address the fundamental coordination chemistry of group 4 metal amidate complexes. In particular, investigations of homoleptic amidate species will be presented, as well as tris(amidate) mono(amido) and bis(amidate) bis(amido) complexes. Solution phase and solid-state molecular structure characterization of these compounds, as well as density functional theory (DFT) calculations, will shed light on exchange processes, amidate hemilability, and geometric isomerization. Exploratory reactivity studies of these complexes will only be introduced, as this will be more fully explored in Chapters 4 and 5.

2.2 Homoleptic Amidate Complexes

2.2.1 Introduction

Amidate ligands bearing both N and O donor atoms are ideally suited to bind hard, high valent early transition metals, such as Ti, Zr, and Hf. While a preliminary report by Arnold and coworkers illustrated that amidate ligands could be installed on Ti, no studies had been performed with the heavier congeners of group 4 (Zr and Hf).³⁹ The potential of amidate ligands to coordinate in three possible forms (N- κ^1 , O- κ^1 , or κ^2), as well as the possibility of geometric isomerism, made the study of fundamental coordination chemistry an important place to start investigations.

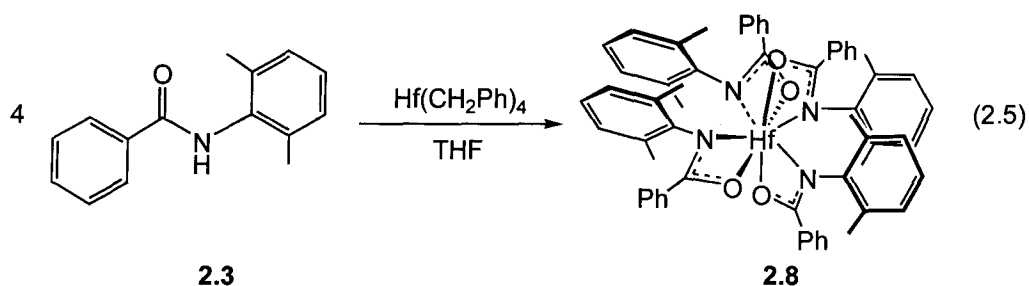
Previous work in the Schafer research group has demonstrated that a maximum of two amidate ligands will coordinate to Ti in a bidentate κ^2 -fashion. Addition of a third equiv of amidate ligand to the small Ti center resulted in complexes that had two κ^2 -amidate ligands, with the third amidate ligand bound in a κ^1 -fashion through the oxygen donor.⁴⁶ Given these results, it was deemed that 8-coordinate homoleptic Ti complexes would not be accessible, and attempts at synthesizing such species were abandoned. The considerably larger Zr and Hf centers are well known to have expanded coordination numbers, allowing for up to 9- and 10-coordinate complexes.⁴⁷⁻⁴⁹ The homoleptic complexes of Zr and Hf were thus targeted for preliminary investigations. In addition to their potential for interesting coordination chemistry, homoleptic amidate complexes of Zr and Hf may have applications as precursors for metal-organic chemical vapor deposition (MOCVD) to generate controlled metal oxide surfaces for materials applications.⁵⁰⁻⁵²

2.2.2 Results and Discussion

It was reported by Arnold and coworkers that salt metathesis of amidate ligands is problematic, resulting in products that are ill-defined and difficult to separate from their salt byproducts.³⁹ By comparison, protonolysis of the amidate ligands with reactive amido starting materials such as Ti(NMe₂)₄ is clean and results in easily isolable amido

complexes. For this reason, protonolysis routes into homoleptic species are preferable to more traditional salt metathesis protocols. Given the fact that the pK_a of the amide proligands is approximately 15, protonolysis of amido and alkyl metal starting materials is extremely facile.⁵³

The homoleptic complex $[\text{DMP}(\text{NO})^{\text{Ph}}]_4\text{Hf}$, **2.8**, is formed through protonolysis of $\text{Hf}(\text{CH}_2\text{Ph})_4$ with four equiv of $[\text{DMP}(\text{NO})^{\text{Ph}}]\text{H}$ (**2.3**) in THF, and is isolated as a white microcrystalline solid in 94 % yield, Eq. 2.5. High symmetry is observed in solution for this complex, as evidenced by a single resonance for the aryl methyl protons at δ 2.51, consistent with all four ligands being equivalent. Electron impact mass spectrometry verifies formation of the homoleptic complex, with a parent ion peak appearing at m/z 1076. While the proposed structure shown in Eq. 2.5 matches the solution phase data, the geometric conformation of the amidate ligands could not be confirmed without solid-state molecular structure evidence.



Colorless single crystals of **2.8** can be grown in moderate yield from concentrated hexanes or pentane solutions, and the solid-state molecular structure for **2.8** was determined by single crystal X-ray diffraction, verifying the hypothesized dodecahedral (DD) structure, as shown in Fig. 2.1. Selected bond lengths and angles are given in Table 2.1, and summarized crystallographic data are located in Table A2.1 in Appendix A. The solid-state molecular structure of **2.8** exhibits pseudo- D_{2d} symmetry, where one of the C_2 axes bisects N1 and N1_1, and also bisects N1_2 and N1_3. This axis also lies at the intersection of the two pseudo-mirror planes within the molecule. The two perpendicular C_2 axes of symmetry lie between the aforementioned mirror planes, bisecting O1 and O1_3, as well as O1 and O1_2. The most notable feature of interest in this complex is the π -stacking interactions that stabilize the N-*cis* conformation, which would otherwise be sterically unfavorable.

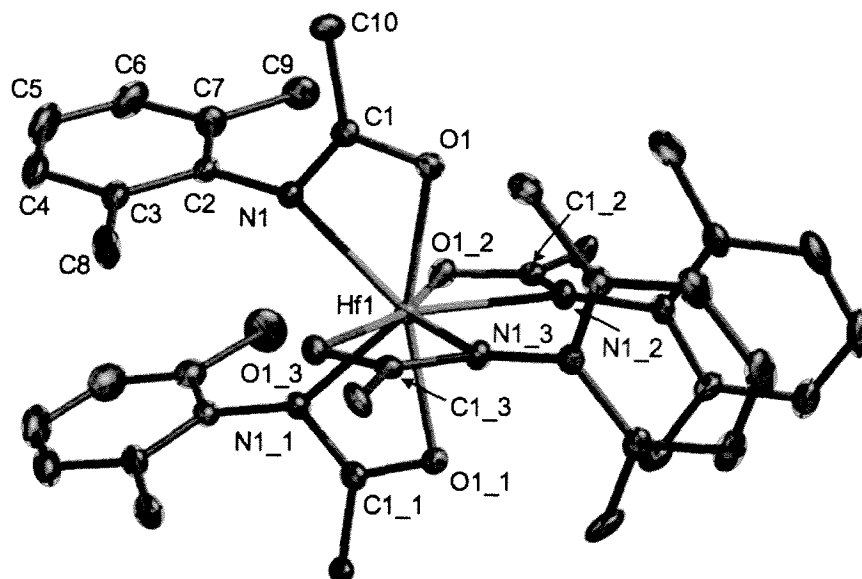


Figure 2.1 ORTEP depiction (ellipsoids at 30% probability) of solid-state molecular structure of $[\text{DMP}(\text{NO})^{\text{Ph}}]_4\text{Hf}$, **2.8** (hydrogens and non-ipso phenyl carbons omitted for clarity)

Table 2.1 Selected Bond Distances (Å) and Angles (°) for $[\text{DMP}(\text{NO})^{\text{Ph}}]_4\text{Hf}$, **2.8**

Lengths		Angles		Angles	
Hf(1)-N(1)	2.325(3)	O(1)-Hf(1)-O(1_1)	159.43(14)	N(1)-Hf(1)-N(1_1)	83.81(18)
Hf(1)-O(1)	2.163(3)	O(1)-Hf(1)-O(1_2)	91.83(3)	N(1_1)-Hf(1)-N(1_3)	123.64(11)
C(1)-O(1)	1.306(5)	O(1)-Hf(1)-O(1_3)	91.83(3)	O(1)-Hf(1)-N(1)	58.39(12)
C(1)-N(1)	1.285(5)	O(1_2)-Hf(1)-O(1_3)	159.43(14)	O(1)-C(1)-N(1)	115.7(4)

The inter-ring distance for the π -stacked groups, as measured from the ring centroids is approximately 4.03 Å, however, the *ipso* carbons are only 3.56 Å apart, falling near the range typically expected for π -stacking (~ 3.6 Å).^{54, 55}

The solid-state molecular structure in Fig. 2.1 appears to be maintained in solution as there is no change in the ^1H NMR spectrum over a wide range of temperatures. Eight-coordinate complexes tend to exist in one of three polyhedral parent shapes: cubic, square antiprismatic, or dodecahedral.⁵⁶ Complex **2.8** is best described as derived from a dodecahedral parent shape. The simplified illustration in Fig 2.2 shows how a dodecahedron can be visualized from **2.8**.

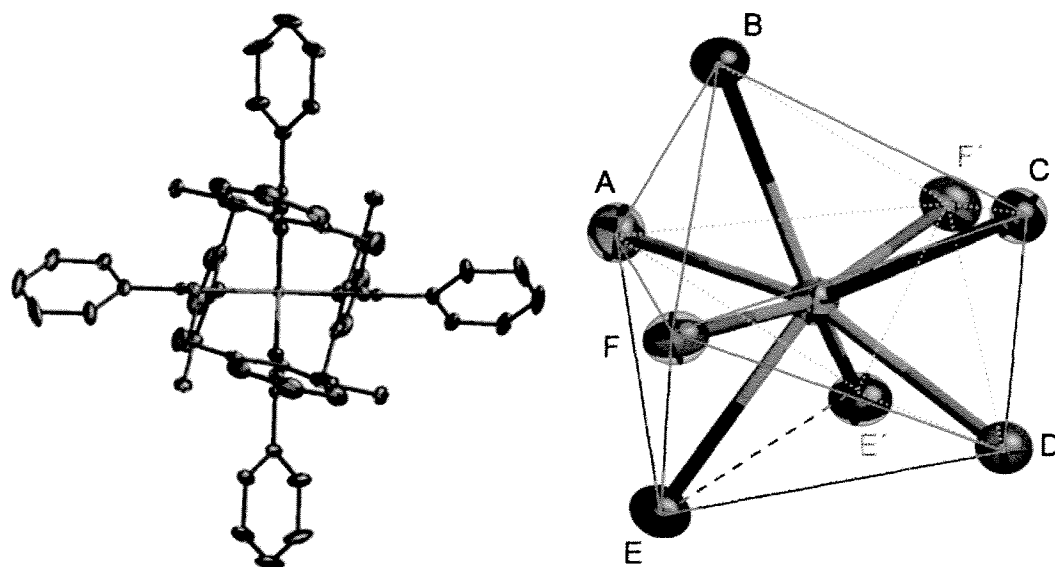


Figure 2.2 View of $[\text{DMP}(\text{NO})\text{Ph}]_4\text{Hf}$ (**2.8**) down C_2 axis of symmetry (left), and view of dodecahedral core structure (right)

Dodecahedra are classically defined as 12 faced Platonic solids.^{57, 58} Whereas a regular dodecahedron is composed of 12 pentagonal faces, the dodecahedron presented in Fig. 2.2 is a truncated dodecahedron with triangular faces.^{57, 58} The overall polyhedron is essentially composed of two pentagonal prisms, which share three of their five edges (AB, BC, and CD).

A related Zr complex can be synthesized following the same method shown in Eq. 2.5, starting with $\text{Zr}(\text{CH}_2\text{Ph})_4$ rather than $\text{Hf}(\text{CH}_2\text{Ph})_4$, and utilizing proligand **2.4** ($[\text{DMP}(\text{NO})^{\text{tBu}}]\text{H}$) rather than proligand **2.3**. While the size difference between Zr and Hf is negligible, the effect of ligand electronics can be explored by varying the backbone group of the amidate ligand from an electron withdrawing phenyl group to an electron donating *tert*-butyl group. The resulting complex, $[\text{DMP}(\text{NO})^{\text{tBu}}]_4\text{Zr}$ (**2.9**), is isolated in high yield (85 %) as a white microcrystalline solid. ^1H NMR spectroscopy of the crude product is extremely simple, with a diagnostic resonance at δ 1.02 for the *tert*-butyl methyl protons and a resonance at δ 2.40 for the aryl methyl protons. This suggests that the symmetry of **2.9** is analogous to **2.8**, and the solid-state molecular structure verifies this as shown in Fig. 2.3. Selected bond lengths and angles are given in Table 2.2, and crystallographic data are located in Table A2.2 in Appendix A.

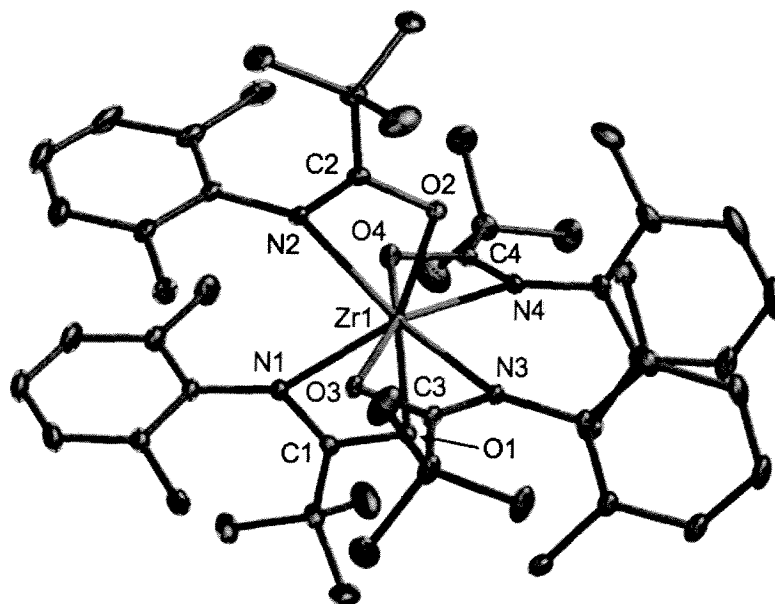


Figure 2.3 ORTEP depiction (ellipsoids at 30% probability) of solid-state molecular structure of $[\text{DMP}(\text{NO})^{\text{tBu}}]_4\text{Zr}$, **2.9** (hydrogens omitted for clarity)

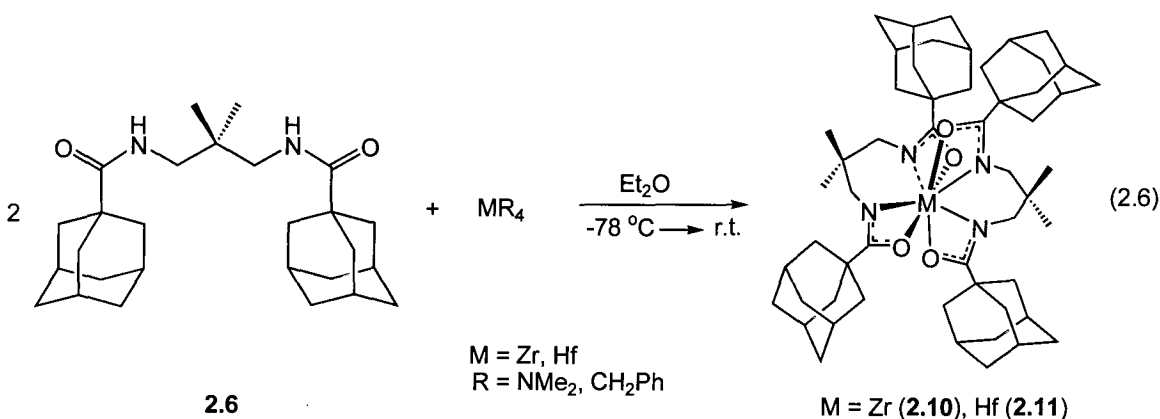
Table 2.2 Selected Bond Distances (Å) and Angles (°) for $[\text{DMP}(\text{NO})^{\text{tBu}}]_4\text{Zr}$, **2.9**

Lengths		Angles		Angles	
Zr(1)-N(1)	2.2911(16)	O(2)-Zr(1)-O(4)	93.13(6)	N(3)-Zr(1)-N(4)	85.83(6)
Zr(1)-N(2)	2.3236(16)	O(2)-Zr(1)-O(1)	159.14(5)	N(1)-Zr(1)-N(2)	85.78(6)
Zr(1)-N(3)	2.2954(16)	O(4)-Zr(1)-O(1)	87.89(6)	N(3)-Zr(1)-N(2)	124.08(6)
Zr(1)-N(4)	2.3203(16)	O(2)-Zr(1)-O(3)	88.01(6)	N(4)-Zr(1)-N(2)	120.19(6)
Zr(1)-O(1)	2.1221(14)	O(4)-Zr(1)-O(3)	159.13(5)	O(1)-Zr(1)-N(1)	57.68(6)
Zr(1)-O(2)	2.1121(14)	O(1)-Zr(1)-O(3)	98.38(6)	O(2)-Zr(1)-N(2)	57.39(5)
Zr(1)-O(3)	2.1251(14)	N(1)-Zr(1)-N(3)	121.55(6)	O(3)-Zr(1)-N(3)	57.62(6)
Zr(1)-O(4)	2.1192(14)	N(1)-Zr(1)-N(4)	124.03(6)	O(4)-Zr(1)-N(4)	57.41(5)

In comparison to **2.8**, the π -stacking interactions in **2.9** are much stronger with centroid distances of 3.61 Å. It is likely that this is due to crystal packing and is not dictated by the actual change in the ligand backbone. However, the additional steric bulk of the distally located *tert*-butyl may force the two π -stacked rings closer together. It is also possible to synthesize **2.9** via protonolysis with the tetrakisamido starting material $\text{Zr}(\text{NMe}_2)_4$ in very similar yield, demonstrating the compatibility of the protonolysis methodology with both alkyl and amido starting materials. While both **2.8** and **2.9** are stable in solution and do not appear to isomerize on the NMR timescale, the possibility

for multiple geometric isomers exists, and the application of a tethered bis(amidate) ligand can be utilized to control which isomer is observed.

The tethered bis(amide) proligand $^{\text{Adf}}[\text{O}_2\text{N}_2]\text{H}_2$, **2.6**, can be synthesized in an analogous manner to the bidentate amide proligands **2.1** – **2.5**, where 1,3-diamino-2,2-dimethylpropane is utilized as the diamine, and is reacted with two equiv of 1-adamantoyl chloride. The addition of two equiv of proligand **2.6** to $\text{Zr}(\text{NMe}_2)_4$ or $\text{Hf}(\text{CH}_2\text{Ph})_4$ results in the formation of the homoleptic species $^{\text{Adf}}[\text{O}_2\text{N}_2]_2\text{M}$ ($\text{M} = \text{Zr}$ (**2.10**) and Hf (**2.11**)). The ^1H NMR spectra of **2.10** and **2.11** are completely analogous to each other, and are consistent with D_{2d} symmetry in solution, similar to **2.8** and **2.9**, as illustrated in Eq. 2.6.



A single resonance is observed at δ 1.28 for the backbone methyls in **2.10**, implying that they are equivalent by static symmetry, or by exchanging through a ‘wagging’ process which occurs more rapidly than the NMR timescale. In addition, single resonances are observed for the adamantyl methylene and methine environments as well as the backbone methylene groups, indicating that the two coordinated ligands are chemically and magnetically equivalent. These complexes are isolated as white microcrystalline solids in high yields (80 % for **2.10** and 81 % for **2.11**) and can be recrystallized as colorless prisms suitable for X-ray crystallographic analysis. The solid-state molecular structure of **2.10** is shown in Fig. 2.4 (core structure shown in Fig. 2.5), with selected bond lengths and angles given in Table 2.3, and crystallographic data summarized in Table A2.3 in Appendix A.

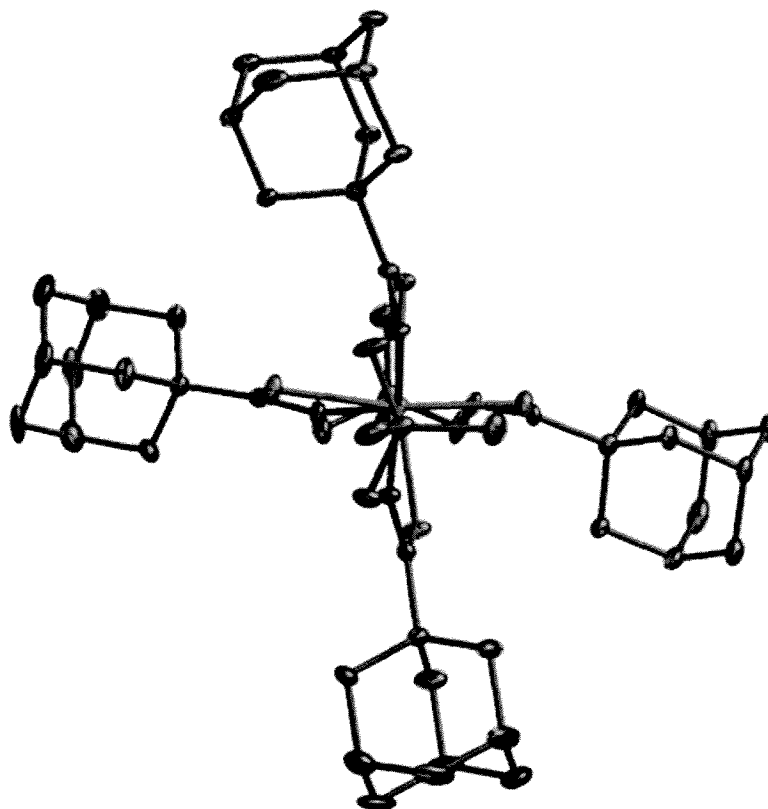


Figure 2.4 ORTEP depiction (ellipsoids at 30% probability) of solid-state molecular structure of $^{\text{Ad}}[\text{O}_2\text{N}_2]_2\text{Zr}$, **2.10** (hydrogens omitted for clarity)

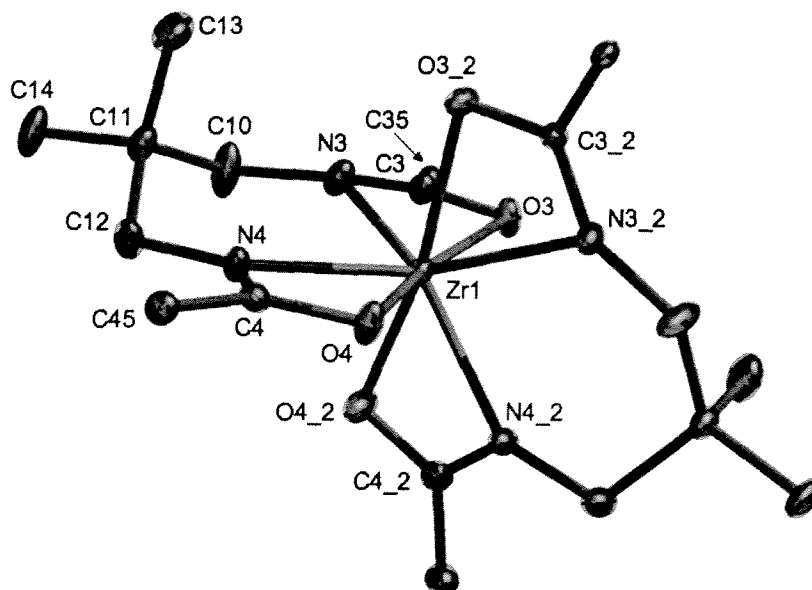


Figure 2.5 ORTEP depiction (ellipsoids at 30% probability) of core structure of $^{\text{Ad}}[\text{O}_2\text{N}_2]_2\text{Zr}$, **2.10** (hydrogens and adamantyl groups omitted for clarity)

Table 2.3 Selected Bond Distances (Å) and Angles (°) for $^{\text{Ad}}[\text{O}_2\text{N}_2]_2\text{Zr}$, **2.10**

	Lengths		Angles		Angles
Zr(1)-O(3)	2.202(4)	O(3)-Zr(1)-O(3_2)	87.3(2)	O(3)-Zr(1)-N(3)	58.09(15)
Zr(1)-N(3)	2.260(4)	N(4)-Zr(1)-N(4_2)	117.2(2)	O(3)-C(3)-N(3)	113.3(4)
Zr(1)-O(4)	2.252(4)	O(3)-Zr(1)-O(4_2)	84.16(15)	O(4)-C(4)-N(4)	113.4(5)
Zr(1)-N(4)	2.240(4)	O(3)-Zr(1)-O(4)	164.14(13)		
C(3)-N(3)	1.300(7)	N(4)-Zr(1)-O(4)	58.17(15)		
C(3)-O(3)	1.293(6)	O(4)-Zr(1)-O(4_2)	107.1(2)		

As Fig. 2.4 illustrates, the tethered bis(amidate) ligand binds in a planar fashion to the Zr center, with the second bis(amidate) ligand adopting the same planar conformation, but at 90° to the first ligand. The complex is octa-coordinate with approximate D_{2d} symmetry, matching the observed solution phase behavior. While the adamantyl groups offer substantial steric bulk, they only protect the Zr center in a planar conformation, where each of the four adamantyl groups in Fig. 2.4 lies approximately in the plane of the page. This arrangement leaves the metal center relatively exposed, and **2.10** still exhibits a high degree of air/moisture sensitivity, decomposing in less than an hour when exposed to air, similar to **2.8** and **2.9**. A simplified core structure is shown in Fig. 2.5, with the adamantyl groups removed for ease of viewing. The amidate ligand backbone binds to the Zr in a planar fashion; however, the tethering unit between the amidate N donors is bent out of the plane to satisfy the geometric constraints of the sp^3 -hybridized three carbon tether. The presence of a single resonance for these methyl groups in the ^1H NMR spectrum verifies the supposition that the tethering unit for the ligand is ‘wagging’ up and down rapidly in solution, making C(13) and C(14) equivalent on the NMR timescale. In general, the bond lengths and angles for **2.10** are unremarkable.

The analogous Hf complex $^{\text{Ad}}[\text{O}_2\text{N}_2]_2\text{Hf}$ (**2.11**) is isostructural with its Zr congener. The simplified solid-state molecular structure of **2.11** as determined by X-ray crystallography is illustrated in Appendix A in Fig. A1, with selected bond lengths and angles located in Table A2.4, and crystallographic data given in Table A2.5. Although isostructural, the Hf complex **2.11** actually has marginally shorter M-N and M-O bonds than the Zr complex **2.10**. This is a trend that has been seen in the literature for Hf complexes, and is due to relativistic effects.⁵⁹

The coordination geometry observed for these homoleptic species is akin to that seen for mixed nitrate acetoacetonato (acac) complexes of Zr and Hf published by Fay and coworkers.^{56, 60, 61} In contrast, the homoleptic acac complexes adopt a square antiprismatic (SAP) geometry.⁶² The six-membered chelate formed by acac is better suited to bridge the longer edges of a SAP than the shorter edges of a dodecahedron (DD). While acetylacetonato ligands have a bite angle of approximately 75-80° owing to their six-membered chelate ring, the amidate ligands have a much tighter bite angle, at approximately 60°.^{61, 63} Thus, the substitution of acac ligands with nitrate ligands, having four-membered chelates, results in a shift in coordination geometry from SAP to DD.^{60, 61} It is therefore logical that the homoleptic amidate complexes, with bite angles closer to that of nitrate than acac ligands, exist in a DD geometry.

2.2.3 Summary

The synthesis of homoleptic amidate complexes of Zr and Hf was accomplished through protonolysis of tetrakis(amido) and tetrabenzyl Zr and Hf starting materials with amide proligands. Due to the smaller size of Ti, and its inability to facilitate coordination numbers greater than six, homoleptic complexes of Ti were not pursued. Both bidentate and tetradentate amidate ligands were utilized successfully, and the resulting complexes were all coordinatively non-fluxional in solution. In the solid-state, these complexes are of pseudo- D_{2d} symmetry, with similar core molecular structures regardless of the amidate ligand utilized. While the tetradentate bis(amidate) ligand enforces the observed coordination geometry through its three carbon bridging unit, the bidentate amidate ligands exhibit unique π -stacking interactions that reinforce the observed *N-cis* dodecahedral geometry. The tight bite angle of the amidate ligands distorts these complexes from the ideal geometry that has been seen with other similar complexes in the literature. While these homoleptic complexes exhibit interesting coordination geometries, and may have potential as MOCVD precursors,⁵⁰⁻⁵² the focus of this project was to utilize amidate ligands to examine metal-element bond reactivities. As such, the synthesis of amido complexes was undertaken to examine the reactivity of M-N bonds, and is discussed in the following section.

2.3 Amidate Amido Complexes

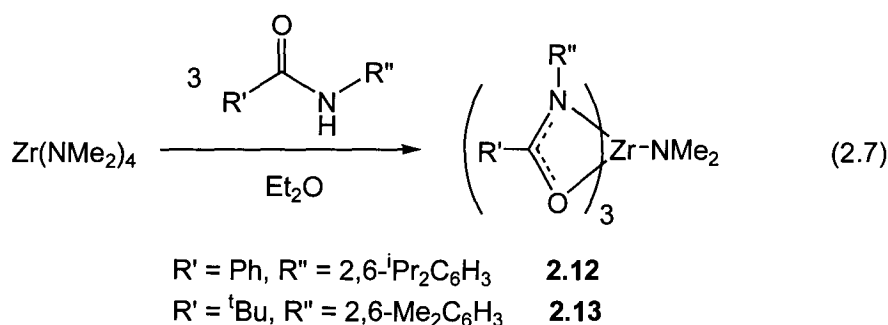
2.3.1 Introduction

Amido complexes of the group 4 metals have been shown to undergo a diverse range of reactivity.⁶⁴ These reactive functionalities have been utilized in catalytic transamidation,⁴⁴ hydroamination catalysis,⁶⁵⁻⁷¹ imine metathesis,⁷² and selected insertion reactivity.^{73, 74} Since the synthesis of 8-coordinate homoleptic amidate complexes resulted in novel coordination complexes exhibiting unique geometries, the 7-coordinate tris(amidate) mono(amido) complexes were targeted. Due to the strong π -donating character of amido ligands, the orbital interactions with the amidate ligands could be dramatically affected by the introduction of an amido unit, and the coordination chemistry for these species was not readily predicted. As was noted in the previous section, the small size of Ti precluded its use in the synthesis of 7-coordinate tris(amidate) mono(amido) complexes. Thus, these studies focused on Zr, where Hf was not investigated in the interest of time, and may be the subject of future work. Previous isolation and characterization of tris(amidate) mono(amido) complexes of Ti in the Schafer lab have shown these complexes to adopt a 6-coordinate pseudo-octahedral ligation motif, with two bidentate amidate ligands, and a third ligand coordinated in a monodentate fashion through the O donor.⁴⁶ While tris(amidate) mono(amido) complexes may offer interesting protonolysis and insertion chemistry, bis(amidate) bis(amido) complexes would offer the possibility of accessing multiply bonded species, where this is possible due to the presence of two reactive ligands at the metal center. Both Ti and Zr species of this type will be discussed, while the Hf congeners will be left as possible future work.

2.3.2 Results and Discussion

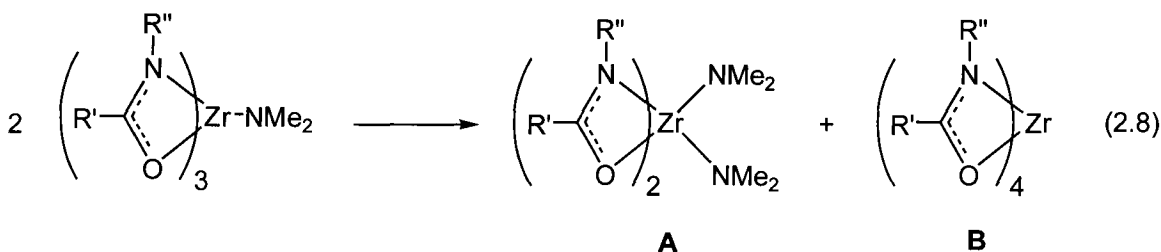
2.3.2.1 Tris(amidate) Mono(amido) Complexes of Zr

Due to the larger size of Zr and the possibility of expanded coordination numbers, the Zr complexes were anticipated to be much different than the previously isolated Ti species. Synthesis of tris(amidate) mono(amido) complexes can be readily achieved by simply combining three equiv of the amide proligand with one equiv of a tetrakis(amido) metal starting material.

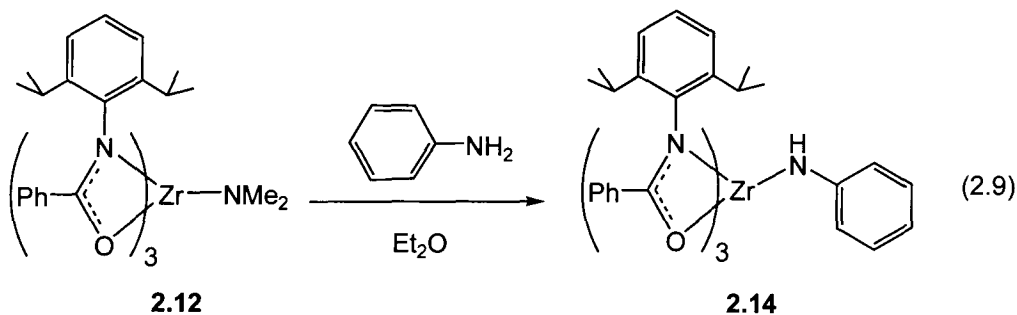


Preparation of $[\text{}^{\text{DIPP}}(\text{NO})^{\text{Ph}}]_3\text{ZrNMe}_2$, **2.12**, and $[\text{}^{\text{DMP}}(\text{NO})^{\text{tBu}}]_3\text{ZrNMe}_2$, **2.13**, is accomplished as shown in Eq. 2.7. The ^1H NMR spectrum of **2.13** is consistent with a C_3 symmetric structure in solution, as would be expected for a complex with three equivalent ligands, or rapidly exchanging amidate ligands. All three amidate ligands in **2.13** are equivalent on the NMR timescale, due to rapid exchange. In contrast, **2.12** exhibits hindered rotation about the N-C_{ipso} bonds. This constraint is manifested by three doublets for the isopropyl methyl groups at δ 0.88, 1.07, and 1.26. These peaks exist in a 18:6:12 ratio, which can be rationalized by free rotation about two of the N-C_{ipso} bonds, which are inequivalent, and hindered rotation about the N-C_{ipso} bond of the third amidate ligand. This results in two isopropyl doublets, one of which overlaps with the signal for one of the other amidate ligands, giving rise to the observed ratio. A single broad septet resonance is observed at δ 3.75 for the isopropyl methine protons, and the expected singlet for the dimethylamido ligand is present at δ 3.29, indicating free rotation of this ligand in solution. In addition to ^1H NMR spectra of **2.12** and **2.13**, mass spectral data and elemental analysis confirm their composition as tris(amidate) mono(amido) species.

In mixed ligand complexes, the possibility of disproportionation always exists. The tris(amidate) mono(amido) complexes **2.12** and **2.13** could undergo ligand exchange to generate the homoleptic complexes and bis(amidate) bis(amido) complexes as illustrated in Eq. 2.8. As demonstrated in section 2.2, homoleptic complexes such as the generic example **B** shown in Eq. 2.8 are readily accessible in high yields. Bis(amidate) bis(amido) complexes (**A**) will be discussed in the following section. Although **2.12** and **2.13** can be isolated readily, allowing the reaction shown in Eq. 2.7 to proceed for extended periods (greater than 24 hours) can result in formation of both products **A** and **B**, where **2.12** is especially prone to this, presumably due to the large degree of steric encumbrance about the Zr with the very bulky 2,6-diisopropylphenyl groups. A possible intermolecular ligand exchange mechanism may involve κ^1 -bound amidate ligands bridging between metal centers prior to ligand transfer. Evidence for this proposal will be discussed at length in the following section.



The reactive amido ligands in **2.12** and **2.13** can undergo protonolysis reactions with acidic groups such as amines. For example, protonolysis of **2.12** with one equiv of aniline results in the formation of a new tris(amidate) mono(amido) complex, where the dimethylamido unit has been replaced with a monoanionic anilido unit, as illustrated in Eq. 2.9. The resulting complex $[\text{DIPP}(\text{NO})^{\text{Ph}}]_3\text{ZrNHPh}$, **2.14**, can be isolated as a yellow microcrystalline solid.



Unlike precursor **2.12**, which exhibits a relatively simple ^1H NMR spectrum, the spectrum of **2.14** is very complicated, where hindered rotation about all three amidate N- C_{ipso} bonds is evident. In particular, 12 distinct doublets are seen between δ -0.08 and 1.81. In addition, 6 septet resonances are observed between δ 2.72 and 4.55, where three of the resonances overlap and are difficult to distinguish, and the remaining three correspond to single methine protons. The aromatic region is necessarily complicated, and does not offer much useful information apart from stoichiometry verification. Single crystals of **2.14** suitable for X-ray diffraction can be isolated from a 1:1 toluene/hexanes mixture, and the solid-state molecular structure is given in Fig. 2.6, with selected bond lengths and angles given in Table 2.4, and crystallographic data summarized in Table A2.6 (Appendix A). The low symmetry of this complex is readily apparent, where **2.14** exists in the solid-state as a 7-coordinate complex, which is best described as a distorted pentagonal bipyramid, in which the axial positions are occupied by the anilido ligand, and the N(2) donor of one of the amidate ligands. The remaining amidate donors (O(2), N(1), O(1), N(3), and O(3)) define the pentagonal plane in **2.14**.

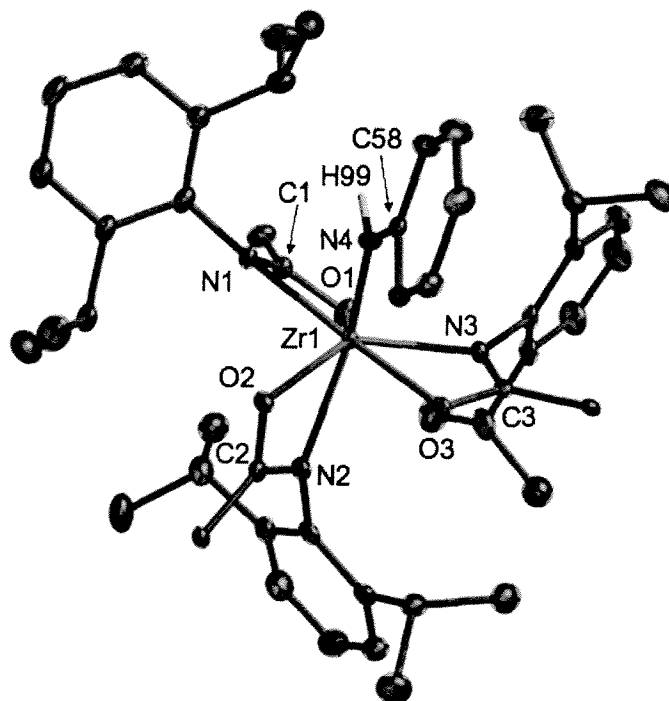


Figure 2.6 ORTEP depiction (ellipsoids at 30% probability) of solid-state molecular structure of $[\text{DIPP}(\text{NO})^{\text{Ph}}]_3\text{ZrNHPPh}$, **2.14** (non-ipso phenyl carbons and hydrogens omitted)

Table 2.4 Selected Bond Distances (Å) and Angles (°) for $[\text{DIPP}(\text{NO})^{\text{Ph}}]_3\text{ZrNHPPh}$, **2.14**

	Lengths		Angles		Angles
Zr(1)-O(1)	2.1411(16)	N(4)-Zr(1)-O(2)	93.63(7)	O(3)-Zr(1)-N(3)	58.43(6)
Zr(1)-O(2)	2.1383(15)	N(4)-Zr(1)-O(1)	117.53(8)	N(4)-Zr(1)-N(2)	151.03(8)
Zr(1)-O(3)	2.1965(15)	O(1)-Zr(1)-O(2)	132.00(6)	O(1)-Zr(1)-N(2)	89.26(7)
Zr(1)-N(1)	2.3586(19)	N(4)-Zr(1)-O(3)	86.24(7)	O(3)-Zr(1)-N(2)	83.07(6)
Zr(1)-N(2)	2.3367(19)	O(2)-Zr(1)-O(3)	82.24(6)	N(3)-Zr(1)-N(2)	99.99(7)
Zr(1)-N(3)	2.2642(19)	O(1)-Zr(1)-O(3)	131.76(6)	N(4)-Zr(1)-N(1)	85.20(8)
Zr(1)-N(4)	2.068(2)	N(4)-Zr(1)-N(3)	97.13(8)	O(2)-Zr(1)-N(1)	92.61(6)
O(2)-C(2)	1.311(3)	O(2)-Zr(1)-N(3)	138.17(6)	O(3)-Zr(1)-N(1)	169.71(6)
N(2)-C(2)	1.309(3)	O(1)-Zr(1)-N(3)	76.45(6)	Zr(1)-N(4)-C(58)	137.66(17)

While the monoamido complexes illustrate the solution fluxionality of the amidate ligands, and the ability of the amido ligands to undergo protonolysis reactions, the bis(amidate) bis(amido) complexes were deemed more desirable targets. Related bis(amidinate)⁷⁵ and bis(guanidinate)⁷⁶⁻⁷⁹ complexes of Ti and Zr have demonstrated unique stoichiometric and catalytic reactivity. Specifically, a bis(guanidinate) imido complex has been shown to facilitate alkyne hydroamination catalysis, a reaction which will be discussed in detail in Chapter 5.⁷⁶ In addition, for many catalytic transformations the availability of two reactive ligand sites is critical to the success of these reactions, and new and exciting reactivity may be gleaned from the study of bis(amidate) complexes.

2.3.2.2 Bis(amidate) Bis(amido) Complexes of Ti and Zr

The combination of two equiv of the amide proligand $[\text{tBu}(\text{NO})^{\text{Ph}}]\text{H}$ (**2.1**) with one equiv of the starting material $\text{Zr}(\text{NEt}_2)_4$ in Et_2O results in clean formation of the desired bis(amidate) bis(amido) complex $[\text{tBu}(\text{NO})^{\text{Ph}}]_2\text{Zr}(\text{NEt}_2)_2$ (**2.15**), as illustrated in Eq. 2.10. To prevent over-speciation by the amidate ligands, these reactions are performed at reduced temperature and allowed to warm to room temperature over a couple of hours prior to workup. Isolation of **2.15** is readily achieved in high yield (80 %) as a pale yellow microcrystalline solid. Typically the crude isolated material is very pure, but can be further purified by recrystallization from a concentrated hexanes solution. This reaction is general and can be applied to a wide range of amidate ligands on both Ti and

Zr. The solid-state molecular structure of **2.15** is shown in Figure 2.7, with selected bond lengths and angles given in Table 2.5 and crystallographic details located in Table A2.7 (Appendix A). The complex is pseudo- C_2 symmetric in the solid-state with the amido ligands *cis* disposed and the N-donors of the amidate ligands *cis* oriented. Although the *tert*-butyl substituents on the amidate ligands are relatively bulky, the tight bite angle of the amidate ligands ($\sim 58^\circ$) pulls these groups away from each other such that this conformation is not sterically unfavorable. The amido ligands in **2.15** can be considered as formal $4 e^-$ donors. The Zr-N bond distances of $2.043(3) \text{ \AA}$ are on the short side expected for Zr-N single bonds,⁸⁰ and N(4) is planar, with the sum of angles about N equal to 360° . The sum of angles about N(3) is approximately 348° , which is likely an artifact of the large degree of disorder present in this diethylamido ligand.

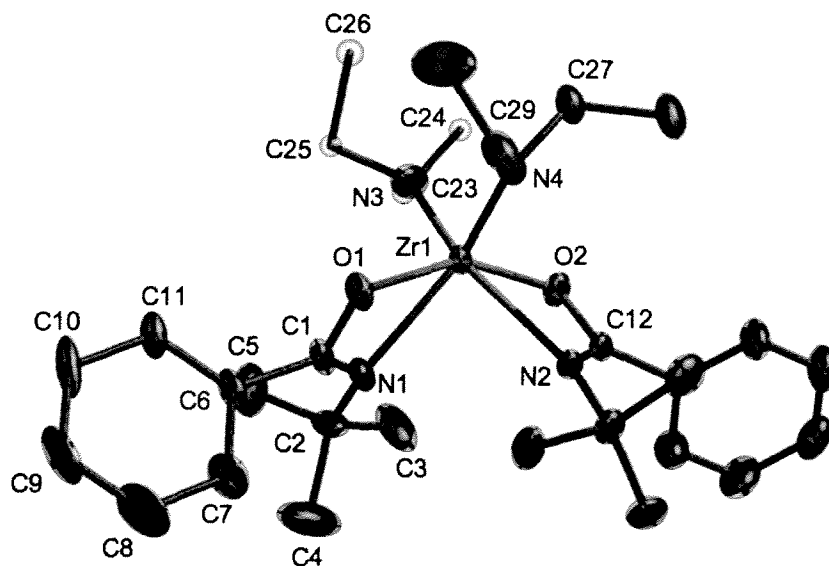
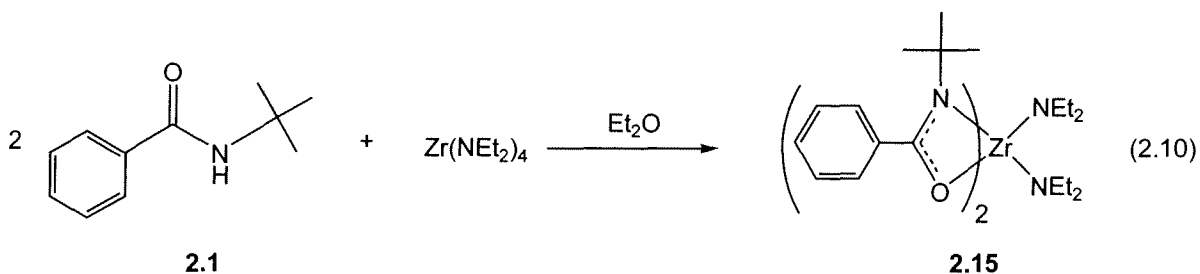


Figure 2.7 ORTEP depiction (ellipsoids at 30% probability) of solid-state molecular structure of $[\text{tBu}(\text{NO})^{\text{Ph}}]_2\text{Zr}(\text{NEt}_2)_2$, **2.15** (hydrogens omitted for clarity)

Table 2.5 Selected Bond Distances (Å) and Angles (°) for $[\text{t}^{\text{Bu}}(\text{NO})^{\text{Ph}}]_2\text{Zr}(\text{NEt}_2)_2$, **2.15**

	Lengths		Angles		Angles
Zr(1)-N(4)	2.043(3)	N(4)-Zr(1)-N(3)	100.93(15)	N(4)-Zr(1)-N(2)	95.15(12)
Zr(1)-N(3)	2.043(3)	N(4)-Zr(1)-O(2)	109.93(11)	N(3)-Zr(1)-N(2)	144.08(16)
Zr(1)-O(2)	2.186(3)	N(3)-Zr(1)-O(2)	86.22(15)	O(2)-Zr(1)-N(2)	58.03(9)
Zr(1)-O(1)	2.187(3)	N(4)-Zr(1)-O(1)	85.55(12)	O(1)-Zr(1)-N(2)	102.61(11)
Zr(1)-N(1)	2.318(3)	N(3)-Zr(1)-O(1)	110.44(15)	N(1)-Zr(1)-N(2)	87.48(11)
Zr(1)-N(2)	2.327(3)	O(2)-Zr(1)-O(1)	155.19(11)	N(1)-C(1)-O(1)	114.8(3)
O(1)-C(1)	1.310(5)	N(4)-Zr(1)-N(1)	142.98(13)	N(2)-C(12)-O(2)	114.4(3)
O(2)-C(12)	1.317(4)	N(3)-Zr(1)-N(1)	98.09(13)	C(29)-N(4)-Zr(1)	133.0(3)
N(1)-C(1)	1.286(5)	O(2)-Zr(1)-N(1)	102.72(12)	C(27)-N(4)-Zr(1)	112.5(3)
N(2)-C(12)	1.292(5)	O(1)-Zr(1)-N(1)	58.01(12)	C(27)-N(4)-C(29)	114.4(3)

In solution, **2.15** retains C_2 symmetry as evidenced by a single resonance in the ^1H NMR spectrum for the *tert*-butyl methyl protons, at δ 1.26, which overlaps with a single triplet resonance for the diethylamido methyl protons. Likewise, a single quartet resonance for the diethylamido methylene protons is observed at δ 3.78.

Synthesis of the Ti analogue of **2.15** is readily accomplished upon combination of 2 equiv of the amide proligand with $\text{Ti}(\text{NEt}_2)_4$ in Et_2O . Protonolysis to generate the product is rapid, and the dark red solution generated indicates successful formation of the bis(amido) complex in 82 % yield. The use of hydrocarbon solvents, such as toluene, results in formation of the desired product; however, mixtures of geometric isomers are often formed, and need to be converted to a single isomeric product via heating. Thus, synthesis of the bis(amidate) bis(amido) complexes is typically performed in ethereal solvents, which promote isomerization of the complex. The ^1H NMR spectrum of $[\text{t}^{\text{Bu}}(\text{NO})^{\text{Ph}}]_2\text{Ti}(\text{NEt}_2)_2$ (**2.16**) is largely analogous to that discussed for **2.15**.

Crystals suitable for X-ray diffraction can be isolated from a toluene/hexanes mixture at room temperature. The solid-state molecular structure is shown in Fig. 2.8, and is completely isostructural to its Zr analogue, exhibiting pseudo- C_2 symmetry in the solid-state. Selected bond lengths and angles are located in Table 2.6, with crystallographic details listed in Appendix A in Table A2.8. Again, the amido ligands are planar indicating sp^2 -hybridization at the N atoms, with significant lone pair donation to the Ti center. Interestingly, both **2.15** and **2.16** display unsymmetrical bonding of the

amidate ligands to the metal center. Clearly, the backbone of the amidate ligand is not fully delocalized with the larger contributor being the alkoxy-imine tautomer shown in Fig. 2.9, as illustrated by the longer C-O bonds and shorter C=N bonds (C(1)-O(1) = 1.310(5) Å vs. C(1)-N(1) = 1.286(5) Å in **2.15**, and C(1)-O(1) = 1.329(8) Å vs. C(1)-N(1) = 1.283(8) Å in **2.16**). The M-N and M-O bond lengths in **2.15** and **2.16** reflect this, with shorter Zr-O bond lengths (Zr(1)-O(1) = 2.187(3) Å) versus the Zr-N amidate bond lengths (Zr(1)-N(1) = 2.318(3) Å) in **2.15**, and shorter Ti-O bond lengths (Ti(1)-O(1) = 2.035(4) Å) versus the Ti-N amidate bond lengths (Ti(1)-N(1) = 2.234(5) Å) in **2.16**.

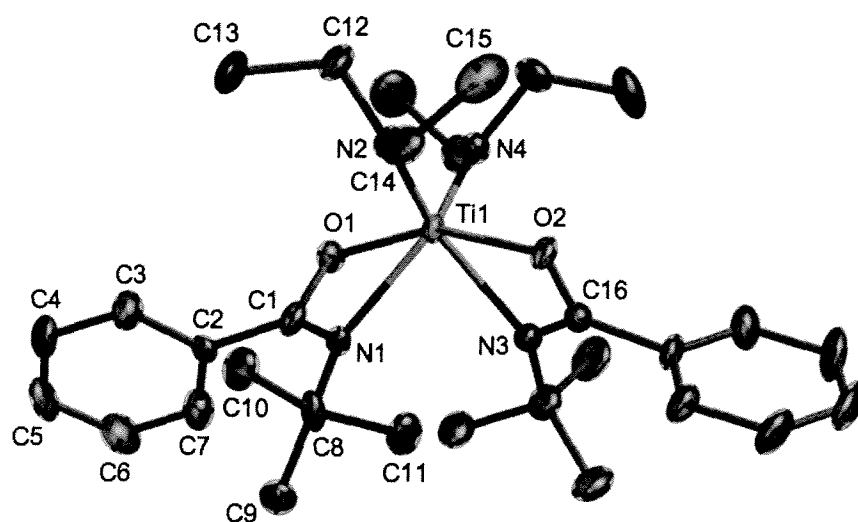


Figure 2.8 ORTEP depiction (ellipsoids at 30% probability) of solid-state molecular structure of $[\text{tBu}(\text{NO})^{\text{Ph}}]_2\text{Ti}(\text{NEt}_2)_2$, **2.16** (hydrogens omitted for clarity)

Table 2.6 Selected Bond Distances (Å) and Angles (°) for $[\text{tBu}(\text{NO})^{\text{Ph}}]_2\text{Ti}(\text{NEt}_2)_2$, **2.16**

Lengths		Angles		Angles	
Ti(1)-N(1)	2.234(5)	N(4)-Ti(1)-N(2)	98.6(3)	N(4)-Ti(1)-N(3)	95.0(2)
Ti(1)-N(2)	1.907(6)	N(4)-Ti(1)-O(2)	104.9(2)	N(2)-Ti(1)-N(3)	150.4(2)
Ti(1)-N(3)	2.254(5)	N(2)-Ti(1)-O(2)	89.6(2)	O(2)-Ti(1)-N(3)	61.43(19)
Ti(1)-N(4)	1.892(6)	N(4)-Ti(1)-O(1)	89.0(2)	O(1)-Ti(1)-N(3)	100.52(19)
Ti(1)-O(1)	2.035(4)	N(2)-Ti(1)-O(1)	105.9(2)	N(1)-Ti(1)-N(3)	85.5(2)
Ti(1)-O(2)	2.027(4)	O(2)-Ti(1)-O(1)	157.59(19)	N(1)-C(1)-O(1)	113.9(6)
O(1)-C(1)	1.329(8)	N(4)-Ti(1)-N(1)	149.9(2)	N(3)-C(16)-O(2)	114.3(6)
O(2)-C(16)	1.327(8)	N(2)-Ti(1)-N(1)	95.4(2)	C(12)-N(2)-Ti(1)	122.3(5)
N(1)-C(1)	1.283(8)	O(2)-Ti(1)-N(1)	101.68(19)	C(14)-N(2)-Ti(1)	124.1(5)
N(3)-C(16)	1.286(8)	O(1)-Ti(1)-N(1)	61.50(19)	C(12)-N(2)-C(14)	113.5(6)

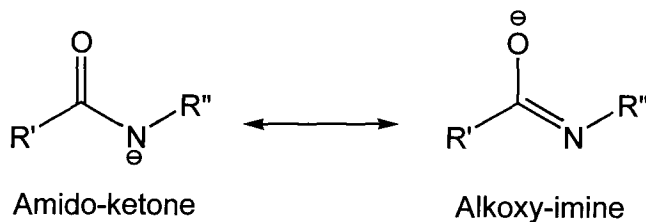


Figure 2.9 Tautomers of amidate ligand

While the diethylamido groups result in clean crystalline material for complexes **2.15** and **2.16**, in general, the presence of these ligands results in greasy isolated materials, which are highly soluble and difficult to recrystallize. The starting material $\text{Ti}(\text{NMe}_2)_4$ can be utilized in analogous protonolysis reactions to isolate more crystalline materials. The resulting dimethylamido complexes are less soluble in hydrocarbon solvents, and recrystallized material is more easily accessed for these complexes. As seen for **2.15** and **2.16**, isolation of $[\text{tBu}(\text{NO})^{\text{Ph}}]_2\text{Ti}(\text{NMe}_2)_2$ (**2.17**) can be achieved in yields as high as 75 %. The solid-state molecular structure of the dimethylamido analogue of **2.16** ($[\text{tBu}(\text{NO})^{\text{Ph}}]_2\text{Ti}(\text{NMe}_2)_2$, **2.17**) was determined by X-ray crystallography and is given in Appendix A in Fig. A2. This complex is isostructural with **2.16**, and relevant bond lengths and angles are given in Table A2.9, and crystallographic data are located in Table A2.10 (Appendix A). It is obvious that the smaller methyl groups on the amido ligands lead to no appreciable difference in coordination geometry of **2.17** vs. **2.16**. In addition to more favorable solubility characteristics, the NMR spectroscopic properties of the resulting material are simplified, with a single resonance for the *tert*-butyl protons at δ 1.28 and a single resonance at δ 3.62 for the amido methyl protons. For the aforementioned reasons, most of the remaining amido chemistry was performed using dimethylamido Ti and Zr starting materials.

The effect of an aryl substituent on the amidate N can also be probed for comparison with the alkyl substituted complexes discussed previously. Utilizing the proligand $[\text{DMP}(\text{NO})^{\text{tBu}}]\text{H}$ (**2.4**), the same protonolysis reaction is performed with $\text{Zr}(\text{NMe}_2)_4$ rather than $\text{Zr}(\text{NEt}_2)_4$, with an isolated yield of 75 %. The dimethylamido starting material has the added advantage of being a solid rather than a liquid, which allows for simple combination of the two solids in a single reaction flask, rather than

cannula transfer of a solution of one reactant into the other. The solid-state molecular structure of $[\text{DMP}(\text{NO})^{\text{tBu}}]_2\text{Zr}(\text{NMe}_2)_2$ (**2.18**) was determined by X-ray crystallography and is C_1 symmetric, where the two amidate ligands are bound in a *trans* N,O configuration rather than the *trans* O,O configuration observed previously for complexes bearing ligand **2.1** ($[\text{tBu}(\text{NO})^{\text{Ph}}]$). Figure 2.10 illustrates the solid-state molecular structure of **2.18**, with selected bond lengths and angles located in Table 2.7, and crystallographic details found in Table A2.11 (Appendix A).

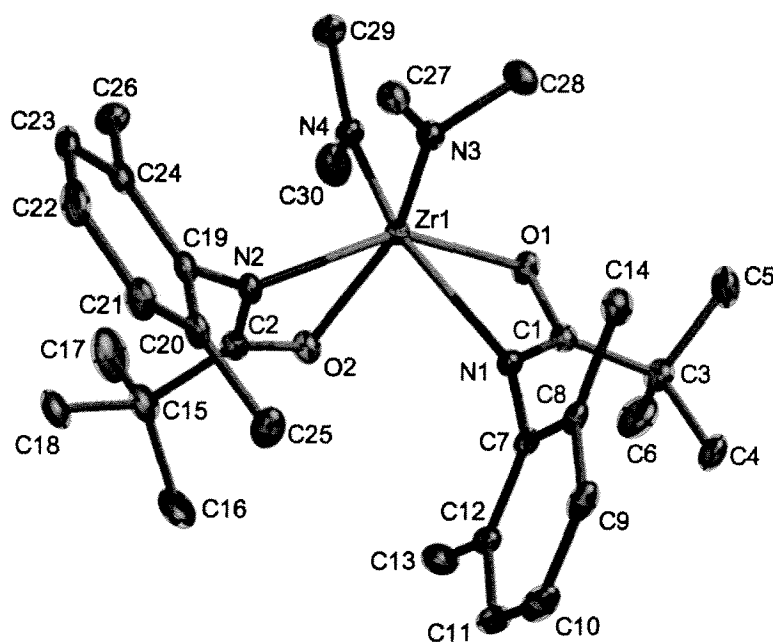
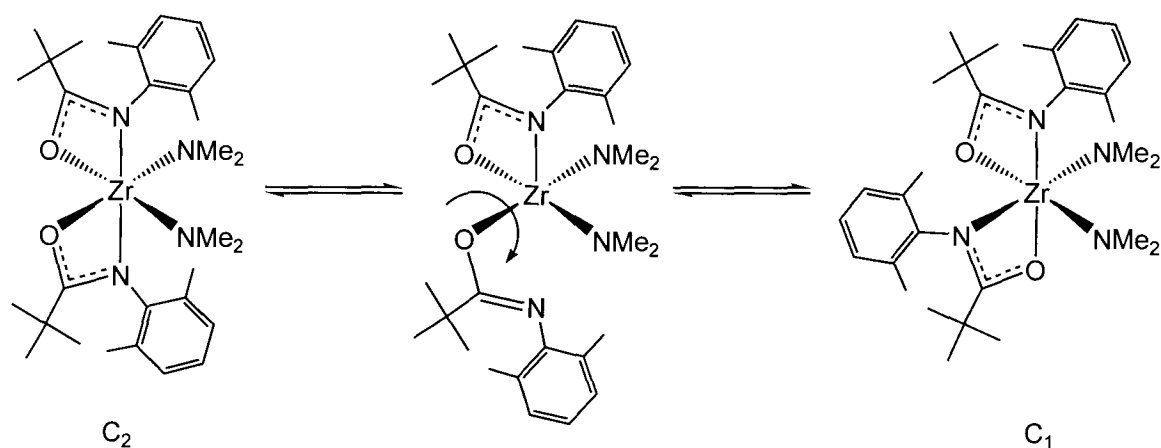


Figure 2.10 ORTEP depiction (ellipsoids at 30% probability) of solid-state molecular structure of $[\text{DMP}(\text{NO})^{\text{tBu}}]_2\text{Zr}(\text{NMe}_2)_2$, **2.18** (hydrogens omitted)

Table 2.7 Selected Bond Distances (Å) and Angles (°) for $[\text{DMP}(\text{NO})^{\text{tBu}}]_2\text{Zr}(\text{NMe}_2)_2$, **2.18**

Lengths		Angles		Angles	
Zr(1)-N(3)	2.038(3)	N(3)-Zr(1)-N(4)	98.36(10)	N(3)-Zr(1)-N(1)	95.62(9)
Zr(1)-N(4)	2.044(2)	N(3)-Zr(1)-O(1)	110.73(9)	N(4)-Zr(1)-N(1)	152.61(9)
Zr(1)-O(1)	2.1524(19)	N(4)-Zr(1)-O(1)	95.66(8)	O(1)-Zr(1)-N(1)	57.25(8)
Zr(1)-O(2)	2.201(2)	N(3)-Zr(1)-O(2)	149.81(9)	O(2)-Zr(1)-N(1)	87.12(9)
Zr(1)-N(2)	2.3055(19)	N(4)-Zr(1)-O(2)	92.40(9)	N(2)-Zr(1)-N(1)	99.76(9)
Zr(1)-N(1)	2.403(2)	O(1)-Zr(1)-O(2)	96.04(8)	N(1)-C(1)-O(1)	113.8(3)
N(2)-C(2)	1.301(4)	N(3)-Zr(1)-N(2)	92.48(10)	N(2)-C(2)-O(2)	113.5(2)
O(2)-C(2)	1.295(3)	N(4)-Zr(1)-N(2)	103.03(9)	C(28)-N(3)-Zr(1)	107.15(18)
O(1)-C(1)	1.325(3)	O(1)-Zr(1)-N(2)	147.72(10)	C(27)-N(3)-Zr(1)	142.5(2)
N(1)-C(1)	1.294(3)	O(2)-Zr(1)-N(2)	57.53(8)	C(27)-N(3)-C(28)	110.3(2)

While the solid-state molecular structure of **2.18** exhibits C_1 symmetry, the solution phase behavior is consistent with a C_2 symmetric structure. The ^1H NMR spectrum of **2.18** is extremely simple with a single resonance for the *tert*-butyl methyl protons at δ 1.03. In addition, a single resonance is observed for the aryl methyl protons at δ 2.12, indicating free rotation about the N-C_{ipso} bonds of the amidate ligands. The expected amido methyl resonance is present at δ 2.93, along with resonances for the aryl protons at δ 6.86-6.92. This high symmetry species suggests that the amidate ligands are labile enough to undergo rapid isomerization in solution. The possibility of κ^1 -intermediates during the isomerization process is likely, given that the amidate ligand is bound in an alkoxy-imine motif. A potential isomerization pathway is illustrated in Scheme 2.1, where the κ^1 -intermediate can rotate and the N donor can re-coordinate in a new geometric conformation. If this process is sufficiently rapid in comparison to the NMR timescale, in solution an average structure should be observed for this transformation.



Scheme 2.1

To test this hypothesis for isomerization, a competitive donor was added to Zr complex **2.18**. Upon addition of one equiv of pyridine (Py) to **2.18**, the ^1H NMR spectrum becomes more complicated, with multiple resonances for both the *tert*-butyl protons and the aryl methyl protons. The appearance of these new signals is consistent with a C_1 symmetric structure such as that shown in Eq. 2.11. Variable temperature ^1H NMR spectroscopic studies reveal that the complex is highly fluxional, and the coordinated pyridine is labile. At room temperature or above, the signals for pyridine appear where free pyridine would be expected. However, the ligand based resonances are more complicated than expected, suggesting rapid exchange of pyridine. Heating this reaction mixture to 50 °C or greater liberates pyridine, and the spectrum is essentially identical to **2.18** prior to addition of pyridine.

The solid-state molecular structure of $\kappa^2\text{-}[\text{DMP}(\text{NO})^{\text{tBu}}]\text{-}\kappa^1\text{-}[\text{DMP}(\text{NO})^{\text{tBu}}]\text{Zr}(\text{NMe}_2)_2(\text{Py})$ (**2.19**) was determined and is shown in Fig. 2.11, with selected bond lengths and angles given in Table 2.8, and crystallographic details located in Table A2.12 in Appendix A. One of the amidate ligands isomerizes to a κ^1 -form, where the amidate N donor is labile and is replaced with pyridine. The solid-state molecular structure of **2.19** definitively illustrates that the amidate ligands can undergo hemilability to a monodentate form. The Zr(1)-N(5) bond of the bound pyridine is long at 2.469(2) Å, consistent with being located *trans* to a dimethylamido ligand, which is a strong π -donor. Additionally, the solid-state structure of **2.19** confirms the notion that the amidate ligands tend to bind in an alkoxy-imine form, as the κ^1 -coordinated ligand is

bound through the oxygen rather than the nitrogen. Examination of the bond lengths in the κ^1 -amidate ligand also support this interpretation, where the C(2)-N(2) bond length of 1.267(3) Å is consistent with a C=N double bond,⁸¹ and the C(2)-O(2) bond length of 1.321(3) Å is best described as a C-O single bond.⁸¹

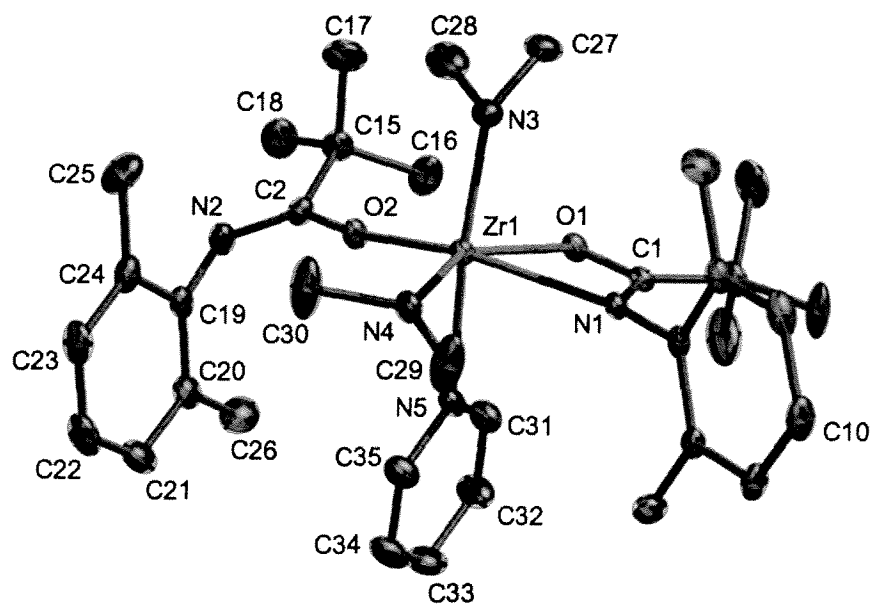
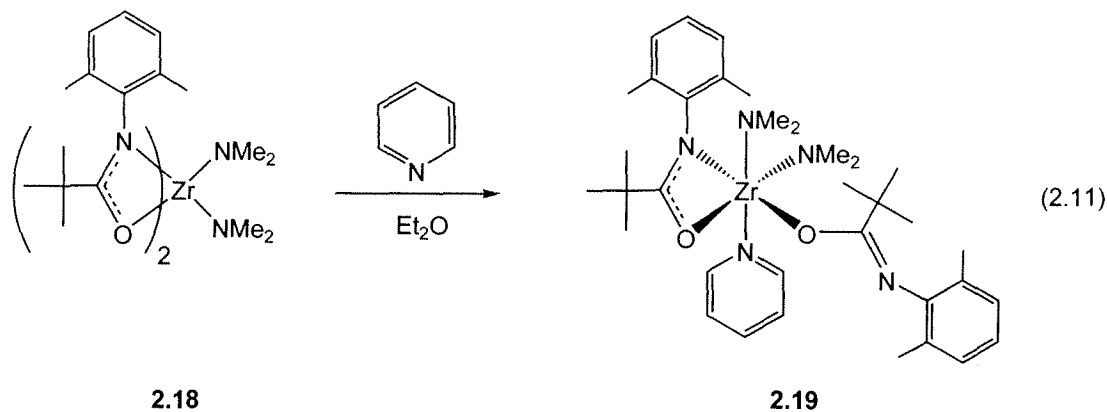


Figure 2.11 ORTEP depiction (ellipsoids at 30% probability) of solid-state molecular structure of κ^2 -[^{DMP}(NO)^{tBu}] $-\kappa^1$ -[^{DMP}(NO)^{tBu}]Zr(NMe₂)₂(Py), **2.19** (hydrogens omitted for clarity)

Table 2.8 Selected Bond Distances (Å) and Angles (°) for κ^2 -[^{DMP}(NO)^{tBu}]₂- κ^1 -[^{DMP}(NO)^{tBu}]Zr(NMe₂)₂(Py), **2.19**

	Lengths		Angles		Angles
Zr(1)-O(2)	2.0148(18)	O(2)-Zr(1)-N(4)	106.24(9)	O(2)-Zr(1)-N(5)	79.00(8)
Zr(1)-N(4)	2.041(2)	O(2)-Zr(1)-N(3)	99.43(9)	N(4)-Zr(1)-N(5)	91.03(9)
Zr(1)-N(3)	2.057(2)	N(4)-Zr(1)-N(3)	100.49(10)	N(3)-Zr(1)-N(5)	168.31(9)
Zr(1)-O(1)	2.1813(18)	O(2)-Zr(1)-O(1)	102.27(7)	O(1)-Zr(1)-N(5)	78.07(7)
Zr(1)-N(1)	2.372(2)	N(4)-Zr(1)-O(1)	146.86(9)	N(1)-Zr(1)-N(5)	82.35(8)
Zr(1)-N(5)	2.469(2)	N(3)-Zr(1)-O(1)	91.06(9)	N(2)-C(2)-O(2)	125.0(2)
O(2)-C(2)	1.321(3)	O(2)-Zr(1)-N(1)	154.84(8)	N(2)-C(2)-C(15)	119.7(3)
N(2)-C(2)	1.267(3)	N(4)-Zr(1)-N(1)	90.75(9)	O(2)-C(2)-C(15)	115.3(2)
O(1)-C(1)	1.306(4)	N(3)-Zr(1)-N(1)	95.43(9)		
N(1)-C(1)	1.296(4)	O(1)-Zr(1)-N(1)	57.05(7)		

Inspection of the extended solid-state structure of **2.19** demonstrates two distinct intermolecular non-covalent interactions within the lattice. The first interaction is a hydrogen bonding interaction between the N(2) atom of the κ^1 -bound amidate ligand and the *meta* aryl proton of C(23) of an adjacent molecule of **2.19**. This interaction is illustrated in Fig. 2.12 (A) by dashed red lines, which form a ladder structure throughout the lattice. The 2.72 Å contact distance for this interaction falls within the sum of van der Waals radii of N and H (N = 1.55 Å, H = 1.20 Å, total = 2.75 Å) indicating that this is a real interaction, and not simply the product of crystal packing.⁸²

The second non-covalent intermolecular interaction present in the lattice is a less intuitive hydrogen bonding interaction between the *meta* proton of the coordinated pyridine at C(32) and the π -system of the N-aryl group on the κ^2 -bound amidate ligand, where the *para* carbon C(10) has the closest contact with the proton at C(32). This interaction is shown in Fig. 2.12 (A) by dashed blue lines, where the contact distance of 2.88 Å falls within the sum of van der Waals radii for C and H (C = 1.70 Å, H = 1.20 Å, total = 2.90 Å).⁸² Similar interactions between protons and π -systems are frequently seen in extended molecular structures.⁵⁵ The result of these two intermolecular forces is the formation of a 1D network defined by two columns of **2.19** related by a C₂ screw axis parallel to the b-axis of the crystallographic unit cell. This extended structure is depicted in Fig. 2.12 (B) as viewed along the C₂ crystallographic screw axis. This extended solid-

state structure supports the notion that amidate ligand exchange/transfer may be possible through bridging interactions between metal centers via κ^1 -amidate ligation.

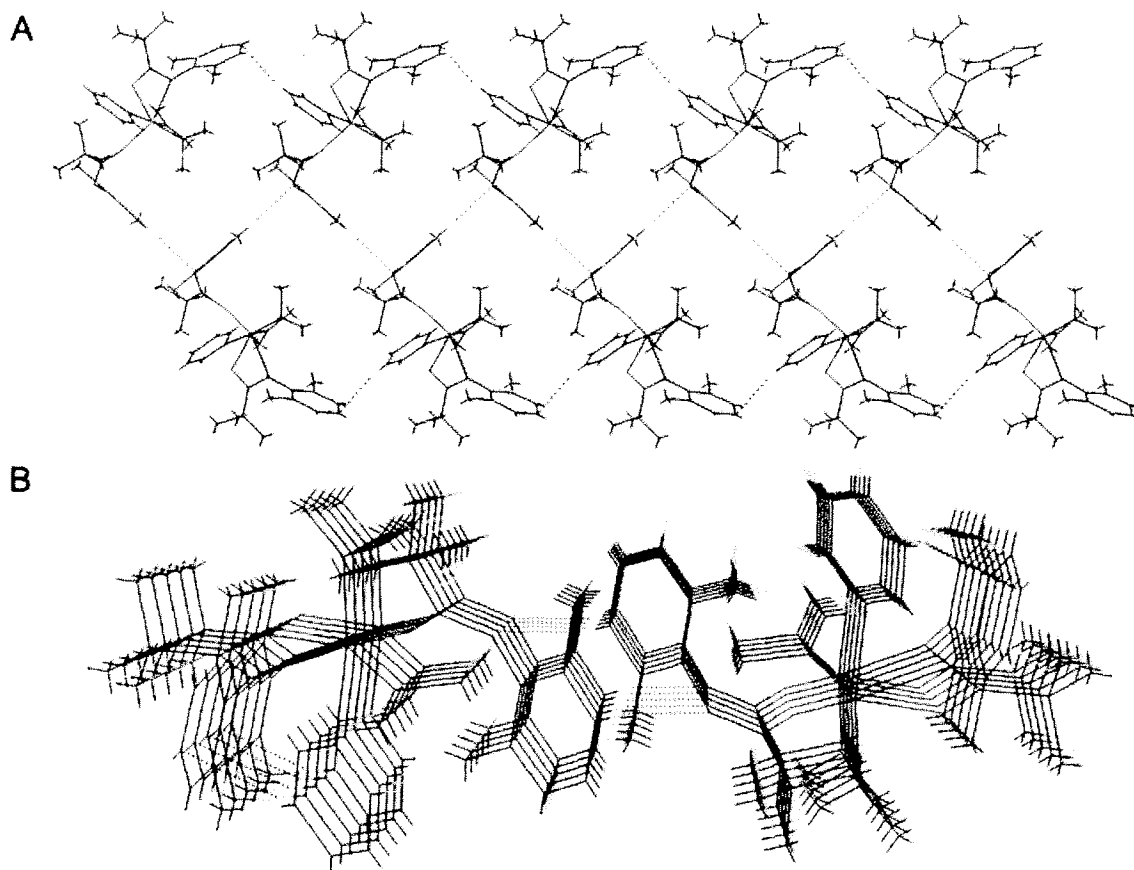
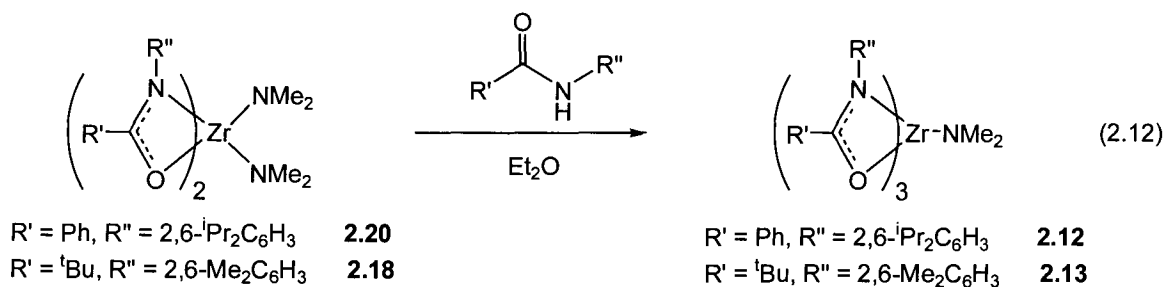
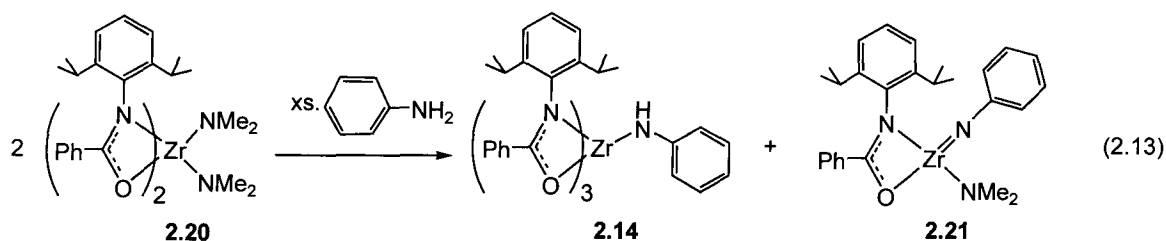


Figure 2.12 Extended structure of **2.19** in the solid-state (**A**), and viewed down crystallographic C_2 screw axis (**B**) (C = gray, H = green, Zr = purple, N = blue, O = red; hydrogen bonds = dashed red and blue lines)

While the tris(amidate) complexes **2.12** and **2.13** are readily synthesized in high yield by the route illustrated in Eq. 2.7, stepwise synthesis is also possible upon combination of a third equiv of the amide proligand with the bis(amidate) bis(amido) complexes, as shown in Eq. 2.12. While beyond the scope of this thesis, the stepwise synthesis of the tris(amidate) complexes implies that complexes bearing two or more different amidate ligands should theoretically be accessible. However, the ligand redistribution issues presented in the previous section suggest that these mixed ligand species would likely be unstable to disproportionation.



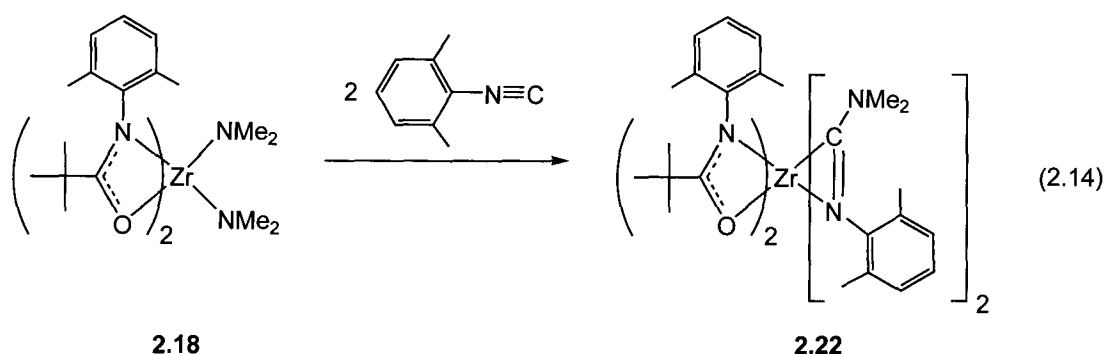
It is also of note that the anilido complex **2.14**, synthesized by protonolysis of **2.12** with aniline, can be isolated by reaction of excess aniline with the bis(amido) bis(amido) complex **2.20** as shown in Eq. 2.13. A potential mechanism for the formation of **2.14** from **2.20** can be envisioned through an intermolecular ligand exchange reaction between two Zr centers, involving a κ^1 -interaction analogous to that seen for **2.19**. The other product formed would be a mono(amidate) imido complex **2.21**. No solution phase or solid-state evidence exists to substantiate the claim of formation of **2.21**, but is inferred from reaction stoichiometry alone. Given the unsuccessful attempts to synthesize mono(amidate) tris(amido) complexes, it is postulated that **2.21** would likely not be monomeric, but rather dimeric or oligomeric in nature.



2.3.2.3 Insertion Reactivity of Amido Ligands

The reaction of **2.12** with aniline to form **2.14** through protonolysis is an important reaction which has implications for the catalytic hydroamination studies to be presented in Chapter 5. Another important fundamental reaction would be insertion of unsaturated organic species into the M-N bonds of the amido complexes presented in the preceding sections. One test reaction to probe the feasibility of such a process for these complexes is the insertion of 2,6-dimethylphenylisocyanide into Zr-N bonds. While isocyanide insertion into metal alkyls is well precedented, the analogous reactivity with

metal amido complexes has received far less attention.^{73, 74, 83} The combination of two equiv of 2,6-dimethylphenylisocyanide with bis(amido) complex $[\text{DMP}(\text{NO})^{\text{tBu}}]_2\text{Zr}(\text{NMe}_2)_2$, **2.18**, results in formation of the η^2 -iminocarbamoyl complex **2.22** ($[\text{DMP}(\text{NO})^{\text{tBu}}]_2\text{Zr}(\eta^2\text{-ArN}=\text{C}(\text{NMe}_2))_2$ (Ar = 2,6-Me₂C₆H₃)) as illustrated in Eq. 2.14. Preliminary sealed NMR tube experiments show this reaction to be essentially instantaneous. Isolation of **2.22** can be accomplished in 65 % yield upon precipitation from Et₂O. The low solubility of this material facilitates its isolation by filtration.



Verification of insertion and η^2 -iminocarbamoyl ligation is most easily shown by ¹³C NMR spectroscopic studies, which show a signal at δ 208.7, which is highly characteristic of such species.⁷⁴ This complex exhibits C₂ symmetry in solution, with hindered rotation about the amidate N-C_{ipso} bonds as well as the iminocarbamoyl N-C_{ipso} bonds. This is manifested by a single resonance for the *tert*-butyl groups in the ¹H NMR spectrum at δ 1.17, and four resonances of equal intensity for the aryl methyl groups at δ 1.66, 1.94, 2.42, and 2.73. Free rotation of the amido NMe₂ groups is observed as a single resonance at δ 2.09. Mass spectrometry also verified the formation of this product with a parent ion at *m/z* 848, and a fragment at *m/z* 673, corresponding to loss of one of the iminocarbamoyl ligands. While some iminoacyl and iminocarbamoyl complexes of this type are known to undergo C=C coupling of the η^2 -bound ligands,^{77, 83, 84} **2.22** does not undergo such reactivity even at elevated temperatures

It is important to note that insertion of the isocyanide moiety into the amidate Zr-N bond does not occur. The steric protection afforded by the bulky groups on the amidate N donors effectively protects these sites from undesirable side reactivity. Insertion of simple alkenes and alkynes into the metal amido linkages of **2.18** would have important implications in the mechanism of catalytic hydroamination; however, attempts

at insertion reactions with styrene, 1-hexene, and phenylacetylene resulted in no reaction. This suggests that these less polar C-C multiple bonds cannot insert into the Zr-N bonds of these amido complexes through σ -bond insertion processes.

2.3.3 Summary

Both bis(amidate) and tris(amidate) amido complexes of Ti and Zr can be synthesized in high yields. The tris(amidate) mono(amido) complexes of Zr are C_3 symmetric in solution, with rapidly exchanging amidate ligands. Solid-state molecular structure analysis of **2.14** shows that these 7-coordinate complexes exist in heavily distorted pentagonal bipyramidal geometries. Large groups on the amidate ligands lead to ligand exchange and disproportionation reactions with these complexes. Intramolecular exchange processes of bis(amidate) bis(amido) complexes are likely facilitated by the hemilabile nature of the amidate ligands, where complexes bearing κ^1 -bound amidate ligands are important intermediates as demonstrated by **2.19**. The tris(amidate) mono(amido) complexes **2.12** and **2.13** can be synthesized in a single step from the precursor $Zr(NMe_2)_4$, or sequentially from the bis(amidate) bis(amido) species **2.18** and **2.20**. This implies that complexes bearing two or more different amidate ligands can be synthesized should the need arise. This synthetic flexibility could prove useful in future high-throughput combinatorial screening for polymerization catalysis and other useful reactivity. The reactive amido ligands in the bis(amidate) bis(amido) and tris(amidate) mono(amido) complexes can undergo protonolysis reactions to form species like anilido complex **2.14**, as well as insertion reactions to form iminocarbamoyl complexes (**2.22**).

2.4 Geometric Isomerization of Amido Complexes

2.4.1 Introduction

The ability of metal complexes to adopt varied coordination geometries is one of their most important features. This geometric flexibility is crucial to the novel reactivity

that metal complexes promote; however, this flexibility also makes characterization of such complexes difficult. The amidate ligands investigated in this thesis are unsymmetrical due to their mixed N,O chelate motif. The potential for multiple geometric isomers makes solution phase characterization complicated. It was previously noted that solution phase isomerization of bis(amidate) bis(amido) complexes may occur through κ^1 -intermediates as shown in Scheme 2.1. The factors controlling the geometric isomer observed, and the interconversion of different geometric isomers were investigated by solid-state molecular structural analysis and density functional theory (DFT) calculations.

2.4.2 Results and Discussion

2.4.2.1 Structural Studies

While the hard N,O chelating motif of the monoanionic amidate ligand set is ideally suited to bind to group 4 metals, the unsymmetrical chelating unit gives rise to several possible geometric isomers. As was alluded to in the previous section, these isomers can be manifested in solution by multiple resonances in the ^1H NMR spectra, or by solid-state structures inconsistent with solution phase behavior (complex **2.18**). There are five isomers possible based on a pseudo-octahedral coordination geometry. These isomers are illustrated in Fig. 2.13.

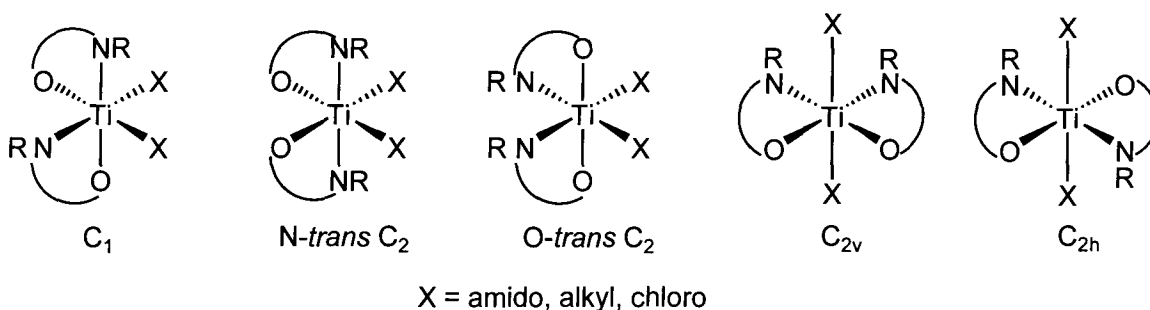


Figure 2.13 Possible geometric isomers of bis(amidate) Ti complexes

Given the presence of bulky substituents on the N donors of the amidate ligands, it could reasonably be predicted that the predominant geometric isomer observed would be the *N-trans* C₂ variant. However, bis(amidate) bis(amido) complexes of ligand **2.1** ([^tBu(NO)^{Ph}]), **2.15** – **2.17**, exist in the *O-trans* C₂ geometry in the solid-state. The observation of this unexpected isomer can be attributed to the tight bite angle of the amidate ligands at approximately 60°, which place the bulky *tert*-butyl substituents farther apart than would typically be expected. In addition, the orientation of the N donors of the amidate ligands *trans* to the amido ligands should be energetically more favorable than having the O donors *trans* to the amido ligands. The alkoxy-imine binding mode of the amidate ligands to the metal centers implies significantly stronger M-O bonds than M-N bonds. Due to the strong *trans* influence of the amido ligands, the overall stability of the metal complex should be enhanced by ensuring that the strong donors are not *trans* to the amido ligands.

Interconversion of the different geometric isomers is proposed to occur through a mechanism involving κ^2 -to- κ^1 -ligand isomerization, as illustrated in Scheme 2.1. Systematic investigation of the factors controlling the prevalent geometric isomer was accomplished by X-ray crystallographic and density functional theory (DFT) studies. While Ti complexes **2.15** – **2.17** clearly illustrate the preference for the *O-trans* C₂ geometric isomer, Zr complex **2.18** demonstrates that the C₁ isomer is also possible for these bis(amidate) bis(amido) species. The difference in size of Ti and Zr is considerable, and to ensure appropriate comparisons of the effects of steric factors influencing coordination geometry of bis(amidate) bis(amido) complexes, a series of Ti complexes was synthesized with amidate ligands sharing a common phenyl carbonyl substituent. In collaboration with the Wang group at UBC, DFT calculations determined the relative energies of the five possible geometric isomers of each of three different bis(amidate) bis(amido) complexes utilized in this study. In addition to complex **2.16** ([^tBu(NO)^{Ph}]₂Ti(NEt₂)₂), complexes **2.23** ([^{DMP}(NO)^{Ph}]₂Ti(NEt₂)₂) and **2.24** ([^{DIPP}(NO)^{Ph}]₂Ti(NEt₂)₂) can be synthesized following the procedure shown in Eq. 2.10.

Using the crystallographically determined solid-state molecular structure of **2.16** as a starting point, DFT models of the five possible geometric isomers were generated. Fig. 2.14 illustrates the computed structures of the isomers of **2.16** and their relative

energetic ordering. The metrical parameters for the crystallographically characterized isomers of **2.16**, **2.23**, and **2.24** and their calculated variants are in good agreement and are given in Tables B2.1, B2.2, and B2.3, respectively, in Appendix B.

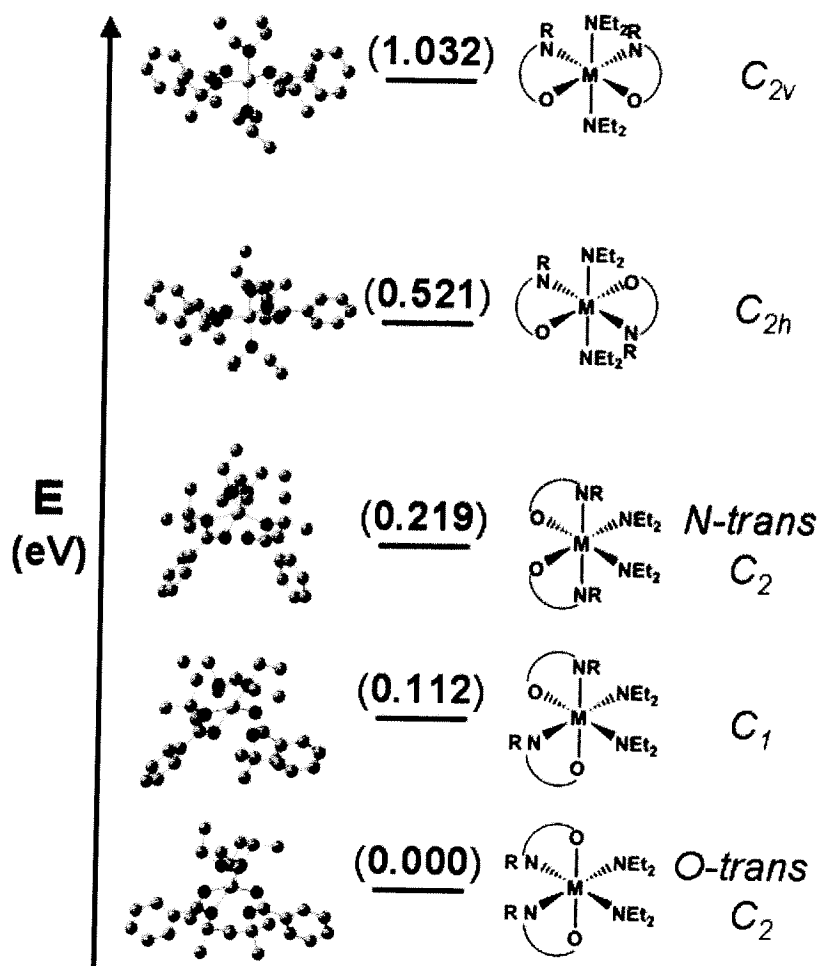


Figure 2.14 Relative energetic ordering of geometric isomers of **2.16** (Ti = white, N = blue, O = red, C = gray)

The *O-trans* C_2 isomer is calculated to be the most energetically favorable, and matches the solid-state molecular structure for **2.16**, which is logical since the crystallized material should represent a thermodynamic minimum. The next highest energy isomer is the C_1 isomer, calculated to be 0.112 eV higher in potential energy. If the isomerization mechanism proposed in Scheme 2.1 is envisioned, κ^2 -to- κ^1 -ligand isomerization of one of the amidate ligands of the *O-trans* C_2 isomer, followed by recoordination of the amidate ligand, would result in the formation of the C_1 isomer. Repeating the

isomerization process with the second amidate ligand would result in generation of the *N-trans* C₂ isomer, which is located 0.107 eV above the C₁ isomer. The two highest energy isomers (C_{2h} and C_{2v}) have *trans* oriented amido ligands and are considerably higher in energy than the C₁ and C₂ isomers. The strong *trans* influence of the amido ligands explains their preference for *cis* orientation, and thus the high energy of the C_{2h} and C_{2v} isomers. Finally, the sterically unfavorable interaction of the *tert*-butyl groups in the C_{2v} isomer places it at the highest relative energy.

At room temperature, **2.16** does not appear to isomerize on the NMR timescale; however, high temperature ¹H NMR spectroscopic experiments suggest solution phase isomerization. At higher temperatures, other signals grow into the spectrum indicating the presence of multiple geometric isomers. As the temperature is increased, the intensities of the signals for the minor geometric isomers increase relative to the signals for the ground state *O-trans* C₂ isomer. In contrast, bond rotation processes can be observed and frozen out at low temperatures. For example, at -25°C the quartet for the diethylamido methylene protons broadens and eventually splits into two broad multiplets of equal intensity at even lower temperatures, indicating hindered rotation about the amido Ti-N bond, resulting in inequivalent ethyl groups. Accompanying this observation, the corresponding methyl protons on the diethylamido ligands separate into two multiplets of equal intensity that inconveniently overlap with the *tert*-butyl signal. The fact that isomerization at room temperature is not observed for **2.16** is reasonable given the relatively large difference in energy between the various geometric isomers.

The solid-state molecular structure of complex **2.23** was determined by X-ray crystallography and is shown in Figure 2.15. Selected bond lengths and angles are located in Table 2.9, and crystallographic data are presented in Table A2.13 (Appendix A). In this case, the sterically larger 2,6-dimethylphenyl groups on the amidate N donors force the amidate ligands from the *O-trans* C₂ conformation seen in **2.16** to one in which the overall symmetry of the complex is C₁. Comparison of the amidate N-Ti-N bond angles for **2.16** and **2.23** show that this rearrangement results in an increase in this bond angle from 85.5(2)° to 94.94(5)°. This C₁ geometric isomer was seen for the related Zr complex [^{DMP}(NO)^{tBu}]₂Zr(NMe₂)₂, **2.18**, which likewise has 2,6-dimethylphenyl substituents on the amidate N donors, but has *tert*-butyl groups at the carbonyl positions

of the amidate ligands. While **2.18** does exhibit asymmetry of the binding of the two amidate ligands, due to one having a N donor *trans* to an amido ligand, and the other having an O donor *trans* to an amido ligand, the effect is more pronounced in **2.23**. This is likely due to the fact that the Ti-O and Ti-N bond lengths are contracted relative to the Zr-O and Zr-N bond lengths in **2.18**, owing to the smaller ionic radius of Ti(IV) vs. Zr(IV), thus resulting in greater steric repulsions within **2.23** vs. **2.18**. For example, the Ti(1)-O(2) bond length in **2.23** is 2.004(1) Å, whereas the Ti(1)-O(1) bond length is significantly longer at 2.076(1) Å, as expected for a donor *trans* to a strong π -donor like diethylamido. Likewise, the Ti(1)-N(3) bond is considerably longer than the Ti(1)-N(1) bond (2.375(1) Å vs. 2.211(1) Å, respectively). It is also interesting to note that the normal alkoxy-imine binding mode for the amidate backbone is shifted to the amido-ketone form (Fig. 2.9) for the amidate ligand that is bound with the O donor *trans* to the amido ligand (C(1)-O(1) = 1.293(2) Å and C(1)-N(1) = 1.310(2) Å).

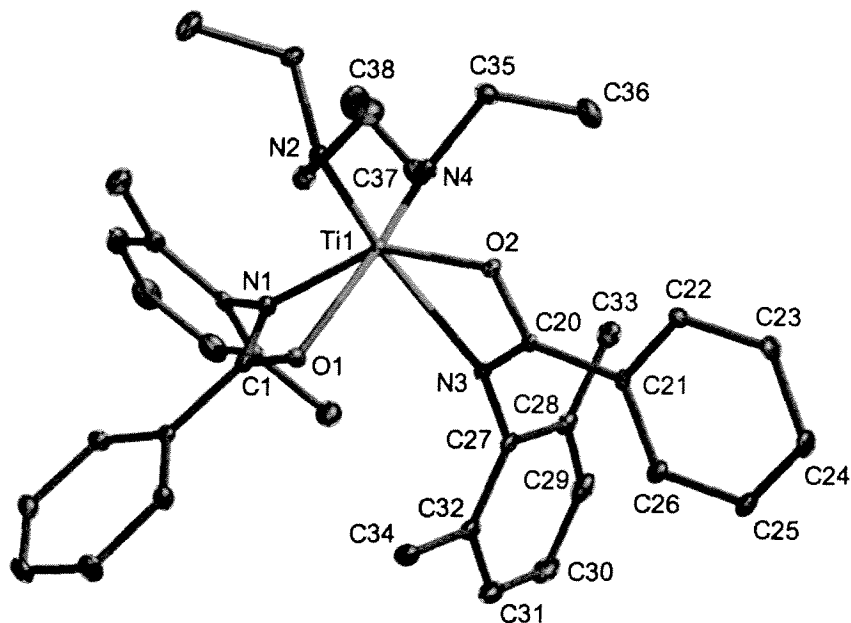


Figure 2.15 ORTEP depiction (ellipsoids at 30% probability) of solid-state molecular structure of $[\text{DMP}(\text{NO})^{\text{Ph}}]_2\text{Ti}(\text{NEt}_2)_2$, **2.23** (hydrogens omitted for clarity)

Table 2.9 Selected Bond Distances (Å) and Angles (°) for $[\text{DMP}(\text{NO})^{\text{Ph}}]_2\text{Ti}(\text{NEt}_2)_2$, **2.23**

Lengths		Angles		Angles	
Ti(1)-N(1)	2.211(1)	O(1)-Ti(1)-O(2)	95.37(5)	O(1)-Ti(1)-N(4)	157.55(5)
Ti(1)-N(2)	1.894(1)	N(1)-Ti(1)-N(3)	94.94(5)	O(2)-Ti(1)-N(1)	148.94(5)
Ti(1)-N(3)	2.375(1)	N(1)-Ti(1)-N(2)	105.06(6)	O(2)-Ti(1)-N(3)	59.62(4)
Ti(1)-N(4)	1.901(1)	N(1)-Ti(1)-N(4)	97.15(6)	O(2)-Ti(1)-N(4)	102.58(5)
Ti(1)-O(1)	2.076(1)	N(2)-Ti(1)-N(4)	99.79(6)	O(2)-Ti(1)-N(2)	95.02(5)
Ti(1)-O(2)	2.004(1)	N(3)-Ti(1)-N(4)	95.83(6)		
O(1)-C(1)	1.293(2)	N(3)-Ti(1)-N(2)	152.73(6)		
N(1)-C(1)	1.310(2)	O(1)-Ti(1)-N(3)	81.63(5)		
O(2)-C(20)	1.318(2)	O(1)-Ti(1)-N(2)	91.86(5)		
N(3)-C(20)	1.296(2)	O(1)-Ti(1)-N(1)	61.09(5)		

As was done for **2.16**, DFT calculations were performed to determine the relative energies of the five possible geometric isomers of **2.23**. The results are illustrated in Fig. 2.16. The most interesting observation with complex **2.23** is that the C_1 isomer characterized in the solid-state is not the ground state isomer determined by computational methods. The ground state isomer for **2.23** is calculated to be the *N-trans* C_2 isomer, which has not been observed crystallographically at this point. The expected C_1 isomer is very close in energy to the ground state, at only 0.036 eV higher energy. In comparison, the energy gap between the ground state and C_1 isomers in **2.16** is 0.113 eV (over three times larger). This small energy gap for **2.23** is manifested experimentally by room temperature geometric isomerization, where the major isomer (> 80%) has NMR spectral properties consistent with the *N-trans* C_2 isomer, calculated to be the thermodynamically most stable isomer. The low energy barrier between the *N-trans* C_2 and C_1 isomers allows for their rapid interconversion at room temperature and higher. Minor isomeric forms (< 20%) are also present in solution, as evidenced by multiple quartets and triplets corresponding to the diethylamido groups. At lower temperatures, multiple isomeric forms can clearly be seen by the appearance of multiple peaks in the region of each expected resonance. As the temperature is raised, line broadening is observed, accompanied by the coalescence of the peaks. For example, the diethylamido quartets for all the different isomers coalesce into one broad hump at temperatures above 60 °C. However, there are no well resolved peaks for any of the possible isomers, even at

temperatures up to 100 °C. This observation suggests that the interconversion of the higher energy isomers is occurring slowly on the NMR timescale at temperatures up to and including 100 °C. If the proposed κ^1 -intermediate isomerization pathway is occurring (Scheme 2.1), the presence of these species would serve to further complicate the ^1H NMR spectrum of **2.23** at higher temperatures. Given the observation that **2.18** and **2.23** both crystallize as C_1 symmetric species, but exhibit C_2 symmetry in solution, it is possible that crystal packing interactions in the solid state compensate for the slightly higher calculated gas-phase ground state energy.

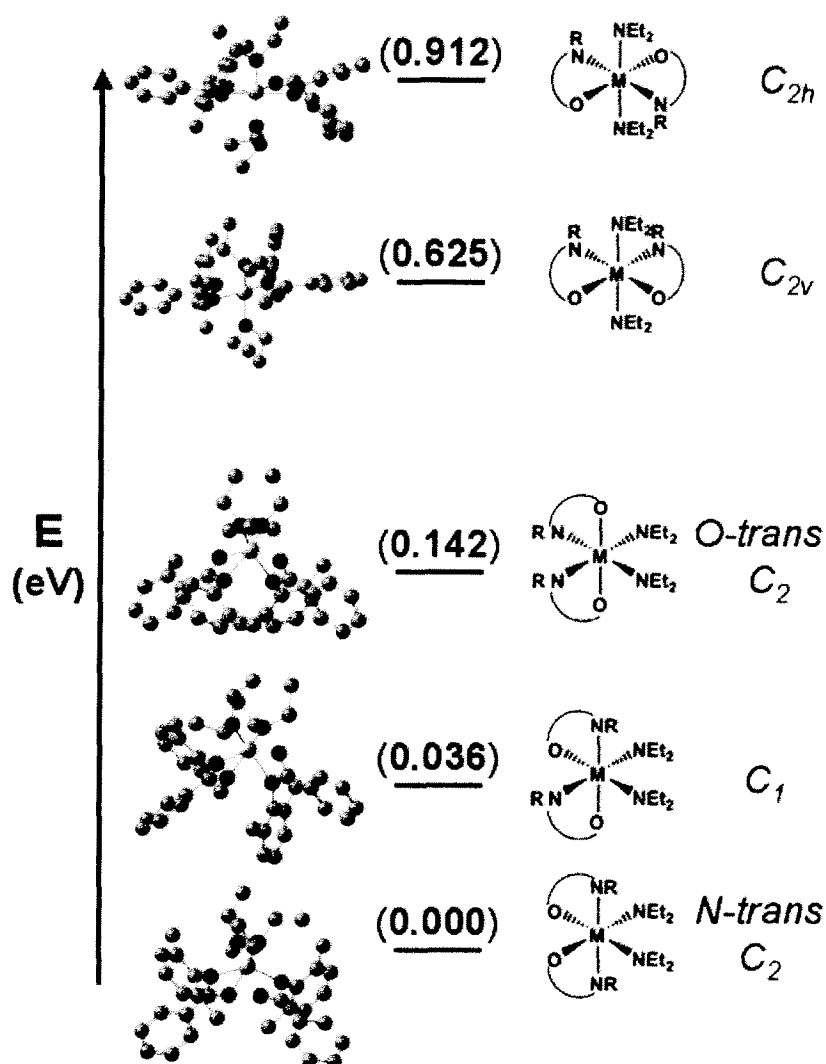


Figure 2.16 Relative energetic ordering of geometric isomers of **2.23** (Ti = white, N = blue, O = red, C = gray)

While the *N-trans* C₂ and C₁ isomers are relatively close in energy, the *O-trans* C₂ isomer is substantially higher in energy, at 0.142 eV above the ground state, which is logical given the degree of steric crowding present in this isomer. As was seen for **2.16**, the C_{2v} and C_{2h} isomers are much higher in energy than the C₂ and C₁ isomers; however, the C_{2v} isomer is stabilized relative to the C_{2h} isomer by a π -stacking interaction between the two 2,6-dimethylphenyl groups on the N donors of the amidate ligands. This is the same interaction that was seen earlier for the homoleptic complexes **2.8** and **2.9**, verifying the stabilization imparted by this non-covalent interaction.

By increasing the steric bulk at the N donors of the amidate ligands to the very large 2,6-diisopropylphenyl groups, the *N-trans* C₂ isomer can be accessed, which is illustrated in the solid-state molecular structure of [^{DIPP}(NO)^{Ph}]₂Ti(NEt₂)₂, **2.24**, in Fig. 2.17. For selected bond lengths and angles see Table 2.10. The solid-state molecular structure of **2.24** was previously elucidated, and is rigorously C₂ symmetric, with the C₂ axis of symmetry passing through the Ti center and relating N(2) and N(2)*, N(1) and N(1)*, etc.⁸⁵ This conformation effectively forces the amidate N-aryl groups apart, with a N(1)-Ti(1)-N(1)* bond angle of 140.42(8)°. The relevant bond lengths are consistent with those seen for **2.16** and **2.23**, where the major observable difference is seen in the amidate backbone distances, with the backbone existing in the amido-ketone tautomer shown in Fig. 2.9 (C(1)-O(1) = 1.283(2) Å and C(1)-N(1) = 1.320(2) Å). In contrast to **2.16** and **2.23**, the amidate Ti-O and Ti-N bond lengths are nearly identical (Ti(1)-N(1) = 2.156(1) Å and Ti(1)-O(1) = 2.146(1) Å). With **2.24**, the preference for the bulky groups to be *trans* to each other competes with the general preference for the amidate ligands to bind with the N donors *trans* to the amido ligands. The resulting geometry forces the amidate ligand into a different tautomeric form than is normally seen. Unfortunately, due to the highly sterically congested nature of **2.24**, the ¹H NMR spectrum is very complicated, and variable temperature ¹H NMR spectroscopic experiments looking at solution phase isomerization could not be accurately interpreted. The complex nature of the ¹H NMR spectrum suggests that hindered rotation exists about the amidate N-C_{ipso} bonds, as well as the amido Ti-N bonds. At elevated temperatures, solution phase isomerization occurs readily, as witnessed by the increased complexity of the ¹H NMR spectra.

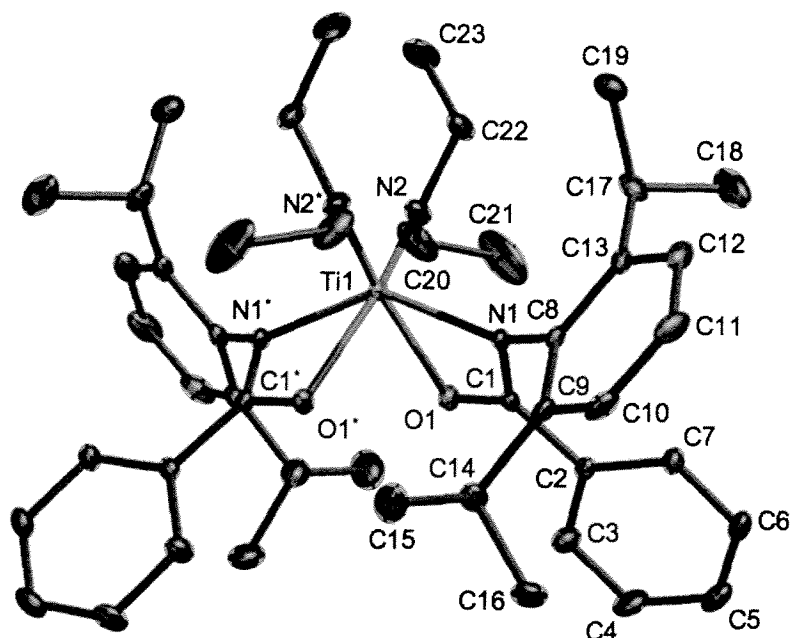


Figure 2.17 ORTEP depiction (ellipsoids at 30% probability) of solid-state molecular structure of $[\text{DIPP}(\text{NO})^{\text{Ph}}]_2\text{Ti}(\text{NEt}_2)_2$, **2.24** (hydrogens omitted for clarity)

Table 2.10 Selected Bond Distances (Å) and Angles (°) for $[\text{DIPP}(\text{NO})^{\text{Ph}}]_2\text{Ti}(\text{NEt}_2)_2$, **2.24**

Lengths		Angles		Angles	
Ti(1)-O(1)	2.146(1)	O(1)-Ti(1)-O(1) [*]	81.92(7)	O(1)-Ti(1)-N(1) [*]	88.30(5)
Ti(1)-N(1)	2.156(1)	N(1)-Ti(1)-N(1) [*]	140.42(8)	O(1)-Ti(1)-N(2)	159.30(5)
Ti(1)-N(2)	1.899(2)	N(1)-Ti(1)-N(2)	99.21(6)	O(1)-Ti(1)-N(1)	61.21(5)
O(1)-C(1)	1.283(2)	N(1)-Ti(1)-N(2) [*]	105.68(6)	O(1)-C(1)-N(1)	114.5(2)
N(1)-C(1)	1.320(2)	N(2)-Ti(1)-N(2) [*]	101.1(1)		

The relative energies of the geometric isomers of **2.24** were calculated using DFT methods, and are shown in Fig. 2.18. The ground state isomer is calculated to be the *N-trans* C_2 isomer, matching the observed solid-state molecular structure of **2.24**. Similarly to **2.16** and **2.23**, the next highest isomer in energy is the C_1 isomer, which is at 0.096 eV relative to the ground state. This larger energy gap explains the less prevalent room temperature isomerization observed for **2.24** vs. **2.23**. As predicted, the *O-trans* C_2 isomer is considerably higher in energy than the C_1 isomer (0.342 eV relative to the C_1) due to the extremely unfavorable steric interactions between the amidate *N*-aryl groups. Again, the C_{2h} and C_{2v} isomers are much higher in energy than the C_2 and C_1 isomers (a consequence of the *trans* influence of the amido ligands). Unlike **2.23**, the π -stacking

stabilization of the C_{2v} isomer of **2.24** is not possible due to the isopropyl groups preventing close approach of the aryl rings. Thus, the C_{2v} isomer is higher in energy than the C_{2h} isomer, as seen for **2.16**.

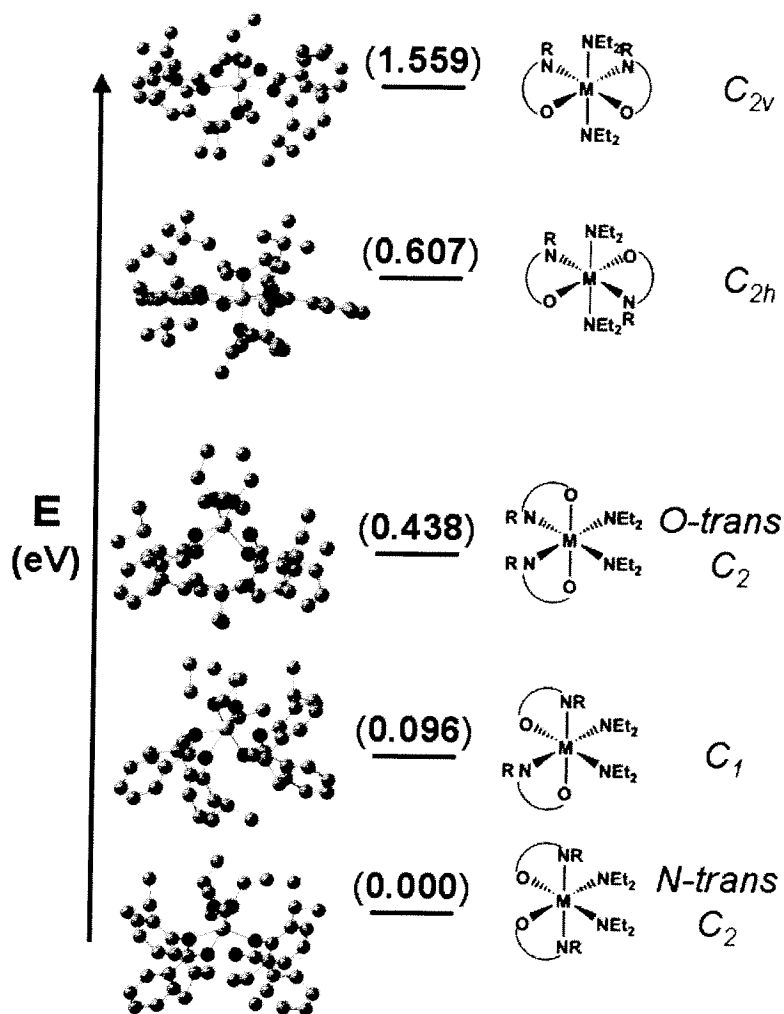


Figure 2.18 Relative energetic ordering of geometric isomers of **2.24** (Ti = white, N = blue, O = red, C = gray)

2.4.2.2 Electronic Structure Analysis

In an attempt to understand the bonding interactions holding the bis(amidate) bis(amido) complexes together, single point DFT calculations were performed on the geometry optimized structures of the five geometric isomers of complexes **2.16**, **2.23**, and **2.24**. Similar interactions are observed for all of the isomers of each of the complexes

investigated; therefore, the following discussion will focus only on the lowest energy isomer of complex **2.16** (*O-trans* C₂). Thermal stability experiments at elevated temperatures (> 110 °C) for periods as long as one week show no appreciable decomposition of the bis(amidate) bis(amido) complexes, indicating that the ancillary amidate bonding interactions are very strong. It was predicted that these interactions would lie well below the frontier orbitals.

The frontier bonding orbitals (HOMO and HOMO-1) are shown in Fig. 2.19. These two energetically similar orbitals are both amido-based π -symmetry orbitals. These orbitals support the previous designation of the amido ligands as 4 e⁻ donors, with the N lone pair of electrons being donated to the Ti center. The $d\pi$ - $p\pi$ interactions in the HOMO and HOMO-1 orbitals involve overlap of the vacant d-orbital with p-orbitals on both amido ligands. Since the amido ligands are the reactive sites for protonolysis reactivity that will be discussed in Chapters 4 and 5, it is logical that the frontier orbitals involve bonding interactions with these ligands.

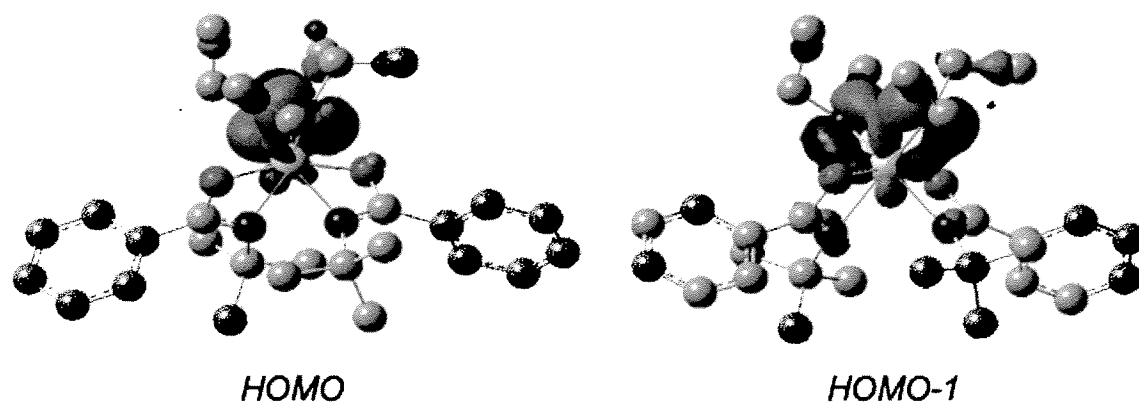


Figure 2.19 Frontier bonding orbitals of ground state isomer of **2.16** (Ti = white, N = blue, O = red, C = gray)

In addition to the π -symmetry bonding interactions of the amido ligands, the requisite σ -bonding interactions are also present. The σ -bond at the HOMO-9 level is shown in Fig. 2.20, and exhibits effective overlap between the d-orbital and hybrid orbitals of both amido ligands.

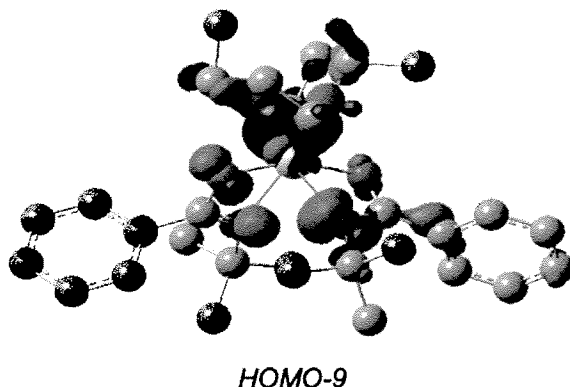


Figure 2.20 Amido σ -bonding orbital of ground state isomer of **2.16** (Ti = white, N = blue, O = red, C = gray)

The LUMO for **2.16** is calculated to be a non-bonding, unoccupied d-orbital, and is shown in Fig. 2.21. The assignment of which d-orbital is the LUMO is difficult owing to the fact that these complexes are severely distorted from a simple octahedral geometry, resulting in hybrid bonding interactions. The vacant d-orbital allows for coordination of Lewis bases, such as amines and phosphines. In particular, the availability of this orbital for amine coordination plays an important role in a precoordination step for catalytic hydroamination. A detailed mechanistic discussion of catalytic hydroamination of alkynes and alkenes will be presented in Chapter 5.

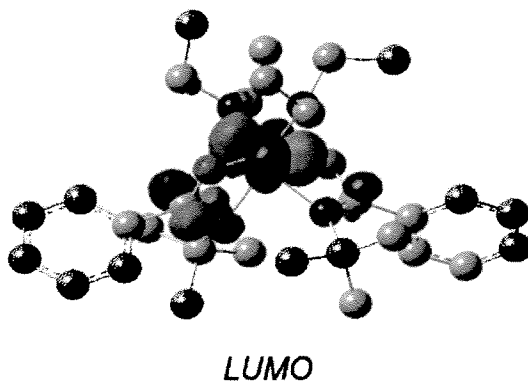


Figure 2.21 Frontier non-bonding orbital of ground state isomer of **2.16** (Ti = white, N = blue, O = red, C = gray)

Bonding interactions involving the amidate ligands are considerably lower in energy than those for the amido ligands, as predicted by the stability of these complexes. The HOMO-10 orbital illustrated in Fig. 2.22 shows d-p σ -interactions between Ti and

the amidate O donors, as well as interactions with the amido ligands. It was previously noted that the amido ligands' strong *trans* influence has a large impact on the nature of the amidate bonding interactions. This influence can be seen in the HOMO-13 orbital (Fig 2.22), where the amidate N donor and the *trans* disposed amido ligand are sharing opposite ends of the same d-orbital.

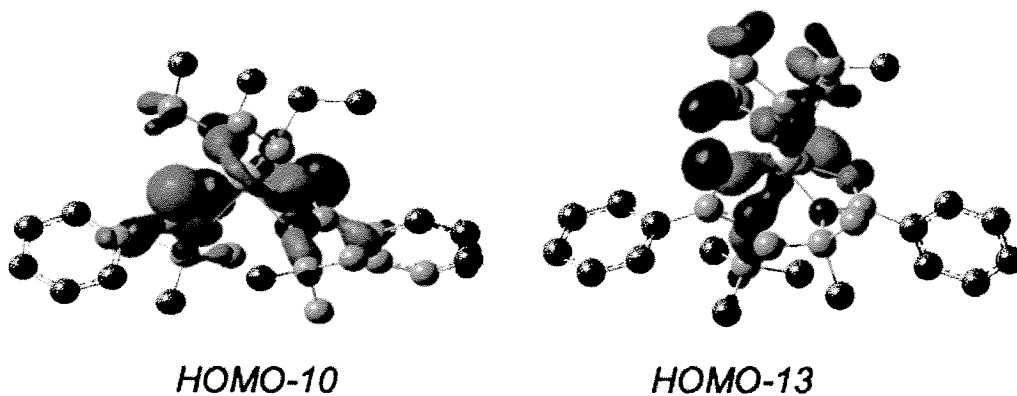


Figure 2.22 Amidate bonding interactions of ground state isomer of **2.16** (Ti = white, N = blue, O = red, C = gray)

The HOMO-LUMO gap for **2.16** is calculated to be 3.681 eV, which is slightly larger than that for **2.23** (3.512 eV) and **2.24** (3.543 eV). For comparative purposes, the UV/vis spectra of **2.16**, **2.23**, and **2.24** were collected. Since these complexes are all d^0 Ti species, the observed spectral features for these complexes are all LMCT bands. Calculated and experimental λ_{\max} values for **2.16**, **2.23**, and **2.24** are presented in Table 2.11.

Table 2.11 Theoretical and Experimental λ_{\max} Values for **2.16**, **2.23**, and **2.24**

Compound	HOMO-LUMO Gap (eV)	λ_{\max} Theoretical (nm)	λ_{\max} Experimental (nm)
2.16	3.681	276	270
2.23	3.512	325	358
2.24	3.543	315	265

For **2.16**, the agreement between the theoretical and experimental values is excellent (276 nm vs. 270 nm); however, the agreement for **2.23** and **2.24** is less impressive. The spectra of **2.23** and **2.24** are much broader, with far less defined features

than that seen for **2.16**. More prevalent solution phase isomerization of **2.23** and **2.24** vs. **2.16** make the presence of multiple geometric isomers highly likely. This implies that the experimental spectra are a combination of 2 or 3 different isomers. In general, the experimental and calculated spectra have very similar features and lineshapes, but the theoretical spectra are shifted in wavelength from the experimental spectra. The experimentally determined UV/vis spectrum for **2.16** is shown in Fig. 2.23, and the theoretical spectrum is shown in Fig. 2.24 (experimental and computational spectra for **2.23** and **2.24** are given in Appendix B for comparative purposes).

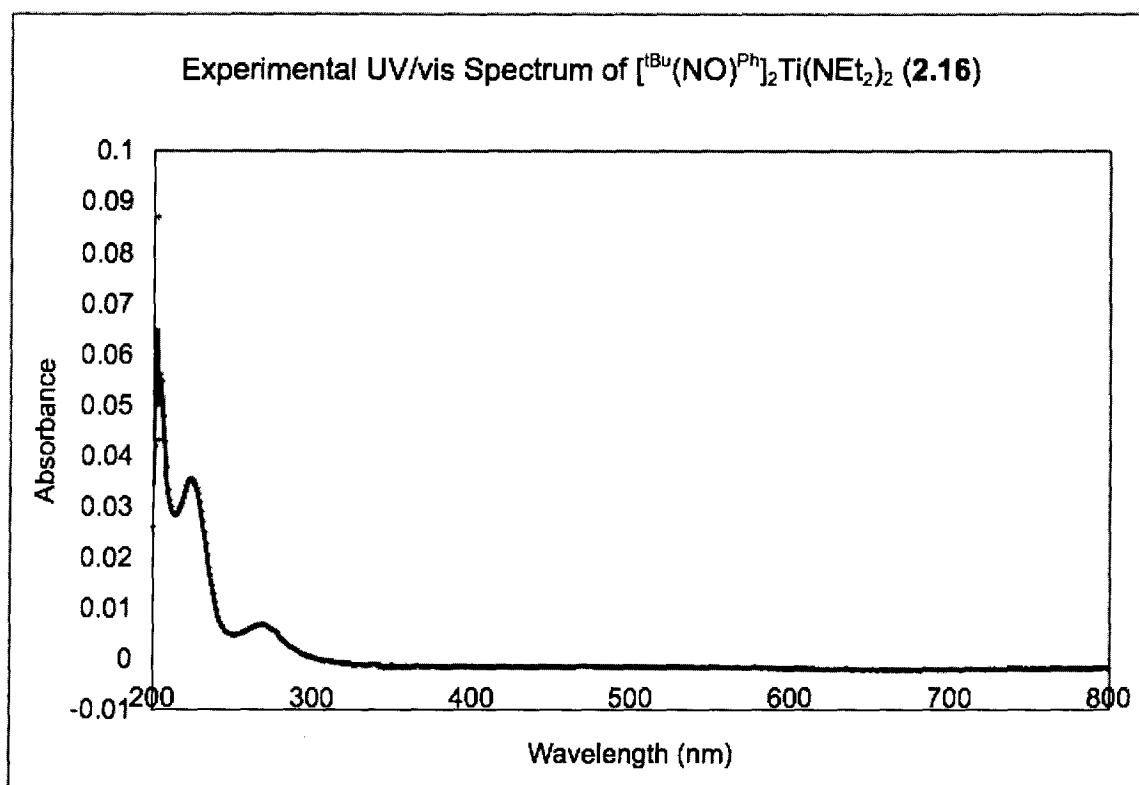


Figure 2.23 Experimental UV/vis absorption spectrum of **2.16**

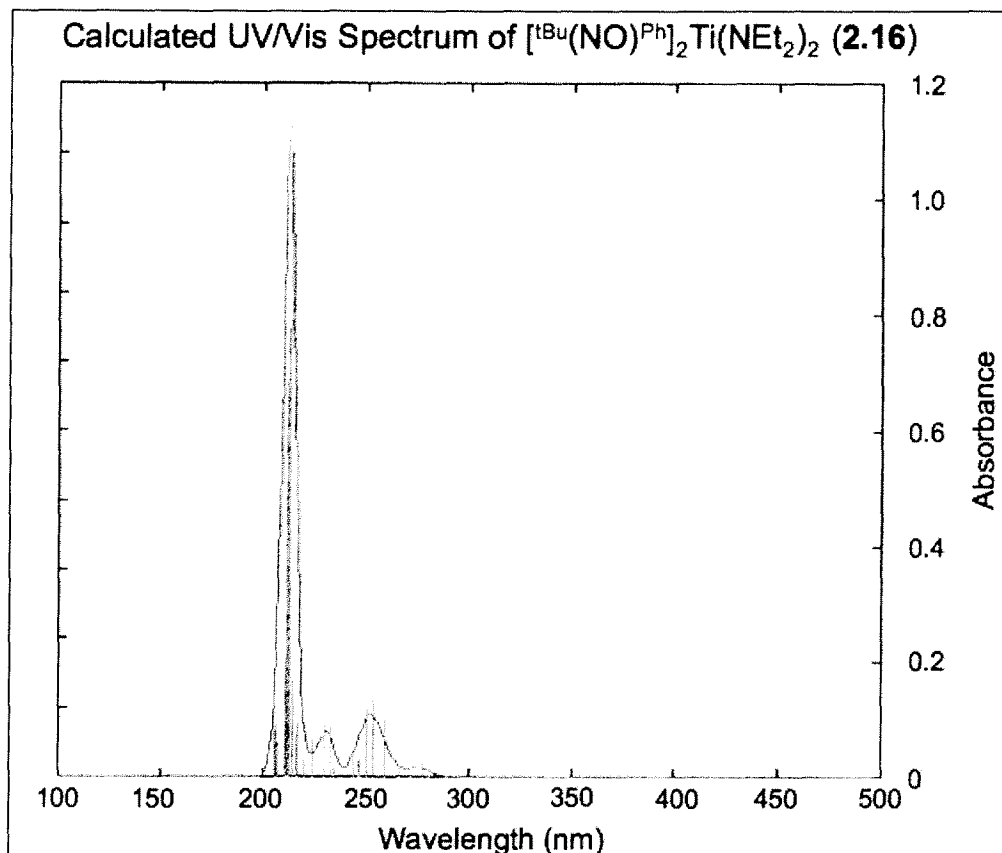


Figure 2.24 Calculated UV/vis absorption spectrum of **2.16**

2.4.3 Summary

While the bis(amidate) bis(amido) complexes of Ti and Zr exist as pseudo-octahedral species, due to the unsymmetric N,O chelate of the amidate ligands, five possible geometric isomers exist for these complexes. Systematic variation of the steric bulk at the N donor of the amidate ligand demonstrates that the geometric isomer observed in the solid-state is largely dictated by the bulk at this position. Density functional theory (DFT) calculations on the five possible isomers of complexes **2.16**, **2.23**, and **2.24** verified the solid-state molecular structures of **2.16** and **2.24** as the energetic minima for these complexes. Complex **2.23** was calculated to be most stable as the *N-trans* C_2 isomer, but was characterized as the C_1 isomer in the solid-state. DFT calculations on the isomers of **2.23** showed that the energy gap between the *N-trans* C_2 and C_1 isomers is very small, explaining the solution phase characterization, which is consistent with C_2 symmetry. As expected, the C_{2v} and C_{2h} isomers, which have *trans*

located amido ligands, are highest in energy due to the strong *trans* influence of these ligands. Geometric isomerization can further be controlled by tethering the amidate ligands together, as with proligand **2.6**. However, this ligand binds to group 4 metals in a planar fashion, as illustrated by the homoleptic complexes **2.10** and **2.11**. This planar coordination is problematic for the formation of amido complexes, as the amido donors prefer to be *cis*, which would leave the metal center highly exposed with this ligand. Proligand **2.6** is useful for the synthesis of bis(alkyl) complexes of Zr and Hf, and is discussed in Chapter 3.

Solution phase isomerization of the bis(amidate) bis(amido) complexes was more pronounced with bulkier groups on the N donors of the amidate ligands. Variable temperature ¹H NMR spectroscopy of **2.16**, **2.23**, and **2.24** support the relative energetic spacing of the geometric isomers of these complexes, where **2.16** has the largest spacing between isomers and demonstrates the least solution phase isomerization.

Bonding interactions determined by DFT calculations for **2.16** support the assignment of bis(amidate) bis(amido) complexes as 16 e⁻ species, where the amido ligands are 4 e⁻ donors, with sp²-hybridized N centers. The π-bonding interactions of the amido ligands for all isomeric forms of **2.16**, **2.23**, and **2.24** are located at the HOMO and HOMO-1 energy levels. In all cases, the LUMO for these species is a vacant d-orbital, which allows for coordination of Lewis bases such as amines. This has important implications for catalytic hydroamination with these complexes, and is discussed in detail in Chapter 5. The amidate bonding interactions for these complexes are located very low in energy in comparison to the frontier orbitals, and suggest that the amidate ligands bind to the Ti center with more electrostatic or ionic bonding character, rather than strictly covalent bonding. This ionic character is instrumental for the unique reactivity that is discussed in Chapters 3 – 5, as it allows these extremely electrophilic metal complexes to approach levels of reactivity for some reactions that are typically only seen with cationic species.

2.5 Conclusions

The amidate ligand set is highly adaptable to the group 4 metals, with novel coordination geometries, dictated largely by the tight bite angle of the amidate ligands. While salt metathesis methods for installing these ligands have been described previously, the products are difficult to isolate, often with disappointing yields.⁸⁶ However, protonolysis methods using tetrakis(amido) and tetrakis(alkyl) starting materials are highly efficient, and are utilized in the synthesis of bis(amidate) bis(amido), tris(amidate) mono(amido), and homoleptic tetrakis(amidate) complexes. Solid-state molecular structure characterization of many of these complexes demonstrates that the amidate ligands are typically bound in a κ^2 -fashion to the metal center, through both the N and O donors.

Given the unsymmetrical nature of the amidate ligand, multiple geometric isomers are possible, and disagreement between solution phase and X-ray crystallographic data suggest that isomer interconversion is possible, and can be observed via variable temperature ¹H NMR spectroscopy. The mechanism of interconversion likely involves κ^1 -intermediates, and experimental evidence supporting this notion exists in the X-ray crystallographic characterization of the mixed κ^1, κ^2 -bis(amidate) bis(amido) pyridine adduct, **2.19**. In general, isomerization can be controlled by modulating the steric bulk on the N donors of the amidate ligands. Despite the hemilability of the amidate ligands, dissociation/exchange in the absence of other donors was not observed for the bis(amidate) bis(amido) complexes.

Density functional theory (DFT) studies, in concert with X-ray crystallography of a series of Ti bis(amidate) bis(amido) complexes (**2.16**, **2.23**, and **2.24**), support sterically controlled geometric isomerization, and are in agreement with variable temperature ¹H NMR spectroscopic studies. The electronic structure of the bis(amidate)-bis(amido) complexes was determined by DFT calculations and supports a strongly ionic bonding character for the amidate ligand set.

The amido complexes in this chapter are reactive precursors for protonolysis reactions to form new amido complexes, such as the anilido complex **2.14**. The bis(amidate) bis(amido) complexes can also react with additional amide proligands to

form tris(amidate) mono(amido) complexes through protonolysis, suggesting the ability to generate mixed amidate complexes for future applications. However, the stability of these species towards disproportionation is limited with very bulky amidate ligands. Insertion of isocyanides into Zr-N amido bonds is also possible (2.22), and the amidate ligands are not affected by this reaction, indicating that these amido complexes are stable for both protonolysis and insertion reactions. Both of these types of reactivity play an important role in the findings reported in the remaining chapters of this thesis.

2.6 Experimental

2.6.1 General Considerations

The general statements presented herein apply to all subsequent chapters in this thesis, and are not reproduced for the sake of space. Except where stated otherwise, all manipulations were performed under an inert atmosphere of dry, oxygen-free dinitrogen using either standard Schlenk or drybox techniques. The work presented was performed in either an MBraun MB150BG-II glovebox (equipped with a dual column purification system and a -35 °C freezer), or an MBraun Labmaster 130 glovebox (equipped with a dual column purification system, a -35 °C freezer, and a parallel synthetic apparatus, capable of controlling the temperature and stir rate of 5 different reaction chambers). Anhydrous hexanes and toluene were purchased from Aldrich, sparged with dry, degassed dinitrogen, and passed through a column of activated alumina and Ridox (or Q-5) catalyst prior to use. Anhydrous benzene, diethyl ether, tetrahydrofuran, and pentane were purchased from Aldrich, sparged with dry, degassed dinitrogen, and purified by passage through an Innovative Technologies SPS-PureSolv-400-4 apparatus. Dimethoxyethane (DME) was purified by distillation from sodium/potassium alloy under reduced pressure, and collected in a sealed flask for later use.

Deuterated NMR solvents were purchased from Cambridge Isotopes Ltd. Deuterated benzene (C_6D_6) and deuterated toluene (C_7D_8) were degassed by successive freeze-pump-thaw cycles, and stored overnight over molecular sieves under an atmosphere of dry dinitrogen prior to use. Deuterated bromobenzene (C_6D_5Br) was

distilled from CaH_2 under vacuum, and stored over molecular sieves under an atmosphere of dry dinitrogen prior to use. Deuterated tetrahydrofuran ($\text{C}_4\text{D}_8\text{O}$) was purified by distillation from sodium/potassium alloy under an atmosphere of dry dinitrogen and stored over molecular sieves prior to use. Deuterated chloroform (CDCl_3) was stored in a darkened flask over molecular sieves prior to use with organic molecules. Deuterated water (D_2O) was used as received. ^1H , $^1\text{H}\{^{31}\text{P}\}$, $^{13}\text{C}\{^1\text{H}\}$, ^{31}P , $^{31}\text{P}\{^1\text{H}\}$, ^{19}F , $^{19}\text{F}\{^1\text{H}\}$, two-dimensional, and NOE spectra were collected on three different Bruker instruments: AV-300 with a 5 mm BBI probe operating at 300.0 MHz for ^1H NMR spectroscopy; AV-400 with a 5 mm inverse BBI probe operating at 400.0 MHz for ^1H NMR spectroscopy; AV-400 with a 5 mm BBI probe operating at 400.0 MHz for ^1H NMR spectroscopy. All three instruments were equipped with cryoprobes capable of variable temperature experiments, ranging between $-150\text{ }^\circ\text{C}$ and $+180\text{ }^\circ\text{C}$. ^1H NMR spectra were referenced to residual protons in deuterated solvents as follows: $\text{C}_6\text{D}_5\text{H}$ (δ 7.15), $\text{C}_7\text{D}_7\text{H}$ (δ 2.09), $\text{C}_4\text{D}_7\text{HO}$ (δ 3.58), CHCl_3 (δ 7.24) with respect to TMS (δ 0.00). ^{31}P NMR spectra were referenced to external $\text{P}(\text{OMe})_3$ (δ 141.0 with respect to 85% H_3PO_4 at δ 0.0). ^{13}C NMR spectra were referenced to (δ 128.39) in deuterated benzene or (δ 77.44) in deuterated chloroform with respect to TMS (δ 0.00). ^{19}F NMR spectra were referenced to external trifluoroacetic acid (δ 0.00).

IR spectra were recorded as KBr pellets on a BOMEM Michelson Series MB-100 FTIR spectrophotometer. UV/vis spectra were recorded on a Perkin Elmer λ 5000 spectrophotometer using air-tight cuvettes. Mass spectra were either collected on an Agilent technologies GCMS equipped with 6890N GC column and a 5793 mass selective detector operating with an electron impact source and quadrupolar detector, or were collected by Mr. M. Lapawa at the University of British Columbia, Department of Chemistry (EIMS on a Kratos MS 50 using a 70 eV electron impact source, unless otherwise stated). Assigned mass clusters for specific ions in the mass spectra show the appropriate isotopic patterns as calculated for the atomic composition of the species. Elemental analyses were performed by Mr. M. Lakha at the University of British Columbia, Department of Chemistry. Due to the air and moisture sensitivity of the metal complexes analyzed, these compounds were handled using glovebox or glovebag techniques during analysis.

Crystallographic details of all solid-state molecular structures are located in Appendix A. All measurements were made on either Rigaku ADSC, Rigaku AFC7, or Bruker X8 Apex CCD area detectors with graphite-monochromated Mo K α radiation. Data sets that were not collected by the author were collected by Dr. Brian O. Patrick. The data were processed⁸⁷ and corrected for Lorentz and polarization effects. The structures were solved by direct methods,⁸⁸ and expanded using Fourier techniques.⁸⁹ All non-hydrogen atoms were refined with anisotropic thermal parameters. Neutral atom scattering factors and anomalous dispersion corrections were taken from the International Tables for X-ray Crystallography.^{90, 91} All structures are visualized as ORTEP-3 depictions.⁹²

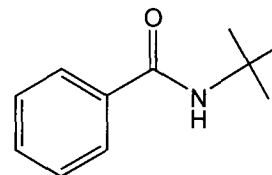
2.6.2 Starting Materials and Reagents

The starting materials listed herein are also utilized in subsequent chapters, and are not reproduced for the sake of space. Wherever particular materials are relevant to individual chapters, details are given regarding the source, synthesis, and purification of these compounds. The following reagents were purchased from Aldrich and purified by distillation: aniline, 2,6-dimethylaniline; 2,6-diisopropylaniline; pyridine; *tert*-butylamine; trimethylsilylchloride; and benzylbromide. The following reagents were purchased from Aldrich and used as received: H₂NCH₂CMe₂CH₂NH₂; benzoyl chloride; trimethylacetyl chloride; triethylamine; NaN(SiMe₃)₂; 1-adamantoyl chloride; benzyl magnesium chloride. Solutions of ⁿBuLi (1.6 M in hexanes) were obtained from Acros Organics and used without further purification. ZrCl₄, TiCl₄, HfCl₄, Ti(NMe₂)₄, Ti(NEt₂)₄, Zr(NMe₂)₄, Zr(NEt₂)₄, and 2,6-dimethylphenylisocyanide were purchased from Strem Chemicals and used without further purification. ZrCl₄(THF)₂,⁹³ TiCl₄(THF)₂,⁹³ Ti(NMe₂)₂Cl₂,⁹⁴ Zr(NMe₂)₂Cl₂(DME),⁹⁵ Zr(CH₂Ph)₄,⁹⁶ and Hf(CH₂Ph)₄,⁹⁶ were prepared via literature methods.

2.6.3 Synthesis

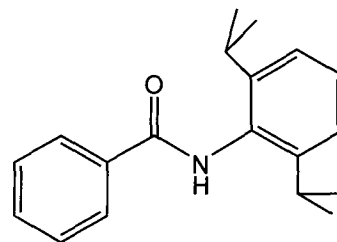
Synthesis of [^tBu(NO)^{Ph}]H, **2.1**

A solution of *tert*-butylamine (7.1 mL, 67.8 mmol) and triethylamine (9.4 mL, 67.8 mmol) in 100 mL of CH₂Cl₂ was cooled to -78 °C prior to dropwise addition of a CH₂Cl₂ solution of benzoyl chloride (6.0 mL, 56.5 mmol). The clear colorless solution was allowed to warm to room temperature while stirring for approximately 2 h. The cloudy white suspension was then extracted with three portions of 1M HCl (3 × 25 mL) until the aqueous washings were acidic. The organic fraction was then extracted with a single 25 mL portion of 1M NaOH, until the aqueous fraction was basic. Finally, the organic fraction was washed with 25 mL of brine and the organic fraction was dried over anhydrous MgSO₄. Gravity filtration of the solution to remove MgSO₄ was performed and excess CH₂Cl₂ was removed by rotary evaporation to give a white powder. The product was purified by recrystallization from a supersaturated toluene solution that was cooled to -15 °C. Colorless crystals of **2.1** were isolated by filtration, ground with a mortar and pestle to a fine white powder, and dried while heating to 75 °C under vacuum in a Schlenk flask to remove air and moisture. The purified product was isolated in 87 % yield (8.74 g). ¹H NMR (CDCl₃, 25 °C, 300 MHz): δ 1.30 (s, 9H, C(CH₃)₃), 5.50 (br, 1H, NH), 7.00-7.10 (m, 3H, *m,p*-Ar-H), 7.65 (d, 2H, ³J_{HH} = 6.6 Hz, *o*-Ar-H). ¹³C{¹H} NMR (CDCl₃, 25 °C, 75 MHz): δ 29.1, 51.6, 127.6, 128.8, 131.2, 137.1, 166.7. IR (KBr/Nujol, cm⁻¹): 1635 (m, C=O), 3326 (w, N-H). EIMS (*m/z*): 177 ([M⁺]). Anal. Calcd for C₁₁H₁₅NO (%): C, 74.54; H, 8.53; N, 7.90. Found: C, 74.77; H, 8.55; N, 7.98.



Synthesis of $[\text{DIPP}(\text{NO})^{\text{Ph}}]\text{H}$, **2.2**

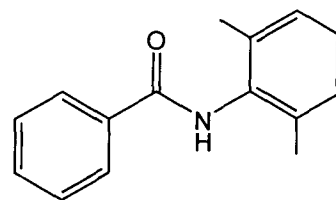
A solution of 2,6-diisopropylaniline (26.6 mL, 141 mmol) and triethylamine (19.7 mL, 141 mmol) in 100 mL of CH_2Cl_2 was cooled to $-78\text{ }^\circ\text{C}$ prior to dropwise addition of a CH_2Cl_2 solution of benzoyl chloride (12.6 mL, 108 mmol). The clear colorless solution was allowed to warm to room



temperature while stirring for approximately 2 h. The cloudy white suspension was then extracted with three portions of 1M HCl ($3 \times 25\text{ mL}$) until the aqueous washings were acidic. The organic fraction was then extracted with a single 25 mL portion of 1M NaOH, until the aqueous fraction was basic. The organic fraction was then washed with 25 mL of brine and the organic fraction was dried over anhydrous MgSO_4 . Gravity filtration of the solution to remove MgSO_4 was performed and excess CH_2Cl_2 was removed by rotary evaporation to give a white powder. The product was purified by recrystallization from a supersaturated toluene solution that was cooled to $-15\text{ }^\circ\text{C}$. Colorless crystals of **2.2** were isolated by filtration, ground with a mortar and pestle to a fine white powder, and dried while heating to $100\text{ }^\circ\text{C}$ under vacuum in a Schlenk flask to remove air and moisture. The purified product was isolated in 53 % yield (16.0 g). ^1H NMR (CDCl_3 , $25\text{ }^\circ\text{C}$, 300 MHz): δ 1.24 (d, 12H, $^3J_{\text{HH}} = 6.9\text{ Hz}$, $\text{CH}(\text{CH}_3)_2$), 3.18 (sept, 2H, $^3J_{\text{HH}} = 6.9\text{ Hz}$, $\text{CH}(\text{CH}_3)_2$), 7.24-7.95 (m, 9H, Ar-H, N-H). $^{13}\text{C}\{^1\text{H}\}$ NMR (CDCl_3 , $25\text{ }^\circ\text{C}$, 75 MHz): δ 23.9, 29.1, 123.8, 127.4, 128.7, 129.0, 131.4, 131.9, 134.8, 146.6, 167.1. EIMS (m/z): 281 ($[\text{M}^+]$). Anal. Calcd for $\text{C}_{19}\text{H}_{23}\text{NO}$ (%): C, 81.10; H, 8.24; N, 4.98. Found: C, 80.62; H, 8.26; N, 4.92.

Synthesis of $[\text{DMP}(\text{NO})^{\text{Ph}}]\text{H}$, **2.3**

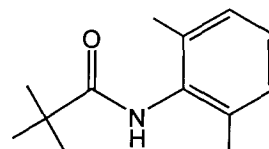
A solution of 2,6-dimethylaniline (11.5 mL, 92.8 mmol) and triethylamine (12.9 mL, 92.8 mmol) in 100 mL of CH_2Cl_2 was cooled to $-78\text{ }^\circ\text{C}$ prior to dropwise addition of a CH_2Cl_2 solution of benzoyl chloride (8.3 mL, 71.4 mmol). The clear, slightly pink solution was allowed to warm to room



temperature while stirring for approximately 3 h. The cloudy white suspension was then extracted with three portions of 1M HCl (3 × 25 mL) until the aqueous washings were acidic. The organic fraction was then extracted with a single 25 mL portion of 1M NaOH, until the aqueous fraction was basic. Finally, the organic fraction was washed with 25 mL of brine and the organic fraction was dried over anhydrous MgSO₄. Gravity filtration of the solution to remove MgSO₄ was performed and excess CH₂Cl₂ was removed by rotary evaporation to give a white powder. The product was purified by recrystallization from a supersaturated toluene solution that was cooled to -15 °C. Colorless crystals of **2.3** were isolated by filtration, ground with a mortar and pestle to a fine white powder, and dried while heating to 70 °C under vacuum in a Schlenk flask to remove air and moisture. The purified product was isolated in 64 % yield (10.3 g). ¹H NMR (CDCl₃, 25 °C, 400 MHz): δ 2.24 (s, 6H, Ph(CH₃)₂), 7.07-7.89 (m, 8H, Ar-H), 7.62 (br, 1H, N-H). ¹³C{¹H} NMR (CDCl₃, 25 °C, 75 MHz): δ 18.4, 127.2, 127.3, 128.1, 128.6, 131.6, 134.0, 134.4, 135.6, 165.9. EIMS (*m/z*): 225 ([M⁺]). Anal. Calcd for C₁₅H₁₅NO (%): C, 79.97; H, 6.71; N, 6.22. Found: C, 80.24; H, 6.72; N, 6.20.

Synthesis of [^{DMP}(NO)^{tBu}]H, **2.4**

A solution of 2,6-dimethylaniline (5.1 mL, 41.5 mmol) and triethylamine (5.8 mL, 41.5 mmol) in 50 mL of CH₂Cl₂ was cooled to -78 °C prior to dropwise addition of a CH₂Cl₂ solution of trimethylacetyl chloride (5.1 mL, 41.5 mmol). The clear

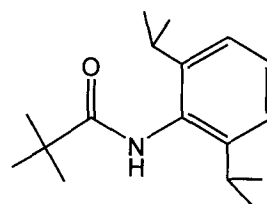


slightly pink solution was allowed to warm to room temperature while stirring for approximately 3 h. The cloudy white suspension was then extracted with three portions of 1M HCl (3 × 25 mL) until the aqueous washings were acidic. The organic fraction was then extracted with a single 25 mL portion of 1M NaOH, until the aqueous fraction was basic. Finally, the organic fraction was washed with 25 mL of brine and the organic fraction was dried over anhydrous MgSO₄. Gravity filtration of the solution to remove MgSO₄ was performed and excess CH₂Cl₂ was removed by rotary evaporation to give a white powder. The product was purified by recrystallization from a supersaturated toluene solution that was cooled to -15 °C. Colorless crystals of **2.4** were isolated by

filtration, ground with a mortar and pestle to a fine white powder, and dried while heating to 100 °C under vacuum in a Schlenk flask to remove air and moisture. The purified product was isolated in 82 % yield (6.98 g). ^1H NMR (CDCl_3 , 25 °C, 300 MHz): δ 1.30 (s, 9H, $\text{C}(\text{CH}_3)_3$), 2.14 (s, 6H, $\text{Ar}(\text{CH}_3)_2$), 7.04 (m, 3H, Ar-H), 7.13 (br, 1H, N-H). $^{13}\text{C}\{^1\text{H}\}$ NMR (CDCl_3 , 25 °C, 75 MHz): δ 18.3, 27.8, 39.3, 127.0, 128.1, 134.3, 135.6, 179.7. EIMS (m/z): 205 ($[\text{M}^+]$). Anal. Calcd for $\text{C}_{13}\text{H}_{19}\text{NO}$ (%): C, 76.06; H, 9.33; N, 6.82. Found: C, 75.94; H, 9.11; N, 6.83.

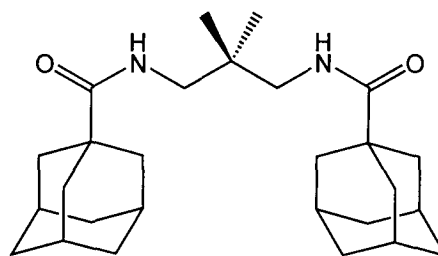
Synthesis of $[\text{DIPP}(\text{NO})^{\text{tBu}}]\text{H}$, **2.5**

A solution of 2,6-diisopropylaniline (10.7 mL, 56.4 mmol) and triethylamine (8.0 mL, 56.4 mmol) in 50 mL of CH_2Cl_2 was cooled to -78 °C prior to dropwise addition of a CH_2Cl_2 solution of trimethylacetyl chloride (6.9 mL, 56.4 mol). The clear pale yellow solution was allowed to warm to room temperature while stirring overnight. The cloudy yellow suspension was then extracted with three portions of 1M HCl (3×25 mL) until the aqueous washings were acidic. The organic fraction was then extracted with a single 25 mL portion of 1M NaOH, until the aqueous fraction was basic. The organic fraction was then washed with 25 mL of brine and the organic fraction was dried over anhydrous MgSO_4 . Gravity filtration of the solution to remove MgSO_4 was performed and excess CH_2Cl_2 was removed by rotary evaporation to give a white powder. The product was purified by recrystallization from a supersaturated toluene solution that was cooled to -15 °C. Colorless crystals of **2.5** were isolated by filtration, ground with a mortar and pestle to a fine white powder, and dried while heating to 100 °C under vacuum in a Schlenk flask to remove air and moisture. The purified product was isolated in 58 % yield (8.54 g). ^1H NMR (CDCl_3 , 25 °C, 300 MHz): δ 1.21 (d, 12H, $^3J_{\text{HH}} = 6.9$ Hz, $\text{CH}(\text{CH}_3)_2$), 1.38 (s, 9H, $\text{C}(\text{CH}_3)_3$), 3.03 (sept, 2H, $^3J_{\text{HH}} = 6.9$ Hz, $\text{CH}(\text{CH}_3)_2$), 6.86 (br, 1H, N-H), 7.18 (d, 2H, $^3J_{\text{HH}} = 7.7$ Hz, $m\text{-Ar-H}$), 7.29 (m, 1H, $p\text{-Ar-H}$). $^{13}\text{C}\{^1\text{H}\}$ NMR (CDCl_3 , 25 °C, 75 MHz): δ 23.6, 27.9, 28.8, 39.3, 123.4, 128.2, 131.6, 146.3, 177.3. EIMS (m/z): 261 ($[\text{M}^+]$). Anal. Calcd for $\text{C}_{17}\text{H}_{27}\text{NO}$ (%): C, 78.11; H, 10.41; N, 5.36. Found: C, 78.22; H, 10.17; N, 5.42.



Synthesis of $\text{Ad}[\text{O}_2\text{N}_2]\text{H}_2$, **2.6**

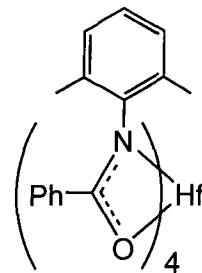
A solution of 1,3-diamino-2,2-dimethylpropane (2.4 mL, 20.1 mmol) and triethylamine (5.6 mL, 40.3 mol) in 100 mL of CH_2Cl_2 was cooled to $-78\text{ }^\circ\text{C}$ prior to dropwise addition of a CH_2Cl_2 solution of 1-adamantane carbonyl chloride (7.98 g, 40.3



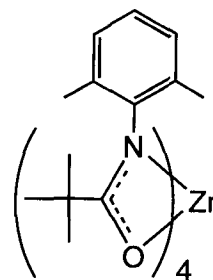
mmol). The clear colorless solution was allowed to warm to room temperature while stirring overnight. The cloudy white suspension was then extracted with three portions of 1M HCl ($3 \times 25\text{ mL}$) until the aqueous washings were acidic. The organic fraction was then extracted with a single 25 mL portion of 1M NaOH, until the aqueous fraction was basic. Finally, the organic fraction was washed with 25 mL of brine and the organic fraction was dried over anhydrous MgSO_4 . Gravity filtration of the solution to remove MgSO_4 was performed, and excess CH_2Cl_2 was removed by rotary evaporation to give a white powder. The product was purified by recrystallization from a supersaturated toluene solution that was cooled to $-15\text{ }^\circ\text{C}$. A white powder was isolated by filtration, ground with a mortar and pestle to a fine white powder, and dried while heating to $120\text{ }^\circ\text{C}$ under vacuum overnight in a Schlenk flask to remove air and moisture. Due to the increased ability of **2.6** to hydrogen bond with water, higher temperatures were used to remove traces of moisture. The purified product was isolated in 67 % yield (5.75 g). ^1H NMR (CDCl_3 , $25\text{ }^\circ\text{C}$, 300 MHz): δ 0.80 (s, 6H, $\text{NCH}_2\text{C}(\text{CH}_3)_2\text{CH}_2\text{N}$), 1.70 (br, 12H, Ad- $(\text{CH}(\text{CH}_2)\text{CH})_3$), 1.86 (d, 12H, $^3J_{\text{HH}} = 2.8\text{ Hz}$, Ad- $\text{C}(\text{CH}_2)_3$), 2.02 (br, 6H, Ad- $(\text{CH})_3$), 2.91 (d, 4H, $^3J_{\text{HH}} = 6.7\text{ Hz}$, $\text{HNCH}_2\text{C}(\text{CH}_3)_2\text{CH}_2\text{NH}$), 6.54 (t, 2H, $^3J_{\text{HH}} = 6.2\text{ Hz}$, NH). $^{13}\text{C}\{^1\text{H}\}$ NMR (CDCl_3 , $25\text{ }^\circ\text{C}$, 75 MHz): δ 23.5, 28.2, 36.5, 39.3, 40.8, 44.9, 178.7 (no signal observed for quaternary C of adamantyl group). CIMS (m/z): 427 ($[\text{M}+1]^+$). Anal. Calcd for $\text{C}_{27}\text{H}_{42}\text{N}_2\text{O}_2$ (%): C, 76.01; H, 9.92; N, 6.57. Found: C, 75.69; H, 9.96; N, 6.70.

Synthesis of $[\text{DMP}(\text{NO})^{\text{Ph}}]_4\text{Hf}$, **2.8**

In a foil wrapped 500 mL round-bottomed Schlenk flask equipped with a stir bar, 3.32 g (14.7 mmol) of **2.3** was combined with 2.00 g (3.68 mmol) of $\text{Hf}(\text{CH}_2\text{Ph})_4$. To this flask was added 100 mL of THF which had been cooled to $-78\text{ }^\circ\text{C}$. The cloudy white mixture was stirred for 2 hours while allowing to warm to room temperature. The clear, colorless solution was then concentrated to dryness *in vacuo* to give a white solid residue. The crude material was washed with approximately 50 mL of hexanes and dried *in vacuo* to yield 3.72 g of a white powder (94 % yield). Single clear colorless crystals suitable for X-ray crystallographic analysis were grown from a saturated hexanes solution at room temperature. ^1H NMR (C_6D_6 , $25\text{ }^\circ\text{C}$, 300 MHz): δ 2.51 (s, 24H, $\text{Ar}(\text{CH}_3)_2$), 6.77-6.87 (m, 24H, Ar-H), 7.70 (d, 8H, $^3J_{\text{HH}} = 6.5\text{ Hz}$, Ar-H). $^{13}\text{C}\{^1\text{H}\}$ NMR (C_6D_6 , $25\text{ }^\circ\text{C}$, 75 MHz): δ 19.8, 125.3, 128.4, 128.8, 129.3, 132.0, 133.4, 134.5, 143.4, 179.2. EIMS (m/z): 1076 ($[\text{M}^+]$), 852 ($[\text{M}^+] - [\text{DMP}(\text{NO})^{\text{Ph}}]$). Anal. Calcd for $\text{C}_{60}\text{H}_{56}\text{N}_4\text{O}_4\text{Hf}$ (%): C, 67.00; H, 5.25; N, 5.21. Found: C, 67.26; H, 5.37; N, 5.09.

Synthesis of $[\text{DMP}(\text{NO})^{\text{tBu}}]_4\text{Zr}$, **2.9**

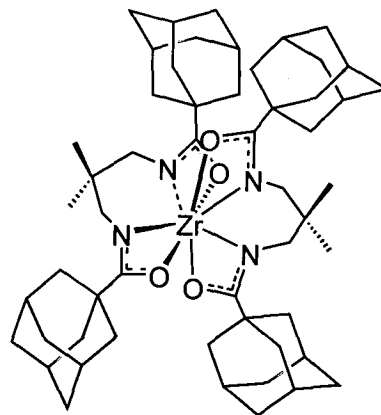
In a foil wrapped 250 mL round-bottomed Schlenk flask equipped with a stir bar, 770 mg (3.76 mmol) of **2.4** was combined with 250 mg (0.939 mmol) of $\text{Zr}(\text{NMe}_2)_4$. To this flask was added 50 mL of THF which had been cooled to $-78\text{ }^\circ\text{C}$. The cloudy white mixture was stirred while allowing to warm to room temperature overnight. The clear, colorless solution was then concentrated to dryness *in vacuo* to give a white solid residue. The crude material was triturated with approximately 30 mL of hexanes, and the product was isolated by filtration and dried *in vacuo* to yield 720 mg of a white powder (85 % yield). Single clear colorless crystals suitable for X-ray crystallographic analysis were grown from a saturated hexanes solution at room temperature. ^1H NMR (C_6D_6 , $25\text{ }^\circ\text{C}$, 300 MHz): δ 1.02 (s, 36H, $\text{C}(\text{CH}_3)_3$) 2.40 (s, 24H,



$\text{Ar}(\text{CH}_3)_2$, 6.62-6.69 (m, 12H, Ar-H). $^{13}\text{C}\{^1\text{H}\}$ NMR (C_6D_6 , 25 °C, 100 MHz): δ 20.5, 28.3, 41.6, 124.7, 128.0, 132.8, 143.3, 189.9.

Synthesis of $^{\text{Ad}}[\text{O}_2\text{N}_2]_2\text{Zr}$, **2.10**

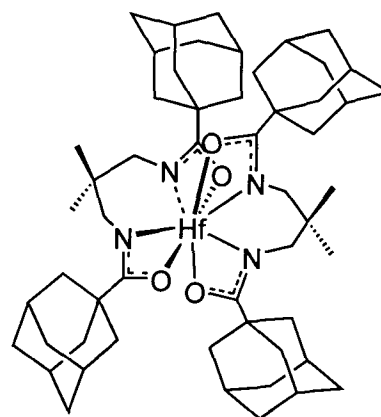
In a 100 mL round-bottomed Schlenk flask equipped with a stir bar, 250 mg (0.587 mmol) of **2.6** was combined with 78 mg (0.293 mmol) of $\text{Zr}(\text{NMe}_2)_4$. To this flask was added 30 mL of THF which had been cooled to -78 °C. The cloudy white mixture was stirred overnight while allowing to warm to room temperature. The clear, colorless solution was then concentrated to dryness to give a white solid residue. The crude material



was triturated with 10 mL of hexanes dried *in vacuo* to give 220 mg of a white powder (80 % yield). Single clear colorless crystals suitable for X-ray crystallographic analysis were grown from a saturated toluene solution at room temperature. ^1H NMR (C_6D_6 , 25 °C, 300 MHz): δ 1.28 (s, 12H, $\text{C}(\text{CH}_3)_2$), 1.60 (m, 24H, $\text{Ad}-(\text{CH}(\text{CH}_2)\text{CH})_3$), 1.90 (br, 12H, $\text{Ad}-(\text{CH})_3$), 2.20 (br, 24H, $\text{Ad}-\text{C}(\text{CH}_2)_3$), 3.63 (s, 8H, $\text{NCH}_2\text{C}(\text{CH}_3)_2\text{CH}_2\text{N}$). $^{13}\text{C}\{^1\text{H}\}$ NMR (C_6D_6 , 25 °C, 75 MHz): δ 25.9, 29.1, 36.8, 37.5, 39.0, 43.0, 56.9, 190.2. EIMS (m/z): 938 ($[\text{M}^+]$), 803 ($[\text{M}^+] - \text{Ad}$).

Synthesis of $^{\text{Ad}}[\text{O}_2\text{N}_2]_2\text{Hf}$, **2.11**

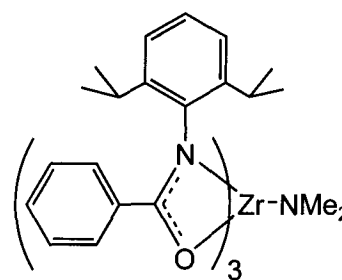
In a foil wrapped 100 mL round-bottomed Schlenk flask equipped with a stir bar, 750 mg (1.76 mmol) of **2.6** was combined with 478 mg (0.880 mmol) of $\text{Hf}(\text{CH}_2\text{Ph})_4$. To this flask was added 50 mL of THF which had been cooled to -78 °C. The cloudy white reaction mixture was then stirred overnight while allowing to warm to room temperature. The clear, pale yellow solution was then concentrated to dryness *in vacuo* to give a pale yellow



solid residue. The crude material was washed with 25 mL of hexanes and filtered to isolate 730 mg of an off-white powder (81 % yield). Single crystals suitable for X-ray crystallographic analysis were grown from a saturated toluene solution at room temperature. ^1H NMR (C_6D_6 , 25 °C, 300 MHz): δ 1.27 (s, 12H, $\text{C}(\text{CH}_3)_2$), 1.56-1.66 (br, 24H, $\text{Ad}-(\text{CH}(\text{CH}_2)\text{CH}_3)$), 1.90-1.95 (br, 12H, $\text{Ad}-(\text{CH})_3$), 2.20 (br, 24H, $\text{Ad}-\text{C}(\text{CH}_2)_3$), 3.67 (s, 8H, $\text{NCH}_2\text{C}(\text{CH}_3)_2\text{CH}_2\text{N}$). $^{13}\text{C}\{^1\text{H}\}$ NMR (C_6D_6 , 25 °C, 75 MHz): δ 25.3, 28.3, 36.8, 38.3, 39.5, 42.6, 56.1, 188.9. EIMS (m/z): 1028 ($[\text{M}^+]$), 893 ($[\text{M}^+] - \text{Ad}$). Anal. Calcd for $\text{C}_{54}\text{H}_{80}\text{N}_4\text{O}_4\text{Hf}$ (%): C, 63.11; H, 7.85; N, 5.45. Found: C, 63.50; H, 7.72; N, 5.58.

Synthesis of $[\text{DIPP}(\text{NO})^{\text{Ph}}]_3\text{ZrNMe}_2$, **2.12**

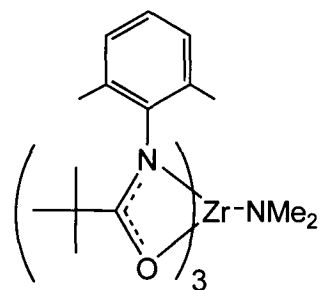
In a 250 mL round bottomed Schlenk flask, 3.15 g (11.2 mmol) of **2.2** was dissolved in approximately 100 mL of Et_2O and cooled to -78 °C while stirring. In a separate flask, 1.00 g (3.73 mmol) of $\text{Zr}(\text{NMe}_2)_4$ was dissolved in about 30 mL of Et_2O prior to addition to the solution of **2.2** via cannula. This solution was allowed to warm to



room temperature overnight while stirring, resulting in a clear colorless solution. Excess Et_2O was removed *in vacuo* to generate a white solid residue. The crude product was dissolved in 20 mL of pentane and filtered through CeliteTM to remove traces of unreacted proligand. The solution was concentrated to dryness and the product was isolated in 86 % yield (3.13 g). ^1H NMR (C_6D_6 , 25 °C, 300 MHz): δ 0.88 (d, 18H, $^3J_{\text{HH}} = 6.4$ Hz, $\text{CH}(\text{CH}_3)_2$), 1.07 (d, 6H, $^3J_{\text{HH}} = 6.6$ Hz, $\text{C}(\text{CH}_3)_2$), 1.26 (d, 12H, $^3J_{\text{HH}} = 6.7$ Hz, $\text{C}(\text{CH}_3)_2$), 3.29 (s, 6H, $\text{N}(\text{CH}_3)_2$), 3.75 (sept, 6H, $^3J_{\text{HH}} = 6.7$ Hz, $\text{CH}(\text{CH}_3)_2$), 6.72-7.60 (m, 24 H total, Ar-H). $^{13}\text{C}\{^1\text{H}\}$ NMR (C_6D_6 , 25 °C, 75 MHz): δ 24.9, 25.5, 28.7, 43.7, 124.8, 126.4, 128.3, 130.8, 131.9, 132.9, 142.6, 143.2, 178.1. EIMS (m/z): 930 ($[\text{M}^+] - \text{NMe}_2$). Anal. Calcd for $\text{C}_{59}\text{H}_{72}\text{N}_4\text{O}_3\text{Zr}$ (%): C, 72.57; H, 7.43; N, 5.74. Found: C, 71.47; H, 8.91; N, 5.20.

Synthesis of $[\text{DMP}(\text{NO})^{\text{tBu}}]_3\text{ZrNMe}_2$, **2.13**

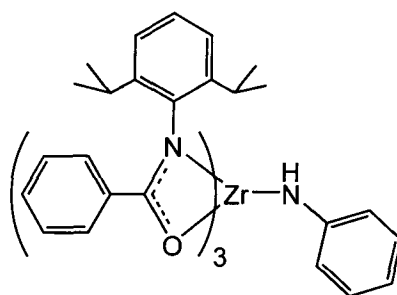
In a 250 mL round bottomed Schlenk flask, 2.30 g (11.2 mmol) of **2.4** was slurried in approximately 120 mL of toluene, which was cooled to $-78\text{ }^\circ\text{C}$. In a 50 mL Schlenk flask, 1.00 g (3.75 mmol) of $\text{Zr}(\text{NMe}_2)_4$ was dissolved in 25 mL of toluene, which was transferred via cannula into the slurry of **2.4**. The reaction mixture was allowed to warm to



room temperature overnight while stirring, resulting in a clear colorless solution. Excess solvent was removed *in vacuo* to give a slightly off-white waxy solid. The crude product was dissolved in 25 mL of pentane and filtered through CeliteTM to remove traces of unreacted proligand. The solution was concentrated to dryness, to give 89 % yield (2.48 g) of **2.13**. ^1H NMR (C_6D_6 , $25\text{ }^\circ\text{C}$, 300 MHz): δ 1.02 (s, 27H, $\text{C}(\text{CH}_3)_3$), 2.31 (br s, 18H, $\text{Ph}(\text{CH}_3)_2$), 2.96 (s, 6H, $\text{N}(\text{CH}_3)_2$), 6.78 (m, 9H, Ar-H). $^{13}\text{C}\{^1\text{H}\}$ NMR (C_6D_6 , $25\text{ }^\circ\text{C}$, 75 MHz): δ 19.6, 27.8, 41.3, 43.2, 124.3, 127.8, 132.4, 143.7, 189.6.

Synthesis of $[\text{DIPP}(\text{NO})^{\text{Ph}}]_3\text{ZrNHPh}$, **2.14**

In a 250 mL round bottomed Schlenk flask, 1.00 g (1.35 mmol) of **2.20** was dissolved in 100 mL Et_2O and cooled to $-78\text{ }^\circ\text{C}$. To this flask was added via syringe 0.1 mL (1.35 mmol) of aniline which had been dissolved in 10 mL of Et_2O . This solution was allowed to warm to room temperature overnight while stirring, resulting in a bright

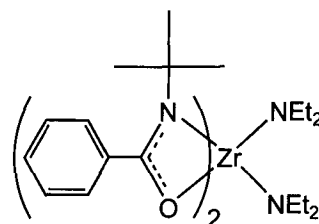


yellow solution. Excess Et_2O was removed *in vacuo* to generate a yellow solid residue. The crude product was dissolved in 15 mL of pentane and filtered through CeliteTM to remove a small amount of pale yellow insoluble material. The solution was concentrated to dryness, resulting in 700 mg (51 % yield) of bright yellow **2.14**. Single crystals were grown from a saturated toluene solution at room temperature. ^1H NMR (C_6D_6 , $25\text{ }^\circ\text{C}$, 300 MHz): δ -0.08 (d, 3H, $^3J_{\text{HH}} = 6.7\text{ Hz}$, $\text{CH}(\text{CH}_3)_2$), 0.18 (d, 3H, $^3J_{\text{HH}} = 6.5\text{ Hz}$, $\text{CH}(\text{CH}_3)_2$), 0.24 (d, 3H, $^3J_{\text{HH}} = 6.6\text{ Hz}$, $\text{CH}(\text{CH}_3)_2$), 0.48 (d, 3H, $^3J_{\text{HH}} = 6.8\text{ Hz}$,

CH(CH₃)₂), 0.59 (d, 3H, ³J_{HH} = 6.5 Hz, CH(CH₃)₂), 0.82 (d, 3H, ³J_{HH} = 6.6 Hz, CH(CH₃)₂), 0.89 (d, 3H, ³J_{HH} = 6.5 Hz, CH(CH₃)₂), 1.08 (d, 3H, ³J_{HH} = 6.5 Hz, CH(CH₃)₂), 1.14 (d, 3H, ³J_{HH} = 6.7 Hz, CH(CH₃)₂), 1.30 (d, 3H, ³J_{HH} = 6.5 Hz, CH(CH₃)₂), 1.48 (d, 3H, ³J_{HH} = 6.7 Hz, CH(CH₃)₂), 1.81 (d, 3H, ³J_{HH} = 6.8 Hz, CH(CH₃)₂), 2.69 (sept, 1H, ³J_{HH} = 6.8 Hz, CH(CH₃)₂), 3.21 (sept, 1H, ³J_{HH} = 6.8 Hz, CH(CH₃)₂), 3.58 (sept, 1H, ³J_{HH} = 6.9 Hz, CH(CH₃)₂), 3.60 (sept, 1H, ³J_{HH} = 6.7 Hz, CH(CH₃)₂), 3.69 (br, 1H, CH(CH₃)₂), 4.54 (sept, 1H, ³J_{HH} = 7.6 Hz, CH(CH₃)₂), 6.57-7.71 (m, 29H, Ar-H), 8.15 (s, 1H, Zr-NH). EIMS (*m/z*): 930 ([M⁺] - NHPH).

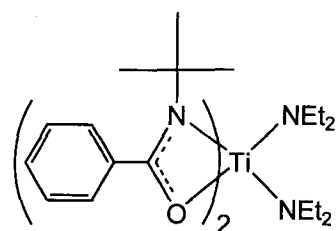
Synthesis of [^tBu(NO)^{Ph}]₂Zr(NEt₂)₂, **2.15**

In a 50 mL round-bottomed Schlenk flask equipped with a stir bar, 4.18 mL (11.3 mmol) of Zr(NEt₂)₄ was dissolved in 10 mL of toluene. In a separate 50 mL round bottomed Schlenk flask, 4.00 g (22.6 mmol) of **2.1** was slurried in 25 mL of toluene at -78 °C. The solution of Zr(NEt₂)₄ was transferred by cannula into the solution of **2.1**. The resulting yellow solution was stirred while warming to room temperature. The clear yellow-orange reaction mixture was evaporated to dryness *in vacuo*, resulting in an orange solid, which was dissolved in hexanes and filtered through CeliteTM to remove contaminants. The hexanes soluble fraction was concentrated to dryness, and the oily yellow-orange solid obtained was subsequently dissolved and triturated in pentane. Removal of pentane *in vacuo* gave a yellow-orange powder in 80% yield (5.31 g). Single crystals suitable for X-ray crystallographic analysis were grown from a saturated 1:1 toluene/hexanes mixture at -37 °C. ¹H NMR (C₆D₆, 25 °C, 400 MHz): δ 1.26 (s, 18 H, C(CH₃)₃), 1.26 (t, 12H, ³J_{HH} = 6.7 Hz, N(CH₂CH₃)₂), 3.78 (q, 8H, ³J_{HH} = 6.7 Hz, N(CH₂CH₃)₂), 7.03-7.06 (m, 6H, Ar-H), 7.39 (d, 4H, ³J_{HH} = 9.5 Hz, Ar-H). ¹³C{¹H} NMR (CDCl₃, 25 °C, 75 MHz): δ 24.00, 37.50, 47.20, 127.50, 129.00, 132.00, 134.55, 168.50. IR (KBr/Nujol, cm⁻¹): 1636 (m, CO). EIMS (*m/z*): 514 ([M⁺] - NEt₂). Anal. Calcd for C₃₀H₄₈N₄O₂Zr (%): C, 61.28; H, 8.23; N, 9.53. Found: C, 58.12; H, 8.25; N, 9.69.



Synthesis of $[\text{tBu}(\text{NO})^{\text{Ph}}]_2\text{Ti}(\text{NEt}_2)_2$, **2.16**

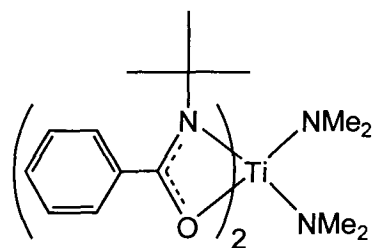
In a 250 mL round-bottomed Schlenk flask equipped with a stir bar, 600 mg (3.39 mmol) of **2.1** was slurried in 60 mL of Et_2O and cooled to $-78\text{ }^\circ\text{C}$. In a separate 100 mL tube Schlenk flask $\text{Ti}(\text{NEt}_2)_4$ (570 mg, 1.69 mmol) was dissolved in 50 mL of Et_2O and cooled to $-78\text{ }^\circ\text{C}$. The solution of $\text{Ti}(\text{NEt}_2)_4$ was



added via cannula transfer to the slurry of **2.1**, and the resulting red-orange mixture was stirred and allowed to warm to room temperature for 5 hours. Excess Et_2O was removed *in vacuo* and the crude product was taken up in hexanes, filtered through CeliteTM, and excess hexanes was removed *in vacuo*. A dark red microcrystalline solid was isolated in 82% yield (755 mg). Single crystals suitable for X-ray crystallographic analysis were grown from a saturated 1:1 toluene/hexanes mixture at $-37\text{ }^\circ\text{C}$. ^1H NMR (C_6D_6 , $25\text{ }^\circ\text{C}$, 300 MHz): δ 1.38 (s, 18H, $\text{C}(\text{CH}_3)_3$), 1.30 (t, 12H, $^3J_{\text{HH}} = 6.9\text{ Hz}$, $\text{N}(\text{CH}_2\text{CH}_3)_2$), 4.17 (q, 8H, $^3J_{\text{HH}} = 6.7\text{ Hz}$, $\text{N}(\text{CH}_2\text{CH}_3)_2$), 7.15-7.23 (m, 6H, Ar-H), 7.50 (d, 4H, $^3J_{\text{HH}} = 6.7\text{ Hz}$, Ar-H). IR (KBr/Nujol, cm^{-1}): 1637 (m, CO). EIMS (m/z): 472 ($[\text{M}^+] - \text{NEt}_2$), 400 ($[\text{M}^+] - 2\text{NEt}_2$). Anal. Calcd for $\text{C}_{30}\text{H}_{48}\text{N}_4\text{O}_2\text{Ti}$ (%): C, 66.16; H, 8.88; N, 10.29. Found: C, 65.76; H, 8.77; N, 10.39.

Synthesis of $[\text{tBu}(\text{NO})^{\text{Ph}}]_2\text{Ti}(\text{NMe}_2)_2$, **2.17**

In a 250 mL round-bottomed Schlenk flask equipped with a stir bar, 8.00 g (45.2 mmol) of **2.1** was slurried in 100 mL of Et_2O and cooled to $-78\text{ }^\circ\text{C}$. In a separate 100 mL tube Schlenk flask $\text{Ti}(\text{NMe}_2)_4$ (5.07 g, 22.6 mmol) was dissolved in 50 mL of Et_2O and cooled to $-78\text{ }^\circ\text{C}$. The solution of

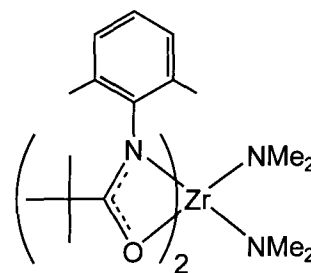


$\text{Ti}(\text{NMe}_2)_4$ was added via cannula transfer to the slurry of **2.1**, and the resulting red-orange mixture was stirred and allowed to warm to room temperature for 3 hours. Excess Et_2O was removed *in vacuo* and the crude product was taken up in hexanes, filtered through CeliteTM, and excess hexanes was removed *in vacuo*. A dark red microcrystalline solid was isolated in 75% yield (8.25 g). Single crystals suitable for X-

ray crystallographic analysis were grown from a saturated 1:1 hexanes solution at room temperature. ^1H NMR (C_6D_6 , 25 °C, 300 MHz): δ 1.28 (s, 18H, $\text{C}(\text{CH}_3)_3$), 3.62 (s, 12H, $\text{N}(\text{CH}_3)_2$), 7.04-7.10 (m, 6H, Ar-H), 7.36-7.39 (m, 4H, Ar-H). $^{13}\text{C}\{^1\text{H}\}$ NMR (CDCl_3 , 25 °C, 75 MHz): δ 32.5, 47.1, 53.2, 127.4, 128.4, 129.8, 139.3, 175.3. EIMS (m/z): 488 ($[\text{M}^+]$), 444 ($[\text{M}^+] - \text{NMe}_2$), 400 ($[\text{M}^+] - 2\text{NMe}_2$). Anal. Calcd for $\text{C}_{26}\text{H}_{40}\text{N}_4\text{O}_2\text{Ti}$ (%): C, 63.93; H, 8.25; N, 11.47. Found: C, 63.72; H, 8.26; N, 11.10.

Synthesis of $[\text{DMP}(\text{NO})^{\text{tBu}}]_2\text{Zr}(\text{NMe}_2)_2$, **2.18**

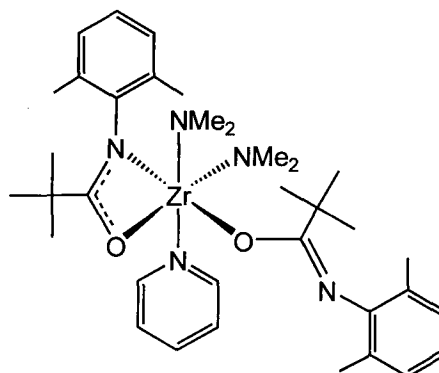
In a 500 mL round-bottomed Schlenk flask equipped with a stir bar, 6.14 g (29.9 mmol) of **2.4** was combined with 4.00 g (15.0 mmol) of $\text{Zr}(\text{NMe}_2)_4$. To this flask was added 150 mL of THF which had been cooled to -78 °C. The cloudy white reaction mixture was then stirred overnight while allowing to warm to room temperature. The clear, colorless solution was



then concentrated to dryness *in vacuo* to give a white solid residue. The crude material was dissolved in 70 mL of pentane and filtered through CeliteTM to remove impurities. The pentane solution was concentrated to approximately 10 mL and cooled to -37 °C. The white precipitate was isolated in 75 % yield (6.55 g) by filtration and dried *in vacuo*. Single crystals suitable for X-ray crystallographic analysis were grown from a saturated pentane solution at room temperature. ^1H NMR (C_6D_6 , 25 °C, 400 MHz): δ 1.03 (s, 18H, $\text{C}(\text{CH}_3)_3$), 2.12 (s, 12H, $\text{Ph}(\text{CH}_3)_2$), 2.93 (s, 12H, $\text{N}(\text{CH}_3)_2$), 6.86-6.92 (m, 6H, Ar-H). $^{13}\text{C}\{^1\text{H}\}$ NMR (C_7D_8 , 25 °C, 100 MHz): δ 18.6, 27.8, 41.1, 41.8, 124.3, 127.9, 131.7, 144.3, 187.1. EIMS (m/z): 586 ($[\text{M}^+]$), 542 ($[\text{M}^+] - \text{NMe}_2$), 498 ($[\text{M}^+] - 2\text{NMe}_2$). Anal. Calcd for $\text{C}_{30}\text{H}_{48}\text{N}_4\text{O}_2\text{Zr}$ (%): C, 61.28; H, 8.23; N, 9.53. Found: C, 61.14; H, 8.47; N, 9.43.

Synthesis of $\kappa^2\text{-}[\text{DMP}(\text{NO})^{\text{tBu}}]\text{-}\kappa^1\text{-}[\text{DMP}(\text{NO})^{\text{tBu}}]\text{Zr}(\text{NMe}_2)_2(\text{Py})$, **2.19**

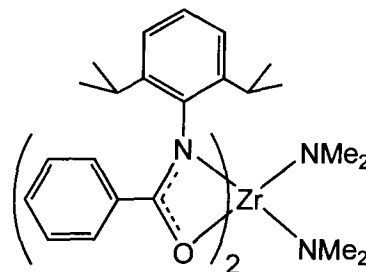
In a 25 mL vial equipped with a stir bar, in a glovebox, 500 mg (0.853 mmol) of **2.18** was dissolved in approximately 15 mL of pentane and stirred at room temperature. In a 5 mL vial 67 mg (0.853 mmol) of Py was dissolved in approximately 3 mL of pentane and added to the stirring solution of **2.18**. The clear colorless solution was filtered



through CeliteTM and concentrated to approximately 3 mL, and an off-white microcrystalline solid was isolated by filtration and dried *in vacuo*. Yield = 79 % (450 mg). Colorless single crystals for X-ray analysis were grown from a saturated pentane solution. ¹H NMR (C₆D₆, 25 °C, 300 MHz): δ 1.03 (s, 18H, C(CH₃)₃), 2.12 (br, 12H, Ph(CH₃)₂), 2.78-2.93 (br, 12H, N(CH₃)₂), 6.63-6.89 (m, 9H, Ar-H, Py-*m,p*-H), 8.46 (d, 2H, ³J_{HH} = 4.3 Hz, Py-*o*-H). ¹³C{¹H} NMR (C₆D₅Br, 25 °C, 100 MHz): δ 17.0, 17.3, 26.7, 28.0, 37.7, 39.7, 40.7, 119.6, 122.6, 122.9, 126.5, 126.8, 135.2, 142.8, 147.9, 148.8, 166.6, 182.7, 185.2. EIMS (*m/z*): 586 ([M⁺] - Py), 542 ([M⁺] - Py - NMe₂), 498 ([M⁺] - Py - 2NMe₂). Anal. Calcd for C₃₅H₅₃N₅O₂Zr (%): C, 63.02; H, 8.01; N, 10.50. Found: C, 61.93; H, 7.81; N, 10.00.

Synthesis of $[\text{DIPP}(\text{NO})^{\text{Ph}}]_2\text{Zr}(\text{NMe}_2)_2$, **2.20**

In a 100 mL round-bottomed Schlenk flask 2.0 g (7.49 mmol) of Zr(NMe₂)₄ was dissolved in approximately 25 mL of Et₂O. In a separate 250 mL round-bottomed Schlenk flask, 4.21 g (14.9 mmol) of **2.2** was slurried in approximately 75 mL of Et₂O. The ligand slurry was stirred and cooled to -78 °C using a dry-ice isopropanol

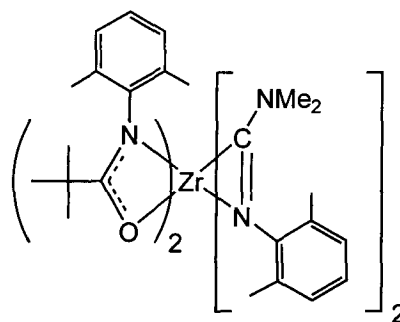


bath. The ethereal Zr(NMe₂)₄ solution was transferred via cannula into the ligand slurry. The reaction mixture was allowed to warm to room temperature overnight, during which time the solution became clear and turned a pale yellow color. Excess Et₂O was removed

in situ to afford a pale yellow solid. The crude product was dissolved in hexanes and filtered through Celite™ to remove insoluble impurities. The pale yellow filtrate was concentrated to dryness, resulting in a pale yellow solid isolated in 92 % yield (5.09 g). Generally, no further purification was required; however, recrystallization from concentrated hexanes or pentane solutions resulted in analytically pure product in moderate yields. ¹H NMR (C₆D₆, 25 °C, 300 MHz): δ 0.91 (d, 12H, ³J_{HH} = 6.8 Hz, CH(CH₃)₂), 1.21 (d, 12H, ³J_{HH} = 6.8 Hz, CH(CH₃)₂), 3.11 (s, 12H, N(CH₃)₂), 3.49 (sept, 4H, ³J_{HH} = 6.8 Hz, CH(CH₃)₂), 6.83-6.92 (m, 6H, Ar-H), 7.15 (br, 6H, Ar-H), 7.75 (d, 4H, ³J_{HH} = 6.8 Hz, Ar-H). ¹³C{¹H} NMR (C₇D₈, 25 °C, 75 MHz): δ 24.8, 28.7, 42.4, 124.5, 124.7, 126.3, 128.3, 130.8, 132.1, 133.1, 142.5, 177.7. EIMS (*m/z*): 738 ([M⁺]), 694 ([M⁺] – NMe₂), 650 ([M⁺] – 2NMe₂). Anal. Calcd for C₄₂H₅₆N₄O₂Zr (%): C, 68.16; H, 7.63; N, 7.57. Found: C, 68.22; H, 7.69; N, 7.23.

Synthesis of [^{DMP}(NO)^{tBu}]₂Zr(η²-(2,6-Me₂C₆H₃)N=C(NMe₂))₂, **2.22**

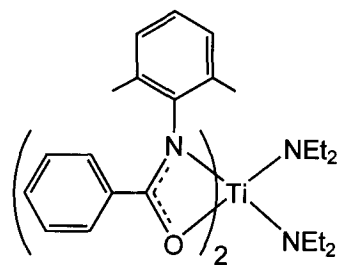
In a 25 mL vial, equipped with a stir bar, in a glovebox, 450 mg (0.768 mmol) of **2.18** and 200 mg (1.54 mmol) of 2,6-Me₂C₆H₃N≡C were dissolved in approximately 5 mL of pentane (approximately 1 mL of toluene added to aid solubility). The colorless reaction mixture was stirred overnight and concentrated to dryness to give a



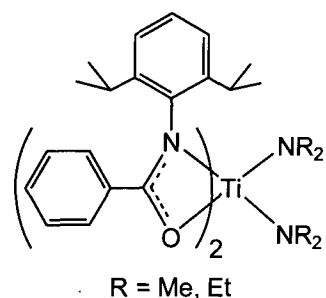
waxy white residue. The crude material was triturated with approximately 5 mL of Et₂O and the white crystalline material was isolated by filtration, and dried *in vacuo*. Yield = 65 % after 3 crops of precipitation and filtration (420 mg). ¹H NMR (C₆D₆, 25 °C, 300 MHz): δ 1.17 (s, 18H, C(CH₃)₃), 1.66 (s, 6H, Ph(CH₃)₂), 1.94 (s, 6H, Ph(CH₃)₂), 2.09 (s, 12H, N(CH₃)₂), 2.42 (s, 6H, Ph(CH₃)₂), 2.73 (s, 6H, Ph(CH₃)₂), 6.77-7.03 (m, 12H, Ar-H). ¹³C{¹H} NMR (C₆D₆, 25 °C, 75 MHz): δ 18.8, 18.9, 19.8, 21.2, 28.8, 36.9, 41.5, 45.0, 124.0, 124.3, 128.1, 128.6, 131.3, 132.9, 133.8, 134.7, 148.5, 151.8, 186.5, 208.7. EIMS (*m/z*): 848 ([M⁺]), 673 ([M⁺] – 2,6-Me₂C₆H₃N=CNMe₂).

Synthesis of $[\text{DMP}(\text{NO})^{\text{Ph}}]_2\text{Ti}(\text{NEt}_2)_2$, **2.23**

In a 250 mL round-bottomed Schlenk flask, a slurry of **2.3** (134 mg, 0.596 mmol) in toluene (40 mL) was cooled to -78 °C. In a separate Schlenk flask, a solution of $\text{Ti}(\text{NEt}_2)_4$ (100 mg, 0.298 mmol) in toluene was cooled to -78 °C and transferred via cannula into the solution of **2.3**. The resulting red-orange mixture was allowed to warm to room temperature while stirring, and was subsequently heated to 100 °C for 7 hours (this reaction can also be performed in Et_2O , without heating to generate the same product). Excess toluene was removed *in vacuo* and the crude product was dissolved in pentane, filtered through CeliteTM, and excess pentane was removed *in vacuo*. A red-orange microcrystalline solid was isolated in 84% yield (160 mg). ^1H NMR (C_6D_6 , 25 °C, 300 MHz): δ 1.19 (t, 12H, $\text{N}(\text{CH}_2\text{CH}_3)_2$), 2.57 (s, 12H, $\text{Ph}(\text{CH}_3)_2$), 4.31 (q, 8H, $\text{N}(\text{CH}_2\text{CH}_3)_2$), 7.12-7.99 (m, 16H, Ar-*H*). EIMS (m/z): 568 ($[\text{M}^+] - \text{NEt}_2$). Anal. Calcd for $\text{C}_{38}\text{H}_{48}\text{N}_4\text{O}_2\text{Ti}$ (%): C, 71.24; H, 7.55; N, 8.74. Found: C, 70.39; H, 7.55; N, 9.12.

Synthesis of $[\text{DIPP}(\text{NO})^{\text{Ph}}]_2\text{Ti}(\text{NR}_2)_2$, **2.24**

This previously reported complex was synthesized from **2.2** and $\text{Ti}(\text{NEt}_2)_4$ following established literature procedures, and characterization data matched expected values. The synthesis of the dimethylamido variant ($\text{R} = \text{Me}$) was accomplished in the same manner as that published for **2.24**.⁸⁵ ^1H NMR ($\text{R} = \text{Me}$) (C_6D_6 , 25 °C, 300 MHz): δ 0.93 (d, 12H, $^3J_{\text{HH}} = 6.8$ Hz, $\text{CH}(\text{CH}_3)_2$), 1.30 (d, 12H, $^3J_{\text{HH}} = 6.8$ Hz, $\text{CH}(\text{CH}_3)_2$), 3.28 (s, 12H, $\text{N}(\text{CH}_3)_2$), 3.61 (sept, 4H, $^3J_{\text{HH}} = 6.8$ Hz, $\text{CH}(\text{CH}_3)_2$), 6.81-6.88 (m, 6H, Ar-*H*), 7.15 (br, 6H, Ar-*H*), 7.69 (d, 4H, $^3J_{\text{HH}} = 7.8$ Hz, Ar-*H*).



2.7 References

1. Liu, F.; Chen, W. *Eur. J. Inorg. Chem.* **2006**, *6*, 1168.
2. Matsumoto, K.; Arai, S.; Ochiai, M.; Chen, W.; Nakata, A.; Nakai, H.; Kinoshita, S. *Inorg. Chem.* **2005**, *44*, 8552.
3. Chen, W.; Yarnada, J.; Matsumoto, K. *Synth. Commun.* **2002**, *32*, 17.
4. Chen, W.; Liu, F.; Nishioka, T.; Matsumoto, K. *Eur. J. Inorg. Chem.* **2003**, *23*, 4234.
5. Henderson, W.; Oliver, A. G.; Rickard, C. E. F. *Inorg. Chim. Acta* **2000**, *307*, 144.
6. Henderson, W.; Oliver, A. G.; Nicholson, B. K. *Inorg. Chim. Acta* **2000**, *298*, 84.
7. Kilpin, K. J.; Henderson, W.; Nicholson, B. K. *Polyhedron* **2007**, *26*, 434.
8. Krot, K. A.; Danil de Namor, A. F.; Aguilar-Cornejo, A.; Nolan, K. B. *Inorg. Chim. Acta* **2005**, *358*, 3497.
9. Wirth, A.; Moers, O.; Jones, P. G.; Blaschette, A. *Acta Crystallogr., Sect. C: Cryst. Struct. Commun.* **1999**, *C55*, 2033.
10. Rothaus, O.; LeRoy, S.; Tomas, A.; Barkigia, K. M.; Artaud, I. *Eur. J. Inorg. Chem.* **2004**, *7*, 1545.
11. Park, J.-H.; Lee, B.-W.; Lee, U.; Doh, M.-K. *Bull. Kor. Chem. Soc.* **2002**, *23*, 903.
12. Ray, M.; Hammes, B.; Yap, G. P. A.; Rheingold, A. L.; Borovik, A. S. *Inorg. Chem.* **1998**, *37*, 1527.
13. Bian, G. Q.; Kuroda-Sowa, T.; Konaka, H.; Maekawa, M.; Munakata, M. *Acta Crystallogr., Sect. C: Cryst. Struct. Commun.* **2004**, *C60*, 338.
14. Lescouezec, R.; Vaissermann, J.; Toma, L. M.; Carrasco, R.; Lloret, F.; Julve, M. *Inorg. Chem.* **2004**, *43*, 2234.
15. Borovik, A. S.; Dewey, T. M.; Raymond, K. N. *Inorg. Chem.* **1993**, *32*, 413.
16. Tolis, E. J.; Teberekidis, V. I.; Raptopoulou, C. P.; Terzis, A.; Sigalas, M. P.; Deligiannakis, Y.; Kabanos, T. A. *Chem. Eur. J.* **2001**, *7*, 2698.

17. Tolis, E. J.; Soulti, K. D.; Kabanos, T. A.; Raptopoulou, C. P.; Terzis, A.; Deligiannakis, Y. *Chem. Commun.* **2000**, 601.
18. Maurya, M. R.; Titinchi, S. J. J.; Chand, S. *J. Mol. Catal. A: Chem.* **2004**, *214*, 257.
19. Davy, R. D.; Hall, M. B. *J. Am. Chem. Soc.* **1989**, *111*, 1268.
20. Liu, W.; Wang, C.-F.; Li, Y.-Z.; Zuo, J.-L.; You, X.-Z. *Inorg. Chem.* **2006**, *45*, 10058.
21. Abraham, S.; Ha, C.-S.; Kim, I. *J. Polym. Sci., Part A: Polym. Chem.* **2006**, *44*, 2774.
22. Ottenwaelder, X.; Aukauloo, A.; Journaux, Y.; Carrasco, R.; Cano, J.; Cervera, B.; Castro, I.; Curreli, S.; Munoz, M. C.; Rosello, A. L.; Soto, B.; Ruiz-Garcia, R. *Dalton Trans.* **2005**, *15*, 2516.
23. Curtin, S. A.; Deming, T. J. *Polym. Prepr. (Am. Chem. Soc., Div. Polym. Chem.)* **2000**, *41*, 464.
24. Zhu, S.; Brennessel, W. W.; Harrison, R. G.; Que, L., Jr. *Inorg. Chim. Acta* **2002**, *337*, 32.
25. Le Henanf, M.; Le Roy, C.; Petillon, F. Y.; Schollhammer, P.; Talarmin, J. *Eur. J. Inorg. Chem.* **2005**, *19*, 3875.
26. Chisholm, M. H.; Clark, R. J. H.; Gallucci, J.; Hadad, C. M.; Patmore, N. J. *J. Am. Chem. Soc.* **2004**, *126*, 8303.
27. Huang, B.-H.; Yu, T.-L.; Huang, Y.-L.; Ko, B.-T.; Lin, C.-C. *Inorg. Chem.* **2002**, *41*, 2987.
28. Hoerter, J. M.; Otte, K. M.; Gellman, S. H.; Stahl, S. S. *J. Am. Chem. Soc.* **2006**, *128*, 5177.
29. Baugh, L. S.; Sissano, J. A. *J. Polym. Sci., Part A: Polym. Chem.* **2002**, *40*, 1633.
30. Montiel-Palma, V.; Huitron-Rattinger, E.; Cortes-Llamas, S.; Munoz-Hernandez, M.-A.; Garcia-Montalvo, V.; Lopez-Honorato, E.; Silvestru, C. *Eur. J. Inorg. Chem.* **2004**, *18*, 3743.
31. Uemura, K.; Yamasaki, K.; Fukui, K.; Matsumoto, K. *Inorg. Chim. Acta* **2007**, *360*, 2623.

32. Uemura, K.; Yamasaki, K.; Fukui, K.; Matsumoto, K. *Eur. J. Inorg. Chem.* **2007**, *6*, 809.
33. Liu, F.; Chen, W.; Wang, D. *Dalton Trans.* **2006**, *28*, 3445.
34. Chen, W.; Liu, F.; Matsumoto, K.; Autschbach, J.; Le Guennic, B.; Ziegler, T.; Maliarik, M.; Glaser, J. *Inorg. Chem.* **2006**, *45*, 4526.
35. Chen, W.; Matsumoto, K. *Inorg. Chim. Acta* **2003**, *342*, 88.
36. Dolmella, A.; Intini, F. P.; Pacifico, C.; Padovano, G.; Natile, G. *Polyhedron* **2002**, *21*, 275.
37. Cini, R.; Intini, F. P.; Maresca, L.; Pacifico, C.; Natile, G. *Eur. J. Inorg. Chem.* **1998**, *9*, 1305.
38. Cotton, F. A.; Donahue, J. P.; Murillo, C. A.; Perez, L. M.; Yu, R. *J. Am. Chem. Soc.* **2003**, *125*, 8900.
39. Giesbrecht, G. R.; Shafir, A.; Arnold, J. *Inorg. Chem.* **2001**, *40*, 6069.
40. Zhou, X.-G.; Zhang, L.-B.; Zhu, M.; Cai, R.-F.; Weng, L.-H.; Huang, Z.-X.; Wu, Q.-J. *Organometallics* **2001**, *20*, 5700.
41. Braunstein, P.; Nobel, D. *Chem. Rev.* **1989**, *89*, 1927.
42. Gambarotta, S.; Strologo, S.; Floriani, C.; Chiesi-Villa, A.; Guastini, C. *Inorg. Chem.* **1985**, *24*, 654.
43. Fujita, K.-I.; Yamashita, M.; Puschmann, F.; Martinez Alvarez-Falcon, M.; Incarvito, C. D.; Hartwig, J. F. *J. Am. Chem. Soc.* **2006**, *128*, 9044.
44. Kissounko, D. A.; Hoerter, J. M.; Guzei, I. A.; Cui, Q.; Gellman, S. H.; Stahl, S. S. *J. Am. Chem. Soc.* **2007**, *129*, 1776.
45. Kissounko, D. A.; Guzei, I. A.; Gellman, S. H.; Stahl, S. S. *Organometallics* **2005**, *24*, 5208.
46. Wan, G.; Schafer, L.L. Unpublished results.
47. Willey, G. R.; Woodman, T. J.; Fisher, M. *Transition Met. Chem.* **1998**, *23*, 467.
48. Morozov, I. V.; Fedorova, A. A.; Palamarchuk, D. V.; Troyanov, S. I. *Russ. Chem. Bull.* **2005**, *54*, 93.
49. Kaiser, V.; Ebinal, S.; Menzel, F.; Stumpp, E. *Z. Anorg. Allg. Chem.* **1997**, *623*, 449.
50. Pasko, S. V.; Abrutis, A.; Hubert-Pfalzgraf, L. G. *Mater. Lett.* **2004**, *59*, 261.

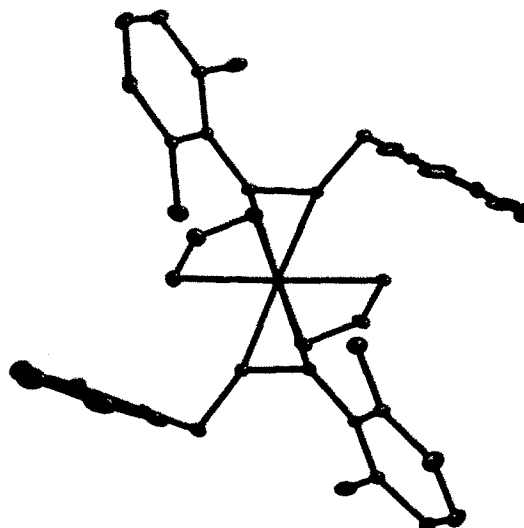
51. Loo, Y. F.; O'Kane, R.; Jones, A. C.; Aspinall, H. C.; Potter, R. J.; Chalker, P. R.; Bickley, J. F.; Taylor, S.; Smith, L. M. *J. Mater. Chem.* **2005**, *15*, 1896.
52. Spijksma, G. I.; Bouwmeester, H. J. M.; Blank, D. H. A.; Fischer, A.; Henry, M.; Kessler, V. G. *Inorg. Chem.* **2006**, *45*, 4938.
53. Smith, M. B.; March, J. *March's Advanced Organic Chemistry: Reactions, Mechanisms, and Structure*. 5th ed.; Wiley: Toronto, **2001**.
54. Mokuolu, Q. F.; Duckmanton, P. A.; Hitchcock, P. B.; Wilson, C.; Blake, A. J.; Shukla, L.; Love, J. B. *Dalton Trans.* **2004**, *13*, 1960.
55. Roesky, H. W.; Andruh, M. *Coord. Chem. Rev.* **2003**, *236*, 91.
56. Fay, R. C. *Coord. Chem. Rev.* **1996**, *154*, 99.
57. Seidel, S. R.; Stang, P. J. *Acc. Chem. Res.* **2002**, *35*, 972.
58. Wenninger, M. J. *Polyhedron Models*. Cambridge University Press: New York, **1970**.
59. Cotton, F. A.; Wilkinson, G.; Murillo, C. A.; Bochmann, M. *Advanced Inorganic Chemistry*. 6th ed.; Wiley: Toronto, **1999**.
60. Muller, E. G.; Day, V. W.; Fay, R. C. *J. Am. Chem. Soc.* **1976**, *98*, 2165.
61. Day, V. W.; Fay, R. C. *J. Am. Chem. Soc.* **1975**, *97*, 5136.
62. Steffen, W. L.; Fay, R. C. *Inorg. Chem.* **1978**, *17*, 779.
63. Fay, R. C.; VonDreele, R. B.; Stezowski, J. J. *J. Am. Chem. Soc.* **1971**, *93*, 2887.
64. Kempe, R. *Angew. Chem. Int. Ed.* **2000**, *39*, 468.
65. Watson, D. A.; Chiu, M.; Bergman, R. G. *Organometallics* **2006**, *25*, 4731.
66. Li, C.; Thomson, R. K.; Gillon, B.; Patrick, B. O.; Schafer, L. L. *Chem. Commun.* **2003**, 2462.
67. Bytschkov, I.; Doye, S. *Eur. J. Org. Chem.* **2003**, *6*, 935.
68. Ackermann, L.; Bergman, R. G. *Org. Lett.* **2002**, *4*, 1475.
69. Walsh, P. J.; Baranger, A. M.; Bergman, R. G. *J. Am. Chem. Soc.* **1992**, *114*, 1708.
70. Gott, A. L.; Clarke, A. J.; Clarkson, G. J.; Scott, P. *Organometallics* **2007**, *26*, 1729.
71. Wood, M. C.; Leitch, D. C.; Yeung, C. S.; Kozak, J. A.; Schafer, L. L. *Angew. Chem. Int. Ed.* **2007**, *46*, 354.

Chapter 2: Coordination Chemistry of Group 4 Amidate Complexes

72. Zuckerman, R. L.; Krska, S. W.; Bergman, R. G. *J. Am. Chem. Soc.* **2000**, *122*, 751.
73. Martins, A. M.; Ascenso, J. R.; de Azevedo, C. G.; Dias, A. R.; Duarte, M. T.; da Silva, J. F.; Veiros, L. F.; Rodrigues, S. S. *Organometallics* **2003**, *22*, 4218.
74. Wu, Z.; Diminnie, J. B.; Xue, Z. *Organometallics* **1999**, *18*, 1002.
75. van Meerendonk, W. J.; Schroder, K.; Brussee, E. A. C.; Meetsma, A.; Hessen, B.; Teuben, J. H. *Eur. J. Inorg. Chem.* **2003**, *3*, 427.
76. Ong, T.-G.; Yap, G. P. A.; Richeson, D. S. *Organometallics* **2002**, *21*, 2839.
77. Ong, T.-G.; Wood, D.; Yap, G. P. A.; Richeson, D. S. *Organometallics* **2002**, *21*, 1.
78. Littke, A.; Sleiman, N.; Bensimon, C.; Richeson, D. S.; Yap, G. P. A.; Brown, S. J. *Organometallics* **1998**, *17*, 446.
79. Mullins, S. M.; Duncan, A. P.; Bergman, R. G.; Arnold, J. *Inorg. Chem.* **2001**, *40*, 6952.
80. A search of the Cambridge Crystallographic Database shows that Ti=N bond lengths as long as 1.928 Å have been reported for double bond character, and bond lengths as long as 2.043 Å have been reported for Zr=N double bond character.
81. Zumdahl, S. S. *Chemical Principles*. 4th ed.; Heath: Toronto, **1995**.
82. Bondi, A. *J. Phys. Chem.* **1964**, *68*, 441.
83. Cano, J.; Sudupe, M.; Royo, P.; Mosquera, M. E. G. *Organometallics* **2005**, *24*, 2424.
84. Scott, M. J.; Lippard, S. J. *Organometallics* **1997**, *16*, 5857.
85. Zhang, Z.; Schafer, L. L. *Org. Lett.* **2003**, *5*, 4733.
86. Beard, J. D. The synthesis of group 3 and group 4 metal amidate chloride complexes and titanium catalysts for olefin hydroamination. Master's Dissertation. University of British Columbia, Vancouver, BC, **2005**.
87. *Molecular Structure Corp. teXsan for Windows* Molecular Structure Corp.: The Woodlands, Texas, **1996**.

88. Altomane, A.; Burla, M. C.; Cammali, G.; Cascarano, M.; Giacovazzo, C.; Gagliardi, A.; Moliterni, A. G. G.; Polidoi, G.; Spagna, A. *SIR-97*. CNR-IRMEC: Bari, Italy, **1999**.
89. Beurkens, P. T.; Admiraal, G.; Bauskens, G.; Bosman, W. P.; de Gelder, R.; Israel, R.; Smits, J. M. M. *DIRDIF-94*. University of Njmegen: Njmegen, The Netherlands, **1994**.
90. *International Union of Crystallography. International tables for X-ray crystallography*. Kynoch Press: Birmingham, UK, **1974**.
91. *International Union of Crystallography. International tables for X-ray crystallography*. Kluwer Academic: Boston, Mass., **1992**.
92. Farrugia, L. J. *J. Appl. Crystallogr.* **1997**, *30*, 565.
93. Manzer, L. E. *Inorg. Synth.* **1982**, *21*, 135.
94. Benzing, E.; Kornicker, W. *Chem. Ber.* **1961**, *94*, 2263.
95. Warren, T. H.; Erker, G.; Froehlich, R.; Wibbeling, B. *Organometallics* **2000**, *19*, 127.
96. Zucchini, U.; Albizzati, E.; Giannini, U. *J. Organomet. Chem.* **1971**, *26*, 357.

CHAPTER 3

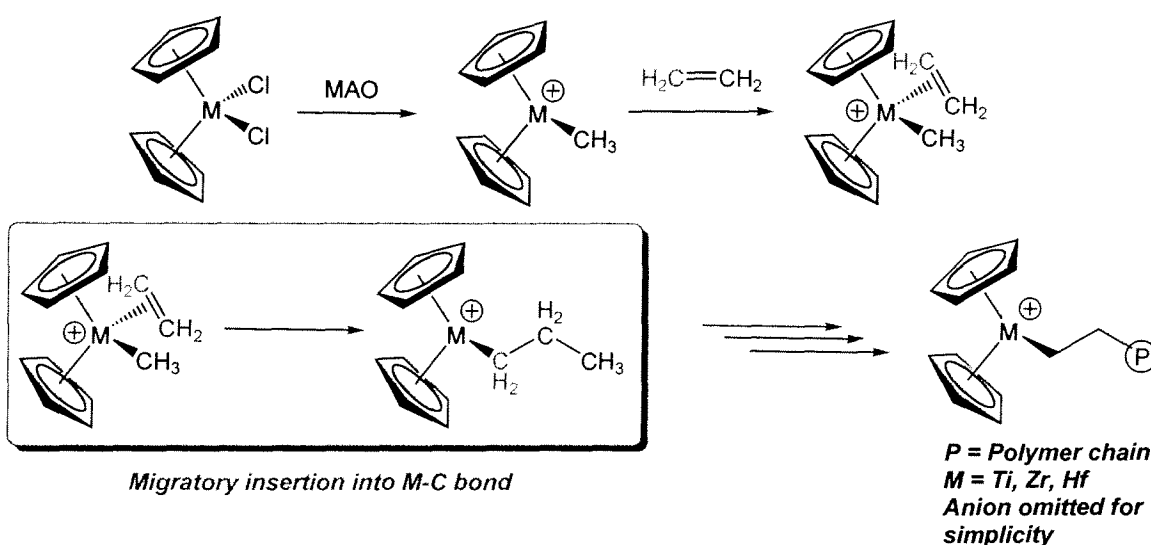


Synthesis, Structure, and Reactivity of Zr and Hf Amidate Benzyl Complexes

3.1 Introduction

Generation of new C-C bonds is an extremely important process in synthetic organic chemistry.¹⁻⁵ The systematic development of methods to facilitate this process has consistently been an important goal for synthetic chemists since the beginning of rationally designed syntheses.^{4, 5} Organometallic chemistry has played an extremely important role in this area of chemistry, due to the frequent requirement of transition metal-carbon bonded species as key intermediates in these processes.⁶⁻¹⁰ Alkyl complexes of transition metals undergo a wide range of reactivity with many divergent pathways, resulting in the formation of new C-E bonds (E = C, N, O, etc.).

Many industrially important processes involve organometallic species. The insertion of unsaturated organic molecules into M-C bonds is a fundamental process that is important to understanding metal-mediated reactions. The best known catalytic process for the formation of new C-C bonds in group 4 chemistry is olefin polymerization.¹¹⁻¹³ This reaction, first discovered in the 1955, is critical for the sustainability of our modern society, which is heavily dependent upon goods constructed from the plastics formed by this process.^{14, 15} Heterogeneous Ziegler-Natta catalysts, composed of mixtures of titanium chloro species and aluminum alkyls, are responsible for the bulk of the polyethylene produced in the world.¹⁶⁻¹⁹ Since this reaction is known to proceed at the surface of crystalline Ti chloro clusters, very little modification of the catalyst is possible, making product flexibility limited.²⁰ By comparison, the homogeneous metallocene catalysts first discovered by Natta¹⁶ and Breslow¹⁷ in 1957, aided by Kaminsky's fortuitous discovery of the methylalumoxane (MAO) cocatalyst in 1980,²¹ offers flexibility in the design of these catalysts systems, due to the ability to modify both the cyclopentadienyl ligands as well as the cocatalytic species. The overall process for ethylene polymerization is illustrated in Scheme 3.1, where M is a group 4 metal (Ti, Zr, or Hf). A key step in this transformation involves the insertion of a C=C bond into a M-C bond. This process is repeated many times before chain termination occurs, resulting in polyethylene.

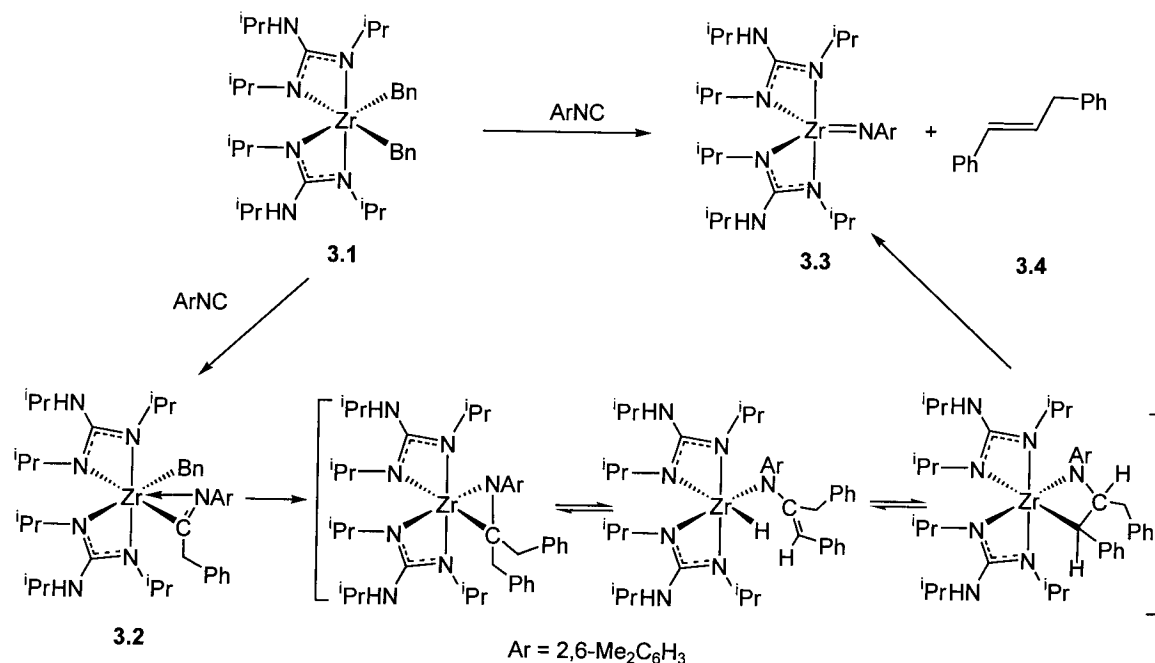


Scheme 3.1

The above olefin polymerization example demonstrates the importance of controlled sequential insertion into M-C bonds, but also illustrates the unique reactivity facilitated by cationic group 4 species, which are accessed by alkyl abstraction reactions. Thus the fundamental abstraction of alkyl groups from group 4 metals is an important reaction to understand for a given ligand system. In section 2.4.2, the highly ionic nature of the amidate bonding to Ti was shown through DFT calculations.²² This results in very electron deficient metal centers that promote reactivity that approaches that of cationic species. Cationic amidate complexes have been generated *in situ* and studied by the Arnold group.²³ In particular, catalytic ethylene polymerization was studied using a cationic Ti complex bearing a phenylene linked bis(amidate) ligand set. This complex was found to be modestly active towards olefin polymerization when dichloro and bis(amido) derivatives were activated with MAO.²³ Chapter 5 will illustrate the unique alkene hydroamination reactivity that is promoted by neutral bis(amidate) complexes, which is seen more commonly with group 3/lanthanide complexes and *cationic* group 4 complexes.

The two most closely related ligand systems to the amidate ligand set are the amidinate²⁴⁻³¹ and guanidinate³²⁻³⁸ ligands, which have been much more widely studied. While these ligands form 4-membered chelates with metal centers similar to the amidate ligand system, they are considerably more electron rich and have increased steric bulk. Insertion studies of C-E multiple bonds (E = N, O, S) into these organometallic species have shown interesting differences to those of other group 4 complexes. For example, the triisopropyl guanidinate Zr benzyl complex studied by Richeson and coworkers (**3.1**) has demonstrated unique reactivity with aryl isocyanides to generate imido species.³⁹ While most alkyl complexes simply insert isocyanides to generate iminoacyl complexes, like **3.2**,⁴⁰ this complex undergoes a novel rearrangement to yield imido complex **3.3**. This is proposed to occur through an interesting mechanism involving intramolecular iminoacyl alkylation, followed by β -hydride elimination/rearrangement and retrocyclization, as shown in Scheme 3.2. Unfortunately, the basic nitrogen donors in the backbone of the guanidinate system also undergo undesirable transamination and alkylation reactivity, which is deleterious to subsequent reactivity.^{33, 34, 41} The absence of

these groups in the backbone of the amidate ligand may reduce the tendency of such unwanted side reactions.



Scheme 3.2

Chapter 2 demonstrated the fundamental properties of Ti and Zr amido complexes bearing amidate ligands, including the exchange and isomerization processes that are possible with these ligand systems. This chapter discusses the synthesis and characterization of alkyl complexes bearing amidate ligands. Preliminary insertion reactivity studies are also presented. Given the fact that no group 4 alkyl complexes bearing amidate ligands had been characterized prior to this work, initiation of alkyl reactivity studies began with the synthesis and characterization of simple benzyl derivatives of Zr and Hf amidate species.⁴² Analogous Ti complexes were not targeted as these species are notoriously thermally and photosensitive.

3.2 Synthesis and Characterization of Dibenzyl Complexes

3.2.1 Introduction

The synthesis of amidate supported amido complexes and homoleptic amidate species via protonolysis with homoleptic tetrakisamido Ti and Zr starting materials was highly successful, and was described in detail in Chapter 2. The generation of homoleptic Hf complexes was also accomplished via an analogous protonolysis route, starting with $\text{Hf}(\text{CH}_2\text{Ph})_4$. By extension, it was reasoned that dibenzyl complexes of Zr and Hf could be synthesized through protonolysis using only 2 equiv of proligand, while starting with $\text{M}(\text{CH}_2\text{Ph})_4$ starting materials ($\text{M} = \text{Zr}, \text{Hf}$), which are easily prepared through literature procedures.⁴³

Exploratory alkyl chemistry is also often plagued by facile decomposition pathways, the most prevalent being β -hydride elimination. In an attempt to generate more stable alkyl species, benzyl complexes were targeted as they lack problematic β -hydrogens. In addition, benzyl ligands are capable of satisfying various electronic requirements by adopting different binding modes.⁴⁴⁻⁴⁹ While structural evidence of η^1 ,⁵⁰⁻⁵³ η^2 ,⁵⁴⁻⁶¹ η^3 ,^{46, 47} η^4 ,^{62, 63} η^5 ,⁶⁴ and even η^7 -bound benzyl ligands have been reported,⁶⁵ the more prevalent hapticities for Zr are η^1 , η^2 , and η^3 , where the η^1 -coordination mode is most common, and η^2 -benzyl ligands are often seen for very electron deficient or cationic complexes (Fig. 3.1).^{48, 66-71} The following section deals with the synthesis of Zr and Hf amidate benzyl species.

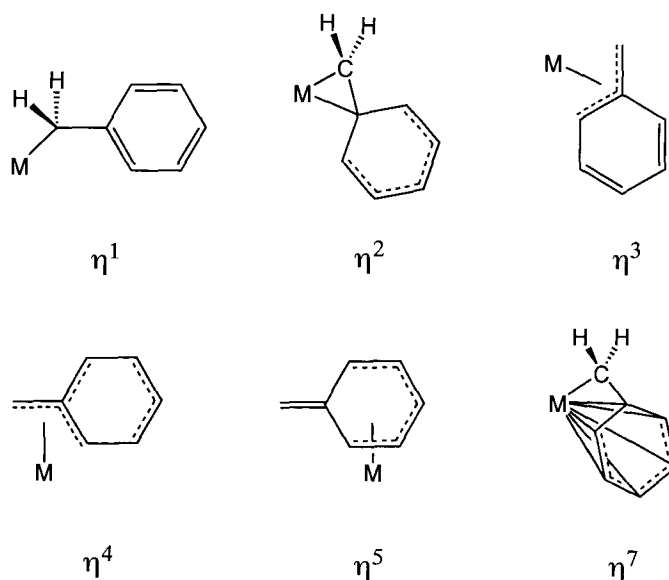
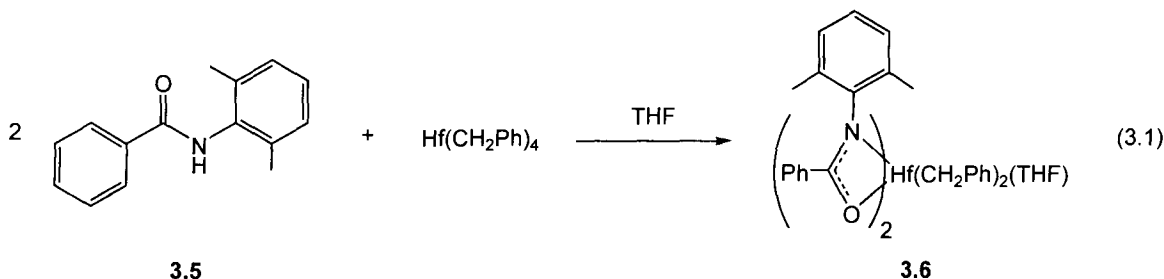


Figure 3.1 Hapticities of benzyl ligands

3.2.2 Results and Discussion

3.2.2.1 Bidentate Amidate Dibenzyl Complexes

The combination of 2 equiv of proligand **3.5** ($[\text{DMP}(\text{NO})^{\text{Ph}}]\text{H}$) and one equivalent of $\text{Hf}(\text{CH}_2\text{Ph})_4$ in THF in the dark at $-78\text{ }^\circ\text{C}$ results in a pale yellow slurry, which upon warming to room temperature, forms a deep red-orange solution. An intense red-orange solid can be isolated, which is stable to ambient light and heat in the solid-state. ^1H NMR spectroscopy of the resulting product **3.6** ($[\text{DMP}(\text{NO})^{\text{Ph}}]_2\text{Hf}(\text{CH}_2\text{Ph})_2(\text{THF})$), is consistent with a THF adduct of the desired bis(amidate) dibenzyl Hf complex as shown in Eq. 3.1. The presence of a single resonance for the aryl methyl groups at δ 2.34, and a single resonance for the benzyl groups at δ 2.55, suggest a highly symmetric species in solution. The coordination of THF is evidenced by resonances at δ 1.64 and 3.83.



The solid-state molecular structure of **3.6** as determined by X-ray diffraction is shown in Fig. 3.2. Selected bond lengths and angles are cited in Table 3.1, and crystallographic data are given in Table A3.1 in Appendix A. The structure is a slightly distorted pentagonal bipyramid, where the amidate ligands and THF are coordinated in the equatorial plane, and the two benzyl groups are *trans* disposed in the axial positions at $169.8(2)^\circ$ from each other. The deviation of the equatorially placed amidate and THF ligands from the equatorial plane is nearly non-existent, with the sum of angles about Hf being 360.16° . As expected, the THF Hf(1)-O(3) distance of $2.236(4)$ Å is considerably longer than the Hf-O bond lengths to the anionic amidate oxygen donors (Hf(1)-O(1) = $2.161(4)$ Å and Hf(1)-O(2) = $2.174(4)$ Å). In contrast to the bis(amido) complexes described in Chapter 2, this complex has the reactive benzyl groups *trans*. This is possibly due to the lack of π -donor character in the benzyl groups. With the amido ligands, they may be forced into a *cis* orientation to avoid unfavorable *trans* influences.

The overall symmetry of **3.6** is pseudo- C_{2v} , and the 2,6-dimethylphenyl groups of the amidate ligands are *cis* oriented, and stabilized by a π -stacking interaction, in which the ring planes are nearly perfectly parallel, with a deviation of only 3.99° . This interaction was seen previously for the homoleptic complexes $[\text{DMP}(\text{NO})^{\text{Ph}}]_4\text{Hf}$ and $[\text{DMP}(\text{NO})^{\text{tBu}}]_4\text{Zr}$ discussed in Chapter 2, where the amidate ligands bind in a planar fashion to the metal center, and the *cis* N-aryl groups are π -stacked in the solid-state. Intramolecular π -stacking interactions with these bulky substituents are relatively rare, but the distance between the ring centroids for the N-aryl groups at approximately 3.6 Å is consistent with a previously reported π -stacking interaction in a Ti - late metal bimetallic species, where the interactions ranged between 3.51 and 3.77 Å.⁷² The obtuse benzyl bond angles (Hf(1)-C(38)-C(39) = $122.3(4)^\circ$ and Hf(1)-C(31)-C(32) = $124.3(4)^\circ$) are consistent with typical η^1 -coordination and formal $2 e^-$ donation.⁵¹⁻⁵³ The amidate ligand set was shown by structural analysis and DFT studies in Chapter 2 to be a $4 e^-$ monoanionic bidentate donor.²² Thus **3.6** can be classified as a $14 e^-$ complex. Given its low electron count, **3.6** is remarkably thermally and photo-stable in the solid-state.

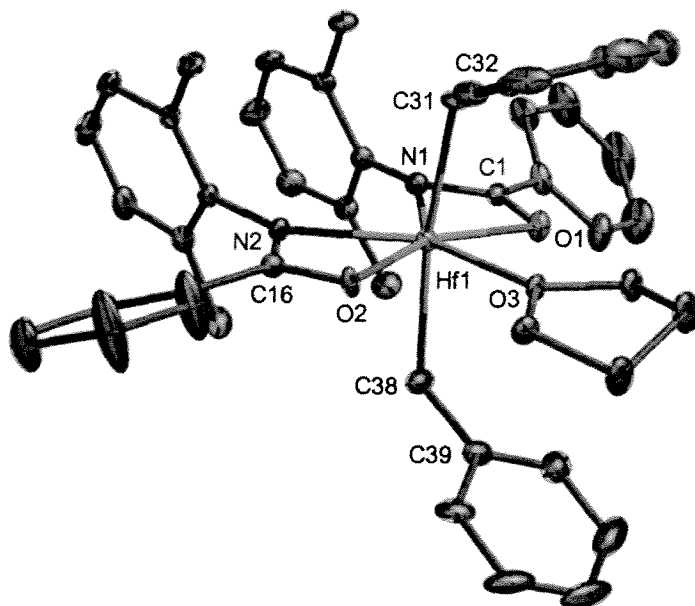


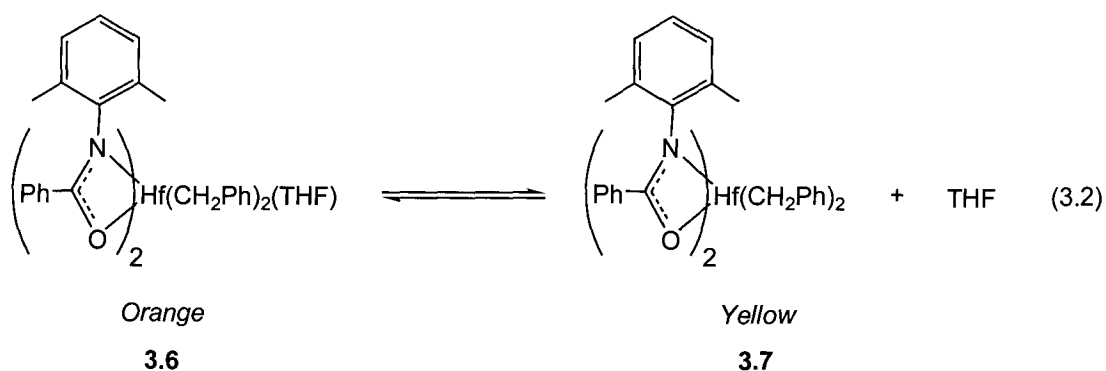
Figure 3.2 ORTEP depiction (ellipsoids at 30% probability) of solid-state molecular structure of $[\text{DMP}(\text{NO})^{\text{Ph}}]_2\text{Hf}(\text{CH}_2\text{Ph})_2(\text{THF})$, **3.6** (hydrogens omitted)

Table 3.1 Selected Bond Distances (Å) and Angles (°) for $[\text{DMP}(\text{NO})^{\text{Ph}}]_2\text{Hf}(\text{CH}_2\text{Ph})_2(\text{THF})$, **3.6**

Lengths		Angles		Angles	
Hf(1)-O(1)	2.161(4)	O(1)-Hf(1)-O(2)	156.60(15)	C(39)-C(38)-Hf(1)	122.3(4)
Hf(1)-O(2)	2.174(4)	O(1)-Hf(1)-O(3)	77.61(15)	O(2)-C(16)-N(2)	114.9(5)
Hf(1)-O(3)	2.236(4)	O(2)-Hf(1)-O(3)	78.76(15)	C(32)-C(31)-Hf(1)	124.3(4)
Hf(1)-N(1)	2.265(5)	O(2)-Hf(1)-N(2)	59.45(16)	O(1)-C(1)-N(1)	114.7(5)
Hf(1)-N(2)	2.258(5)	O(1)-Hf(1)-N(1)	59.53(15)		
Hf(1)-C(31)	2.326(6)	N(2)-Hf(1)-N(1)	84.81(17)		
Hf(1)-C(38)	2.330(5)	C(31)-Hf(1)-C(38)	169.8(2)		

At temperatures below room temperature, **3.6** maintains its solid-state C_{2v} structure in solution; however, warming the solution above room temperature results in a color change from deep orange to yellow. ^1H NMR spectroscopy of this new complex is very similar to that for **3.6**, with the presence of additional signals for free THF. Reoordination of the THF can be observed at temperatures below room temperature by the reappearance of the deep orange color. This reversible thermochromism is presumably due to the large geometrical perturbation of the metal complex upon coordination/decoordination of THF. Isolation of the THF free dibenzyl species is

accomplished by evacuating the yellow solution to dryness under vacuum to give a pale yellow solid. The resulting material, $[\text{DMP}(\text{NO})^{\text{Ph}}]_2\text{Hf}(\text{CH}_2\text{Ph})_2$, **3.7** can also be synthesized independently by the same synthetic protocol shown in Eq. 3.1, but in toluene rather than THF. The ^1H NMR spectrum of the product isolated via independent synthesis is identical to that of the material isolated from **3.6** after THF loss. Unfortunately, no solid-state molecular structural data could be obtained for **3.7**, so it was consistently isolated as an amorphous solid.



The kinetic parameters of the THF exchange process illustrated in Eq. 3.2 were determined by standard NMR line broadening experiments.⁷³ A variable temperature stacked plot of the α -methylene THF region of the ^1H NMR spectrum is shown in Fig. 3.3. Both bound THF peaks are observed to broaden in response to decreased temperature. The peak at δ 3.90 broadens and splits into two peaks at δ 4.12 and 3.50 that sharpen at -50 °C. The coalescence temperature for these two peaks, corresponding to bound and free THF, respectively, occurs at (-25 ± 5) °C. The rate constant (k_{solv}) for the THF exchange process is calculated to be (560 ± 110) s^{-1} by standard methods.⁷³ The activation energy (ΔG^\ddagger) for this process is likewise found to be (47 ± 1.5) kJ mol^{-1} . This value is similar to that seen for benzyl η^2 - η^1 - η^2 interconversion of a pyridine diamido dibenzyl Zr complex, where the activation energy (ΔG^\ddagger) for this process was found to be 47 kJ mol^{-1} (TC = -30 °C).⁷⁴

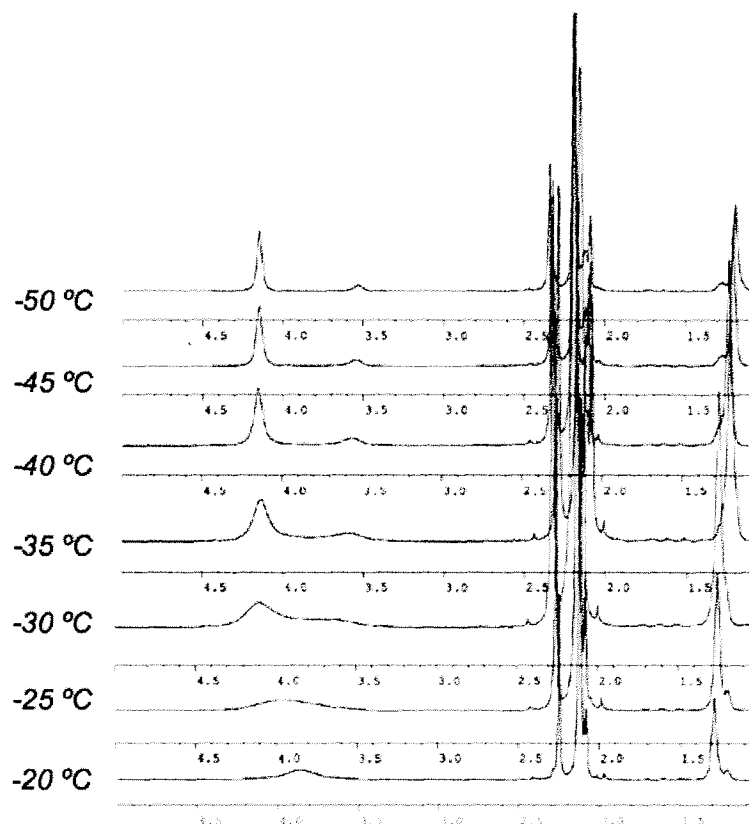


Figure 3.3 Stacked plot ^1H NMR spectrum showing THF exchange on $[\text{DMP}(\text{NO})^{\text{Ph}}]_2\text{Hf}(\text{CH}_2\text{Ph})_2(\text{THF})$, **3.6**

While solid-state molecular structural analysis of the 6-coordinate Hf complex **3.7** was not possible, the proposed structure, based upon solution phase behavior, is a pseudo-octahedral species with *cis* arranged benzyl ligands, exhibiting overall C_2 symmetry. While Zr complexes are known to be more thermally sensitive than Hf species, there are many reported cases of stable Zr alkyls that have been fully characterized.^{50-53, 75, 76} Here a 6-coordinate Zr dibenzyl complex $[\text{DMP}(\text{NO})^{\text{tBu}}]_2\text{Zr}(\text{CH}_2\text{Ph})_2$, **3.9**, can be synthesized using the synthetic protocol presented in Eq. 3.1, with $[\text{DMP}(\text{NO})^{\text{tBu}}]\text{H}$, **3.8**, as the proligand employed. Given the propensity of the N-2,6-dimethylphenyl-substituents to interact via π -stacking interactions, it is anticipated that the Zr complex will exhibit solution and solid-state molecular structures analogous to **3.6**.

Dibenzyl complex **3.9** can be isolated in very high yield as a bright yellow powder, which can be readily recrystallized from a saturated pentane solution, although

the crude material is typically pure enough for subsequent reactivity studies. Solution phase behavior of **3.9** is consistent with C_2 symmetry, as indicated by single resonances for the amidate *tert*-butyl and aryl methyl groups at δ 0.91 and 2.05, respectively. This suggests free rotation about the N-C_{ipso} bonds of the 2,6-dimethylphenyl substituents. Free rotation of the benzyl groups is also observed by a single resonance at δ 2.24. It is important to note that even when THF is the solvent of preparation, **3.9** does not coordinate THF to form a 7-coordinate complex analogous to **3.6**. Variable temperature ^1H NMR experiments on **3.9** do not indicate any slow fluxional processes that can be arrested at low temperature. In comparison to Hf complex **3.6**, **3.9** is significantly more photochemically and thermally prone to degradation. However, controlled thermolysis and photolysis experiments do not result in any easily isolable decomposition products, such as benzylidene species.^{77,78}

Bright yellow crystals of **3.9** can be grown from a saturated pentane solution at low temperature. The solid-state molecular structure of **3.9** is shown in Fig. 3.4, and selected bond lengths and angles are depicted in Table 3.2, with crystallographic data located in Table A3.2 (Appendix A).

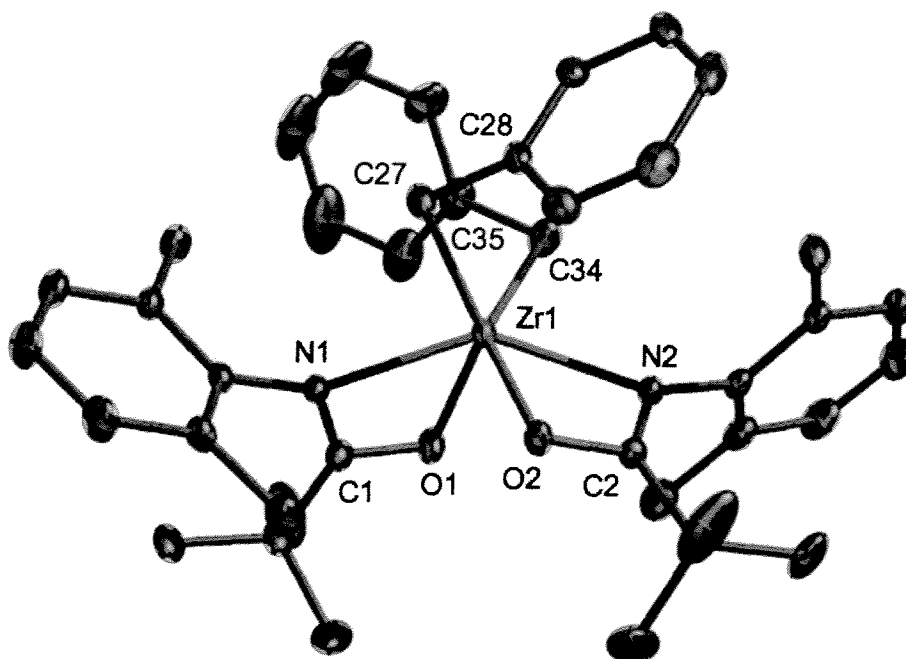


Figure 3.4 ORTEP depiction (ellipsoids at 30% probability) of solid-state molecular structure of $[\text{DMP}(\text{NO})^{\text{tBu}}]_2\text{Zr}(\text{CH}_2\text{Ph})_2$, **3.9** (hydrogens omitted for clarity)

Table 3.2 Selected Bond Distances (Å) and Angles (°) for $[\text{DMP}(\text{NO})^{\text{tBu}}]_2\text{Zr}(\text{CH}_2\text{Ph})_2$, **3.9**

	Lengths		Angles		Angles
Zr(1)-O(1)	2.0988(13)	O(1)-Zr(1)-O(2)	95.75(5)	C(35)-C(34)-Zr(1)	105.08(12)
Zr(1)-O(2)	2.1080(13)	N(1)-Zr(1)-N(2)	142.16(5)	O(1)-Zr(1)-N(1)	58.78(5)
Zr(1)-N(1)	2.2836(14)	N(1)-Zr(1)-C(27)	82.98(6)	O(1)-C(1)-N(1)	112.55(14)
Zr(1)-N(2)	2.2875(13)	O(1)-Zr(1)-C(27)	139.85(5)		
Zr(1)-C(27)	2.2440(18)	C(27)-Zr(1)-C(34)	97.18(8)		
Zr(1)-C(34)	2.2390(19)	C(28)-C(27)-Zr(1)	103.79(11)		

In contrast to the C_1 symmetric solid-state molecular structure of the bis(amido) complex bearing this amidate ligand, $[\text{DMP}(\text{NO})^{\text{tBu}}]_2\text{Zr}(\text{NMe}_2)_2$ (**3.10**) discussed in Chapter 2 (**2.18**), the structure of **3.9** is C_2 symmetric, with the N donors of the amidate ligands *trans* to each other. While η^1 -coordination of the benzyl group is obvious for **3.6**, the hapticity of the benzyl group in **3.9** is less clear. One typical parameter used to evaluate the hapticity of benzyl ligands is the bond angle formed by the *ipso* carbon of the benzyl group, the benzylic carbon, and the metal center.⁵⁵ Another parameter sometimes utilized is the chemical shift of the *ortho* protons of the benzyl group.^{47, 79} Finally, the sum of the van der Waals radii of the metal center and the *ipso* carbon can be used to gauge the presence of an η^2 -benzyl interaction.^{20, 80}

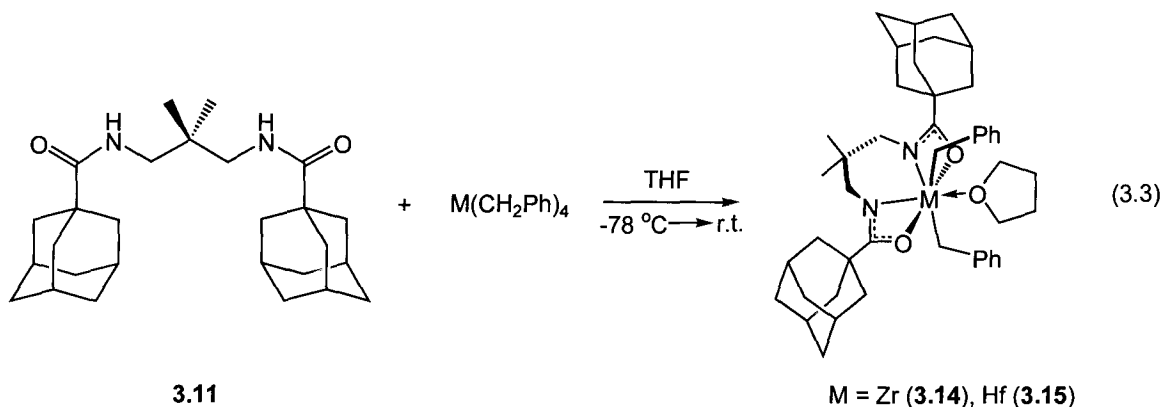
The bond angles at the benzylic carbon atoms in **3.9** are 103.79(11)° and 105.08(12)°, and are considerably more acute than the 122.3(4)° and 124.3(4)° bond angles for **3.6**. However, η^2 -benzyl coordination is generally only designated when this angle is less than 90°. ^{56, 79, 80} In the literature, a wide variation for this bond angle is seen, which is highly dependent upon the steric and electronic requirements of the metal center.⁴⁹ The bond angles in **3.9** can be classified as intermediate between η^1 - and η^2 -hapticity for the benzyl group.⁴⁷ A similar ‘intermediate’ hapticity can be seen for a β -diketiminato tribenzyl species (TTP)Zr(CH₂Ph)₃ (TTP = *p*-tolyl-NC(CH₃)CHC(CH₃)N-*p*-tolyl), where two of the benzyl ligands are clearly η^1 with bond angles of 110.7° and 117.6°, with the intermediate benzyl ligand having a bond angle of 99.1°. ⁵⁰ Another complex exhibiting intermediate hapticity is the Cp complex (CpZr(CH₂Ph)₃), which has a benzyl ligand with a bond angle of 94.5°. ⁸¹

It is generally noted that complexes with multiple benzyl groups having different hapticities in the solid-state often have ^1H NMR spectra that suggest a single type of benzyl environment, usually due to rapid fluxional processes that make the benzyl groups equivalent on the NMR timescale.^{47, 50, 59, 60, 74} Given the acute angles formed at the benzylic carbon atoms and the overall C_2 symmetry of **3.9**, it is surprising that the diastereotopic benzylic protons do not manifest themselves as two different signals. Fluxional processes are likely responsible for this observation. Interconversion between η^1 - and η^2 -coordination modes of the benzyl ligands is possible; however, variable temperature ^1H NMR experiments do not indicate any observable changes at low temperature. With η^2 -benzyl ligands, it is often seen that the *ortho* protons are shifted to higher field, which can be attributed to significant π -donation to the metal center.⁴⁷ This reduces the ring current within the arene ring, and is manifested by greater magnetic shielding. For **3.9**, no arene resonances are observed upfield of approximately δ 6.8, which is generally considered the cutoff for η^2 -behavior,⁴⁷ supporting average η^1 -binding in the solution phase, despite the intermediate hapticity seen in the solid-state. This implies that such an interconversion is extremely rapid for **3.9**. It is also possible that the amidate ligands in **3.9** are undergoing isomerization in solution through a κ^1 -O-bound amidate intermediate as discussed in Chapter 2 for bis(amidate) bis(amido) complexes. However, evidence for this process was not observed through low temperature ^1H NMR spectroscopic experiments. This isomerization process seems less probable for these dibenzyl complexes, as the benzyl ligands offer less electronic stabilization than the amido ligands in the bis(amidate) bis(amido) complexes discussed in Chapter 2.

Inspection of the distances between Zr(1) and the *ipso* carbon atoms (C(28) \sim 2.97 Å and C(35) \sim 2.98 Å) shows that they fall well outside the distance expected for formal Zr-C σ -bonds, which are usually approximately 2.2 - 2.4 Å.^{47, 48} Weak non-covalent interactions between Zr and the *ipso* benzyl carbons are present, since the Zr(1)-C(28) and Zr(1)-C(35) distances fall within the sum of the van der Waals radii of Zr and C (\sim 3.7 Å).⁸² These data taken together suggest a degree of η^2 -character for the benzyl ligands in **3.9**, particularly in the solid-state. However, the solution phase data are indicative of more traditional η^1 -hapticity.

3.2.2.2 Tethered Tetradentate Amidate Dibenzyl Complexes

In contrast to the Ti bis(amidate) bis(amido) complexes described in Chapter 2, the dibenzyl complexes **3.6**, **3.7**, and **3.9** do not appear to undergo amidate ligand isomerization as readily. This reduces the need for a tethered bis(amidate) ligand to control geometric isomerization. However, the ability to access a *trans* type pentagonal bipyramidal geometry for the Hf dibenzyl complex, **3.6**, indicates that the tethered proligand $\text{Ad}^d[\text{O}_2\text{N}_2]\text{H}_2$ (**3.11**) should be suitable for stabilizing bis(alkyl) complexes of Zr and Hf, as this ligand was shown to preferentially bind in a planar fashion in the homoleptic complexes $\text{Ad}^d[\text{O}_2\text{N}_2]_2\text{M}$ (M = Zr (**3.12**), Hf (**3.13**)). Synthesis of the Zr (**3.14**) and Hf (**3.15**) dibenzyl complexes of proligand **3.11** can be accomplished as shown in Eq. 3.3.



While this reaction is completely analogous to the synthesis of **3.6**, **3.7**, and **3.9**, additional care must be taken when performing these protonolysis reactions with proligand **3.11**. The extra entropic driving force provided by the chelate effect of the tetradentate ligand set results in the formation of the homoleptic species **3.12** and **3.13** as byproducts in these reactions, even when performed in a strict 1:1 stoichiometry. The extremely low solubility of **3.11** in nearly all common solvents makes the slow addition of a solution of **3.11** to a solution of $\text{M}(\text{CH}_2\text{Ph})_4$ unfeasible, and addition of cold solvent to an intimate mixture of **3.11** and $\text{M}(\text{CH}_2\text{Ph})_4$ still results in the formation of large quantities of **3.12** and **3.13**. To circumvent this problem, the slow addition of **3.11** to an ethereal solution of $\text{M}(\text{CH}_2\text{Ph})_4$ via solid addition funnel is required. This results in high

yields of the desired dibenzyl species as bright yellow (**3.14**, $\text{Ad}[\text{O}_2\text{N}_2]\text{Zr}(\text{CH}_2\text{Ph})_2(\text{THF})$) and pale yellow (**3.15**, $\text{Ad}[\text{O}_2\text{N}_2]\text{Hf}(\text{CH}_2\text{Ph})_2(\text{THF})$) powders.

As illustrated in Eq. 3.3, these complexes are stabilized by THF in solution, with signals for coordinated THF appearing at δ 1.33 and 3.99 for **3.15**. The ^1H NMR spectra for **3.14** and **3.15** are nearly identical, suggesting that they are isostructural, which was seen previously for homoleptic species **3.12** and **3.13** bearing this ligand (Chapter 2). Solution phase C_{2v} geometry is suggested by the high symmetry of the ^1H NMR spectra of **3.14** and **3.15**, with a single resonance observed for the amidate ligand backbone methyl groups at δ 0.86, suggesting the backbone ‘wagging’ process described in Chapter 2 for **3.12** and **3.13**. Likewise, single resonances for the benzylic and backbone methylene protons are observed at δ 1.73 and 3.19, respectively. The bulky adamantyl groups appear as three resonances in a 12:6:12 ratio at δ 1.66, 1.95, and 2.09, corresponding to the methylene and methine protons. The large number of methylene protons in these complexes required the use of COSY NMR experiments to assign all of the ^1H NMR resonances.

Similar to complexes **3.6**, **3.7**, and **3.9**, **3.14** and **3.15** do not exhibit any solution behavior suggestive of η^2 -coordination of the benzyl groups. Free rotation of the benzyl groups about their M-C bonds in solution is facile, and can not be arrested during low temperature ^1H NMR experiments. Interestingly, unlike **3.6**, the coordinated THF ligand in **3.14** and **3.15** is not labile in solution. Since these THF adducts are formally $14 e^-$ species, the coordination of THF helps fulfill the electronic requirements of the metal centers in these species. The lack of lability is likely due to the fact that this tethered bis(amidate) ligand does not offer sufficient flexibility to assume a more traditional pseudo-octahedral geometry upon loss of THF.⁴² In the case of **3.6**, the π -stacking interaction between the two amidate ligands is easily broken up, and allows for ligand reorganization, likely resulting in a pseudo-octahedral geometry for **3.7**, which is analogous to that seen for **3.9**.⁴²

Verification of the planar binding geometry of the bis(amidate) ligand in complexes **3.14** and **3.15** is given in the solid-state molecular structure of **3.14** in Fig. 3.5, with selected bond lengths and angles in Table 3.3, and crystallographic data located in Table A3.3 (Appendix A).

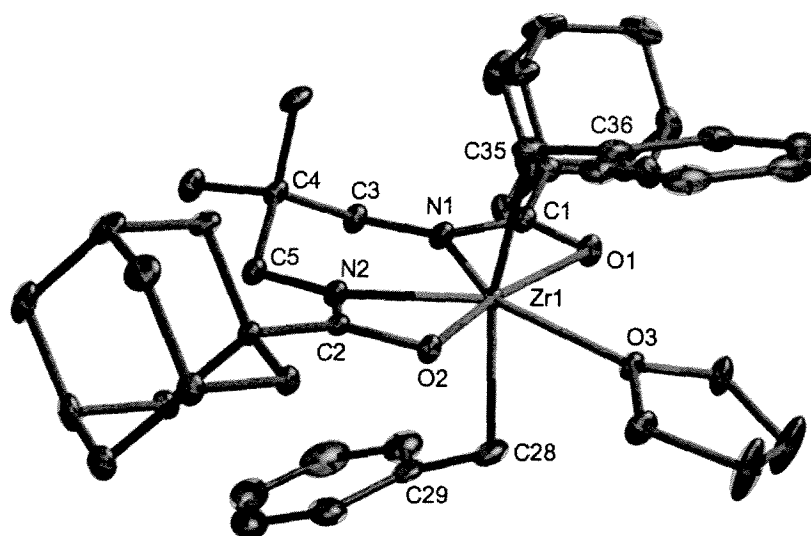


Figure 3.5 ORTEP depiction (ellipsoids at 30% probability) of solid-state molecular structure of $^{\text{Ad}}[\text{O}_2\text{N}_2]\text{Zr}(\text{CH}_2\text{Ph})_2(\text{THF})$, **3.14** (hydrogens omitted)

Table 3.3 Selected Bond Distances (Å) and Angles (°) for $^{\text{Ad}}[\text{O}_2\text{N}_2]\text{Zr}(\text{CH}_2\text{Ph})_2(\text{THF})$, **3.14**

Lengths		Angles		Angles	
Zr(1)-O(1)	2.2083(17)	O(1)-Zr(1)-O(2)	161.62(7)	C(29)-C(28)-Zr(1)	113.52(18)
Zr(1)-O(2)	2.1962(17)	O(1)-Zr(1)-O(3)	82.46(6)	O(2)-C(2)-N(2)	113.3(2)
Zr(1)-O(3)	2.2887(17)	O(2)-Zr(1)-O(3)	81.29(6)	C(36)-C(35)-Zr(1)	116.58(19)
Zr(1)-N(1)	2.183(2)	O(2)-Zr(1)-N(2)	59.84(7)	O(1)-C(1)-N(1)	113.2(2)
Zr(1)-N(2)	2.1867(19)	O(1)-Zr(1)-N(1)	59.68(7)		
Zr(1)-C(28)	2.358(3)	N(2)-Zr(1)-N(1)	77.74(7)		
Zr(1)-C(35)	2.366(3)	C(28)-Zr(1)-C(35)	165.57(10)		

The metrical parameters given in Table 3.3 are unexceptional, and show that **3.14** demonstrates very similar bond lengths and angles to **3.6** and **3.9**, where the amidate unit bite angle in all of these complexes is approximately 60°. The bond angle between the *trans* benzyl groups is 165.57(10)°, which is slightly contracted in comparison to **3.6**, where this angle is 169.8(2)°. The highly exposed nature of the Zr center in **3.14** is apparent in Fig. 3.5, where the bulky adamantyl groups effectively guard the metal center from the sides, but leave the metal center exposed from the top, bottom, and front. As was seen for **3.6**, the THF coordinates in the equatorial position between the two benzyl groups, generating a pentagonal bipyramidal structure. The bond angles at the benzylic carbon atoms are obtuse indicating η^1 -binding of the benzyl ligands to Zr (C(29)-C(28)-

Zr(1) = 113.52(18)° and C(36)-C(35)-Zr(1) = 116.58(19)°. One final interesting feature to note is the *anti* disposition of the benzyl arene units, where the rings are not sandwiching the THF group as was seen in **3.6**. Presumably this is due to reduced steric crowding at the Zr with the tethered ligand; however, crystal packing interactions may also influence the orientation of the benzyl groups in the solid-state. The overall symmetry of **3.14** is C_s . Rapid backbone ‘wagging’ of the amidate backbone, and free rotation of the benzyl groups about the Zr-C linkages gives rise to the observed C_{2v} solution phase structure.

Single crystals of the Hf congener **3.15** were also grown from a saturated pentane solution. The solid-state molecular structure of **3.15** is illustrated in Fig. A3 of Appendix A, with relevant metrical parameters given in Table A3.4, along with crystallographic details in Table A3.5. Aside from a slight contraction of the bond distances between the ligand donor atoms and the metal center, **3.15** is completely isostructural to **3.14**. These bond length reductions can be attributed to the relativistic nature of Hf vs. Zr, as discussed in Chapter 2.²⁰

3.2.3 Summary

The synthesis and characterization of dibenzyl complexes of Zr and Hf was accomplished via protonolysis with tetrabenzyl Zr and Hf starting materials. The Hf dibenzyl complex $[\text{DMP}(\text{NO})^{\text{Ph}}]_2\text{Hf}(\text{CH}_2\text{Ph})_2(\text{THF})$ (**3.6**) was isolated as a 7-coordinate THF adduct. Reversible thermochromism was observed for this complex as a result of THF lability in solution. The activation parameters for THF exchange of this complex were determined by variable temperature NMR experiments. Distorted pentagonal bipyramidal geometry was confirmed in the solid-state for this complex.

A 6-coordinate solvent-free Zr dibenzyl complex $[\text{DMP}(\text{NO})^{\text{tBu}}]_2\text{Zr}(\text{CH}_2\text{Ph})_2$ (**3.9**) was also isolated. The benzyl ligands in this complex were intermediate between η^1 - and η^2 -hapticity in the solid-state, with a propensity to behave as η^1 -ligands in solution. Two dibenzyl complexes supported by a tethered tetradentate bis(amidate) ligand were prepared in an analogous fashion ($^{\text{Ad}}[\text{O}_2\text{N}_2]\text{M}(\text{CH}_2\text{Ph})_2(\text{THF})$, M = Zr (**3.14**), Hf (**3.15**)). Both the Zr and Hf species are 7-coordinate THF adducts in the solid-state, but unlike

3.6, the coordinated THF ligand is not labile in solution. With the development of reliable preparative methods for the synthesis of the metal alkyl complexes in hand, preliminary reactivity investigations were undertaken.

3.3 Insertion Reactions of Isocyanides with $[\text{DMP}(\text{NO})^{\text{tBu}}]_2\text{Zr}(\text{CH}_2\text{Ph})_2$ (3.9**)**

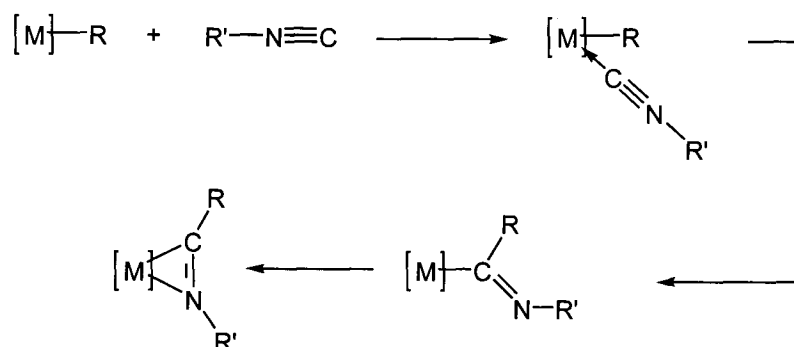
3.3.1 Introduction

The ability of M-C bonds to insert unsaturated organic molecules is the foundation of many catalytic cycles, the most relevant here being catalytic olefin polymerization.¹¹⁻¹³ En route to the development of catalytic reactions, the study of stoichiometric insertion reactions allows for a greater understanding of the factors controlling insertion, stereoselectivity, and subsequent reactivity of the resulting products. This section will address the reactivity patterns observed for the insertion of isocyanides into group 4 metal carbon bonds. Preliminary experiments with the tethered bis(amidate) dibenzyl complexes **3.14** and **3.15** indicated that insertion of unsaturated organic moieties into the M-C bond was possible; however, the very open coordination sphere resulted in a mixture of unidentified products. Fortunately, Zr complex **3.9** offers a good degree of steric stabilization in comparison to **3.14** and **3.15**, and has an extremely simple ¹H NMR spectrum, making it ideal for the exploration of stoichiometric insertion reactivity.

3.3.2 Results and Discussion

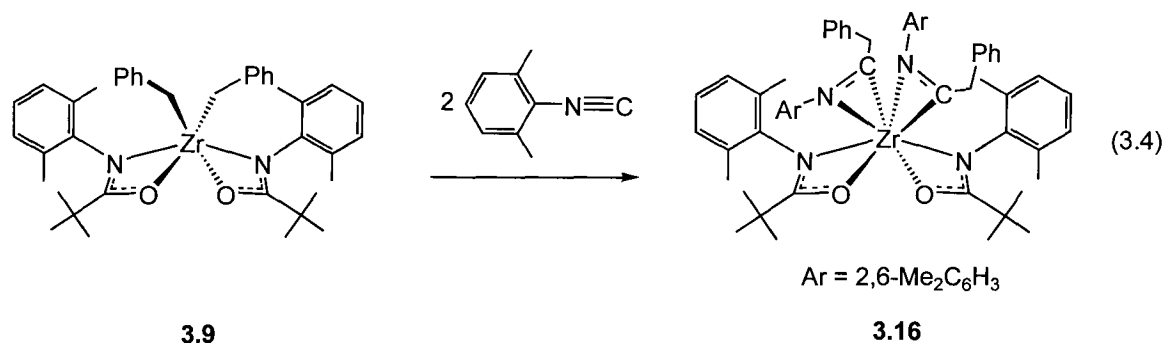
The insertion of isocyanides is a well known process that has been extensively studied, and is an attractive place to begin exploration of amidate supported group 4 organometallic species.⁴⁰ The insertion of isocyanides into group 4 metal carbon bonds is known to proceed through initial coordination of the carbon lone pair of electrons, followed by rapid insertion into the adjacent reactive M-C bond.^{40, 76} This results in the formation of an iminoacyl complex, where the N=C bond is usually coordinated to the metal center in an η^2 -fashion, as illustrated in Scheme 3.3.^{75, 83-86} Unlike the reversible

insertion of CO to form acyl species, the formation of iminoacyl complexes is irreversible, resulting in complexes that are stable to thermally induced deinsertion processes.⁴⁰



Scheme 3.3

The insertion of 2,6-dimethylphenyl isocyanide was investigated with Zr dibenzyl complex **3.9**. Upon addition of two equiv of isocyanide to a solution of **3.9** in C_6D_6 in a J-Young NMR tube, the solution is observed to immediately change from bright yellow to colorless. The 1H NMR spectrum of the reaction mixture indicates formation of a single product in quantitative yield, due to complete disappearance of the signals corresponding to **3.9**. Successful insertion of the isocyanide moieties is suggested by the appearance of canted doublets at δ 3.35 and 3.59 corresponding to the benzylic protons, indicating diastereotopic methylene protons. This was not observed for **3.9**, and was attributed to rapid isomerization processes. The bis(iminoacyl) complex **3.16** ($[^{DMP}(NO)^{tBu}]_2Zr(\eta^2-2,6-Me_2C_6H_3N=CCH_2Ph)_2$), is non-fluxional in solution, and the benzyl ligands cannot undergo isomerization processes due to their distance from the Zr center. The presence of four singlets of equal intensity at δ 0.95, 1.92, 2.12, and 2.62 is suggestive of two unique 2,6-dimethylphenyl groups, each experiencing hindered rotation about the $N-C_{ipso}$ bond. This is possible in a C_2 symmetric species, where the amidate ligand aryl groups experience hindered rotation, and the inserted isocyanide aryl groups also are prevented from rotating freely on the NMR timescale. Thus, the insertion product **3.16** is proposed to have the structure shown in Eq. 3.4.



The η^2 -binding mode in Eq. 3.4 is strongly suggested by ¹³C NMR spectroscopic data, where the resonance at δ 250.6 is characteristic of η^2 -coordinated iminoacyl carbons.^{40, 76} The most commonly observed geometric isomers of bis η^2 -iminoacyls are best described as pseudo-tetrahedral in either a head-to-head (**A**) or head-to-tail (**B**) arrangement, as shown in Fig. 3.6.^{40, 83} Interconversion between these two forms can occur, and in some cases has been observed spectroscopically.⁸⁵ A solution phase head-to-tail arrangement of the two iminoacyl units is required by the observed C₂ symmetry in the ¹H NMR spectrum. The solution phase structure of **3.16** appears static at room temperature, and is consistent with geometric isomer **B** in Fig. 3.6, where the ancillary ligands (L) are κ^2 -amidate groups. Variable temperature ¹H NMR experiments suggest that interconversion between forms **A** and **B** is not particularly facile, as no change in the spectrum is observed over the range of temperatures (-40 °C to 90 °C).

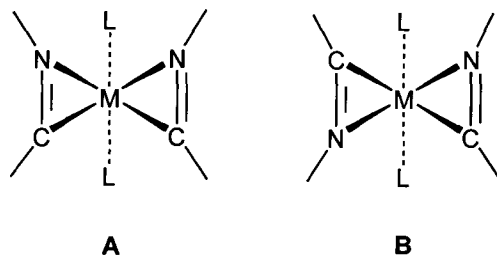


Figure 3.6 Common geometric isomers of bis(η^2 -iminoacyl) complexes

The solid-state molecular structure of **3.16** is shown in Fig. 3.7. Selected bond distances and angles are presented in Table 3.4 and crystallographic details are located in Table A3.6 (Appendix A). The presence of η^2 -ligation of the iminoacyl moieties was verified as shown in Fig. 3.7, where the Zr-N and Zr-C bond lengths are nearly identical

for each of the iminoacyl groups ($\text{Zr}(1)\text{-N}(3) = 2.243(6) \text{ \AA}$, $\text{Zr}(1)\text{-C}(3) = 2.252(7) \text{ \AA}$ and $\text{Zr}(1)\text{-N}(4) = 2.246(6) \text{ \AA}$, $\text{Zr}(1)\text{-C}(4) = 2.249(8) \text{ \AA}$). As expected, the iminoacyl $\text{N}=\text{C}$ bond lengths are consistent with double bonds ($\text{C}(3)\text{-N}(3) = 1.274(10) \text{ \AA}$ and $\text{C}(4)\text{-N}(4) = 1.282(9) \text{ \AA}$),^{87, 88} matching the structure shown in Eq. 3.4. The head-to-tail arrangement of the iminoacyl ligands is also verified in the solid-state, where the overall structure matches that seen for isomer **B** in Fig. 3.6. In many cases where two η^2 -iminoacyl ligands are bound to a group 4 metal, the L-M-L plane is not parallel to the iminoacyl $\text{N}=\text{C}$ bonds, and is twisted substantially from the $\text{C} \rightarrow \text{N}$ vectors (Fig. 3.6).^{40, 83} In the solid-state, the twist angle between the plane defined by $\text{C}(1)\text{-Zr}(1)\text{-C}(2)$ and the iminoacyl $\text{C} \rightarrow \text{N}$ vectors for **3.16** is approximately 26.45° . This is more easily viewed in Fig. 3.8, which shows **3.16** as viewed down its C_2 axis of symmetry. This twist angle is similar to the value seen for a bis(aryloxy) zirconium complex ($\text{Zr}(\text{O}-2,6\text{-}^t\text{BuC}_6\text{H}_3)_2(\eta^2\text{-}^t\text{BuN}=\text{CCH}_2\text{Ph})_2$), which exhibits a twist angle of 21.5° .⁸³

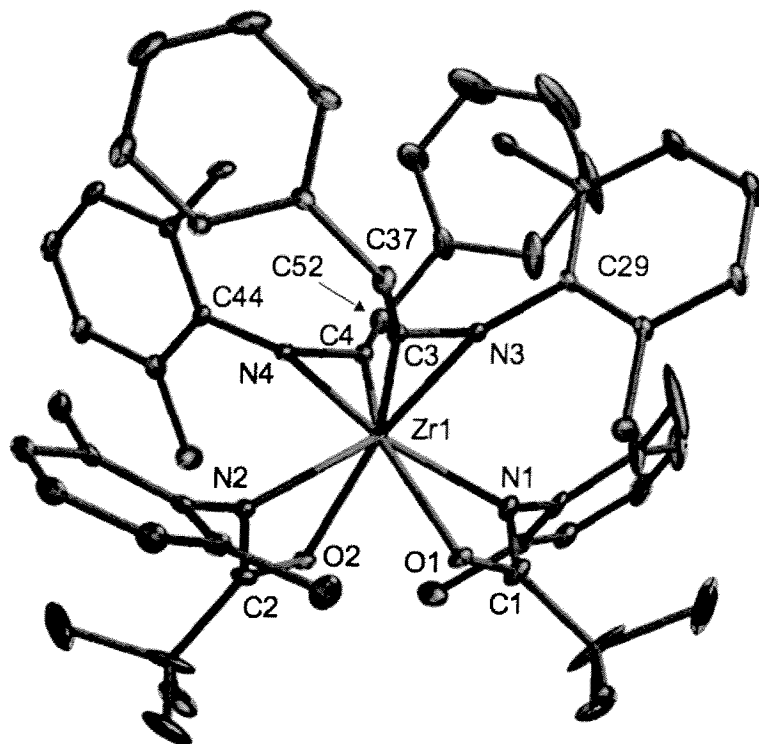
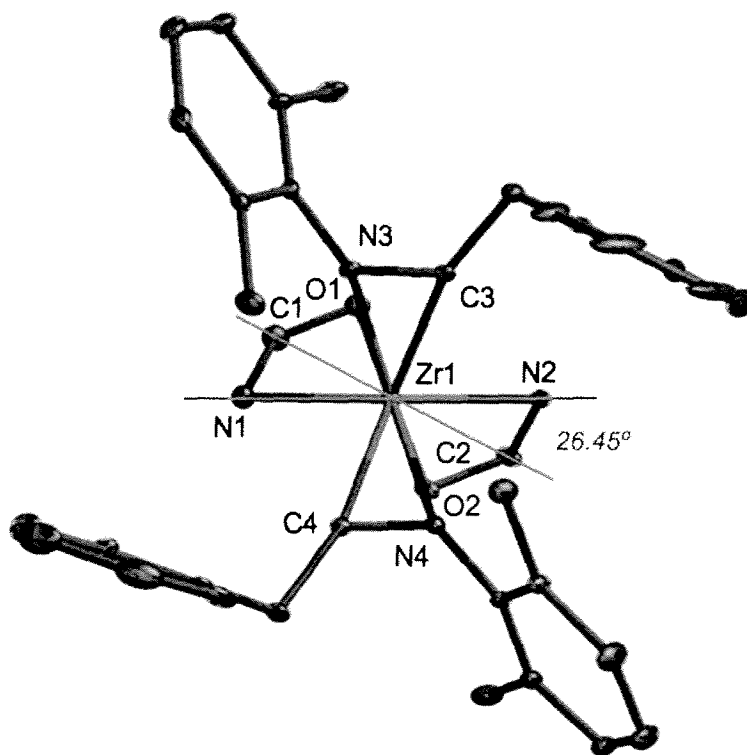


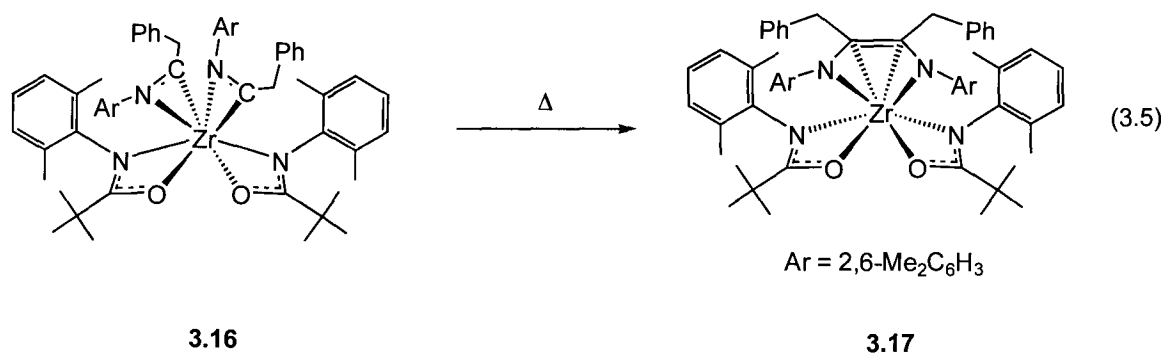
Figure 3.7 ORTEP depiction (ellipsoids at 30% probability) of solid-state molecular structure of $[\text{DMF}(\text{NO})^t\text{Bu}]_2\text{Zr}(\eta^2\text{-}2,6\text{-Me}_2\text{C}_6\text{H}_3\text{N}=\text{CCH}_2\text{Ph})_2$, **3.16** (hydrogens omitted for clarity)

Table 3.4 Selected Bond Distances (Å) and Angles (°) for [^{DMP}(NO)^{tBu}]₂Zr(η²-2,6-Me₂C₆H₃N=CCH₂Ph)₂, **3.16**

Lengths		Angles		Angles	
Zr(1)-O(1)	2.214(5)	O(1)-Zr(1)-O(2)	79.3(2)	C(37)-C(3)-Zr(1)	162.2(6)
Zr(1)-O(2)	2.217(5)	N(1)-Zr(1)-N(2)	129.2(2)	C(37)-C(3)-N(3)	123.2(7)
Zr(1)-N(1)	2.339(6)	C(3)-Zr(1)-C(4)	110.2(3)	N(3)-C(3)-Zr(1)	73.1(4)
Zr(1)-N(2)	2.335(6)	N(3)-Zr(1)-N(4)	108.0(2)	C(52)-C(4)-Zr(1)	161.0(6)
Zr(1)-N(3)	2.243(6)	N(3)-Zr(1)-C(3)	32.9(2)	C(52)-C(4)-N(4)	124.4(7)
Zr(1)-N(4)	2.246(6)	N(4)-Zr(1)-C(4)	33.2(2)	N(4)-C(4)-Zr(1)	73.3(4)
Zr(1)-C(3)	2.252(7)	C(29)-N(3)-C(3)	127.3(6)	C(4)-N(4)-Zr(1)	73.5(4)
Zr(1)-C(4)	2.249(8)	C(29)-N(3)-Zr(1)	158.0(5)	C(44)-N(4)-C(4)	125.6(6)
N(3)-C(3)	1.274(10)	C(3)-N(3)-Zr(1)	73.9(4)	C(44)-N(4)-Zr(1)	159.8(5)
N(4)-C(4)	1.282(9)				

**Figure 3.8** ORTEP depiction (ellipsoids at 30% probability) of simplified structure of **3.16** viewed down the C₂ axis of symmetry (amidate substituents and hydrogens omitted for clarity)

While **3.16** is stable in solution at room temperature, heating this complex to 110 °C for 24 hours results in the formation of a new bright yellow species having C_s symmetry in solution. ^1H NMR spectroscopy of the product of this reaction shows the presence of two resonances for the aryl methyl groups, indicating free rotation about the N- C_{ipso} bonds of the 2,6-dimethylphenyl groups of the inserted isocyanides and the amidate ligands. Additionally, the ^{13}C NMR spectroscopic signal at δ 250.6 characteristic of η^2 -iminoacyl species is replaced with a new signal at δ 115.6, which is indicative of an sp^2 -hybridized carbon center. These results are consistent with a well precedented coupling transformation (Eq. 3.5).^{40, 76, 89-92}



This process requires the iminoacyl ligands to rearrange prior to C=C coupling. This rearrangement is energy intensive for **3.16** as this reaction requires 24 h at 110 °C to go to completion. The formation of new C=C bonds by the coupling of isocyanides in the presence of early transition metals is dependent upon the steric and electronic properties of both the metal center and the isocyanides.⁴⁰ This process is generally intramolecular in nature, and is dictated largely by the energy of the π^*_{CN} orbital.⁹³ Accordingly, C=C coupling is more readily achieved with electron withdrawing groups on the iminoacyl moiety, such as aryl substituents, and less readily achieved with electron donating alkyl groups on the iminoacyl unit.⁹³ The xylyl groups in **3.16** are slightly electron withdrawing, and thus fit this pattern of reactivity.

Formation of a new C=C bond to generate the enediamido complex $[\text{DMP}(\text{NO})^{\text{tBu}}]_2\text{Zr}(\eta^4\text{-ArNC}(\text{CH}_2\text{Ph})=\text{C}(\text{CH}_2\text{Ph})\text{NAr})$, **3.17** (Ar = 2,6-Me₂C₆H₃), is confirmed in the solid-state molecular structure illustrated in Fig. 3.9, with relevant bond lengths and angles given in Table 3.5, and crystallographic details presented in Table A3.7 (Appendix A).

Table 3.5 Selected Bond Distances (Å) and Angles (°) for $[\text{DMP}(\text{NO})^{\text{iBu}}]_2\text{Zr}(\eta^4\text{-ArNC}(\text{CH}_2\text{Ph})=\text{C}(\text{CH}_2\text{Ph})\text{NAr})$, **3.17** (Ar = 2,6-Me₂C₆H₃)

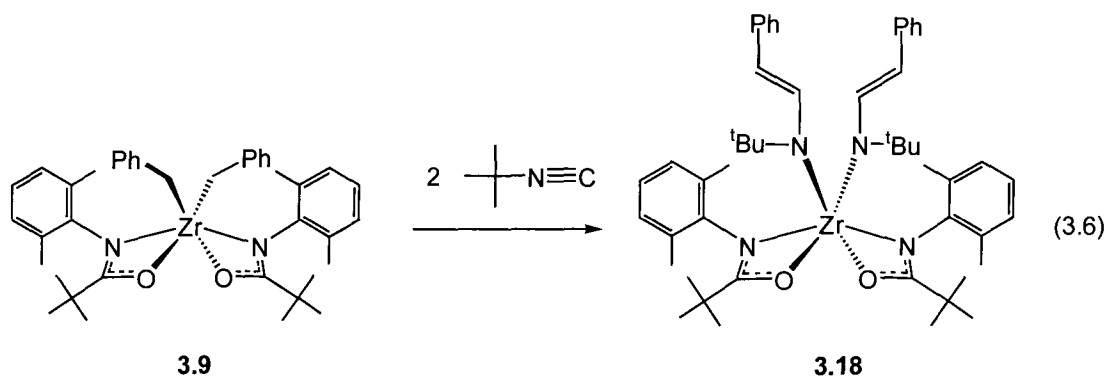
	Lengths		Lengths/ Angles		Angles
Zr(1)-O(1)	2.1344(19)	Zr(1)-C(28)	2.548(2)	C(37)-N(3)-C(28)	121.04(19)
Zr(1)-O(2)	2.1645(19)	C(27)-C(28)	1.381(3)	C(28)-N(3)-Zr(1)	93.85(13)
Zr(1)-N(1)	2.470(2)	N(3)-C(28)	1.406(3)	C(52)-C(28)-N(3)	117.1(2)
Zr(1)-N(2)	2.346(2)	N(4)-C(27)	1.410(3)	C(52)-C(28)-C(27)	123.4(2)
Zr(1)-N(3)	2.0328(19)	O(1)-Zr(1)-N(1)	56.04(7)	C(27)-C(28)-N(3)	118.9(2)
Zr(1)-N(4)	2.069(2)	O(2)-Zr(1)-N(2)	57.69(7)	O(1)-Zr(1)-O(2)	116.11(7)
Zr(1)-C(27)	2.560(2)	C(37)-N(3)-Zr(1)	142.25(17)	N(1)-Zr(1)-N(2)	93.72(7)

Fig. 3.9 shows that **3.17** is not C_s symmetric in the solid-state, indicating that solution fluxionality must be occurring to give rise to the observed ¹H NMR spectrum. Solution phase amidate fluxionality was discussed at length in section 2.4, and the proposed $\kappa^2\text{-}\kappa^1\text{-}\kappa^2$ mechanism for this process must be considered. The new C=C bond formed falls within the range expected for a double bond (C(27)-C(28) = 1.381(3) Å), and the C-N distances of the enediamido backbone are consistent with single bonds (N(3)-C(28) = 1.406(3) Å and N(4)-C(27) = 1.410(3) Å).⁸⁸

A significant fold angle of approximately 54.5° exists between the planes defined by N(4)-C(27)-C(28)-N(3) and N(4)-Zr(1)-N(3). Fold angles of this size are commonly seen for complexes of this type, where one related example is Richeson's bis(guanidinate) enediamido complex, having a fold angle of 44.8°.³⁹ The deviation from planarity has been rationalized by the need to relieve steric interactions, as well as the additional electronic stabilization offered by the η^4 -interaction with the metal center.^{39, 89, 92, 93} While the Zr(1)-C(27) and Zr(1)-C(28) bond distances (2.560(2) Å and 2.548(2) Å, respectively) lie outside the range generally observed for Zr-C σ bonds, they are similar to the distances observed in Cp complexes of Zr, which exhibit π -bonding interactions (average Zr- η^5 -C₅H₅ distances are ~ 2.48-2.55 Å).⁹⁴ It has also been suggested through DFT calculations that the driving force for the folding of the enediamido ligand is the rotation of the nitrogen lone pairs towards the metal center to enhance d π -p π orbital overlap.⁹⁵

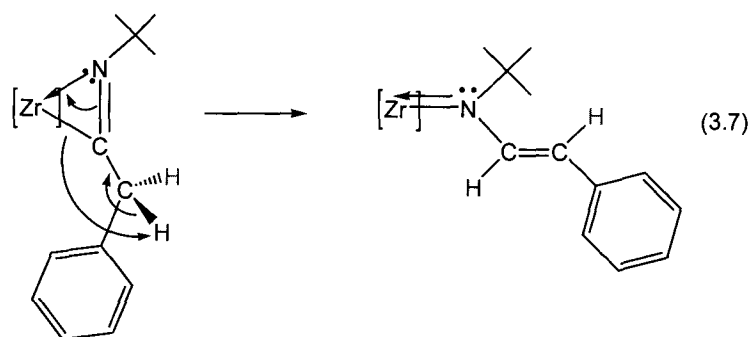
Although it would be desirable to couple different isocyanide units to generate novel diamido ligands, the high reactivity of **3.9** results in rapid insertion of two equivalents of isocyanide per Zr center, even with strict 1:1 stoichiometry. The selective insertion of two equivalents of isocyanide into Zr-C bonds in the presence of only 1 equivalent of isocyanide is not generally seen. In most cases, insertion of a single equivalent of isocyanide results in stable mixed alkyl η^2 -iminoacyl complexes.⁴⁰ However, this observed reactivity is consistent with both the greater steric access and enhanced electrophilic character of Zr afforded by the amidate ligands in **3.9**.

With the knowledge that literature precedence for C-C coupling of iminoacyls is favored with electron withdrawing groups, such as 2,6-dimethylphenyl, and disfavored with electron donating groups, the possibility of divergent behavior was investigated by studying the insertion of *tert*-butyl isocyanide.^{40, 93} Upon addition of two equiv of $t\text{BuN}\equiv\text{C}$ to **3.9**, the solution immediately deepens in color from pale yellow to an intense golden yellow. The ^1H NMR spectrum of insertion product **3.18** is consistent with a C_2 symmetric complex, with one signal for the aryl methyl groups, and two signals for the *tert*-butyl groups of the amidate ligands and inserted isocyanide units. Splitting of the signal for the benzylic protons in **3.18** into two canted doublets is suggestive of isocyanide insertion; however, the chemical shift of these signals is shifted far downfield at δ 5.84 and 7.28. These chemical shifts suggest the presence of vinyl amido ligands as shown in Eq. 3.6.^{36, 40, 96-98} The $^3J_{\text{HH}}$ coupling constants of 13.5 Hz for these signals indicate a *trans* geometry about the double bond.⁸⁸



Vinylamido insertion products like $[\text{DMP}(\text{NO})^{\text{tBu}}]_2\text{Zr}(\text{N}(\text{tBu})\text{CH}=\text{CHPh})_2$ (**3.18**) have been reported in the literature, but are quite rare for group 4 metals.^{36, 96, 98} Rothwell and coworkers reported a vinylamido hafnocene complex which resulted from the insertion of 2,6-dimethylphenyl isocyanide into the Hf-C bonds of $\text{Cp}_2\text{Hf}(\text{CH}_2\text{-py-6-Me})_2$.⁹⁶ The solid-state molecular structure of the insertion product clearly established the *trans* geometry of the vinyl group, and doublets for the *trans* vinyl protons were observed in the ^1H NMR spectrum at δ 4.6-4.8 and 8.5-9.5, with $^3J_{\text{HH}}$ coupling constants of 12-13 Hz. A related bis(guanidinate) dibenzyl Zr complex was shown to insert two equiv of xylyl isocyanide, resulting in the formation of a bis(guanidinate) bis(vinylamido) product, analogous to **3.18**.³⁶ The close similarity in the diagnostic NMR spectroscopic signals between these complexes and those of **3.18** lend further support to the proposed structure in Eq. 3.6.^{36, 96} In addition to the ^1H NMR spectroscopic data, ^{13}C NMR spectroscopy supports the presence of a vinyl unit, with signals at δ 106.2 and 134.4, consistent with sp^2 -hybridized carbon centers. Templeton and coworkers have also reported that vinylamido ligands can be accessed through primary amine additions to alkynes coordinated to W pyrazolyl borate complexes.⁹⁹ In these cases, the ^1H NMR spectroscopic data are very similar to those for **3.18**, supporting the formulation in Eq. 3.6. Finally, mass spectrometry data confirm the insertion of 2 equiv of $\text{tBuN}\equiv\text{C}$ into **3.9**, with an parent ion of $m/z = 846$. While X-ray crystallographic verification of this structure was not possible, the data presented are strongly supportive of the designation given in Eq. 3.6.

The isomerization of η^2 -iminoacyl groups to vinylamides can be explained by a 1,2-hydrogen atom migration as shown in Eq. 3.7.^{96, 97} The difference in reactivity seen for insertion of $\text{tBuN}\equiv\text{C}$ vs. $2,6\text{-Me}_2\text{C}_6\text{H}_3\text{N}\equiv\text{C}$ can be explained by two factors. First, the presence of the electron donating *tert*-butyl group increases the energy of the π^*_{CN} orbital, making the C=C coupling of the η^2 -iminoacyl groups much less favorable.⁴⁰



Secondly, steric bulk has been noted as a factor which can shut down this reactivity in Cp complexes of Hf, where the insertion of 2,6-Me₂C₆H₃N≡C into Cp₂Hf(CHPh-py-6-Me)₂ results in the generation of the bis(η²-iminoacyl) complex, and 1,2-hydrogen atom migration to the bis(vinylamido) complex can not be induced.⁹⁷ It is possible that the steric bulk of the amidate ligands in **3.9** prevents this rearrangement from occurring with 2,6-Me₂C₆H₃N≡C. However, the ^tBuN≡C group is less bulky by comparison and can rearrange to form the bis(vinylamido) complex **3.18**. While observation of the expected intermediate η²-iminoacyl species was not possible for this reaction with **3.9**, an NMR tube scale reaction of Hf complex **3.6** with two equiv of ^tBuN≡C resulted in the formation of the η²-iminoacyl complex [^{DMP}(NO)^{Ph}]₂Hf(η²-^tBuN=CCH₂Ph)₂ (**3.19**), as evidenced by ¹H NMR spectroscopic data, with diastereotopic benzylic resonances at δ 2.88 and 3.68. When the NMR tube was heated to 80 °C over 24 h, the solution changes color from yellow-orange to emerald green, showing diagnostic resonances at δ 6.02 and 7.47 for the *trans* vinyl group, indicating formation of the bis(vinylamido) complex [^{DMP}(NO)^{Ph}]₂Hf(N(^tBu)CH=CHPh)₂ (**3.20**). Unfortunately, this reaction is not clean, and a number of other signals are observed in the ¹H NMR spectrum, and this reaction will not be discussed in any further detail.

While these results are promising, detailed investigations of insertion reactivity patterns with other unsaturated organics (ketones, isocyanates, carbodiimides, etc.) are beyond the scope of this thesis, and preliminary NMR tube scale exploratory insertion reactions are discussed briefly in Chapter 6, as the basis for future investigations.

3.3.3 Summary

Preliminary insertion reactivity studies of bis(amidate) dibenzyl complex **3.9** with isocyanides were undertaken. The insertion of 2 equiv of 2,6-Me₂C₆H₃N≡C into the Zr-C bonds of **3.9** resulted in the formation of the bis(η²-iminoacyl) complex **3.16** ([^{DMP}(NO)^{tBu}]₂Zr(η²-2,6-Me₂C₆H₃N=CCH₂Ph)₂), which was verified in the solid-state. Attempts to insert one equiv of 2,6-Me₂C₆H₃N≡C resulted in a mixture of **3.9** and the double insertion product **3.16**, rather than the expected mono-iminoacyl complex. Complex **3.16** underwent thermally induced C=C coupling to generate the enediamido complex [^{DMP}(NO)^{tBu}]₂Zr(η⁴-ArNC(CH₂Ph)=C(CH₂Ph)NAr), **3.17** (Ar = 2,6-Me₂C₆H₃), which was also characterized in the solid-state. In the solid-state this complex exhibits η⁴-binding of the enediamido ligand to the Zr center, but the amidate ligands are fluxional in solution giving rise to a very simple ¹H NMR spectrum. In contrast to these results, the reaction of 2 equiv of ^tBuN≡C with **3.9** resulted in rapid formation of the bis(vinylamido) complex [^{DMP}(NO)^{tBu}]₂Zr(N(^tBu)CH=CHPh)₂ (**3.18**), which was characterized in solution, and found to have *trans* oriented vinylamido ligands. Formation of the vinylamido ligands is proposed to occur through a 1,2-hydrogen atom migration mechanism, as illustrated by Rothwell and coworkers.⁹⁷

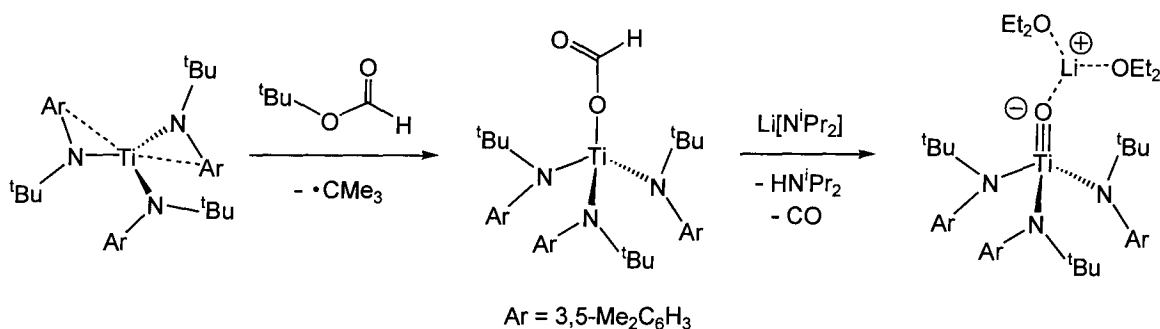
3.4 Hydrolysis of Dibenzyl Complex [^{DMP}(NO)^{Ph}]₂Hf(CH₂Ph)₂(THF) (**3.6**)

3.4.1 Introduction

It is well known that M-C bonds are susceptible to protolytic cleavage by acidic protons. Amines,^{100, 101} phosphines,¹⁰² and alcohols⁸⁵ are among the most common reagents that have been shown to undergo this type of reactivity with metal alkyls. The synthesis of amidate benzyl species via protonolysis in section 3.2 demonstrated that organic amides can be installed through protonolysis reactions.⁴² Protonolysis routes into metal speciation are advantageous as they do not generate salt byproducts, which can be difficult to separate from the desired products. Additionally, in the case of the dibenzyl

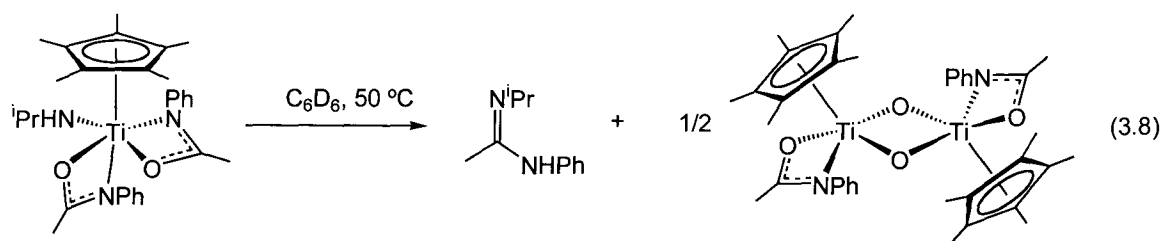
complexes **3.6**, **3.7**, **3.9**, **3.14**, and **3.15**, the byproduct of protonolysis is toluene, which can easily be removed under vacuum.

Protonolysis of organometallic species can be utilized to access many types of metal-element linkages. Metal-oxo species, bearing M=O multiple bonds, are one example of the different types of complexes accessible via protonolysis. Oxo complexes have been extensively studied as they are important intermediates in biological oxidation processes,¹⁰³ as well as industrially relevant chemical oxidations.¹⁰⁴ Oxo complexes of the group 4 metals have not been studied extensively, due in large part to the difficulties associated with controlled isolation of these species. However, the synthesis of terminal Ti oxo complexes has been accomplished by a number of different routes. For example, Cummins and coworkers have demonstrated that anionic terminal Ti oxo complexes can be accessed upon deprotonation and decarbonylation of a complexed formate ligand, as illustrated in Scheme 3.4.¹⁰⁵

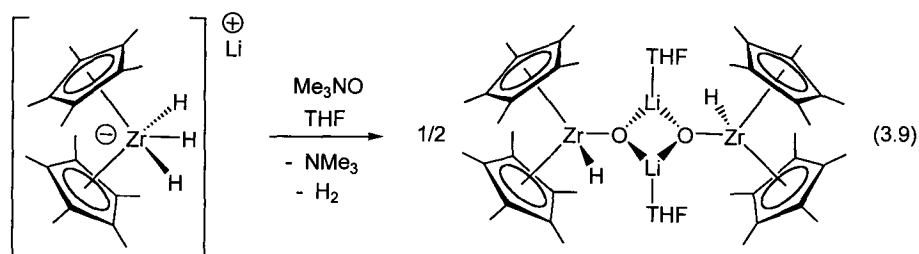


Scheme 3.4

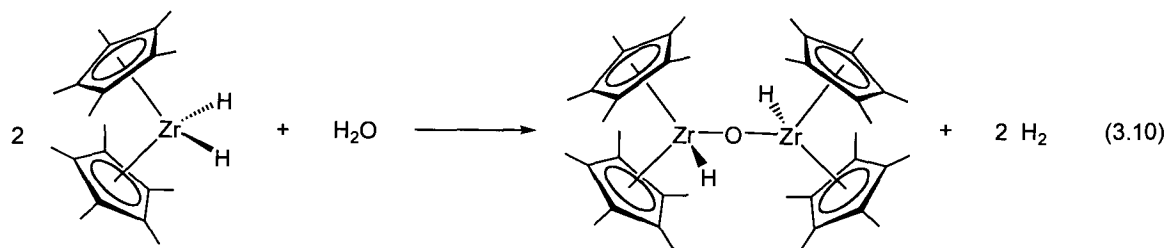
Stahl and coworkers have also shown that bridging Ti oxo dimers can be generated through transamidation of sterically unprotected amidate ligands with primary amines, to form amidines, as shown in Eq. 3.8.¹⁰⁶ Oxidation of Ti(II) species, such as (C₅Me₅)₂Ti(C₂H₄), with nitrous oxide has also been utilized to generate terminal Ti(IV) oxo complexes.¹⁰⁷ At elevated temperatures, these complexes decompose to tetranuclear oxo clusters.¹⁰⁷ Ti oxo complexes have also been synthesized through the addition of a small excess of H₂O to a Ti(III) hydrido complex,¹⁰⁸ and a Ti(IV) η²-imine complex.¹⁰⁹



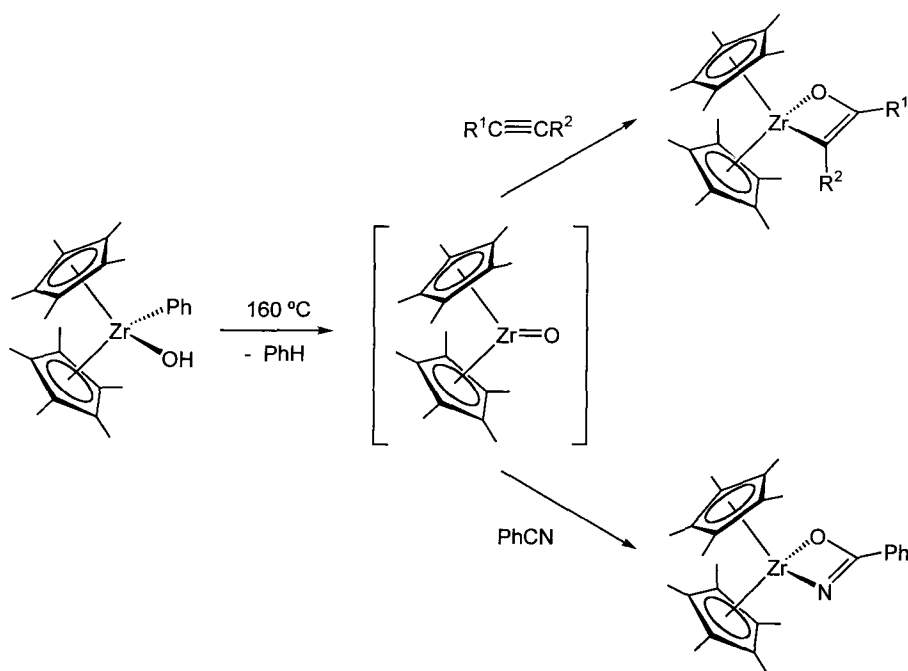
Dimeric oxo complexes of Zr have been isolated and structurally characterized. Recent results from the Stephan group have shown that oxo transfer agents, such as Me_3NO , can react with an anionic zirconium hydride complex to furnish a bridging Zr oxo dimer as shown in Eq. 3.9.¹¹⁰



Related work by Hillhouse and Bercaw demonstrated that careful hydrolysis of a neutral hydride complex of Zr results in the formation of a μ -oxo hydrido dimer, as demonstrated in Eq. 3.10.¹¹¹



Terminal oxo complexes of Zr and Hf are less prevalent, given their tendency to oligomerize due to the greater size of Zr and Hf vs. Ti. However, a terminal zirconium oxo complex has been trapped by Bergman and coworkers through thermolysis of a phenyl hydroxyl zirconium complex as illustrated in Scheme 3.5.¹¹² The highly reactive oxo fragment was trapped through cycloaddition reactions with unsaturated organics, such as alkynes and nitriles, forming new C-O bonds in the process.¹¹²

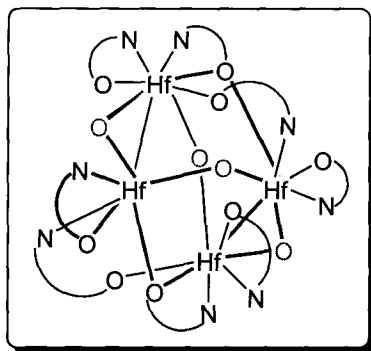
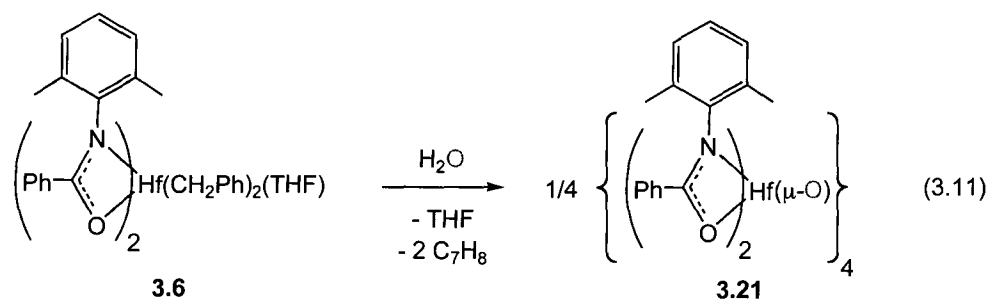


Scheme 3.5

This last route into terminal oxo complexes closely resembles the methodology used to access terminal imido complexes, which will be discussed in detail in Chapter 4. The possibility of using oxo complexes, such as the one in Scheme 3.5, in catalytic C=O bond-forming transformations provided the motivation to analyze amidate complexes bearing the metal-oxygen linkage. The following section discusses the fortuitous isolation of a Hf oxo complex, as the result of slow hydrolysis of the Hf bis(amidate) dibenzyl complex **3.6**.

3.4.2 Results and Discussion

Early transition metal oxo complexes are difficult targets to access reliably, and are typically isolated as dimeric^{106, 108, 110, 111} or oligomeric species,¹¹³⁻¹¹⁵ due to the sterically unprotected nature of the oxo ligand. Slow diffusion of trace amounts of H₂O into single crystals of **3.6** results in the fortuitous isolation of the hydrolysis byproduct $\{[{}^{\text{DMP}}(\text{NO})^{\text{Ph}}]_2\text{Hf}(\mu\text{-O})\}_4$, **3.21**.⁴² This complex has a tetrameric formulation, and is the result of addition of 1 equiv of H₂O to the dibenzyl species **3.6**, as shown in Eq. 3.11.



The solid-state molecular structure of **3.21** is shown in Fig. 3.10. Selected bond lengths and angles are available in Table 3.6 and crystallographic data are located in Appendix A in Table A3.8. The most important feature to note regarding the solid-state molecular structure of **3.21** is that the amidate ligands are intact, and only the benzyl ligands are eliminated from the metal center. This speaks to the robust nature of the amidate linkages to the Hf centers. While this complex is partially hydrolyzed under mild conditions, the resulting product is still unstable to further hydrolysis in the presence of excess H_2O , making it unlikely that group 4 amidate complexes would be useful in the presence of moist air.

Independent synthesis of **3.21** was attempted using a stoichiometric quantity of water with **3.6**.¹¹¹ The resulting oxo complex is completely insoluble in all solvents making solution characterization impossible. Due to the high molecular weight of **3.21** (2572 g mol^{-1}), conventional EI mass spectrometry is not possible for bulk structure analysis of molecular mass. However, fragments are observed in the mass spectrum, indicating that the resulting material still has coordinated amidate ligands ($m/z = 1076$, $[\text{DMP}(\text{NO})^{\text{Ph}}]_4\text{Hf}$; $m/z = 852$, $[\text{DMP}(\text{NO})^{\text{Ph}}]_3\text{Hf}$; $m/z = 643$, $[\text{DMP}(\text{NO})^{\text{Ph}}]_2\text{Hf}=\text{O}$). In an attempt to characterize the bulk material, MALDI mass spectrometric analysis was undertaken on **3.21**. The MALDI instrument in the chemistry department at UBC is not

compatible with air-free analysis, thus analysis was performed as quickly as possible under aerobic conditions. No signal was observed corresponding to the tetrameric oxo complex; however, the mass fragment at $m/z = 643.3$, corresponding to the monomeric oxo complex $[\text{DMP}(\text{NO})^{\text{Ph}}]_2\text{Hf}=\text{O}$, was observed again, along with the fragment at $m/z = 852.2$ ($[\text{DMP}(\text{NO})^{\text{Ph}}]_3\text{Hf}$).

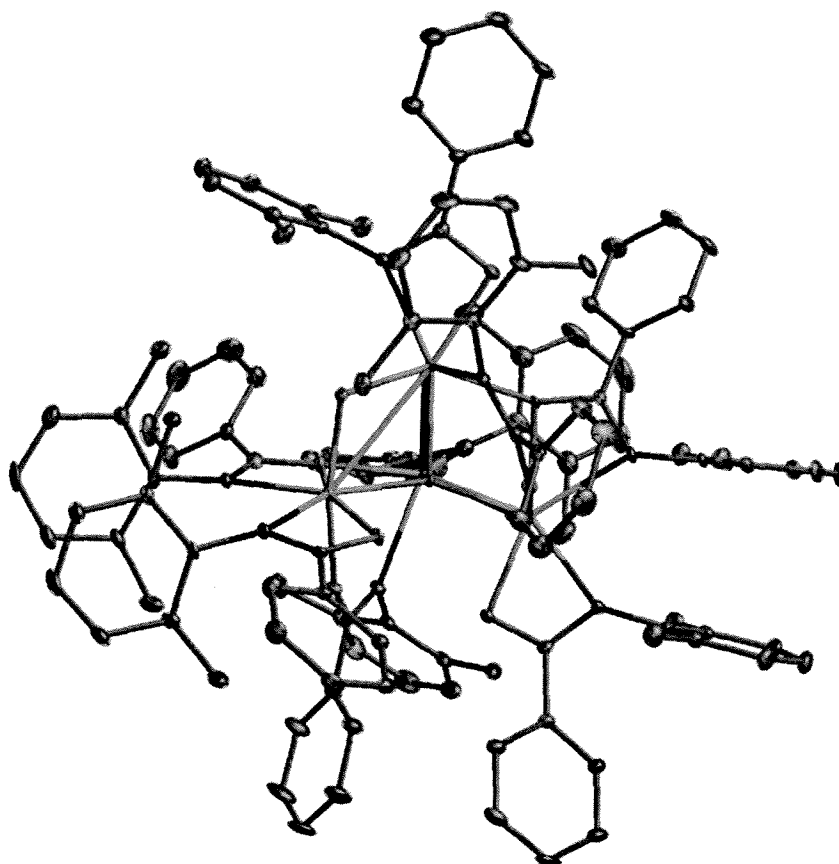


Figure 3.10 ORTEP depiction (ellipsoids at 30% probability) of solid-state molecular structure of $\{[\text{DMP}(\text{NO})^{\text{Ph}}]_2\text{Hf}(\mu\text{-O})\}_4$, **3.21** (hydrogens omitted)

A simplified structure of **3.21** is given in Fig. 3.11, which clearly shows the multiple binding motifs possible with the amidate ligands. While κ^1 - and κ^2 -binding of the amidate ligands was shown in Chapter 2, this is the first example where these bulky amidate ligands have been observed to bridge between multiple metal centers. The π -stacking interactions observed in the dibenzyl precursor **3.6** are also present in the oxo cluster for four of the eight amidate ligands. Interestingly, in each of the two pairs of π -stacked amidate ligands, one amidate is bound in a standard κ^2 -fashion, while the other is

bound κ^2 to one Hf and bridged through the oxygen to another Hf center. In addition to the π -stacked amidate ligands in the oxo cluster, there are two κ^2 -amidate ligands bound to single Hf centers. Finally, there are two amidate ligands bridging between two Hf centers that are bound κ^1 to both metals.

The four Hf atoms are arranged in a kite-like geometry, with each Hf bridging to two other Hf centers through a μ -oxo ligand. The four oxo ligands (O(9), O(10), O(11), and O(12)) are arranged such that the overall symmetry of **3.21** is approximately C_2 symmetric, with the C_2 axis of symmetry lying along the vector connecting O(9) and O(11). This is most easily seen in Fig 3.11, in which **3.21** is viewed down the approximate C_2 axis of symmetry, and has all of the amidate substituents omitted for clarity. In general, oxo clusters of Hf tend to exist as very large units, having more than a dozen Hf centers, making direct comparison of bond lengths in **3.21** difficult.¹¹⁵ The oxo Hf-O distances range between 1.944(3) Å and 2.259(3) Å, and are similar to the Zr-O and Hf-O distances seen in the cluster compounds $Zr_3O(O^tBu)_{10}$ and $Hf_6O_2(OEt)_{20}(EtOH)_2$, where the oxo ligands are bridging to three Zr or Hf centers.¹¹⁴ Select Hf-Hf bonds are given as a visual guide, and do not represent actual bonding interactions. These distances range between 3.2423(5) and 3.5288(3) Å, whereas the ionic radius of Hf(IV) is only 0.85 Å (6-coordinate) or 0.97 Å (8-coordinate).²⁰ As such Hf(2) and Hf(4) are best considered as 7-coordinate, with distorted pentagonal bipyramidal geometries. In contrast, Hf(1) and Hf(3) are better viewed as highly distorted octahedra.

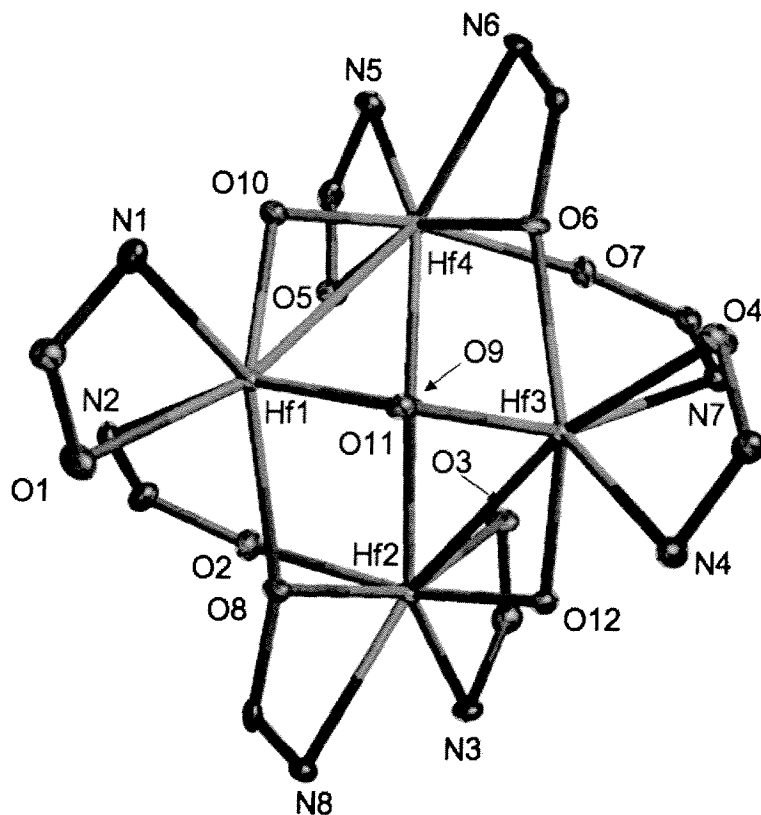


Figure 3.11 ORTEP depiction (ellipsoids at 30% probability) of core solid-state molecular structure of $\{[{}^{\text{DMP}}(\text{NO})^{\text{Ph}}]_2\text{Hf}(\mu\text{-O})\}_4$, **3.21** (hydrogens and amidate substituents omitted)

Table 3.6 Selected Bond Distances (Å) and Angles ($^\circ$) for $\{[{}^{\text{DMP}}(\text{NO})^{\text{Ph}}]_2\text{Hf}(\mu\text{-O})\}_4$, **3.21**

Lengths		Lengths		Lengths/ Angles	
Hf(1)-N(1)	2.327(4)	Hf(2)-O(3)	2.177(3)	Hf(4)-O(10)	1.948(3)
Hf(1)-N(2)	2.474(4)	Hf(3)-O(4)	2.196(3)	Hf(1)-O(10)	2.000(3)
Hf(2)-N(3)	2.272(4)	Hf(4)-O(5)	2.196(3)	Hf(3)-O(11)	1.969(3)
Hf(3)-N(4)	2.296(4)	Hf(3)-O(6)	2.206(3)	Hf(1)-O(11)	1.978(3)
Hf(4)-N(5)	2.265(4)	Hf(4)-O(6)	2.244(3)	Hf(2)-O(12)	1.944(3)
Hf(4)-N(6)	2.358(3)	Hf(4)-O(7)	2.086(7)	Hf(3)-O(12)	2.011(3)
Hf(3)-N(7)	2.457(4)	Hf(1)-O(8)	2.230(3)	Hf(4)-O(9)-Hf(2)	146.59(16)
Hf(2)-N(8)	2.341(4)	Hf(2)-O(8)	2.259(3)	Hf(4)-O(10)-Hf(1)	110.40(14)
Hf(1)-O(1)	2.182(3)	Hf(4)-O(9)	2.115(3)	Hf(3)-O(11)-Hf(1)	113.06(15)
Hf(2)-O(2)	2.088(3)	Hf(2)-O(9)	2.117(3)	Hf(3)-O(12)-Hf(2)	109.73(13)

3.4.3 Summary

A tetrametallic Hf oxo cluster, $\{[\text{DMP}(\text{NO})^{\text{Ph}}]_2\text{Hf}(\mu\text{-O})\}_4$, **3.21**, was isolated by adventitious hydrolysis of the Hf dibenzyl complex $[\text{DMP}(\text{NO})^{\text{Ph}}]_2\text{Hf}(\text{CH}_2\text{Ph})_2(\text{THF})$, **3.6**, in the solid-state. The insolubility of this complex precluded solution phase characterization; however, solid-state molecular structure characterization was possible through X-ray crystallographic studies. The resulting cluster complex retains all of the amidate ligands present in the benzyl precursor, where three distinct amidate binding modes are seen, including two bridging modes that had not previously been observed with these bulky ligands. Although Zr and Hf oxo clusters of this type are desirable for materials applications such as MOCVD, the inability to synthesize this cluster reliably makes this a poor candidate for such studies.¹¹⁶⁻¹¹⁸ This novel oxo complex demonstrates the robust nature of the amidate linkages, and the flexibility of the amidate ligand set in different coordination environments.

3.5 Abstraction Reactivity of Bis(Amidate) Dibenzyl Complexes

3.5.1 Introduction

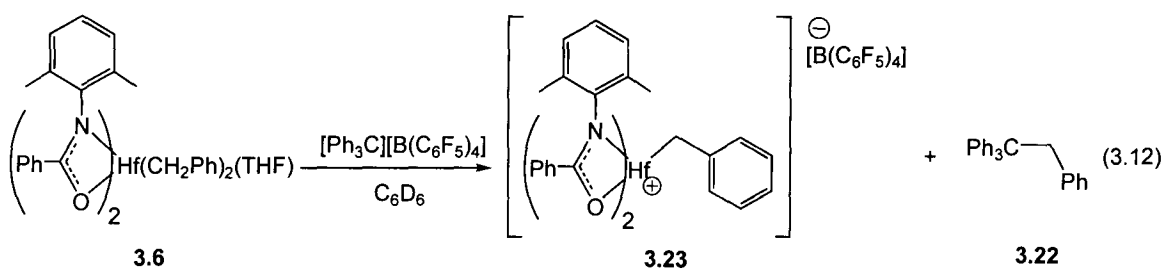
The ability to generate cationic metal complexes is an extremely important consideration when developing a new ligand system. In particular, cationic group 4 metals are well known to be excellent catalysts for ethylene polymerization.¹¹⁻¹³ The isolation of well defined cationic species is often extremely difficult or impossible, and thus generation of cationic complexes *in situ* is often the preferred method for studying these species.^{11, 13, 18} Abstraction of alkyl ligands is most often performed by strong Lewis acids like Al(III) and B(III).¹¹⁹ In most polymerization applications, partially hydrolyzed Al alkyl species (MAO) are utilized as co-catalysts to activate dichloro or bis(alkyl) group 4 metals for the rapid polymerization of ethylene.^{21, 119}

In contrast, studies that focus on the generation of cationic complexes for careful stoichiometric studies are generally performed with boron based abstraction agents.¹¹⁹ Preliminary studies by Arnold and coworkers revealed that a phenylene bridged

bis(amidate) Ti complex was a modestly active catalyst for ethylene polymerization.²³ In a collaboration with Exxon-Mobil, the dibenzyl complexes **3.6**, **3.9**, **3.14**, and **3.15** have been investigated for ethylene polymerization. The tethered systems **3.14** and **3.15** show particular promise for this process, and are being investigated in more detail. Furthermore, cationic group 4 complexes have been reported as alkene hydroamination precatalysts.^{120, 121} Thus, the generation of cationic amidate complexes was investigated.

3.5.2 Results and Discussion

The isolation of the first amidate supported bis(alkyl) complex (**3.6**, $[\text{DMP}(\text{NO})^{\text{Ph}}]_2\text{Hf}(\text{CH}_2\text{Ph})_2(\text{THF})$) enabled the study of alkyl abstraction reactions with amidate supported group 4 complexes.⁴² The combination of **3.6** and $[\text{Ph}_3\text{C}][\text{B}(\text{C}_6\text{F}_5)_4]$ in a 1:1 ratio in a J-Young NMR tube in C_6D_6 results in an immediate color change from light orange to deep red. The solution immediately separates into two immiscible phases, where a bright yellow solution floats above a red oil. ^1H NMR spectroscopy of the mixture is complicated; however, the two phases can be separated by decanting the yellow solution away from the red oil. The ^1H NMR spectrum of the yellow solution is simple, with a diagnostic signal at δ 3.80, which can be attributed to the methylene group of 1,1,1,2-tetraphenylethane (**3.22**), the expected organic product generated by benzyl abstraction, as shown in Eq. 3.12.

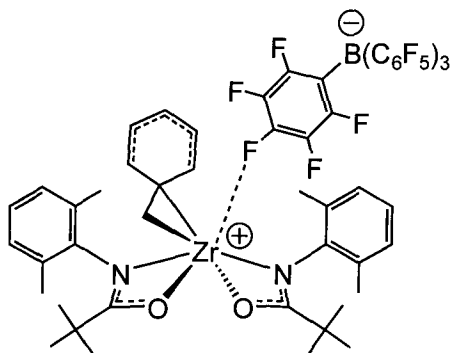


Unfortunately, spectroscopic data on the resulting cationic hafnium species $[\text{DMP}(\text{NO})^{\text{Ph}}]_2\text{HfCH}_2\text{Ph}[\text{B}(\text{C}_6\text{F}_5)_4]$, **3.23**, are extremely broad and of limited usefulness. However, the clean spectrum of **3.22** suggests that generation of **3.23** is occurring, and isolation of the desired complex may be possible. It has been noted in the literature that THF is a suitable ancillary ligand for stabilizing cationic group 4 complexes.^{122, 123}

Combination of **3.6** and $[\text{Ph}_3\text{C}][\text{B}(\text{C}_6\text{F}_5)_4]$ in THF at $-78\text{ }^\circ\text{C}$, followed by warming to room temperature results in a bright yellow solution. After several hours, this solution solidifies upon polymerization of the THF solvent. Polymerization of THF has been noted for many different Lewis acidic metals and acids, though rarely reported for cationic group 4 complexes.¹²⁴⁻¹²⁶

Cationic Zr complexes have recently been utilized in the catalytic hydroamination of aminoalkenes, and the mechanism of this reaction, promoted by neutral Ti and Zr complexes, is probed in detail in Chapter 5.^{120, 121} In order to evaluate two contrasting mechanistic proposals for this reaction, the use of cationic amidate Zr complexes in the hydroamination of aminoalkenes is necessary. While the cationic Hf complex **3.23** is not cleanly accessible, the abstraction reaction illustrated in Eq. 3.12, when performed with Zr dibenzyl complex **3.9**, cleanly yields the cationic complex $[[^{\text{DMP}}(\text{NO})^{\text{tBu}}]_2\text{ZrCH}_2\text{Ph}][\text{B}(\text{C}_6\text{F}_5)_4]$, **3.24**. Due to the low solubility of **3.23** in C_6D_6 , the reaction of **3.9** and $[\text{Ph}_3\text{C}][\text{B}(\text{C}_6\text{F}_5)_4]$ was performed in $\text{C}_6\text{D}_5\text{Br}$, instantly generating a blood red solution. Generation of 1,1,1,2-tetraphenylethane is observed by a single resonance at δ 3.93. In addition, the integration for the benzyl resonance is reduced in intensity from 4 protons to 2, and is downfield shifted to δ 2.60. Single resonances for the *tert*-butyl and aryl methyl protons at δ 0.83 and 2.00, respectively, indicate rapid exchange of the amidate ligands in solution. The *ortho* proton resonances for the benzyl group are shifted upfield to δ 6.55, suggesting that the benzyl ligand may be bound in an η^2 -fashion.

A significant change is observed in the ^{19}F NMR spectrum for the $[\text{B}(\text{C}_6\text{F}_5)_4]^-$ anion of **3.24**, where the *para* fluorine atoms appear at δ -162.1 ($^3J_{\text{FF}} = 22.2$ Hz). The *ortho* and *meta* fluorine atoms appear at δ -165.9 and -131.6. In $[\text{Ph}_3\text{C}][\text{B}(\text{C}_6\text{F}_5)_4]$, the ^{19}F NMR spectrum indicates that all fluorine atoms are equivalent on the NMR timescale. This indicates that the *para* fluorine atoms in **3.24** are potentially involved in a weak interaction with the Zr center, as illustrated in Figure 3.12. The presence of three signals in a 2:1:2 ratio in the ^{19}F NMR spectrum indicate that the pentafluorophenyl groups of the anion are equivalent on the NMR timescale, likely due to rapid exchange at the metal center.



3.24

Figure 3.12 Proposed structure of **3.24** in solution

Characterization of discrete cationic complexes in the solid-state is extremely difficult. These complexes are often too unstable to isolate, and in many cases are not crystalline, but are amorphous in nature.¹²⁷ The relative scarcity of well characterized cationic complexes in the literature is a testament to the difficulty associated with the isolation of such compounds.^{48, 71, 127-132} In most cases the generation of cationic complexes *in situ* is sufficient, even preferable, for reactivity studies. An exciting application of cationic group 4 complexes is the catalytic hydroamination of aminoalkenes to generate N-heterocyclic products.^{120, 121} Complex **3.24** and a closely related compound, will be revisited in Chapter 5 during the study of the mechanism of catalytic aminoalkene hydroamination, where the clean *in situ* generation of **3.24** facilitates these studies.

3.5.3 Summary

The generation of amidate supported cationic Hf and Zr complexes was possible through the combination of the dibenzyl complexes **3.6** and **3.9** with $[\text{Ph}_3\text{C}][\text{B}(\text{C}_6\text{F}_5)_4]$. Generation of the cationic complexes $[[^{\text{DMP}}(\text{NO})^{\text{Ph}}]_2\text{HfCH}_2\text{Ph}][\text{B}(\text{C}_6\text{F}_5)_4]$, **3.23**, and $[[^{\text{DMP}}(\text{NO})^{\text{tBu}}]_2\text{ZrCH}_2\text{Ph}][\text{B}(\text{C}_6\text{F}_5)_4]$, **3.24** was supported by the appearance of 1,1,1,2-tetraphenylethane as a result of benzyl abstraction by the trityl cation.

NMR spectroscopic data of **3.23** are complicated, indicating a mixture of products and possibly unstable cationic species in solution. In contrast, the NMR spectroscopic data for **3.24** are well resolved, suggesting generation of a single cationic complex in

solution. ^{19}F NMR data indicate that the tetrakis(pentafluorophenyl) borate anion is weakly coordinating to the Zr through the *para* F atoms of the pentafluorophenyl rings.

While ethylene polymerization studies of these complexes is beyond the scope of this thesis, **3.23** was found to polymerize THF at room temperature, indicating that the Hf center is strongly Lewis acidic.

3.6 Conclusions

Amidate supported Zr and Hf dibenzyl species can be reliably accessed in high yields through protonolysis of tetrabenzyl Zr and Hf starting materials with organic amide proligands. Both bidentate and tetradentate amidate ligands were successful at stabilizing these complexes. While the Hf complex **3.6** was stable to ambient light and heat, it underwent THF exchange in solution, oscillating between 7-coordinate pentagonal bipyramidal and 6-coordinate pseudo-octahedral species. The Zr complex **3.9** was less stable to heat and light than **3.6**, and exhibited intermediate η^1/η^2 -hapticity of the benzyl ligands in the solid-state, but behaved as an η^1 -benzyl species in solution.

Migratory insertion of aryl isocyanides was observed for **3.9**, resulting in η^2 -iminoacyl complex **3.16**, which could undergo thermal coupling to form enediamido complex **3.17**. Insertion of $^t\text{BuN}\equiv\text{C}$ resulted in the formation of a vinylamido complex, **3.18**, which was generated through a 1,2-hydrogen atom migration mechanism. The inability to controllably insert one equivalent of isocyanide is indicative of the extremely electrophilic nature of **3.9**, further supporting the highly ionic character of the amidate bonding interactions discussed in Chapter 2.

Although the amidate ligands are poor at donating electron density to the group 4 metals, they bind strongly to these metals, such that partial hydrolysis of **3.6** results in the formation of a tetrametallic Hf oxo cluster, where all of the amidate ligands are intact. This complex demonstrates the variety of bonding modes possible with the amidate ligand set, as κ^1 - and κ^2 -binding modes are noted, and for the first time, these ligands are observed to bridge between metal centers.

In addition to the insertion and protonolysis reactivity possible with these bis(amidate) dibenzyl complexes, benzyl abstraction is also readily accomplished. The

ability of cationic Hf complex **3.23** to polymerize THF at room temperature is strongly supportive of the potential of these complexes to polymerize ethylene and polar monomers in future investigations.

The benzyl complexes discussed in this chapter are readily isolated in high yields, and undergo reliable insertion, protonolysis, and abstraction chemistry. While most of the chemical reactivity of the dibenzyl complexes follows patterns previously seen in the literature, some of the deviations noted can be attributed to the highly ionic nature of the amidate bonding to Zr and Hf. These highly electrophilic benzyl complexes thus exhibit reactivity which approaches levels seen more often for cationic group 4 complexes.

3.7 Experimental

3.7.1 General Considerations

See Chapter 2, section 2.6.1. Reactions with $\text{Zr}(\text{CH}_2\text{Ph})_4$ and $\text{Hf}(\text{CH}_2\text{Ph})_4$ were performed in the absence of light to avoid photo-initiated decomposition.

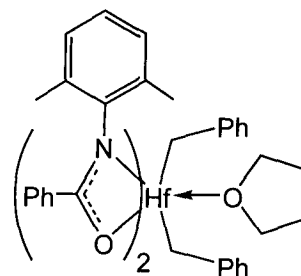
3.7.2 Starting Materials and Reagents

See Chapter 2, section 2.6.2.

3.7.3 Synthesis

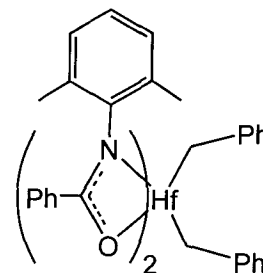
Synthesis of $[\text{DMP}(\text{NO})^{\text{Ph}}]_2\text{Hf}(\text{CH}_2\text{Ph})_2(\text{THF})$, **3.6**

In a foil wrapped Schlenk flask, 3.50 g (6.5 mmol) of $\text{Hf}(\text{CH}_2\text{Ph})_4$ and 2.90 g (12.9 mmol) of $[\text{DMP}(\text{NO})^{\text{Ph}}]\text{H}$ (**3.5**) were combined. To this mixture of solids, approximately 125 mL of THF was added at $-78\text{ }^\circ\text{C}$ via cannula. The reaction mixture was allowed to warm to room temperature while stirring overnight. Excess THF was removed from the bright red-orange solution *in vacuo*, resulting in the isolation of 5.60 g of the crude product as an intense red-orange solid (98% yield). The crude product was dissolved in approximately 150 mL of hexanes at room temperature and filtered through a fritted disk. A small amount of a pale yellow hexanes insoluble product ($[\text{DMP}(\text{NO})^{\text{Ph}}]_2\text{Hf}(\text{CH}_2\text{Ph})_2$, **3.7**) was isolated by filtration, and the dark red-orange filtrate was concentrated and cooled to $-37\text{ }^\circ\text{C}$ overnight. Microcrystals of the red-orange product (**3.6**) suitable for X-ray crystallographic analysis were isolated in 34% yield from the first batch. Repeated concentration and crystallization of the mother liquor resulted in a combined yield of approximately 65%. The spectroscopic properties of the isolated microcrystals are identical to that seen for the crude isolated material. ^1H NMR (C_6D_6 , $25\text{ }^\circ\text{C}$, 300 MHz): δ 1.40 (t, 4H, $^3J_{\text{HH}} = 6.4\text{ Hz}$, $\text{O}(\text{CH}_2\text{CH}_2)_2$), 2.10 (s, 12H, $\text{Ph}(\text{CH}_3)_2$), 2.30 (s, 4H, $\text{Hf}(\text{CH}_2\text{Ph})_2$), 3.59 (t, 4H, $^3J_{\text{HH}} = 6.4\text{ Hz}$, $\text{O}(\text{CH}_2\text{CH}_2)_2$), 6.78-6.92 (m, 14H total, Ar-H), 7.10-7.24 (m, 8H total, Ar-H), 7.61 (d, 4H, $^3J_{\text{HH}} = 7.4\text{ Hz}$, Ar-H). $^{13}\text{C}\{^1\text{H}\}$ NMR (C_6D_6 , $25\text{ }^\circ\text{C}$, 75 MHz): δ 18.7, 25.8, 68.0, 81.6, 122.1, 126.0, 128.6, 128.7, 128.9, 129.1, 132.0, 132.3, 133.1, 142.1, 144.7, 179.6. EIMS (m/z): 719 ($[\text{M}^+] - \text{THF} - \text{CH}_2\text{Ph}$), 627 ($[\text{M}^+] - \text{THF} - 2\text{ CH}_2\text{Ph}$). Anal. Calcd for $\text{C}_{48}\text{H}_{50}\text{N}_2\text{O}_3\text{Hf}$ (%): C, 65.41; H, 5.72; N, 3.18. Found: C, 65.15; H, 6.00; N, 3.54.



Synthesis of $[\text{DMP}(\text{NO})^{\text{Ph}}]_2\text{Hf}(\text{CH}_2\text{Ph})_2$, **3.7**

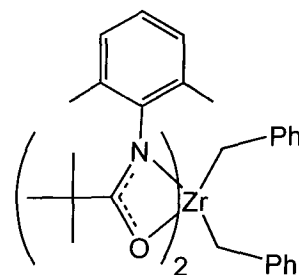
In a foil wrapped Schlenk flask, 0.93 g (1.7 mmol) of $\text{Hf}(\text{CH}_2\text{Ph})_4$ and 0.77 g (3.4 mmol) of $[\text{DMP}(\text{NO})^{\text{Ph}}]\text{H}$ (**3.5**) were combined. To this mixture of solids, approximately 75 mL of toluene was added at $-78\text{ }^\circ\text{C}$ via cannula. The reaction mixture was allowed to warm to room temperature while stirring for approximately 4 h. Excess toluene was removed, resulting in the isolation of a bright yellow



solid residue. The crude product was dissolved in approximately 25 mL of hexanes at room temperature and concentrated until a yellow powder precipitated out of solution. This powder was isolated in 62 % yield (0.86 g) by filtration through a fritted disk, and dried *in vacuo*. ^1H NMR (C_6D_6 , $25\text{ }^\circ\text{C}$, 300 MHz): δ 2.10 (s, 12H, $\text{Ph}(\text{CH}_3)_2$), 2.30 (s, 4H, $\text{Hf}(\text{CH}_2\text{Ph})_2$), 6.78-6.94 (m, 14H total, Ar-H), 7.10-7.24 (m, 8H total, Ar-H), 7.61 (d, 4H, $^3J_{\text{HH}} = 7.3\text{ Hz}$, Ar-H). $^{13}\text{C}\{^1\text{H}\}$ NMR (C_6D_6 , $25\text{ }^\circ\text{C}$, 75 MHz): δ 19.0, 82.9, 122.1, 126.4, 129.0, 128.7, 129.3, 129.5, 130.1, 132.3, 132.7, 133.5, 142.5, 144.7, 179.6. EIMS (m/z): 719 ($[\text{M}^+] - \text{CH}_2\text{Ph}$), 627 ($[\text{M}^+] - 2\text{ CH}_2\text{Ph}$). Anal. Calcd for $\text{C}_{44}\text{H}_{42}\text{N}_2\text{O}_2\text{Hf}$ (%): C, 65.30; H, 5.23; N, 3.46. Found: C, 64.41; H, 5.36; N, 3.81.

Synthesis of $[\text{DMP}(\text{NO})^{\text{tBu}}]_2\text{Zr}(\text{CH}_2\text{Ph})_2$, **3.9**

In a foil wrapped 250 mL round-bottomed Schlenk flask equipped with a stir bar, 0.90 g (4.4 mmol) of $[\text{DMP}(\text{NO})^{\text{tBu}}]\text{H}$ (**3.8**) was combined with 1.00 g (2.2 mmol) of $\text{Zr}(\text{CH}_2\text{Ph})_4$. To this flask was added 75 mL of toluene which had been cooled to $-78\text{ }^\circ\text{C}$. The reaction mixture was then stirred for 3.5 hours while allowing to warm to $\sim 10\text{ }^\circ\text{C}$. Given the thermal and

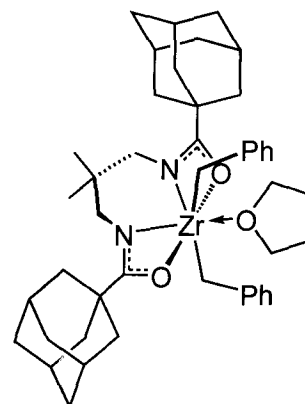


photosensitivity of $\text{Zr}(\text{CH}_2\text{Ph})_4$, care was taken to ensure reaction occurred in the absence of ambient light, and the reaction was not allowed to exceed $10\text{ }^\circ\text{C}$. The clear bright yellow solution was then concentrated to dryness *in vacuo* to give a bright yellow solid residue. The crude material was dissolved in 30 mL of pentane and filtered through CeliteTM to remove impurities. The pentane solution was concentrated to approximately

10 mL and cooled to $-37\text{ }^{\circ}\text{C}$. The yellow precipitate was isolated in 57 % yield (0.85 g) by filtration and dried *in vacuo*. Successive concentration/filtration cycles allow access to > 80 % yield of pure **3.9**. Single crystals suitable for X-ray crystallographic analysis were grown in the dark from a saturated pentane solution at $-37\text{ }^{\circ}\text{C}$. ^1H NMR (C_6D_6 , $25\text{ }^{\circ}\text{C}$, 300 MHz): δ 0.91 (s, 18H, $\text{C}(\text{CH}_3)_3$), 2.05 (s, 12H, $\text{Ph}(\text{CH}_3)_2$), 2.24 (s, 4H, $\text{Zr}(\text{CH}_2\text{Ph})_2$), 6.86-6.89 (m, 8H, Ar-H), 7.11-7.15 (m, 8H, Ar-H). $^{13}\text{C}\{^1\text{H}\}$ NMR (C_6D_6 , $25\text{ }^{\circ}\text{C}$, 75 MHz): δ 19.4, 27.5, 41.2, 75.8, 123.1, 125.5, 128.6, 129.4, 129.9, 132.1, 142.9, 143.2, 190.7. EIMS (m/z): 589 ($[\text{M}^+] - \text{CH}_2\text{Ph}$), 497 ($[\text{M}^+] - 2\text{ CH}_2\text{Ph}$). Anal. Calcd for $\text{C}_{40}\text{H}_{50}\text{N}_2\text{O}_2\text{Zr}$ (%): C, 70.44; H, 7.39; N, 4.11. Found: C, 69.71; H, 7.60; N, 4.67.

Synthesis of $^{\text{Ad}}[\text{N}_2\text{O}_2]\text{Zr}(\text{CH}_2\text{Ph})_2(\text{THF})$, **3.14**

A foil wrapped 250 mL round-bottomed Schlenk flask equipped with a stir bar, was loaded with 0.75 g (1.7 mmol) of $\text{Zr}(\text{CH}_2\text{Ph})_4$. To this flask was added 50 mL of THF via cannula, and the resulting solution was cooled to $-78\text{ }^{\circ}\text{C}$. Using a solid addition funnel, 0.70 g (1.7 mmol) of **3.11** was added to the THF solution of $\text{Zr}(\text{CH}_2\text{Ph})_4$ over a period of 5 minutes. The cloudy yellow reaction mixture was then stirred while allowing to warm to $0\text{ }^{\circ}\text{C}$ over the course of 4 hours. The clear

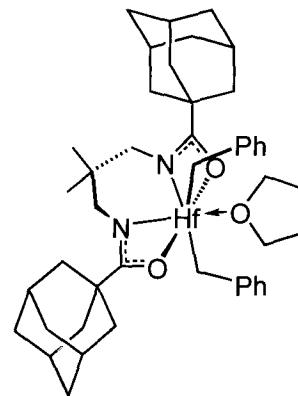


bright yellow-orange solution was concentrated to dryness *in vacuo* to give a bright yellow solid residue, while ensuring that the reaction temperature did not exceed $\sim 10\text{ }^{\circ}\text{C}$. The crude material was washed with 25 mL of pentane and dried under vacuum to give a bright yellow powder in 73 % yield (0.92 g). Single crystals suitable for X-ray crystallographic analysis were grown in the dark from a saturated hexanes solution at $-37\text{ }^{\circ}\text{C}$. ^1H NMR (C_6D_6 , $25\text{ }^{\circ}\text{C}$, 400 MHz): δ 0.72 (s, 6H, $\text{C}(\text{CH}_3)_2$), 1.38 (m, 4H, $\text{O}(\text{CH}_2\text{CH}_2)_2$), 1.61 (br, 12H, Ad- $(\text{CH}(\text{CH}_2)\text{CH})_3$), 1.90 (br, 6H, Ad- $(\text{CH})_3$), 2.04 (br, 12H, Ad- $\text{C}(\text{CH}_2)_3$), 2.25 (s, 4H, $\text{Hf}(\text{CH}_2\text{Ph})_2$), 3.08 (s, 4H, $\text{NCH}_2\text{C}(\text{CH}_3)_2\text{CH}_2\text{N}$), 3.66 (m, 4H, $\text{O}(\text{CH}_2\text{CH}_2)_2$), 6.86 (m, 2H, Ar-H), 7.19-7.24 (m, 8H, Ar-H). $^{13}\text{C}\{^1\text{H}\}$ NMR (C_6D_6 , $25\text{ }^{\circ}\text{C}$, 100 MHz): δ 24.9, 26.0, 28.9, 35.8, 37.2, 38.5, 43.0, 56.3, 62.4, 68.8, 120.2, 127.9, 128.5, 148.2, 192.3. EIMS (m/z): 605 ($[\text{M}^+] - \text{THF} - \text{CH}_2\text{Ph}$). Anal. Calcd

for $C_{45}H_{62}N_2O_3Zr$ (%): C, 70.17; H, 8.11; N, 3.64. Found: C, 65.01; H, 7.99; N, 4.14. (incomplete combustion through possible carbide formation may be responsible for low carbon analysis).

Synthesis of $^{Ad}[N_2O_2]Hf(CH_2Ph)_2(THF)$, **3.15**

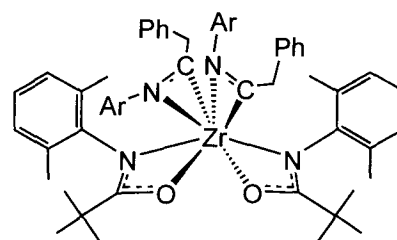
A foil wrapped 250 mL round-bottomed Schlenk flask equipped with a stir bar, was loaded with 3.00 g (5.5 mmol) of $Hf(CH_2Ph)_4$. To this flask was added 100 mL of THF via cannula, and the resulting solution was cooled to $-78\text{ }^\circ\text{C}$. Using a solid addition funnel, 2.36 g (5.5 mmol) of **3.11** was added to the THF solution of $Hf(CH_2Ph)_4$ over a period of 5 minutes. The cloudy yellow reaction mixture was then stirred while allowing to warm to room temperature overnight. The clear



yellow solution was then concentrated to dryness *in vacuo* to give a light yellow solid residue. The crude material was triturated with ~ 30 mL of pentane and filtered over a fritted disk to give 2.75 g (58 % yield) of **3.15** as a pale yellow powder. The pentane washings were concentrated until product began to precipitate. After cooling to aid precipitation, and additional 0.50 g (11 % yield) of **3.15** was isolated by filtration, resulting in an overall isolated yield of 70 %. Single crystals suitable for X-ray crystallographic analysis were grown in the dark from a saturated hexanes solution at $-37\text{ }^\circ\text{C}$. ^1H NMR (C_6D_6 , $25\text{ }^\circ\text{C}$, 400 MHz): δ 0.83 (s, 6H, $C(CH_3)_2$), 1.33 (m, 4H, $O(CH_2CH_2)_2$), 1.66 (br, 12H, Ad- $(CH(CH_2)CH)_3$), 1.72 (s, 4H, $Hf(CH_2Ph)_2$), 1.95 (br, 6H, Ad- $(CH)_3$), 2.09 (br, 12H, Ad- $C(CH_2)_3$), 3.19 (s, 4H, $NCH_2C(CH_3)_2CH_2N$), 3.99 (m, 4H, $O(CH_2CH_2)_2$), 6.76 (m, 2H, Ar- H), 7.04 (d, 4H, $^3J_{HH} = 7.6$ Hz, Ar- H), 7.19 (m, 4H, Ar- H). $^{13}\text{C}\{^1\text{H}\}$ NMR (C_6D_6 , $25\text{ }^\circ\text{C}$, 75 MHz): δ 24.9, 25.0, 28.2, 35.8, 36.5, 37.8, 42.8, 55.3, 57.3, 70.0, 117.9, 125.4, 127.4, 153.9, 190.9. EIMS (m/z): 695 ($[M^+]$ – THF – CH_2Ph). Anal. Calcd for $C_{45}H_{62}N_2O_3Hf$ (%): C, 63.03; H, 7.29; N, 3.27. Found: C, 61.96; H, 7.64; N, 3.50.

Synthesis of $[\text{DMP}(\text{NO})^{\text{tBu}}]_2\text{Zr}(\eta^2\text{-ArN=CCH}_2\text{Ph})_2$ (Ar = 2,6-Me₂C₆H₃), **3.16**

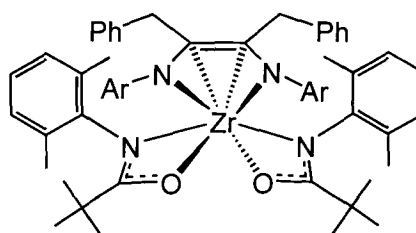
In a 50 mL Schlenk flask, 150 mg (0.2 mmol) of **3.9** was dissolved in approximately 5 mL of toluene at room temperature. To this solution was added 58 mg (0.4 mmol) of 2,6-Me₂C₆H₃N≡C dissolved in 5 mL of toluene. The bright yellow solution was stirred at room



temperature, and became colorless within minutes. Excess toluene was removed *in vacuo* to give a white residue. This material was triturated with 5 mL of pentane, and the insoluble white powder was isolated by filtration in 52 % yield (108 mg). Higher yields are possible, but due to static electricity, the product sticks to glass very well, and small scale reactions suffer from this. Single crystals were grown from a saturated pentane solution at -37 °C. ¹H NMR (C₆D₆, 25 °C, 300 MHz): δ 0.95 (s, 6H, Ph(CH₃)₂), 1.11 (s, 18H, C(CH₃)₃), 1.92 (s, 6H, Ph(CH₃)₂), 2.12 (s, 6H, Ph(CH₃)₂), 2.62 (s, 6H, Ph(CH₃)₂), 3.35 (d, 2H, ²J_{HH} = 12.0 Hz, CH₂Ph), 3.59 (d, 2H, ²J_{HH} = 12.2 Hz, CH₂Ph), 6.19 (d, 4H, ³J_{HH} = 6.6 Hz, Ar-H), 6.83-7.09 (m, 18H, Ar-H). ¹³C {¹H} NMR (C₆D₆, 25 °C, 75 MHz): δ 18.2, 19.1, 19.4, 20.6, 28.5, 41.3, 44.3, 125.7, 125.8, 126.6, 129.0, 130.0, 130.2, 130.8, 133.5, 133.9, 135.8, 147.8, 149.1, 187.3, 250.6. EIMS (*m/z*): 942 ([M⁺]), 720 ([M⁺] - PhCH₂C=N(2,6-Me₂C₆H₃)). Anal. Calcd for C₅₈H₆₈N₄O₂Zr₁ (%): C, 73.76; H, 7.26; N, 5.93. Found: C, 70.62; H, 7.25; N, 5.63 (incomplete combustion through possible carbide formation may be responsible for low carbon analysis).

Synthesis of $[\text{DMP}(\text{NO})^{\text{tBu}}]_2\text{Zr}(\eta^4\text{-ArNC}(\text{CH}_2\text{Ph})=\text{C}(\text{CH}_2\text{Ph})\text{NAr})$ (Ar = 2,6-Me₂C₆H₃), **3.17**

In a 100 mL Schlenk flask, 360 mg (0.5 mmol) of **3.9** and 139 mg (1.0 mmol) of 2,6-Me₂C₆H₃N≡C was dissolved in approximately 35 mL of toluene at room temperature. The bright yellow solution was stirred and heated to 110 °C overnight, resulting in a yellow

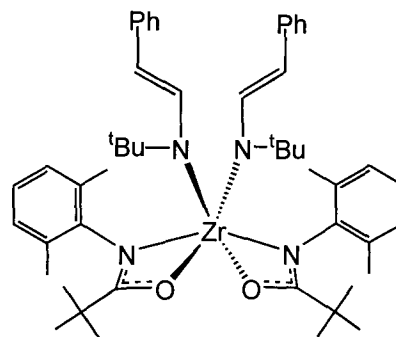


orange solution. Excess toluene was removed *in vacuo* to give a yellow-orange solid. This material was dissolved in 10 mL of pentane, and filtered through CeliteTM to remove

3.16. Excess pentane was removed *in vacuo*, resulting in 81 % yield (403 mg) of **3.17** as a yellow orange solid. This complex can also be synthesized by heating **3.17** to 110 °C overnight. Single crystals for X-ray analysis were grown from a saturated toluene solution at room temperature. ¹H NMR (C₆D₆, 25 °C, 400 MHz): δ 0.82 (s, 18H, C(CH₃)₃), 1.95 (s, 12H, Ph(CH₃)₂), 2.19 (s, 12H, Ph(CH₃)₂), 3.99 (s, 4H, CH₂Ph), 6.65-7.08 (m, 22H, Ar-H). ¹³C{¹H} NMR (C₆D₆, 25 °C, 100 MHz): δ 20.2, 21.2, 28.1, 37.8, 41.4, 115.6, 124.1, 124.8, 126.3, 128.0, 128.3, 128.6, 130.5, 132.1, 133.3, 140.4, 143.9, 147.3, 187.6.

Synthesis of [^{DMP}(NO)^{tBu}]₂Zr(N^{tBu}CH=CHPh)₂, **3.18**

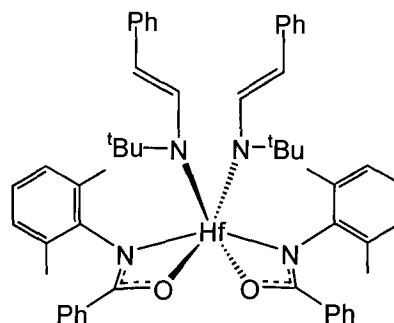
In a 100 mL Schlenk flask, 360 mg (0.5 mmol) of **3.9** was dissolved in approximately 30 mL of toluene at room temperature. To this solution was added 88 mg (1.0 mmol) of ^tBuN≡C dissolved in 5 mL of toluene at room temperature. The solution immediately became an intense yellow color. Excess toluene was removed *in vacuo* to give a vibrant yellow solid. This material was triturated



with 10 mL of pentane, and isolated by filtration in 86 % yield (385 mg). ¹H NMR (C₆D₆, 25 °C, 300 MHz): δ 1.02 (s, 18H, O=CC(CH₃)₃), 1.35 (s, 18H, NC(CH₃)₃), 2.31 (s, 12H, Ph(CH₃)₂), 5.84 (d, 2H, ³J_{HH} = 13.5 Hz, NCH=CHPh), 6.91-7.12 (m, 16H, Ar-H), 7.28 (d, 2H, ³J_{HH} = 13.5 Hz, NCH=CHPh). ¹³C{¹H} NMR (C₆D₆, 25 °C, 75 MHz): δ 20.9, 28.3, 30.4, 41.3, 58.4, 106.2, 124.7, 125.2, 125.9, 128.1, 129.0, 132.1, 134.4, 139.5, 144.7 (no signal seen for C=O). EIMS (*m/z*): 846 ([M⁺]). Anal. Calcd for C₅₀H₆₈N₄O₂Zr₁ (%): C, 70.79; H, 8.08; N, 6.60. Found: C, 69.42; H, 7.73; N, 6.16.

NMR tube reaction of **3.6** and ${}^t\text{BuN}\equiv\text{C}$ to generate $[\text{DMP}(\text{NO})^{\text{Ph}}]_2\text{Hf}(\eta^2\text{-}{}^t\text{BuN}=\text{CCH}_2\text{Ph})_2$, **3.19** and $[\text{DMP}(\text{NO})^{\text{Ph}}]_2\text{Hf}(\text{N}{}^t\text{BuCH}=\text{CHPh})_2$, **3.20**

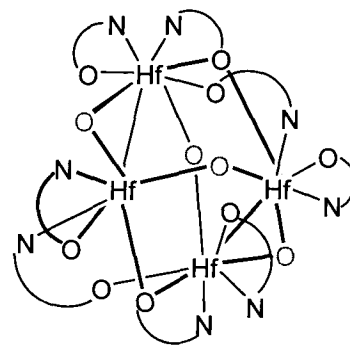
In a small vial in a glovebox, 100 mg (0.1 mmol) of **3.6** was dissolved in approximately 0.5 mL C_6D_6 and transferred into a J-Young NMR tube. In another vial 19 mg (0.2 mmol) of ${}^t\text{BuN}\equiv\text{C}$ was dissolved in approximately 0.5 mL of C_6D_6 and added to the NMR tube. An immediate color change from orange to yellow-orange occurred upon mixing the two solutions.



While the ${}^1\text{H}$ NMR spectrum was complicated and indicated a mixture of products, signals characteristic of an η^2 -iminoacyl were observed. ${}^1\text{H}$ NMR (C_6D_6 , 25 °C, 300 MHz): δ 2.88 (d, 2H, ${}^2J_{\text{HH}} = 13.3$ Hz, ${}^t\text{BuN}=\text{CCH}_2\text{Ph}$), 3.68 (d, 2H, ${}^2J_{\text{HH}} = 13.7$ Hz, ${}^t\text{BuN}=\text{CCH}_2\text{Ph}$). Heating the NMR tube to 80 °C for 24 h resulted in a gradual color change from yellow-orange to red-brown, and finally to emerald green. Again, the ${}^1\text{H}$ NMR spectrum was complicated with signals for multiple products, signals characteristic of a *trans* vinylamido complex analogous to **3.18** were observed. ${}^1\text{H}$ NMR (C_6D_6 , 25 °C, 300 MHz): δ 6.02 (d, 2H, ${}^2J_{\text{HH}} = 12.8$ Hz, ${}^t\text{BuN}=\text{CCH}_2\text{Ph}$), 7.47 (d, 2H, ${}^2J_{\text{HH}} = 11.9$ Hz, ${}^t\text{BuN}=\text{CCH}_2\text{Ph}$).

Attempted synthesis of $\{[\text{DMP}(\text{NO})^{\text{Ph}}]_2\text{Hf}(\mu\text{-O})\}_4$, **3.21**

In a 100 mL round bottomed Schlenk flask 710 mg (0.8 mmol) of **3.6** was dissolved in approximately 50 mL toluene. This solution was frozen in a liquid nitrogen bath prior to addition of 15 μL of H_2O via microsyringe. The reaction mixture was slowly warmed to -78 °C using a dry-ice/isopropanol bath, and was left to gradually warm to room temperature while stirring overnight. The red-orange



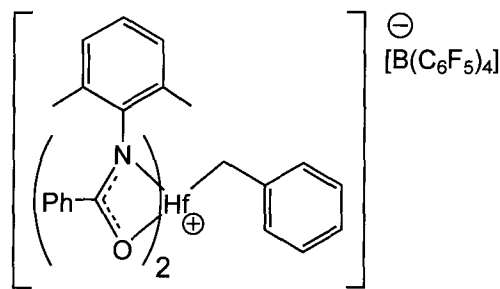
solution was observed to turn into a cloudy white suspension. Excess toluene was removed *in vacuo* to give a white powder. The crude product was triturated with 10 mL

of hexanes and filtered over a fritted disk. This material was completely insoluble in all organic solvents, and was uncharacterizable in the solution phase. While microanalysis did not verify the composition of **3.21** as determined by X-ray crystallography, mass spectral data suggested formation of oxo species. EIMS (m/z): 1076 ($[\text{DMP}(\text{NO})^{\text{Ph}}]_4\text{Hf}$), 852 ($[\text{DMP}(\text{NO})^{\text{Ph}}]_3\text{Hf}$), 643 ($[\text{DMP}(\text{NO})^{\text{Ph}}]_2\text{Hf}=\text{O}$). MALDIMS (m/z) = 643.3 ($[\text{DMP}(\text{NO})^{\text{Ph}}]_2\text{Hf}=\text{O}$), 852.2 ($[\text{DMP}(\text{NO})^{\text{Ph}}]_3\text{Hf}$).

Synthesis of cationic species **3.23** and **3.24**

In situ generation of **3.23**

In a small vial in a glovebox 100 mg (0.1 mmol) of **3.6** was dissolved in approximately 0.5 mL of C_6D_6 at room temperature. In a separate vial 105 mg (0.1 mmol) of $[\text{Ph}_3\text{C}][\text{B}(\text{C}_6\text{F}_5)_4]$ was dissolved in approximately 1 mL of C_6D_6 . The two solutions were transferred into a J-Young



NMR tube, and an immediate color change to deep red was observed. The solution partitioned into two phases, with a dense red oil settling on the bottom of the tube, and light yellow solution rising to the top. NMR spectroscopy of the red oil was not informative. ¹H NMR spectroscopy of the yellow solution indicated the formation of $\text{Ph}_3\text{CCH}_2\text{Ph}$ as a result of benzyl abstraction by the trityl cation. ¹H NMR (C_6D_6 , 25 °C, 300 MHz): δ 3.93 (s, 2H, $\text{Ph}_3\text{CCH}_2\text{Ph}$), 6.71-7.22 (m, 20H, Ar-H).

Attempted isolation of **3.23**

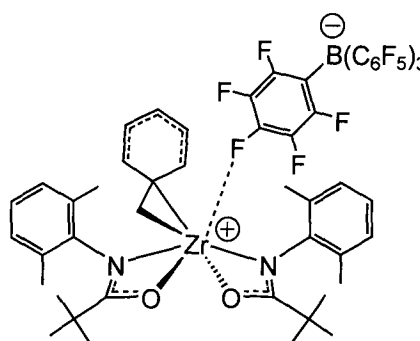
In a 250 mL round bottomed Schlenk flask 812 mg (0.9 mmol) of **3.6** and 850 mg (0.9 mmol) of $[\text{Ph}_3\text{C}][\text{B}(\text{C}_6\text{F}_5)_4]$ were combined prior to addition of approximately 100 mL of THF which had been cooled to -78 °C. The yellow solution was allowed to warm to room temperature while stirring overnight, during which time the solution solidified. The reaction mixture was quenched with 6M HCl and agitated with a spatula to break up the

polymeric material. The white solid was isolated by filtration and dried under vacuum. GPC data indicated generation of poly-THF ($M_n = 106884$, $M_w = 299222$, PDI = 2.80). ^1H NMR (C_6D_6 , 25 °C, 300 MHz): δ 1.58 (m, 4H, $-(\text{OCH}_2\text{CH}_2\text{CH}_2\text{CH}_2)_n-$), 1.83 (m, 2H, $\text{O}(\text{CH}_2\text{CH}_2)_2$), 2.33 (s, 0.2H, CH_2Ph , benzyl end group), 3.39 (m, 4H, $-(\text{OCH}_2\text{CH}_2\text{CH}_2\text{CH}_2)_n-$), 3.72 (m, 2H, $\text{O}(\text{CH}_2\text{CH}_2)_2$), 7.16-7.23 (m, 0.5H, Ar-H, benzyl end group).

In situ generation of **3.24**

In a small vial in a glovebox 30 mg (0.04 mmol) of **3.9** was dissolved in approximately 0.5 mL of $\text{C}_6\text{D}_5\text{Br}$. In a separate vial, 41 mg (0.04 mmol) of $[\text{Ph}_3\text{C}][\text{B}(\text{C}_6\text{F}_5)_4]$ was dissolved in approximately 0.5 mL of $\text{C}_6\text{D}_5\text{Br}$. The two solutions were added to a J-Young NMR tube at room temperature, and a deep red solution formed immediately. ^1H NMR ($\text{C}_6\text{D}_5\text{Br}$, 25 °C, 300 MHz): δ

0.83 (s, 18H, $\text{C}(\text{CH}_3)_3$), 2.00 (s, 12H, Ar-H), 2.60 (s, 2H, ZrCH_2Ph), 3.93 (s, 2H, $\text{Ph}_3\text{CCH}_2\text{Ph}$), 6.55 (d, 2H, $^3J_{\text{HH}} = 7.1$ Hz, $\text{ZrCH}_2(o\text{-Ph-H})$), 6.73-7.39 (m, 29H, Ar-H ($\text{Ph}_3\text{CCH}_2\text{Ph}$ and **3.24**)). ^{19}F NMR ($\text{C}_6\text{D}_5\text{Br}$, 25 °C, 282 MHz): δ -165.9 (br, 8F, *o* or *m*-Ar-F), -162.1 (t, 4F, $^3J_{\text{FF}} = 22.2$ Hz, *p*-Ar-F), -131.6 (br, 8F, *o* or *m*-Ar-F).



3.8 References

1. Nicolaou, K. C.; Bulger, P. G.; Sarlah, D. *Angew. Chem. Int. Ed.* **2005**, *44*, 4490.
2. Nicolaou, K. C.; Bulger, P. G.; Sarlah, D. *Angew. Chem. Int. Ed.* **2005**, *44*, 4442.
3. Corey, E. J. *Angew. Chem. Int. Ed.* **2002**, *41*, 1650.
4. Tatsuta, K.; Hosokawa, S. *Chem. Rev.* **2005**, *105*, 4707.
5. Yet, L. *Chem. Rev.* **2000**, *100*, 2963.
6. Luh, T.-Y.; Leung, M.-K.; Wong, K.-T. *Chem. Rev.* **2000**, *100*, 3187.
7. Smith, N. D.; Mancuso, J.; Lautens, M. *Chem. Rev.* **2000**, *100*, 3257.
8. Gansaeuer, A.; Bluhm, H. *Chem. Rev.* **2000**, *100*, 2771.
9. Sato, F.; Urabe, H.; Okamoto, S. *Chem. Rev.* **2000**, *100*, 2835.
10. Kulinkovich, O. G.; de Meijere, A. *Chem. Rev.* **2000**, *100*, 2789.
11. Kaminsky, W. *Catal. Today* **2000**, *62*, 23.
12. Coates, G. W. *Dalton Trans.* **2002**, *4*, 467.
13. Alt, H. G.; Koepl, A. *Chem. Rev.* **2000**, *100*, 1205.
14. Natta, G.; Pino, P.; Corradini, P.; Danusso, F.; Mantica, E.; Mazzanti, G.; Moraglio, G. *J. Am. Chem. Soc.* **1955**, *77*, 1708.
15. Ziegler, K.; Holzkamp, E.; Breil, H.; Martin, H. *Angew. Chem.* **1955**, *67*, 426.
16. Natta, G.; Pino, P.; Mazzanti, G.; Giannini, U. *J. Am. Chem. Soc.* **1957**, *79*, 2975.
17. Breslow, D. S.; Newburg, N. R. *J. Am. Chem. Soc.* **1957**, *79*, 5072.
18. Sinn, H.; Kaminsky, W. *Adv. Organomet. Chem.* **1980**, *18*, 99.
19. Breslow, D. S.; Newburg, N. R. *J. Am. Chem. Soc.* **1959**, *81*, 81.
20. Cotton, F. A.; Wilkinson, G.; Murillo, C. A.; Bochmann, M. *Advanced Inorganic Chemistry*. 6th ed. Wiley: Toronto, **1999**.
21. Sinn, H.; Kaminsky, W.; Vollmer, H. J.; Woldt, R. *Angew. Chem.* **1980**, *92*, 396.
22. Thomson, R. K.; Zahariev, F. E.; Zhang, Z.; Patrick, B. O.; Wang, Y. A.; Schafer, L. L. *Inorg. Chem.* **2005**, *44*, 8680.
23. Giesbrecht, G. R.; Shafir, A.; Arnold, J. *Inorg. Chem.* **2001**, *40*, 6069.
24. Hagadorn, J. R.; Arnold, J. *Organometallics* **1994**, *13*, 4670.
25. Stewart, P. J.; Blake, A. J.; Mountford, P. *Inorg. Chem.* **1997**, *36*, 3616.

26. Littke, A.; Sleiman, N.; Bensimon, C.; Richeson, D. S.; Yap, G. P. A.; Brown, S. *J. Organometallics* **1998**, *17*, 446.
27. Stewart, P. J.; Blake, A. J.; Mountford, P. *J. Organomet. Chem.* **1998**, *564*, 209.
28. Stewart, P. J.; Blake, A. J.; Mountford, P. *Organometallics* **1998**, *17*, 3271.
29. Keaton, R. J.; Koterwas, L. A.; Fettinger, J. C.; Sita, L. R. *J. Am. Chem. Soc.* **2002**, *124*, 5932.
30. van Meerendonk, W. J.; Schroder, K.; Brussee, E. A. C.; Meetsma, A.; Hessen, B.; Teuben, J. H. *Eur. J. Inorg. Chem.* **2003**, *3*, 427.
31. Guiducci, A. E.; Boyd, C. L.; Mountford, P. *Organometallics* **2006**, *25*, 1167.
32. Wood, D.; Yap, G. P. A.; Richeson, D. S. *Inorg. Chem.* **1999**, *38*, 5788.
33. Mullins, S. M.; Duncan, A. P.; Bergman, R. G.; Arnold, J. *Inorg. Chem.* **2001**, *40*, 6952.
34. Ong, T.-G.; Yap, G. P. A.; Richeson, D. S. *Organometallics* **2002**, *21*, 2839.
35. Ong, T.-G.; Yap, G. P. A.; Richeson, D. S. *Chem. Commun.* **2003**, *20*, 2612.
36. Ong, T.-G.; Yap, G. P. A.; Richeson, D. S. *Organometallics* **2003**, *22*, 387.
37. Bazinet, P.; Wood, D.; Yap, G. P. A.; Richeson, D. S. *Inorg. Chem.* **2003**, *42*, 6225.
38. Duncan, A. P.; Mullins, S. M.; Arnold, J.; Bergman, R. G. *Organometallics* **2001**, *20*, 1808.
39. Ong, T.-G.; Wood, D.; Yap, G. P. A.; Richeson, D. S. *Organometallics* **2002**, *21*, 1.
40. Durfee, L. D.; Rothwell, I. P. *Chem. Rev.* **1988**, *88*, 1059.
41. Thirupathi, N.; Yap, G. P. A.; Richeson, D. S. *Organometallics* **2000**, *19*, 2573.
42. Thomson, R. K.; Patrick, B. O.; Schafer, L. L. *Can. J. Chem.* **2005**, *83*, 1037.
43. Zucchini, U.; Albizzati, E.; Giannini, U. *J. Organomet. Chem.* **1971**, *26*, 357.
44. Kilbourn, B. T.; Davies, G. R.; Jarvis, J. A. J.; Pioli, A. J. P. *Chem. Commun.* **1971**, 677.
45. Davies, G. R.; Jarvis, J. A. J.; Kilbourn, B. T. *Chem. Commun.* **1971**, *23*, 1511.
46. Cotton, F. A.; Marks, T. J. *J. Am. Chem. Soc.* **1969**, *91*, 1339.
47. Latesky, S. L.; McMullen, A. K.; Niccolai, G. P.; Rothwell, I. P.; Huffman, J. C. *Organometallics* **1985**, *4*, 902.

48. Jordan, R. F.; LaPointe, R. E.; Bajgur, C. S.; Echols, S. F.; Willett, R. *J. Am. Chem. Soc.* **1987**, *109*, 4111.
49. Carmona, E.; Marin, J. M.; Paneque, M.; Poveda, M. L. *Organometallics* **1987**, *6*, 1757.
50. Qian, B.; Scanlon, W. J.; Smith, M. R., III; Motry, D. H. *Organometallics* **1999**, *18*, 1693.
51. Lowes, T. A.; Ward, B. D.; Whannel, R. A.; Dubberley, S. R.; Mountford, P. *Chem. Commun.* **2005**, 113.
52. Fryzuk, M. D.; Love, J. B.; Rettig, S. J. *Organometallics* **1998**, *17*, 846.
53. Hughes, A. K.; Meetsma, A.; Teuben, J. H. *Organometallics* **1993**, *12*, 1936.
54. Dryden, N. H.; Legzdins, P.; Sayers, S. F.; Trotter, J.; Yee, V. C. *Can. J. Chem.* **1995**, *73*, 1035.
55. Dryden, N. H.; Legzdins, P.; Trotter, J.; Yee, V. C. *Organometallics* **1991**, *10*, 2857.
56. Warren, T. H.; Schrock, R. R.; Davis, W. M. *Organometallics* **1996**, *15*, 562.
57. Ciruelo, G.; Cuenca, T.; Gomez, R.; Gomez-Sal, P.; Martin, A.; Rodriguez, G.; Royo, P. *J. Organomet. Chem.* **1997**, *547*, 287.
58. Schrock, R. R.; Seidel, S. W.; Schrodi, Y.; Davis, W. M. *Organometallics* **1999**, *18*, 428.
59. Morgan, A. R.; Kloskowski, M.; Kalischewski, F.; Phillips, A. H.; Petersen, J. L. *Organometallics* **2005**, *24*, 5383.
60. Legzdins, P.; Smith, K. M.; Rettig, S. J. *Can. J. Chem.* **2001**, *79*, 502.
61. Cloke, F. G. N.; Geldbach, T. J.; Hitchcock, P. B.; Love, J. B. *J. Organomet. Chem.* **1996**, *506*, 343.
62. Mintz, E. A.; Moloy, K. G.; Marks, T. J.; Day, V. W. *J. Am. Chem. Soc.* **1982**, *104*, 4692.
63. Bassi, I. W.; Allegra, G.; Scordamaglia, R.; Chioccola, G. *J. Am. Chem. Soc.* **1971**, *93*, 3787.
64. Hamon, J. R.; Astruc, D.; Roman, E.; Batail, P.; Mayerle, J. J. *J. Am. Chem. Soc.* **1981**, *103*, 2431.

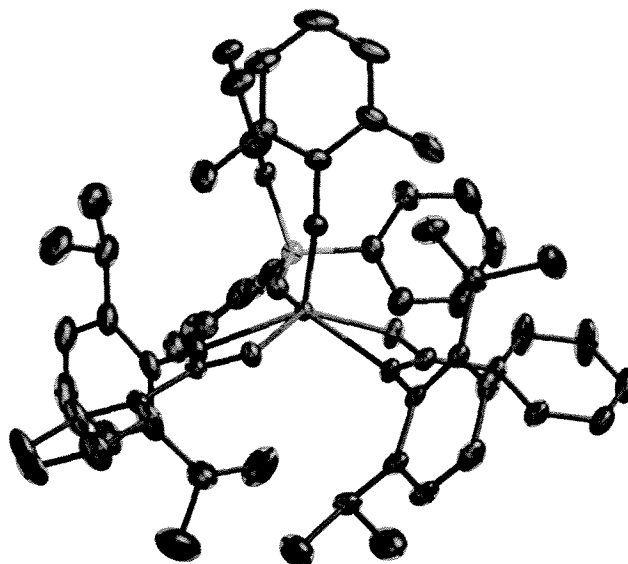
65. Pellecchia, C.; Immirzi, A.; Pappalardo, D.; Peluso, A. *Organometallics* **1994**, *13*, 3773.
66. Coles, M. P.; Dalby, C. I.; Gibson, V. C.; Little, I. R.; Marshall, E. L.; Ribeiro da Costa, M. H.; Mastroianni, S. *J. Organomet. Chem.* **1999**, *591*, 78.
67. Bochmann, M.; Lancaster, S. J.; Hursthouse, M. B.; Malik, K. M. A. *Organometallics* **1994**, *13*, 2235.
68. Bochmann, M.; Lancaster, S. J. *Organometallics* **1993**, *12*, 633.
69. O'Connor, P. E.; Morrison, D. J.; Steeves, S.; Burrage, K.; Berg, D. J. *Organometallics* **2001**, *20*, 1153.
70. Horton, A. D.; de With, J.; van der Linden, A. J.; van de Weg, H. *Organometallics* **1996**, *15*, 2672.
71. Bei, X.; Swenson, D. C.; Jordan, R. F. *Organometallics* **1997**, *16*, 3282.
72. Mokuolu, Q. F.; Duckmanton, P. A.; Hitchcock, P. B.; Wilson, C.; Blake, A. J.; Shukla, L.; Love, J. B. *Dalton Trans.* **2004**, *13*, 1960.
73. Friebolin, H. *Basic one- and two-dimensional NMR spectroscopy*. 2nd ed. VCH: Toronto, **1993**.
74. Guerin, F.; McConville, D. H.; Vittal, J. J.; Yap, G. A. P. *Organometallics* **1998**, *17*, 5172.
75. Spencer, L. P.; Fryzuk, M. D. *J. Organomet. Chem.* **2005**, *690*, 5788.
76. Scott, M. J.; Lippard, S. J. *Organometallics* **1997**, *16*, 5857.
77. Fryzuk, M. D.; Mao, S. S. H.; Zaworotko, M. J.; MacGillivray, L. R. *J. Am. Chem. Soc.* **1993**, *115*, 5336.
78. Fryzuk, M. D.; Duval, P. B.; Mao, S. S. H.; Rettig, S. J.; Zaworotko, M. J.; MacGillivray, L. R. *J. Am. Chem. Soc.* **1999**, *121*, 1707.
79. Dryden, N. H.; Legzdins, P.; Phillips, E. C.; Trotter, J.; Yee, V. C. *Organometallics* **1990**, *9*, 882.
80. Legzdins, P.; Phillips, E. C.; Trotter, J.; Yee, V. C.; Einstein, F. W. B.; Jones, R. H. *Organometallics* **1991**, *10*, 986.
81. Scholz, J.; Rehbaum, F.; Thiele, K.-H.; Goddard, R.; Betz, P.; Krueger, C. *J. Organomet. Chem.* **1993**, *443*, 93.
82. Bondi, A. *J. Phys. Chem.* **1964**, *68*, 441.

83. Chamberlain, L. R.; Durfee, L. D.; Fanwick, P. E.; Kobriger, L.; Latesky, S. L.; McMullen, A. K.; Rothwell, I. P.; Foltin, K.; Huffman, J. C.; et al. *J. Am. Chem. Soc.* **1987**, *109*, 390.
84. Giannini, L.; Caselli, A.; Solari, E.; Floriani, C.; Chiesi-Villa, A.; Rizzoli, C.; Re, N.; Sgamellotti, A. *J. Am. Chem. Soc.* **1997**, *119*, 9198.
85. Thorn, M. G.; Lee, J.; Fanwick, P. E.; Rothwell, I. P. *Dalton Trans.* **2002**, *17*, 3398.
86. Sebastian, A.; Royo, P.; Gomez-Sal, P.; Ramirez de Arellano, C. *Eur. J. Inorg. Chem.* **2004**, *19*, 3814.
87. Zumdahl, S. S. *Chemical Principles*. Heath: Toronto, **1995**.
88. Smith, M. B.; March, J. *March's Advanced Organic Chemistry: Reactions, Mechanisms, and Structure*. 5th ed. Wiley: Toronto, **2001**.
89. Chamberlain, L. R.; Durfee, L. D.; Fanwick, P. E.; Kobriger, L. M.; Latesky, S. L.; McMullen, A. K.; Steffey, B. D.; Rothwell, I. P.; Foltin, K.; Huffman, J. C. *J. Am. Chem. Soc.* **1987**, *109*, 6068.
90. McMullen, A. K.; Rothwell, I. P.; Huffman, J. C. *J. Am. Chem. Soc.* **1985**, *107*, 1072.
91. Ramos, C.; Royo, P.; Lanfranchi, M.; Pellinghelli, M. A.; Tiripicchio, A. *Eur. J. Inorg. Chem.* **2005**, *19*, 3962.
92. Giannini, L.; Caselli, A.; Solari, E.; Floriani, C.; Chiesi-Villa, A.; Rizzoli, C.; Re, N.; Sgamellotti, A. *J. Am. Chem. Soc.* **1997**, *119*, 9709.
93. Durfee, L. D.; McMullen, A. K.; Rothwell, I. P. *J. Am. Chem. Soc.* **1988**, *110*, 1463.
94. Barger, P. T.; Santarsiero, B. D.; Armantrout, J.; Bercaw, J. E. *J. Am. Chem. Soc.* **1984**, *106*, 5178.
95. Boncella, J.M. Personal Communication. **2007**.
96. Beshouri, S. M.; Fanwick, P. E.; Rothwell, I. P.; Huffman, J. C. *Organometallics* **1987**, *6*, 891.
97. Beshouri, S. M.; Chebi, D. E.; Fanwick, P. E.; Rothwell, I. P.; Huffman, J. C. *Organometallics* **1990**, *9*, 2375.
98. Lee, L.; Berg, D. J.; Bushnell, G. W. *Organometallics* **1997**, *16*, 2556.

99. Feng, S. G.; White, P. S.; Templeton, J. L. *Organometallics* **1995**, *14*, 5184.
100. Pohlki, F.; Doye, S. *Angew. Chem. Int. Ed.* **2001**, *40*, 2305.
101. McGrane, P. L.; Jensen, M.; Livinghouse, T. *J. Am. Chem. Soc.* **1992**, *114*, 5459.
102. Douglass, M. R.; Marks, T. J. *J. Am. Chem. Soc.* **2000**, *122*, 1824.
103. Montellano, P. R. O. D. *Cytochrome P-450: Structure, Mechanism, and Biochemistry*. Plenum: New York, **1995**.
104. Centi, G.; Trifiro, F.; Ebner, J. R.; Franchetti, V. M. *Chem. Rev.* **1988**, *88*, 55.
105. Mendiratta, A.; Figueroa, J. S.; Cummins, C. C. *Chem. Commun.* **2005**, 3403.
106. Kissounko, D. A.; Hoerter, J. M.; Guzei, I. A.; Cui, Q.; Gellman, S. H.; Stahl, S. S. *J. Am. Chem. Soc.* **2007**, *129*, 1776.
107. Smith, M. R., III; Matsunaga, P. T.; Andersen, R. A. *J. Am. Chem. Soc.* **1993**, *115*, 7049.
108. Lukens, W. W., Jr.; Matsunaga, P. T.; Andersen, R. A. *Organometallics* **1998**, *17*, 5240.
109. Hill, J. E.; Fanwick, P. E.; Rothwell, I. P. *Inorg. Chem.* **1989**, *28*, 3602.
110. Hoskin, A. J.; Stephan, D. W. *Organometallics* **1999**, *18*, 2479.
111. Hillhouse, G. L.; Bercaw, J. E. *J. Am. Chem. Soc.* **1984**, *106*, 5472.
112. Carney, M. J.; Walsh, P. J.; Hollander, F. J.; Bergman, R. G. *J. Am. Chem. Soc.* **1989**, *111*, 8751.
113. Babcock, L. M.; Klemperer, W. G. *Inorg. Chem.* **1989**, *28*, 2003.
114. Starikova, Z. A.; Turevskaya, E. P.; Kozlova, N. I.; Turova, N. Y.; Berdyev, D. V.; Yanovsky, A. I. *Polyhedron* **1999**, *18*, 941.
115. Dalgarno, S. J.; Atwood, J. L.; Raston, C. L. *Inorg. Chim. Acta* **2007**, *360*, 1344.
116. Loo, Y. F.; O'Kane, R.; Jones, A. C.; Aspinall, H. C.; Potter, R. J.; Chalker, P. R.; Bickley, J. F.; Taylor, S.; Smith, L. M. *J. Mater. Chem.* **2005**, *15*, 1896.
117. Spijksma, G. I.; Bouwmeester, H. J. M.; Blank, D. H. A.; Fischer, A.; Henry, M.; Kessler, V. G. *Inorg. Chem.* **2006**, *45*, 4938.
118. Pasko, S. V.; Abrutis, A.; Hubert-Pfalzgraf, L. G. *Mater. Lett.* **2004**, *59*, 261.
119. Chen, E. Y.-X.; Marks, T. J. *Chem. Rev.* **2000**, *100*, 1391.
120. Gribkov, D. V.; Hultsch, K. C. *Angew. Chem. Int. Ed.* **2004**, *43*, 5542.

121. Knight, P. D.; Munslow, I.; O'Shaughnessy, P. N.; Scott, P. *Chem. Commun.* **2004**, 894.
122. Ma, K.; Piers, W. E.; Parvez, M. *J. Am. Chem. Soc.* **2006**, *128*, 3303.
123. Pellecchia, C.; Grassi, A.; Zambelli, A. *J. Mol. Catal. A: Chem.* **1993**, *82*, 57.
124. Burrows, R. C. *Polym. Prepr. (Am. Chem. Soc., Div. Polym. Chem.)* **1965**, *6*, 600.
125. Dreyfuss, P.; Dreyfuss, M. P.; Pruckmayr, G. *Encycl. Polym. Sci. Eng.* **1989**, *16*, 649.
126. Kozhevnikov, I. V. *Chem. Rev.* **1998**, *98*, 171.
127. Bochmann, M. *Dalton Trans.* **1996**, *3*, 255.
128. Guo, Z.; Swenson, D. C.; Guram, A. S.; Jordan, R. F. *Organometallics* **1994**, *13*, 766.
129. Mehrkhodavandi, P.; Schrock, R. R.; Pryor, L. L. *Organometallics* **2003**, *22*, 4569.
130. Mehrkhodavandi, P.; Schrock, R. R. *J. Am. Chem. Soc.* **2001**, *123*, 10746.
131. Yang, X.; Stern, C. L.; Marks, T. J. *Angew. Chem. Int. Ed.* **1992**, *31*, 1375.
132. Sishta, C.; Hathorn, R. M.; Marks, T. J. *J. Am. Chem. Soc.* **1992**, *114*, 1112.

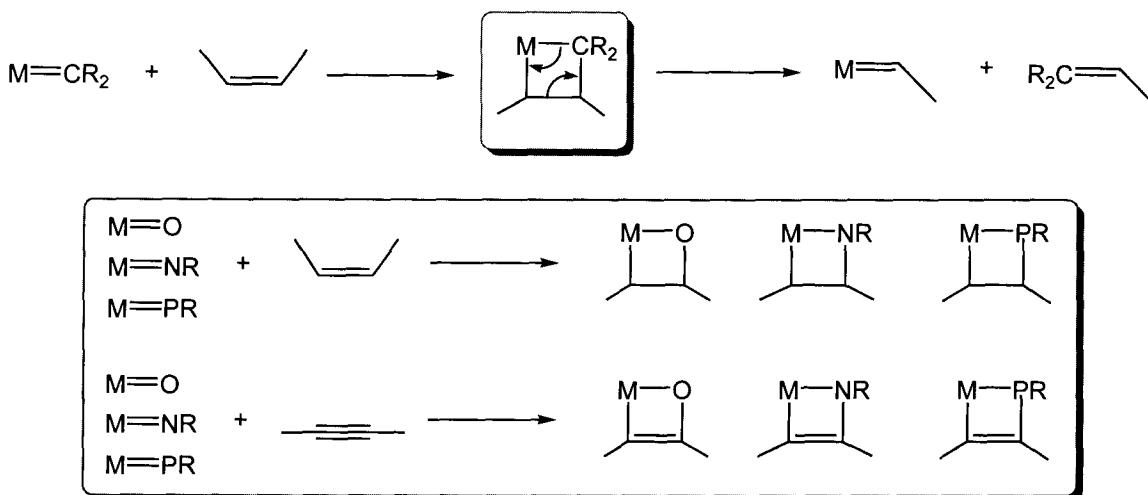
CHAPTER 4



Synthesis, Structure, and Reactivity of Amidate Supported Imido Complexes

4.1 Introduction

Many stoichiometric and catalytic reactions promoted by transition metals are dependent upon an intermediate involving a metal-element multiple bond. The most famous example of this being the olefin metathesis reaction, which proceeds through an alkylidene intermediate, having a $M=CR_2$ double bond.¹⁻⁵ In 2005, the Nobel prize in chemistry was awarded to Yves Chauvin, Richard R. Schrock, and Robert H. Grubbs for “development of the metathesis method in organic synthesis,” where the multiply bonded $M=CR_2$ species were the key to this extremely important reaction.^{6, 7} The $M=C$ double bond allows for a switching of partners, or metathesis, through a cycloaddition reaction, resulting in a metallacyclobutane intermediate (Scheme 4.1).^{8, 9}



Scheme 4.1

By comparison, the related oxo ($M=O$),¹⁰⁻²² imido ($M=NR$),²³⁻³⁵ and phosphinidene ($M=PR$)³⁶⁻⁴⁹ complexes have been less extensively studied than the alkylidenes. Similar cycloaddition pathways can be envisioned for these species, which would result in the formation of new C-E bonds, where E = O, N, P, etc. While catalytic C-C bond formation via olefin metathesis and ring-closing metathesis (RCM) has proven extremely useful in organic synthesis,^{50, 51} the analogous exploitation of other metal-mediated catalytic C-E bond formations in organic synthesis has only recently come to gain widespread attention.^{17, 52-57} One particular catalytic process that has seen an explosion of interest in the last 5 years is catalytic hydroamination, which is the formal addition of an N-H bond across a C-C multiple bond.^{55, 58-67} With certain early transition metal based catalysts, especially group 4 and 5 complexes, the mechanism of alkyne hydroamination is understood to proceed through a cycloaddition reaction between the alkyne and an imido complex, such as the reaction illustrated in Scheme 4.1.^{58, 68}

In order to develop a complete understanding of the olefin metathesis reaction, a comprehensive investigation of metal alkylidene species was required. Systematic investigation of the steric and electronic influences imparted by the ancillary ligands led to vastly improved catalysts for this process.^{2, 4, 69-73} An excellent example of this development process can be observed upon studying the evolution of the Grubbs'-type olefin metathesis catalysts.⁴ The earliest commercialized catalyst developed by Grubbs and coworkers was a benzylidene species stabilized by two chloro ancillary ligands, and

two phosphine ligands, to generate a square pyramidal complex, as shown in Fig. 4.1 (4.1).⁷³⁻⁷⁶ While this catalyst exhibited excellent functional group tolerance for the metathesis reaction in comparison to the Schrock catalyst (4.2), the activity of the Ru complex was far lower than that of the Mo complex.^{3, 70, 71} By changing one of the ancillary phosphine ligands to an N-heterocyclic carbene (4.3), the activity of the resulting complex was vastly increased, while still maintaining excellent functional group tolerance.^{4, 77}

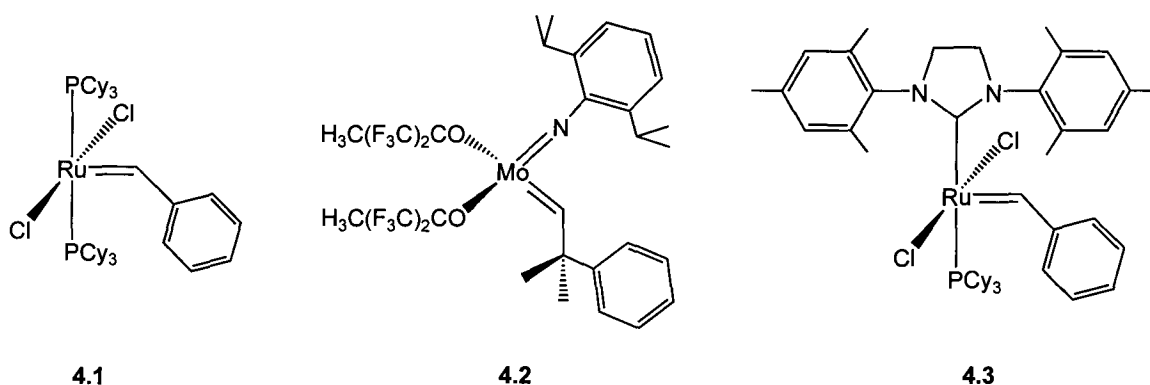


Figure 4.1 Grubbs and Schrock olefin metathesis catalysts

The Schrock catalyst (4.2) also illustrates the usage of imido ligands as ancillary groups for mid to late transition metals. Imido ligands have been lauded as new tunable alternatives to Cp ligands, due to the isolobal nature of their bonding interactions.⁷⁸⁻⁸⁰ This has found important application in olefin polymerization catalysis.^{78, 80-83} The dianionic nature of the imido ligand typically requires the utility of neutral ancillaries on group 4 metals to maintain the essential cationic monoalkyl reactive site. A couple of representative complexes developed by the Mountford group are shown in Fig. 4.2 (4.4 and 4.5), where the supporting ancillaries are derived from the triazacyclononane (tacn) framework.^{80, 84} These complexes exhibit high to very high activity in the polymerization of ethylene.⁸² An exciting new development in this area has also been observed for a chiral *ansa*-titanocene imido complex capable of syndiospecific polymerization of methylmethacrylate, also highlighted in Fig 4.2 (4.6).⁸⁵

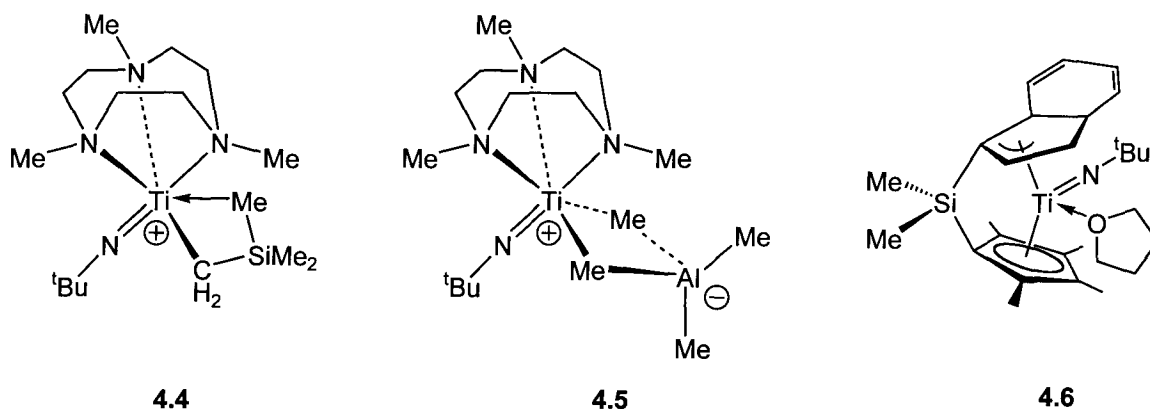
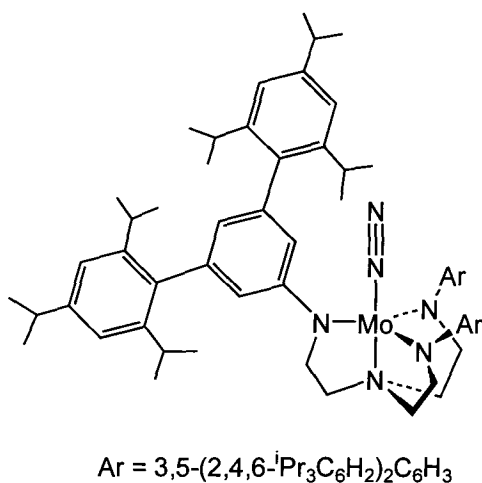
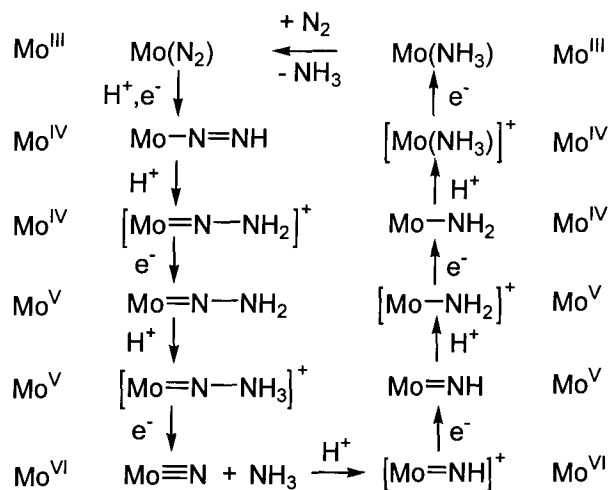


Figure 4.2 New Ti imido polymerization catalysts

Whereas the modification of cyclopentadienyl rings can be laborious and difficult, steric and electronic modification of the imido ligand can be readily accomplished by starting with the appropriate amine.^{33, 78, 79, 82, 83, 86} For example, access to the metal center can be moderated by incorporation of large groups in the 2 and 6 positions of the aryl ring, as in the case of the Schrock metathesis catalyst (**4.2**).^{1, 2} While imido ligands can be utilized as non-reactive ancillaries, a wealth of interesting reactivity can also be accessed with these ligands.^{33, 87} For example, the enzymatic fixation of dinitrogen has been postulated to involve an imido intermediate en route to the formation of ammonia. Recent studies of a model Mo system (**4.7**) have characterized imido species as intermediates along the catalytic pathway for the reduction of N₂ to NH₃ by stepwise addition of protons and electrons.⁸⁸ This system, studied by Schrock and coworkers, was the first synthetic complex to facilitate catalytic conversion of atmospheric N₂ to NH₃ under mild conditions, and the overall process is illustrated in Scheme 4.2.⁸⁸



4.7



Scheme 4.2

While imido species are known for many transition metals, the group 4 imido complexes display the most notable reactivity.^{32, 33} The first reported group 4 imido complexes were isolated by the Wolczanski and Bergman groups in 1988 (Fig. 4.3).^{89, 90} The Bergman system (4.8) was stabilized by traditional Cp ligands,⁹⁰ whereas the Wolczanski complex (4.9) was stabilized by the bulky tri(*tert*-butyl)silylamido ligands (tBu_3SiNH).⁸⁹ These imido complexes were highly reactive and could not be characterized in the solid-state, but their molecular structures were inferred from subsequent reactivity. It was noted that both of these imido complexes were capable of reversible C-H bond activation.^{89, 90} Particularly impressive was the observed activation of methane by the amido ligated imido complex.⁸⁹

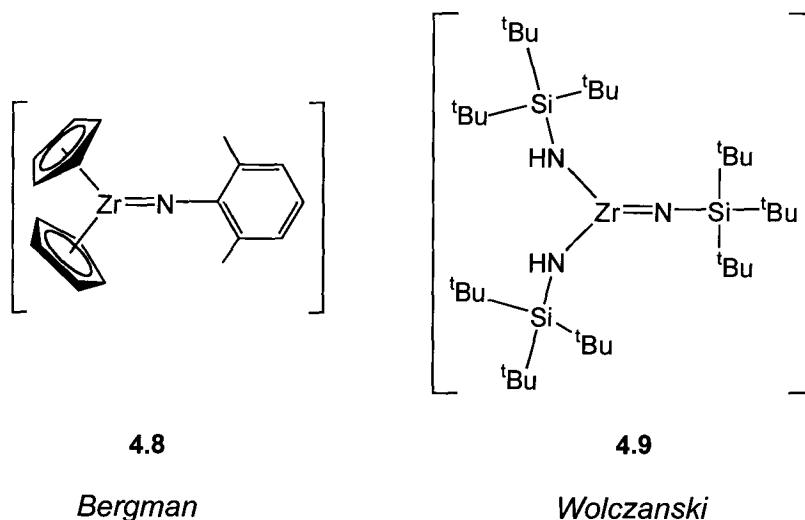
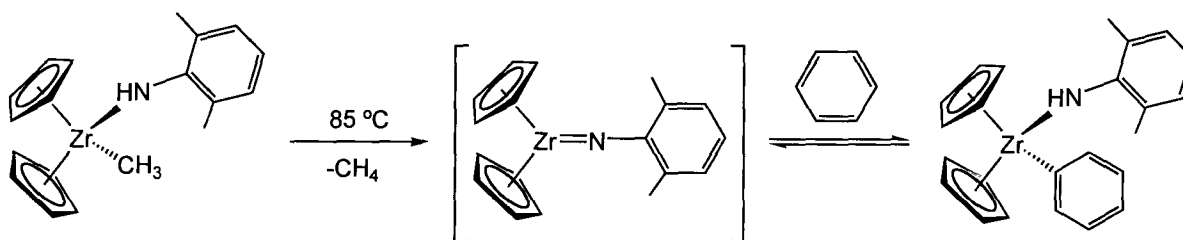


Figure 4.3 The first group 4 imido complexes

In these activation reactions, the C-H bond adds across the Zr=N bond in a 1,2-addition type reaction, resulting in an alkyl-amido, or aryl-amido complex, which can reversibly eliminate the alkane or arene, and regenerate the transient imido complex as illustrated in Scheme 4.3.⁹⁰ Since these early Zr imido complexes were not stable isolable species, they were generated *in situ* by alkane or arene elimination from mixed alkyl-amido or aryl-amido species, also shown in Scheme 4.3.

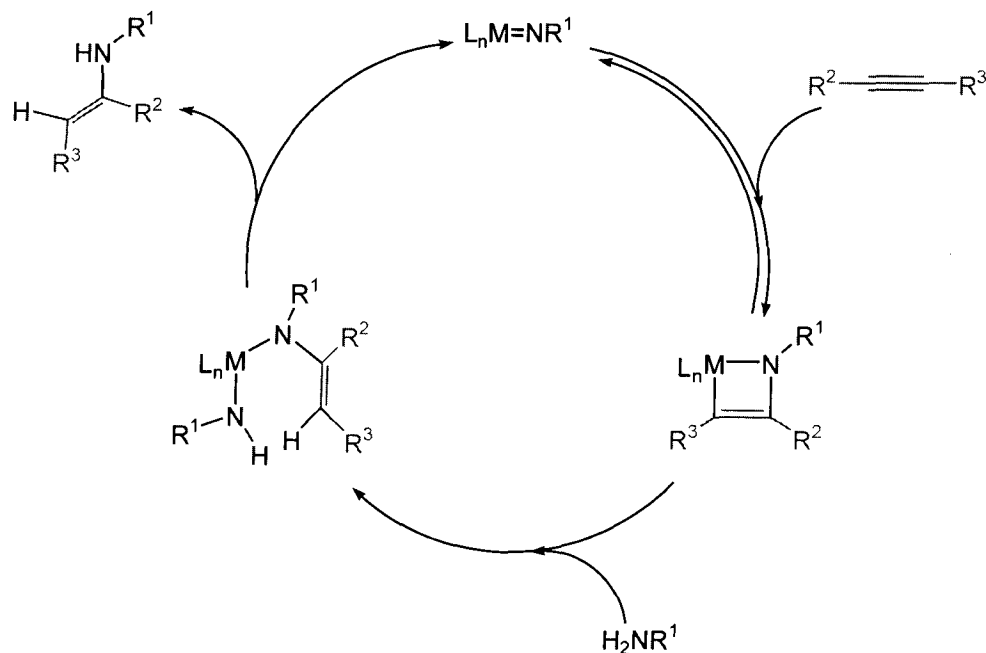


Scheme 4.3

While the activation of C-H bonds has many potential applications in the formation of new C-E bonds, the bulk of observed reactivity with imido complexes has involved cycloaddition reactions of unsaturated organic species with the M=N bond.^{32, 33, 91} The cycloaddition of ketones,^{52, 92, 93} isocyanates,^{94, 95} carbodiimides,^{87, 96-98} imines,^{99, 100} phosphalkynes,^{101, 102} alkynes,^{93, 103} alkenes,^{93, 104, 105} and allenes¹⁰⁶ with imido

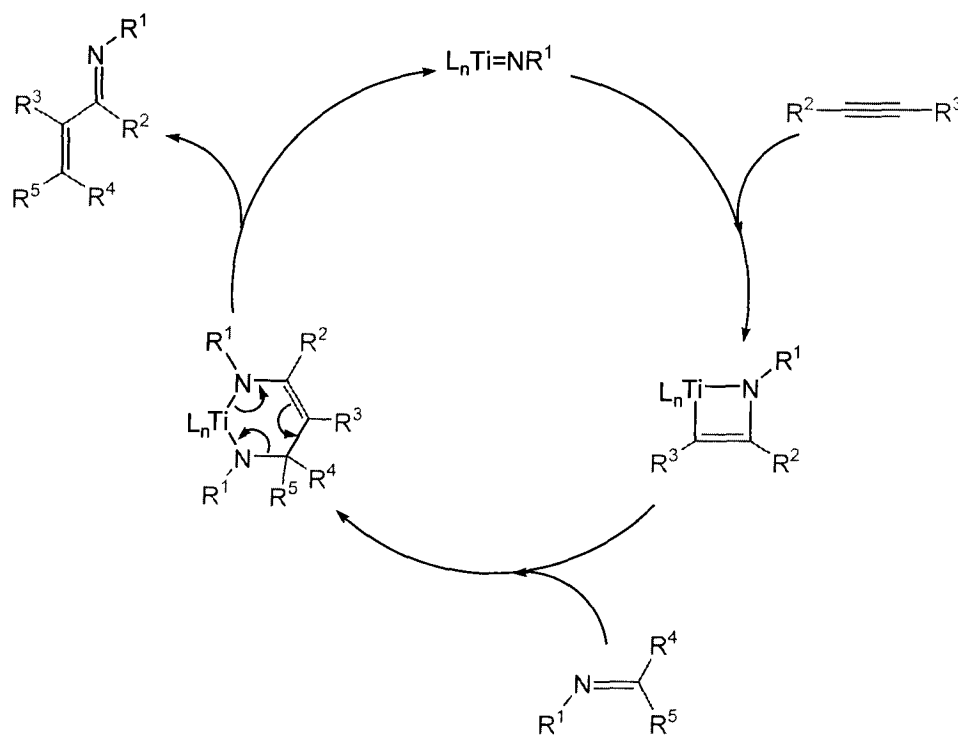
fragments have all been noted in the literature. This type of stoichiometric reactivity is important for the fundamental study of new N-C bond formation; however, application of such reactions to catalytic processes has seen relatively limited success. Three important applications of imido cycloaddition reactivity are catalytic hydroamination,^{53, 58, 60, 61, 68, 107} catalytic carboamination,¹⁰⁸⁻¹¹¹ and catalytic transamidation.¹¹²⁻¹¹⁴

The most widely studied application of group 4 imido complexes is catalytic alkyne hydroamination.^{53, 58, 60, 61, 68, 107} The mechanism for this reaction was first described in detail by Bergman and coworkers, where the key step in this transformation involves the cycloaddition of a zirconocene imido fragment with the triple bond of the alkyne.⁶⁸ This results in the formation of an azametallacyclobutene complex, shown in Scheme 4.4. Addition of another equivalent of amine to the metallacyclic intermediate results in cleavage of the Zr-C bond, and formation of a new amido-eneamido complex.⁶⁸ Regeneration of the imido complex is accomplished by α -H abstraction, facilitating the elimination of the enamine product.⁶⁸ This reaction has been widely exploited by a number of research groups, and considerable progress has been made in the development of new catalysts for this important reaction.^{58, 115}



Scheme 4.4

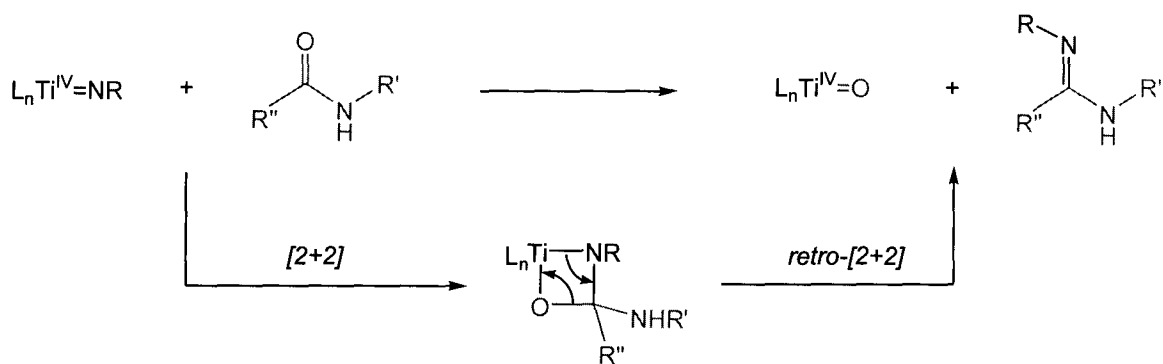
Catalytic carboamination has been observed recently for Ti and Zr complexes. This process results in a three component coupling of an amine, an alkyne, and an imine. ¹⁰⁸⁻¹¹¹ The necessity of an imido linkage has also been illustrated for this reaction, which proceeds through the mechanism illustrated in Scheme 4.5. ¹⁰⁸ The mechanism for catalytic carboamination is identical to that for hydroamination until the formation of the azametallacyclobutene species. In catalytic carboamination, an imine is inserted into the M-C bond of the metallacycle, generating a new diazametallacyclohexene complex. ¹⁰⁸ Cycloreversion of this metallacycle results in the regeneration of the active imido catalyst, while eliminating the α , β -unsaturated imine product. These products are analogous to α , β -unsaturated ketones, and are useful as precursors for hetero-Diels-Alder type reactions for the formation of new N-heterocycles. ^{116, 117}



Scheme 4.5

Catalytic transamidation has been described recently by Stahl and coworkers with Al and Ti complexes. ^{112-114, 118} In the case of Ti-based catalysts, the mechanism is proposed to involve nucleophilic attack of primary amines on Ti-coordinated secondary organic amides, analogous to that presented for the Al catalysts in Chapter 1 (Scheme

1.4).^{114, 118} The overall result of this process is the cleavage of a N-C bond, and formation of a new N-C bond, to generate a new secondary organic amide. A competing side reaction in this process is the cycloaddition of secondary organic amides with Ti imido species, resulting in the formation of an azaoxytitanacyclobutane complex, with an N,O chelating motif. This complex can subsequently cyclorevert to generate a Ti oxo complex and eliminate the organic amidine as shown in Scheme 4.6.^{113, 114}



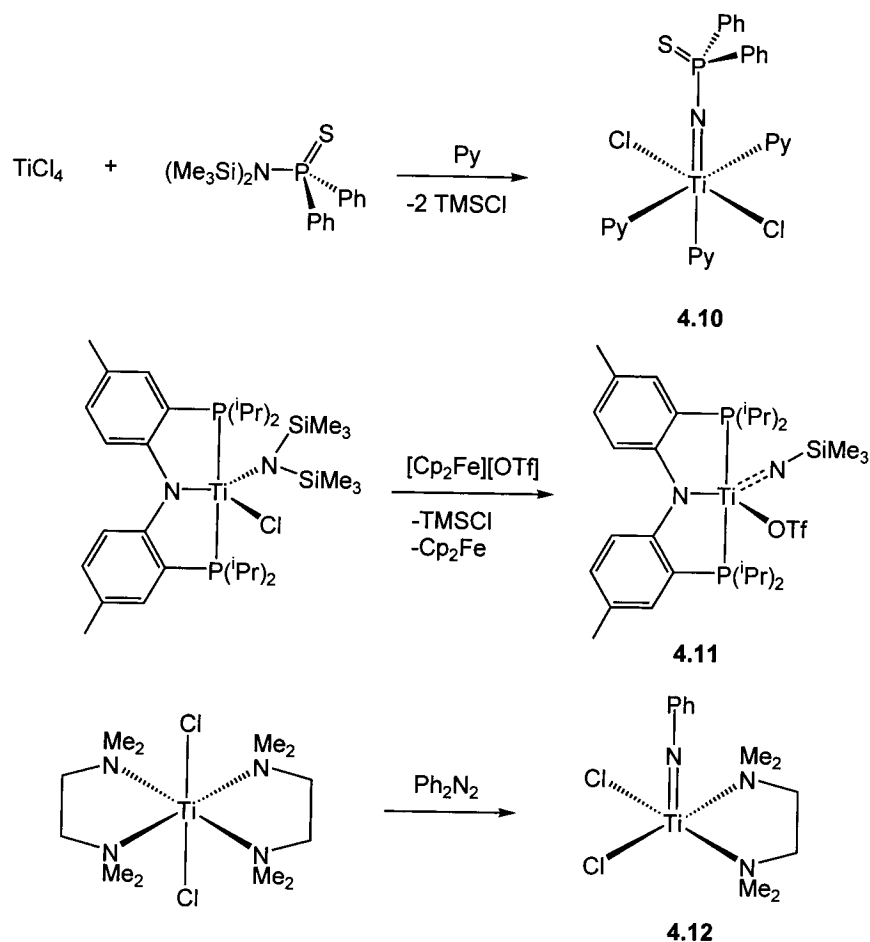
Scheme 4.6

Amidate supported Ti complexes have recently been exploited for the catalytic hydroamination of terminal alkynes.¹¹⁹⁻¹²² These complexes are highly reactive for this process and exhibit excellent regioselectivity for the anti-Markovnikov imine product, and this process is discussed at length in Chapter 5.¹²⁰ The unique reactivity patterns seen for these complexes, and the known intermediacy of imido species in this process, required the detailed study of amidate supported imido complexes. This chapter will discuss the synthesis, characterization, and fundamental reactivity of Ti and Zr imido complexes supported by amidate ligands.

4.2 Synthesis and Structure of Terminal Imido Complexes

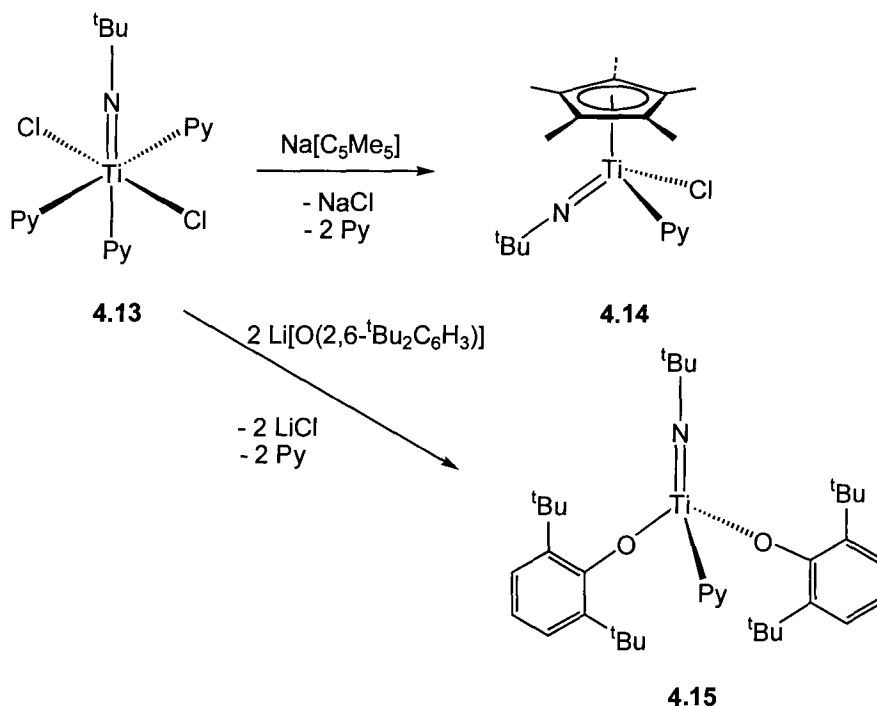
4.2.1 Introduction

A number of synthetic routes into imido complexes have been developed for group 4 metals. The first terminal Ti imido complexes were structurally authenticated by the Roesky¹²³ and Rothwell¹²⁴ groups in 1990. The complex isolated by Roesky was accessed by a TMS-Cl elimination route. By combining TiCl_4 with $(\text{Me}_3\text{Si})_2\text{NP}(\text{S})\text{Ph}_2$ in the presence of pyridine, the tris(pyridine) imido adduct (**4.10**) shown in Scheme 4.7 was isolated.¹²³ A similar strategy was recently utilized by Mindiola and coworkers, where oxidatively induced TMS-Cl elimination was accomplished by addition of ferrocenium triflate to a Ti(III) precursor.¹²⁵ This resulted in the generation of the Ti(IV) imido complex (**4.11**). Ti(II) precursors have also been utilized to access Ti(IV) imido species through oxidative cleavage of azobenzene ligands, as illustrated by complex (**4.12**) in Scheme 4.7.¹²⁶



Scheme 4.7

More common strategies for accessing imido species involve N-H bond cleavage or salt metathesis reactions. As noted in section 4.1, the earliest Zr imido complexes were accessed via alkane or arene elimination from mixed amido-alkyl or amido-aryl complexes (Scheme 4.3).^{89, 90} These precursor species were accessed by salt metathesis reactions with metal chloro starting materials. While the low-coordinate complexes generated by the Bergman and Wolczanski groups were not isolable, trapping of the imido complexes was possible in the presence of Lewis bases, such as pyridine or THF. The most heavily exploited routes into imido complexes involve the utility of mixed chloro imido starting materials. In 1995, Mountford and coworkers reported the synthesis of the Ti dichloro imido complex (**4.13**) shown in Scheme 4.8.^{127, 128} This complex allowed for the facile installation of a variety of ancillary ligands through salt metathesis, and a couple of select examples are given in Scheme 4.8.^{129, 130}

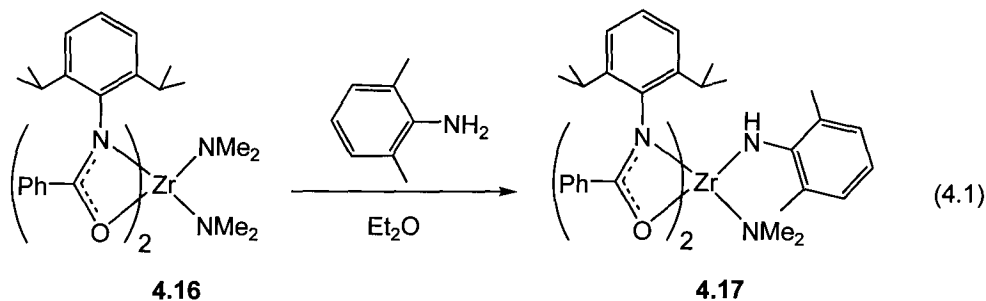


Scheme 4.8

4.2.2 Results and Discussion

4.2.2.1 Synthesis and Structure of Amido Anilido Complex

As mentioned in Chapter 2, salt metathesis routes for the installation of amidate ligands are problematic, and protonolysis routes are much more successful. Thus, protonolysis routes into imido complexes, analogous to those utilized by the Bergman and Wolczanski groups, were utilized for the formation of isolable imido complexes.^{89, 90} Unlike the mixed alkyl-amido precursor complexes used by the Bergman and Wolczanski groups, the bis(amidate) bis(amido) species described in section 2.3.2.2 were utilized as precursors for aminolysis routes into imido complexes. Upon addition of 1 equiv. of 2,6-dimethylaniline to the Zr bis(amido) complex [^{DIPP}(NO)^{Ph}]₂Zr(NMe₂)₂ (**4.16**) (introduced in Chapter 2 as **2.20**), the mixed amido complex [^{DIPP}(NO)^{Ph}]₂Zr(NH-2,6-Me₂C₆H₃)(NMe₂) (**4.17**) can be isolated in high yield (Eq. 4.1).



Reduced symmetry is apparent in the ^1H NMR spectrum of **4.17**, as indicated by four doublets for the isopropyl groups on the N aryl units of the amidate ligands. These signals exist in a 6:6:6:6 ratio, suggestive of chemically inequivalent aryl groups, where two of the arene rings exhibit hindered rotation about the N-C_{ipso} bond. As expected, a single resonance at δ 2.12 is observed for the aryl methyl groups, indicating free rotation of the anilido group on the NMR timescale. Finally, the dimethylamido ligand appears as a single resonance at δ 3.47. The presence of an N-H group is confirmed by IR spectroscopy, where a weak signal is observed at 3316 cm^{-1} . This is very similar to results seen by Zuckermann and Bergman, where the mixed alkyl-amido complex $\text{Cp}_2\text{Zr}(\text{NH}(2,6\text{-}^i\text{Pr}_2\text{C}_6\text{H}_3))(\text{CH}_3)$ exhibits a weak NH stretch in the IR spectrum at 3311 cm^{-1} .³⁵

Verification of the structure of **4.17** was accomplished by a single crystal X-ray diffraction study, which resulted in the solid-state molecular structure shown in Fig. 4.4. Relevant bond lengths and angles are listed in Table 4.1, and crystallographic details are presented in Table A4.1 in Appendix A. The pseudo-octahedral geometry about the Zr center is similar to that seen for the other bis(amidate) bis(amido) complexes discussed in Chapter 2. The overall symmetry of **4.17** is C_1 , with the two amido ligands oriented *cis* to each other, as expected for these strong π -donor ligands. Both the dimethylamido and 2,6-dimethylanilido ligands are sp^2 -hybridized, with planar N donors (sum of angles about N4 = 359.74°), suggesting π -donation. The double bond character of the dimethylamido ligand is further supported by the Zr(1)-N(4) bond length of $2.031(3)\text{ \AA}$, which is similar to the analogous bond lengths in Zr bis(amido) complexes $[\text{tBu}(\text{NO})^{\text{Ph}}]_2\text{Zr}(\text{NEt}_2)_2$ **4.18**, $[\text{DMP}(\text{NO})^{\text{tBu}}]_2\text{Zr}(\text{NMe}_2)_2$ **4.19**, and $\kappa^2\text{-}[\text{DMP}(\text{NO})^{\text{tBu}}]\text{-}\kappa^1\text{-}[\text{DMP}(\text{NO})^{\text{tBu}}]\text{Zr}(\text{NMe}_2)_2(\text{Py})$ **4.20**, which were discussed in Chapter 2. A slightly longer bond length is observed for the Zr(1)-N(3) linkage of the anilido ligand ($2.099(3)\text{ \AA}$),

which can be rationalized by delocalization of the nitrogen lone pair electrons into the arene ring, thereby weakening the Zr-N bond. The tris(amidate) anilido complex $[\text{DIPP}(\text{NO})^{\text{Ph}}]_3\text{ZrNHPh}$ (**4.21**), presented in Chapter 2 (**2.14**), has a similar Zr-NHR ligand, where the Zr-N-C_{ipso} bond angle is 137.66(17)°. In **4.17**, the Zr(1)-N(3)-C(39) bond angle is very similar at 140.9(2)°, significantly distorted from the 120° bond angle expected for an sp²-hybridized N center. The obtuse angle is likely a product of reduced steric repulsions achieved upon moving the aryl group further from the sterically congested metal center.

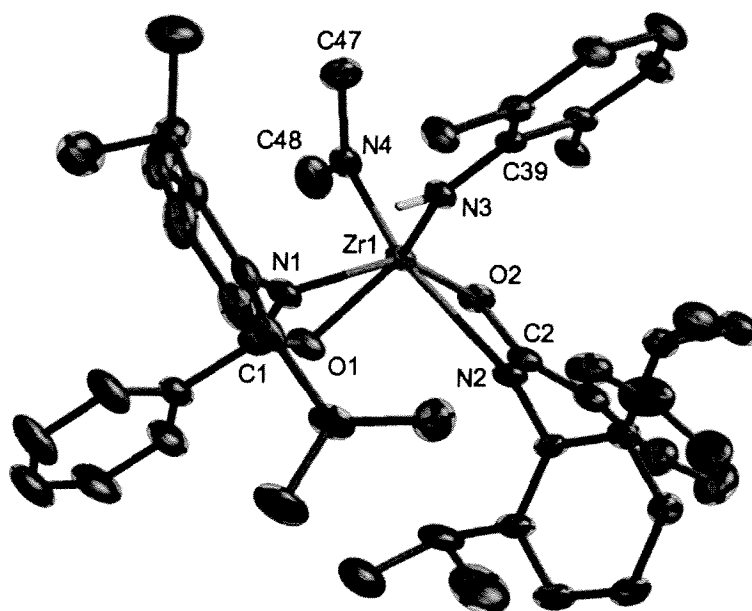
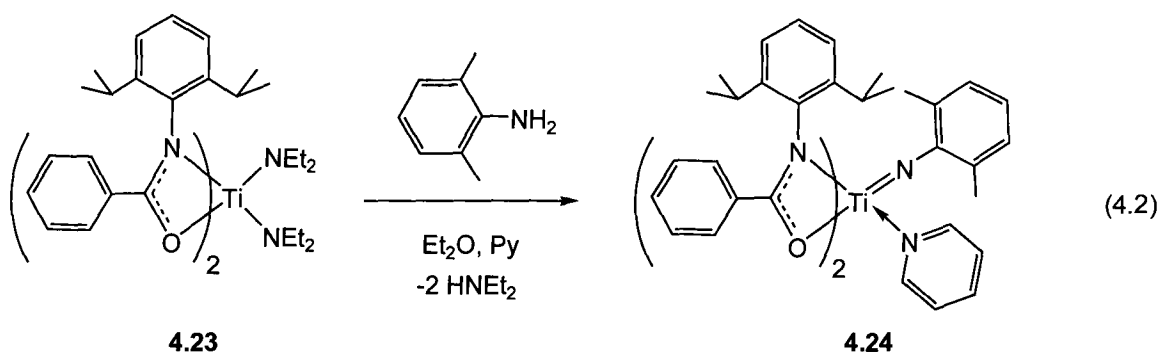


Figure 4.4 ORTEP depiction (ellipsoids at 30% probability) of solid-state molecular structure of $[\text{DIPP}(\text{NO})^{\text{Ph}}]_2\text{Zr}(\text{NH}-2,6\text{-Me}_2\text{C}_6\text{H}_3)(\text{NMe}_2)$, **4.17** (non-N-H hydrogens omitted)

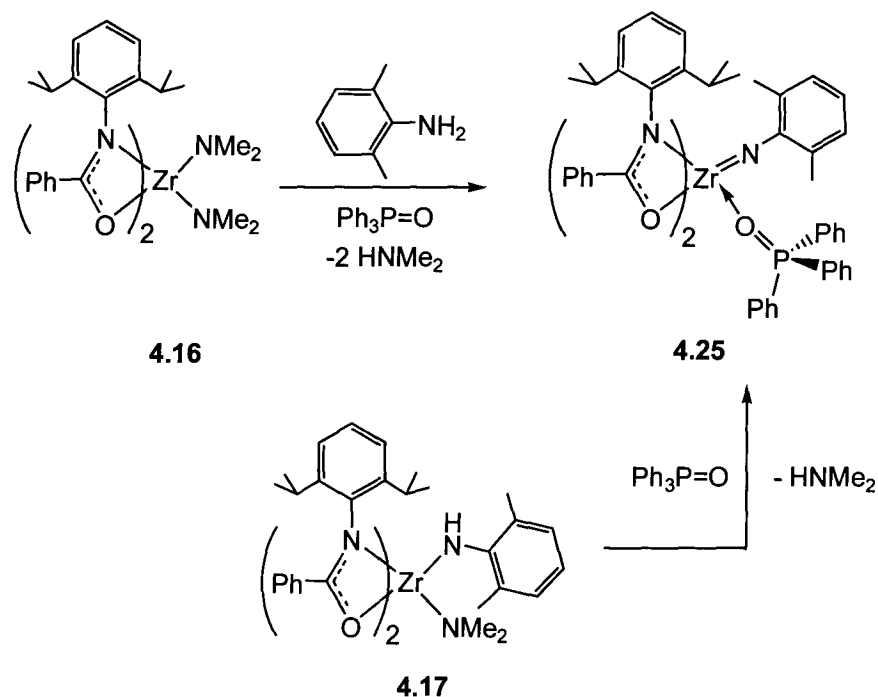
Table 4.1 Selected Bond Distances (Å) and Angles (°) for $[\text{DIPP}(\text{NO})^{\text{Ph}}]_2\text{Zr}(\text{NH}-2,6\text{-Me}_2\text{C}_6\text{H}_3)(\text{NMe}_2)$, **4.17**

Lengths		Angles		Angles	
Zr(1)-O(1)	2.193(2)	O(1)-Zr(1)-N(1)	58.05(10)	O(2)-Zr(1)-N(4)	90.97(12)
Zr(1)-O(2)	2.164(3)	O(2)-Zr(1)-N(2)	57.21(10)	O(1)-Zr(1)-N(3)	138.09(11)
Zr(1)-N(1)	2.288(3)	N(1)-Zr(1)-N(2)	105.26(11)	O(1)-Zr(1)-N(4)	95.68(11)
Zr(1)-N(2)	2.385(3)	N(3)-Zr(1)-N(4)	100.69(13)	O(2)-Zr(1)-N(1)	143.13(10)
Zr(1)-N(3)	2.099(3)	O(1)-Zr(1)-O(2)	87.11(10)	O(1)-Zr(1)-N(2)	87.06(10)
Zr(1)-N(4)	2.031(3)	N(2)-Zr(1)-N(4)	147.95(12)	C(47)-N(4)-C(48)	110.8(3)
O(1)-C(1)	1.299(5)	N(2)-Zr(1)-N(3)	98.24(11)	C(47)-N(4)-Zr(1)	128.9(3)
N(1)-C(1)	1.313(5)	N(1)-Zr(1)-N(3)	80.64(11)	C(48)-N(4)-Zr(1)	120.0(3)
O(2)-C(2)	1.304(4)	N(1)-Zr(1)-N(4)	103.17(12)	C(39)-N(3)-Zr(1)	140.9(2)
N(2)-C(2)	1.299(5)	O(2)-Zr(1)-N(3)	130.45(10)		

While **4.17** could potentially eliminate dimethylamine to generate a 5-coordinate imido complex, thermolysis of this species does not result in the formation of an imido complex. Although 5-coordinate imido complexes of Zr are known for the related guanidinate ligand system (**4.22**) (Fig. 4.5), the amidate ligand set has two features that make this unlikely:^{131, 132} first, due to the nature of the amidate N,O chelate vs. the N,N chelate of guanidinate ligands, the amidate system only has steric protection on one side of the amidate ligand, and this coupled with the tight bite angle of the four-membered chelate results in a relatively open coordination sphere; second, while guanidinate ligands have been described in the literature as 4 e⁻ donors, electronically similar to amidate ligands, the NR₂ donor in the guanidinate backbone allows for additional electron donation to the metal center,^{133, 134} which is not possible with amidate ligands.¹³⁵ The increased capacity for electron donation is exemplified by resonance structure **B** shown in Fig. 4.5. This increased electron donation could be important for stabilizing a coordinatively unsaturated 5-coordinate complex.



Isolation of a TPPO stabilized imido complex is possible upon combining $[\text{DIPP}(\text{NO})^{\text{Ph}}]_2\text{Zr}(\text{NMe}_2)_2$ (**4.16**) with one equiv. of 2,6-dimethylaniline in a solution of toluene, followed by addition of one equiv. of TPPO, as illustrated in Scheme 4.9. The initial reaction between **4.16** and $\text{H}_2\text{N}(2,6\text{-Me}_2\text{C}_6\text{H}_3)$ results in a subtle deepening of the pale yellow color of the solution, presumably corresponding to the formation of **4.17**. Upon addition of TPPO, the solution color changes dramatically from light yellow to a deep golden yellow. Isolation of the imido complex $[\text{DIPP}(\text{NO})^{\text{Ph}}]_2\text{Zr}=\text{NAr}(\text{TPPO})$, **4.25** ($\text{Ar} = 2,6\text{-Me}_2\text{C}_6\text{H}_3$), is facilitated by its low solubility in pentane, allowing it to be collected by filtration in high yield (82%). Coordination of TPPO is indicated by a downfield shift of the signal in the ^{31}P NMR spectrum to δ 42.7 from 25.4 for free TPPO.



Scheme 4.9

In solution, **4.25** exhibits C_1 symmetry as shown by ^1H NMR spectroscopy, with three distinct isopropyl doublet resonances in a 12:6:6 ratio. This indicates that the two amidate N-aryl groups are chemically inequivalent on the NMR timescale, where one of the aryl groups can freely rotate about its N- C_{ipso} bond, and the other is sterically hindered from rotating. This behavior is mirrored by the isopropyl methine signals, where two distinct resonances are seen at δ 3.57 and 4.00. The resonance at δ 4.00 is broad, suggesting that it corresponds to the isopropyl methine protons on the ring experiencing hindered rotation. Correlation of the two isopropyl signals of equal intensity to the broad methine resonance at δ 4.00 by COSY NMR spectroscopy confirmed the peak assignment for the ^1H NMR spectrum. The appearance of a single resonance at δ 2.47 verifies the installation of the 2,6-dimethylphenyl imido unit, which can freely rotate about its N- C_{ipso} bond. A resonance at δ 142.4 in the $^{13}\text{C}\{^1\text{H}\}$ NMR spectrum is diagnostic of arene carbons adjacent to imido fragments.^{32, 35, 95, 127, 129, 137-139} Variable temperature ^1H and ^{31}P NMR spectroscopic experiments suggest that two C_1 symmetric isomers are interconverting in solution. Free TPPO is not observed by ^{31}P NMR spectroscopy, indicating that it is not coordinatively labile, and this process occurs through an inner-sphere ligand exchange mechanism.

While **4.25** can be synthesized directly from the bis(amido) precursor **4.16**, it is also possible to access **4.25** via addition of TPPO to the mixed amido species **4.17**, as illustrated in Scheme 4.9. This result suggests that imido formation occurs through an associative unimolecular pathway, where sterically induced α -H transfer of the anilido proton to the dimethylamido ligand results in dimethylamine elimination and concomitant imido formation. An alternative reaction pathway would involve the addition of 2 equiv. of 2,6-dimethylaniline to form a bis(anilido) complex, which would then eliminate 2,6-dimethylaniline through a sterically induced α -H transfer. Attempts to synthesize and isolate such a bis(2,6-dimethylanilido) complex have been unsuccessful, and suggest that this mechanism for imido formation is unlikely. Furthermore, addition of one equiv. of 2,6-dimethylaniline to imido complex **4.25** does not result in a bis(anilido) complex, suggesting that the back reaction to a mixed amido complex is not favorable once the imido complex is formed. It is possible that the sterically bulky 2,6-dimethylphenyl substituents are too large to support such a bis(anilido) complex.

Single crystals of **4.25** were grown from a saturated benzene solution and analyzed by X-ray crystallographic analysis. The solid-state molecular structure of **4.25** is shown in Fig. 4.6, with relevant bond lengths and angles listed in Table 4.2, and crystallographic data located in Table A4.2 (Appendix A). The solid-state molecular structure of **4.25** exhibits a unique distorted pentagonal pyramidal coordination geometry. This type of coordination geometry is very uncommon, and has not previously been observed for group 4 complexes. In this structure, the amidate and TPPO ligands are located in the pseudo-equatorial plane, with the imido ligand located in the axial position.

The zirconium center is situated 0.571 Å above the mean plane defined by the amidate and TPPO donors (N(2)-O(2)-N(1)-O(1)-O(3)). The pentagonal base of the complex is most easily seen in bottom view, as shown in Fig. 4.7 (outlined in green). The imido ligand is axially located, perpendicular to the mean plane defined by the amidate and TPPO ligands, which makes an 89.8° angle with the plane defined by C(57)-N(3)-Zr(1).

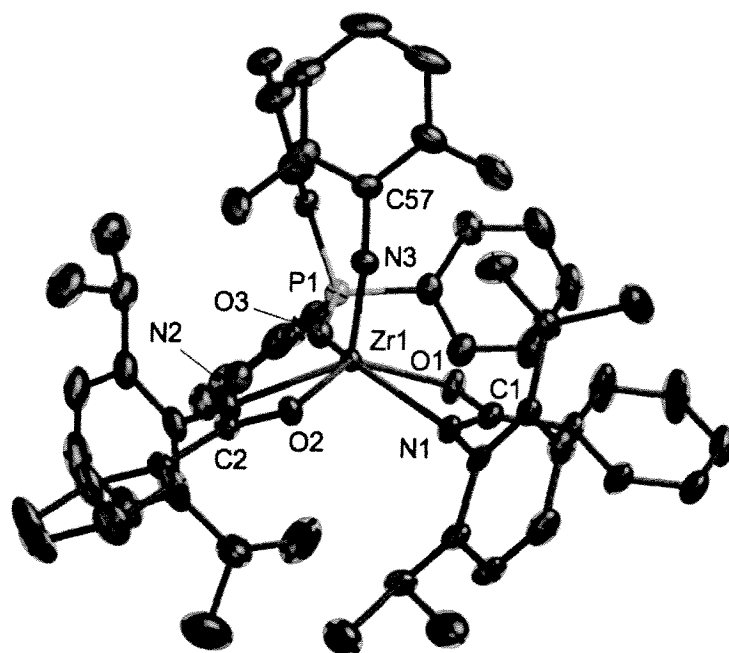
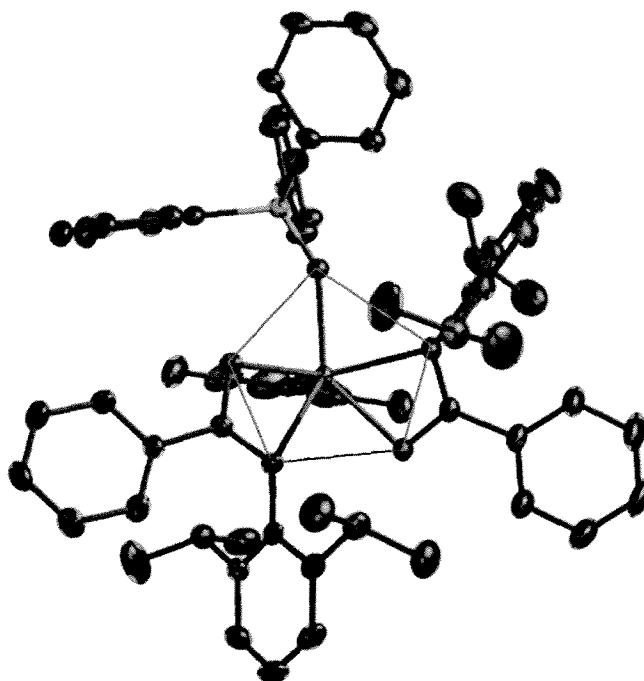


Figure 4.6 ORTEP depiction (ellipsoids at 30% probability) of solid-state molecular structure of $[\text{DIP}^{\text{P}}(\text{NO})^{\text{Ph}}]_2\text{Zr}=\text{N}(2,6\text{-Me}_2\text{C}_6\text{H}_3)(\text{TPPO})$, **4.25** (hydrogens omitted for clarity)

Table 4.2 Selected Bond Distances (Å) and Angles (°) for $[\text{DIPP}(\text{NO})^{\text{Ph}}]_2\text{Zr}=\text{N}(2,6\text{-Me}_2\text{C}_6\text{H}_3)(\text{TPPO})$, **4.25**

Lengths		Angles		Angles	
Zr(1)-O(1)	2.2034(15)	O(1)-Zr(1)-N(1)	57.93(6)	O(2)-Zr(1)-N(1)	78.72(6)
Zr(1)-O(2)	2.2391(15)	O(2)-Zr(1)-N(2)	57.45(6)	O(1)-Zr(1)-N(3)	105.85(7)
Zr(1)-O(3)	2.2086(14)	N(1)-Zr(1)-N(2)	121.90(7)	O(2)-Zr(1)-N(3)	96.89(7)
Zr(1)-N(1)	2.3124(18)	N(1)-Zr(1)-N(3)	103.37(7)	P(1)-O(3)-Zr(1)	147.87(9)
Zr(1)-N(2)	2.3114(18)	O(1)-Zr(1)-O(2)	134.33(6)	O(3)-Zr(1)-N(1)	134.26(6)
Zr(1)-N(3)	1.8531(18)	N(2)-Zr(1)-N(3)	116.92(8)	O(3)-Zr(1)-O(2)	136.32(5)
O(1)-C(1)	1.294(3)	O(3)-Zr(1)-N(3)	100.07(7)		
N(1)-C(1)	1.310(3)	C(57)-N(3)-Zr(1)	173.54(16)		
O(2)-C(2)	1.290(3)	O(1)-Zr(1)-O(3)	78.14(6)		
N(2)-C(2)	1.315(3)	N(2)-Zr(1)-O(3)	79.01(6)		

**Figure 4.7** ORTEP depiction (ellipsoids at 30% probability) of bottom view of solid-state molecular structure of $[\text{DIPP}(\text{NO})^{\text{Ph}}]_2\text{Zr}=\text{N}(2,6\text{-Me}_2\text{C}_6\text{H}_3)(\text{TPPO})$, **4.25** (hydrogens omitted for clarity)

The overall symmetry of **4.25** is C_1 , and the solid-state molecular structure is consistent with the solution characterization data. As can be seen in Fig. 4.6, the aryl group located on the N(1) donor of one of the amidate ligands is less sterically encumbered than the other amidate aryl group at N(2), which is adjacent to the bulky

TPPO ligand. This structure matches the ^1H NMR spectrum for this complex, where one of the amidate N-aryl groups gives rise to two signals for the isopropyl groups, due to hindered rotation, and the other is observed as a single resonance. The imido group is best envisioned as a triply-bonded ligand, with an sp-hybridized N center. Triple bond character is supported by the very short Zr(1)-N(3) bond distance of 1.8531(18) Å, and the nearly linear C(57)-N(3)-Zr(1) bond angle of 173.54(16)°. While the solution phase data are supportive of the pentagonal pyramidal structure observed in the solid-state, a C_1 symmetric pseudo-octahedral solution phase structure cannot be ruled out. Density functional theory (DFT) calculations have been undertaken to determine the electronic structure of **4.25** and assist in the interpretation of its unique geometry and reactivity.

4.2.2.3 Electronic Structure of Pentagonal Pyramidal Imido Complex **4.25**

Geometric optimization of the structure of **4.25** was accomplished using the solid-state molecular structure determined by X-ray crystallography as the input, and computational details are given in Appendix B. The energetically minimized structure closely matches the experimentally determined structure, and a single point calculation was performed to determine the electronic structure of this complex. As was observed in the DFT calculations of the bis(amido) complexes in Chapter 2, the amidate bonding interactions in **4.25** are energetically well below the frontier bonding interactions, which are dominated by the imido ligand. The amidate ligands have poor orbital overlap with the metal center, and the interactions are largely electrostatic in nature.¹³⁵ The TPPO ligand is also located at relatively low energy, having poor orbital overlap with Zr.

The HOMO and HOMO-1 orbitals of **4.25** are two orthogonal π - $d\pi$ bonding interactions between the d_{xz} and d_{yz} orbitals of Zr and the p_x and p_y orbitals of the sp-hybridized imido nitrogen. These interactions are shown in Figs. 4.8 and 4.9.

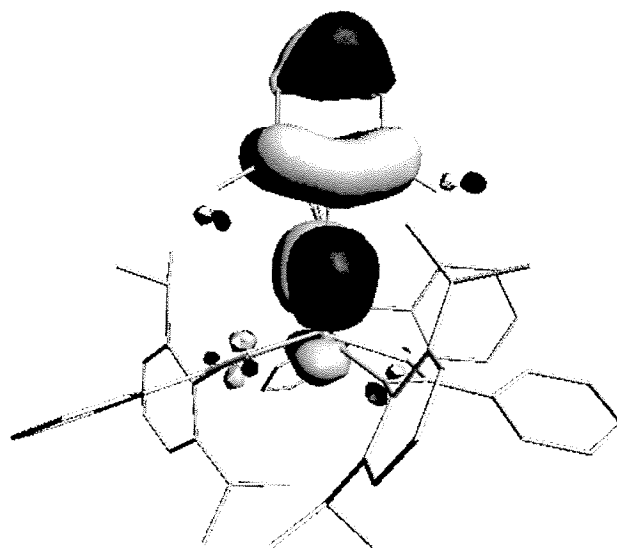


Figure 4.8 HOMO of $[\text{DIPP}(\text{NO})^{\text{Ph}}]_2\text{Zr}=\text{N}(2,6\text{-Me}_2\text{C}_6\text{H}_3)(\text{TPPO})$, **4.25**

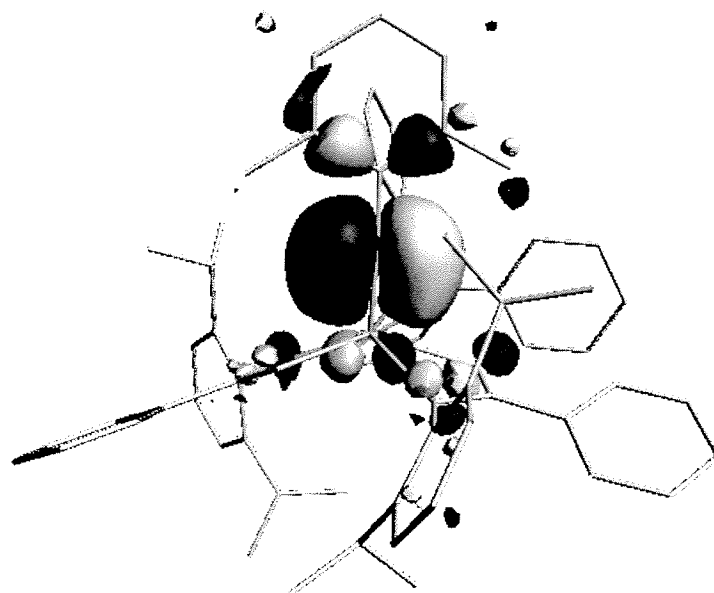


Figure 4.9 HOMO-1 of $[\text{DIPP}(\text{NO})^{\text{Ph}}]_2\text{Zr}=\text{N}(2,6\text{-Me}_2\text{C}_6\text{H}_3)(\text{TPPO})$, **4.25**

The required σ -symmetry bonding interaction for the imido ligand is located at a substantially lower energy than the π -interactions (HOMO-59, 4.217 eV below relative energy of HOMO-1). The intervening orbitals are largely ligand based in nature. Overlap of the d_{z^2} orbital of Zr with the sp -hybrid orbital of the imido nitrogen results in the σ -bond illustrated in Fig. 4.10.

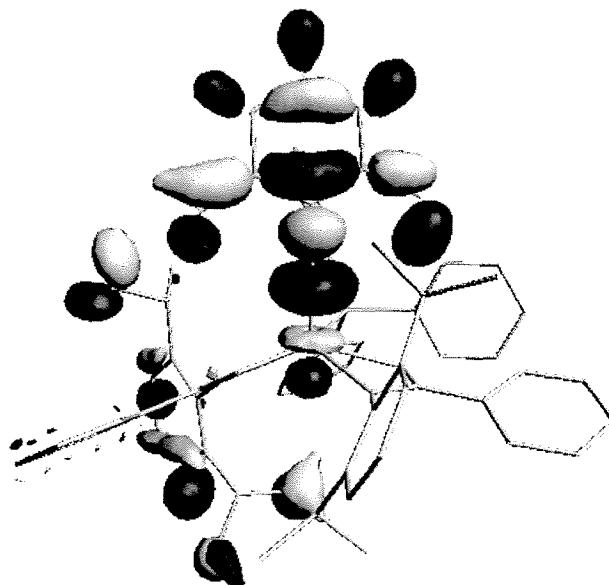


Figure 4.10 HOMO-59 of $[\text{D}^{\text{IPP}}(\text{NO})^{\text{Ph}}]_2\text{Zr}=\text{N}(2,6\text{-Me}_2\text{C}_6\text{H}_3)(\text{TPPO})$, **4.25**

These bonding interactions verify the triple bond status of the imido linkage in **4.25**, and reinforce the notion that the amidate ligand set binds to the metal center with largely electrostatic character, allowing for optimal imido overlap. The six electrons donated by the imido ligand effectively satisfy the bonding interactions in the axial direction of **4.25**, which leads to the question as to whether the position *trans* to the imido group is accessible for further electron donors. While displacement of the TPPO ligand is observed for **4.25** upon addition of an excess of pyridine, no 7-coordinate adduct could be cleanly isolated upon addition of one equiv. of pyridine to **4.25**. The lack of steric accessibility of the position *trans* to the imido ligand is illustrated in the space-filling models of **4.25** shown in Fig. 4.11.

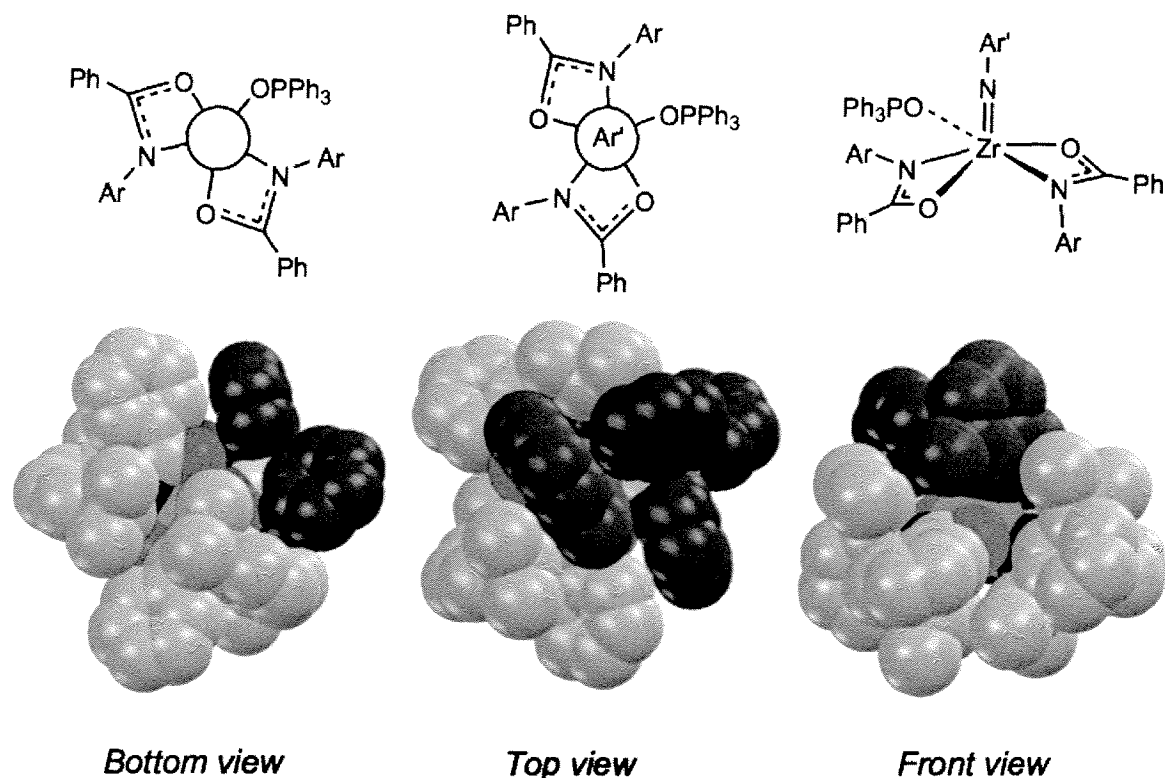


Figure 4.11 Space-filling models of **4.25** (imido ligand = purple balls, amidate ligands = green balls, TPPO ligand = gray balls)

While the front and top views of **4.25** show that the imido ligand is relatively accessible, the bottom view illustrates how the 2,6-diisopropylphenyl groups offer significant steric protection, where very little of the Zr center appears accessible. As previously observed for bis(amidate) bis(amido) complexes of Ti,¹³⁵ the amidate ligands in Zr imido complex **4.25** have poor orbital overlap with Zr, thereby generating a very electrophilic metal center that maximizes orbital overlap with the imido fragment, resulting in a formal triple bond.

4.2.2.4 Ligand Lability Investigations

While the TPPO ligand in **4.25** is not coordinatively labile in solution, the addition of an excess of a small donor such as THF or pyridine results in loss of TPPO, as observed by ³¹P NMR spectroscopy, where the signal at δ 42.7 is replaced by the signal at δ 25.4 for free TPPO. This suggests that under catalytic hydroamination conditions, the

TPPO donor can be readily displaced by another donor, such as an amine. These results are consistent with an associative mechanism for ligand substitution, proceeding through a 7-coordinate intermediate.

It has been noted in the literature that Ti complexes are much more reactive for alkyne hydroamination than Zr complexes,^{58, 115, 140} and thus the Ti analogue of **4.25** was synthesized for comparison. Direct synthesis of $[\text{DIPP}(\text{NO})^{\text{Ph}}]_2\text{Ti}=\text{N}(2,6\text{-Me}_2\text{C}_6\text{H}_3)(\text{TPPO})$ (**4.26**) is possible by combination of $[\text{DIPP}(\text{NO})^{\text{Ph}}]_2\text{Ti}(\text{NMe}_2)_2$, the dimethylamido variant of **4.23**, with 2,6-dimethylaniline in the presence of TPPO. In solution, **4.26** behaves much the same as **4.25**, with ¹H, ¹³C, and ³¹P NMR spectra that are essentially identical to those for **4.25**. While solid-state structural characterization of this complex was not possible, mass spectral data and elemental analysis support the composition of **4.26** as designated. While the isopropyl methyl region of the ¹H NMR spectrum for **4.26** is nearly identical to that of **4.25**, suggesting a C₁ symmetric complex with hindered rotation about one of the N aryl groups and free rotation about the other, the smaller size of Ti may force the more traditional pseudo-octahedral geometry. The solid-state molecular structures of two bis(amidate) Ti imido complexes isolated in the Schafer lab exhibit distorted octahedral geometries, supporting this hypothesis for the smaller Ti complex.^{122, 141} As seen previously for **4.25**, the addition of amine donors to **4.26** results in the displacement of TPPO, presumably through an associative mechanism.

4.2.3 Summary

Terminal Ti and Zr imido complexes were isolated in high yields through an aminolysis methodology, starting with bis(amidate) bis(amido) complexes. Generation of the imido complexes occurs through initial generation of a mixed amido species $[\text{DIPP}(\text{NO})^{\text{Ph}}]_2\text{Zr}(\text{NH}-2,6\text{-Me}_2\text{C}_6\text{H}_3)(\text{NMe}_2)$, **4.17**. This complex can undergo sterically induced α -hydrogen abstraction upon addition of the Lewis base TPPO, liberating dimethylamine and generating the desired imido complex $[\text{DIPP}(\text{NO})^{\text{Ph}}]_2\text{Zr}=\text{N}(2,6\text{-Me}_2\text{C}_6\text{H}_3)(\text{TPPO})$, **4.25**. In the solid-state, **4.25** exists in a rare pentagonal pyramidal geometry. Bond lengths and angles for the imido fragment in **4.25** are indicative of triple bond character, and DFT calculations support this bonding picture. Although the bound

TPPO is not coordinatively labile, it is possible to displace this ligand upon addition of an excess of donor ligand. An associative mechanism involving a 7-coordinate imido complex is postulated for this process, and the following section describes the synthesis and characterization of such a species.

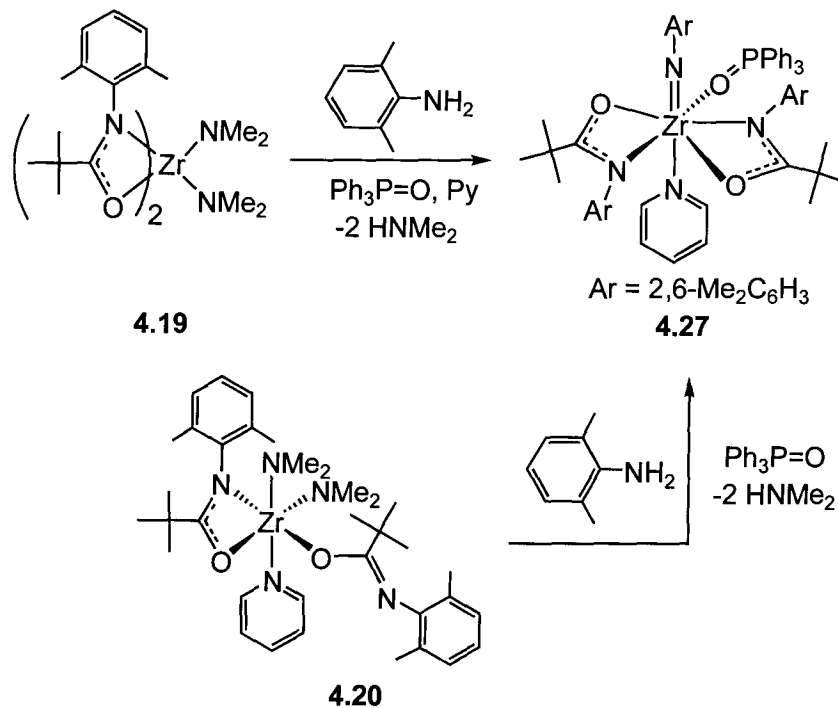
4.3 Synthesis and Structure of a Seven-Coordinate Imido Complex

4.3.1 Introduction

The structural results for **4.25** demonstrated that amidate supported terminal imido species are readily accessible, and adopt a pyramidal geometry in the solid-state. It was possible to observe ancillary ligand exchange of TPPO with other donors, and 7-coordinate imido complexes are postulated as intermediates in this process. However, characterization of a 7-coordinate imido complex was not possible with the bulky [^{DIPP}(NO)^{Ph}] amidate ligand. Space-filling models of **4.25** indicate that the position *trans* to the imido ligand is difficult to access due to the bulky 2,6-diisopropylphenyl substituents on the amidate ligands. By reducing the steric bulk of the amidate ligands it was anticipated that 7-coordinate imido species could be accessed.

4.3.2 Results and Discussion

In an attempt to isolate a 7-coordinate imido complex, the steric bulk at the N of the amidate ligands was reduced from 2,6-diisopropylphenyl to 2,6-dimethylphenyl, to allow access to the site *trans* to the imido fragment. The ¹H NMR spectrum of the bis(amido) complex [^{DMP}(NO)^{tBu}]₂Zr(NMe₂)₂ (**4.19**) is much simpler than that for [^{DIPP}(NO)^{Ph}]₂Zr(NMe₂)₂ (**4.16**), and it was hoped that this simplicity would facilitate solution phase characterization of the resulting imido complex. Two routes into a 7-coordinate imido complex are illustrated in Scheme 4.10.



Direct synthesis of the 7-coordinate distorted pentagonal bipyramidal imido complex $[\text{DMP}(\text{NO})^{\text{tBu}}]_2\text{Zr}=\text{N}(2,6\text{-Me}_2\text{C}_6\text{H}_3)(\text{TPPO})(\text{Py})$, **4.27**, can be accomplished by combining the bis(amido) precursor $[\text{DMP}(\text{NO})^{\text{tBu}}]_2\text{Zr}(\text{NMe}_2)_2$, **4.19**, with one equiv. of 2,6-dimethylaniline in the presence of one equiv. of TPPO and one equiv. of pyridine. In solution, a single resonance is observed at δ 1.08 corresponding to the *tert*-butyl protons, indicating two equivalent amidate ligands. However, the 2,6-dimethylphenyl groups of the amidate ligands appear as two overlapping broad signals at δ 2.13 and 2.22, suggesting hindered rotation of these groups. This was confirmed by variable temperature ^1H NMR spectroscopic experiments, which show coalescence and sharpening of the broad signals into a single sharp singlet at elevated temperatures. A singlet resonance at δ 2.37 indicates free rotation of the imido group at room temperature. Coordination of TPPO can be seen in the ^{31}P NMR spectrum of **4.27**, where the downfield shifted signal at δ 41.2 is similar to that seen for **4.25** and **4.26**. Finally, coordination of pyridine is confirmed by signals at δ 8.70, 7.61, and 6.59 in the ^1H NMR spectrum. The broadness of these signals suggests fluxional behavior and a relatively weakly coordinated pyridine moiety. This fluxionality is also inferred by the appearance

of free pyridine signals in the ^1H NMR spectrum at elevated temperatures. Generation of **4.27** is also possible through reaction of one equiv. of 2,6-dimethylaniline and one equiv. of TPPO with the bis(amidate) bis(amido) pyridine adduct **4.20** (introduced in Chapter 2 as compound **2.19**), where the coordinated pyridine in **4.20** remains coordinated to the resulting imido complex.

As was the case for **4.25** and **4.26**, isolation of **4.27** is facilitated by its low solubility in pentane and hexanes, and high yields of the product can be isolated as a bright yellow microcrystalline material. Electron impact mass spectrometry of the crude material supports the formation of the imido complex, with a signal at m/z 895, corresponding to M^+ - pyridine. Confirmation of pyridine coordination in the solid-state was possible through X-ray crystallographic studies of single crystals grown from a saturated toluene solution at $-37\text{ }^\circ\text{C}$. The solid-state molecular structure of **4.27** is illustrated in Fig. 4.12, with relevant bond lengths and angles listed in Table 4.3, and crystallographic details given in Table A4.3 (Appendix A).

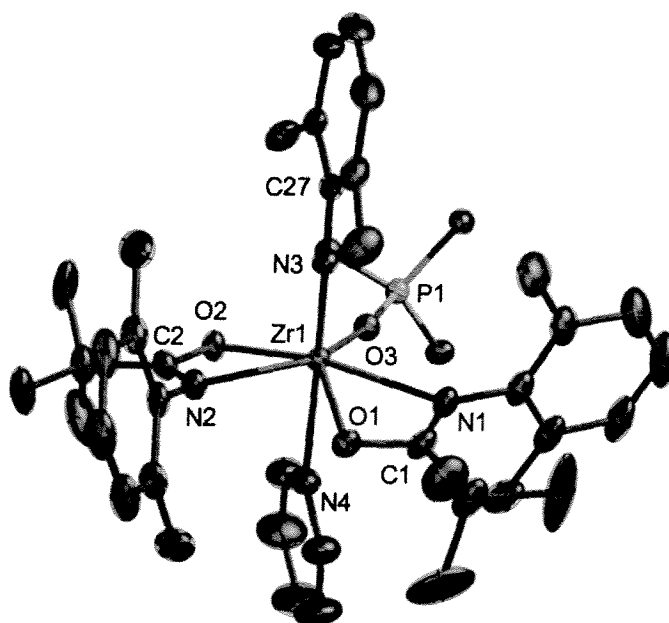


Figure 4.12 ORTEP depiction (ellipsoids at 30% probability) of solid-state molecular structure of $[\text{DMP}(\text{NO})^{\text{tBu}}]_2\text{Zr}=\text{N}(2,6\text{-Me}_2\text{C}_6\text{H}_3)(\text{TPPO})(\text{Py})$, **4.27** (non-ipso phenyl carbons and hydrogens omitted for clarity)

Table 4.3 Selected Bond Distances (Å) and Angles (°) for [^{DMP}(NO)^{tBu}]₂Zr=N(2,6-Me₂C₆H₃)(TPPO)(Py), **4.27**

Lengths		Angles		Angles	
Zr(1)-O(1)	2.213(3)	O(1)-Zr(1)-N(3)	103.64(14)	N(3)-Zr(1)-N(4)	175.32(14)
Zr(1)-O(2)	2.243(3)	N(1)-Zr(1)-N(3)	98.08(14)	O(1)-Zr(1)-N(1)	56.95(11)
Zr(1)-O(3)	2.223(3)	O(3)-Zr(1)-N(3)	98.36(13)	O(2)-Zr(1)-N(2)	56.92(11)
Zr(1)-N(1)	2.391(3)	O(2)-Zr(1)-N(3)	101.97(13)	P(1)-O(3)-Zr(1)	167.73(19)
Zr(1)-N(2)	2.334(3)	N(2)-Zr(1)-N(3)	93.66(14)	O(3)-Zr(1)-N(1)	82.80(11)
Zr(1)-N(3)	1.880(4)	O(1)-Zr(1)-N(4)	81.02(12)	O(3)-Zr(1)-O(2)	80.09(10)
Zr(1)-N(4)	2.601(4)	N(1)-Zr(1)-N(4)	84.76(13)	N(2)-Zr(1)-O(1)	79.23(12)
P(1)-O(3)	1.504(3)	O(3)-Zr(1)-N(4)	78.25(12)	C(27)-N(3)-Zr(1)	178.0(3)
O(1)-C(1)	1.300(5)	O(2)-Zr(1)-N(4)	74.37(12)		
N(1)-C(1)	1.317(5)	N(2)-Zr(1)-N(4)	86.77(13)		

It is clear that the smaller amidate ligands in **4.27** allow access to the site *trans* to the imido ligand, with a N(3)-Zr(1)-N(4) bond angle of 175.32(14)°, but the Zr(1)-N(4) bond length of 2.601(4) Å indicates that the bound pyridine is very weakly coordinated to the Zr center. A graphical representation of the steric accessibility of the site *trans* to the imido ligand is shown in Fig. 4.13, where the coordinated pyridine has been removed from the space-filling model to demonstrate the increased access to the bottom coordination site in **4.27**.

The imido bond length (Zr(1)-N(3) = 1.880(4) Å) is very similar to the analogous distance in **4.25**, indicating that the presence of the pyridine ligand results in very little perturbation of the imido ligand. Complementing the short Zr-N bond length of the imido ligand is the nearly linear C(27)-N(3)-Zr(1) bond angle of 178.0(3)°. Taken together, these observations indicate triple bond formation between the imido nitrogen and the zirconium center, as was seen in complex **4.25**. The pentagonal plane defined by the amidate and TPPO ligands in **4.27** is considerably more planar than that for **4.25**, where the sum of equatorial angles about Zr is 356.01° for **4.27** and only 351.2° for **4.25**. As expected, the deviation of Zr from the mean plane defined by N(1)-O(1)-N(2)-O(2)-O(3) in **4.27** is substantially less than that seen for **4.25** (0.359 Å (**4.27**) vs. 0.571 Å (**4.25**)).

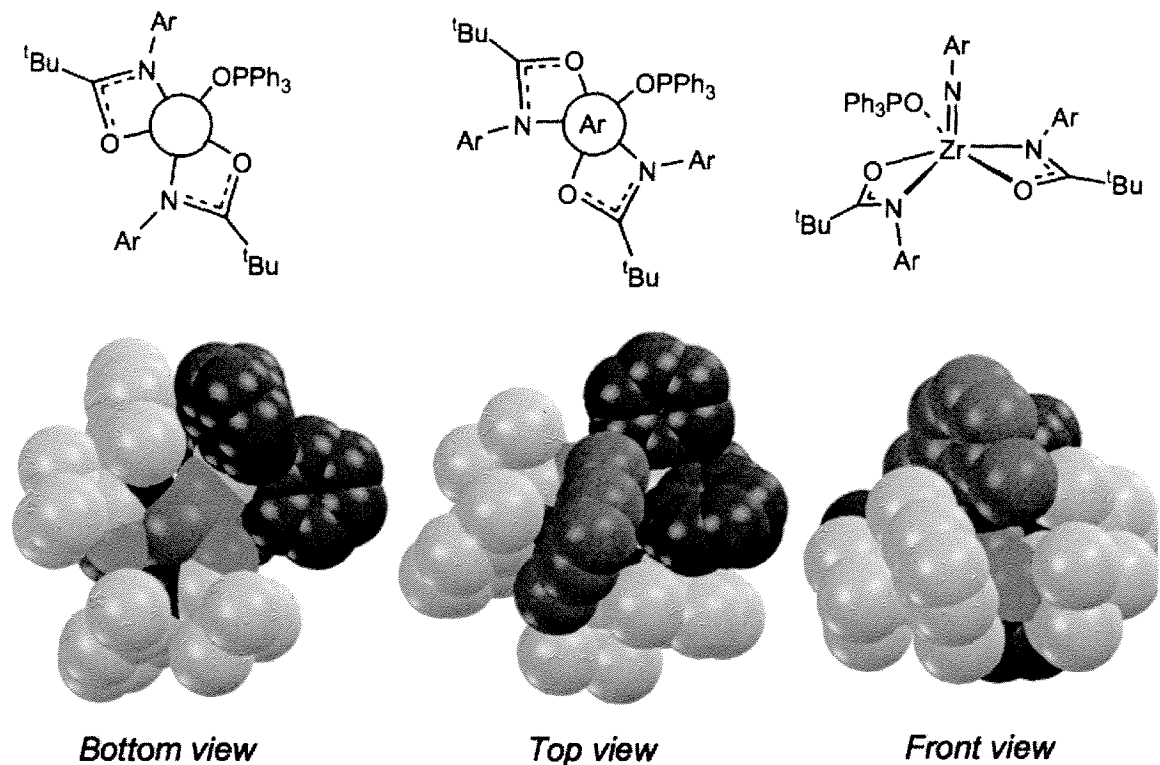


Figure 4.13 Space-filling models of **4.27** with pyridine removed (imido ligand = purple balls, amidate ligands = green balls, TPPO ligand = gray balls)

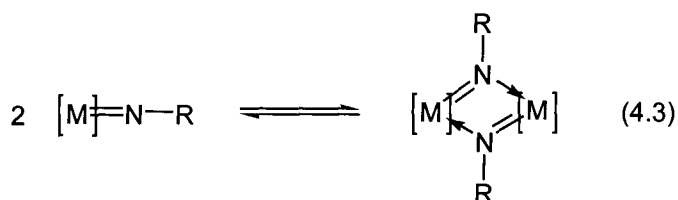
4.3.3 Summary

By judicious choice of the less bulky amidate ligand [$\text{DMP}(\text{NO})^{\text{tBu}}$], a 7-coordinate terminal imido complex **4.27** was isolable, where the position *trans* to the imido fragment is sterically accessible to electron donors like pyridine. Solid-state molecular structure characterization verified a pentagonal bipyramidal geometry. The coordinated pyridine is labile in solution phase, allowing for rapid exchange of coordinated ligands at this site. This complex is the first 7-coordinate Zr imido complex structurally authenticated, and is strong supporting evidence for an associative mechanism for ligand substitution at Zr. This complex will be revisited in Chapter 5 as a transition state model in the catalytic hydroamination of aminoalkenes.

4.4 Structural Characterization of Dimeric Zr Imido Complexes

4.4.1 Introduction

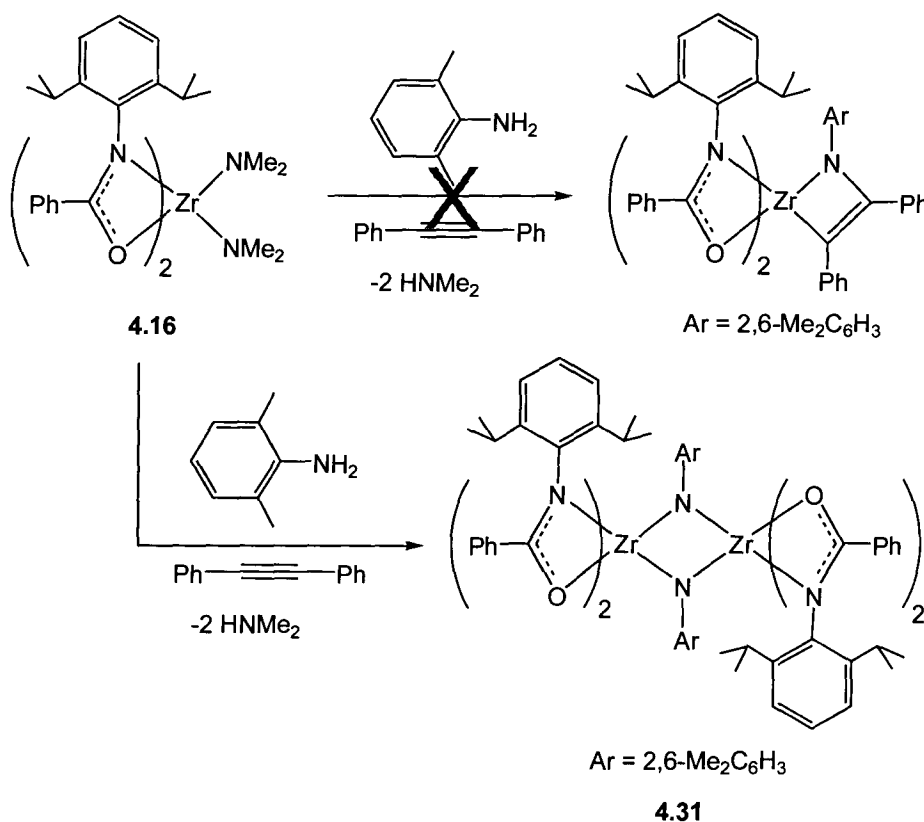
With many early transition metals, terminal imido complexes are in equilibrium with their dimeric forms (Eq. 4.3).^{68, 90, 93, 129, 130, 142} Complexes exhibiting this type of behavior generally have low coordination numbers, are electron deficient, or have highly labile ancillary ligands in their coordination sphere. The presence of dimeric imido complexes is an important consideration in hydroamination catalysis, as these species are considered catalytically inactive and reduce the availability of the catalytically active terminal imido complex.^{68, 143, 144}



A dimeric Ti imido complex supported by amidate ligands has been characterized by mass spectrometry, and has the empirical formula $[\text{tBu}(\text{NO})^{\text{C6F5}}]_2\text{Ti}(\mu\text{-NPh})_2\text{Ti}[\text{tBu}(\text{NO})^{\text{C6F5}}]_2$ (**4.28**).¹⁴¹ This complex could not be characterized in solution or by X-ray crystallography due to its extremely low solubility in all common organic solvents. While the fluorinated bis(amido) precatalyst $[\text{tBu}(\text{NO})^{\text{C6F5}}]_2\text{Ti}(\text{NEt}_2)_2$ (**4.29**) is highly reactive for alkyne hydroamination, the non-fluorinated congener $[\text{tBu}(\text{NO})^{\text{Ph}}]_2\text{Ti}(\text{NEt}_2)_2$ (**4.30**) is only modestly active in comparison to the much bulkier complex $[\text{DIPP}(\text{NO})^{\text{Ph}}]_2\text{Ti}(\text{NEt}_2)_2$ (**4.23**).^{119, 120} The difference in reactivity between **4.30** and **4.23** can be rationalized by the reduced propensity of imido complexes bearing the very bulky $[\text{DIPP}(\text{NO})^{\text{Ph}}]$ amidate ligand to dimerize in solution. In the hopes of determining the relative importance of dimeric imido species in hydroamination catalysis with amidate supported group 4 complexes, isolation of these complexes was attempted.

4.4.2 Results and Discussion

Given the rich imido chemistry observed for Zr amidate vs. Ti amidate complexes, attempts to synthesize dimeric imido complexes focused on Zr species. It was previously noted that pyridine adducts of bulky Ti and Zr imido complexes were ill-defined and difficult to characterize. Solution characterization of any dynamic monomer-dimer equilibria was therefore impossible with these systems. While the TPPO stabilized imido complexes **4.25** – **4.27** are easier to characterize in solution, the strongly donating TPPO ligand is not sufficiently labile to permit dimer formation. As a result, no solution phase evidence for the existence of dimeric imido complexes could be obtained. However, attempts to form azazirconacyclobutene species *in situ* from bis(amido) precursor $[\text{DIPP}(\text{NO})^{\text{Ph}}]_2\text{Zr}(\text{NMe}_2)_2$ (**4.16**) fortuitously resulted in solid-state evidence for the formation of a dimeric Zr imido complex, as illustrated in Scheme 4.11.



Scheme 4.11

The reaction of **4.16** with one equiv. of 2,6-dimethylaniline and one equiv. of diphenylacetylene resulted in a color change from pale yellow to yellow-orange. The ^1H NMR spectrum of this complex is extremely complicated and of limited usefulness. The product isolated is a waxy yellow-orange paste that is very difficult to manipulate. The crude material is soluble in toluene, and this solution was left to crystallize at room temperature for several months. Single crystals were isolable in extremely low yield after crystallization, and were analyzed by X-ray diffraction. It is unlikely that the crystals isolated are representative of the bulk material, and are likely only a small fraction of the products formed in this reaction. However, this experiment afforded the first crystallographically characterized example of bridging imido ligands with ancillary amidate ligands. The solid-state molecular structure of $[\text{DIPP}(\text{NO})^{\text{Ph}}]_2\text{Zr}(\mu\text{-N}(2,6\text{-Me}_2\text{C}_6\text{H}_3))_2\text{Zr}[\text{DIPP}(\text{NO})^{\text{Ph}}]_2$ (**4.31**) is shown in Fig. 4.14, with relevant bond lengths and angles listed in Table 4.4 and crystallographic data located in Appendix A (Table A4.4).

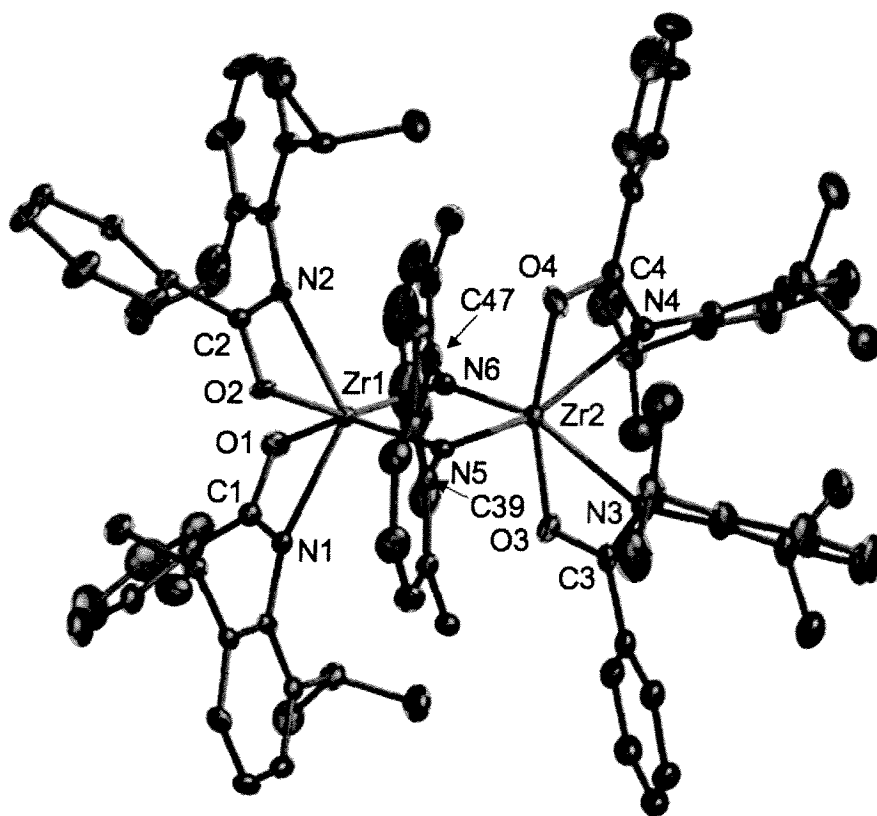
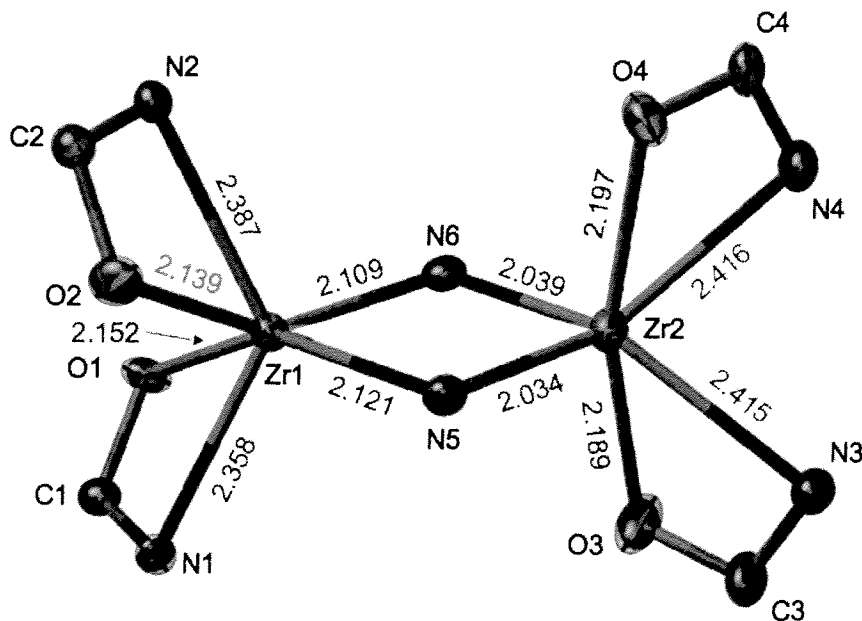


Figure 4.14 ORTEP depiction (ellipsoids at 30% probability) of solid-state molecular structure of $[\text{DIPP}(\text{NO})^{\text{Ph}}]_2\text{Zr}(\mu\text{-N}(2,6\text{-Me}_2\text{C}_6\text{H}_3))_2\text{Zr}[\text{DIPP}(\text{NO})^{\text{Ph}}]_2$, **4.31** (hydrogens omitted)

Table 4.4 Selected Bond Distances (Å) and Angles (°) for $[\text{DIPP}(\text{NO})^{\text{Ph}}]_2\text{Zr}(\mu\text{-N}(2,6\text{-Me}_2\text{C}_6\text{H}_3))_2\text{Zr}[\text{DIPP}(\text{NO})^{\text{Ph}}]_2$, **4.31**

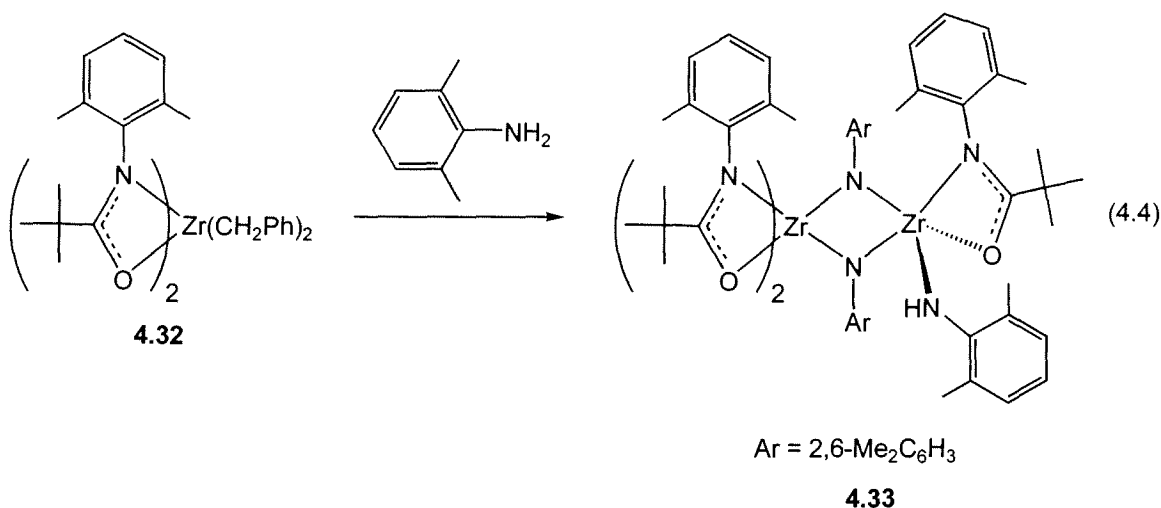
Lengths		Lengths		Angles	
Zr(1)-O(1)	2.152(3)	Zr(1)-N(5)	2.109(4)	Zr(1)-N(5)-Zr(2)	99.03(16)
Zr(1)-O(2)	2.139(3)	Zr(1)-N(6)	2.121(4)	Zr(1)-N(6)-Zr(2)	99.26(16)
Zr(2)-O(3)	2.189(4)	Zr(2)-N(3)	2.415(4)	N(5)-Zr(1)-N(6)	79.01(15)
Zr(2)-O(4)	2.197(3)	Zr(2)-N(4)	2.416(4)	N(5)-Zr(2)-N(6)	82.70(15)
Zr(1)-N(1)	2.358(4)	Zr(2)-N(5)	2.034(4)	N(1)-Zr(1)-N(2)	125.94(12)
Zr(1)-N(2)	2.387(4)	Zr(2)-N(6)	2.039(4)	O(3)-Zr(1)-O(4)	163.85(13)

The considerable steric congestion present in **4.31** is readily apparent in Fig. 4.14, where the 2,6-diisopropylphenyl groups on N(1) and N(2) of the amidate ligands impart steric protection to the bridging imido ligands. While having the N donors of the amidate ligands *trans* disposed is sterically favored, the amidate ligands bound to Zr(2) are forced into the *O-trans* geometry. This is likely due to the extreme steric pressure that would be experienced by the complex if all of the N-2,6-diisopropylphenyl groups were adjacent to the imido core. The core interactions in **4.31** are illustrated in Fig. 4.15, with bond lengths listed in red.

**Figure 4.15** ORTEP depiction (ellipsoids at 30% probability) of core molecular structure of $[\text{DIPP}(\text{NO})^{\text{Ph}}]_2\text{Zr}(\mu\text{-N}(2,6\text{-Me}_2\text{C}_6\text{H}_3))_2\text{Zr}[\text{DIPP}(\text{NO})^{\text{Ph}}]_2$, **4.31** (bond distances in Å)

The Zr_2N_2 core of **4.31** is planar with the sum of angles within the core being exactly 360° . In addition, both bridging imido ligands are planar, with the sum of bond angles around N(5) and N(6) being approximately 360° ($\Sigma_{N5} = 359.45^\circ$ and $\Sigma_{N6} = 359.81^\circ$). Due to the contrasting coordination geometries about the two different Zr centers, the overall symmetry of **4.31** is pseudo- C_2 , with the C_2 axis of symmetry passing through both Zr centers. The different coordination geometries about the Zr centers result in differing imido ligand distances to Zr(1) and Zr(2). As illustrated in Fig. 4.15, the imido distances to Zr(2) are 2.034(4) and 2.039(4) Å vs. the analogous distances to Zr(1), which are 2.109(4) and 2.121(4) Å. These distances are all considerably longer than those seen in the terminal imido complexes **4.25** (1.8531(18) Å) and **4.27** (1.880(4) Å). While an electronic argument based on the *trans* influence can be given to rationalize the different Zr-N(imido) bond distances in **4.31**, it is likely that the main factor is steric congestion at Zr(1) imposed by the N-2,6-diisopropylphenyl groups at N(1) and N(2). These bulky groups force the bridging imido ligands closer to Zr(2), which is less sterically encumbered.

The formation of **4.31** appears to be highly unfavorable given steric considerations. While terminal alkynes, such as phenylacetylene, undergo rapid hydroamination reactions with bis(amidate)-imido complexes, internal alkynes, like diphenylacetylene, do not react with these species (Scheme 4.11).¹²⁰ This lack of reactivity, coupled with an open environment where other volatile donors can escape, likely results in the slow formation of **4.31** over a very long period of time. Bis(amido) complexes such as **4.16** liberate dimethylamine in protonolysis reactions, which can act as a potential ligand for any subsequent products.¹⁴¹ To eliminate the possible formation of neutral donors *in situ*, it was logical to pursue dimeric imido formation using dibenzyl species as reactive precursors. The steric bulk of the amidate ligands must also be reduced to favor imido dimer formation. Thus, the Zr dibenzyl complex $[^{DMP}(NO)^{tBu}]_2Zr(CH_2Ph)_2$ (**4.32**), discussed in Chapter 3 (**3.9**), was chosen as a precursor for imido dimer formation, and upon reaction with one equiv. of 2,6-dimethylaniline, an interesting dimeric imido complex was isolated as shown in Eq. 4.4.



Solid-state characterization of this complex clearly shows that the protonolysis reaction was successful; however, the bimetallic Zr imido species formed is not the expected symmetrical dimer. The crystallographically determined solid-state molecular structure of **4.33** is shown in Fig. 4.16, with selected bond lengths and angles given in Table 4.5, and crystallographic data located in Table A4.5 (Appendix A).

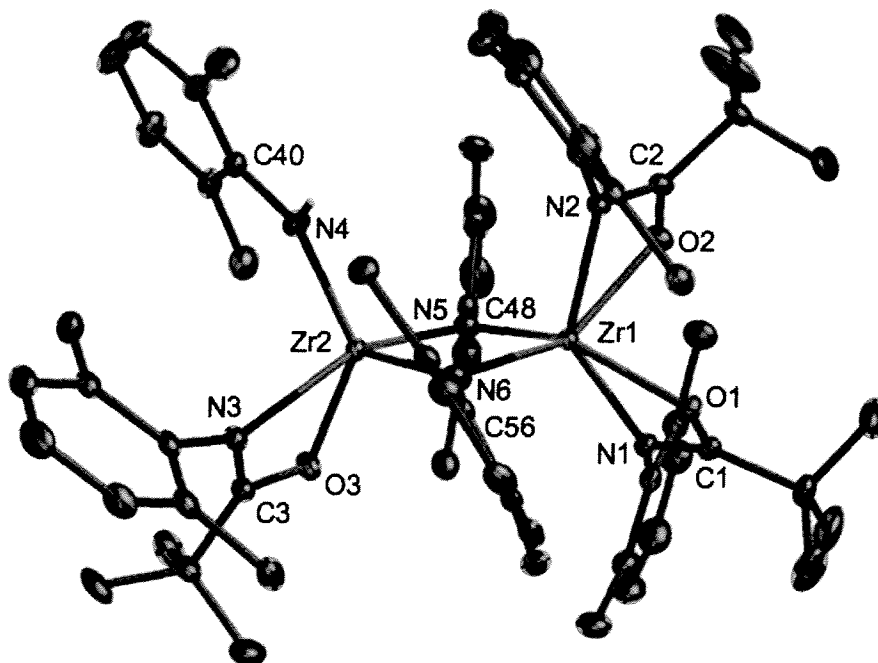


Figure 4.16 ORTEP depiction (ellipsoids at 30% probability) of solid-state molecular structure of [^{DMP}(NO)^{tBu}]₂Zr(μ-N(2,6-Me₂C₆H₃))₂Zr[^{DMP}(NO)^{tBu}]NH(2,6-Me₂C₆H₃), **4.33** (non-N-H hydrogens omitted)

Table 4.5 Selected Bond Distances (Å) and Angles (°) for $[\text{DMP}(\text{NO})^{\text{tBu}}]_2\text{Zr}(\mu\text{-N}(2,6\text{-Me}_2\text{C}_6\text{H}_3))_2\text{Zr}[\text{DMP}(\text{NO})^{\text{tBu}}]\text{NH}(2,6\text{-Me}_2\text{C}_6\text{H}_3)$, **4.33**

Lengths		Lengths/Angles		Angles	
Zr(1)-O(1)	2.1623(19)	Zr(1)-N(6)	2.112(2)	N(4)-Zr(2)-N(5)	107.00(10)
Zr(1)-O(2)	2.147(2)	Zr(2)-N(5)	2.077(2)	O(3)-Zr(2)-N(4)	131.77(10)
Zr(2)-O(3)	2.113(2)	Zr(2)-N(6)	1.987(2)	N(3)-Zr(2)-N(4)	95.81(10)
Zr(1)-N(1)	2.301(2)	N(5)-Zr(1)-N(6)	80.50(9)	C(40)-N(4)-Zr(2)	141.2(2)
Zr(1)-N(2)	2.283(2)	O(2)-Zr(1)-O(1)	87.24(8)	Zr(1)-N(5)-Zr(2)	98.53(10)
Zr(2)-N(3)	2.326(2)	N(1)-Zr(1)-N(2)	138.38(8)	Zr(1)-N(6)-Zr(2)	98.43(10)
Zr(2)-N(4)	2.071(3)	N(4)-Zr(2)-N(6)	110.60(10)		
Zr(1)-N(5)	2.019(2)	N(5)-Zr(2)-N(6)	82.10(9)		

Similar to **4.31**, the Zr_2N_2 core of **4.33** is planar, with the sum of angles about the core being 359.56° . Due to the two different Zr centers, the core bonding interactions are unsymmetrical, with bond distances largely being dictated by steric interactions. For example, the Zr(2)-N(6) imido distance of 1.987(2) Å is substantially shorter than the Zr(1)-N(6) distance of 2.112(2) Å, which can be attributed to the increased steric crowding about Zr(1), where the N donors of the amidate ligands are *cis* to the Zr_2N_2 core. Likewise, the Zr(2)-N(5) bond distance of 2.077(2) Å is longer than the Zr(1)-N(5) distance of 2.019(2) Å, due to the ability of the 2,6-dimethylanilido ligand to rotate into the Zr_2N_2 core. These bond distances are very similar to those seen for the bridging imido ligands in **4.31**, and are much longer than those for the terminal imido complexes discussed in sections 4.2 and 4.3. The 2,6-dimethylanilido ligand is bound to the Zr center with double bond character, having a bond length of 2.071(3) Å, and a C(40)-N(4)-Zr(2) bond angle of $141.2(2)^\circ$. These values are similar to those seen for the 2,6-dimethylanilido ligand in **4.17** (Zr(1)-N(3) = 2.099(3) Å, and C(39)-N(3)-Zr(1) = $140.9(2)^\circ$).

In order to generate **4.33**, either protonolysis of an amidate ligand by 2,6-dimethylaniline or ligand redistribution must occur. No evidence of protonolysis of amidate ligands with primary amines has been observed for these bulky amidate ligands; however, ligand redistribution was noted in Chapter 2 for a tris(amidate) mono(amido) Zr complex $[\text{DIPP}(\text{NO})^{\text{Ph}}]_3\text{ZrNMe}_2$ (**2.12**), making this a more likely possibility. While **4.33** was structurally authenticated in the solid-state, solution phase ^1H NMR spectroscopy is

extremely complex and suggests that multiple unidentified products are present in solution, and a dimeric imido species is not prevalent. Attempts to reproduce the formation of **4.33** have not been successful, and indicate that **4.33** is likely generated as one of several different species in solution. It is reasonable that the reduced steric crowding with the 2,6-dimethylphenyl-substituted amidate ligands may favor ligand redistribution of the bridged bimetallic imido complex **4.33** more readily than the more sterically encumbered imido dimer **4.31**.

4.4.3 Summary

Two bimetallic bridging imido complexes were characterized in the solid-state. Both complexes were found to have a Zr_2N_2 core, with 2,6-dimethylphenyl groups on the μ -imido ligands. The diamond shaped cores of **4.31** and **4.33** are planar, indicating sp^2 -hybridization at both of the imido N donors. Solution phase characterization was not possible for either of these complexes, due to the presence of multiple products and possible dynamic behavior. Reproducibility of these results is poor, and suggests that these bridged imido species are not formed in appreciable quantities, especially in the presence of excess donors, as would be encountered during catalytic hydroamination conditions. With sterically less encumbered ligands, ligand redistribution may be occurring to generate the observed unsymmetrical bimetallic bridged imido complex **4.33**. While solid-state molecular structural data confirm that dimeric imido species can be formed from bis(amidate) bis(amido) and bis(amidate) dibenzyl complexes, the inability to reproduce these data suggest that these species are a very minor contributor in catalytic hydroamination, especially when very bulky amidate ligands are employed.

4.5 Cycloaddition Reactivity with Terminal Imido Complexes

4.5.1 Introduction

Cycloaddition reactions of unsaturated organic molecules with metal-element multiple bonds have been a major driving force behind studying the formation of these interesting metal complexes.^{1, 3-7, 33, 44, 45, 78, 79} Alkylidene complexes have been heavily exploited in this regard, finding widespread application in organic synthesis and ring-opening metathesis polymerization (ROMP).^{2-5, 50} Imido complexes have likewise been utilized to great effect in catalytic hydroamination,^{53, 58, 60, 61, 68, 107, 115} carboamination,¹⁰⁸⁻¹¹¹ and transamidation reactivity.¹¹²⁻¹¹⁴

Stoichiometric cycloadditions of imido complexes with alkynes^{90, 145} and alkenes^{93, 104} have been noted in the literature; however, imido complexes had not been successfully utilized in the catalytic hydroamination of alkenes prior to this research. Two structurally characterized metallacycles of importance to hydroamination catalysis are presented in Fig. 4.17. The diamidopyridine ligated Ti complex (**4.34**) results from the cycloaddition of the aryl imido complex with phenylacetylene.¹⁴⁵ This complex is an important hydroamination intermediate in the generation of the *anti*-Markovnikov imine product.¹⁴⁵ The zirconocene complex (**4.35**) likewise results from the cycloaddition of the *tert*-butyl imido complex with norbornene.⁹³ While this would represent an important intermediate in the catalytic hydroamination of alkenes, this reaction is not catalytically viable with these zirconocene species.⁹³

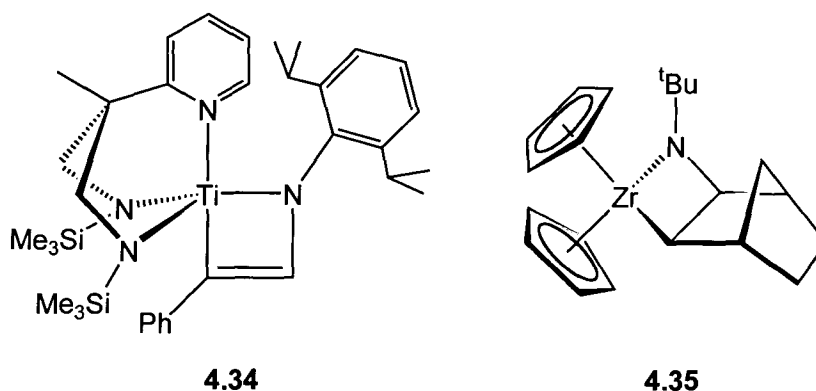


Figure 4.17 Metallacycles relevant to catalytic hydroamination

Catalytic hydroamination is a unifying theme in the Schafer research group, and imido complexes are important proposed intermediates for this process.^{68, 143} The following section investigates some preliminary fundamental reactivity of the imido complexes discussed earlier in this chapter. In particular, this section seeks to demonstrate the ability of these amidate supported imido complexes to undergo cycloaddition-type reactivity, as would be required for successful hydroamination catalysis.^{68, 143}

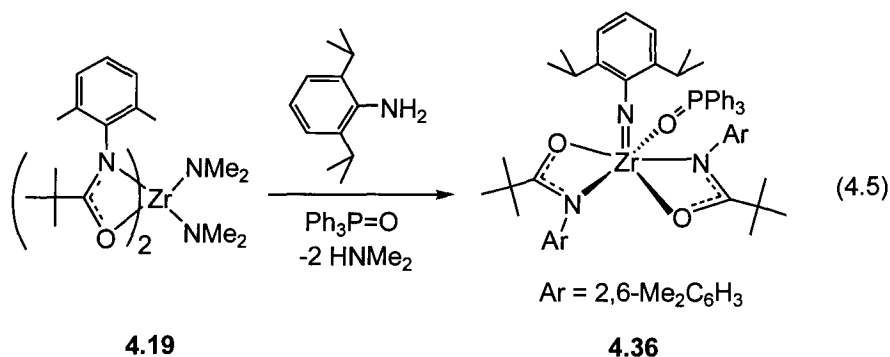
4.5.2 Results and Discussion

4.5.2.1 Development of Spectroscopically Simpler Imido Complexes

Azametallacyclobutane complexes like **4.35** are potential intermediates in imido-mediated alkene hydroamination, and thus these complexes were targeted through stoichiometric investigations. While the complex isolated by Bergman and coworkers (**4.35**) has been characterized crystallographically, this complex is not a viable intermediate in *catalytic* alkene hydroamination, since these zirconocene species do not mediate catalytic hydroamination of alkenes.⁹³

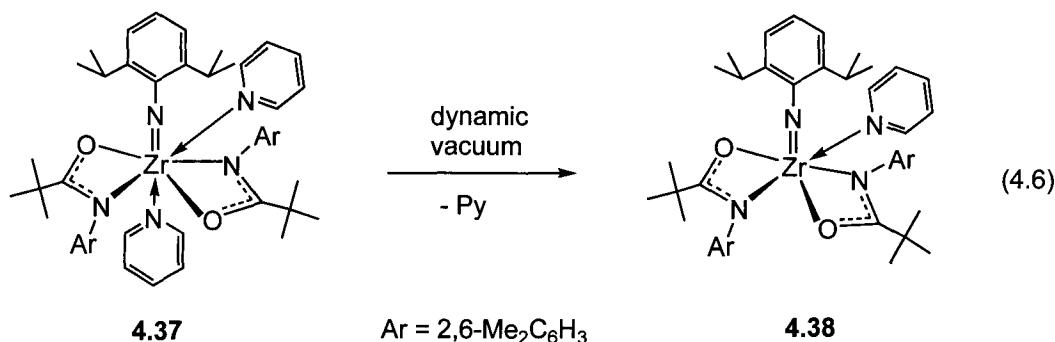
Despite numerous attempts to react imido complex **4.25** with alkenes, no metallacyclic products could be isolated. Norbornene, styrene, 1-hexene, and vinyl trimethylsilylether do not react with **4.25** to generate the expected azametallacyclobutane complexes. Monitoring these reactions by ¹H NMR spectroscopy highlights another difficulty associated with using **4.25** for exploratory cycloaddition reactions. The sterically congested nature of **4.25** results in complicated ¹H NMR spectra when attempting to observe *in situ* reactivity. As such, spectroscopically simpler imido complexes were targeted, bearing the less bulky [^{DMP}(NO)^{tBu}] amidate ligand. Likewise, the non-volatile nature of TPPO makes separation of any metal containing materials from liberated TPPO a potential problem. A volatile stabilizing ligand like pyridine would facilitate separation, as the liberated pyridine could be readily pumped away under vacuum.

Previous attempts at synthesizing well-defined pyridine adducts of Ti and Zr imido complexes were unsuccessful when 2,6-dimethylaniline was utilized to generate the imido ligand. By increasing the steric bulk at the imido ligand, it was hoped that pyridine would stabilize imido complexes bearing the simpler and less bulky $[\text{DMP}(\text{NO})^{\text{tBu}}]$ amidate ligand. Combination of one equiv. of 2,6-diisopropylaniline with bis(amido) complex **4.19** in pentane followed by addition of one equiv. of TPPO results in the generation of a golden yellow solution, from which yellow microcrystals of imido complex $[\text{DMP}(\text{NO})^{\text{tBu}}]_2\text{Zr}=\text{N}(2,6\text{-}^i\text{Pr}_2\text{C}_6\text{H}_3)(\text{TPPO})$ (**4.36**) precipitate over time in 67 % yield, as shown in Eq. 4.5.

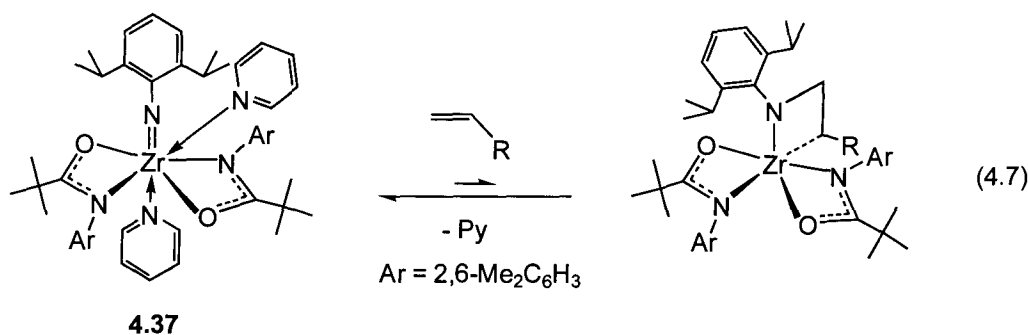


As anticipated, the ^1H NMR spectrum of the resulting complex is extremely simple, having a single resonance for the *tert*-butyl protons at δ 1.07, and two overlapping singlets at δ 2.17 and 2.22 corresponding to the methyl protons on the aryl groups of the amidate ligands. This suggests hindered rotation about the N-C_{ipso} bonds of the amidate ligands, and was confirmed by variable temperature ^1H NMR spectroscopic experiments, which show that these two peaks coalesce at elevated temperatures. The imido ligand appears as a doublet at δ 1.13 for the isopropyl methyl protons and a septet at δ 4.18 for the isopropyl methine protons. Coordination of TPPO is verified by a signal at δ 41.4 in the $^{31}\text{P}\{^1\text{H}\}$ NMR spectrum. While X-ray crystallographic analysis was not performed, mass spectrometry and elemental analysis confirmed the composition of **4.36**. While the proposed structure of **4.36** in Eq. 4.5 is a C₁ symmetric complex, based on previously observed results for **4.25** and **4.27**, the solution phase behavior indicate that the amidate ligands are rapidly exchanging positions, making them appear equivalent on the NMR timescale.

The successful generation of **4.36** supports the notion that the bulk at the amidate ligands can be reduced as long as it is compensated for by additional bulk at the imido ligand. Replacement of the TPPO ligand by a pyridine ligand would generate an ideal complex for stoichiometric cycloaddition studies. Repeating the experiment in Eq. 4.5 with an excess of pyridine instead of TPPO results in a bright yellow solution, which precipitates bright yellow crystalline material in excellent yield (80 %). The new imido complex $[\text{DMP}(\text{NO})^{\text{tBu}}]_2\text{Zr}=\text{N}(2,6\text{-}^i\text{Pr}_2\text{C}_6\text{H}_3)(\text{Py})_2$ (**4.37**), exists as a dipyridine adduct as shown in Eq. 4.6. Coordination of two equiv. of pyridine is evident via integrations in the ^1H NMR spectrum of **4.37**. Similar to **4.27**, the pyridine coordinated *trans* to the imido ligand is labile and can be removed under dynamic vacuum to generate the mono pyridine adduct **4.38**, which has also been characterized, and can be synthesized directly in 93 % yield by using a single equiv. of pyridine, rather than an excess.



Despite the simpler ^1H NMR spectroscopic characteristics of **4.37**, cycloaddition attempts with assorted alkenes do not result in isolable metallacyclic complexes. Given the ideal orbital overlap between the imido ligand and the Zr center, it is reasonable to expect that the cycloaddition of a C=C bond with the imido fragment would generate a much less stable complex, having greatly diminished orbital overlap. Such a metallacyclic complex could rapidly cyclorevert to regenerate the stable imido complex and eject the alkene unit as shown by the equilibrium in Eq. 4.7. Unfortunately these metallacyclic species are not detectable on the NMR timescale, suggesting that the equilibrium, if present, lies far to the left.

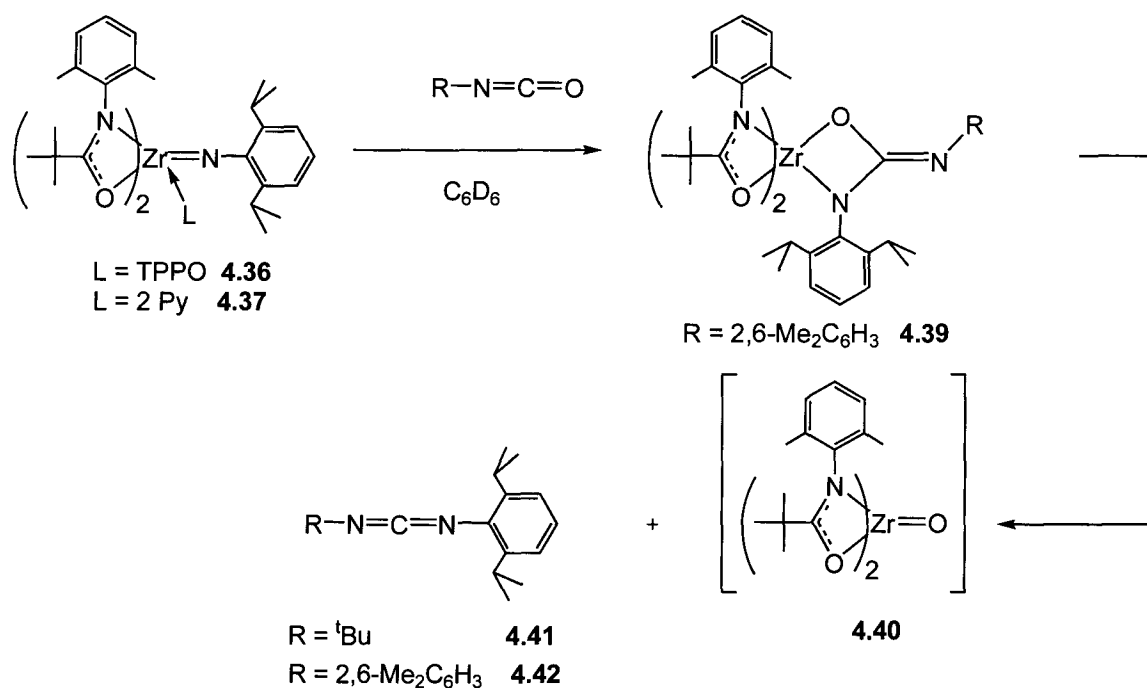


It is unfortunate that the observation of an azametallacyclobutane complex is not possible; however, the unique hydroamination reactivity presented later in this chapter may be a consequence of a highly unstable metallacycle. Such an unstable species would act as a driving force for catalytic turnover in the presence of excess amine, whereas many other systems generate stable metallacycles that show no further reactivity.

4.5.2.2 Cycloadditions of C=O Bonds

If the highly stabilized pyramidal imido complexes generate unstable metallacycles upon cycloaddition of C=C multiple bonds, perhaps the poorer orbital overlap of the metallacycles can be compensated for by the addition of a hard donor to the coordination sphere of the metallacycle. Oxygen is an excellent donor for Zr(IV), and cycloadditions of ketones^{52, 92, 93} and isocyanates^{94, 95} with imido complexes have been well documented. Armed with spectroscopically simple imido complexes (**4.36** and **4.37**), cycloaddition reactions with RN=C=O (R = ^tBu or 2,6-Me₂C₆H₃) and Ph₂C=O have been attempted.

While intermediates in the reaction of ^tBuN=C=O with **4.36** are difficult to observe by ¹H NMR spectroscopy, it is possible to isolate the carbodiimide **4.41** (^tBuN=C=N(2,6-ⁱPr₂C₆H₃)), which results from metathesis between the imido **4.36** and ^tBuN=C=O. Fortunately, the addition of one equiv. of 2,6-Me₂C₆H₃N=C=O to **4.36** in C₆D₆ at room temperature results in a relatively simple ¹H NMR spectrum that corresponds to the ureate complex **4.39**, generated upon cycloaddition of **4.36** with the C=O bond of the isocyanate, as shown in Scheme 4.12.

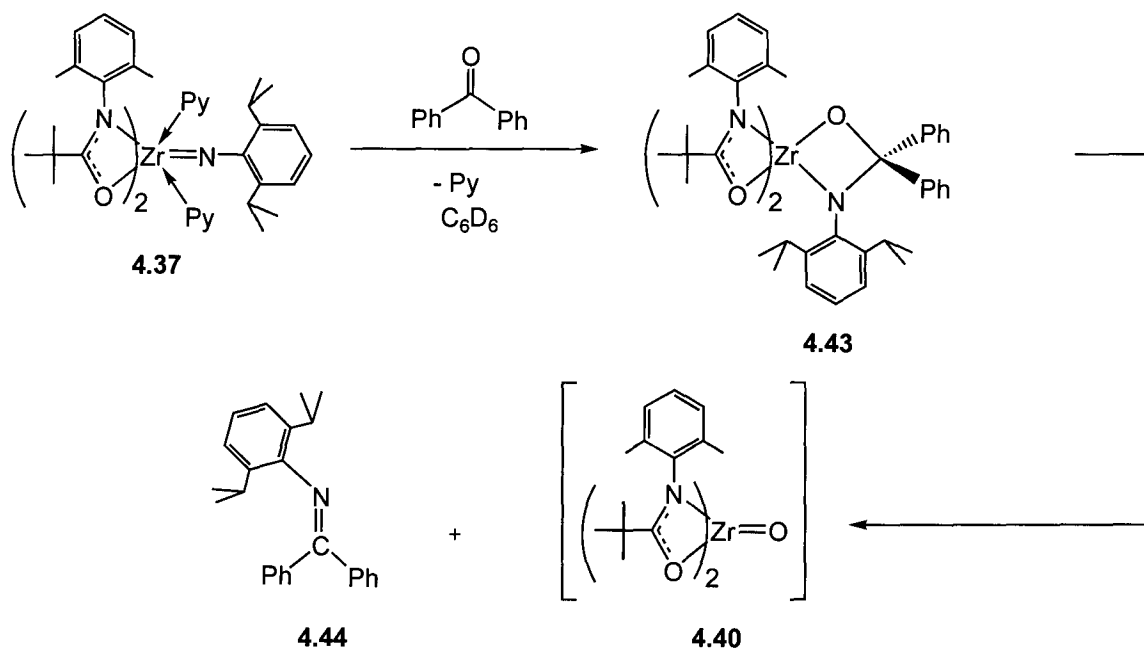


Scheme 4.12

In **4.39**, the *tert*-butyl protons appear at δ 1.00, and the aryl methyl protons of the amidate ligands can be seen at δ 2.01 and 2.10. The isopropyl groups appear as two doublets at δ 1.45 and 1.60 (methyl protons), and a broad septet at δ 4.02 (methine protons). The 2,6-dimethylphenyl group derived from the isocyanate exhibits free rotation about its N-C_{ipso} bond, appearing as a single resonance at δ 2.49. Heating the NMR tube reaction to 110 °C results in complete cycloreversion to generate **4.42**, and the carbodiimide was isolated after hydrolysis of the reaction mixture, and characterized by ¹H NMR spectroscopy, as well as GCMS. The oxo complex **4.40** has not been characterized, but is inferred from reaction stoichiometry and literature precedence for cycloaddition reactions of this type.⁹⁸ It is also possible to perform these reactions with the pyridine stabilized imido complex **4.37** and obtain the same carbodiimide products.

In analogous fashion, the cycloaddition of **4.37** with benzophenone results in the generation of the imine Ph₂C=N(2,6-ⁱPr₂C₆H₃) (**4.44**), presumably along with the oxo complex **4.40**, as illustrated in Scheme 4.13. Unfortunately, the ¹H NMR spectrum of the intermediate amino-alkoxide complex **4.43** is not very informative, and generation of the oxo complex occurs more rapidly than for the isocyanate cycloadditions. The identity of

the resulting imine was confirmed by ^1H NMR spectroscopy and GCMS after hydrolysis of the reaction mixture and isolation of the organic product.



Scheme 4.13

4.5.3 Summary

Attempts at generating azametallacyclobutane complexes as intermediate model species for alkene hydroamination studies were unsuccessful. The synthesis of spectroscopically simple imido complexes $[\text{DMP}(\text{NO})^{\text{tBu}}]_2\text{Zr}=\text{N}(2,6\text{-}^i\text{Pr}_2\text{C}_6\text{H}_3)(\text{L})$ ($\text{L} = \text{TPPO}$, **4.36**; $\text{L} = 2 \text{ Py}$, **4.37**) was accomplished, and these complexes were used in stoichiometric cycloaddition reactions with benzophenone, *tert*-butylisocyanate, and 2,6-dimethylphenylisocyanate. In all cases, cycloreversion to generate a proposed oxo complex occurs, releasing the imine or carbodiimide products. In the case of the reaction with 2,6-dimethylphenylisocyanate, the intermediate ureate complex **4.39**, was characterized *in situ* by ^1H NMR spectroscopy. These results suggest that amidate supported imido complexes can undergo cycloaddition reactivity, and while the metallacycles generated by cycloaddition to $\text{C}=\text{O}$ bonds are typically somewhat stable, it is postulated that metallacycles generated by cycloaddition to $\text{C}=\text{C}$ bonds are highly

unstable if formed. In an attempt to probe the possibility of C=C bond cycloaddition with imido complexes *in situ*, catalytic hydroamination of aminoalkenes was investigated.

4.6 Catalytic Hydroamination of Aminoalkenes

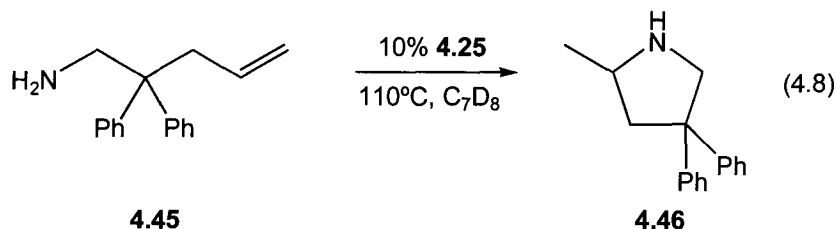
4.6.1 Introduction

Catalytic hydroamination is an important process, with many possible applications in organic synthesis.^{32, 62, 63, 146} As mentioned in the introduction, this is the formal addition of a N-H bond across a carbon-carbon multiple bond.^{63, 68, 107, 147} The cyclohydroamination of aminoalkene substrates represents a convenient method of accessing functionalized N-heterocycles, which are ubiquitous in natural products and pharmaceuticals.^{146, 148-151} While group 4 catalyzed alkyne hydroamination is well preceded,^{32, 53, 58, 60, 68, 121} the analogous reaction with alkenes has only recently seen some success.¹⁵²⁻¹⁵⁸ The first group 4 catalysts reported to promote the cyclization of aminoalkenes were cationic,^{152, 153} and thus formally isoelectronic with the rare-earth catalysts previously reported for this reaction.^{63, 147} Very recently, select neutral group 4 complexes have been reported for this reaction.¹⁵⁴⁻¹⁵⁹ These neutral complexes are proposed to proceed through imido complex intermediates, but prior to this work, no isolable imido complexes had been reported to promote aminoalkene hydroamination. Imido complex **4.25** was thus investigated as the first group 4 imido precatalyst for aminoalkene hydroamination.¹⁶⁰

4.6.2 Results and Discussion

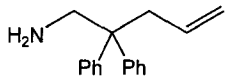
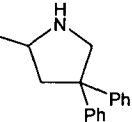
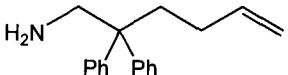
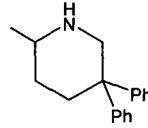
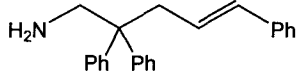
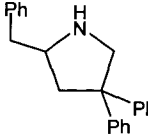
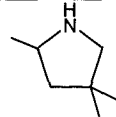
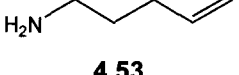
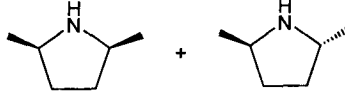
The application of a group 4 imido complex for the cyclohydroamination reaction of aminoalkenes is a strong piece of supporting evidence for an imido-based cycloaddition mechanism, similar to that presented in Scheme 4.4. Reaction of aminoalkene substrate **4.45** in Eq. 4.8 with 10 mol % of imido complex **4.25** in C₇D₈ at 110 °C, results in the generation of the pyrrolidine product **4.46** in 98% isolated yield

after 4 hours. This was the first successful application of a group 4 imido complex in the catalytic hydroamination of an unactivated alkene. Reaction of the analogous secondary, N-methylated, aminoalkene under the same conditions resulted in no reaction, even after several days at 145 °C. Since this substrate can not form a Zr=N double bond, this is supportive of an imido-cycloaddition mechanism. Detailed investigations of the mechanism for this reaction are presented in Chapter 5.



Preliminary substrate scope investigations are summarized in Table 4.6, which demonstrates that the formation of pyrrolidine products (entries 1, 3-5) can be accomplished at 110 °C with 5 or 10 mol % of catalyst. The increase in reaction times with decreasing bulk at the β -position of the substrate is consistent with a chair-like transition state, where the decrease in size in both the Thorpe-Ingold and reactive rotamer effects contribute to the observed reduction in reaction rate.¹⁶¹ The cyclization of 6-membered rings is also possible with this complex (entry 2), but the reaction times are longer, as would be expected for the expanded transition state required. It is important to note that activated internal alkenes are also cyclized by the Zr imido complex (entry 3). However, this reaction requires a considerable amount of time, even with increased catalyst loadings, to proceed to moderate completion (48 % after 8 days). Most excitingly, the α -methyl substituted substrate (entry 5), which lacks reactivity enhancing geminal disubstituents at the β -position, is cyclized in reasonable yield, with very high diastereoselectivity (92 % d.e.), with the *anti* regioselectivity being favored. A mechanistic rationale for this result will be presented in Chapter 5.

Table 4.6 – Unoptimized alkene hydroamination results with precatalyst **4.25**^e

Entry	Aminoalkene	Product	Yield % (h)
1	 4.45	 4.46	98 (4) ^a
2	 4.47	 4.48	82 (24) ^a
3	 4.49	 4.50	38 (96) ^a 48 (192) ^{b,d}
4	 4.51	 4.52	73 (120) ^b 87 (96) ^{b,d}
5	 4.53	 4.54	72 (96) ^{b,d} 'syn': 'anti': 1:11.3 ^c

^aIsolated yield. ^bYield determined by ¹H NMR (internal standard 1,3,5-trimethoxybenzene). ^cRatio determined by ¹H NMR. ^d10 mol % catalyst loading. ^eUnless otherwise stated, 5 mol % of catalyst was utilized and reaction times were unoptimized.

4.6.3 Summary

Imido complex **4.25** was successfully applied as the first group 4 imido derivative capable of performing catalytic cyclohydroamination of unactivated aminoalkenes. The lack of reactivity of an N-methylated substrate supports the intermediacy of an imido complex, which undergoes cycloaddition with the pendant olefin to generate a transient metallacycle. Cyclization of aminoalkene **4.53** results in the formation of the pyrrolidine **4.54** in very high diastereoselectivity. Detailed investigations in Chapter 5 are directed at elucidating the mechanism of this important reaction.

4.7 Conclusions

Terminal imido complexes can be accessed reliably in high yields by protonolysis of bis(amidate) bis(amido) Ti and Zr starting materials with primary amines. Addition of Lewis bases, such as pyridine or TPPO is required to induce elimination of dimethylamine from intermediate mixed amido species. Once formed, the imido complexes are very stable, and stoichiometric quantities of primary amines do not add to these species to regenerate bis(amido) complexes. The imido complexes generated exhibit novel pyramidal structures, including a very rare pentagonal pyramidal structure for **4.25**. Ancillary TPPO and pyridine ligand substitution is possible upon addition of other donors to **4.25**, and an associative mechanism is envisioned for this process, involving 7-coordinate imido species.

The site *trans* to the imido ligand can be accessed by varying the steric bulk in the amidate ligands, resulting in the first 7-coordinate group 4 imido complex (**4.27**). While two bridging μ imido Zr complexes were structurally characterized in the solid-state, the lack of reproducibility of these results, and the absence of supporting data in the solution phase suggests that dimeric imido complexes are not a major contributor. Under catalytic hydroamination conditions, where an excess of amine donor is present, it is unlikely that stable dimeric imido complexes are persistent in solution.

DFT studies support a triple bond for the terminal imido moiety, with the amidate ligands largely bound in an electrostatic fashion. The strength of the imido linkage appears to be difficult to overcome, and stoichiometric cycloaddition of C=C bonds with amidate supported imido complexes does not result in any observable metallacyclic species. However, cycloaddition of C=O bonds with the imido fragment was observed, and it is proposed that the hard oxygen donor helps stabilize the resulting metallacycle. Even these metallacycles proved to be fairly unstable, undergoing cycloreversion to generate proposed oxo complexes, eliminating the resulting organic metathesis products.

The instability of the formed metallacycles is unique in comparison to many other imido complexes,^{32, 33, 35, 93, 104} and this is possibly the reason that **4.25** is the only group 4 imido complex to date that can promote catalytic cyclohydroamination of unactivated

aminoalkenes. A detailed mechanistic analysis of cyclohydroamination of aminoalkenes is presented in Chapter 5.

4.8 Experimental

4.8.1 General Considerations

Refer to Chapter 2, section 2.6.1.

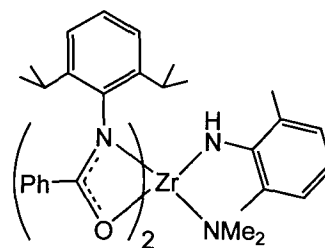
4.8.2 Starting Materials and Reagents

Refer to Chapter 2, section 2.6.2. Aminoalkenes **4.45**, **4.47**, **4.49**, **4.51** and **4.53** were synthesized according to literature procedures.¹⁶² Hydroamination products **4.46**, **4.48**, **4.50**, **4.52**, and **4.54** are known compounds, and NMR spectroscopic data for these compounds matches literature values.¹⁶²

4.8.3 Synthesis

Synthesis of $[\text{DIPP}(\text{NO})^{\text{Ph}}]_2\text{Zr}(\text{NH}-2,6\text{-Me}_2\text{C}_6\text{H}_3)(\text{NMe}_2)$, **4.17**

In a 250 mL round-bottomed Schlenk flask, 3.00 g (4.05 mmol) of $[\text{DIPP}(\text{NO})^{\text{Ph}}]_2\text{Zr}(\text{NMe}_2)_2$ (**4.16**) was dissolved in approximately 75 mL of Et_2O and cooled to $-78\text{ }^\circ\text{C}$ while stirring. In a separate 100 mL Schlenk flask, 0.491 g (4.05 mmol) of 2,6-dimethylaniline was dissolved in

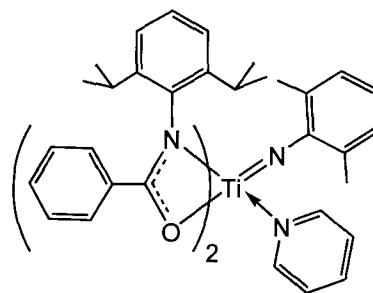


approximately 25 mL of Et_2O and added via cannula to the solution of **4.16**. The resulting solution was allowed to warm to room temperature overnight while stirring. The bright yellow solution was concentrated to a foamy yellow solid, which was dissolved in approximately 50 mL of hexanes and filtered through a plug of CeliteTM. The bright yellow solution was concentrated and allowed to crystallize at room temperature. Bright yellow crystals were isolated by filtration and dried *in vacuo* to give

2.15 g of **4.17** (65 % yield) in the first crop. Single crystals suitable for X-ray crystallography were grown from a saturated hexanes solution. ^1H NMR (C_6D_6 , 25 °C, 300 MHz): δ 0.72 (d, 6H, $^3J_{\text{HH}} = 6.4$ Hz, $\text{CH}(\text{CH}_3)_2$), 0.82 (d, 6H, $^3J_{\text{HH}} = 6.4$ Hz, $\text{CH}(\text{CH}_3)_2$), 0.91 (d, 6H, $^3J_{\text{HH}} = 6.8$ Hz, $\text{CH}(\text{CH}_3)_2$), 0.98 (br, 6H, $\text{CH}(\text{CH}_3)_2$), 2.13 (s, 6H, Ar- CH_3), 3.26 (br, 4H, $\text{CH}(\text{CH}_3)_2$), 3.47 (s, 6H, $\text{N}(\text{CH}_3)_2$), 6.69-7.06 (m, 15H, Ar- H), 7.76 (d, 4H, $^3J_{\text{HH}} = 7.3$ Hz, *m*-Ar- H). IR (KBr/Nujol, cm^{-1}): 3316 (w, N-H), 1585 (m, C=O). Anal. Calcd for $\text{C}_{48}\text{H}_{60}\text{N}_4\text{O}_2\text{Zr}$ (%): C, 70.63; H, 7.41; N, 6.86. Found: C, 70.45; H, 7.56; N, 6.86.

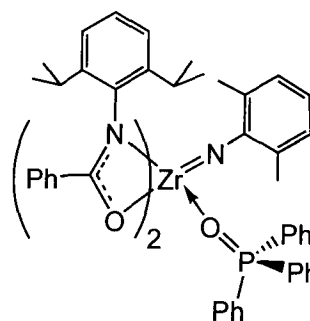
Synthesis of $[\text{DIPP}(\text{NO})^{\text{Ph}}]_2\text{Ti}=\text{N}(2,6\text{-Me}_2\text{C}_6\text{H}_3)(\text{Py})$, **4.24**

In a 250 mL Schlenk flask 1.10 g (1.58 mmol) of $[\text{DIPP}(\text{NO})^{\text{Ph}}]_2\text{Ti}(\text{NMe}_2)_2$ was dissolved in approximately 50 mL of THF and cooled to -78 °C while stirring. In a separate 50 mL Schlenk flask 0.191 g (1.58 mmol) of 2,6-dimethylaniline was dissolved in approximately 25 mL of THF, and added via cannula to the solution of $[\text{DIPP}(\text{NO})^{\text{Ph}}]_2\text{Ti}(\text{NMe}_2)_2$. Finally, 2.0 mL of pyridine (approximately 40 equiv.) was added to the red-orange reaction mixture via syringe. The solution was allowed to warm to room temperature while stirring overnight, resulting in a dark red-brown solution. Excess THF was removed *in vacuo* yielding a dark olive-green foamy solid. The resulting product was taken up in hexanes and filtered through a CeliteTM plug on a fritted disk. The dark red-brown filtrate was collected in an Erlenmeyer flask and placed in the freezer to crystallize at -37 °C. An olive-green solid precipitated out of solution overnight. The solution was concentrated and 828 mg of **4.24** was isolated by filtration and dried *in vacuo* (65 % yield). $^{13}\text{C}\{^1\text{H}\}$ NMR (C_6D_6 , 25 °C, 75 MHz): δ 21.4, 23.8, 29.2, 123.7, 125.6, 127.5, 127.8, 128.2, 128.5, 128.7, 129.0, 129.3, 131.5, 132.2, 135.0, 137.8, 146.9, 167.5. EIMS (m/z): 727 ($[\text{M}^+] - \text{Py}$). Anal. Calcd for $\text{C}_{51}\text{H}_{58}\text{N}_4\text{O}_2\text{Ti}$ (%): C, 75.91; H, 7.25; N, 6.94. Found: C, 75.51; H, 7.35; N, 6.54.



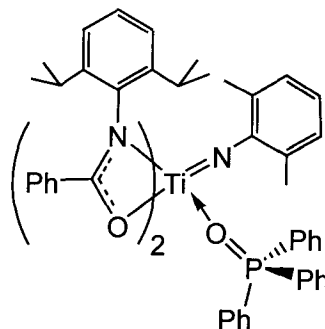
Synthesis of $[\text{DIPP}(\text{NO})^{\text{Ph}}]_2\text{Zr}=\text{N}(2,6\text{-Me}_2\text{C}_6\text{H}_3)(\text{TPPO})$, **4.25**

In a 500 mL round-bottomed Schlenk flask, 5.00 g (6.76 mmol) of $[\text{DIPP}(\text{NO})^{\text{Ph}}]_2\text{Zr}(\text{NMe}_2)_2$ (**4.16**) and 1.88 g (6.76 mmol) of triphenylphosphine oxide (TPPO) were combined, and the flask was cooled to $-78\text{ }^\circ\text{C}$ before adding approximately 100 mL of Et_2O via cannula. In a separate 100 mL Schlenk flask, 0.820 g (6.76 mmol) of 2,6-dimethylaniline was dissolved in approximately 20 mL of Et_2O . To the slurry of **4.16** and TPPO (TPPO has low solubility in Et_2O) was added the solution of 2,6-dimethylaniline via cannula. The reaction mixture was allowed to warm to room temperature while stirring overnight. The TPPO completely dissolved and the solution changed color from pale yellow to a bright golden yellow. Excess Et_2O was removed under vacuum, and a golden yellow solid was isolated. The golden yellow product was washed with approximately 30 mL of hexanes and collected by filtration and dried *in vacuo*. Yield = 5.75 g (82 %). Single crystals suitable for X-ray crystallographic analysis were grown from a saturated benzene solution at room temperature. ^1H NMR (C_6D_6 , $25\text{ }^\circ\text{C}$, 300 MHz): δ 0.90 (d, 12H, $^3J_{\text{HH}} = 6.8\text{ Hz}$, $\text{CH}(\text{CH}_3)_2$), 1.02 (br d, 6H, $^3J_{\text{HH}} = 4.8\text{ Hz}$, $\text{CH}(\text{CH}_3)_2$), 1.15 (br d, 6H, $^3J_{\text{HH}} = 6.4\text{ Hz}$, $\text{CH}(\text{CH}_3)_2$), 2.47 (s, 6H, Ar- CH_3), 3.57 (br m, 2H, $\text{CH}(\text{CH}_3)_2$), 3.94 (br m, 2H, $\text{CH}(\text{CH}_3)_2$), 6.78-7.18 (m, 24H, Ar- H), 7.61-7.67 (m, 10H, Ar- H). $^{13}\text{C}\{^1\text{H}\}$ NMR (C_6D_6 , $25\text{ }^\circ\text{C}$, 75 MHz): δ 19.9, 24.1, 28.7, 116.4, 123.8, 124.1, 125.4, 127.1, 127.8, 128.7, 128.9, 129.3, 129.8, 130.2, 131.0, 131.9, 132.9, 133.6, 142.4, 157.3. $^{31}\text{P}\{^1\text{H}\}$ NMR (C_6D_6 , $25\text{ }^\circ\text{C}$, 121 MHz): δ 42.7. EIMS (m/z): 1049 ($[\text{M}^+]$), 930 ($[\text{M}^+] - \text{N}(2,6\text{-Me}_2\text{C}_6\text{H}_3)$), 277 (TPPO). Anal. Calcd for $\text{C}_{64}\text{H}_{68}\text{N}_3\text{O}_3\text{PZr}$ (%): C, 73.25; H, 6.53; N, 4.00. Found: C, 73.65; H, 6.93; N, 4.32.



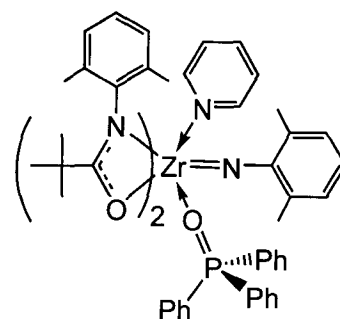
Synthesis of $[\text{DIPP}(\text{NO})^{\text{Ph}}]_2\text{Ti}=\text{N}(2,6\text{-Me}_2\text{C}_6\text{H}_3)(\text{TPPO})$, 4.26

In a 250 mL round-bottomed Schlenk flask, 2.00 g (2.87 mmol) of $[\text{DIPP}(\text{NO})^{\text{Ph}}]_2\text{Ti}(\text{NMe}_2)_2$ and 0.800 g (2.87 mmol) of TPPO were combined and the mixture was cooled to $-78\text{ }^\circ\text{C}$. To this mixture of solids was added approximately 100 mL of Et_2O . The resulting slurry was stirred rapidly and the temperature was maintained at $-78\text{ }^\circ\text{C}$. In a separate 25 mL Schlenk flask, 0.4 mL (2.87 mmol) of 2,6-dimethylaniline was dissolved in approximately 15 mL of Et_2O . The dimethylaniline solution was then transferred via cannula into the reaction mixture. The dark red-orange solution was then allowed to warm to room temperature and stir overnight. During this time, all remaining TPPO was observed to dissolve, and the solution turned a dark red-brown color. Excess Et_2O was removed *in vacuo* to yield a red-brown solid. The crude product was washed with hexanes, isolated by filtration and dried under vacuum. Yield = 2.30 g (80 %). ^1H NMR (C_6D_6 , $25\text{ }^\circ\text{C}$, 300 MHz): δ 0.81 (d, 12H, $^3J_{\text{HH}} = 6.8\text{ Hz}$, $\text{CH}(\text{CH}_3)_2$), 0.98 (d, 6H, $^3J_{\text{HH}} = 6.4\text{ Hz}$, $\text{CH}(\text{CH}_3)_2$), 1.04 (d, 6H, $^3J_{\text{HH}} = 6.5\text{ Hz}$, $\text{CH}(\text{CH}_3)_2$), 2.25 (s, 6H, Ar- CH_3), 3.65 (br m, 2H, $\text{CH}(\text{CH}_3)_2$), 4.14 (br m, 2H, $\text{CH}(\text{CH}_3)_2$), 6.62-7.22 (m, 24H, Ar- H), 7.74-8.00 (m, 10H, Ar- H). $^{13}\text{C}\{^1\text{H}\}$ NMR (C_6D_6 , $25\text{ }^\circ\text{C}$, 75 MHz): δ 19.3, 24.7, 28.2, 119.7, 124.1, 124.3, 125.6, 127.0, 127.6, 128.7, 128.9, 130.7, 132.9, 133.4, 133.6, 134.5, 143.1. $^{31}\text{P}\{^1\text{H}\}$ NMR (C_6D_6 , $25\text{ }^\circ\text{C}$, 121 MHz): δ 41.3. EIMS (m/z): 887 ($[\text{M}^+]$ – N(2,6-Me₂C₆H₃)), 727 ($[\text{M}^+]$ – TPPO), 277 (TPPO). Anal. Calcd for $\text{C}_{64}\text{H}_{68}\text{N}_3\text{O}_3\text{PTi}$ (%): C, 76.40; H, 6.81; N, 4.18. Found: C, 76.80; H, 7.04; N, 4.50.

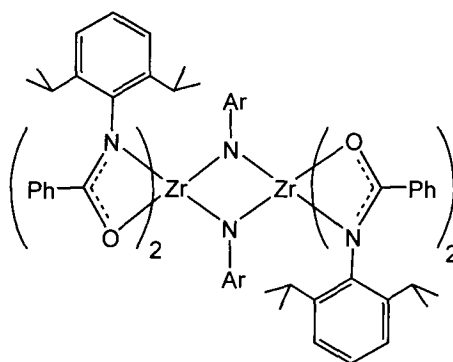


Synthesis of $[\text{DMP}(\text{NO})^{\text{tBu}}]_2\text{Zr}=\text{N}(2,6\text{-Me}_2\text{C}_6\text{H}_3)(\text{TPPO})(\text{Py})$, **4.27**

In a 25 mL vial equipped with a small stir bar in a glovebox, 500 mg (0.850 mmol) of $[\text{DMP}(\text{NO})^{\text{tBu}}]_2\text{Zr}(\text{NMe}_2)_2$ (**4.19**) was dissolved in 15 mL of pentane and stirred at room temperature. To this clear colorless solution was added 103 mg (0.850 mmol) of 2,6-dimethylaniline dissolved in approximately 3 mL of pentane. The reaction mixture was observed to turn a slightly yellow color. To this solution was added 237 mg (0.850 mmol) of TPPO and 67 mg (0.850 mmol) of pyridine pre-dissolved in approximately 5 mL of pentane. The solution immediately turned an intense yellow color, and was allowed to stir for several hours. During this time bright yellow microcrystals precipitated out of solution, which were isolated by filtration and dried *in vacuo*, resulting in 84 % yield (700 mg) of **4.27**. ^1H NMR (C_6D_6 , 25 °C, 300 MHz): δ 1.08 (2, 18H, $\text{C}(\text{CH}_3)_3$), 2.13 (s, 6H, Ar- CH_3), 2.22 (s, 6H, Ar- CH_3), 2.37 (s, 6H, $\text{Zr}=\text{NAr}(\text{CH}_3)_2$), 6.59 (br, 2H, Py-*m-H*), 6.75-7.03 (m, 20H, Ar-*H*), 7.61 (m, 5H, Py-*p-H*, Ar-*H*), 8.70 (br, 2H, Py-*o-H*). $^{13}\text{C}\{^1\text{H}\}$ NMR (C_7D_8 , 25 °C, 75 MHz): δ 20.2, 20.6, 28.5, 41.5, 116.0, 123.6, 124.0, 126.0, 127.5, 129.1, 129.7, 131.5, 132.6, 133.1, 134.0, 145.9, 151.0, 151.4, 185.3. $^{31}\text{P}\{^1\text{H}\}$ NMR (C_6D_6 , 25 °C, 121 MHz): 41.2. EIMS (m/z): 895 ($[\text{M}^+] - \text{Py}$), 277 (TPPO). Anal. Calcd for $\text{C}_{57}\text{H}_{65}\text{N}_4\text{O}_3\text{PZr}$ (%): C, 70.12; H, 6.71; N, 5.74. Found: C, 70.27; H, 6.93; N, 5.29.

Synthesis of $[\text{DIPP}(\text{NO})^{\text{Ph}}]_2\text{Zr}(\mu\text{-N}(2,6\text{-Me}_2\text{C}_6\text{H}_3))_2\text{Zr}[\text{DIPP}(\text{NO})^{\text{Ph}}]_2$, **4.31**

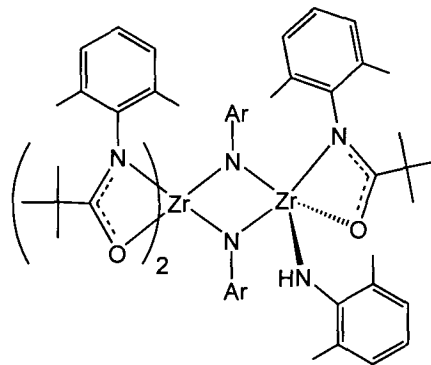
In a 250 mL round-bottomed Schlenk flask, 3.89 g (5.25 mmol) of $[\text{DIPP}(\text{NO})^{\text{Ph}}]_2\text{Zr}(\text{NMe}_2)_2$ (**4.16**) was dissolved in approximately 125 mL of Et_2O and cooled to -78 °C. In a separate 100 mL Schlenk flask 0.636 g (5.25 mmol) of 2,6-dimethylaniline was dissolved in approximately 25 mL of Et_2O and transferred via cannula into the solution of **4.16**.



The reaction was allowed to warm to room temperature while stirring for approximately 5 h, resulting in a bright yellow solution. In a 50 mL Schlenk flask, 0.936 g (5.25 mmol) of diphenylacetylene was dissolved in approximately 30 mL of Et₂O. The reaction mixture was cooled to -78 °C before cannula addition of the ethereal diphenylacetylene solution. The reaction mixture was allowed to warm to room temperature while stirring overnight. The dull yellow solution was concentrated to dryness *in vacuo* to give a light yellow-green oily solid residue. The product was dissolved in approximately 100 mL of hexanes (due to low solubility) and filtered through CeliteTM. The yellow solution was concentrated to dryness *in vacuo* giving a bright yellow oily solid. The crude material was redissolved in hexanes with a small amount of toluene and allowed to crystallize very slowly. While ¹H NMR spectroscopic data of **4.31** was extremely complicated and impossible to interpret, single crystals of **4.31** suitable for X-ray crystallography were isolated from the hexanes/toluene solution over many months.

Synthesis of [^{DMP}(NO)^{tBu}]₂Zr(μ-N(2,6-Me₂C₆H₃))₂Zr[^{DMP}(NO)^{tBu}]NH(2,6-Me₂C₆H₃), **4.33**

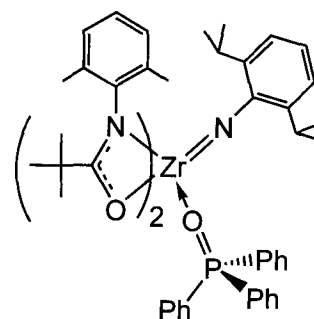
In a glovebox, 341 mg (0.500 mmol) of [^{DMP}(NO)^{tBu}]₂Zr(CH₂Ph)₂ (**4.32**) was dissolved in approximately 15 mL of toluene in a darkened 100 mL Erlenmeyer flask and the solution was stirred at room temperature. To this solution was added 61 mg (0.500 mmol) of 2,6-dimethylaniline dissolved in approximately 5 mL of toluene. The bright yellow



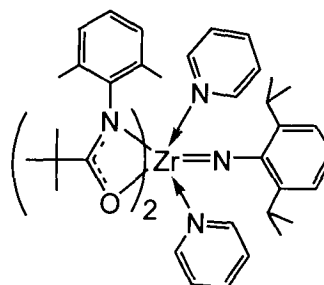
solution was allowed to stir overnight at room temperature. Excess solvent was removed *in vacuo* to give a yellow-orange oil. This oil was dissolved in approximately 25 mL of pentane and filtered through a plug of CeliteTM and concentrated. Yellow single crystals form out of solution in low yield (less than 5 %). The ¹H NMR spectrum is complicated and cannot be readily assigned. X-ray crystallographic analysis was performed using the remaining crystals of **4.33**.

Synthesis of $[\text{DMP}(\text{NO})^{\text{tBu}}]_2\text{Zr}=\text{N}(2,6\text{-iPr}_2\text{C}_6\text{H}_3)(\text{TPPO})$, **4.36**

In a 100 mL Erlenmeyer flask in a glovebox, 588 mg (1.00 mmol) of $[\text{DMP}(\text{NO})^{\text{tBu}}]_2\text{Zr}(\text{NMe}_2)_2$ (**4.19**) was dissolved in 30 mL of pentane and the solution was stirred at room temperature. To this was added 177 mg (1.00 mmol) of 2,6-diisopropylaniline dissolved in approximately 5 mL of pentane. The yellow solution was observed to darken slightly upon addition of 2,6-diisopropylaniline. Addition of 278 mg (1.00 mmol) of solid TPPO resulted in the generation of an intense yellow solution. Approximately 5 mL of toluene was added to the reaction mixture to ensure dissolution of the TPPO (sparingly soluble in pentane). The reaction mixture was allowed to stir overnight at room temperature, during which time a yellow powder precipitated out of solution. The product was isolated by filtration in 67 % yield (636 mg) and dried *in vacuo*. ^1H NMR (C_6D_6 , 25 °C, 300 MHz): δ 1.07 (s, 18H, $\text{C}(\text{CH}_3)_3$), 1.13 (d, 12H, $^3J_{\text{HH}} = 6.8$ Hz, $\text{CH}(\text{CH}_3)_2$), 2.17 (s, 6H, Ar- CH_3), 2.22 (s, 6H, Ar- CH_3), 4.18 (sept, 2H, $^3J_{\text{HH}} = 6.8$ Hz, $\text{CH}(\text{CH}_3)_2$), 6.85-7.19 (m, 18H, Ar- H), 7.59 (br, 6H, Ar- H). $^{13}\text{C}\{^1\text{H}\}$ NMR (C_7D_8 , 25 °C, 100 MHz): δ 19.6, 24.4, 27.8, 28.2, 41.2, 117.1, 121.9, 123.9, 128.2, 128.3, 128.7, 129.2, 132.4, 132.8, 133.4, 142.3, 145.2, 154.0, 186.3. $^{31}\text{P}\{^1\text{H}\}$ NMR (C_6D_6 , 25 °C, 121 MHz): 41.4. EIMS (m/z): 951 ($[\text{M}^+]$), 673 ($[\text{M}^+] - \text{TPPO}$). Anal. Calcd for $\text{C}_{56}\text{H}_{68}\text{N}_3\text{O}_3\text{PZr}$ (%): C, 70.55; H, 7.19; N, 4.41. Found: C, 70.43; H, 7.02; N, 4.80.

Synthesis of $[\text{DMP}(\text{NO})^{\text{tBu}}]_2\text{Zr}=\text{N}(2,6\text{-iPr}_2\text{C}_6\text{H}_3)(\text{Py})_2$, **4.37**

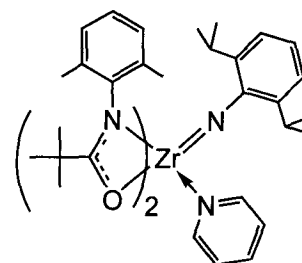
In a 50 mL Schlenk flask, 800 mg (1.36 mmol) of $[\text{DMP}(\text{NO})^{\text{tBu}}]_2\text{Zr}(\text{NMe}_2)_2$ (**4.19**) was dissolved in approximately 30 mL of toluene and the solution was stirred at room temperature. To this solution was added 241 mg (1.36 mmol) of 2,6-diisopropylaniline dissolved in approximately 5 mL of toluene, resulting in a pale yellow solution. An excess of pyridine (approximately 250 mg, 2.5 equiv.) was added to the



reaction mixture, resulting in an immediate color change to intense yellow. The solution was concentrated to dryness and dissolved in minimal pentane. The resulting solution was cooled to -37 °C and a bright yellow solid precipitated out of solution. The solid was isolated by filtration and dried *in vacuo*, resulting in 680 mg (60 % yield) of **4.37** from the first crop. Successive concentration and filtration cycles allow for the isolation of up to 80 % yield overall. ¹H NMR (C₆D₅Br, 30 °C, 300 MHz): δ 1.17 (s, 18H, C(CH₃)₃), 1.25 (d, 12H, ³J_{HH} = 6.7 Hz, CH(CH₃)₂), 2.14 (br s, 12H, Ar-CH₃), 4.32 (sept, 2H, ³J_{HH} = 6.7 Hz, CH(CH₃)₂), 6.82-7.44 (m, 15H, Ar-H), 8.81 (br, 4H, *o*-Py-H).

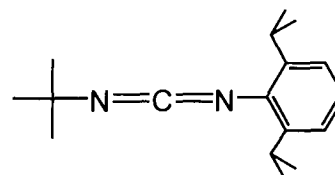
Synthesis of [^{DMP}(NO)^{tBu}]₂Zr=N(2,6-ⁱPr₂C₆H₃)(Py), **4.38**

In a 50 mL Schlenk flask, 800 mg (1.36 mmol) of [^{DMP}(NO)^{tBu}]₂Zr(NMe₂)₂ (**4.19**) was dissolved in approximately 20 mL of pentane and the solution was stirred at room temperature. To the reaction mixture was added a 10 mL pentane solution of 241 mg (1.36 mmol) of 2,6-diisopropylaniline via syringe. Syringe addition of 108 mg (1.36 mmol) of pyridine in 5 mL of pentane results in an immediate color change to intense yellow-orange. Yellow crystals immediately started forming on the walls of the reaction flask. Excess solvent was removed *in vacuo* to give a bright yellow solid residue. This material was triturated with approximately 15 mL of cold pentane and isolated by filtration and dried *in vacuo*. Isolated yield = 960 mg (93 %). ¹H NMR (C₆D₆, 25 °C, 300 MHz): δ 1.09 (s, 18H, C(CH₃)₃), 1.33 (d, 12H, ³J_{HH} = 6.8 Hz, CH(CH₃)₂), 2.14 (br, 12H, Ar-CH₃), 4.40 (sept, 2H, ³J_{HH} = 6.8 Hz, CH(CH₃)₂), 6.30-7.25 (m, 12H, Ar-H), 8.75 (br, 2H, *o*-Py-H). EIMS (*m/z*): 673 ([M⁺] - 2 Py).



Reaction of [^{DMP}(NO)^{tBu}]₂Zr=N(2,6-ⁱPr₂C₆H₃)(TPPO) (**4.36**) with ^tBuN=C=O

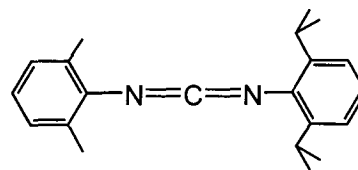
In a 5 mL vial in a glovebox, 100 mg (0.105 mmol) of imido complex **4.36** was dissolved in approximately 0.5 mL of C₆D₆. In another 5 mL vial, 10.4 mg (0.105 mmol) of



${}^t\text{BuN}=\text{C}=\text{O}$ was dissolved in approximately 0.5 mL of C_6D_6 . The two solutions were added to a J-Young NMR tube with a Teflon valve, shaken and a time zero ${}^1\text{H}$ NMR spectrum was collected. The spectrum was complicated and difficult to interpret. The NMR tube was heated to 110 °C overnight, during which time the yellow solution became colorless. ${}^1\text{H}$ NMR spectroscopy of the reaction mixture showed broad peaks in the baseline, with sharp peaks indicating the formation of ${}^t\text{BuN}=\text{C}=\text{N}(2,6\text{-}{}^i\text{Pr}_2\text{C}_6\text{H}_3)$ (**4.41**). ${}^{31}\text{P}\{{}^1\text{H}\}$ NMR spectroscopy indicated the presence of free TPPO, and a new species with coordinated TPPO, tentatively assigned as $[\text{DMP}(\text{NO}){}^t\text{Bu}]_2\text{Zr}=\text{O}(\text{TPPO})$. ${}^1\text{H}$ NMR (C_6D_6 , 25 °C, 300 MHz): δ 1.18 (s, 9H, $\text{C}(\text{CH}_3)_3$), 1.23 (d, 12H, ${}^3J_{\text{HH}} = 6.9$ Hz, $\text{CH}(\text{CH}_3)_2$), 3.63 (sept, 2H, ${}^3J_{\text{HH}} = 6.9$ Hz, $\text{CH}(\text{CH}_3)_2$), 6.81-7.05 (m, 3H, Ar-H). ${}^{31}\text{P}\{{}^1\text{H}\}$ NMR (C_6D_6 , 25 °C, 121 MHz): 25.6 (free TPPO), 39.0 (coordinated TPPO). The contents of the NMR tube were transferred into a 5 mL vial on the bench top and quenched with 2 mL of wet pentane, which caused the solution to become opaque. The insoluble material was removed by filtration through a silica plug, and the filtrate was concentrated to a colorless oil, and analyzed by ${}^1\text{H}$ NMR spectroscopy. The organic material isolated (${}^t\text{BuN}=\text{C}=\text{N}(2,6\text{-}{}^i\text{Pr}_2\text{C}_6\text{H}_3)$) gave a ${}^1\text{H}$ NMR spectrum that was identical to that given above, with the absence of broad peaks in the baseline.

Reaction of $[\text{DMP}(\text{NO}){}^t\text{Bu}]_2\text{Zr}=\text{N}(2,6\text{-}{}^i\text{Pr}_2\text{C}_6\text{H}_3)(\text{TPPO})$ (**4.36**) with $(2,6\text{-Me}_2\text{C}_6\text{H}_3)\text{N}=\text{C}=\text{O}$

In a 5 mL vial in a glovebox, 73.1 mg (0.0767 mmol) of imido complex **4.36** was dissolved in approximately 1 mL of C_6D_6 . In a separate 5 mL vial 11.3 mg (0.0767 mmol) of $2,6\text{-Me}_2\text{C}_6\text{H}_3\text{N}=\text{C}=\text{O}$ was dissolved in approximately 0.5

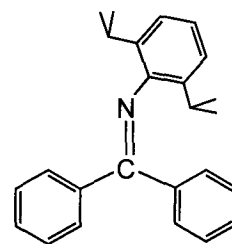


mL of C_6D_6 . The two solutions were transferred into a J-Young NMR tube equipped with a Teflon valve, which was sealed and shaken to ensure efficient mixing. After reaction at room temperature for 2 h, a ${}^1\text{H}$ NMR spectrum was collected. The ${}^1\text{H}$ NMR spectrum of this product is consistent with the metallacyclic complex **4.39**, where both free TPPO and coordinated TPPO can be observed by ${}^{31}\text{P}$ NMR spectroscopy. ${}^1\text{H}$ NMR (C_6D_6 , 25 °C, 300 MHz): δ 1.01 (s, 18H, $\text{C}(\text{CH}_3)_3$), 1.45 (d, 6H, ${}^3J_{\text{HH}} = 5.0$ Hz, $\text{CH}(\text{CH}_3)_2$), 1.60 (d, 6H, ${}^3J_{\text{HH}} = 5.2$ Hz, $\text{CH}(\text{CH}_3)_2$), 2.01 (s, 6H, Ar- CH_3 (amidate)), 2.10

(s, 6H, Ar-CH₃(amidate)), 2.49 (s, 6H, Ar-CH₃), 4.02 (br, 2H, CH(CH₃)₂), 6.79-7.40 (m, 27H, Ar-H). ³¹P{¹H} NMR (C₆D₆, 25 °C, 121 MHz): 25.6 (free TPPO), 45.4 (coordinated TPPO). The NMR tube was heated to 110 °C overnight, and a ¹H NMR spectrum was collected, which was much simpler than that observed for **4.39**, and indicated formation of the carbodiimide (2,6-Me₂C₆H₃)N=C=N(2,6-ⁱPr₂C₆H₃) (**4.42**). Broad signals were observed in the baseline of the spectrum, as was seen for the generation of **4.41**, indicating the presence of the oxo complex **4.40**. The reaction was quenched with 2 mL of wet pentane and an insoluble white powder (**4.40**) was removed by filtration through a silica plug. The filtrate was concentrated and the residue was dissolved in C₆D₆ and analyzed by ¹H NMR spectroscopy and GCMS and found to be carbodiimide **4.42**. ¹H NMR (C₆D₆, 25 °C, 300 MHz): δ 1.31 (d, 12H, ³J_{HH} = 6.9 Hz, CH(CH₃)₂), 2.45 (s, 6H, Ar-CH₃), 3.68 (sept, 2H, ³J_{HH} = 6.9 Hz, CH(CH₃)₂), 6.60-7.27 (m, 6H, Ar-H). GCMS (EI) (*m/z*): 306 ([M⁺]), 291 ([M⁺] - CH₃).

Reaction of [^{DMP}(NO)^{tBu}]₂Zr=N(2,6-ⁱPr₂C₆H₃)(Py)₂ (**4.37**) with Ph₂C=O

In a 5 mL vial in a glovebox, 50.0 mg (0.060 mmol) of imido complex **4.37** was dissolved in approximately 1 mL of C₆D₆. In a separate 5 mL vial 10.9 mg (0.060 mmol) of benzophenone was dissolved in approximately 0.5 mL of C₆D₆. The two solutions were added to a J-Young NMR tube equipped with a Teflon valve, which was then shaken to ensure adequate mixing. ¹H NMR spectroscopy of the reaction mixture was not informative. Broad signals in the baseline suggested the generation of oxo complex **4.40**. The contents of the NMR tube were transferred into a 25 mL vial on the bench top, and approximately 2 mL of wet CH₂Cl₂ was added to the vial. After allowing the reaction mixture to sit overnight, the resulting cloudy yellow-orange mixture was filtered through a CeliteTM plug to remove insoluble material. The clear yellow solution obtained was concentrated and analyzed by ¹H NMR spectroscopy and GCMS. ¹H NMR (CDCl₃, 25 °C, 300 MHz): δ 1.29 (d, 12H, ³J_{HH} = 6.8 Hz, CH(CH₃)₂), 2.98 (sept, 2H, ³J_{HH} = 6.8 Hz, CH(CH₃)₂), 7.04-7.83 (m, 13H, Ar-H). GCMS (EI) (*m/z*): 341 ([M⁺]).



General procedure for NMR tube hydroamination experiments:

All catalytic runs with NMR yields were run using the same general procedure, changing only the catalyst loading (5 or 10 mol %) and the substrate utilized.

Example: Catalytic hydroamination of 2,2-diphenyl-pent-4-enylamine (4.45) to generate 2-methyl-4,4-diphenylpyrrolidine (4.46)

In a 5 mL vial in a glovebox, 150 mg (0.632 mmol) of aminoalkene **4.45** was dissolved in approximately 0.2 mL of D₈-toluene. In a separate vial, 33.2 mg (0.032 mmol, 5 mol %) of imido precatalyst **4.25** was dissolved in approximately 0.5 mL of D₈-toluene, and in a third vial 35.4 mg (0.211 mmol, 33 mol %) of the internal standard 1,3,5-trimethoxybenzene was dissolved in approximately 0.3 mL of D₈-toluene. The three solutions were transferred quantitatively into a J-Young NMR tube equipped with a Teflon valve, which was then sealed and shaken vigorously before collecting a time zero ¹H NMR spectrum. The NMR tube was then placed in an oil bath at 110 °C, and the reaction progress was monitored periodically by ¹H NMR spectroscopy. Yields were determined by comparison of integration values for product peaks (**4.46**) to the integration of the internal standard peaks.

Isolated yields quoted in Table 4.6 were determined by a colleague Jason Bexrud. In general, these reactions were performed using 1.0 mmol of substrate, in a Schlenk flask under an atmosphere of N₂. After being heated to 110 °C for the designated amount of time, the solution was concentrated under reduced pressure and subjected directly to column chromatography (CH₂Cl₂ / 5 % MeOH, SiO₂) to afford the purified pyrrolidine or piperidine product.

4.9 References

1. Schrock, R. R.; Hoveyda, A. H. *Angew. Chem. Int. Ed.* **2003**, *42*, 4592.
2. Schrock, R. R.; Czekelius, C. *Adv. Synth. Catal.* **2007**, *349*, 55.
3. Schrock, R. R. *Acc. Chem. Res.* **1990**, *23*, 158.
4. Trnka, T. M.; Grubbs, R. H. *Acc. Chem. Res.* **2001**, *34*, 18.
5. Schrock, R. R. *Chem. Rev.* **2002**, *102*, 145.
6. Grubbs, R. H. *Angew. Chem. Int. Ed.* **2006**, *45*, 3760.
7. Schrock, R. R. *Angew. Chem. Int. Ed.* **2006**, *45*, 3748.
8. Chauvin, Y. *Angew. Chem. Int. Ed.* **2006**, *45*, 3741.
9. Romero, P. E.; Piers, W. E. *J. Am. Chem. Soc.* **2005**, *127*, 5032.
10. Shaik, S.; Hirao, H.; Kumar, D. *Acc. Chem. Res.* **2007**, *40*, 532.
11. Que, L., Jr.; Tolman, W. B. *Angew. Chem. Int. Ed.* **2002**, *41*, 1114.
12. Gibson, V. C. *Modern Coord. Chem.* **2002**, 140.
13. Sharp, P. R. *Dalton Trans.* **2000**, 2647.
14. West, B. O. *Polyhedron* **1989**, *8*, 219.
15. Mayer, J. M. *Acc. Chem. Res.* **1998**, *31*, 441.
16. Centi, G.; Trifiro, F.; Ebner, J. R.; Franchetti, V. M. *Chem. Rev.* **1988**, *88*, 55.
17. Carney, M. J.; Walsh, P. J.; Hollander, F. J.; Bergman, R. G. *J. Am. Chem. Soc.* **1989**, *111*, 8751
18. Lukens, W. W., Jr.; Matsunaga, P. T.; Andersen, R. A. *Organometallics* **1998**, *17*, 5240.
19. Hoskin, A. J.; Stephan, D. W. *Organometallics* **1999**, *18*, 2479.
20. Hill, J. E.; Fanwick, P. E.; Rothwell, I. P. *Inorg. Chem.* **1989**, *28*, 3602.
21. Smith, M. R., III; Matsunaga, P. T.; Andersen, R. A. *J. Am. Chem. Soc.* **1993**, *115*, 7049.
22. Mendiratta, A.; Figueroa, J. S.; Cummins, C. C. *Chem. Commun.* **2005**, 3403.
23. Nugent, W. A.; Haymore, B. L. *Coord. Chem. Rev.* **1980**, *31*, 123.
24. Wigley, D. E. *Prog. Inorg. Chem.* **1994**, *42*, 239.
25. Romao, C. C.; Kuehn, F. E.; Herrmann, W. A. *Chem. Rev.* **1997**, *97*, 3197.

26. Oro, L. A.; Ciriano, M. A.; Tejel, C.; Shi, Y.-M.; Modrego, J. *Met. Clust. Chem.* **1999**, *1*, 381.
27. Eikey, R. A.; Abu-Omar, M. M. *Coord. Chem. Rev.* **2003**, *243*, 83.
28. Giesbrecht, G. R.; Gordon, J. C. *Dalton Trans.* **2004**, 2387.
29. Muniz, K. *Chem. Soc. Rev.* **2004**, *33*, 166.
30. Schrock, R. R. *J. Mol. Catal. A: Chem.* **2004**, *213*, 21.
31. Mehn, M. P.; Peters, J. C. *J. Inorg. Biochem.* **2006**, *100*, 634.
32. Duncan, A. P.; Bergman, R. G. *Chem. Rec.* **2002**, *2*, 431.
33. Hazari, N.; Mountford, P. *Acc. Chem. Res.* **2005**, *38*, 839.
34. Basuli, F.; Kilgore, U. J.; Brown, D.; Huffman, J. C.; Mindiola, D. J. *Organometallics* **2004**, *23*, 6166.
35. Zuckerman, R. L.; Bergman, R. G. *Organometallics* **2000**, *19*, 4795.
36. Basuli, F.; Bailey, B. C.; Watson, L. A.; Tomaszewski, J.; Huffman, J. C.; Mindiola, D. J. *Organometallics* **2005**, *24*, 1886.
37. Bailey, B. C.; Huffman, J. C.; Mindiola, D. J.; Weng, W.; Ozerov, O. V. *Organometallics* **2005**, *24*, 1390.
38. Basuli, F.; Tomaszewski, J.; Huffman, J. C.; Mindiola, D. J. *J. Am. Chem. Soc.* **2003**, *125*, 10170.
39. Mathey, F. *Dalton Trans.* **2007**, 1861.
40. Mathey, F. *Angew. Chem. Int. Ed.* **2003**, *42*, 1578.
41. Mindiola, D. J. *Acc. Chem. Res.* **2006**, *39*, 813.
42. Basuli, F.; Bailey, B. C.; Huffman, J. C.; Baik, M.-H.; Mindiola, D. J. *J. Am. Chem. Soc.* **2004**, *126*, 1924.
43. Lammertsma, K.; Vlaar, M. J. M. *Eur. J. Org. Chem.* **2002**, 1127.
44. Cowley, A. H. *Acc. Chem. Res.* **1997**, *30*, 445.
45. Stephan, D. W. *Angew. Chem. Int. Ed.* **2000**, *39*, 315.
46. Breen, T. L.; Stephan, D. W. *J. Am. Chem. Soc.* **1995**, *117*, 11914.
47. Ho, J.; Rousseau, R.; Stephan, D. W. *Organometallics* **1994**, *13*, 1918.
48. Hou, Z.; Breen, T. L.; Stephan, D. W. *Organometallics* **1993**, *12*, 3158.
49. Hou, Z.; Stephan, D. W. *J. Am. Chem. Soc.* **1992**, *114*, 10088.
50. Grubbs, R. H.; Miller, S. J.; Fu, G. C. *Acc. Chem. Res.* **1995**, *28*, 446.

51. Nicolaou, K. C.; Bulger, P. G.; Sarlah, D. *Angew. Chem. Int. Ed.* **2005**, *44*, 4490.
52. Lee, S. Y.; Bergman, R. G. *J. Am. Chem. Soc.* **1996**, *118*, 6396.
53. Odom, A. L. *Dalton Trans.* **2005**, 225.
54. Barnea, E.; Eisen, M. S. *Coord. Chem. Rev.* **2006**, *250*, 855.
55. Hultsch, K. C. *Adv. Synth. Catal.* **2005**, *347*, 367.
56. Douglass, M. R.; Ogasawara, M.; Hong, S.; Metz, M. V.; Marks, T. J. *Organometallics* **2002**, *21*, 283.
57. Douglass, M. R.; Stern, C. L.; Marks, T. J. *J. Am. Chem. Soc.* **2001**, *123*, 10221.
58. Pohlki, F.; Doye, S. *Chem. Soc. Rev.* **2003**, *32*, 104.
59. Mueller, T. E. *Rec. Res. Dev. Org. Chem.* **2002**, *6*, 625.
60. Bytschkov, I.; Doye, S. *Eur. J. Org. Chem.* **2003**, 935.
61. Nobis, M.; Driessen-Holscher, B. *Angew. Chem. Int. Ed.* **2001**, *40*, 3983.
62. Hartwig, J. F. *Pure Appl. Chem.* **2004**, *76*, 507.
63. Hong, S.; Marks, T. J. *Acc. Chem. Res.* **2004**, *37*, 673.
64. Marks, T. J.; Gagne, M. R.; Nolan, S. P.; Schrock, L. E.; Seyam, A. M.; Stern, D. *Pure Appl. Chem.* **1989**, *61*, 1665.
65. Seayad, J.; Tillack, A.; Hartung, C. G.; Beller, M. *Adv. Synth. Catal.* **2002**, *344*, 795.
66. Muller, T. E.; Beller, M. *Chem. Rev.* **1998**, *98*, 675.
67. Eisen, M. S.; Straub, T.; Haskel, A. *J. Alloys Compd.* **1998**, *271*, 116.
68. Walsh, P. J.; Baranger, A. M.; Bergman, R. G. *J. Am. Chem. Soc.* **1992**, *114*, 1708.
69. Schrock, R. R.; Feldman, J.; Cannizzo, L. F.; Grubbs, R. H. *Macromolecules* **1987**, *20*, 1172.
70. Murdzek, J. S.; Schrock, R. R. *Organometallics* **1987**, *6*, 1373.
71. Oskam, J. H.; Schrock, R. R. *J. Am. Chem. Soc.* **1992**, *114*, 7588.
72. Oskam, J. H.; Schrock, R. R. *J. Am. Chem. Soc.* **1993**, *115*, 11831.
73. Schwab, P.; Grubbs, R. H.; Ziller, J. W. *J. Am. Chem. Soc.* **1996**, *118*, 100.
74. Nguyen, S. T.; Johnson, L. K.; Grubbs, R. H.; Ziller, J. W. *J. Am. Chem. Soc.* **1992**, *114*, 3974.
75. Nguyen, S. T.; Grubbs, R. H.; Ziller, J. W. *J. Am. Chem. Soc.* **1993**, *115*, 9858.

76. Schwab, P.; France, M. B.; Ziller, J. W.; Grubbs, R. H. *Angew. Chem. Int. Ed.* **1995**, *34*, 2039.
77. Scholl, M.; Ding, S.; Lee, C. W.; Grubbs, R. H. *Org. Lett.* **1999**, *1*, 953.
78. Bolton, P. D.; Mountford, P. *Adv. Synth. Catal.* **2005**, *347*, 355.
79. Mountford, P. *Chem. Commun.* **1997**, 2127.
80. Bolton, P. D.; Clot, E.; Adams, N.; Dubberley, S. R.; Cowley, A. R.; Mountford, P. *Organometallics* **2006**, *25*, 2806.
81. Coles, M. P.; Dalby, C. I.; Gibson, V. C.; Little, I. R.; Marshall, E. L.; Ribeiro da Costa, M. H.; Mastroianni, S. *J. Organomet. Chem.* **1999**, *591*, 78.
82. Adams, N.; Arts, H. J.; Bolton, P. D.; Cowell, D.; Dubberley, S. R.; Friederichs, N.; Grant, C. M.; Kranenburg, M.; Sealey, A. J.; Wang, B.; Wilson, P. J.; Cowley, A. R.; Mountford, P.; Schroeder, M. *Chem. Commun.* **2004**, 434.
83. Owen, C. T.; Bolton, P. D.; Cowley, A. R.; Mountford, P. *Organometallics* **2007**, *26*, 83.
84. Bolton, P. D.; Clot, E.; Cowley, A. R.; Mountford, P. *J. Am. Chem. Soc.* **2006**, *128*, 15005.
85. Jin, J.; Chen, E. Y.-X. *Organometallics* **2002**, *21*, 13.
86. Bigmore, H. R.; Dubberley, S. R.; Kranenburg, M.; Lawrence, S. C.; Sealey, A. J.; Selby, J. D.; Zuideveld, M. A.; Cowley, A. R.; Mountford, P. *Chem. Commun.* **2006**, 436.
87. Kilgore, U. J.; Basuli, F.; Huffman, J. C.; Mindiola, D. J. *Inorg. Chem.* **2006**, *45*, 487.
88. Yandulov, D. V.; Schrock, R. R. *Science* **2003**, *301*, 76.
89. Cummins, C. C.; Baxter, S. M.; Wolczanski, P. T. *J. Am. Chem. Soc.* **1988**, *110*, 8731.
90. Walsh, P. J.; Hollander, F. J.; Bergman, R. G. *J. Am. Chem. Soc.* **1988**, *110*, 8729.
91. Gade, L. H.; Mountford, P. *Coord. Chem. Rev.* **2001**, *216*, 65.
92. Wang, H.; Chan, H.-S.; Xie, Z. *Organometallics* **2005**, *24*, 3772.
93. Walsh, P. J.; Hollander, F. J.; Bergman, R. G. *Organometallics* **1993**, *12*, 3705.

94. Blake, A. J.; Mountford, P.; Nikonov, G. I.; Swallow, D. *Chem. Commun.* **1996**, 1835.
95. Ward, B. D.; Orde, G.; Clot, E.; Cowley, A. R.; Gade, L. H.; Mountford, P. *Organometallics* **2005**, *24*, 2368.
96. Thorman, J. L.; Guzei, I. A.; Young, V. G., Jr.; Woo, L. K. *Inorg. Chem.* **1999**, *38*, 3814.
97. Ong, T.-G.; Yap, G. P. A.; Richeson, D. S. *Chem. Commun.* **2003**, 2612.
98. Blake, A. J.; McInnes, J. M.; Mountford, P.; Nikonov, G. I.; Swallow, D.; Watkin, D. J. *Dalton Trans.* **1999**, 379.
99. Meyer, K. E.; Walsh, P. J.; Bergman, R. G. *J. Am. Chem. Soc.* **1994**, *116*, 2669.
100. Meyer, K. E.; Walsh, P. J.; Bergman, R. G. *J. Am. Chem. Soc.* **1995**, *117*, 974.
101. Cloke, F. G. N.; Hitchcock, P. B.; Nixon, J. F.; James Wilson, D.; Mountford, P. *Chem. Commun.* **1999**, 661.
102. Pugh, S. M.; Troesch, D. J. M.; Wilson, D. J.; Bashall, A.; Cloke, F. G. N.; Gade, L. H.; Hitchcock, P. B.; McPartlin, M.; Nixon, J. F.; Mountford, P. *Organometallics* **2000**, *19*, 3205.
103. Harlan, C. J.; Tunge, J. A.; Bridgewater, B. M.; Norton, J. R. *Organometallics* **2000**, *19*, 2365.
104. Polse, J. L.; Andersen, R. A.; Bergman, R. G. *J. Am. Chem. Soc.* **1998**, *120*, 13405.
105. Bennett, J. L.; Wolczanski, P. T. *J. Am. Chem. Soc.* **1994**, *116*, 2179.
106. Bashall, A.; McPartlin, M.; Collier, P. E.; Mountford, P.; Gade, L. H.; Trosch, D. J. M. *Chem. Commun.* **1998**, 2555.
107. McGrane, P. L.; Jensen, M.; Livinghouse, T. *J. Am. Chem. Soc.* **1992**, *114*, 5459.
108. Ruck, R. T.; Zuckerman, R. L.; Krska, S. W.; Bergman, R. G. *Angew. Chem. Int. Ed.* **2004**, *43*, 5372.
109. Ruck, R. T.; Bergman, R. G. *Organometallics* **2004**, *23*, 2231.
110. Basuli, F.; Aneetha, H.; Huffman, J. C.; Mindiola, D. J. *J. Am. Chem. Soc.* **2005**, *127*, 17992.
111. Aneetha, H.; Basuli, F.; Bollinger, J.; Huffman, J. C.; Mindiola, D. J. *Organometallics* **2006**, *25*, 2402.

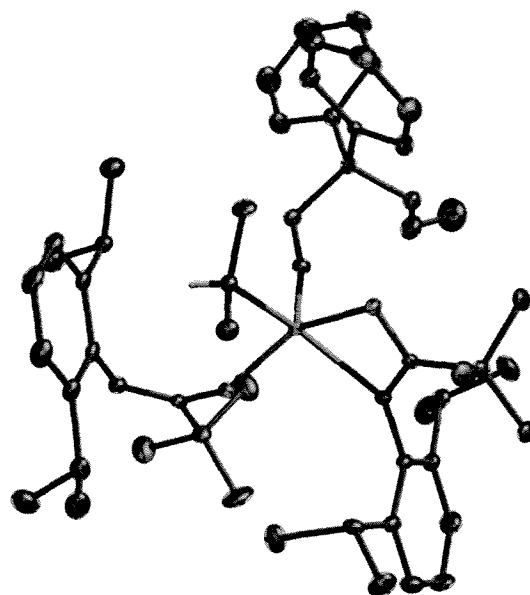
112. Eldred, S. E.; Stone, D. A.; Gellman, S. H.; Stahl, S. S. *J. Am. Chem. Soc.* **2003**, *125*, 3422.
113. Kissounko, D. A.; Guzei, I. A.; Gellman, S. H.; Stahl, S. S. *Organometallics* **2005**, *24*, 5208.
114. Kissounko, D. A.; Hoerter, J. M.; Guzei, I. A.; Cui, Q.; Gellman, S. H.; Stahl, S. S. *J. Am. Chem. Soc.* **2007**, *129*, 1776.
115. Doye, S. *Synlett* **2004**, 1653.
116. Boger, D. L.; Corbett, W. L.; Curran, T. T.; Kasper, A. M. *J. Am. Chem. Soc.* **1991**, *113*, 1713.
117. He, M.; Struble, J. R.; Bode, J. W. *J. Am. Chem. Soc.* **2006**, *128*, 8418.
118. Hoerter, J. M.; Otte, K. M.; Gellman, S. H.; Stahl, S. S. *J. Am. Chem. Soc.* **2006**, *128*, 5177.
119. Li, C.; Thomson, R. K.; Gillon, B.; Patrick, B. O.; Schafer, L. L. *Chem. Commun.* **2003**, 2462.
120. Zhang, Z.; Schafer, L. L. *Org. Lett.* **2003**, *5*, 4733.
121. Lee, A. V.; Schafer, L. L. *Eur. J. Inorg. Chem.* **2007**, 2243.
122. Zhang, Z.; Leitch, D. C.; Lu, M.; Patrick, B. O.; Schafer, L. L. *Chem.--Eur. J.* **2007**, *13*, 2012.
123. Roesky, H. W.; Voelker, H.; Witt, M.; Noltemeyer, M. *Angew. Chem. Int. Ed.* **1990**, *29*, 669.
124. Hill, J. E.; Profflet, R. D.; Fanwick, P. E.; Rothwell, I. P. *Angew. Chem. Int. Ed.* **1990**, *29*, 664.
125. Bailey, B. C.; Basuli, F.; Huffman, J. C.; Mindiola, D. J. *Organometallics* **2006**, *25*, 2725.
126. Duchateau, R.; Williams, A. J.; Gambarotta, S.; Chiang, M. Y. *Inorg. Chem.* **1991**, *30*, 4863.
127. Blake, A. J.; Collier, P. E.; Dunn, S. C.; Li, W.-S.; Mountford, P.; Shishkin, O. V. *Dalton Trans.* **1997**, 1549.
128. Collier, P. E.; Dunn, S. C.; Mountford, P.; Shishkin, O. V.; Swallow, D. *Dalton Trans.* **1995**, 3743.
129. Collier, P. E.; Blake, A. J.; Mountford, P. *Dalton Trans.* **1997**, 2911.

130. Dunn, S. C.; Mountford, P.; Robson, D. A. *Dalton Trans.* **1997**, 293.
131. Ong, T.-G.; Wood, D.; Yap, G. P. A.; Richeson, D. S. *Organometallics* **2002**, *21*, 1.
132. Ong, T.-G.; Yap, G. P. A.; Richeson, D. S. *Organometallics* **2002**, *21*, 2839.
133. Wood, D.; Yap, G. P. A.; Richeson, D. S. *Inorg. Chem.* **1999**, *38*, 5788.
134. Mullins, S. M.; Duncan, A. P.; Bergman, R. G.; Arnold, J. *Inorg. Chem.* **2001**, *40*, 6952.
135. Thomson, R. K.; Zahariev, F. E.; Zhang, Z.; Patrick, B. O.; Wang, Y. A.; Schafer, L. L. *Inorg. Chem.* **2005**, *44*, 8680.
136. Adams, N.; Bigmore, H. R.; Blundell, T. L.; Boyd, C. L.; Dubberley, S. R.; Sealey, A. J.; Cowley, A. R.; Skinner, M. E. G.; Mountford, P. *Inorg. Chem.* **2005**, *44*, 2882.
137. Li, Y.; Shi, Y.; Odom Aaron, L. *J. Am. Chem. Soc.* **2004**, *126*, 1794.
138. Blake, A. J.; Collier, P. E.; Gade, L. H.; Mountford, P.; Lloyd, J.; Pugh, S. M.; Schubart, M.; Skinner, M. E. G.; Troesch, D. J. M. *Inorg. Chem.* **2001**, *40*, 870.
139. Dubberley, S. R.; Evans, S.; Boyd, C. L.; Mountford, P. *Dalton Trans.* **2005**, 1448.
140. Heutling, A.; Doye, S. *J. Org. Chem.* **2002**, *67*, 1961.
141. Li, C. New Bis(Amidate) Titanium-Bis(Amido) Complexes as Hydroamination Precatalysts: Synthetic and Mechanistic Investigations. Master's Dissertation. University of British Columbia, Vancouver, BC, **2003**.
142. Smolensky, E.; Kapon, M.; Eisen, M. S. *Organometallics* **2005**, *24*, 5495.
143. Pohlki, F.; Doye, S. *Angew. Chem. Int. Ed.* **2001**, *40*, 2305.
144. Straub, B. F.; Bergman, R. G. *Angew. Chem. Int. Ed.* **2001**, *40*, 4632.
145. Ward, B. D.; Maisse-Francois, A.; Mountford, P.; Gade, L. H. *Chem. Commun.* **2004**, 704.
146. Molander, G. A.; Dowdy, E. D.; Pack, S. K. *J. Org. Chem.* **2001**, *66*, 4344.
147. Gagne, M. R.; Marks, T. J. *J. Am. Chem. Soc.* **1989**, *111*, 4108.
148. Arredondo, V. M.; Tian, S.; McDonald, F. E.; Marks, T. J. *J. Am. Chem. Soc.* **1999**, *121*, 3633.
149. Trost, B. M.; Tang, W. *J. Am. Chem. Soc.* **2002**, *124*, 14542.

Chapter 4: Synthesis, Structure, and Reactivity of Amidate Supported Imido Complexes

150. Schar, P.; Cren, S.; Renaud, P. *Chimia* **2006**, *60*, 131.
151. Michael, J. P. *Nat. Prod. Rep.* **2007**, *24*, 191.
152. Knight, P. D.; Munslow, I.; O'Shaughnessy, P. N.; Scott, P. *Chem. Commun.* **2004**, 894.
153. Gribkov, D. V.; Hultsch, K. C. *Angew. Chem. Int. Ed.* **2004**, *43*, 5542.
154. Bexrud, J. A.; Beard, J. D.; Leitch, D. C.; Schafer, L. L. *Org. Lett.* **2005**, *7*, 1969.
155. Wood, M. C.; Leitch, D. C.; Yeung, C. S.; Kozak, J. A.; Schafer, L. L. *Angew. Chem. Int. Ed.* **2007**, *46*, 354.
156. Mueller, C.; Loos, C.; Schulenberg, N.; Doye, S. *Eur. J. Org. Chem.* **2006**, 2499.
157. Watson, D. A.; Chiu, M.; Bergman, R. G. *Organometallics* **2006**, *25*, 4731.
158. Kim, H.; Lee, P. H.; Livinghouse, T. *Chem. Commun.* **2005**, 5205.
159. Stubbert, B. D.; Marks, T. J. *J. Am. Chem. Soc.* **2007**, *129*, 6149.
160. Thomson, R. K.; Bexrud, J. A.; Schafer, L. L. *Organometallics* **2006**, *25*, 4069.
161. Jung, M. E.; Piizzi, G. *Chem. Rev.* **2005**, *105*, 1735.
162. Gagne, M. R.; Stern, C. L.; Marks, T. J. *J. Am. Chem. Soc.* **1992**, *114*, 275.

CHAPTER 5



Catalytic Hydroamination Mechanistic Studies

5.1 Introduction

5.1.1 General Introduction

In synthetic organic chemistry, the ability to selectively form new C-E bonds (E = N, O, P, S, etc.) dictates the selected disconnections in developing a synthetic strategy for a given target molecule. Thus, research into selective C-E bond formation is of the utmost importance, as it allows a greater degree of flexibility in designing organic syntheses in a predictable and efficient manner. Heterocycles with C-N bonds are ubiquitous in natural products and pharmaceuticals.¹⁻⁵ Molecules belonging to the alkaloid family are characterized by the presence of one or more N-heterocycles.^{2, 3, 6-15} For example, the alkaloids hygrine,^{16, 17} cuscohygrine,¹⁶ and nicotine^{18, 19} share the

© Reproduced in part with permission from a.) Li, C.; Thomson, R. K.; Gillon, B.; Patrick, B. O.; Schafer, L. L. *Chem. Commun.* **2003**, 2462 (Copyright 2003 Royal Society of Chemistry). b.) Thomson, R. K.; Bexrud, J. A.; Schafer, L. L. *Organometallics* **2006**, *25*, 4069 (Copyright 2006 American Chemical Society).

pyrrolidine heterocyclic functionality as a part of their skeletal framework.^{6, 16, 17} Similarly, the piperidine²⁰ heterocycle is a key component of the alkaloids piperine,^{21, 22} coniine,²³⁻²⁶ and sparteine.²⁷⁻³² Two common tropane alkaloids are also illustrated in Fig. 5.1, cocaine³³ and atropine,^{33, 34} which feature a 5- and 6-membered bicyclic ring system with a bridgehead N.^{5, 15} These selected compounds have varying pharmacological effects on humans, and at their core all share a N-containing heterocycle that must be formed in a selective manner. In this vein, the ability to selectively form C-N bonds is a particularly important application in the preparation of target molecules containing N-heterocycles.

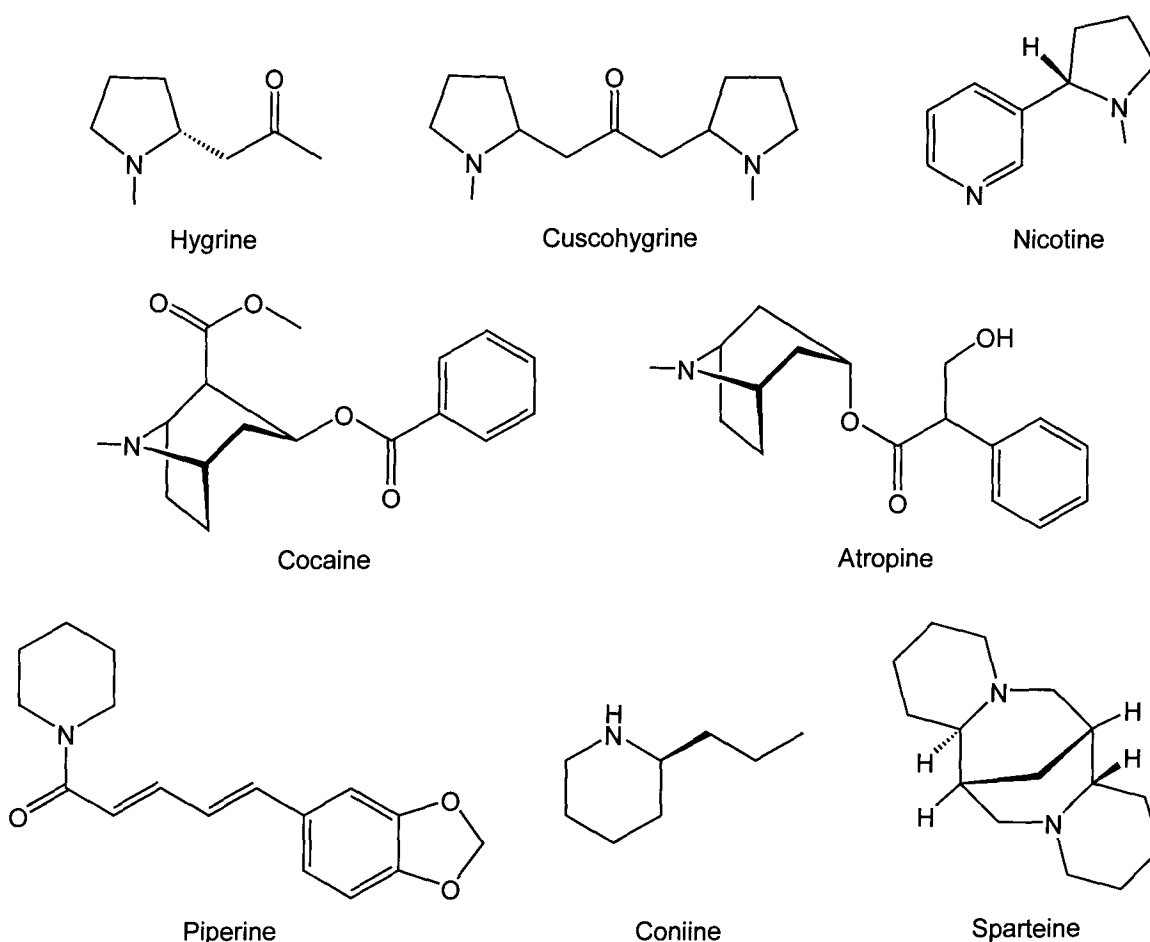


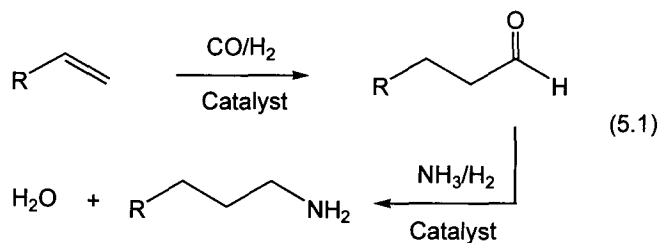
Figure 5.1 Structures of alkaloid natural products

Many traditional synthetic organic methods exist for the formation of C-N bonds, which typically require stoichiometric quantities of reagents, and generate a number of byproducts that can be deleterious for subsequent reactions.³⁵ Synthetic methodologies to install N groups often utilize carbonyl groups prior to installation of the nitrogen during synthesis.³⁵ The inherent reactivity of the carbonyl functionality may require numerous protection and deprotection steps during the evolution of a synthetic pathway. By contrast, alkyne and alkene functionalities are generally less reactive, increasing their stability under a variety of synthetic conditions. In addition, alkynes can be installed with relative ease through nucleophilic substitution or Sonagashira coupling.³⁵⁻³⁸ In this manner, alkenes and alkynes can act as masked carbonyl equivalents for later reactivity.

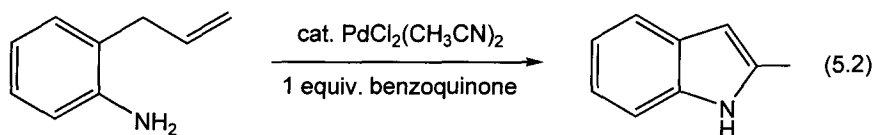
Atom economy in reactions is always an important consideration. When trying to implement synthetic methodology for large scale industrial or pharmaceutical applications, this consideration is critical. Generation of new C-N bonds has a theoretical maximum atom economy of 100% when an amine N-H bond is added directly to a C-C multiple bond in a 1,2-fashion. Although select cases have been reported of direct addition of amines to C-C multiple bonds, these substrates are generally highly activated by electron withdrawing groups or conjugation (Michael-type reactions).³⁹⁻⁴² In general, a transition metal is involved in mediating this addition reaction.

Metal catalyzed versions of this reaction, known as hydroamination, were developed as long ago as 1954, when Howk and coworkers demonstrated that ammonia and ethylene could be combined to form mixtures of ethyl, diethyl, and triethylamines.⁴³ This reaction was performed under the basic conditions of metallic sodium, and required high temperatures (~ 200 °C) and pressures (1000 bar).⁴³ Early hydroamination routes utilized highly toxic mercurial reagents, and often required forcing conditions, employing both high temperatures and pressures.^{44, 45} While the most desirable amine substrate for hydroamination would be ammonia (NH₃), the direct addition of ammonia to ethylene has not been accomplished at ambient temperatures and pressures. The related hydroaminomethylation reaction has been accomplished with ammonia.^{46, 47} This process results in the formation of amine products analogous to hydroamination, with the incorporation of an additional methylene unit (Eq. 5.1). While this reaction has good atom economy, water is still generated as a byproduct. Water can be a problematic

byproduct for subsequent reactions, necessitating rigorous purification of intermediates. Due to the volatility and poor nucleophilic character of ammonia, most hydroamination studies have focused on the use of primary or secondary amines with substituted alkynes and alkenes.⁴⁸⁻⁵⁴



The earliest homogeneous system for the catalytic hydroamination of simple olefins under mild conditions was discovered by Coulson and coworkers in 1971, where RhCl₃ was found to catalyze the addition of secondary amines to ethylene.⁵⁵ Shortly after this discovery, Hegedus and coworkers found that PdCl₂(CH₃CN)₂ was active for both the addition of secondary amines to simple monoolefins, and the intramolecular cyclization of *o*-allylanilines to generate functionalized indoles, as shown in Eq. 5.2.^{56, 57} In this reaction, a stoichiometric quantity of benzoquinone was required as a reoxidant for the Pd.



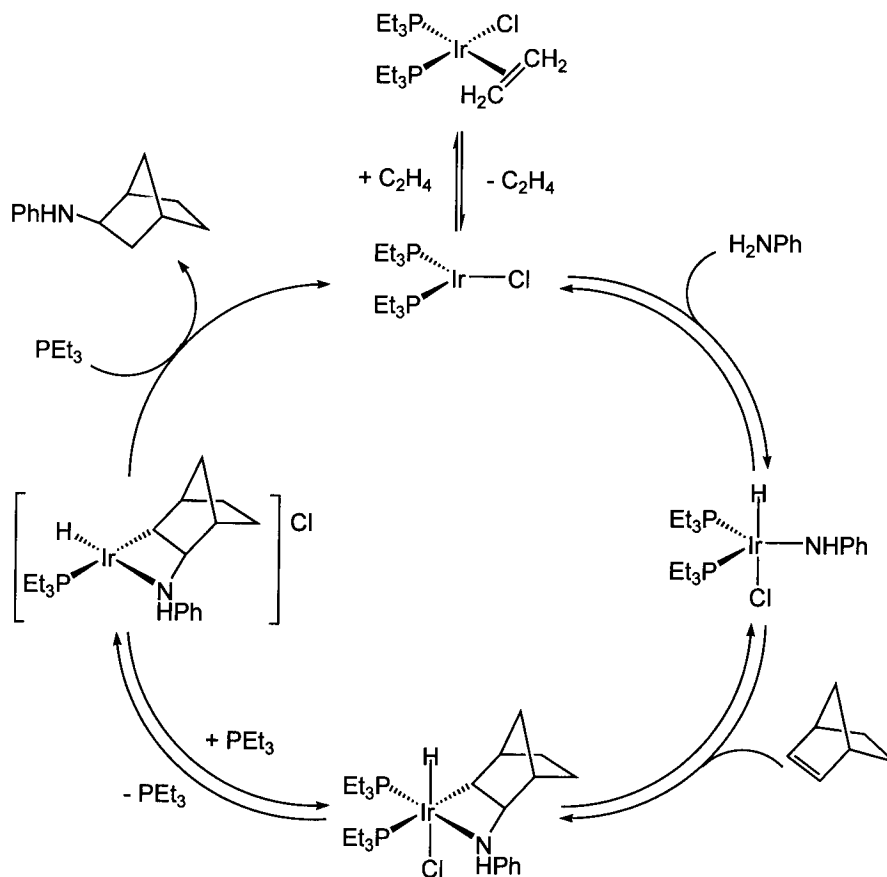
In 1988, scientists at Dupont discovered that aniline could add to norbornene in the presence of catalytic quantities of [Ir(PEt₃)₂(C₂H₄)Cl].⁵⁸ Subsequent studies by Togni and coworkers showed that analogous systems with chiral diphosphine ligands, in the presence of fluoride anions, could affect this transformation in an enantioselective fashion.⁵⁹ While these early systems were promising, they were limited to activated olefins. In the wake of these results, numerous catalytic systems have been developed for various hydroamination reactions, resulting in additions of primary and secondary amines to alkynes, allenes, and alkenes.⁴⁹⁻⁵⁴

The operative mechanisms for different hydroamination reactions have been intensely investigated, and in some cases there is wide agreement for the proposed route. However, in other cases, the mechanism of reaction is still unclear, and investigations are

ongoing for these systems. The following sections outline some of the key mechanisms proposed for different transition metal catalyzed homogeneous hydroamination reactions.

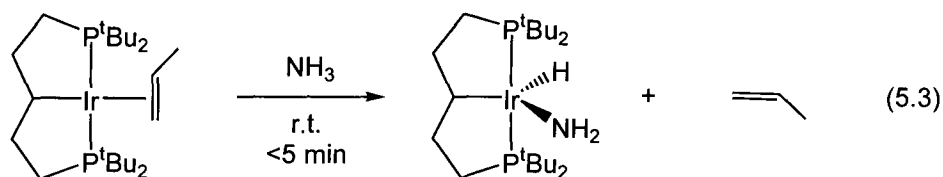
5.1.2 Late Transition Metal Catalyst Mechanisms

As noted in the previous section, some of the earliest hydroamination results were achieved with late transition metals. Owing to the ability of many of these metal complexes to undergo facile oxidative addition and reductive elimination reactions, as well as stabilize alkenes and alkynes for nucleophilic attack, a few distinct mechanisms have been suggested for these reactions. Some late metal systems proceed through an initial oxidative addition of amine to the metal center, followed by migratory insertion of the alkyne or alkene, with subsequent C-H reductive elimination of the product. Milstein and coworkers were the first to demonstrate hydroamination proceeding through an N-H activation mechanism.⁵⁸ The proposed mechanism is illustrated in Scheme 5.1, where careful mechanistic investigations clearly demonstrated the plausibility of this mechanism, including the solid-state characterization of the pseudo-octahedral alkyl-amino-hydrido complex generated upon insertion of norbornene into the Ir-N bond of the amido-hydrido precursor.⁵⁸

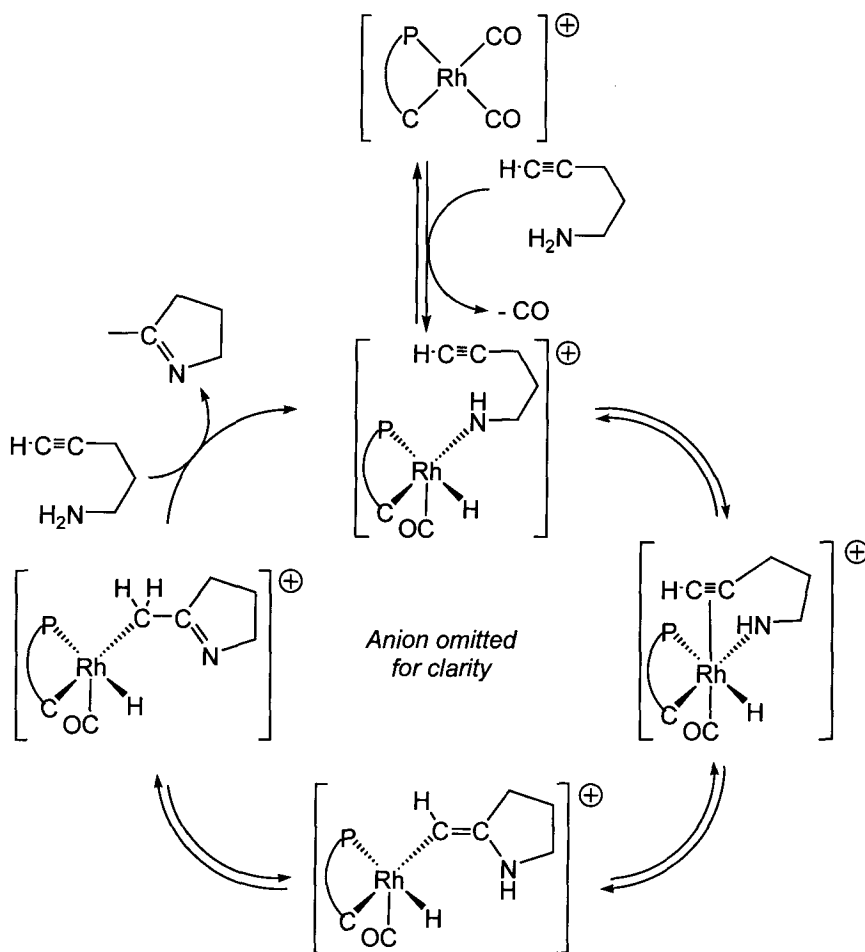


Scheme 5.1

The direct synthesis of primary amines through hydroamination with ammonia is a highly desirable goal. Hydroamination reactions with ammonia proceeding through the above mechanism would require that oxidative addition of the ammonia N-H bond to the metal occur. It has long been known that ammonia is an excellent ligand for transition metals, and simple coordination of the N to the metal center prevails.⁶⁰ Recent results from the Hartwig and Goldman groups illustrate that the oxidative addition of ammonia to Ir(I) is possible, when an electron rich PCP ligand is utilized at the Ir center.⁶¹ The resulting amido-hydrido complex was fully characterized, including structural analysis by X-ray crystallography (Eq. 5.3). Thus far, this novel complex has not been shown to promote catalytic hydroamination with ammonia or any other amine, but the generation of this species is a milestone achievement in this area, suggesting that the ultimate goal of hydroamination with ammonia using late transition metals may be possible.

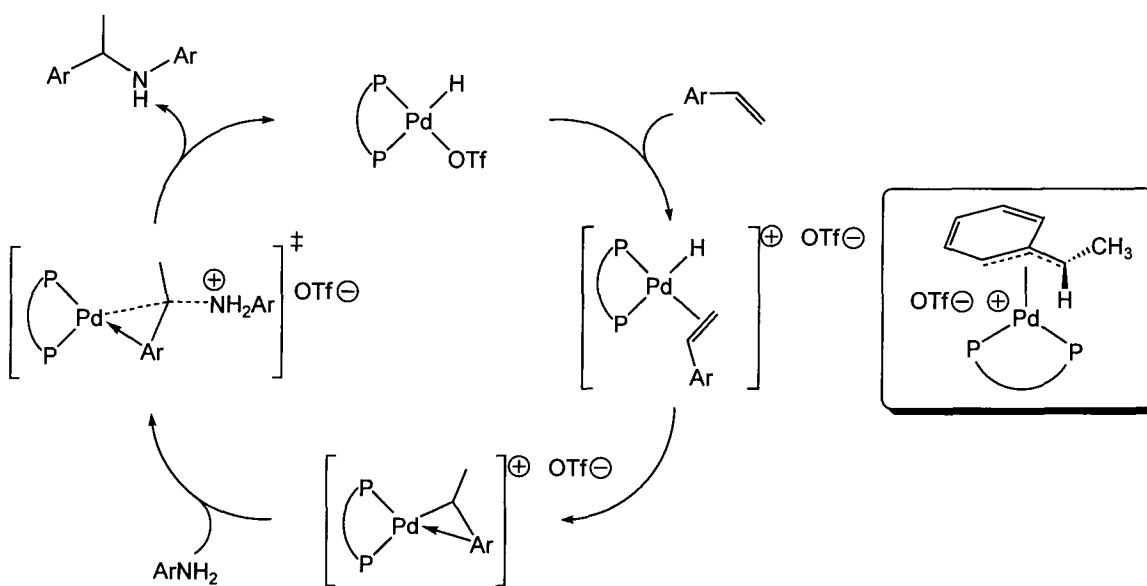


Results by Messerle and coworkers demonstrate that intramolecular cyclization of aminoalkynes by a Rh(I) phosphine-carbene catalyst proceeds through an alternate mechanism, where N-H activation by a precatalytic carbonyl species generates an amido-hydrido complex.⁶² Coordination of the alkyne is followed by nucleophilic attack of the coordinated amido ligand on the alkyne, generating an alkyl-hydrido species. Rather than reductive elimination to liberate the pyrroline product, analogous to the results seen by Casalnuovo and coworkers, the complex undergoes protonolysis to liberate the product regenerating the cationic Rh(III) amido-hydrido complex as shown in Scheme 5.2.⁶²



Scheme 5.2

While late transition metal mediated nucleophilic attack of alkenes and alkynes is a common process, Hartwig and coworkers have recently illustrated an alternate mechanism for select palladium catalysts as shown in Scheme 5.3, where the metal center forms a π -complex with the alkene substrate as an initial step.⁶³ This mechanism has only been seen for additions to vinylarenes, which can be resonance stabilized in an allylic form (inset Scheme 5.3). The resulting η^3 - π -complex can then be attacked by the amine nucleophile in a Wacker-type addition to generate the bound adduct, which is subsequently liberated with concomitant regeneration of a metal hydride species, through proton transfer to the Pd center. Confirmation of this π -species as an intermediate in the catalytic pathway was accomplished by successful use of the isolated η^3 -arene complex (inset) in catalysis.⁶³ Inversion of stereochemistry at the benzylic carbon suggested that external nucleophilic addition of the amine to the coordinated alkene was occurring, rather than metal-mediated amine transfer, which would result in retention of stereochemistry.⁶³



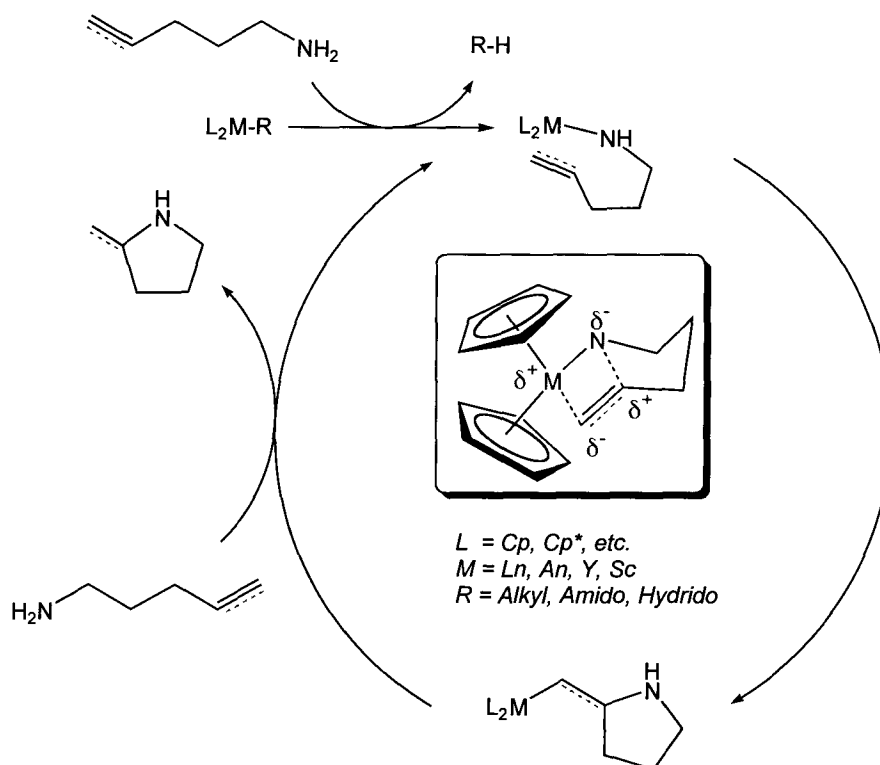
Scheme 5.3

While the late transition metal catalysts presented in this section offer good functional group tolerance, and are relatively insensitive to air and moisture, they still suffer from two major drawbacks. First, these complexes do not catalyze the

hydroamination of non-activated olefins under mild conditions. Second, the high price of the metals utilized in these complexes makes their application to potential industrial scale processes limited unless very low catalyst loadings can be used. Successful hydroamination of non-activated olefins has been accomplished recently through the use of lanthanide and actinide catalysts, as outlined in the following section.

5.1.3 Rare-Earth Metal Catalyst Mechanism

Lanthanide alkyl and hydride bonds have long been known to exhibit extremely high reactivity towards the insertion of olefins.⁶⁴⁻⁷² In 1989, Marks and coworkers recognized that coupling a proton transfer process to the olefin insertion reaction would affect the net addition of H-X to olefins. By utilizing aminoalkenes, the intramolecular cyclization of these substrates to pyrrolidine and piperidine products could be affected in the presence of catalytic quantities of $(Cp^*_2LaH)_2$.⁷³ It was subsequently demonstrated that the entire lanthanide series was capable of facilitating this transformation, with the rate of cyclization being strongly correlated to the ionic radius of the lanthanide. The largest lanthanide, lanthanum, was found to have the highest turnover number (TON) for aminoalkene cyclohydroamination.⁷⁴ Careful kinetic and mechanistic studies showed that the mechanism involved initial protonolysis of the precatalyst to generate an amido complex. This complex was highly susceptible to σ -bond olefin insertion, resulting in a new alkyl complex, which was rapidly protonated by the next equiv. of substrate. This liberated the cyclized product and regenerated the active amido complex, as illustrated in Scheme 5.4. The turnover-limiting step for this process was found to be olefin insertion, resulting in a zero-order dependence of the reaction on substrate concentration.⁷⁵ The highly electrophilic nature of these complexes, along with their diffuse orbitals, allows them to perform cyclization of amine substrates bearing unactivated double and triple bonds. Lanthanide complexes have also been utilized in the catalytic cyclization of phosphinoalkenes, entirely analogous to the aminoalkenes previously described.⁷⁶ This reaction is believed to proceed through the same mechanism as catalytic hydroamination, with a highly polarized transition state for the insertion reaction (inset Scheme 5.4).⁷⁷



Scheme 5.4

The development of these catalyst systems was an important contribution to the field of hydroamination, as these were the first efficient catalysts for the hydroamination of unactivated alkenes. Application of these complexes to the total synthesis of (+)-Pyrrolidine 197B, and (+)-Xenovenine (Fig. 5.2) demonstrated the importance of this new catalytic methodology.⁷⁸

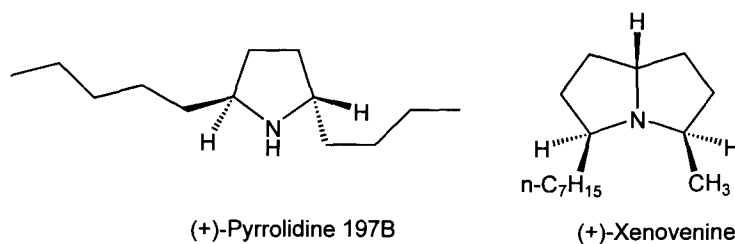


Figure 5.2 Biologically active N-heterocycles synthesized via hydroamination

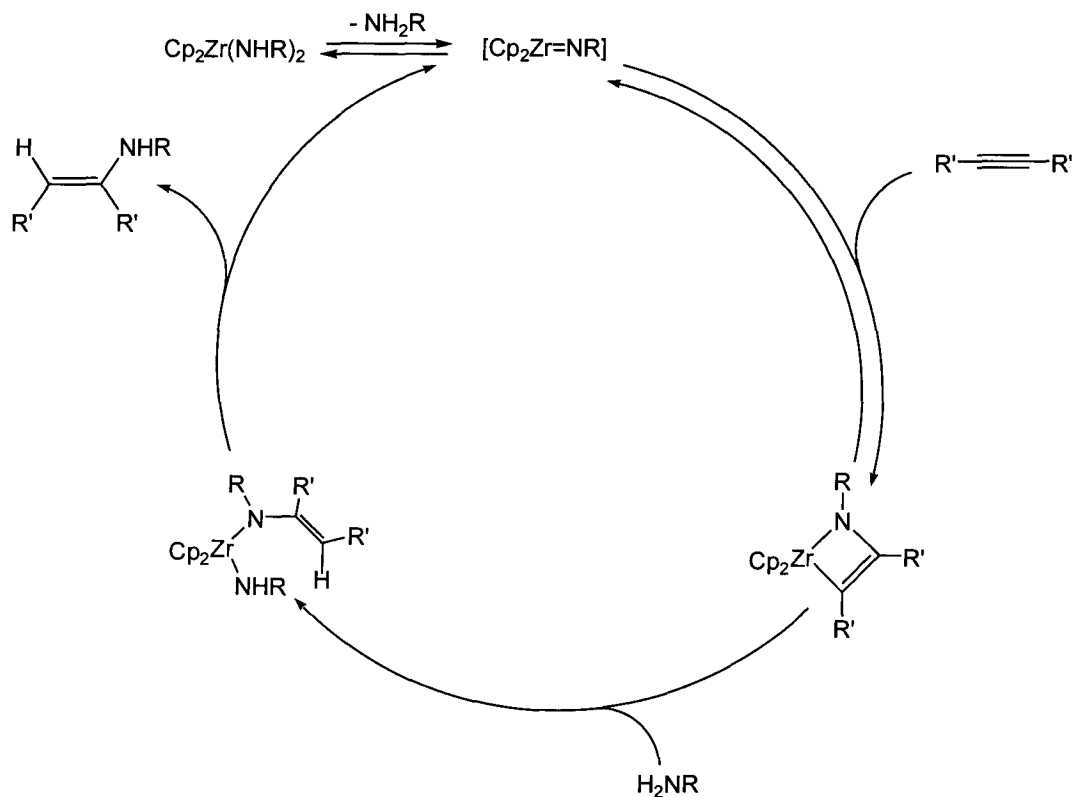
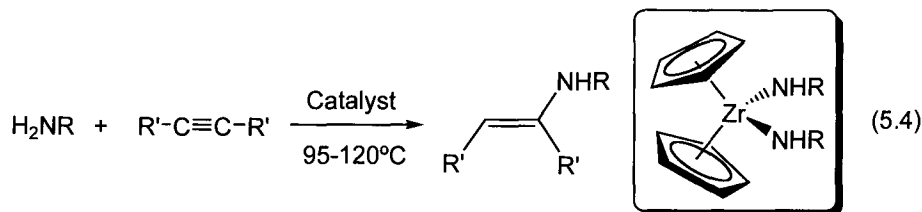
Chiral variants of these lanthanide (III) complexes have also recently been successfully applied in enantioselective cyclizations of aminoalkenes, opening doors for

the enantioselective synthesis of N-heterocyclic targets, without requiring the use of a chiral auxiliary or chiral starting material.⁷⁹⁻⁸⁸ Despite their high reactivity towards intramolecular cyclizations of alkenes and alkynes, these catalysts have not been found to be synthetically useful for the intermolecular variant of this reaction with either alkenes or alkynes.⁸⁹⁻⁹¹ In addition to this substrate scope limitation, these complexes are extremely moisture sensitive. This makes the application of these complexes problematic for synthetic organic chemists lacking specialized anaerobic equipment or knowledge of Schlenk techniques.

The application of group 4 metals for catalytic hydroamination offers the potential advantages of high reactivity, low toxicity, lower cost than late transition metals, and reduced air sensitivity with respect to lanthanides and actinides. Great progress has been made in the past 15 years using group 4 metals for catalytic hydroamination, with fantastic leaps occurring over the past 5 years.^{49, 50, 53, 92, 93} The following section outlines some of the current progress in this area, and the current understanding of how these reactions proceed.

5.1.4 Group 4 Catalyst Mechanism

Early work with zirconocene complexes showed that the intermolecular addition of amines to alkynes could be achieved with long reaction times, and relatively high temperatures (Eq. 5.4).⁹⁴ Mechanistic studies of this reaction revealed that the formation of an imido species, bearing a Zr=N double bond, is a critical step. This is followed by a [2+2] cycloaddition reaction, resulting in the generation of an azazirconacyclobutene species. The Zr-C bond in this intermediate is cleaved by σ -bond metathesis with the N-H bond of incoming amine substrate. Finally, the resulting mixed amido complex can undergo elimination of the enamine product through α -H abstraction, regenerating the imido complex in the process.⁹⁴ For this mechanism, the rate-limiting step has been determined to be the α -elimination of amine to generate the imido species, manifested by an inverse first-order dependence of the catalytic reaction on amine.⁹⁴ The overall mechanism of this reaction is shown in Scheme 5.5, as developed by Bergman and coworkers.



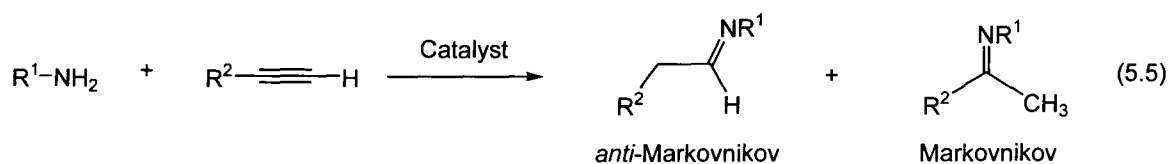
While allenes were also shown to undergo reaction with arylamines in a catalytic fashion with these zirconocene precatalysts,⁹⁴ unactivated alkenes were completely unreactive in this reaction. The ability to facilitate the direct addition of amines across unactivated alkenes is highly desirable, as the products generated from such a process are chiral amines. This compares favorably to the achiral imines derived from alkyne hydroamination, which must be subsequently reduced.⁹⁵ Despite a large research effort directed towards catalytic hydroamination, a general catalyst with wide applicability remains elusive. Considering the ubiquity with which N-C bonds exist in organic molecules, and particularly N-heterocycles, the fulfillment of this goal could have

widespread implications in many areas of synthetic chemistry. This chapter will address the application of group 4 amidate complexes in catalytic hydroamination. As this has been an ongoing research theme in the Schafer laboratory, this project will focus specifically on achieving alkene hydroamination with group 4 metals, and the mechanistic elucidation of this reactivity.

5.2 Alkyne Hydroamination

5.2.1 Introduction

While the catalytic hydroamination of alkenes had not been realized with group 4 metals at the outset of this work, there was good precedent for the application of these metals in catalytic alkyne hydroamination.^{48-50, 52, 53, 92} Early investigations into catalytic hydroamination with zirconocenes revealed that only sluggish reactivity with alkynes could be accomplished.⁹⁴ Considerable progress was noted upon switching to the related titanocene species, which exhibited larger turnover numbers and were more regioselective by comparison.^{96, 97} Addition of an amine to a terminal alkyne can result in two regioisomeric products. Formation of the new C-N bond at the terminal carbon generates the *anti*-Markovnikov product, whereas bond formation at the internal carbon generates the Markovnikov product, as illustrated in Eq. 5.5. Non-Cp based ligand systems have also been exploited for this reactivity.⁹⁸⁻¹⁰³ Many of the ligand systems utilized for this type of reactivity consist of N or O donors, and some selected examples of non-Cp alkyne hydroamination catalysts are illustrated in Fig. 5.3 along with the principal investigators responsible for their development.



Conspicuously absent from this list are mixed-N,O chelate ligand systems. It was interesting to note that the N-based guanidinate (**5.6**) system was active for intermolecular alkyne hydroamination.¹⁰³ Along with the related amidinate ligand

system,¹⁰⁴⁻¹⁰⁷ these ligands bind to the metal center with a tight bite angle, forming a 4-membered metallacycle, resulting in unique coordination chemistry when compared to more traditional 5- and 6-membered ring chelates. It was hoped that the unstudied bis(amidate) bis(amido) complexes presented in Chapter 2 would exhibit novel reactivity, due to their tight bite angles and unique mixed N,O-chelate motif. Additionally, it was reasoned that the tunable nature of the amidate ligands should allow for the systematic study of structure-activity relationships, which would facilitate rational ligand design.

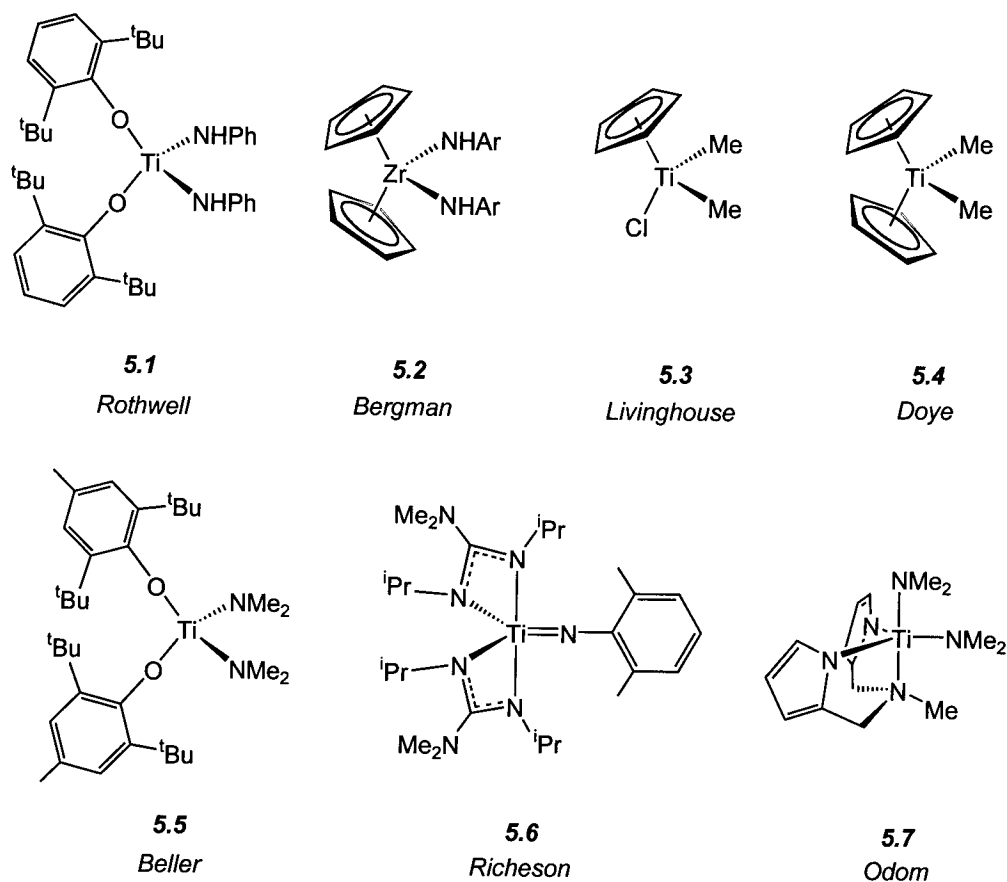
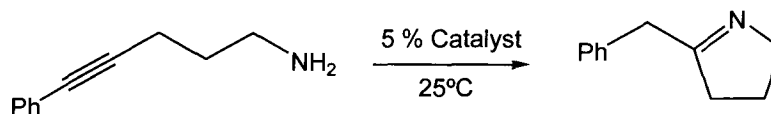


Figure 5.3 Selected group 4 alkyne hydroamination catalysts

5.2.2 Results and Discussion

For entropic reasons, it was decided that intramolecular reactivity would be more readily accomplished, and preliminary studies were directed at the cyclization of 5- and 6-membered rings, to form imine products. As can be seen in Table 5.1, the Ti amidate complexes utilized in this comparison are isosteric, with ^tBu groups on the N-donors of the amidate ligands. The substituent on the backbone of the amidate ligand is varied to provide different electronic environments. Complex **5.8** contains an electron-donating isopropyl group, while complex **5.9** has an electron-withdrawing phenyl group, and finally, complex **5.10** incorporates a strongly electron-withdrawing pentafluorophenyl moiety. X-ray crystallographic studies of **5.9** (Chapter 2) and **5.10** illustrate that the coordination geometry of the solid-state molecular structures of these complexes is unaffected by the electronic modification of the amidate backbone.¹⁰⁸ As expected, the amidate Ti bond distances for **5.10** are elongated, albeit slightly, with respect to **5.9**, consistent with higher ionic bonding character, due to the reduced electron donating capacity of the fluorinated ligand. Selected comparative bond lengths for complexes **5.9** and **5.10** are given in Table 5.2. In keeping with the reduced electron donating capacity of the fluorinated amidate ligand in **5.10**, the amido ligand bond distances are decreased, illustrating a higher degree of π -donation to the metal center versus **5.9**.

Table 5.1 – Effect of electronic modification of amidate ligands on alkyne cyclohydroamination efficiency

Entry	Catalyst (5 mol %)	Yield (%)*	Time (h)
1 Complex 5.8		99	14
2 Complex 5.9		98	3.5
3 Complex 5.10		97	0.25

* NMR yield versus internal standard 1,3,5-trimethoxybenzene.

Table 5.2 – Comparison of bond distances for bis(amidate) bis(amido) complex 5.9 and fluorinated variant 5.10

Entry	Bis(amidate)-Bis(amido) Complex	Bond	Distance (Å)
1 Complex 5.9		Ti-N(amidate)	2.234(5)
		Ti-O(amidate)	2.035(4)
		Ti-N(amido)	1.907(6)
2 Complex 5.10		Ti-N(amidate)	2.356(7)
		Ti-O(amidate)	2.044(6)
		Ti-N(amido)	1.887(7)

The use of electron-withdrawing groups on the amidate framework effectively reduces the degree of electron donation to the metal center. This affords extremely electrophilic metal centers, which are well suited to bring electron rich reagents together, such as amines and alkynes. A strong correlation can be seen in Table 5.1, in which the relative reactivity of the metal complexes increases dramatically with the electron-withdrawing capability of the amidate ligand. Complex **5.10** is to date one of the most reactive complexes known for this particular cyclization reaction.¹⁰⁸ In addition, other work performed in the Schafer laboratories has shown that enhanced reactivity, and increased regioselectivity in intermolecular alkyne hydroamination reactions is possible with larger substituents at the amidate N donors.¹⁰⁹ This is proof of concept that the amidate ligand motif is a truly useful modular ligand framework, which can be systematically investigated.

Ti imido complexes isolated by the Schafer group are also active catalysts for alkyne hydroamination,¹¹⁰ and mechanistic studies are consistent with a mechanism analogous to the one developed by the Bergman group, as illustrated in Scheme 5.5.⁹⁴ Isolated imido species, kinetic studies, and isotopic labeling experiments are all supportive of this mechanistic proposal.¹¹⁰

5.2.3 Summary

The Ti bis(amidate) bis(amido) complexes discussed in Chapter 2 were successfully applied as alkyne hydroamination catalysts. Cyclizations of aminoalkyne substrates were found to be rapid and resulted in high yields. It was found that strongly electron withdrawing substituents within the amidate backbone resulted in greatly accelerated reactions. Subsequent to this work, other results from the Schafer laboratory have demonstrated that intermolecular hydroamination of alkynes can be affected by these complexes, and the regioselectivity and rate of reaction is strongly influenced by the size of the substituents on the amidate nitrogen donors. Mechanistic investigations performed in the Schafer laboratory are consistent with an imido based mechanism analogous to that shown in Scheme 5.5. While the imine products of alkyne hydroamination using these complexes have been exploited in further organic elaboration

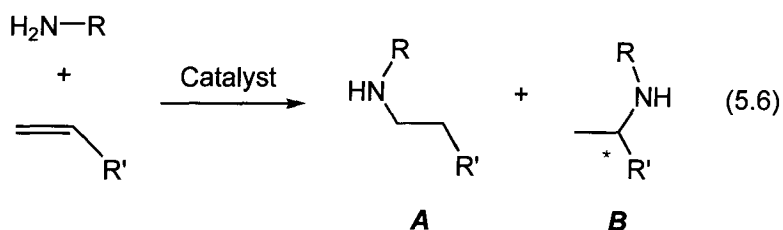
within the Schafer group,¹¹¹ the goal of this project was to extend this reactivity to alkenes, which is discussed in the following section.

5.3 Alkene Hydroamination

5.3.1 Introduction

5.3.1.1 Cationic Group 4 Catalysts

Unlike alkyne hydroamination, which has wide-spread precedence for group 4 metals, the related hydroamination of alkenes using these metals has not been widely studied. The addition of amines to alkenes is an intrinsically more difficult reaction to accomplish than its alkyne variant. Thermodynamically, the alkene addition reaction is approximately thermoneutral, with a higher calculated energy of activation vs. that seen for the exothermic addition of amines to alkynes.^{112, 113} Advantageously, the resulting products of this reaction are amines, in comparison to alkyne hydroamination, which generates imines that must subsequently be reduced to amines. As can be seen in Eq. 5.6, the generalized addition reaction leads to regioisomeric products **A** and **B**, in which product **B** contains a stereogenic carbon α to the nitrogen.



Although lanthanide complexes have been known to catalyze the intramolecular cyclohydroamination of aminoalkenes since the late 1980's,⁷³ no group 4 catalysts were known to facilitate alkene hydroamination until 2004.^{114, 115} The first two complexes developed for the catalytic cyclohydroamination of aminoalkenes are shown in Fig. 5.4. The well known cationic zirconocene complex **5.11** was studied by Hultsch and coworkers,¹¹⁴ whereas the phenolate system **5.12** was developed simultaneously by Scott and coworkers.¹¹⁵ Both of these complexes are cationic, and thus are formally isovalent

with their neutral lanthanide and group 3 counterparts. Preliminary investigations by both Hultsch and Scott and their coworkers showed that these catalysts were capable of cyclizing secondary, or N-disubstituted, aminoalkenes in high yields and relatively short reaction times (Eq. 5.7). Scott's system, being chiral, also exhibited enantioselectivity for this transformation, with enantiomeric excesses up to 82%.¹¹⁵ This was the first asymmetric group 4 catalyst for alkene hydroamination, and provided the highest enantioselectivity for the cyclization of the substrate in Eq. 5.7 known at the time.

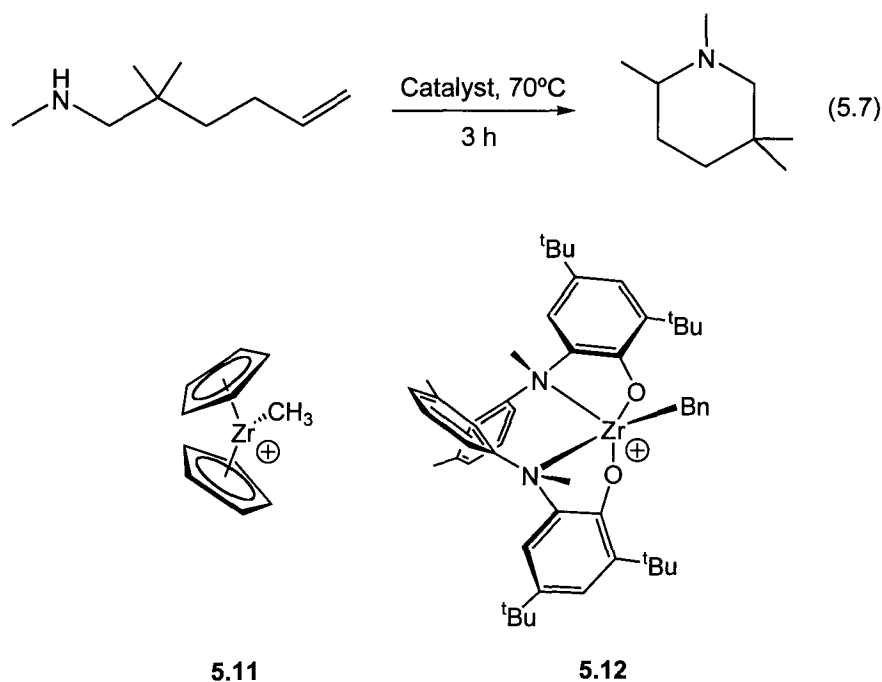
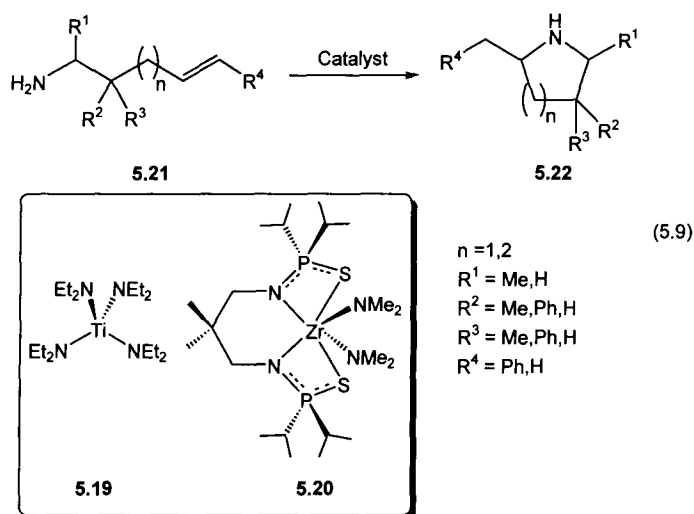


Figure 5.4 Cationic precatalysts for alkene hydroamination

Interestingly, both Scott and Hultsch and their coworkers noted that primary aminoalkenes were not cyclized by these complexes.^{114, 115} The lack of reactivity for these species was reasoned to be due to the formation of catalytically inactive imido complexes, such as **5.14** shown in Eq. 5.8. This could be envisioned to occur through loss of a proton under the basic conditions of excess amine during catalysis, resulting in a neutral imido complex.

5.3.1.2 Neutral Group 4 Catalysts

In light of the observations of the Hultsch, Scott, and Sita groups, we were curious about the plausibility of active neutral imido species in the catalytic hydroamination of alkenes with other group 4 complexes. Cationic complexes tend to be extremely reactive due to their enhanced electrophilic nature. Consequently, handling these complexes can be problematic, limiting their usefulness in organic synthesis. Additionally, the possibility of hydroamination catalysis by H^+ liberated by cationic complexes of this type makes mechanistic investigations of these species complicated.¹¹⁷ These complications make the development of charge neutral catalysts for this reaction an important goal. Two neutral group 4 catalysts were discovered to catalyze cyclohydroamination of primary aminoalkenes, as illustrated in Eq. 5.9. The first complex, $Ti(NMe_2)_4$ (**5.19**) was shown by the Schafer group to be reactive for cyclization of primary aminoalkene substrates to form pyrrolidine and piperidine products.¹¹⁸ Unfortunately, this complex suffers from limited substrate scope, and exhibits very low diastereoselectivity for substrates such as **5.21** (Eq. 5.9), $R^1 = H$, $R^2 = Me$, $R^3 = Ph$, $R^4 = H$ (58 % d.e.). The second system developed by the Livinghouse group features a tetradentate thiophosphinic amidate ligand (**5.20**).¹¹⁹ This complex is more reactive than **5.19**, allowing for greater substrate scope and reduced reaction times. Additional neutral Ti and Zr complexes have since been found to promote catalytic alkene hydroamination, including enantioselective reactivity that exceeds that seen by Scott and coworkers (Fig. 5.5).¹²⁰⁻¹²⁴



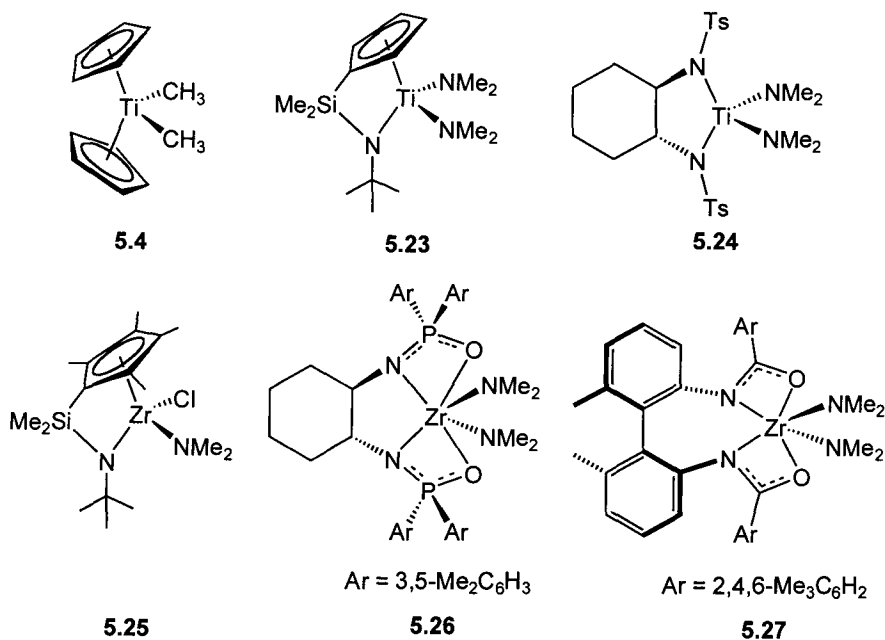


Figure 5.5 Selected neutral Ti and Zr alkene hydroamination precatalysts

Most of the neutral complexes described above have been postulated to promote catalytic alkene hydroamination through an imido intermediate. The lack of reactivity of these complexes with secondary aminoalkenes has been cited as a major piece of supporting evidence, as these substrates cannot form a M=N double bond.^{118, 119, 121} The Zr complex **5.25** is an exception, where Marks and coworkers have proposed a σ -bond insertion mechanism for catalysis. This complex is capable of cyclohydroamination of primary and secondary aminoalkenes with low activity. Prior to the work presented in Chapter 4, no isolable imido complexes had been found to promote this reactivity, in spite of nearly 20 years of study in the area.¹²⁵ The following section discusses the utility of amidate supported amido and imido complexes in the catalytic cyclohydroamination of primary aminoalkenes.

5.3.2 Results and Discussion

5.3.2.1 Imido Precatalyst Kinetic Analysis

While complexes **5.4**, **5.19**, **5.20**, **5.23**, **5.24**, **5.26** and **5.27** are postulated to catalyze alkene cyclohydroamination through an imido intermediate, no isolated imido species have been demonstrated to facilitate this transformation. Excitingly, the Zr imido complex **5.31** developed and discussed in Chapter 4 (**4.25**) has been shown to promote the catalytic cyclohydroamination of primary aminoalkenes, making this the first imido complex to show activity for this reaction.¹²⁵ This observation is strong supporting evidence for an imido-based reaction mechanism; however, alternative mechanisms must also be considered. Mechanistic aspects of this reaction have been probed through kinetic analysis. The Zr imido complex **5.31** is much more reactive than the Ti congener **5.30** for catalytic hydroamination, thus the studies presented herein focus on Zr complex **5.31** shown in Fig. 5.6.

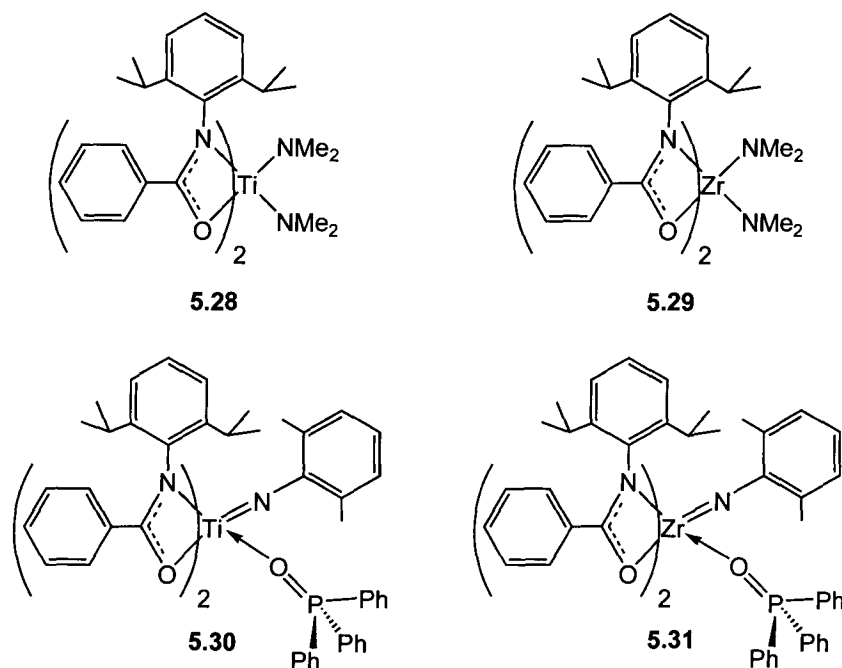


Figure 5.6 Amidate Ti and Zr aminoalkene cyclohydroamination precatalysts

Preliminary screening experiments discussed in Chapter 4, Table 4.6, showed that 2,2-diphenyl-pent-4-enylamine was the most rapidly cyclized substrate, and has thus been chosen for the kinetic studies that follow. The conversion of this substrate (**5.32**) to the N-heterocycle, 1-methyl-3,3-diphenylpyrrolidine (**5.33**), as shown in Eq. 5.10, is observed by ^1H NMR spectroscopy at 110 °C in deuterated toluene. In the presence of 10 mol % of **5.31** as precatalyst, the reaction is monitored every 10 minutes by the consumption of the substrate vs. an internal standard (1,3,5-trimethoxybenzene). A stacked plot showing time-resolved spectra for this reaction is shown in Fig. 5.7, where reaction progress is followed by the disappearance of the olefinic resonances for the substrate at δ 4.96 and 5.44.

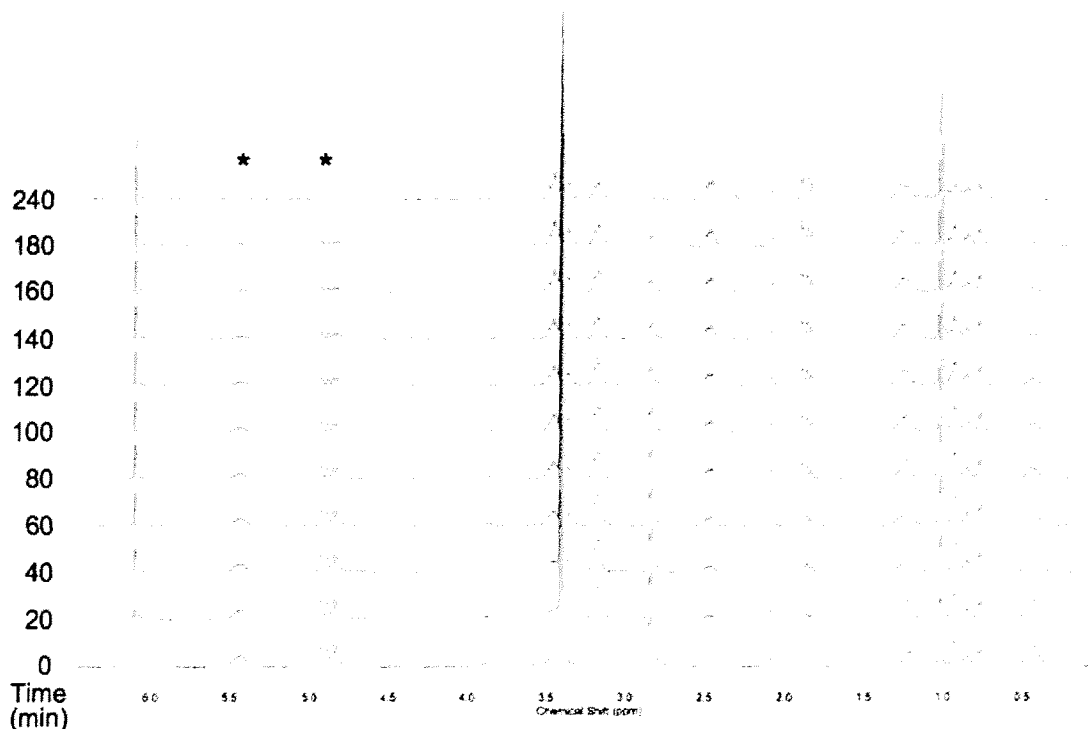
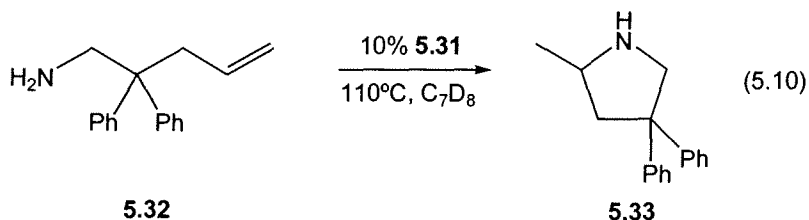


Figure 5.7 Time-resolved 300 MHz ^1H NMR spectra showing consumption of substrate (olefinic signals (*) at δ 4.96 and 5.44)

The dependence of this reaction on substrate concentration can be determined by plotting the concentration of substrate with respect to time. Since the reaction is performed with 10 mol % of catalyst, the substrate is in large excess, exhibiting pseudo-first-order conditions. Plotting the natural logarithm of substrate concentration vs. time for the aforementioned reaction shows a very high linear correlation, as shown in Fig. 5.8. Standard analysis of this behavior is consistent with first-order dependence of this reaction on substrate concentration. First-order substrate dependence suggests that the turnover-limiting step for this process involves an intermolecular reaction between one equivalent of substrate and another species, presumably the catalytically active complex. Two alternative mechanisms for this reaction are presented in Scheme 5.7, where one features an imido-cycloaddition as a key step, and the other involves a σ -bond insertion into an amido Zr-N bond. The imido based mechanism featured on the left is completely analogous to that proposed for alkyne hydroamination with group 4 complexes (Scheme 5.5).⁹⁴ In contrast, the σ -bond insertion mechanism illustrated on the right is analogous to that seen for the rare-earth catalysts (Scheme 5.4).⁷³

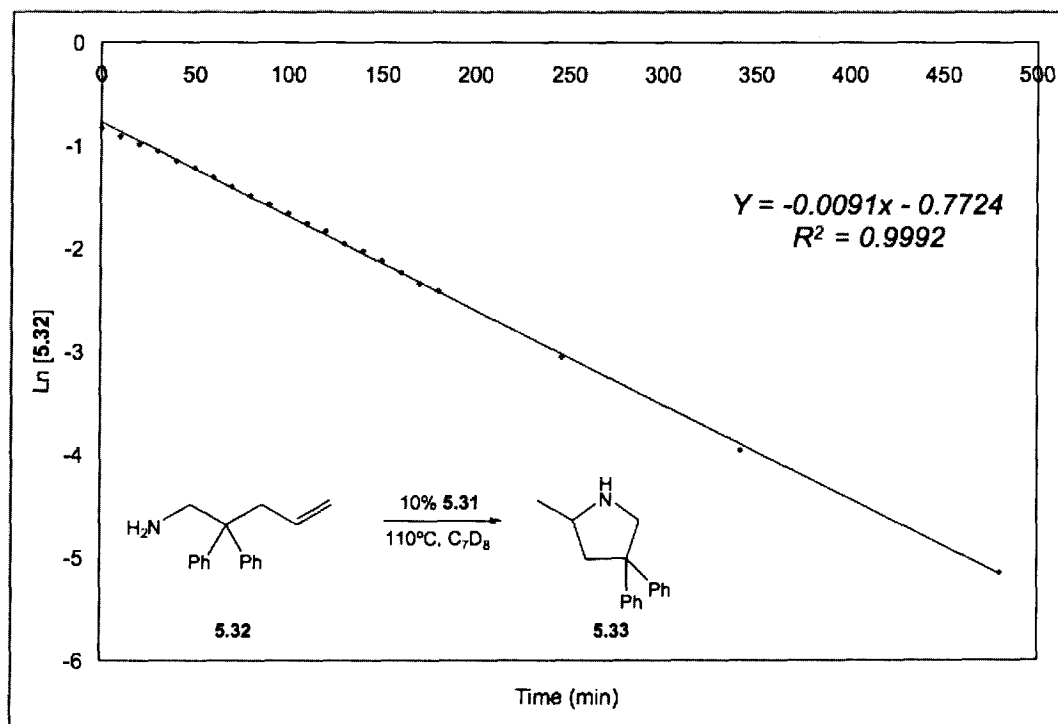
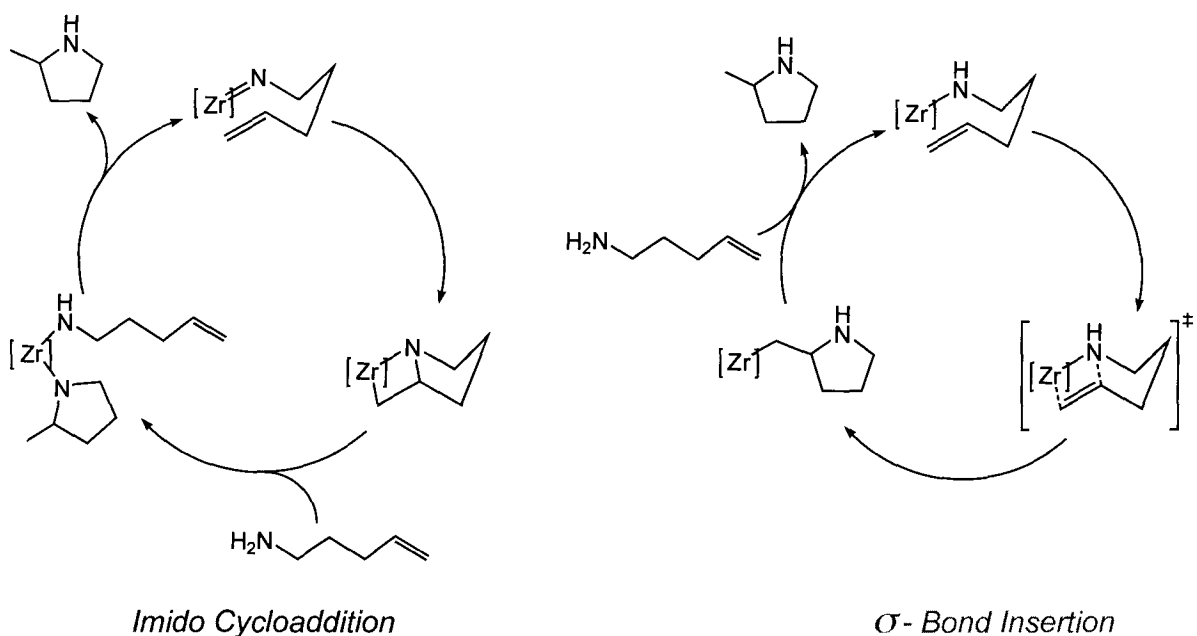


Figure 5.8 Natural log of [5.32] vs. time plot showing first-order substrate dependence



For both of these possible mechanisms, the intermolecular processes are protonolysis reactions between the incoming substrate and an organometallic species. While the σ -bond insertion mechanism in Scheme 5.7 has not been exhaustively examined for group 4 complexes as already mentioned on page 250, this proposal has been suggested for the cationic group 4 complexes **5.11**¹¹⁴ and **5.12**,¹¹⁵ and the neutral chloro-amido Zr complex **5.25**.¹²⁴ Careful mechanistic studies by Marks and coworkers have demonstrated that lanthanide complexes, isoelectronic to the cationic group 4 complexes **5.11** and **5.12**, proceed through this mechanism, where the catalytic reaction shows no dependence on substrate concentration.⁷⁵ Zero-order substrate dependence for these complexes suggests that the turnover-limiting process is the insertion step. If a similar rate-determining step occurs for the amidate precatalysts **5.30** and **5.31**, zero-order substrate dependence would be expected. The observed first-order substrate dependence shown in Fig. 5.8 is consistent with the cycloaddition pathway shown on the left of Scheme 5.7, with the rate-limiting step being the cleavage of the azazirconacyclobutane intermediate.

In an effort to understand the nature of the active catalytic complex for alkene cyclohydroamination, catalyst dependence studies were undertaken. Kinetic analysis of the reaction in Eq. 5.10 at different catalyst loadings clearly demonstrates that first-order

substrate dependence is maintained between 2.5 and 10 mol % of catalyst. Changes in catalyst concentration throughout an individual run are, by definition, negligible, as the catalyst is regenerated at the end of each cycle. Fig. 5.9 shows the natural log plots of substrate consumption vs. time for 2.5, 5.0, 7.5, and 10.0 mol % of imido precatalyst **5.31**, where $[5.32']$ refers to the normalized concentrations of **5.32**.^{75, 125} The linear plots are consistent with first-order substrate dependence for these four catalyst loadings.

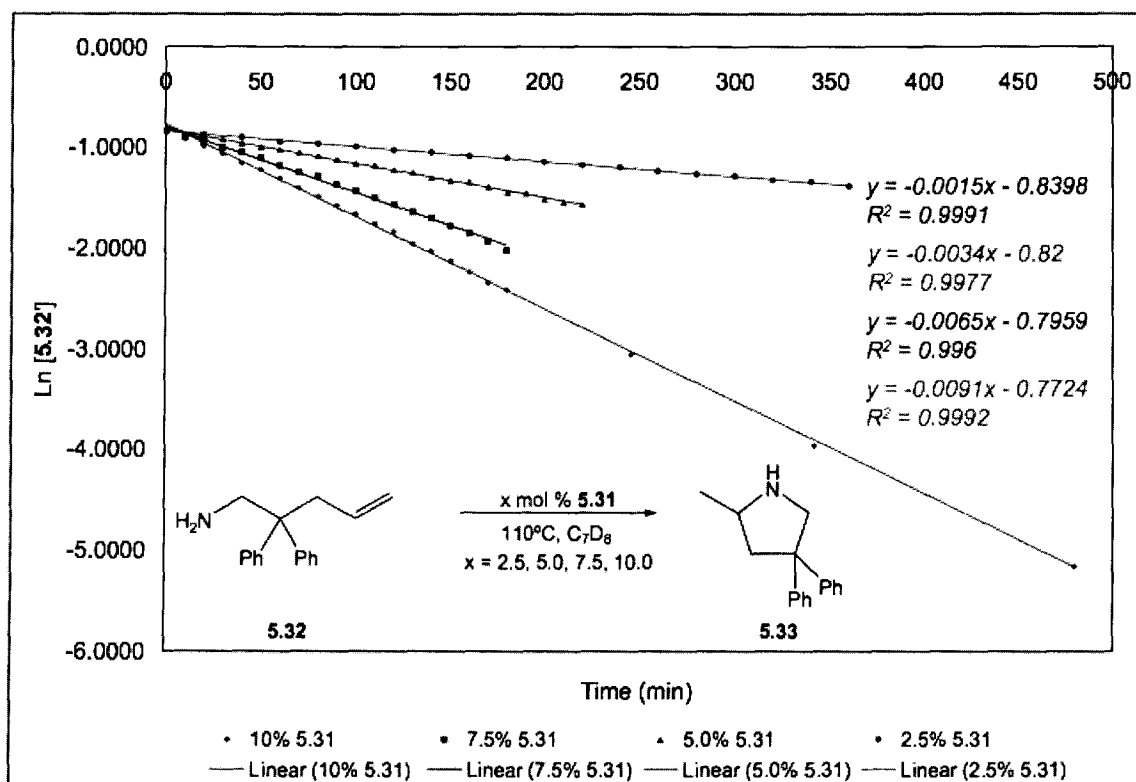


Figure 5.9 $\ln [5.32']$ vs. time plot for 4 different catalyst loadings showing first-order substrate dependence over a wide range of catalyst loadings

Derivation of the rate law for a first-order process dictates that the variation of the natural log of the observable quantity ($[\text{substrate}]$) with time is a linear relationship, and the slope of the line defining this relationship is the pseudo-first-order rate constant for which this variation occurs. By examining the relationship between the rate of reaction and the catalyst loading, the nature of the catalyst and its role in the reaction can be elucidated. Fig. 5.10 demonstrates that the observed rate constants (k_{obs}), derived from the slopes of the lines in Fig. 5.9, vary with catalyst concentration in a linear fashion,

with higher catalyst loadings resulting in larger values of k_{obs} . This behavior is also consistent with first-order dependence of the reaction on the catalyst. While this does not verify that a monometallic complex is involved in the catalytic reaction, the first-order dependence on catalyst loading indicates that a well defined metal complex is responsible for the catalytic reaction. In addition to these kinetic results, which are in accord with the imido cycloaddition mechanism proposed in Scheme 5.7, the inability to cyclize secondary aminoalkene substrates, such as **5.33** shown in Eq. 5.11, is supportive of the intermediacy of an imido complex, since the formation of Zr=N bonds is not possible for secondary aminoalkene substrates.

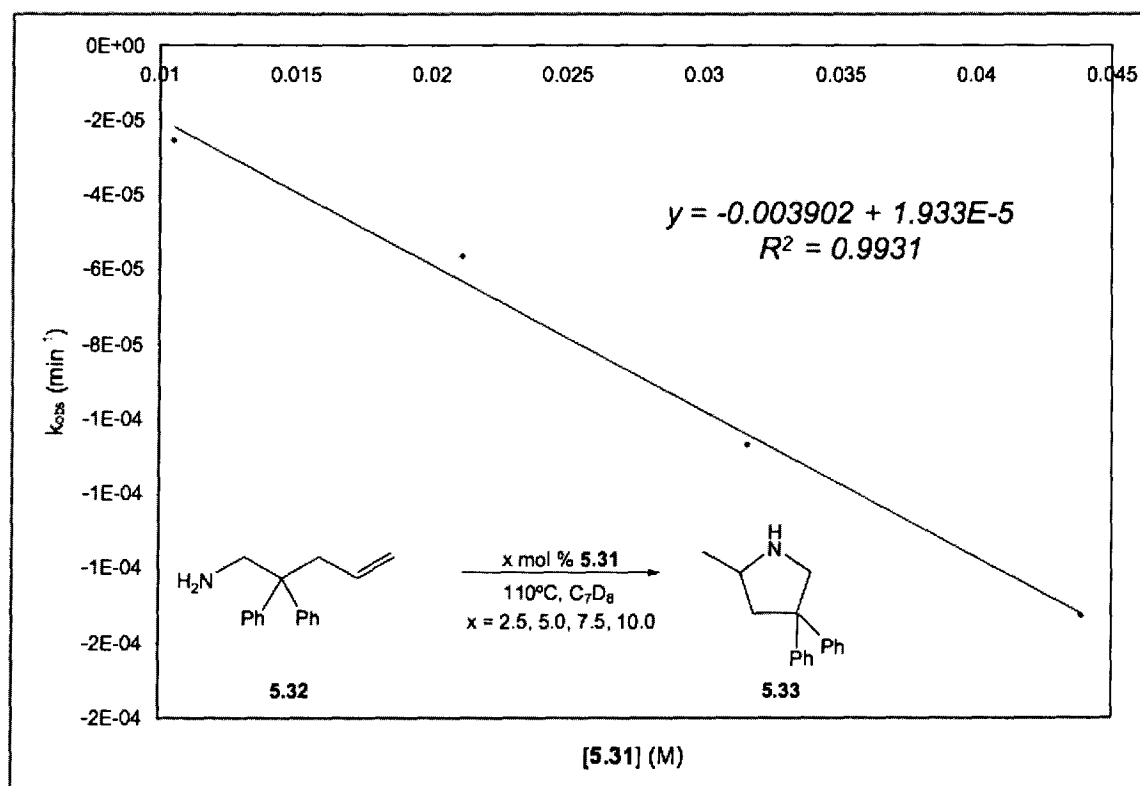
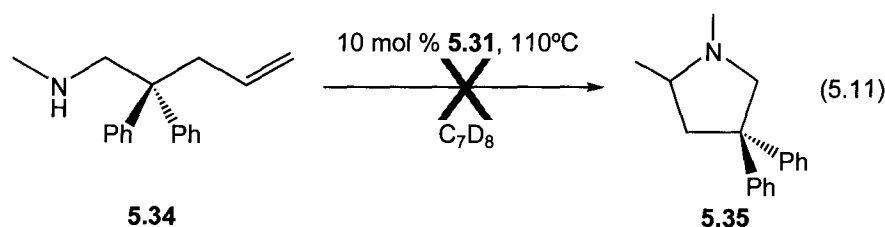


Figure 5.10 Plot of k_{obs} vs. [catalyst] (**5.31**) showing first-order catalyst dependence



It has been demonstrated that dimeric imido species are not catalytically active for hydroamination catalysis.^{94, 126-128} In Chapter 4, the dimeric imido complex $\{[\text{DIPP}(\text{NO})^{\text{Ph}}]_2\text{Zr}(\mu\text{-N}(2,6\text{-Me}_2\text{C}_6\text{H}_3))\}_2$ (**4.31**), was characterized in the solid-state. This complex could not be reliably isolated, and solution phase data suggested that this dimeric imido complex did not remain intact in solution. These facts, combined with the observed catalytic viability of imido complex **5.31** in catalytic cyclohydroamination of aminoalkenes, suggest that a monomeric terminal imido complex is responsible for hydroamination catalysis with amidate-based precatalysts.

5.3.2.2 Bis(amido) Precatalyst Kinetic Analysis

Many group 4 imido complexes that facilitate alkyne hydroamination catalysis are known to suffer from long induction periods, where the catalytically active imido complexes are slowly generated.¹²⁹ In contrast, the imido complexes **5.30** and **5.31** are generated very rapidly upon addition of TPPO to a solution of amine and bis(amido) precursor (**5.28** and **5.29**, respectively).¹²⁵ While these imido complexes have been fully characterized and are accessible in high yields, they are more difficult to prepare than their bis(amido) precursors. The ability to utilize the bis(amido) precursors rather than the imido complexes would greatly simplify mechanistic studies, and would make these catalysts more useful for synthetic organic applications. In order to use bis(amido) precatalysts in place of imido species for kinetics investigations, the conversion of the bis(amido) complex to the imido complex must be rapid in comparison to the rate-determining step. Qualitative observations of nearly instantaneous formation of imido **5.31** from the bis(amido) complex **5.29**, described in Chapter 4 suggest this is the case. Direct comparison of the bis(amido) complex **5.29** and the imido complex **5.31** in

identical catalytic runs of the reaction in Eq. 5.10 verify that this simplification is justified (Fig. 5.11).

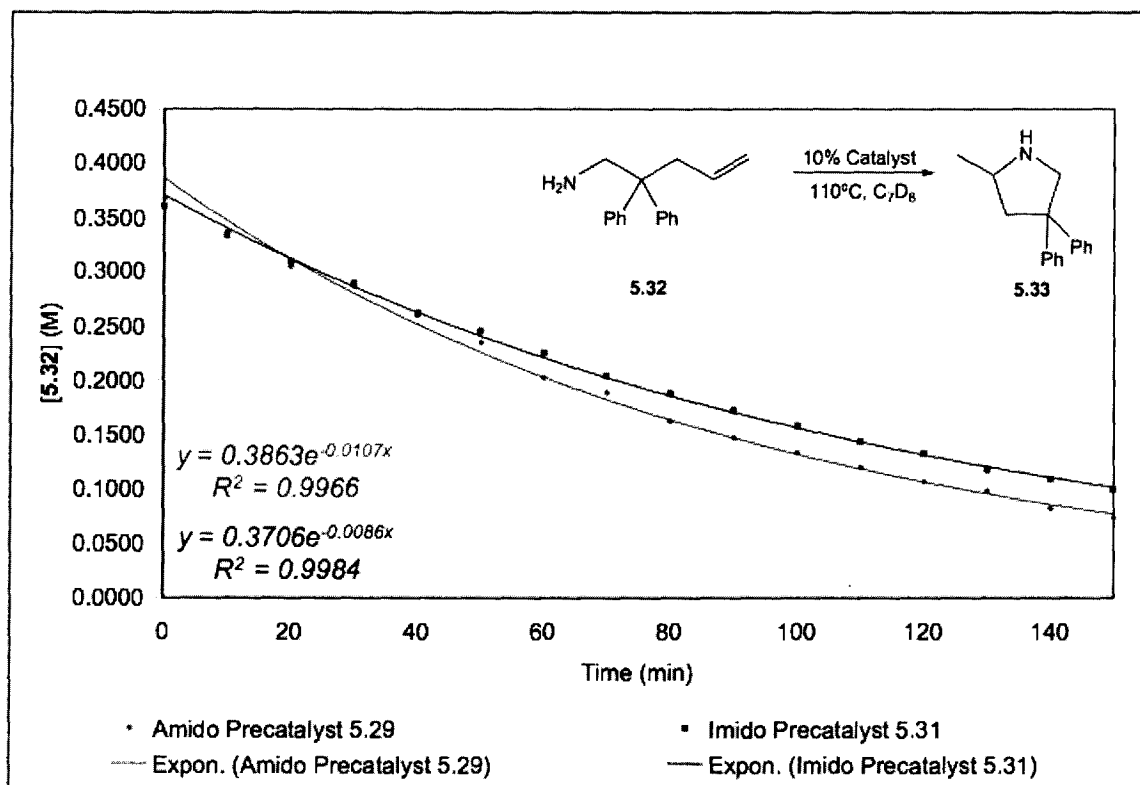


Figure 5.11 Kinetic profile comparison of Zr amido **5.29** vs. imido **5.31** for cyclization of aminoalkene **5.32** ($[5.32]$ vs. time)

While it is apparent in Fig. 5.11 that these two complexes have similar kinetic profiles, the imido complex (blue line) is actually slightly slower to react, particularly at lower concentrations of substrate. This can be rationalized by the fact that the imido complex releases its coordinated TPPO ligand into solution during catalysis, as witnessed by ³¹P NMR spectroscopy. As the reaction proceeds, the substrate is depleted, and competition between the substrate and TPPO for coordination to the metal center becomes more pronounced. This is supported by the fact that the data points for the two kinetic runs are nearly overlaid at low conversions (up to ~ 40 min), and begin to diverge at higher conversion. To test the hypothesis that TPPO is acting as a catalyst poison, 1 equiv. of TPPO was added to the bis(amido) precatalyst **5.29**, and the reaction was monitored by ¹H NMR spectroscopy and compared to the results obtained for the

identical reaction with **5.31** as precatalyst. As illustrated in Fig. 5.12, the kinetic profiles for the cyclization of **5.32** catalyzed by **5.31** and **5.29** plus 1 equiv. of TPPO demonstrate that TPPO inhibits the reaction, with the imido catalyzed reaction occurring more rapidly than the bis(amido)/TPPO catalyzed reaction.

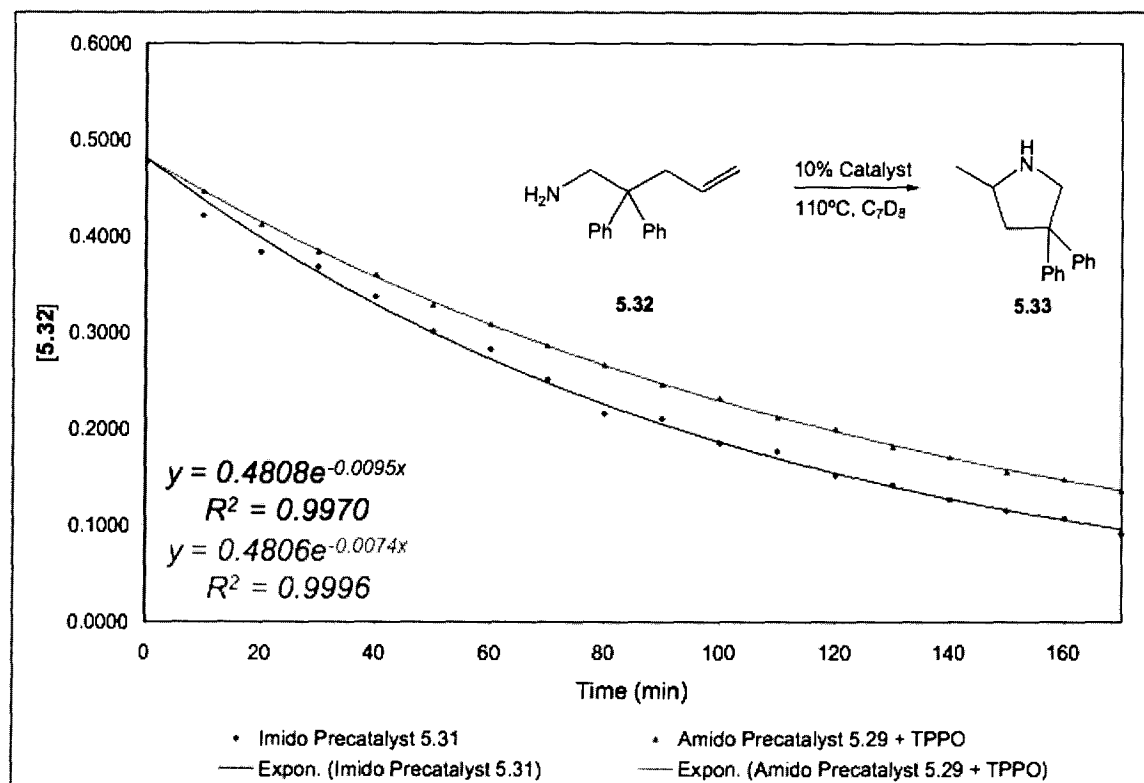


Figure 5.12 Kinetic profile comparison of Zr imido **5.31** and amido **5.29** + TPPO for cyclization of aminoalkene **5.32** ([**5.32**] vs. time)

Bis(amido) complex **5.29** is easier to synthesize than imido complex **5.31**; however, the use of the very bulky [^{DIPP}(NO)^{Ph}] amidate ligand results in relatively slow reactivity, due to excessive steric congestion about the metal center. Switching to a slightly less bulky bis(amido) complex results in shorter reaction times, and increased substrate scope. The Zr bis(amido) complex [^{DMP}(NO)^{tBu}]₂Zr(NMe₂)₂ (**5.36**) discussed in Chapter 2 (**2.18**) has very simple ¹H NMR spectroscopic characteristics, and is easily isolated in very high yields. Comparison of this complex bearing the less bulky 2,6-dimethylphenyl substituents on the amidate N to the bulkier 2,6-diisopropylphenyl substituted complex **5.29**, shows the rate enhancement possible by reducing the steric

bulk of the amidate ligand. The rate constant (k_{obs}) for the cyclization of **5.32** by precatalyst **5.36** was found to be $1.34 \times 10^{-2} \text{ min}^{-1}$, in comparison to that for **5.29** at $0.91 \times 10^{-2} \text{ min}^{-1}$. The remainder of the kinetic analysis was thus performed with **5.36** as a precatalyst.

It was noted earlier that first-order substrate dependence suggests that the rate-determining step for the cyclohydroamination of aminoalkenes is the protonolysis of the azazirconacyclobutane intermediate complex. Verification of this supposition was possible through the use of kinetic isotope effect studies. The N-dideuterated isotopomer of substrate **5.32** (**5.32-*d*₂**) was synthesized through H/D exchange between **5.32** and D₂O in THF (~ 92 % deuterium incorporation). The reaction was monitored as previously described by ¹H NMR spectroscopy, and the natural log plot of the consumption of substrate vs. time was generated for three different runs. For comparative purposes, three different catalytic runs for the cyclization of the protiated substrate **5.32** were also performed. As Fig. 5.13 illustrates, these results are highly reproducible, and representative of the error margins for the kinetic studies presented in this chapter. Comparison of the relative rates of consumption of **5.32** and **5.32-*d*₂** is presented in Fig. 5.13, where the ratio of $k_{\text{H}}/k_{\text{D}}$ for this reaction is 2.14 ± 0.28 . These values are consistent with a small primary kinetic isotope effect, as expected for the proposed rate-limiting protonolysis reaction.

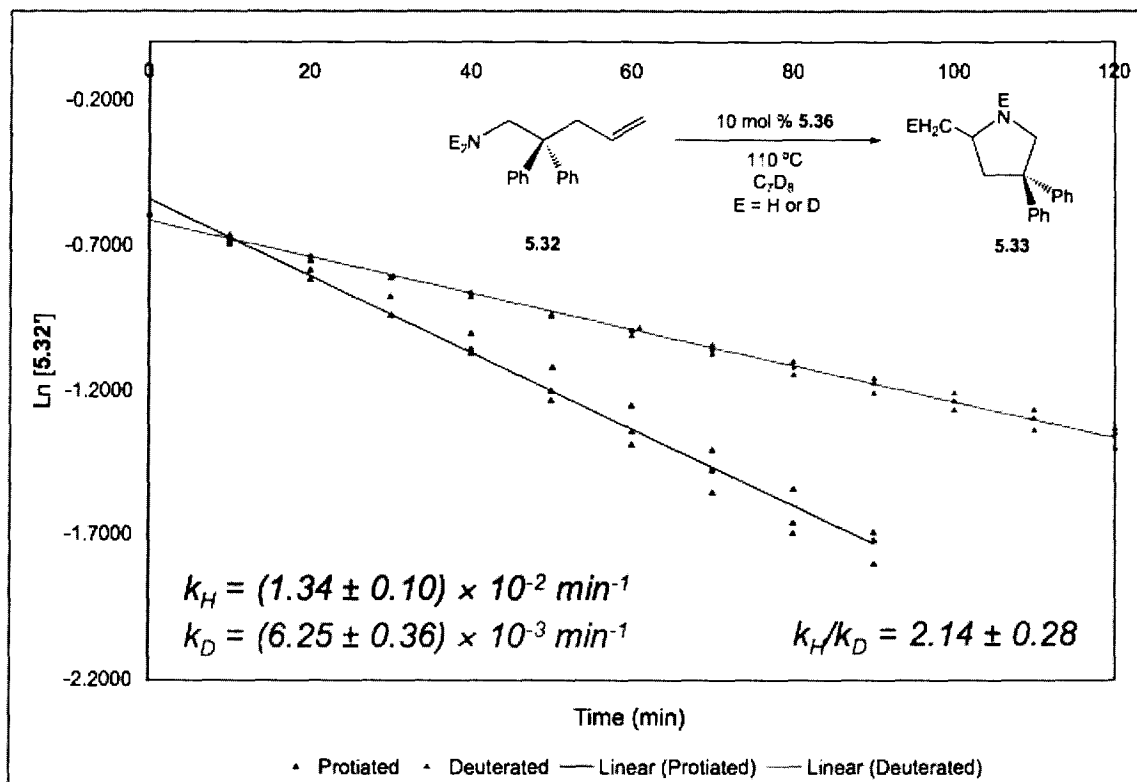


Figure 5.13 Kinetic isotope effect experiment showing small primary kinetic isotope effect for cyclization of aminoalkene **5.32** ($\ln [5.32']$ vs. time)

Kinetic investigations by Marks and coworkers also show a primary kinetic isotope effect for the rate-determining insertion step of the rare-earth catalyst mechanism shown in Scheme 5.4. The values seen by Marks and coworkers for similar substrates are large (2.7-5.2) considering the proposed lack of a discrete N-H bond cleavage process in the rate-determining insertion step.⁷⁵ This has been suggested to be caused by cooperative enhancement by the N-H protons of extra coordinated amine in the transition state for the insertion reaction.⁷⁵

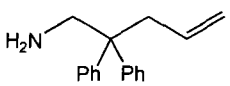
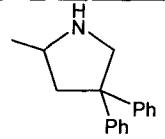
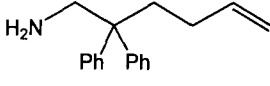
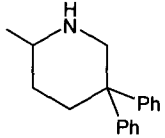
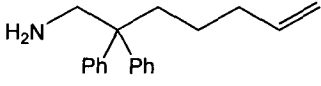
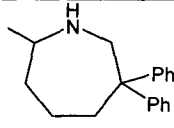
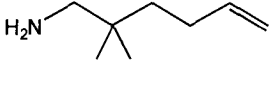
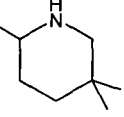
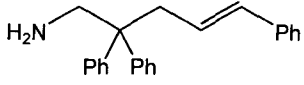
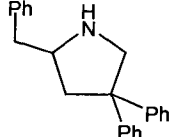
5.3.2.3 Substrate Scope and Reaction Optimization

While the preliminary results shown for imido precatalyst **5.31** in Chapter 4 were promising, the presence of TPPO and the very sterically encumbering amidate ligands resulted in slow reactivity. Other recent results in the Schafer laboratory have shown that a tetradentate bis(amidate) complex with reduced steric bulk (**5.27**) was capable of

performing aminoalkene cyclization in a rapid manner.¹²³ The drawback to this system was a reduced substrate scope, particularly for substrates lacking bulky geminal substituents at the β -position.¹²³ With this in mind, it was reasoned that reduction in steric bulk at amidate N, while retaining the more bulky non-tethered bis(amidate) motif, would allow for increased reaction rates, while maintaining a broad substrate scope. Given the increased observed reactivity of **5.36** towards aminoalkene **5.32**, this precatalyst was investigated for substrate scope. Table 5.3 illustrates that the utility of complex **5.36**, with less bulky 2,6-dimethylphenyl substituents at the amidate N donors, results in accelerated reaction rates and expanded substrate scope.

Complex **5.36** is able to cyclize substrates to form 5-membered pyrrolidine rings (entries 1 and 5) and 6-membered piperidine rings (entries 2 and 4), as was seen previously for imido precatalyst **5.31** (Table 4.6). Entry 3 in Table 5.3 also illustrates that 7-membered rings can be cyclized to form substituted homopiperidines. This is an important advance over other neutral catalysts, which have not been reported to cyclize substrates of this type. Conversion times for the substrates in entries 1, 2, and 3 are consistent with the expanded transition states for entries 2 and 3 being less favored than that for entry 1. While formation of the 2,2-diphenyl substituted pyrrolidine (**5.33**) requires only 2.5 h for complete conversion at 110 °C with 10 mol % catalyst, the 2,2-diphenyl substituted piperidine (**5.38**) requires 3.5 hours for complete conversion under identical reaction conditions. Cyclization of the 2,2-diphenyl substituted homopiperidine product (**5.40**) requires elevated temperatures (145 °C) and increased catalyst loading (20 mol %) to afford complete conversion within 96 h. As previously noted in Table 4.6, reducing the size of the substituents at the β -position of the substrate increases reaction times, due to geminal disubstituent effects.¹³⁰ While the 2,2-dimethyl substituted substrate (**5.41**) in entry 4 can be cyclized overnight at 110 °C, increasing the temperature to 145 °C dramatically reduced the reaction time to 3.5 h for quantitative conversion. Similarly, the internal alkene in entry 5 (**5.43**) was completely cyclized in 36 h at a temperature of 145 °C. This compares favorably to the results obtained with the bulkier imido complex **5.31**, which resulted in only 48% yield of **5.44** in 8 days. These preliminary ligand structure/catalytic activity results suggest that fine tuning of the amidate ligand set should allow for optimized reactivity with a wide variety of substrates.

Table 5.3 – Optimized hydroamination results with precatalytic complex **5.36**

Entry	Aminoalkene	Product	Time to 100% Conversion*
1	 5.32	 5.33	2.5 h, 110°C 10 % Catalyst
2	 5.37	 5.38	3.5 h, 110°C 10 % Catalyst
3	 5.39	 5.40	96 h, 145°C 20 % Catalyst
4	 5.41	 5.42	3.5 h, 145°C 10 % Catalyst
5	 5.43	 5.44	36 h, 145°C 10 % Catalyst

* Monitored by ^1H NMR with respect to 1,3,5-trimethoxybenzene as internal standard

5.3.2.4 Protonolysis Transition State Studies

The sterically accessible bis(amidate) bis(amido) complex $[\text{DMP}(\text{NO})^{\text{tBu}}]_2\text{Zr}(\text{NMe}_2)_2$ (**5.36**), allows for the synthesis of a 7-coordinate imido complex $[\text{DMP}(\text{NO})^{\text{tBu}}]_2\text{Zr}=\text{N}(2,6\text{-Me}_2\text{C}_6\text{H}_3)(\text{TPPO})(\text{Py})$ (**5.45**), which was described in Chapter 4 (4.27). This complex is characterized by a weak interaction of a molecule of pyridine *trans* to the axial imido fragment, as shown in Fig. 5.14 (A). In addition to the equatorially-placed amidate ligands, a triphenylphosphine oxide ligand rounds out the coordination sphere of the zirconium center. The proposed metallacyclic intermediate in

catalytic aminoalkene cyclohydroamination would force a geometric requirement for the complex that would be very similar to the geometry present in the pentagonal pyramidal Zr imido complex **5.31**. As such, this complex is an excellent model for this intermediate. Similarly, the 7-coordinate imido complex **5.45** is a suitable model for the transition state of the metallacycle protonolysis process. In this model, the neutral coordinated pyridine occupies the site reserved for the incoming substrate. As shown in Fig. 5.14 **B**, this model places the substrate N-H bond in the perfect geometry for σ -bond metathesis with the proposed azazirconacyclobutane fragment.

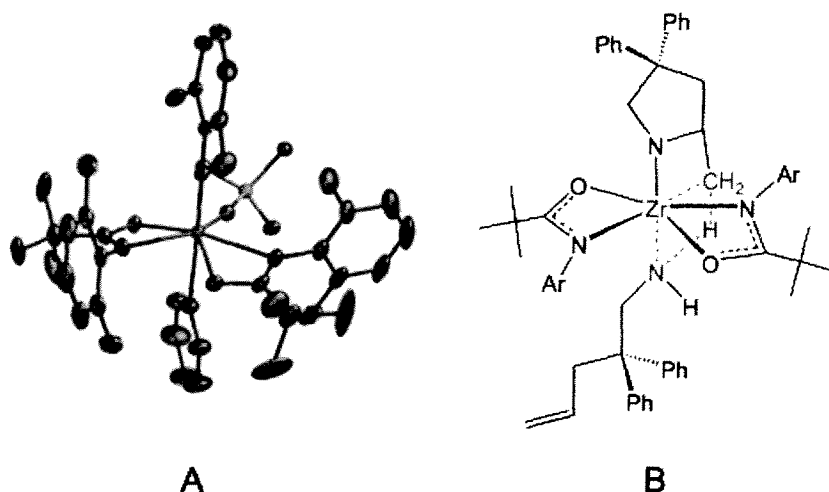


Figure 5.14 ORTEP depiction of solid-state molecular structure of 7-coordinate imido (**A**) and proposed protonolysis transition state (**B**)

As the rate-limiting process for the catalytic reaction is proposed to be the protonolysis of the metallacycle shown in Fig. 5.14, the activation parameters for this process are accessible through kinetic analysis. A highly organized, 7-coordinate transition state (Fig. 5.14 **B**) should have a large negative entropy of activation associated with it. Kinetic analysis of the cyclization reaction in Eq. 5.10 was performed by ^1H NMR spectroscopy at a series of temperatures, and an Eyring plot derived from these studies is shown in Fig. 5.15.¹³¹ As illustrated, extrapolation of the line fitting to the y-axis gives a value of $-30(3)$ e.u. for the entropy of activation (ΔS^\ddagger) for the cyclization reaction. Comparison of this value to data seen in the literature for other highly ordered transition states is in strong agreement with the transition state proposed in Fig 5.14.^{75, 124}

The enthalpy of activation (ΔH^\ddagger) was similarly determined to be +14(2) kcal mol⁻¹, supportive of the cleavage of a Zr-C bond coupled with the formation of a more favorable Zr-N bond.^{75, 124}

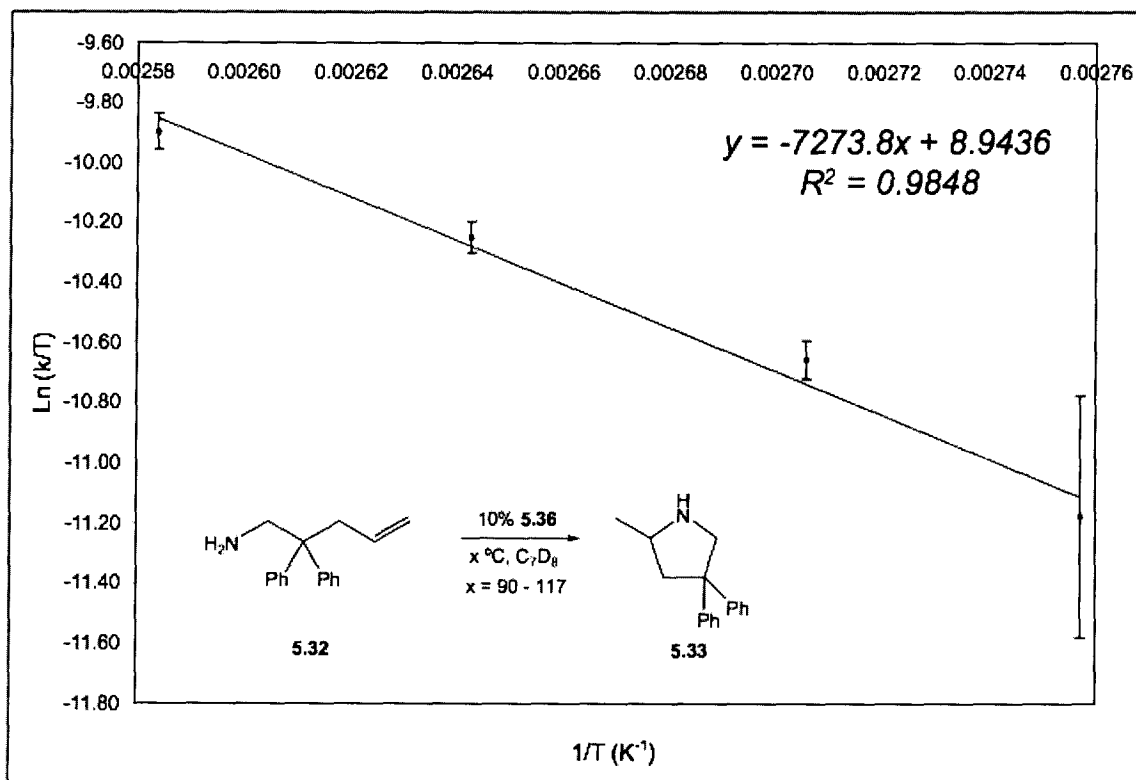


Figure 5.15 Eyring plot for cyclization of substrate **5.32** between 90 and 117 °C using amido precatalyst **5.36**

An Arrhenius plot is also shown in Fig. 5.16, where an activation energy (E_a) value of 15(2) kcal mol⁻¹ was extracted from this plot.¹³¹ This large value is consistent with a high energy transition state for the protonolysis reaction.¹²⁴ The inability to isolate the proposed metallacyclic intermediate is supportive of the fact that the metallacyclic intermediate is unstable, and will either be cleaved through a high energy protonolysis reaction, or revert to the imido precursor by retrocyclization.

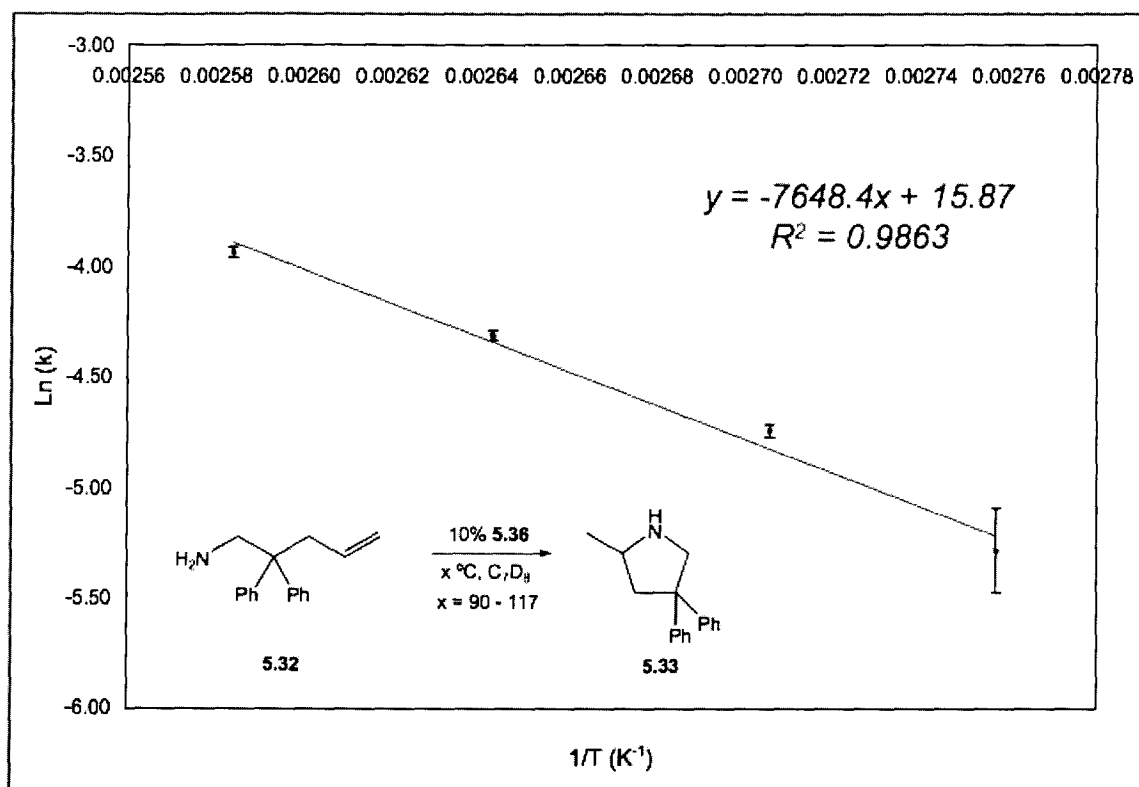


Figure 5.16 Arrhenius plot for cyclization of substrate **5.32** between 90 and 117 °C using amido precatalyst **5.36**

5.3.2.5 Stoichiometric Experiments

The kinetic analysis provided valuable insight into the reaction mechanism, and further supporting evidence in the form of structurally characterized intermediates was sought, with the primary goal being isolation of the proposed metallacyclic intermediate. Initial attempts were based on stoichiometric experiments between the Zr precatalytic species $[\text{DIPP}(\text{NO})^{\text{tBu}}]_2\text{Zr}(\text{NMe}_2)_2$ (**5.46**) and the aminoalkene substrate **5.32**. Preliminary investigations were done on NMR tube scale for ease of analysis. Complex **5.46** was chosen because of its simple ^1H NMR spectroscopic signature, as it would allow for easier characterization of the substrate centered resonances. The bulky 2,6-diisopropylphenyl groups were chosen as they offer steric protection, which could be important in stabilizing reactive intermediates. The reaction illustrated in Eq. 5.12 was performed at room temperature and monitored by ^1H NMR spectroscopy. It is evident from the ^1H NMR spectrum shown in Fig. 5.17 that the complex formed is the amido

species generated by protonolysis of one of the dimethylamido ligands by the aminoalkene molecule ($[\text{DIPP}(\text{NO})^{\text{tBu}}]_2\text{ZrNHCH}_2\text{CPh}_2\text{CH}_2\text{CH}=\text{CH}_2(\text{NMe}_2)$, (**5.47**)). The presence of two diastereomers in an approximately 1.6:1 ratio is indicated by the pairing of several peaks in the spectrum. This mixed amido complex is entirely analogous to the mixed amido complex $[\text{DIPP}(\text{NO})^{\text{Ph}}]_2\text{ZrNH}(2,6\text{-Me}_2\text{C}_6\text{H}_3)(\text{NMe}_2)$ (**4.17**) isolated as a precursor to the pentagonal pyramidal imido species **5.31** described in Chapter 4. Attempts at isolating **5.47** on a preparative scale resulted in an oily material that was resistant to recrystallization.

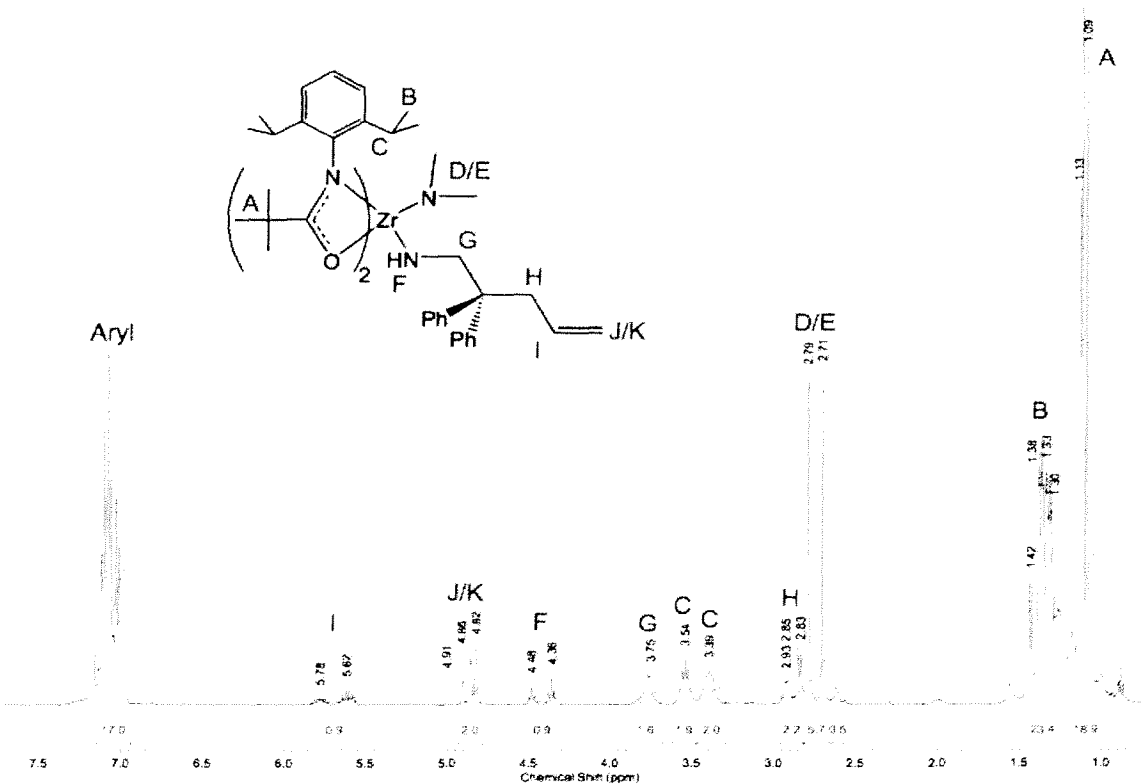
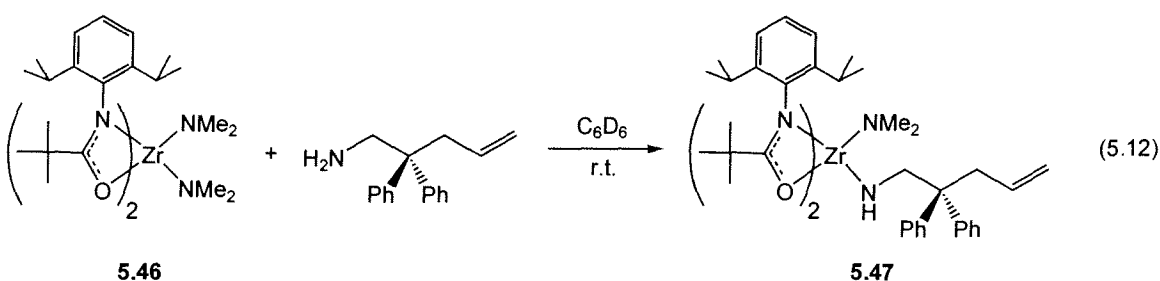
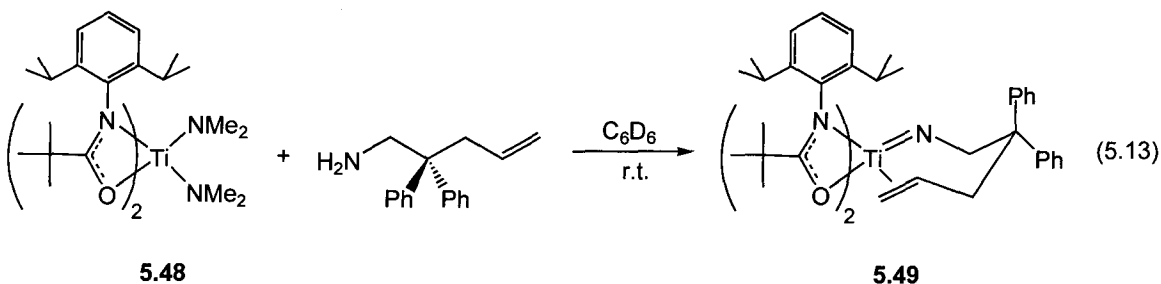


Figure 5.17 400 MHz ^1H NMR spectrum of Zr mixed amido complex **5.47**

Addition of one equiv. of TPPO to a solution of **5.47** does not result in a TPPO stabilized imido complex analogous to **5.31**. ^1H NMR spectroscopy of the reaction mixture is complicated and impossible to assign. Heating the NMR tube to catalytically relevant temperatures for the aforementioned reaction leads to turnover, rather than isolation of the desired metallacyclic species, suggesting that a metallacyclic species is too reactive to isolate, and the probable identity of this material is a mixed amido complex, with bound product. Given the previous observation that Ti is substantially less reactive than Zr for catalytic cyclohydroamination, it was hoped that intermediates could be more easily isolated using the less reactive Ti center. The reaction in Eq. 5.13 was attempted on NMR tube scale, with unexpected results. The ^1H NMR spectrum of the resulting product **5.49** is illustrated in Fig. 5.18. Although complicated, the spectrum can be completely interpreted through a series of 2D NMR experiments, as well a NOESY experiment.



The ^1H NMR spectrum of **5.49** indicates formation of a single product, with multiplet olefinic resonances observed at δ 4.94 and 5.95, and two diastereotopic doublet methylene resonances for the substrate at δ 4.07 and 4.51, as well as two diastereotopic doublet of doublet resonances for the methylene group adjacent to the olefin unit at δ 3.13 and 3.78. All of the expected amidate based resonances are also present, with four septets for the isopropyl methine protons at δ 2.55, 2.93, 3.50, and 4.02, and eight corresponding doublets for the isopropyl methyl groups, which are all inequivalent due to hindered rotation and overall C₁ symmetry. The COSY NMR spectrum clearly shows cross correlation between the two diastereotopic peaks at δ 4.07 and 4.51 for the methylene group adjacent to the N, as illustrated in the proposed structure shown in Fig. 5.18. Likewise cross peaks are seen between the expected diastereotopic doublets of doublets at δ 3.13 and 3.78, for the methylene protons adjacent to the olefin unit. The

wide separation between these diastereotopic peaks is consistent with a chair-like geometry for the complex, as illustrated in Fig. 5.18.

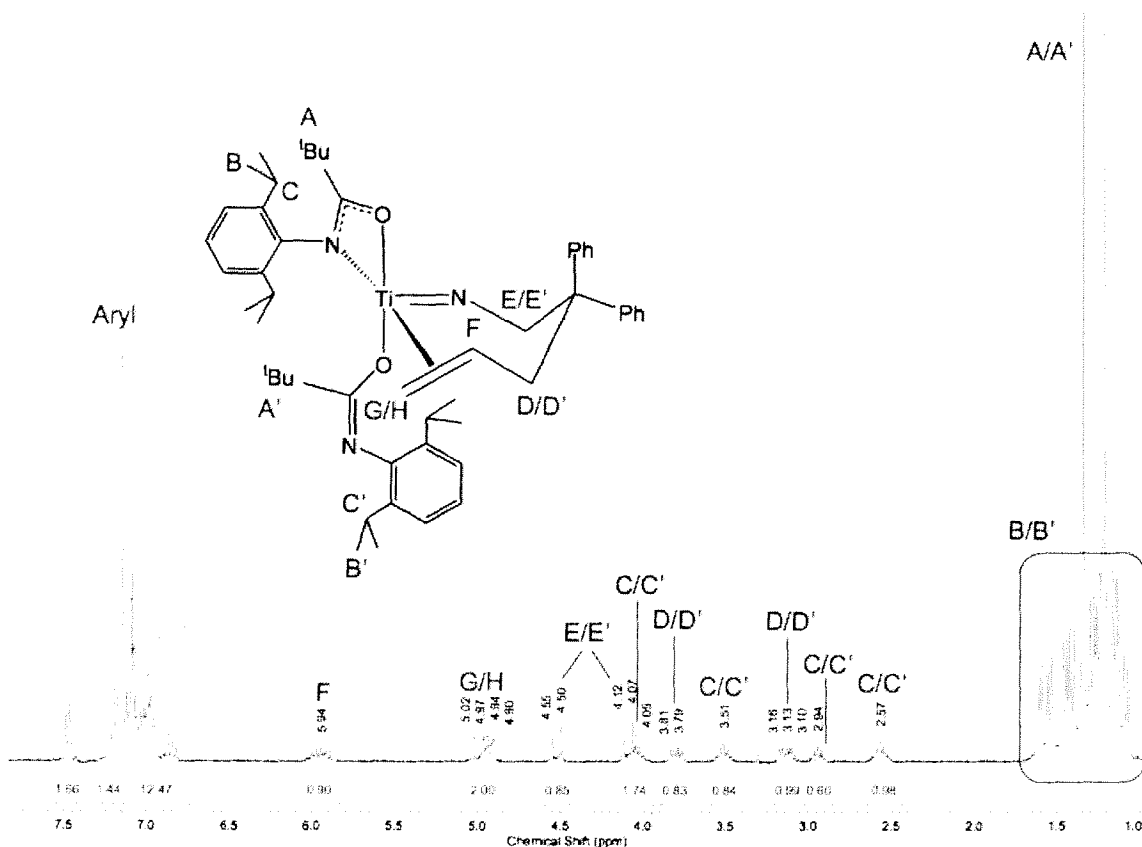


Figure 5.18 400 MHz ¹H NMR spectrum of Ti imido complex **5.49**

Additional support for the structural assignment in Fig. 5.18 was obtained by selective NOE experiments on the aminoalkene resonances for complex **5.49**. Strong NOE enhancements are observed between the two methylene groups, particularly for one of the two signals of each pair of diastereotopic resonances. This is suggestive of a chair-like conformation where 1,3-diaxial through-space interactions are observable by a nuclear Overhauser effect. Analogous NOE experiments performed on the free substrate showed no strong enhancements, supporting the notion that the metal complex is exhibiting a rigid conformational structure that is not present in the uncomplexed form. Coordination of the olefin to the metal center is speculative, but may be indicated by a shift of the olefinic resonances from δ 4.96 and 5.44 in the free substrate to δ 4.94 and

5.94 in **5.49** as seen in Fig 5.18. Finally, an imido type linkage is supported by a ^{13}C resonance at δ 78.7 ppm, which was correlated to the methylene group adjacent to the N by an HMQC experiment. Related alkyl substituted Ti imido complexes studied by Mountford and coworkers exhibit similar chemical shifts for the carbon adjacent to the imido fragment.¹³² By comparison, the chemical shift for the analogous methylene group in the mixed amido Zr complex **5.47** appears much farther upfield at δ 52.8. The downfield shift of this carbon in the imido complex **5.49** indicates that substantial deshielding is occurring due to strong π -donation of the imido N to the Ti center. The other resonances observed in the ^{13}C NMR spectrum of **5.49** are consistent with the proposed structure and are unremarkable.

Although the solution phase data for **5.49** is highly supportive of an imido-olefin complex with a chair-like conformation, additional confirmation of the structure of this species was sought in the form of X-ray crystallographic studies. A preparative scale synthesis of **5.49** was undertaken, and the ^1H NMR spectrum for the isolated material is identical to that seen for the NMR tube reaction discussed above. Isolation of the brown solid was accomplished in high yield, and crystals suitable for X-ray crystallographic analysis were isolated from a saturated toluene solution. The solid-state molecular structure of **5.49** $\cdot\text{HNMe}_2$ is shown in Fig. 5.19, with selected bond lengths and angles listed in Table 5.4 and crystallographic details located in Table A5.1 (Appendix A).

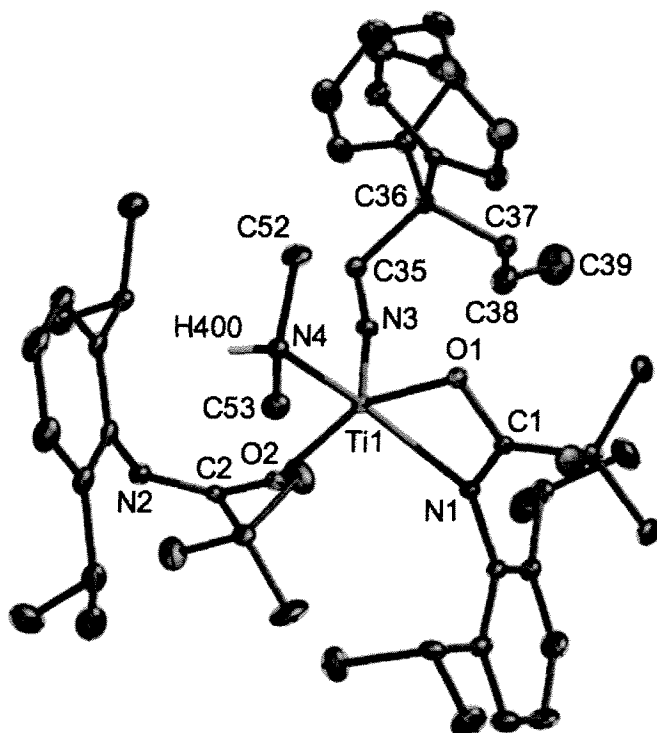


Figure 5.19 ORTEP depiction of solid-state molecular structure (ellipsoids at 30% probability) of κ^2 -[^{DIPP}(NO)^{tBu}]- κ^1 -[^{DIPP}(NO)^{tBu}]₂Ti=NCH₂CPh₂CH₂CH=CH₂ (NHMe₂), **5.49·HNMe₂** (non-N-H hydrogens omitted for clarity)

Table 5.4 Selected Bond Distances (Å) and Angles (°) for κ^2 -[^{DIPP}(NO)^{tBu}]- κ^1 -[^{DIPP}(NO)^{tBu}]₂Ti=NCH₂CPh₂CH₂CH=CH₂(NHMe₂), **5.49·HNMe₂**

Lengths		Lengths/Angles		Angles	
Ti(1)-N(1)	2.171(3)	N(2)-C(2)	1.275(5)	N(4)-Ti(1)-O(2)	91.82(12)
Ti(1)-N(3)	1.688(3)	C(38)-C(39)	1.300(7)	O(1)-Ti(1)-N(3)	106.47(13)
Ti(1)-N(4)	2.166(3)	N(1)-Ti(1)-N(3)	116.50(13)	O(1)-Ti(1)-O(2)	145.46(11)
Ti(1)-O(1)	2.068(2)	N(1)-Ti(1)-N(4)	131.73(12)	O(2)-Ti(1)-N(3)	108.02(13)
Ti(1)-O(2)	1.904(3)	N(1)-Ti(1)-O(1)	61.85(11)	C(2)-O(2)-Ti(1)	145.8(2)
O(1)-C(1)	1.296(4)	N(1)-Ti(1)-O(2)	100.30(11)	N(2)-C(2)-O(2)	124.5(3)
N(1)-C(1)	1.314(5)	N(4)-Ti(1)-N(3)	103.22(14)	C(35)-C(36)-C(37)	108.9(3)
O(2)-C(2)	1.334(4)	N(4)-Ti(1)-O(1)	82.06(12)	C(37)-C(38)-C(39)	125.9(5)

The solid-state molecular structure of **5.49·HNMe₂** clearly differs from the proposed solution phase structure. The complex is characterized by an imido Ti=N linkage, with a very short Ti(1)-N(3) bond length of 1.688(3) Å. This assignment is further supported by the nearly linear C(35)-N(3)-Ti(1) bond angle of 169.4(3)°. It is also

notable that one of the amidate ligands in **5.49**·HNMe₂ is bound to the Ti center in a κ^1 -form, which was seen previously for complex κ^2 -[^{DMP}(NO)^{tBu}]- κ^1 -[^{DMP}(NO)^{tBu}]Zr(NMe₂)₂(Py) (**2.19**) in Chapter 2. In this case, dimethylamine liberated during the formation of the imido complex is coordinated to the Ti center, displacing one of the amidate N donors. It was noted previously in Chapter 2 that the amidate ligand set tends to bind to Ti, Zr, and Hf in an unsymmetric fashion, consistent with an alkoxyimine bonding description. The relevance of this description is particularly apparent for the κ^1 -bound amidate ligand, which has a C(2)-O(2) distance of 1.334(4) Å, consistent with a single bond, and a C(2)-N(2) distance of 1.275(5) Å, which falls in the range expected for a double bond. A simplified core structure of complex **5.49**·HNMe₂ is shown in Fig. 5.20, where it is readily apparent that the imido complex exhibits a distorted square pyramidal geometry. This pyramidalization was previously discussed in Chapter 4, where the weakly donating amidate ligands resulted in a highly unusual pentagonal pyramidal Zr imido complex. The pyramidalization of this complex optimized the orbital overlap for the imido fragment. A similar effect is being observed with complex **5.49**·HNMe₂.

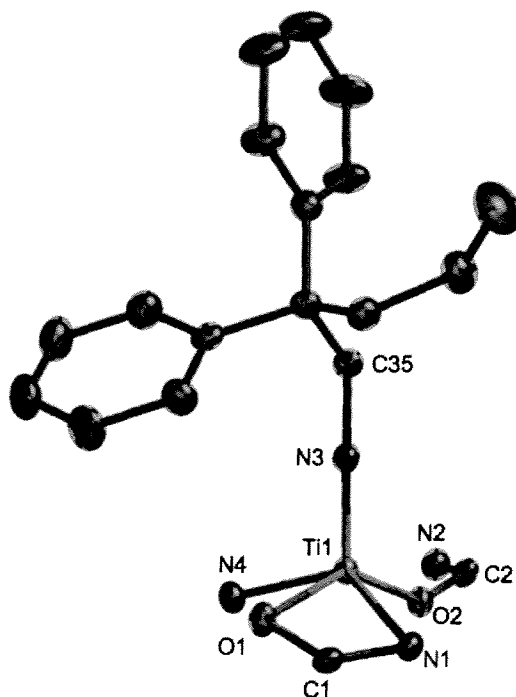


Figure 5.20 ORTEP depiction of core structure of **5.49**·HNMe₂ (hydrogen atoms and amidate/dimethylamine substituents removed for clarity)

There is no evidence for coordinated dimethylamine in the ^1H NMR spectrum of **5.49**, which suggests that the material characterized in the solid-state is preferentially crystallized from the bulk material, where the dimethylamine is present as a byproduct of the transamination reaction to generate the imido complex. It is reasonable that the dimethylamine with its hard N donor acts as a better ligand for Ti in the solid-state than the olefin unit of the aminoalkene substrate. In the solution phase, the highly volatile dimethylamine could be lost and coordination of the alkene could dominate, where the entropically favorable chelate effect generated by coordination of the alkene would be a likely driving force for this process. ^1H NMR spectroscopy of the single crystals matches that seen for the bulk material, suggesting that the proposed solution phase structure is dominant, and the crystallographically determined solid-state molecular structure is largely due to the different solubility characteristics of the amine stabilized imido and the olefin stabilized imido complex. Electron impact mass spectrometry shows a peak at m/z 803, likewise suggesting a lack of coordinated dimethylamine. However, with this harsh ionization method, it is not atypical that a relatively labile ligand such as dimethylamine would be lost from the metal center in the mass spectrometer.

While it was hoped that a short lived azametallacyclobutane complex might be observable at high temperatures, variable temperature ^1H NMR experiments on **5.49** showed no changes over a temperature range of $-30\text{ }^\circ\text{C}$ to $110\text{ }^\circ\text{C}$, indicating that the imido form of this complex must be much more stable than a proposed metallacyclic species. In order to ensure that **5.49** is a catalytically relevant complex, a catalytic hydroamination experiment was performed, which clearly illustrates that this species is capable of performing the catalysis for which it is invoked as an intermediate. Cyclization of substrate **5.32**, as shown in Eq. 5.10, by the Ti imido complex **5.49** was compared directly to its bis(amido) precursor **5.48**, and the natural log plots of substrate consumption vs. time are shown in Fig. 5.21 for the two complexes. Here the imido complex is slightly faster than the bis(amido) complex, which can be attributed to the presence of an additional equivalent of competitive donor, dimethylamine, in the NMR tube for the catalytic run with the bis(amido) complex.

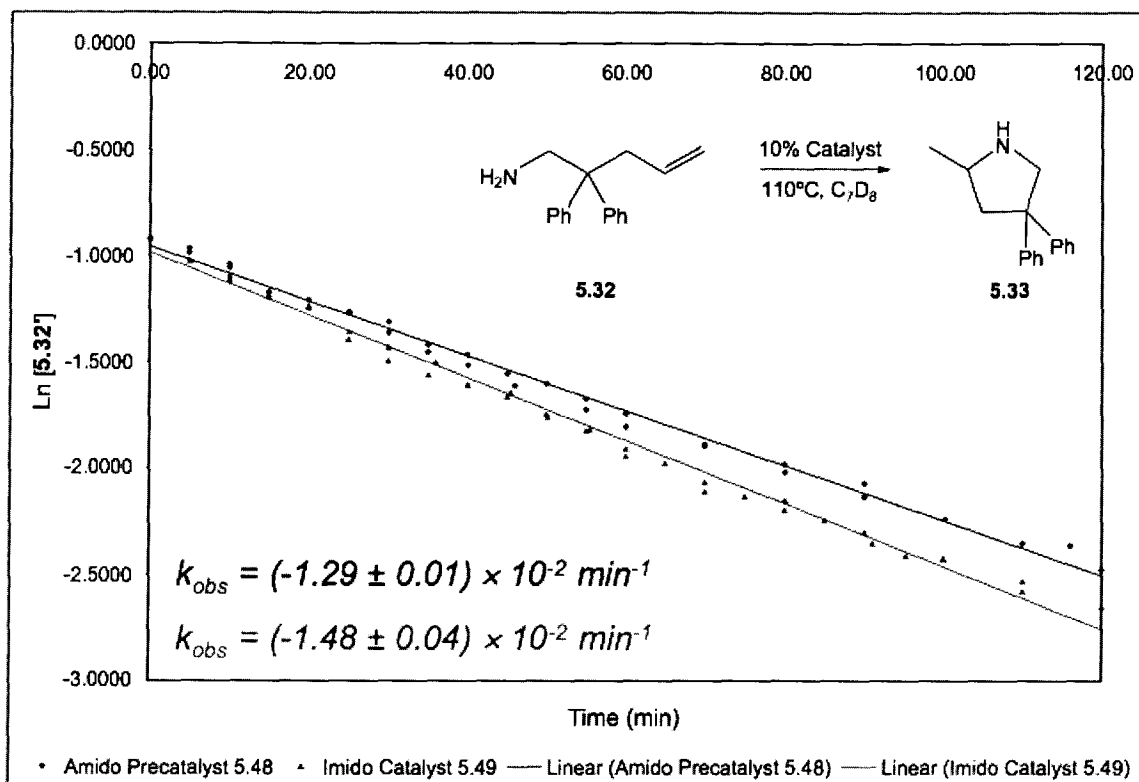


Figure 5.21 $\ln[\text{substrate}]$ vs. time for Ti imido **5.49** and Ti bis(amido) **5.48** showing similar rates and first-order substrate consumption

Given the observation of coordinated dimethylamine in the solid-state molecular structure of **5.49**· HNMe_2 , we favor the assignment of the resting state for this catalytic system as an amine stabilized imido complex, where either the eliminated dimethylamine, or extra substrate or product is coordinated to the imido complex to stabilize it. It is reasonable, based on the data presented thus far, that a very high energy metallacyclic species may form at catalytically relevant temperatures. Due to the far poorer orbital overlap in such a complex as compared to the optimal overlap possible for the pyramidalized imido complex, this reactive metallacycle could either revert to the open imido form, or be protolytically cleaved by substrate (under catalytic conditions). The rate-determining protonolysis step therefore is likely impacted by the extremely high energy of the metallacyclic intermediate. As mentioned earlier, a primary kinetic isotope effect (KIE) of 2.14 ± 0.28 was observed for the cyclization of **5.32**, which is small compared to larger values between 5 and 10, which might be expected for such a reaction. The presence of coordinated substrate in the catalyst resting state may be to

blame for this low KIE value, where the importance of coordinated substrate in other steps may lead to lower than expected KIE values.

5.3.2.6 Diastereoselectivity

The proposed solution phase structure of **5.49** suggests a chair-like transition state for the cyclization of the alkene unit with the imido fragment. Examination of the diastereoselectivity for this reaction supports this transition state for cyclization. In Chapter 4, an α -methyl substituted substrate (**4.51**) was cyclized in reasonable yield, with very high diastereomeric excess (92 %), with the *anti* regioselectivity being favored. This is consistent with minimized 1,3-diaxial interactions, which would place the α -methyl preferentially in the equatorial position of the pseudo-6-membered ring transition state. The two transition state conformations and their resulting hydroamination products are illustrated in Fig. 5.22.

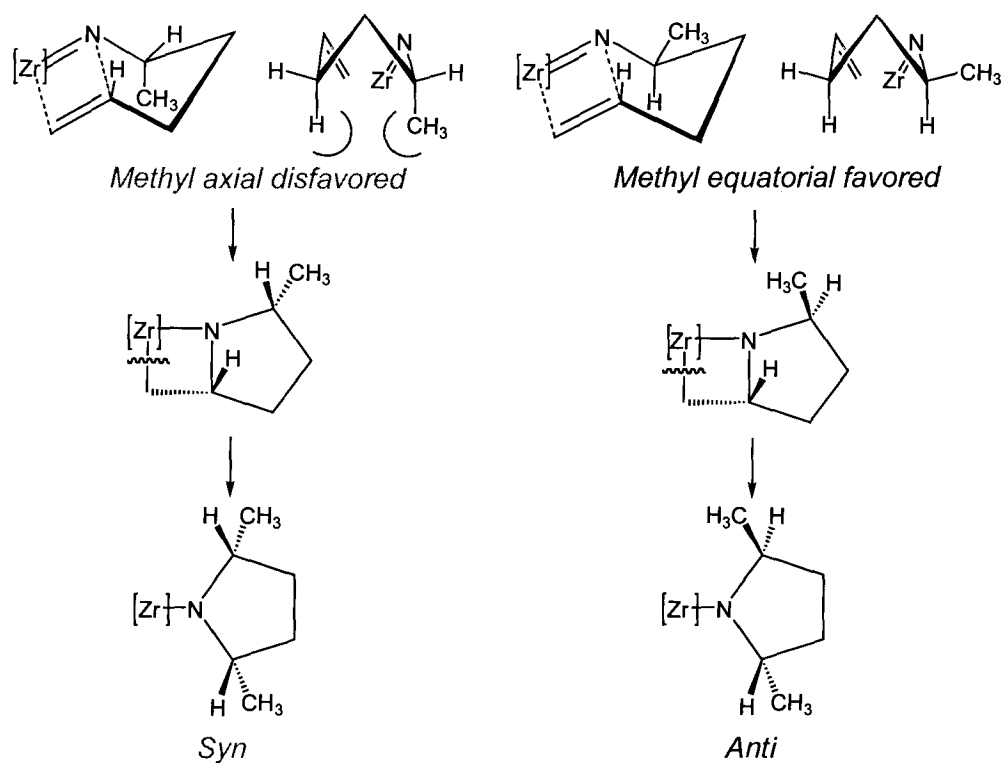
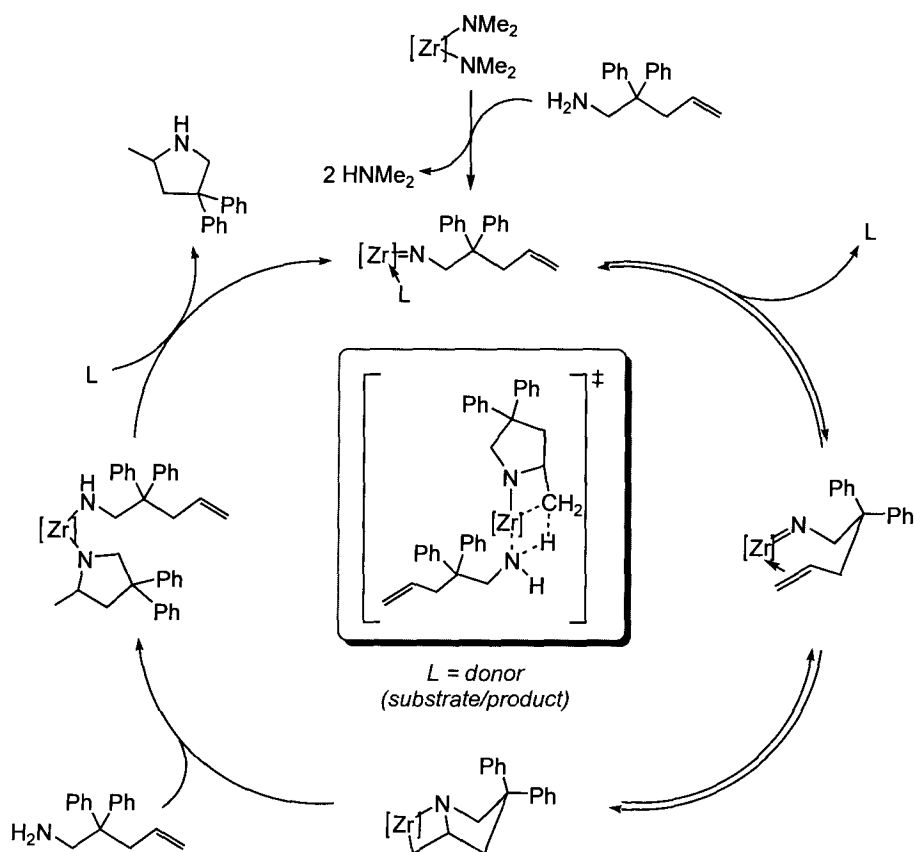


Figure 5.22 Rationalization of diastereoselectivity of cyclization

5.3.3 Summary of Neutral Catalyst Studies

Neutral bis(amidate) bis(amido) complexes are proposed to cyclize primary aminoalkenes through an imido intermediate, which undergoes a cycloaddition reaction with the pendant alkene. This is supported by the solid-state molecular structure characterization of the amine stabilized Ti imido complex **5.49**·HNMe₂, and the successful application of this complex in the catalytic hydroamination of aminoalkene **5.32**. Amine stabilized imido complexes of this type are thus believed to be the resting state of this family of catalysts. A chair-like geometry for this imido complex in solution is supported by NMR spectroscopic studies, which indicate that the coordinated amine is displaced by the pendant alkene unit. In addition, the high diastereoselectivity observed for the cyclization of an α -methyl substituted aminoalkene is supportive of a chair-like geometry for the cycloaddition transition state. The lack of reactivity of these neutral complexes with the N-methyl substituted substrate **5.34** also supports an imido mechanistic proposal, where these secondary aminoalkene substrates cannot form a M=N imido linkage.

Kinetic investigations support an imido cycloaddition mechanism, with first-order dependence of the reaction on substrate concentration, indicating metallacycle protonolysis as the rate-determining process in the catalytic cycle. This was verified by a primary kinetic isotope effect of 2.14 ± 0.28 . The metallacycle formed through cycloaddition was not isolable, and is proposed to be a high energy intermediate en route to product formation. A 7-coordinate transition state is proposed for the rate-determining protonolysis reaction, and reaction parameters determined by an Eyring plot support this proposal, with $\Delta S^\ddagger = -30(3)$ e.u. and $\Delta H^\ddagger = +14(2)$ kcal mol⁻¹. The high energy nature of this transition state is also supported by an $E_a = 15(2)$ kcal mol⁻¹, indicating that the metallacycle formed is unstable, reverting back to the open imido form in the absence of additional protic donors. The overall mechanistic proposal for this process is given in Scheme 5.8.



Scheme 5.8

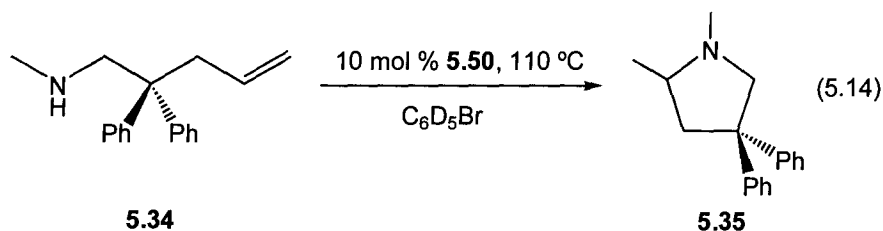
5.4 Cationic Alkene Hydroamination Investigations

5.4.1 Introduction

While the lack of reactivity of neutral imido and bis(amido) precatalysts with the secondary aminoalkene substrate **5.34** is supportive of an imido-based mechanism for cyclohydroamination of alkenes, the possibility of a σ -bond insertion mechanism was probed with cationic alkyl complexes supported by amidate ligands. Reports by the groups of Hultsch and Scott indicate that cationic Ti and Zr species are capable of the catalytic cyclohydroamination of secondary aminoalkenes.^{114, 115} The σ -bond insertion mechanism proposed for these species was described in Scheme 5.7, and is entirely analogous to that demonstrated by Marks and coworkers for rare-earth catalysis.^{73, 75}

5.4.2 Results and Discussion

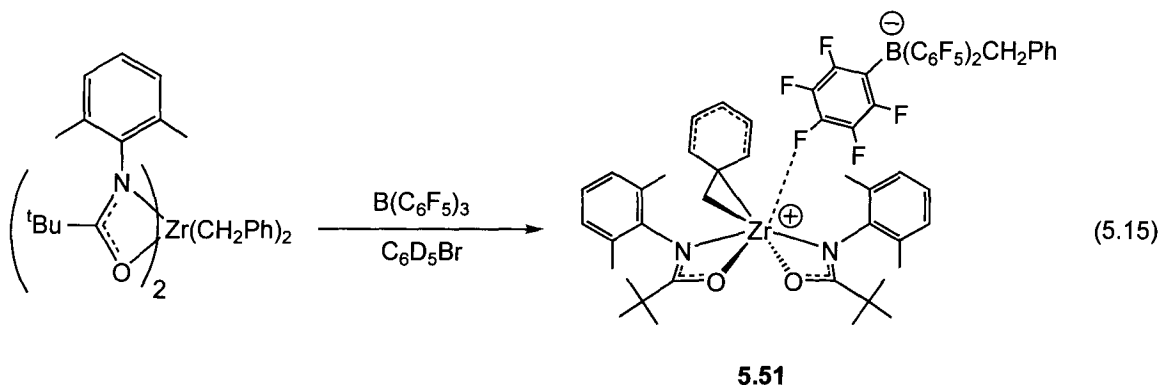
Alkyl abstraction to generate cationic alkyl complexes was investigated in Chapter 3, through reaction of $[\text{Ph}_3\text{C}][\text{B}(\text{C}_6\text{F}_5)_4]$ with the dibenzyl complex $[\text{DMP}(\text{NO})^{\text{tBu}}]_2\text{Zr}(\text{CH}_2\text{Ph})_2$ (**3.9**) to generate a cationic benzyl complex $[[\text{DMP}(\text{NO})^{\text{tBu}}]_2\text{ZrCH}_2\text{Ph}][\text{B}(\text{C}_6\text{F}_5)_4]$, **5.50** (**3.24**). To test the feasibility of cationic amidate complexes as hydroamination precatalysts, 10 mol % of the *in situ* generated cationic benzyl complex **5.50** was reacted with the N-methylated substrate **5.34** and monitored by ^1H NMR spectroscopy, as shown in Eq. 5.14. This reaction is extremely rapid at 110 °C, and complete conversion of **5.34** to **5.35** is observed in less than 1 hour. This reaction can also be performed at lower temperatures (65 °C), but requires extended reaction times (~ 24 h).



Given the *in situ* generation of **5.50** and the inability to isolate this complex, it is possible that unreacted $[\text{Ph}_3\text{C}][\text{B}(\text{C}_6\text{F}_5)_4]$ or $[\text{DMP}(\text{NO})^{\text{tBu}}]_2\text{Zr}(\text{CH}_2\text{Ph})_2$ is responsible for the cyclization of **5.34**. To test this hypothesis, both $[\text{DMP}(\text{NO})^{\text{tBu}}]_2\text{Zr}(\text{CH}_2\text{Ph})_2$ and $[\text{Ph}_3\text{C}][\text{B}(\text{C}_6\text{F}_5)_4]$ were reacted with **5.34** to determine if any background reaction was occurring. The dibenzyl complex $[\text{DMP}(\text{NO})^{\text{tBu}}]_2\text{Zr}(\text{CH}_2\text{Ph})_2$ does not cyclize **5.34** even after several days at 110 °C. However, with 10 mol % of $[\text{Ph}_3\text{C}][\text{B}(\text{C}_6\text{F}_5)_4]$, **5.34** is cyclized at 110 °C in less than 1 hour. This background reaction makes it impossible to verify that the cationic complex **5.50** is responsible for the cyclization of **5.34**.

Since $[\text{Ph}_3\text{C}][\text{B}(\text{C}_6\text{F}_5)_4]$ is an active catalyst for the cyclization of aminoalkene **5.34**, alternate routes were investigated for the synthesis of cationic alkyl complexes. Unlike $[\text{Ph}_3\text{C}][\text{B}(\text{C}_6\text{F}_5)_4]$, combination of the neutral borane $\text{B}(\text{C}_6\text{F}_5)_3$ with aminoalkene **5.34** results in no cyclization at 110 °C. As demonstrated in Eq. 5.15, $\text{B}(\text{C}_6\text{F}_5)_3$ is able to abstract a benzyl group from $[\text{DMP}(\text{NO})^{\text{tBu}}]_2\text{Zr}(\text{CH}_2\text{Ph})_2$ to yield the cationic complex $[[\text{DMP}(\text{NO})^{\text{tBu}}]_2\text{ZrCH}_2\text{Ph}][\text{B}(\text{C}_6\text{F}_5)_3\text{CH}_2\text{Ph}]$, **5.51**. ^1H NMR spectroscopic data of **5.51** are very similar to those for **5.50**, which was discussed in Chapter 3 (**3.24**), and support the

structure shown in Eq. 5.15. Interestingly, while the two Zr bound benzylic protons in **5.51** appear as a singlet at δ 3.48, the two B bound benzylic protons are not observed in the ^1H NMR spectrum. This is likely due to the neighboring quadrupolar B nucleus causing excessive line broadening for these protons.



Utilizing 10 mol % of **5.51** generated *in situ*, the catalytic cyclohydroamination of **5.34** to **5.35** is extremely rapid, going to completion in less than 1 hour at 110 °C. Monitoring this reaction by ^1H NMR spectroscopy indicates that room temperature reactivity is occurring, with nearly 50 % of the substrate olefinic peaks consumed within 15 minutes. The tertiary amine **5.35** generated upon cyclization of **5.34** is an excellent donor for the highly electrophilic cationic Zr center, and product inhibition likely stalls the reaction after approximately 5 turnovers. As Fig 5.23 illustrates, the cyclization of **5.34** has no dependence on substrate concentration (blue line). As the concentration of product (**5.35**) increases, a shift in the slope of the line can be observed (red line), corresponding to product inhibition. Zero-order substrate dependence for reactions of this type has been observed by Marks and coworkers for isoelectronic rare-earth catalysts.⁷⁵ Assuming that the energetics of σ -bond insertion for the cationic Zr center is similar to that for rare-earth complexes, the observed zero-order dependence of this reaction on substrate is supportive of the σ -bond insertion mechanism illustrated in Scheme 5.7.

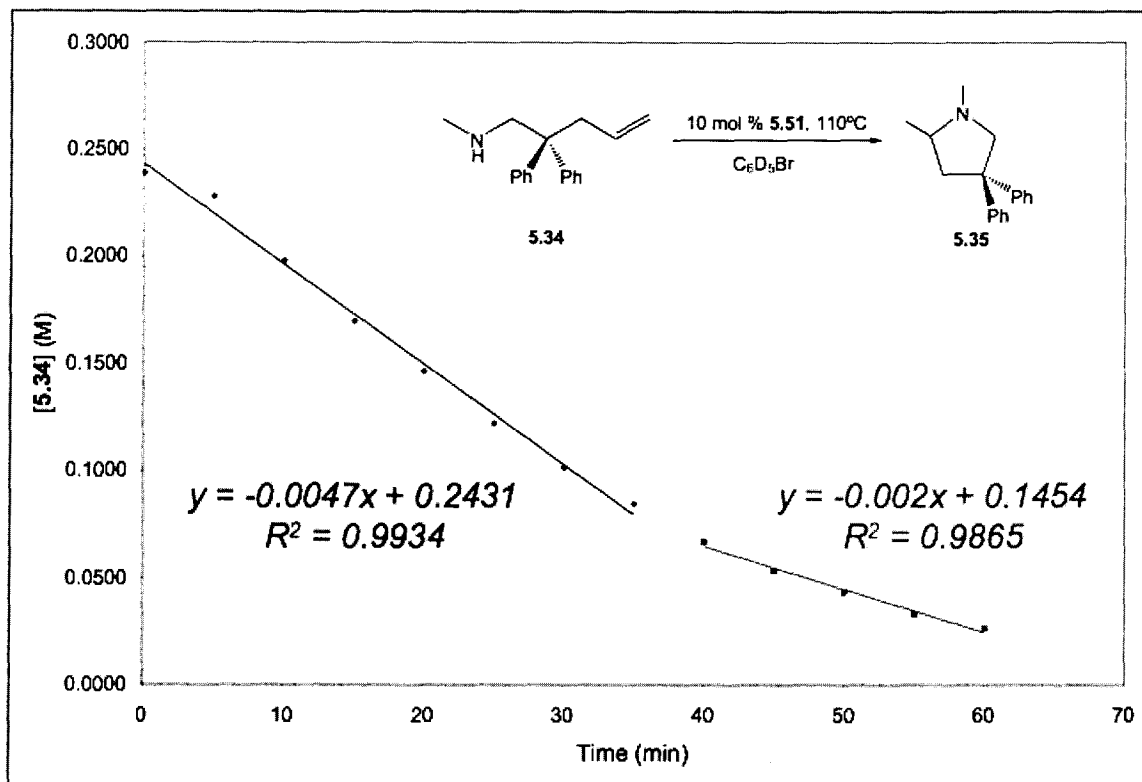
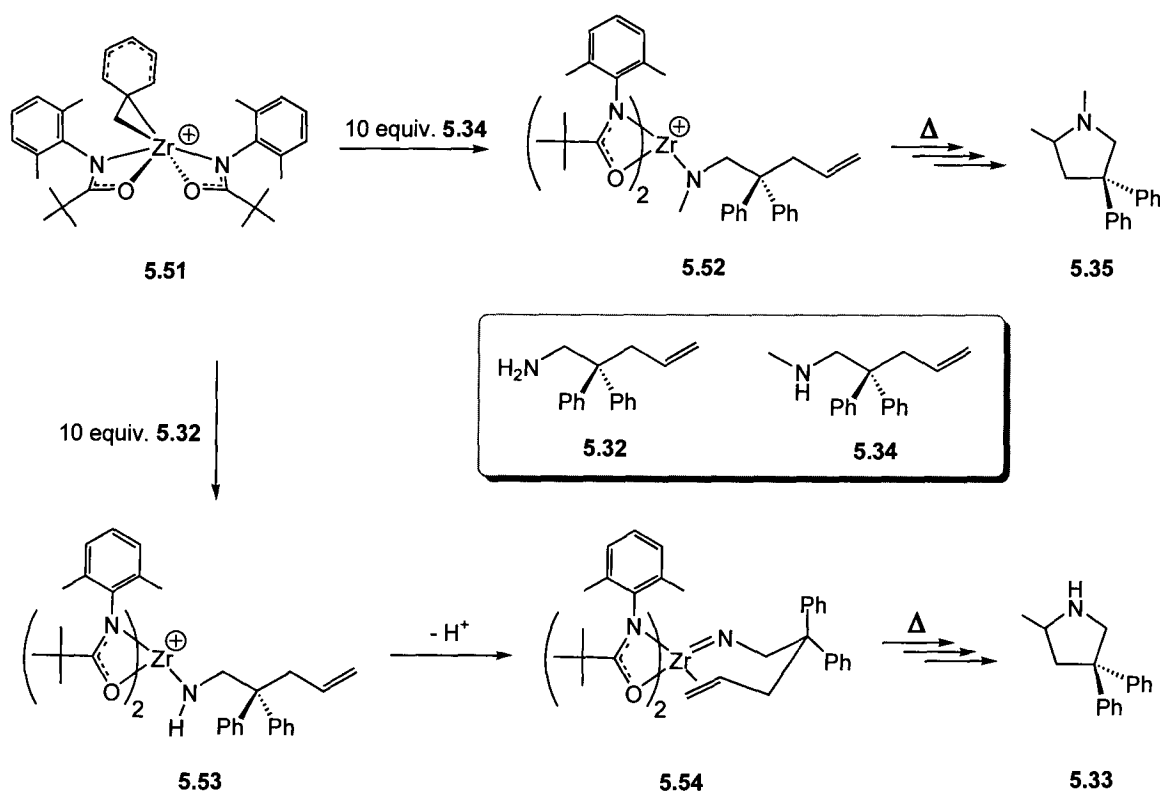


Figure 5.23 [5.34] vs. time plot for cationic Zr precatalyst **5.51** showing zero-order substrate dependence and product inhibition

Upon addition of aminoalkene **5.34** to the blood red solution of **5.51**, an immediate color change to bright yellow is observed, presumably corresponding to the formation of a cationic amido complex (**5.52**) as shown in Scheme 5.9. Over time this solution fades and becomes colorless, possibly indicating the formation of an amine coordinated cationic amido complex. The cationic Zr catalysts reported by Hultsch¹¹⁴ and Scott¹¹⁵ are inactive for the cyclohydroamination of primary aminoalkenes. It was proposed that proton loss, resulting in generation of catalytically inactive imido complexes, was responsible for this lack of reactivity. However, attempts by Sita and coworkers to deprotonate the Zr-N-H proton in cationic amido complexes supported by amidinate and Cp* ligands indicate that amine coordination is a more likely deactivation pathway than deprotonation.¹¹⁶ Reaction of 10 mol % of **5.51** with primary aminoalkene substrate **5.32** results in the same color changes noted for previously for the reaction of **5.51** with **5.34**. However, monitoring the reaction of **5.32** with **5.51** by 1H NMR spectroscopy at room temperature shows that no cyclization of the substrate occurs at

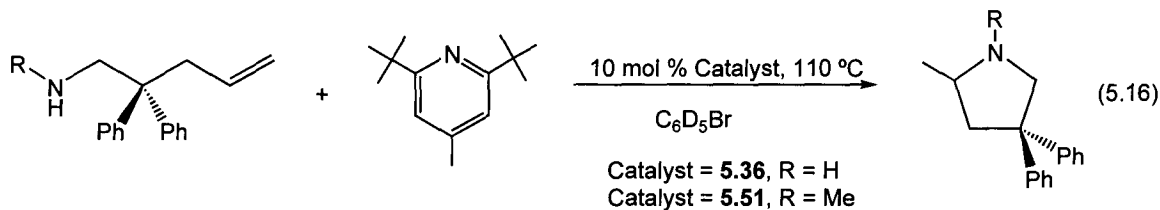
room temperature, in contrast to the observations for the N-methyl substituted substrate **5.34**. While the cationic catalysts described by Hultsch and Scott possibly generate catalytically inactive imido complexes, imido complexes supported by amidate ligands have been shown to facilitate aminoalkene cyclohydroamination.¹²⁵ Upon heating the NMR tube to 110 °C, complete cyclization of **5.32** to **5.33** is observed overnight. This is supportive of the generation of an amido complex **5.53**, which undergoes rapid H⁺ loss to generate an imido complex **5.54**, which is catalytically active for cyclization at elevated temperatures, as shown in Scheme 5.9.



Scheme 5.9 [B(C₆F₅)₃CH₂Ph] anion omitted for clarity

In addition to the imido cycloaddition and σ -bond insertion mechanisms presented previously, H⁺ catalyzed hydroamination is also a possibility, and has been demonstrated by Bergman and coworkers.¹¹⁷ To test for this possibility for both the neutral bis(amido) precatalyst **5.36** and the cationic precatalyst **5.51**, catalytic reactions were performed with 1 equiv. of a bulky base (4-methyl-2,6-di*tert*-butylpyridine), as

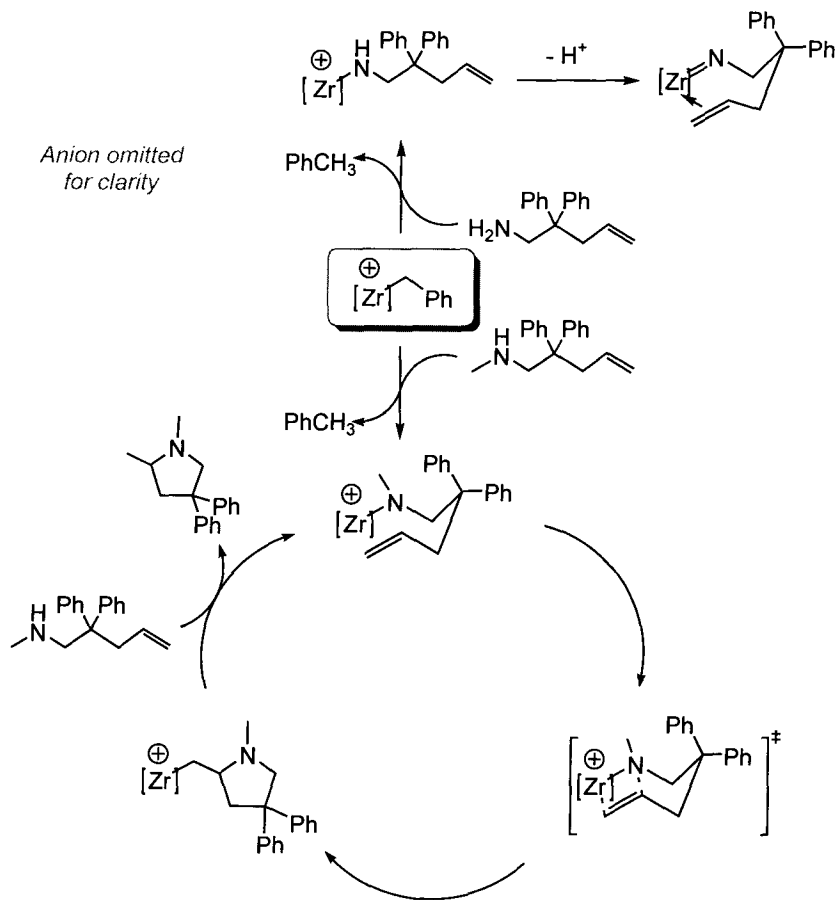
shown in Eq. 5.16. This bulky base was chosen to eliminate the possibility of inhibition through coordination of the base to the metal center.



For both the neutral and cationic precatalysts, this reaction is uninhibited by the presence of the base. This supports the assertion that the neutral amidate supported bis(amido) precatalysts are operating via an imido-based mechanism, and the cationic amidate supported precatalysts are proceeding through a σ -bond insertion mechanism.

5.4.3 Summary of Cationic Catalyst Systems

A σ -bond insertion mechanism is proposed for the cyclohydroamination of secondary aminoalkenes with cationic bis(amidate) benzyl complexes, and is shown in Scheme 5.10. This proposal is supported by kinetic studies that demonstrate zero-order substrate dependence, implying that the insertion process is rate-determining for this reaction. Control experiments verified that the *in situ* generated cationic complex was responsible for the catalytic reactivity, and activating reagents and adventitious protons were not facilitating this transformation. The cationic amidate complexes are also active for the cyclization of primary aminoalkene substrates. However, this reaction does not begin to occur at room temperature, as seen for the secondary substrates. Loss of H^+ to generate imido complexes identical to those derived from neutral bis(amido) precatalysts is proposed. Unlike the imido complexes proposed by Hultsch and Scott, these imido species are catalytically active as had been seen previously, and proceed through the mechanism shown in Scheme 5.8.



Scheme 5.10

5.5 Conclusions

Investigations with intramolecular cyclizations of aminoalkynes illustrated that bis(amidate) bis(amido) complexes were active for alkyne hydroamination. Using these precatalytic species, enhanced reactivity was observed upon increasing the electron withdrawing character of the amidate ligands. This demonstrated the ability to tune reactivity with this new modular ligand system. Extension of hydroamination catalysis to aminoalkenes was also possible with amidate supported Zr imido complexes, as presented in Chapter 4.

An imido mediated cycloaddition mechanism is proposed for the catalytic cyclohydroamination of primary aminoalkenes with neutral amidate supported precatalysts. This mechanism is supported by the lack of reactivity with secondary aminoalkene substrates, which are unable to form M=N imido linkages. A series of

kinetic investigations likewise support this mechanistic proposal, including substrate and catalyst dependence studies, and primary kinetic isotope effect studies. Solid-state characterization of an amine stabilized imido complex with the substrate further supports this mechanistic proposal, and this complex is proposed to be the resting state of the catalytic system. The chair-like geometry proposed in solution for this structure is supported by NMR spectroscopic studies, and rationalizes the diastereoselectivity observed for the cyclization of an α -methyl substituted primary aminoalkene. A 7-coordinate intermediate is proposed for the rate-determining protonolysis reaction, as illustrated in Scheme 5.8. This is further supported by reaction parameters determined from Eyring and Arrhenius plots.

In contrast to the neutral amidate complexes, cationic bis(amidate) benzyl complexes are proposed to cyclize secondary aminoalkenes through the σ -bond insertion mechanism shown in Scheme 5.10. Control experiments and preliminary kinetic studies of substrate dependence support this mechanistic proposal. Reactivity with primary aminoalkenes leads to proton loss, generating a proposed neutral imido complex analogous to those seen for the neutral bis(amidate) bis(amido) precatalysts. In contrast to all other known group 4 hydroamination catalysts, the amidate catalyst family can function through both imido-cycloaddition and σ -bond insertion mechanisms depending on the nature of the substrate and the catalyst.

5.6 Experimental

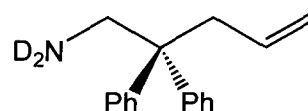
5.6.1 General Considerations

Refer to Chapter 2, section 2.6.1

5.6.2 Starting Materials and Reagents

Refer to Chapter 2, section 2.6.2. Aminoalkenes **5.32**, **5.34**, **5.37**, **5.39**, **5.41**, and **5.43** were synthesized according to literature procedures.⁷⁵ Hydroamination products **5.33**, **5.35**, **5.38**, **5.40**, **5.42** and **5.44** are known compounds, and NMR spectroscopic data for these compounds matches literature values.⁷⁵

Deuterated substrate **5.32-*d*₂** was synthesized through H/D exchange between D₂O and **5.32**. Due to the poor miscibility of **5.32** in water, **5.32** was first dissolved in THF and an excess of D₂O was added (~ 50 equiv.). The solution was stirred for 18 h, and then extracted with Et₂O. The organic fraction was collected and excess solvent was removed under reduced pressure to yield the product as an oil. This procedure was repeated two more times to ensure sufficient incorporation of deuterium. The resulting oil was vacuum distilled at 165 °C, and degassed by successive freeze-pump-thaw cycles, before storing in the glovebox. The deuterated substrate was not stored over molecular sieves due to the possible presence of traces of H⁺. By ¹H NMR spectroscopy, **5.32-*d*₂** was isolated with 92% incorporation of deuterium.



5.6.3 Kinetic Investigations

All NMR tube kinetic investigations were performed in the same manner to ensure consistency. As much as possible, the same spectrometer (300 MHz Bruker Avance, equipped with a variable temperature probe) was utilized to reduce the possibility of random errors. All neutral precatalyst kinetics experiments were performed with **5.32** as substrate. Reaction progress was monitored by the disappearance of the olefinic signals of the substrate over time (δ 4.96 and 5.44), and the average value of the integrations for the two signals was utilized. In general, kinetic runs were collected two or three times to ensure reproducibility, and error limits were derived from the observed errors associated with these duplicate runs. An internal standard (1,3,5-trimethoxybenzene) was utilized to compare the integration of peaks during the course of

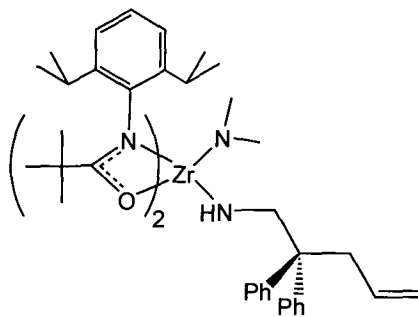
the catalytic reaction. Samples were prepared in an inert atmosphere glovebox, and J-Young NMR tubes with Teflon valves were utilized as reaction vessels. Solutions were generated in 1 mL volumetric flasks to ensure accurate concentrations of all reagents. In cases where multiple runs were considered, the substrate concentrations were normalized. This consisted of multiplication of individual runs by a factor to ensure that initial concentrations were the same for all runs. This process does not influence the slope of the resulting line, and thus does not affect any k_{obs} values determined from the data.

Upon preparing the NMR tube samples, they were immediately immersed in a bath of dry-ice/isopropanol to ensure that a minimum of reactivity occurred prior to kinetic analysis. The spectrometer was preheated to a given temperature using the edte command interface, and a temperature calibration was performed using an 80 % ethylene glycol/DMSO standard. Actual temperatures were determined through measuring the difference in chemical shift ($\Delta\delta$) for the OH and CH₂ protons of ethylene glycol. The actual temperature, in Kelvin, was determined from the relationship $T(\text{K}) = -108.33(\Delta\delta) + 460.41$, provided by Bruker. Upon completing the temperature calibration, the sample was inserted into the NMR probe and locked and shimmed while allowing the tube to equilibrate to the probe temperature (5 min.) before beginning collection. In general, ¹H NMR spectra were collected every 10 min. (using 8 scans) for a given period of time. Collections were either performed manually with a stopwatch, or were automated using the multizg_vd routine, with the delay time set to compensate for the experiment collection time (i.e. delay time = 10 min – collection time). Data workup was performed using Microsoft Excel.

5.6.4 Synthesis

Synthesis of $[\text{DIPP}(\text{NO})^{\text{tBu}}]_2\text{ZrNHCH}_2\text{CPh}_2\text{CH}_2\text{CH}=\text{CH}_2(\text{NMe}_2)$, **5.47**

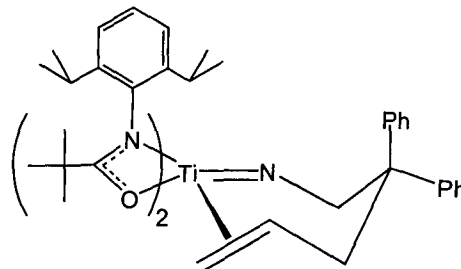
In a 25 mL glass vial in a glovebox, 700 mg (1.00 mmol) of $[\text{DIPP}(\text{NO})^{\text{tBu}}]_2\text{Zr}(\text{NMe}_2)_2$ (**5.46**) was dissolved in approximately 1.5 mL of C_6D_6 at room temperature, generating a clear colorless solution. To this solution was added 237 mg (1.00 mmol) of $\text{H}_2\text{NCH}_2\text{CPh}_2\text{CH}_2\text{CH}=\text{CH}_2$ (**5.32**) dissolved in



approximately 0.5 mL of C_6D_6 . The resulting solution was allowed to stir at room temperature overnight, during which time the solution slowly changed color to pale yellow. The vial was left open to the atmosphere during this time to allow any liberated HNMe_2 (g) to escape. Attempts to scale up this reaction and isolate material were unsuccessful. For several of the NMR signals there are two diastereomeric signals (1.6:1 ratio, as illustrated in Fig. 5.18). ^1H NMR (C_6D_6 , 25 °C, 400 MHz): δ 1.09 (s, 9H, $\text{C}(\text{CH}_3)_3$), 1.13 (s, 9H, $\text{C}(\text{CH}_3)_3$), 1.30 (d, 6H, $^3J_{\text{HH}} = 6.6$ Hz, $\text{CH}(\text{CH}_3)_2$), 1.33 (d, 6H, $^3J_{\text{HH}} = 6.6$ Hz, $\text{CH}(\text{CH}_3)_2$), 1.38 (d, 6H, $^3J_{\text{HH}} = 6.6$ Hz, $\text{CH}(\text{CH}_3)_2$), 1.42 (d, 6H, $^3J_{\text{HH}} = 6.6$ Hz, $\text{CH}(\text{CH}_3)_2$), 2.71 (s, 3H, $\text{Zr-N}(\text{CH}_3)_2$), 2.79 (s, 3H, $\text{Zr-N}(\text{CH}_3)_2$), 2.84 and 2.93 (d, 2H, $^3J_{\text{HH}} = 7.3$ Hz, $-\text{CPh}_2\text{CH}_2\text{CH}=\text{CH}_2$), 3.39 (sept, 2H, $^3J_{\text{HH}} = 8.4$ Hz, $\text{CH}(\text{CH}_3)_2$), 3.54 (sept, 2H, $^3J_{\text{HH}} = 8.9$ Hz, $\text{CH}(\text{CH}_3)_2$), 3.75 (br, 2H, $\text{Zr-NHCH}_2\text{CPh}_2-$), 4.36 and 4.48 (t, 1H, $^3J_{\text{HH}} = 8.8$ Hz, $\text{Zr-NHCH}_2\text{CPh}_2-$), 4.86 (m, 2H, $\text{Zr-NHCH}_2\text{CPh}_2\text{CH}_2\text{CH}=\text{CH}_2$), 5.62 and 5.78 (m, 1H, $\text{Zr-NHCH}_2\text{CPh}_2\text{CH}_2\text{CH}=\text{CH}_2$), 6.95-7.15 (m, 16H, Ar-H). Full assignment of these signals was possible through the use of a COSY NMR spectrum. $^{13}\text{C}\{^1\text{H}\}$ NMR (C_6D_6 , 25 °C, 75 MHz): δ 24.1, 24.2, 28.6, 28.7, 41.7, 42.1, 42.2, 42.3, 52.8, 53.1, 55.4, 55.9, 117.4, 117.7, 123.8, 124.0, 126.0, 126.2, 126.3, 129.2, 129.4, 135.9, 136.3, 140.6, 141.4, 141.8, 142.3, 142.6, 147.4, 147.6, 189.7.

Synthesis of $[\text{DIPP}(\text{NO})^{\text{tBu}}]_2\text{Ti}=\text{NCH}_2\text{CPh}_2\text{CH}_2\text{CH}=\text{CH}_2$, **5.49**

In a 50 mL Erlenmeyer flask in a glovebox, 657 mg (1.00 mmol) of $[\text{DIPP}(\text{NO})^{\text{tBu}}]_2\text{Ti}(\text{NMe}_2)_2$ (**5.48**) was dissolved in approximately 30 mL of pentane at room temperature, generating a clear deep red solution. To this solution was added 237 mg (1.00

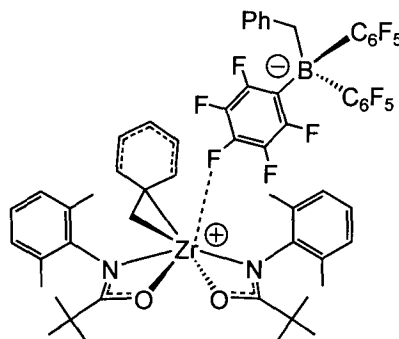


mmol) of $\text{H}_2\text{NCH}_2\text{CPh}_2\text{CH}_2\text{CH}=\text{CH}_2$ (**5.32**) dissolved in approximately 5 mL of pentane. The resulting solution was allowed to stir at room temperature overnight, during which time the solution slowly changed color to pale yellow. The vial was left open to the atmosphere during this time to allow any liberated HNMe_2 (g) to escape. Excess solvent was removed *in vacuo* to give a yellow/tan powder in 99 % yield (796 mg). ^1H NMR (C_6D_6 , 25 °C, 400 MHz): δ 1.09 (d, 3H, $^3J_{\text{HH}} = 6.8$ Hz, $\text{CH}(\text{CH}_3)_2$), 1.16 (d, 3H, $^3J_{\text{HH}} = 6.7$ Hz, $\text{CH}(\text{CH}_3)_2$), 1.22 (s, 9H, $\text{C}(\text{CH}_3)_3$), 1.25 (d, 3H, $^3J_{\text{HH}} = 6.9$ Hz, $\text{CH}(\text{CH}_3)_2$), 1.29 (d, 3H, $^3J_{\text{HH}} = 6.8$ Hz, $\text{CH}(\text{CH}_3)_2$), 1.35 (s, 9H, $\text{C}(\text{CH}_3)_3$), 1.41 (d, 3H, $^3J_{\text{HH}} = 6.8$ Hz, $\text{CH}(\text{CH}_3)_2$), 1.45 (d, 3H, $^3J_{\text{HH}} = 6.8$ Hz, $\text{CH}(\text{CH}_3)_2$), 1.55 (d, 3H, $^3J_{\text{HH}} = 6.7$ Hz, $\text{CH}(\text{CH}_3)_2$), 1.60 (d, 3H, $^3J_{\text{HH}} = 5.7$ Hz, $\text{CH}(\text{CH}_3)_2$), 2.57 (sept, 1H, $^3J_{\text{HH}} = 6.7$ Hz, $\text{CH}(\text{CH}_3)_2$), 2.94 (sept, 1H, $^3J_{\text{HH}} = 6.7$ Hz, $\text{CH}(\text{CH}_3)_2$), 3.15 (m, 1H, $\text{Ti}=\text{NCH}_2\text{CPh}_2\text{CH}_2\text{CH}=\text{CH}_2$), 3.51 (sept, 1H, $^3J_{\text{HH}} = 6.6$ Hz, $\text{CH}(\text{CH}_3)_2$), 3.80 (m, 1H, $\text{Ti}=\text{NCH}_2\text{CPh}_2\text{CH}_2\text{CH}=\text{CH}_2$), 4.05 (sept, 1H, $^3J_{\text{HH}} = 6.6$ Hz, $\text{CH}(\text{CH}_3)_2$), 4.10 (d, 1H, $^2J_{\text{HH}} = 15.0$ Hz, $\text{Ti}=\text{NCH}_2\text{CPh}_2\text{CH}_2\text{CH}=\text{CH}_2$), 4.53 (d, 1H, $^2J_{\text{HH}} = 15.1$ Hz, $\text{Ti}=\text{NCH}_2\text{CPh}_2\text{CH}_2\text{CH}=\text{CH}_2$), 4.96 (m, 2H, $\text{Ti}=\text{NCH}_2\text{CPh}_2\text{CH}_2\text{CH}=\text{CH}_2$), 5.94 (m, 1H, $\text{Ti}=\text{NCH}_2\text{CPh}_2\text{CH}_2\text{CH}=\text{CH}_2$), 6.85-7.55 (m, 16H, Ar-H). $^{13}\text{C}\{^1\text{H}\}$ NMR (C_6D_6 , 25 °C, 75 MHz): δ 23.3, 23.5, 24.7, 25.1, 28.5, 28.6, 29.0, 29.3, 29.4, 36.8, 39.3, 41.9, 43.0, 54.1, 78.7, 117.4, 121.8, 122.6, 123.2, 123.5, 123.9, 124.3, 126.1, 126.4, 130.6, 136.9, 138.4, 138.5, 141.6, 141.9, 142.5, 147.4, 147.8, 148.4, 170.2, 185.3. Assignment of these signals and conformational analysis was possible through the use of COSY, HMQC, and NOESY NMR spectra. EIMS (m/z): 803 ($[\text{M}^+]$), 568 ($[\text{M}^+] - \text{NCH}_2\text{CPh}_2\text{CH}_2\text{CH}=\text{CH}_2$). Crystals suitable for X-ray crystallographic studies were grown from a saturated toluene solution at room temperature.

In situ generation of $[[^{\text{DMP}}(\text{NO})^{\text{tBu}}]_2\text{ZrCH}_2\text{Ph}][\text{B}(\text{C}_6\text{F}_5)_3\text{CH}_2\text{Ph}]$, **5.51**

In a small vial in a glovebox 50 mg (0.07 mmol) of $[[^{\text{DMP}}(\text{NO})^{\text{tBu}}]_2\text{Zr}(\text{CH}_2\text{Ph})_2$ (**3.9**) was dissolved in approximately 0.5 mL of $\text{C}_6\text{D}_5\text{Br}$. In a separate vial, 38 mg (0.07 mmol) of $\text{B}(\text{C}_6\text{F}_5)_3$ was dissolved in approximately 0.5 mL of $\text{C}_6\text{D}_5\text{Br}$. The two solutions were added to a J-Young NMR tube at room temperature, and a deep red solution formed

immediately. ^1H NMR ($\text{C}_6\text{D}_5\text{Br}$, 25 °C, 300 MHz): δ 1.14 (s, 18H, $\text{C}(\text{CH}_3)_3$), 2.33 (br, 12H, Ar-CH_3), 3.48 (br, 2H, ZrCH_2Ph), 6.68-7.50 (m, 16H, Ar-H), BCH_2Ph protons not observed. ^{19}F NMR ($\text{C}_6\text{D}_5\text{Br}$, 25 °C, 282 MHz): δ -164.9 (br, 6F, *m*- Ar-F), -161.1 (br, 3F, *p*- Ar-F), -130.5 (d, 6F, $^3J_{\text{FF}} = 22.6$ Hz, *o*- Ar-F).



5.7 References

1. Tatsuta, K.; Hosokawa, S. *Chem. Rev.* **2005**, *105*, 4707.
2. Ciufolini, M. A. *Farmaco Ed. Sci.* **2005**, *60*, 627.
3. Michael, J. P. *Nat. Prod. Rep.* **2007**, *24*, 191.
4. Yet, L. *Chem. Rev.* **2000**, *100*, 2963.
5. O'Hagan, D.; Robins, R. J. *Chem. Soc. Rev.* **1998**, *27*, 207.
6. Trost, B. M.; Dong, G. *Org. Lett.* **2007**, *9*, 2357.
7. Vanecko, J. A.; Wan, H.; West, F. G. *Tetrahedron* **2006**, *62*, 1043.
8. Rigby, J. H.; Burke, P. J. *Heterocycles* **2006**, *67*, 643.
9. Harrity, J. P. A.; Provoost, O. *Org. Biomol. Chem.* **2005**, *3*, 1349.
10. Brenneman, J. B.; Martin, S. F. *Curr. Org. Chem.* **2005**, *9*, 1535.
11. Baxendale, I. R.; Ley, S. V. *Ind. Eng. Chem. Res.* **2005**, *44*, 8588.
12. Martin, S. F. *Acc. Chem. Res.* **2002**, *35*, 895.
13. Martin, S. F. *Pure Appl. Chem.* **1997**, *69*, 571.
14. Martin, S. F.; Desai, S. R.; Philips, G. W.; Miller, A. C. *J. Am. Chem. Soc.* **1980**, *102*, 3294.
15. Robins, R. J.; Walton, N. J. *Alkaloids* **1993**, *44*, 115.
16. Novak, M.; Salemink, C. A.; Khan, I. *J. Ethnopharmacol.* **1984**, *10*, 261.
17. Hemscheidt, T. *Top. Curr. Chem.* **2000**, *209*, 175.
18. Wagner, F. F.; Comins, D. L. *Tetrahedron* **2007**, *63*, 8065.
19. Yerger, V. B.; Malone, R. E. *Nicotine & Tobacco Res.* **2006**, *8*, 487.
20. Buffat, M. G. P. *Tetrahedron* **2004**, *60*, 1701.
21. Szallasi, A. *Trends Pharmacol. Sci.* **2005**, *26*, 437.
22. Pei, Y. Q. *Epilepsia* **1983**, *24*, 177.
23. Etxebarria, J.; Vicario, J. L.; Badia, D.; Carrillo, L. *Tetrahedron* **2007**, *63*, 11421.
24. Lebrun, S.; Couture, A.; Deniau, E.; Grandclaoudon, P. *Org. Lett.* **2007**, *9*, 2473.
25. Nagata, K.; Nishimura, K.; Yokoya, M.; Itoh, T. *Heterocycles* **2006**, *70*, 335.
26. Girard, N.; Pouchain, L.; Hurvois, J.-P.; Moinet, C. *Synlett* **2006**, 1679.
27. Chuzel, O.; Riant, O. *Top. Organomet. Chem.* **2005**, *15*, 59.

28. Okamoto, Y. *J. Polym. Sci., Part A: Polym. Chem.* **2004**, 42, 4480.
29. Iyengar, R.; Gracias, V. *Chemtracts* **2004**, 17, 92.
30. Schuetz, T. *Synlett* **2003**, 901.
31. Buttler, T.; Fleming, I. *Chem. Commun.* **2004**, 2404.
32. Hermet, J.-P. R.; McGrath, M. J.; O'Brien, P.; Porter, D. W.; Gilday, J. *Chem. Commun.* **2004**, 1830.
33. Fodor, G.; Dharanipragada, R. *Nat. Prod. Rep.* **1985**, 2, 221.
34. Hashimoto, T.; Yamada, Y. *Curr. Top. Plant Physiol.* **1991**, 7, 262.
35. Smith, M. B.; March, J. *March's Advanced Organic Chemistry: Reactions, Mechanisms, and Structure*. 5th ed.; Wiley: Toronto, **2001**.
36. Yin, L.; Liebscher, J. *Chem. Rev.* **2007**, 107, 133.
37. Ozawa, F.; Yoshifuji, M. *Dalton Trans.* **2006**, 4987.
38. Nicolaou, K. C.; Bulger, P. G.; Sarlah, D. *Angew. Chem. Int. Ed.* **2005**, 44, 4442.
39. Le Blanc, M.; Santini, G.; Gallucci, J.; Riess, J. G. *Tetrahedron* **1977**, 33, 1453.
40. Roesky, P. W.; Muller, T. E. *Angew. Chem. Int. Ed.* **2003**, 42, 2708.
41. Brunet, J. J.; Fixari, B.; Caubere, P. *Tetrahedron* **1974**, 30, 2931.
42. Soloshonok, V. A. *Curr. Org. Chem.* **2002**, 6, 341.
43. Howk, B. W.; Little, E. L.; Scott, S. L.; Whitman, G. M. *J. Am. Chem. Soc.* **1954**, 76, 1899.
44. Larock, R. *Angew. Chem. Int. Ed.* **1978**, 17, 27.
45. Barluenga, J.; Aznar, F. *Synthesis* **1975**, 704.
46. Zimmermann, B.; Herwig, J.; Beller, M. *Angew. Chem. Int. Ed.* **1999**, 38, 2372.
47. Seayad, A.; Ahmed, M.; Klein, H.; Jackstell, R.; Gross, T.; Beller, M. *Science* **2002**, 297, 1676.
48. Muller, T. E.; Beller, M. *Chem. Rev.* **1998**, 98, 675.
49. Bytschkov, I.; Doye, S. *Eur. J. Org. Chem.* **2003**, 935.
50. Pohlki, F.; Doye, S. *Chem. Soc. Rev.* **2003**, 32, 104.
51. Hong, S.; Marks, T. J. *Acc. Chem. Res.* **2004**, 37, 673.
52. Duncan, A. P.; Bergman, R. G. *Chem. Rec.* **2002**, 2, 431.
53. Odom, A. L. *Dalton Trans.* **2005**, 225.
54. Hartwig, J. F. *Pure Appl. Chem.* **2004**, 76, 507.

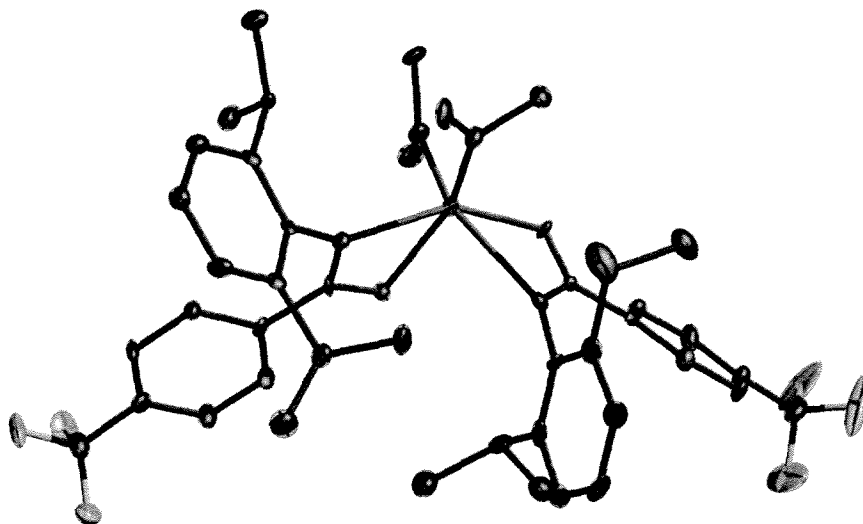
55. Coulson, D. R. *Tetrahedron Lett.* **1971**, 429.
56. Hegedus, L. S.; Allen, G. F.; Waterman, E. L. *J. Am. Chem. Soc.* **1976**, *98*, 2674.
57. Akermark, B.; Baechvall, J. E.; Hegedus, L. S.; Zetterberg, K.; Siirala-Hansen, K.; Sjöberg, K. *J. Organomet. Chem.* **1974**, *72*, 127.
58. Casalnuovo, A. L.; Calabrese, J. C.; Milstein, D. *J. Am. Chem. Soc.* **1988**, *110*, 6738.
59. Dorta, R.; Egli, P.; Zuercher, F.; Togni, A. *J. Am. Chem. Soc.* **1997**, *119*, 10857.
60. Kauffman, G. B. *ACS Symp. Ser.* **1994**, *565*, 3.
61. Zhao, J.; Goldman, A. S.; Hartwig, J. F. *Science* **2005**, *307*, 1080.
62. Field, L. D.; Messerle, B. A.; Vuong, K. Q.; Turner, P. *Organometallics* **2005**, *24*, 4241.
63. Nettekoven, U.; Hartwig, J. F. *J. Am. Chem. Soc.* **2002**, *124*, 1166.
64. Jeske, G.; Lauke, H.; Mauermann, H.; Swepston, P. N.; Schumann, H.; Marks, T. J. *J. Am. Chem. Soc.* **1985**, *107*, 8091.
65. Jeske, G.; Schock, L. E.; Swepston, P. N.; Schumann, H.; Marks, T. J. *J. Am. Chem. Soc.* **1985**, *107*, 8103.
66. Jeske, G.; Lauke, H.; Mauermann, H.; Schumann, H.; Marks, T. J. *J. Am. Chem. Soc.* **1985**, *107*, 8111.
67. Mauermann, H.; Swepston, P. N.; Marks, T. J. *Organometallics* **1985**, *4*, 200.
68. Watson, P. L.; Parshall, G. W. *Acc. Chem. Res.* **1985**, *18*, 51.
69. Hou, Z.; Wakatsuki, Y. *Coord. Chem. Rev.* **2002**, *231*, 1.
70. Barbier-Baudry, D.; Dormond, A. *New Trends in Organolanthanide Hydride Chemistry*. Elsevier: Toronto; **2001**, p249-270.
71. Hou, Z.; Kaita, S.; Wakatsuki, Y. *Pure Appl. Chem.* **2001**, *73*, 291.
72. Anwander, R. *Top. Organomet. Chem.* **1999**, *2*, 1.
73. Gagne, M. R.; Marks, T. J. *J. Am. Chem. Soc.* **1989**, *111*, 4108.
74. Ki, Y.; Marks, T. J. *J. Am. Chem. Soc.* **1996**, *118*, 9295.
75. Gagne, M. R.; Stern, C. L.; Marks, T. J. *J. Am. Chem. Soc.* **1992**, *114*, 275.
76. Douglass, M. R.; Marks, T. J. *J. Am. Chem. Soc.* **2000**, *122*, 1824.
77. Douglass, M. R.; Stern, C. L.; Marks, T. J. *J. Am. Chem. Soc.* **2001**, *123*, 10221.

78. Arredondo, V. M.; Tian, S.; McDonald, F. E.; Marks, T. J. *J. Am. Chem. Soc.* **1999**, *121*, 3633.
79. Giardello, M. A.; Conticello, V. P.; Brard, L.; Gagne, M. R.; Marks, T. J. *J. Am. Chem. Soc.* **1994**, *116*, 10241.
80. Douglass, M. R.; Ogasawara, M.; Hong, S.; Metz, M. V.; Marks, T. J. *Organometallics* **2002**, *21*, 283.
81. Hong, S.; Kawaoka, A. M.; Marks, T. J. *J. Am. Chem. Soc.* **2003**, *125*, 15878.
82. Hong, S.; Tian, S.; Metz, M. V.; Marks, T. J. *J. Am. Chem. Soc.* **2003**, *125*, 14768.
83. O'Shaughnessy, P. N.; Knight, P. D.; Morton, C.; Gillespie, K. M.; Scott, P. *Chem. Commun.* **2003**, 1770.
84. Gribkov, D. V.; Hultsch, K. C. *Chem. Commun.* **2004**, 730.
85. Hultsch, K. C.; Gribkov, D. V.; Hampel, F. *J. Organomet. Chem.* **2005**, *690*, 4441.
86. Gribkov, D. V.; Hultsch, K. C.; Hampel, F. *J. Am. Chem. Soc.* **2006**, *128*, 3748.
87. Kim, J. Y.; Livinghouse, T. *Org. Lett.* **2005**, *7*, 1737.
88. O'Shaughnessy, P. N.; Gillespie, K. M.; Knight, P. D.; Munslow, I. J.; Scott, P. *Dalton Trans.* **2004**, 2251.
89. Ryu, J.-S.; Li, G. Y.; Marks, T. J. *J. Am. Chem. Soc.* **2003**, *125*, 12584.
90. Li, Y.; Marks, T. J. *Organometallics* **1996**, *15*, 3770.
91. Li, Y.; Marks, T. J. *J. Am. Chem. Soc.* **1998**, *120*, 1757.
92. Doye, S. *Synlett* **2004**, 1653.
93. Lee, A. V.; Schafer, L. L. *Eur. J. Inorg. Chem.* **2007**, 2243.
94. Walsh, P. J.; Baranger, A. M.; Bergman, R. G. *J. Am. Chem. Soc.* **1992**, *114*, 1708.
95. Siebeneicher, H.; Doye, S. *Eur. J. Org. Chem.* **2002**, 1213.
96. Haak, E.; Bytschkov, I.; Doye, S. *Angew. Chem. Int. Ed.* **1999**, *38*, 3389.
97. Bytschkov, I.; Doye, S. *Tetrahedron Lett.* **2002**, *43*, 3715.
98. Cao, C.; Ciszewski, J. T.; Odom, A. L. *Organometallics* **2001**, *20*, 5011.
99. Shi, Y.; Hall, C.; Ciszewski, J. T.; Cao, C.; Odom, A. L. *Chem. Commun.* **2003**, 586.

100. Hill, J. E.; Proffitt, R. D.; Fanwick, P. E.; Rothwell, I. P. *Angew. Chem. Int. Ed.* **1990**, *29*, 664.
101. McGrane, P. L.; Jensen, M.; Livinghouse, T. *J. Am. Chem. Soc.* **1992**, *114*, 5459.
102. Khedkar, V.; Tillack, A.; Beller, M. *Org. Lett.* **2003**, *5*, 4767.
103. Ong, T.-G.; Yap, G. P. A.; Richeson, D. S. *Organometallics* **2002**, *21*, 2839.
104. Hagadorn, J. R.; Arnold, J. *Organometallics* **1998**, *17*, 1355.
105. Hagadorn, J. R.; Arnold, J. *Inorg. Chem.* **1997**, *36*, 2928.
106. Hagadorn, J. R.; Arnold, J. *J. Am. Chem. Soc.* **1996**, *118*, 893.
107. Hagadorn, J. R.; Arnold, J. *Organometallics* **1994**, *13*, 4670.
108. Li, C.; Thomson, R. K.; Gillon, B.; Patrick, B. O.; Schafer, L. L. *Chem. Commun.* **2003**, 2462.
109. Zhang, Z.; Schafer, L. L. *Org. Lett.* **2003**, *5*, 4733.
110. Zhang, Z.; Leitch, D. C.; Lu, M.; Patrick, B. O.; Schafer, L. L. *Chem.--Eur. J.* **2007**, *13*, 2012.
111. Lee, A. V.; Schafer, L. L. *Synlett* **2006**, 2973.
112. Marks, T. J.; Gagne, M. R.; Nolan, S. P.; Schock, L. E.; Seyam, A. M.; Stern, D. *Pure Appl. Chem.* **1989**, *61*, 1665.
113. Barnea, E.; Eisen, M. S. *Coord. Chem. Rev.* **2006**, *250*, 855.
114. Gribkov, D. V.; Hultsch, K. C. *Angew. Chem. Int. Ed.* **2004**, *43*, 5542.
115. Knight, P. D.; Munslow, I.; O'Shaughnessy, P. N.; Scott, P. *Chem. Commun.* **2004**, 894.
116. Kissounko, D. A.; Epshteyn, A.; Fettinger, J. C.; Sita, L. R. *Organometallics* **2006**, *25*, 1076.
117. Anderson, L. L.; Arnold, J.; Bergman, R. G. *J. Am. Chem. Soc.* **2005**, *127*, 14542.
118. Bexrud, J. A.; Beard, J. D.; Leitch, D. C.; Schafer, L. L. *Org. Lett.* **2005**, *7*, 1969.
119. Kim, H.; Lee, P. H.; Livinghouse, T. *Chem. Commun.* **2005**, 5205.
120. Watson, D. A.; Chiu, M.; Bergman, R. G. *Organometallics* **2006**, *25*, 4731.
121. Mueller, C.; Loos, C.; Schulenberg, N.; Doye, S. *Eur. J. Org. Chem.* **2006**, 2499.

122. Gott, A. L.; Clarke, A. J.; Clarkson, G. J.; Scott, P. *Organometallics* **2007**, *26*, 1729.
123. Wood, M. C.; Leitch, D. C.; Yeung, C. S.; Kozak, J. A.; Schafer, L. L. *Angew. Chem. Int. Ed.* **2007**, *46*, 354.
124. Stubbert, B. D.; Marks, T. J. *J. Am. Chem. Soc.* **2007**, *129*, 6149.
125. Thomson, R. K.; Bexrud, J. A.; Schafer, L. L. *Organometallics* **2006**, *25*, 4069.
126. Pohlki, F.; Doye, S. *Angew. Chem. Int. Ed.* **2001**, *40*, 2305.
127. Walsh, P. J.; Hollander, F. J.; Bergman, R. G. *Organometallics* **1993**, *12*, 3705.
128. Li, Y.; Shi, Y.; Odom Aaron, L. *J. Am. Chem. Soc.* **2004**, *126*, 1794.
129. Johnson, J. S.; Bergman, R. G. *J. Am. Chem. Soc.* **2001**, *123*, 2923.
130. Jung, M. E.; Piizzi, G. *Chem. Rev.* **2005**, *105*, 1735.
131. Espenson, J. H. *Chemical Kinetics and Reaction Mechanisms*. 2nd ed.; McGraw-Hill, Inc.: New York, **1995**.
132. Dunn, S. C.; Mountford, P.; Shishkin, O. V. *Inorg. Chem.* **1996**, *35*, 1006.

CHAPTER 6



Concluding Remarks and Future Directions

6.1 Summary and Conclusions

The objective of this thesis was to examine the feasibility of modular amidate ancillary ligands for group 4 transition metals and to develop new reactivity modes promoted by this new class of complexes. Being the initiation of a research program in the Schafer group, fundamental studies were performed to build a foundation for future researchers to work from.

Traditional salt metathesis with amidate ligands is complicated by oligomer and 'ate' complex formation. Fortunately, amidate complexes of Ti, Zr, and Hf could be reliably accessed through the use of a protonolysis methodology, where organic amide proligands were combined with alkyl or amido metal starting materials.^{1, 2} A wide range

of different substitution patterns on the amidate ligand are possible, making this ligand set amenable to combinatorial methods for the generation of a library of complexes, which can be utilized for exploratory reactivity studies. Furthermore, both amido and alkyl derivatives can be accessed using the amidate ancillary framework, allowing for the study of M-N and M-C bond reactivity.^{1,2}

Protonolysis and insertion reactivity of amidate complexes proceeds without deleterious reactivity of the amidate ligands. This is effectively controlled through the use of bulky substituents on the N of the amidate ligands, and prevents potential side reactions like transamidation from occurring.³⁻⁵ Although amidate ligated Ti, Zr, and Hf complexes are very stable, they are highly dynamic in solution, undergoing fluxional processes.¹ Solution phase isomerization of κ^2 -amidate complexes occurs through κ^1 -bound species. The ability of the hemilabile amidate ligand set to adopt a κ^1 -coordination mode may facilitate some of the novel reactivity observed with these complexes. Weak covalent bonding character of the amidate ligands was illustrated through structural studies and density functional theory calculations, where the amidate-metal interactions are more electrostatic or ionic in character.¹ The minimal electron donation provided by the amidate ligands, coupled with substantial steric protection of the metal center, allows for the generation of extremely electrophilic metal centers, which promote reactivity not previously observed for neutral group 4 complexes. Despite the poor electron donating abilities of the amidate ligands, *in situ* generation of cationic benzyl amidate complexes is possible, opening further possibilities for reactivity.

Benzyl complexes supported by amidate ligands displayed predictable insertion behavior, and reactions with isocyanides generate the expected η^2 -iminoacyl complexes. While these species are stable with aryl isocyanides, heating these complexes results in C-C coupling to generate enediamido complexes. In contrast, alkyl substituted η^2 -iminoacyl complexes are unstable and undergo spontaneous 1,2-hydrogen atom migration, generating vinyl amido complexes as shown in Chapter 3.

The formation of stable terminal imido complexes was also possible using the amidate ancillary ligand set, and these complexes displayed remarkable reactivity.⁶ In particular, the amidate supported Zr imido complexes discussed in Chapter 4 are the first imido species to display catalytic viability in the cyclohydroamination of primary

aminoalkenes.⁶ Detailed mechanistic investigations support the intermediacy of imido species in this catalytic process. Secondary aminoalkenes can also be cyclized with cationic amidate supported Zr benzyl complexes. Preliminary investigations support an alternative σ -bond insertion mechanism for these reactions. Cationic amidate complexes can react with primary aminoalkenes to generate neutral imido complexes through H^+ loss, similar to what has been proposed for other cationic systems.^{7, 8} However, in contrast to the other known cationic catalyst systems, the amidate supported imido complexes generated are catalytically viable, and mechanistic investigations support an imido cycloaddition pathway.⁶

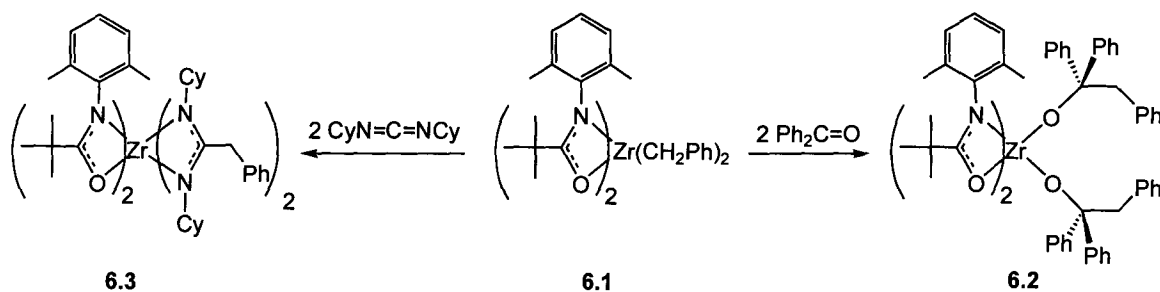
The ability of the amidate ligand set to support two alternative mechanistic pathways for catalytic hydroamination, depending on the nature of the substrate and the catalyst, is an indication of the potentially diverse reactivity that can be exploited through the use of these ancillary ligands. In addition, the easily modified nature of these ligands makes them amenable to combinatorial methods, and detailed structure-activity relationship studies. In addition to the rich hydroamination chemistry promoted by this family of complexes,^{6, 9-15} olefin polymerization using these species is currently being explored through a collaboration with Imperial Oil and Exxon-Mobil.

6.2 Future Work

6.2.1 Insertion Reactivity of Alkyl Complexes

While the insertion of isocyanides into the Zr-C bonds of benzyl derivatives was investigated in detail, preliminary experiments were performed with ketones and carbodiimides, which indicated successful insertion reactivity. Preliminary NMR tube experiments are summarized in Scheme 6.1. The proposed insertion product for the reaction of benzophenone with dibenzyl complex **6.1** (**3.9**) is the alkoxide **6.2**. Likewise, insertion of dicyclohexylcarbodiimide (DCC) into the Zr-C bonds of **6.1** appears to generate the amidinate complex **6.3**. In particular, the appearance of slightly overlapping diastereotopic doublet resonances in the 1H NMR spectrum for the benzylic protons at δ 3.64 and 3.71, suggests the formation of **6.3**. While complexes **6.2** and **6.3** have not been

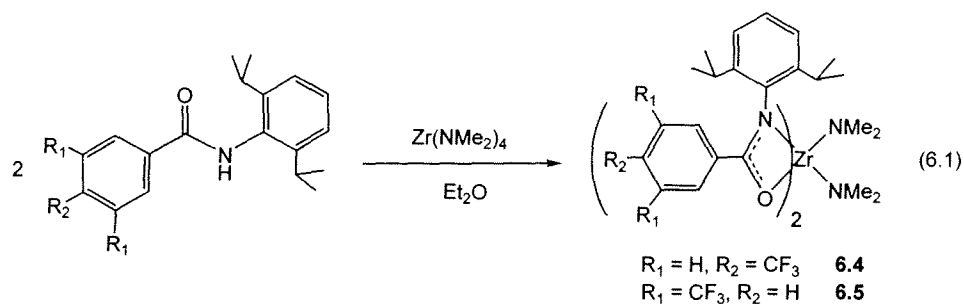
fully characterized, preliminary ^1H NMR spectroscopic data, and mass spectral data support the formation of these complexes. Excellent functional group tolerance of bis(amidate) bis(amido) complexes has been noted for alkyne hydroamination.^{10, 12, 15} If the C=O and C=N insertion processes illustrated above could be coupled with olefin polymerization, using cationic amidate complexes, novel block copolymers could be accessed. The observed polymerization of THF by $[[^{\text{DMP}}(\text{NO})^{\text{Ph}}]_2\text{HfCH}_2\text{Ph}][\text{B}(\text{C}_6\text{F}_5)_4]$ suggests that this may be possible to realize, and should be a future avenue of investigation.



Scheme 6.1

6.2.2 Fluorinated Amidate Ligands for Enhanced Reactivity

The realization of catalytic cyclohydroamination of alkenes using neutral bis(amidate) bis(amido) and bis(amidate) imido complexes is considered to be a fantastic achievement, and may prove useful in the generation of N-heterocyclic frameworks in natural product synthesis. However, fine chemicals production is dependent on the ability to combine a wide variety of amines and alkenes. Extension of this catalytic reactivity to *intermolecular* hydroamination is an important goal.¹⁶⁻²² The use of electron withdrawing substituents on amidate ligands was successful for increasing the efficiency of alkyne hydroamination.⁹ Applying the same concept to alkene hydroamination may be similarly successful. The synthesis of two bis(amidate) bis(amido) complexes bearing fluorinated amidate ligands was attempted, as illustrated in Eq. 6.1.



While full characterization of these complexes was not accomplished, one of these complexes (**6.4**) was characterized by X-ray crystallography, verifying its composition as a bis(amidate) bis(amido) complex. The solid-state molecular structure of this complex is given in Fig. 6.1. The data collected for this structure is of poor quality and this structure provides only connectivity and general coordination geometry. A new graduate student, Courtney Turner, is pursuing this project further, and preliminary results indicate that these complexes are more efficient for the intramolecular cyclohydroamination of aminoalkenes than their non-fluorinated congeners. In particular, sterically hindered substrates are cyclized with greatly reduced reaction times.²³

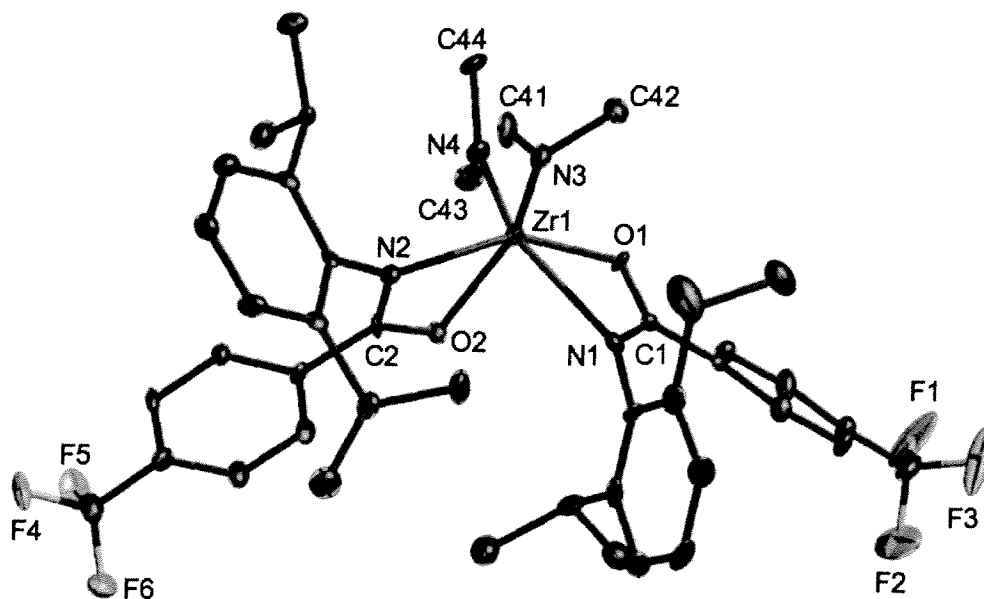
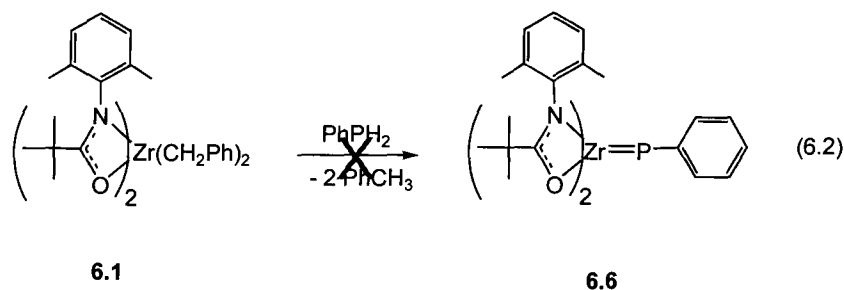


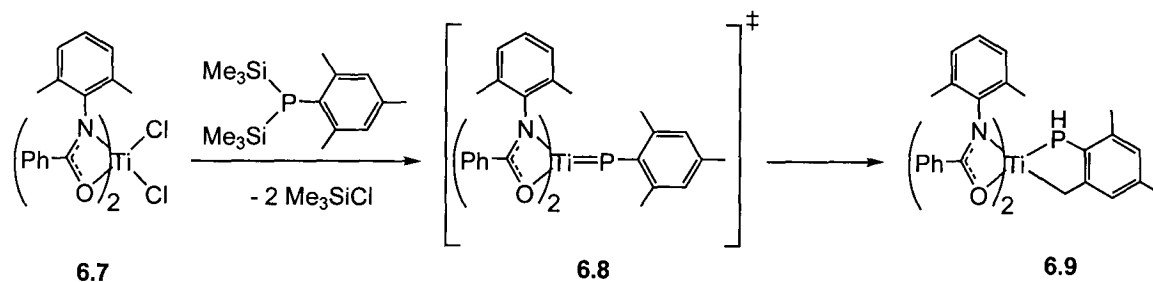
Figure 6.1 ORTEP depiction (ellipsoids at 30% probability) of solid-state molecular structure of $[\text{DIPP}(\text{NO})^{\text{Ph-p-CF}_3}]_2\text{Zr}(\text{NMe}_2)_2$, **6.4** (hydrogens omitted)

6.2.3 Phosphinidene Complexes

Given the unique behavior of the imido complexes presented in Chapter 6, and their application in alkene hydroamination catalysis,⁶ novel catalytic reactivity with the analogous phosphinidene (M=PR) complexes was envisioned. Unfortunately, protonolysis routes into these complexes, analogous to those utilized to access imido complexes, were unsuccessful (Eq. 6.2). While the desired phosphinidene complex **6.6** was not generated through this route, a mixture of products was formed, one of which contains a P-H bond (as witnessed by ³¹P NMR spectroscopy). It is believed that this product is the mixed benzyl phosphide complex ([^{DMP}(NO)^{tBu}]₂Zr(PHPh)(CH₂Ph)), however, the presence of multiple products makes confirmation of this product a problem. It is likely that the much lower polarity of P-H bonds vs. N-H bonds is responsible for the poor efficiency of the protonolysis reaction for the formation of phosphinidene complexes. However, a TMS-Cl elimination route into phosphinidene complexes has shown promise.²⁴

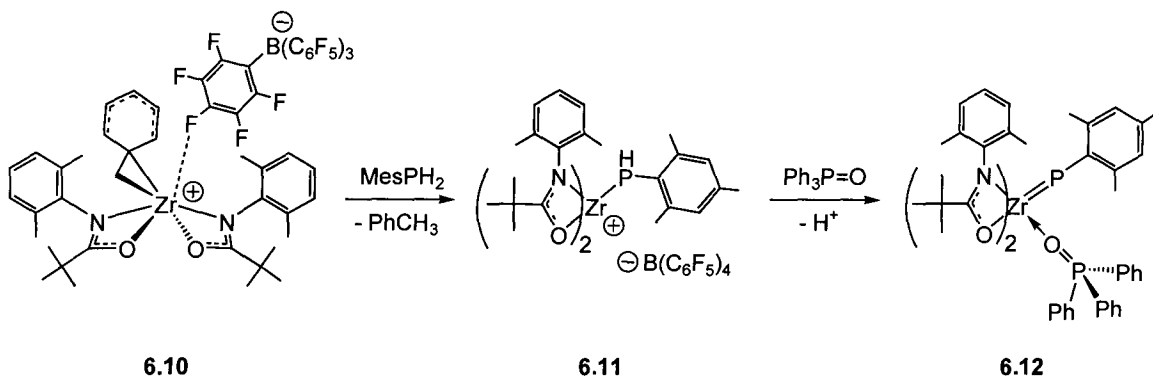


Combination of the Ti dichloro complex **6.7** with (Me₃Si)₂P(2,4,6-Me₃C₆H₂) under forcing conditions results in the elimination of TMS-Cl to generate a proposed transient phosphinidene complex **6.8**. While direct observation of **6.8** was not possible in solution, evidence for the presence of such a complex is supported by *in situ* NMR spectroscopic studies. In particular, generation of a new P-H bond is observed by ³¹P NMR spectroscopy, where a doublet is present at δ -78.9 (¹J_{PH} = 244 Hz). The proposed structure for the resulting complex (**6.9**) is given in Scheme 6.2, and is supported by ¹H NMR spectroscopy. The C-H activation of one of the *ortho* methyl groups would result in the observed complex. Activation of sp³-C-H bonds is challenging,²⁵⁻²⁷ and controlling this reactivity for useful intermolecular reactions is an important goal.^{28, 29}



Scheme 6.2

Given the hard/soft mismatch between Ti and P, it is logical that this project should be extended to the synthesis of Zr phosphinidene complexes.³⁰⁻³² Likewise, the low reactivity of the P-H bonds may be circumvented by the use of cationic amidate precursors. As demonstrated in Chapter 5, these cationic complexes can lose H⁺ upon reaction with primary amines to generate new multiply bonded imido complexes.^{7, 8, 33} A similar technique should be applied to the formation of Zr=PR phosphinidenes, as illustrated in Scheme 6.3.



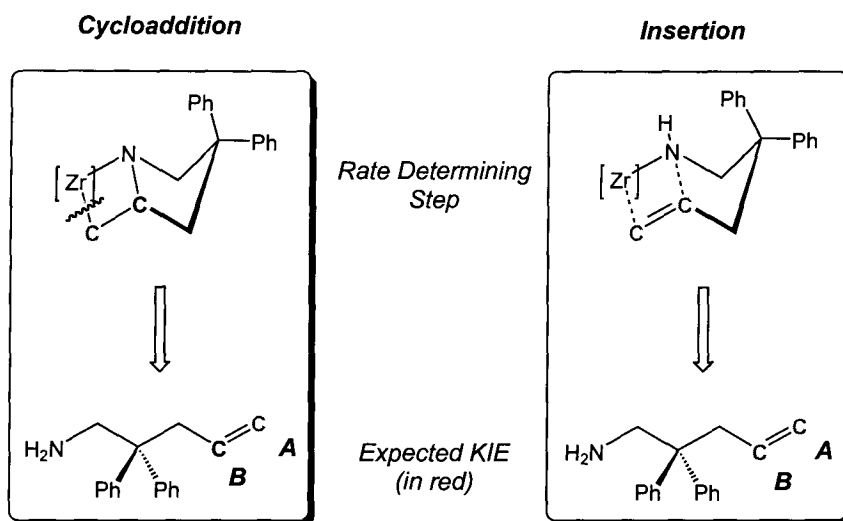
Scheme 6.3

6.2.4 Further Catalytic Hydroamination Mechanistic Investigations

Mechanistic insight into the cyclohydroamination of aminoalkenes using Ti and Zr amidate complexes has provided a rationale for the diastereoselectivities (see Chapter 5)⁶ and enantioselectivities observed for catalysis with these complexes.¹⁴ While the data presented in Chapter 5 are very supportive of an imido cycloaddition mechanism for the cyclohydroamination of primary aminoalkenes, another experiment that could provide

additional evidence for this mechanism is a ^{13}C natural abundance (NA) kinetic isotope effect (KIE) experiment. This technique takes advantage of the difference in reaction rates for isotopomers in the rate-determining step of a given reaction, where the slower reacting isotope (^{13}C) becomes enhanced in the remaining starting material, when reactions are taken to near completion. Singleton and coworkers have described an NMR-based quantitative ^{13}C NA method for examining KIE's for various reactions.³⁴⁻³⁹

As applied to the cyclohydroamination of primary aminoalkenes, this technique can distinguish between σ -bond insertion and cycloaddition pathways, as illustrated in Scheme 6.4. For neutral catalysts the rate-determining step for the imido cycloaddition pathway is cleavage of the Zr-C bond of the proposed azirconacyclobutane intermediate. This would be manifested as a ^{13}C KIE at carbon **A** of the substrate in Scheme 6.4. In contrast, the rate-determining step for the σ -bond insertion mechanism is believed to be insertion into the Zr-N bond of the amido complex. This would show a ^{13}C KIE at carbons **A** and **B** of the substrate.



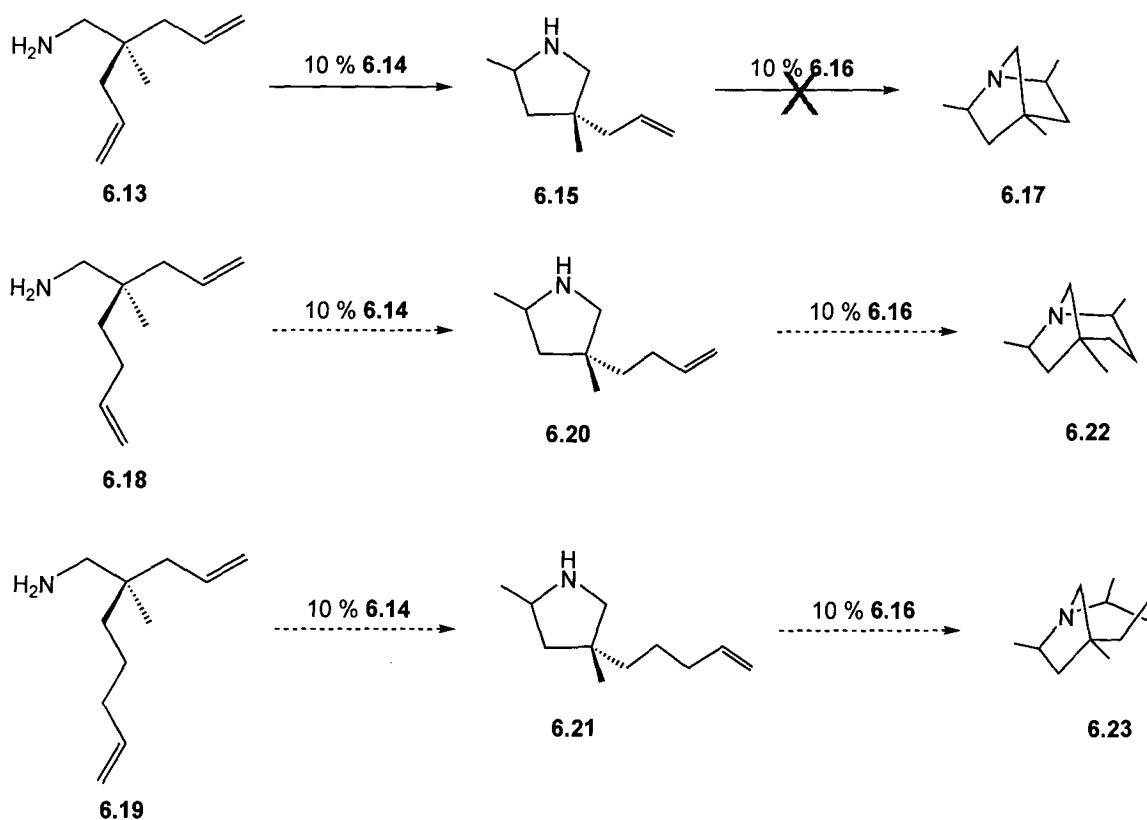
Scheme 6.4

Conditions for this experiment have been determined, including delay times for the ^{13}C NMR spectroscopic experiment; however, isolation of small quantities of the aminoalkene substrate from the pyrrolidine product (Scheme 6.4) is difficult. If the

aminoalkene can be isolated cleanly in acceptable yields after catalysis, this experiment should provide additional mechanistic insight for this important reaction.

Density functional theory (DFT) calculations have provided useful information regarding the mechanism of hydroamination.⁴⁰ Computational methods have been successfully applied to amido and imido complexes bearing amidate ligands,¹ suggesting that similar methods should be amenable to mechanistic studies. Kinetic data presented in Chapter 5 support a high energy metallacycle, which has not thus far been isolable. DFT calculations could be used to verify this supposition, and the energy of other species in the catalytic cycle could also be compared in this manner. Given the dynamic behavior of the amidate ligands and their tendency to isomerize between κ^2 - and κ^1 -forms, accurately modeling this catalytic system will be non-trivial, and a dedicated theoretical chemist should undertake these studies.

Preliminary kinetic results support a σ -bond insertion mechanism for the cyclization of secondary aminoalkenes using cationic amidate precatalytic species. Due to the very rapid nature of this reaction, initial-rate kinetic analysis was not possible. However, full kinetic analysis of this reaction should be feasible through the use of vacuum-transfer techniques to ensure that no reaction occurs prior to beginning kinetic analysis. Combination of the imido cycloaddition and σ -bond insertion mechanisms was attempted using the substrate **6.13**, where cyclization of the pyrrolidine ring is readily accomplished with the bis(amido) precatalyst $[\text{DMP}(\text{NO})^{\text{tBu}}]_2\text{Zr}(\text{NMe}_2)_2$ (**6.14**), generating **6.15** (Scheme 6.5). However, upon addition of the cationic precatalyst **6.16**, $[\text{DMP}(\text{NO})^{\text{tBu}}]_2\text{ZrCH}_2\text{Ph}[\text{B}(\text{C}_6\text{F}_5)_3\text{CH}_2\text{Ph}]$ (**5.51**), no additional cyclization to the desired product **6.17** was observed. It is possible that the transition state is too strained to allow for this to occur with these catalysts. An analogous reaction could be attempted with substrate **6.18** or **6.19**, where the pyrrolidine ring should form preferentially, leaving a pendant olefin available for cyclization of the piperidine (**6.22**) or homopiperidine (**6.23**) fused ring systems by the cationic precatalyst **6.16**.



Scheme 6.5

While the experiments listed above are by no means a comprehensive list of future work, these reactions provide a few convenient starting points for future workers to elaborate on the work presented in this dissertation.

6.3 References

1. Thomson, R. K.; Zahariev, F. E.; Zhang, Z.; Patrick, B. O.; Wang, Y. A.; Schafer, L. L. *Inorg. Chem.* **2005**, *44*, 8680.
2. Thomson, R. K.; Patrick, B. O.; Schafer, L. L. *Can. J. Chem.* **2005**, *83*, 1037.
3. Eldred, S. E.; Stone, D. A.; Gellman, S. H.; Stahl, S. S. *J. Am. Chem. Soc.* **2003**, *125*, 3422.
4. Kissounko, D. A.; Guzei, I. A.; Gellman, S. H.; Stahl, S. S. *Organometallics* **2005**, *24*, 5208.
5. Kissounko, D. A.; Hoerter, J. M.; Guzei, I. A.; Cui, Q.; Gellman, S. H.; Stahl, S. S. *J. Am. Chem. Soc.* **2007**, *129*, 1776.
6. Thomson, R. K.; Bexrud, J. A.; Schafer, L. L. *Organometallics* **2006**, *25*, 4069.
7. Gribkov, D. V.; Hultsch, K. C. *Angew. Chem. Int. Ed.* **2004**, *43*, 5542.
8. Knight, P. D.; Munslow, I.; O'Shaughnessy, P. N.; Scott, P. *Chem. Commun.* **2004**, 894.
9. Li, C.; Thomson, R. K.; Gillon, B.; Patrick, B. O.; Schafer, L. L. *Chem. Commun.* **2003**, 2462.
10. Zhang, Z.; Schafer, L. L. *Org. Lett.* **2003**, *5*, 4733.
11. Ayinla, R. O.; Schafer, L. L. *Inorg. Chim. Acta* **2006**, *359*, 3097.
12. Lee, A. V.; Schafer, L. L. *Synlett* **2006**, 2973.
13. Lee, A. V.; Schafer, L. L. *Eur. J. Inorg. Chem.* **2007**, 2243.
14. Wood, M. C.; Leitch, D. C.; Yeung, C. S.; Kozak, J. A.; Schafer, L. L. *Angew. Chem. Int. Ed.* **2007**, *46*, 354.
15. Zhang, Z.; Leitch, D. C.; Lu, M.; Patrick, B. O.; Schafer, L. L. *Chem.--Eur. J.* **2007**, *13*, 2012.
16. Zhang, J.; Yang, C.-G.; He, C. *J. Am. Chem. Soc.* **2006**, *128*, 1798.
17. Ryu, J.-S.; Li, G. Y.; Marks, T. J. *J. Am. Chem. Soc.* **2003**, *125*, 12584.
18. Kawatsura, M.; Hartwig, J. F. *J. Am. Chem. Soc.* **2000**, *122*, 9546.
19. Nettekoven, U.; Hartwig, J. F. *J. Am. Chem. Soc.* **2002**, *124*, 1166.
20. Utsunomiya, M.; Hartwig, J. F. *J. Am. Chem. Soc.* **2003**, *125*, 14286.

Chapter 6: Concluding Remarks and Future Directions

21. Utsunomiya, M.; Kuwano, R.; Kawatsura, M.; Hartwig, J. F. *J. Am. Chem. Soc.* **2003**, *125*, 5608.
22. Takaya, J.; Hartwig, J. F. *J. Am. Chem. Soc.* **2005**, *127*, 5756.
23. Turner, C. Unpublished work, **2007**.
24. Smit, C. N.; Van der Knaap, T. A.; Bickelhaupt, F. *Tetrahedron Lett.* **1983**, *24*, 2031.
25. Hoyt, H. M.; Michael, F. E.; Bergman, R. G. *J. Am. Chem. Soc.* **2004**, *126*, 1018.
26. Schaller, C. P.; Cummins, C. C.; Wolczanski, P. T. *J. Am. Chem. Soc.* **1996**, *118*, 591.
27. Cummins, C. C.; Baxter, S. M.; Wolczanski, P. T. *J. Am. Chem. Soc.* **1988**, *110*, 8731.
28. Tsang, J. Y. K.; Fujita-Takayama, C.; Buschhaus, M. S. A.; Patrick, B. O.; Legzdins, P. *J. Am. Chem. Soc.* **2006**, *128*, 14762.
29. Tsang, J. Y. K.; Buschhaus, M. S. A.; Legzdins, P. *J. Am. Chem. Soc.* **2007**, *129*, 5372.
30. Hou, Z.; Stephan, D. W. *J. Am. Chem. Soc.* **1992**, *114*, 10088.
31. Hou, Z.; Breen, T. L.; Stephan, D. W. *Organometallics* **1993**, *12*, 3158.
32. Breen, T. L.; Stephan, D. W. *J. Am. Chem. Soc.* **1995**, *117*, 11914.
33. Kissounko, D. A.; Epshteyn, A.; Fettingner, J. C.; Sita, L. R. *Organometallics* **2006**, *25*, 1076.
34. Vo, L. K.; Singleton, D. A. *Org. Lett.* **2004**, *6*, 2469.
35. Singleton, D. A.; Thomas, A. A. *J. Am. Chem. Soc.* **1995**, *117*, 9357.
36. Frantz, D. E.; Singleton, D. A.; Snyder, J. P. *J. Am. Chem. Soc.* **1997**, *119*, 3383.
37. Keating, A. E.; Merrigan, S. R.; Singleton, D. A.; Houk, K. N. *J. Am. Chem. Soc.* **1999**, *121*, 3933.
38. Singleton, D. A.; Szymanski, M. J. *J. Am. Chem. Soc.* **1999**, *121*, 9455.
39. Ussing, B. R.; Hang, C.; Singleton, D. A. *J. Am. Chem. Soc.* **2006**, *128*, 7594.
40. Straub, B. F.; Bergman, R. G. *Angew. Chem. Int. Ed.* **2001**, *40*, 4632.

Appendix A

X-Ray Crystallographic Data

Table A2.1 Crystallographic Data and Refinement Details for $[\text{DMP}(\text{NO})^{\text{Ph}}]_4\text{Hf}$, **2.8**

Empirical Formula	$\text{C}_{60}\text{H}_{56}\text{N}_4\text{O}_4\text{Hf}_1$	Crystal system	Tetragonal
Formula Weight	1075.58	Space group	$P-4\ 21\ c$
a, b, c (Å)	11.0080(7), 11.0080(7), 21.3182(18)		
$V, \text{Å}^3$	2583.3(3)	Total reflections	20445
Z	2	Unique reflections	3104
$D_{\text{calc}}, \text{g cm}^{-3}$	1.383	Parameters	156
μ (Mo $K\alpha$), cm^{-1}	2.070	R_1^a	0.0497
T, K	173 ± 1	R_w^a	0.0839
2θ range ($^\circ$)	55.8	Goodness-of-fit	1.050

$$^a R_1 = \frac{\sum ||F_o| - |F_c||}{\sum |F_o|}; R_w = \frac{\sum w((|F_o|^2 - |F_c|^2)|)^2 / \sum w |F_o|^2)^{1/2}}$$

Table A2.2 Crystallographic Data and Refinement Details for $[\text{DMP}(\text{NO})^{\text{iBu}}]_4\text{Zr}$, **2.9**

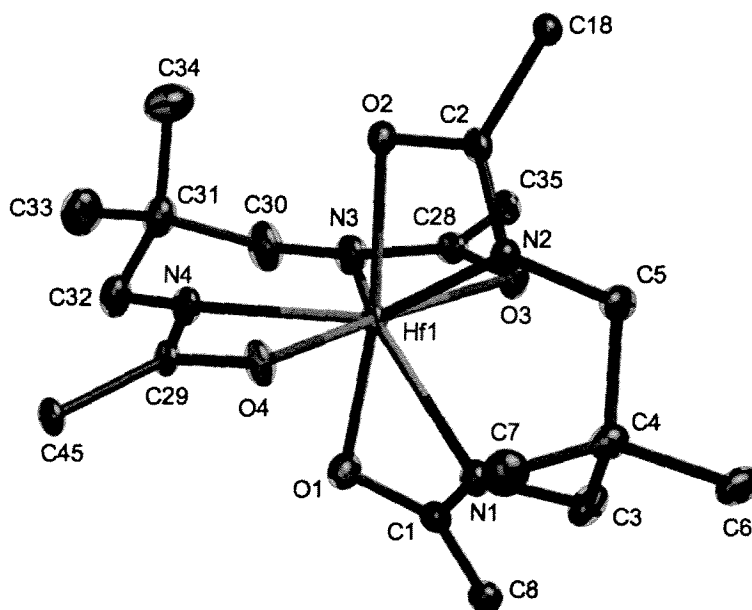
Empirical Formula	$\text{C}_{52}\text{H}_{72}\text{N}_4\text{O}_4\text{Zr}_1$	Crystal system	Triclinic
Formula Weight	908.36	Space group	$P-1$ (#2)
a, b, c (Å); α, β, γ ($^\circ$)	11.908(2), 11.901(2), 18.641(3); 82.392(11), 82.608(11), 80.628(11)		
$V, \text{Å}^3$	2568.1(8)	Total reflections	33550
Z	2	Unique reflections	12691
$D_{\text{calc}}, \text{g cm}^{-3}$	1.175	Parameters	550
μ (Mo $K\alpha$), cm^{-1}	2.59	R_1^a	0.0489
T, K	173 ± 1	R_w^a	0.1243
2θ range ($^\circ$)	57.1	Goodness-of-fit	1.125

$$^a R_1 = \frac{\sum ||F_o| - |F_c||}{\sum |F_o|}; R_w = \frac{\sum w((|F_o|^2 - |F_c|^2)|)^2 / \sum w |F_o|^2)^{1/2}}$$

Table A2.3 Crystallographic Data and Refinement Details for $^{Ad}[O_2N_2]_2Zr$, **2.10**

Empirical Formula	$C_{54}H_{80}N_4O_4Zr_1$	Crystal system	Orthorhombic
Formula Weight	940.44	Space group	$P 2_1 2_1 2_1$
a, b, c (Å)	11.7771(2), 12.7491(3), 19.7018(4)		
$V, \text{Å}^3$	2958.17(10)	Total reflections	39395
Z	2	Unique reflections	7051
$D_{\text{calc}}, \text{g cm}^{-3}$	1.056	Parameters	285
μ (Mo $K\alpha$), cm^{-1}	2.26	R_1^a	0.0915
T, K	173 ± 1	R_w^a	0.2409
2θ range ($^\circ$)	55.9	Goodness-of-fit	1.132

$$^a R_1 = \frac{\sum ||F_o| - |F_c||}{\sum |F_o|}; R_w = \frac{\sum w((|F_o|^2 - |F_c|^2)|^2 / \sum w |F_o|^2)^{1/2}}$$

**Figure A1** ORTEP depiction (ellipsoids at 30% probability) of core solid-state molecular structure of $^{Ad}[O_2N_2]_2Hf$, **2.11** (hydrogens and adamantyl groups omitted for clarity)

Appendix A: X-Ray Crystallographic Data

Table A2.4 Selected Bond Distances (Å) and Angles (°) for ^{Ad}[O₂N₂]₂Hf, **2.11**

	Lengths		Angles		Angles
Hf(1)-N(1)	2.248(3)	O(4)-Hf(1)-O(2)	91.71(10)	N(4)-Hf(1)-N(2)	132.08(11)
Hf(1)-N(2)	2.253(3)	O(4)-Hf(1)-O(1)	95.70(10)	N(3)-Hf(1)-N(2)	127.66(11)
Hf(1)-N(3)	2.248(3)	O(2)-Hf(1)-O(1)	163.44(9)	N(4)-Hf(1)-N(1)	126.54(11)
Hf(1)-N(4)	2.237(3)	O(4)-Hf(1)-O(3)	164.85(9)	N(3)-Hf(1)-N(1)	123.18(11)
Hf(1)-O(1)	2.192(3)	O(2)-Hf(1)-O(3)	84.71(10)		
Hf(1)-O(2)	2.184(2)	O(1)-Hf(1)-O(3)	91.70(10)		
Hf(1)-O(3)	2.203(2)	O(4)-Hf(1)-N(4)	58.79(10)		
Hf(1)-O(4)	2.168(2)	N(4)-Hf(1)-N(3)	77.28(11)		

Table A2.5 Crystallographic Data and Refinement Details for ^{Ad}[O₂N₂]₂Hf, **2.11**

Empirical Formula	C ₅₄ H ₈₀ N ₄ O ₄ Hf ₁	Crystal system	Orthorhombic
Formula Weight	1027.71	Space group	<i>P</i> 21 21 21
<i>a</i> , <i>b</i> , <i>c</i> (Å)	12.2394(3), 18.5760(3), 21.4268(5)		
<i>V</i> , Å ³	4871.58(18)	Total reflections	94258
<i>Z</i>	4	Unique reflections	11564
<i>D</i> _{calc} , g cm ⁻³	1.402	Parameters	568
μ (Mo K α), cm ⁻¹	2.191	<i>R</i> ₁ ^a	0.0300
<i>T</i> , K	173±1	<i>R</i> _w ^a	0.0634
2 θ range (°)	55.8	Goodness-of-fit	1.034

$$^a R_1 = \frac{\sum |F_o| - |F_c|}{\sum |F_o|}; R_w = \frac{\sum w((|F_o^2| - |F_c^2|)^2 / \sum w |F_o^2|^2)}{1/2}$$

Appendix A: X-Ray Crystallographic Data

Table A2.6 Crystallographic Data and Refinement Details for
 $[\text{DIPP}(\text{NO})^{\text{Ph}}]_3\text{ZrNHPh}$, **2.14**

Empirical Formula	$\text{C}_{63}\text{H}_{72}\text{N}_4\text{O}_3\text{Zr}_1\cdot\text{C}_7\text{H}_8$	Crystal system	Triclinic
Formula Weight	1116.60	Space group	<i>P</i> -1 (#2)
<i>a</i> , <i>b</i> , <i>c</i> (Å); α , β , γ (°)	13.6110(10), 15.3137(9), 18.6038(11); 69.509(3), 74.711(2), 70.850(2)		
<i>V</i> , Å ³	3382.4(4)	Total reflections	41052
<i>Z</i>	2	Unique reflections	11859
<i>D</i> _{calc} , g cm ⁻³	1.096	Parameters	707
μ (Mo K α), cm ⁻¹	2.07	<i>R</i> ₁ ^a	0.0637
<i>T</i> , K	173±1	<i>R</i> _w ^a	0.1120
2 θ range (°)	50.4	Goodness-of-fit	1.017

$${}^aR_1 = \sum \left| \frac{|F_o| - |F_c|}{\sum |F_o|} \right|; R_w = \sum w \left(\frac{(|F_o|^2 - |F_c|^2)|}{\sum w |F_o|^2} \right)^2 \Bigg)^{1/2}$$

Table A2.7 Crystallographic Data and Refinement Details for
 $[\text{tBu}(\text{NO})^{\text{Ph}}]_2\text{Zr}(\text{NEt}_2)_2$, **2.15**

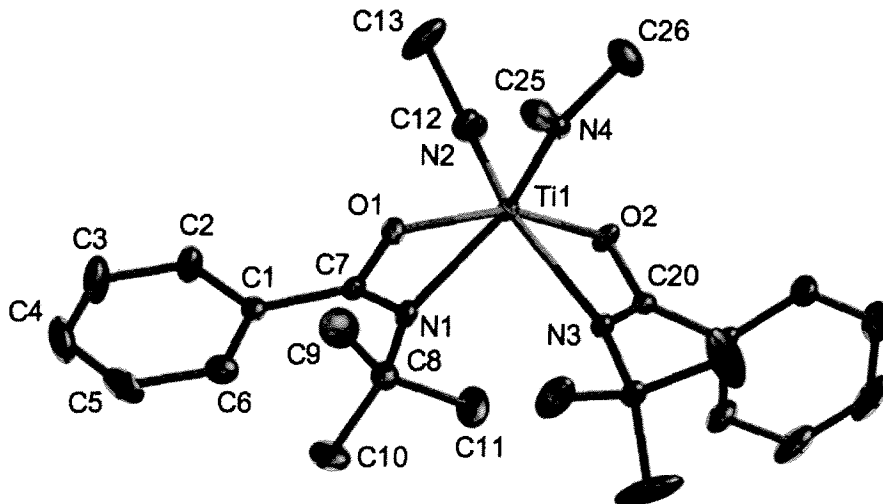
Empirical Formula	$\text{C}_{30}\text{H}_{48}\text{N}_4\text{O}_2\text{Zr}_1$	Crystal system	Triclinic
Formula Weight	587.95	Space group	<i>P</i> -1 (#2)
<i>a</i> , <i>b</i> , <i>c</i> (Å); α , β , γ (°)	10.785(1), 11.012(1), 13.861(2); 101.987(6), 92.387(5), 96.418(5)		
<i>V</i> , Å ³	1596.7(3)	Total reflections	14292
<i>Z</i>	2	Unique reflections	6491
<i>D</i> _{calc} , g cm ⁻³	1.223	Parameters	395
μ (Mo K α), cm ⁻¹	3.74	<i>R</i> ₁ ^a	0.080
<i>T</i> , K	173±1	<i>R</i> _w ^a	0.154
2 θ range (°)	55.7	Goodness-of-fit	0.95

$${}^aR_1 = \sum \left| \frac{|F_o| - |F_c|}{\sum |F_o|} \right|; R_w = \sum w \left(\frac{(|F_o|^2 - |F_c|^2)|}{\sum w |F_o|^2} \right)^2 \Bigg)^{1/2}$$

Table A2.8 Crystallographic Data and Refinement Details for $[\text{tBu}(\text{NO})^{\text{Ph}}]_2\text{Ti}(\text{NET}_2)_2$, **2.16**

Empirical Formula	$\text{C}_{30}\text{H}_{48}\text{N}_4\text{O}_2\text{Ti}_1 \cdot \text{C}_4\text{H}_8\text{O}$	Crystal system	Triclinic
Formula Weight	616.73	Space group	$P-1$ (#2)
a, b, c (Å); α, β, γ (°)	9.561(2), 10.519(2), 19.121(3); 102.30(1), 90.63(1), 110.60(1)	Total reflections	24329
$V, \text{Å}^3$	1751.0(6)	Unique reflections	5687
Z	2	Parameters	378
$D_{\text{calc}}, \text{g cm}^{-3}$	1.170	R_1^a	0.142
μ (Mo $K\alpha$), cm^{-1}	2.81	R_w^a	0.270
T, K	173±1	Goodness-of-fit	1.10
2θ range (°)	50.0		

$$^a R_1 = \frac{\sum ||F_o| - |F_c||}{\sum |F_o|}; R_w = \frac{\sum w((|F_o|^2) - |F_c|^2)^2 / \sum w |F_o|^2)^{1/2}}$$

**Figure A2** ORTEP depiction (ellipsoids at 30% probability) of solid-state molecular structure of $[\text{tBu}(\text{NO})^{\text{Ph}}]_2\text{Ti}(\text{NMe}_2)_2$, **2.17** (hydrogens omitted for clarity)

Appendix A: X-Ray Crystallographic Data

Table A2.9 Selected Bond Distances (Å) and Angles (°) for $[\text{tBu}(\text{NO})^{\text{Ph}}]_2\text{Ti}(\text{NMe}_2)_2$, **2.17**

	Lengths		Angles		Angles
Ti(1)-N(1)	2.2449(16)	N(2)-Ti(1)-N(4)	98.08(7)	N(2)-Ti(1)-N(1)	93.96(7)
Ti(1)-N(2)	1.8998(17)	N(2)-Ti(1)-O(2)	88.97(7)	N(4)-Ti(1)-N(1)	149.83(7)
Ti(1)-N(3)	2.2335(16)	N(4)-Ti(1)-O(2)	108.04(6)	O(2)-Ti(1)-N(1)	99.71(6)
Ti(1)-N(4)	1.9086(16)	N(2)-Ti(1)-O(1)	101.82(6)	O(1)-Ti(1)-N(1)	61.39(5)
Ti(1)-O(1)	2.0423(13)	N(4)-Ti(1)-O(1)	89.02(6)	N(3)-Ti(1)-N(1)	87.37(6)
Ti(1)-O(2)	2.0276(14)	O(2)-Ti(1)-O(1)	158.48(6)	N(1)-C(7)-O(1)	114.75(17)
O(1)-C(7)	1.314(2)	N(2)-Ti(1)-N(3)	150.17(7)	N(3)-C(20)-O(2)	113.76(17)
O(2)-C(20)	1.316(2)	N(4)-Ti(1)-N(3)	95.45(6)	C(12)-N(2)-Ti(1)	127.57(15)
N(1)-C(7)	1.292(2)	O(2)-Ti(1)-N(3)	61.51(5)	C(13)-N(2)-Ti(1)	121.55(15)
N(3)-C(20)	1.295(2)	O(1)-Ti(1)-N(3)	104.89(6)	C(12)-N(2)-C(13)	110.85(18)

Table A2.10 Crystallographic Data and Refinement Details for $[\text{tBu}(\text{NO})^{\text{Ph}}]_2\text{Ti}(\text{NMe}_2)_2$, **2.17**

Empirical Formula	$\text{C}_{26}\text{H}_{40}\text{N}_4\text{O}_2\text{Ti}_1$	Crystal system	Monoclinic
Formula Weight	488.52	Space group	$P 2_1$ (#4)
a, b, c (Å); β (°)	11.6743(9), 13.902(1), 17.195(1); 98.27(1)		
$V, \text{Å}^3$	2761.8(4)	Total reflections	50633
Z	2	Unique reflections	6534
$D_{\text{calc}}, \text{g cm}^{-3}$	1.175	Parameters	322
μ (Mo $K\alpha$), cm^{-1}	3.37	R_1^a	0.068
T, K	173±1	R_w^a	0.122
2θ range (°)	55.8	Goodness-of-fit	0.99

$$^a R_1 = \frac{\sum ||F_o| - |F_c||}{\sum |F_o|}; R_w = \frac{\sum w(|F_o|^2 - |F_c|^2)|^2}{\sum w |F_o|^2}^{1/2}$$

Appendix A: X-Ray Crystallographic Data

Table A2.11 Crystallographic Data and Refinement Details for
 $[\text{DMP}(\text{NO})^{\text{tBu}}]_2\text{Zr}(\text{NMe}_2)_2$, **2.18**

Empirical Formula	$\text{C}_{30}\text{H}_{48}\text{N}_4\text{O}_2\text{Zr}_1$	Crystal system	Orthorhombic
Formula Weight	587.94	Space group	$Pna21$
a, b, c (Å)	17.237(1), 18.746(1), 9.8196(1)		
$V, \text{Å}^3$	3172.98(44)	Total reflections	27716
Z	4	Unique reflections	6575
$D_{\text{calc}}, \text{g cm}^{-3}$	1.231	Parameters	334
μ (Mo $K\alpha$), cm^{-1}	3.77	R_1^a	0.0367
T, K	173±1	R_w^a	0.0938
2θ range (°)	56.3	Goodness-of-fit	0.793

$$^a R_1 = \frac{\sum ||F_o| - |F_c||}{\sum |F_o|}; R_w = \frac{\sum w((|F_o|^2 - |F_c|^2)^2 / \sum w |F_o|^2)^{1/2}}$$

Table A2.12 Crystallographic Data and Refinement Details for
 $\kappa^2\text{-}[\text{DMP}(\text{NO})^{\text{tBu}}]\text{-}\kappa^1\text{-}[\text{DMP}(\text{NO})^{\text{tBu}}]\text{Zr}(\text{NMe}_2)_2(\text{Py})$, **2.19**

Empirical Formula	$\text{C}_{35}\text{H}_{53}\text{N}_5\text{O}_2\text{Zr}_1$	Crystal system	Monoclinic
Formula Weight	667.04	Space group	$P2_1$ (#4)
a, b, c (Å); β (°)	10.5351(6), 9.9729(6), 18.0024(12); 106.273(2)		
$V, \text{Å}^3$	1815.66(19)	Total reflections	26681
Z	2	Unique reflections	8413
$D_{\text{calc}}, \text{g cm}^{-3}$	1.22	Parameters	388
μ (Mo $K\alpha$), cm^{-1}	3.38	R_1^a	0.0536
T, K	173±1	R_w^a	0.0949
2θ range (°)	55.9	Goodness-of-fit	0.980

$$^a R_1 = \frac{\sum ||F_o| - |F_c||}{\sum |F_o|}; R_w = \frac{\sum w((|F_o|^2 - |F_c|^2)^2 / \sum w |F_o|^2)^{1/2}}$$

Appendix A: X-Ray Crystallographic Data

Table A2.13 Crystallographic Data and Refinement Details for
 $[\text{DMP}(\text{NO})^{\text{Ph}}]_2\text{Ti}(\text{NEt}_2)_2$, **2.23**

Empirical Formula	$\text{C}_{38}\text{H}_{48}\text{N}_4\text{O}_2\text{Ti}_1$	Crystal system	Monoclinic
Formula Weight	640.72	Space group	$P 2_1/c$ (#14)
a, b, c (Å); β (°)	18.407(1), 9.8394(5), 21.126(1); 114.821(2)		
$V, \text{Å}^3$	3472.9(3)	Total reflections	31182
Z	4	Unique reflections	7739
$D_{\text{calc}}, \text{g cm}^{-3}$	1.225	Parameters	406
μ (Mo $K\alpha$), cm^{-1}	2.85	R_1^a	0.062
T, K	173±1	R_w^a	0.123
2θ range (°)	55.7	Goodness-of-fit	1.10

$$^a R_1 = \frac{\sum ||F_o| - |F_c||}{\sum |F_o|}; R_w = \frac{\sum w((|F_o|^2 - |F_c|^2)|)^2 / \sum w |F_o|^2}{\sum w |F_o|^2}^{1/2}$$

Table A3.1 Crystallographic Data and Refinement Details for
 $[\text{DMP}(\text{NO})^{\text{Ph}}]_2\text{Hf}(\text{CH}_2\text{Ph})_2(\text{THF})$, **3.6**

Empirical Formula	$\text{C}_{48}\text{H}_{50}\text{N}_2\text{O}_3\text{Hf}_1$	Crystal system	Triclinic
Formula Weight	881.39	Space group	$P-1$ (#2)
a, b, c (Å); α, β, γ (°)	11.605(5), 12.207(5), 16.353(5); 103.027(5), 102.455(5), 106.651(5)		
$V, \text{Å}^3$	2062.6(14)	Total reflections	18282
Z	2	Unique reflections	8417
$D_{\text{calc}}, \text{g cm}^{-3}$	1.419	Parameters	491
μ (Mo $K\alpha$), cm^{-1}	2.572	R_1^a	0.0608
T, K	173±1	R_w^a	0.1106
2θ range (°)	55.7	Goodness-of-fit	1.158

$$^a R_1 = \frac{\sum ||F_o| - |F_c||}{\sum |F_o|}; R_w = \frac{\sum w((|F_o|^2 - |F_c|^2)|)^2 / \sum w |F_o|^2}{\sum w |F_o|^2}^{1/2}$$

Appendix A: X-Ray Crystallographic Data

Table A3.2 Crystallographic Data and Refinement Details for
 $[\text{DMP}^{\text{tBu}}(\text{NO})]_2\text{Zr}(\text{CH}_2\text{Ph})_2$, **3.9**

Empirical Formula	$\text{C}_{40}\text{H}_{50}\text{N}_2\text{O}_2\text{Zr}_1$	Crystal system	Triclinic
Formula Weight	682.04	Space group	<i>P</i> -1 (#2)
<i>a</i> , <i>b</i> , <i>c</i> (Å); α , β , γ (°)	9.719(2), 12.169(3), 16.612(4); 72.624(10), 85.866(11), 76.118(10)		
<i>V</i> , Å ³	1820.3(7)	Total reflections	52902
<i>Z</i>	2	Unique reflections	15411
<i>D</i> _{calc} , g cm ⁻³	1.244	Parameters	406
μ (Mo K α), cm ⁻¹	3.37	<i>R</i> ₁ ^a	0.0707
<i>T</i> , K	173±1	<i>R</i> _w ^a	0.1359
2 θ range (°)	73.1	Goodness-of-fit	1.044

$$^a R_1 = \frac{\sum ||F_o| - |F_c||}{\sum |F_o|}; R_w = \frac{\sum w((|F_o|^2 - |F_c|^2)|)^2 / \sum w |F_o|^2}{\sum w |F_o|^2}^{1/2}$$

Table A3.3 Crystallographic Data and Refinement Details for
 $^{\text{Ad}}[\text{O}_2\text{N}_2]\text{Zr}(\text{CH}_2\text{Ph})_2(\text{THF})$, **3.14**

Empirical Formula	$\text{C}_{45}\text{H}_{62}\text{N}_2\text{O}_3\text{Zr}_1$	Crystal system	Triclinic
Formula Weight	770.19	Space group	<i>P</i> -1 (#2)
<i>a</i> , <i>b</i> , <i>c</i> (Å); α , β , γ (°)	8.8174(7), 11.5483(9), 21.155(3); 86.984(10), 82.894(9), 69.810(6)		
<i>V</i> , Å ³	2006.2(3)	Total reflections	17662
<i>Z</i>	2	Unique reflections	8114
<i>D</i> _{calc} , g cm ⁻³	1.275	Parameters	462
μ (Mo K α), cm ⁻¹	3.15	<i>R</i> ₁ ^a	0.0494
<i>T</i> , K	173±1	<i>R</i> _w ^a	0.1127
2 θ range (°)	55.8	Goodness-of-fit	1.087

$$^a R_1 = \frac{\sum ||F_o| - |F_c||}{\sum |F_o|}; R_w = \frac{\sum w((|F_o|^2 - |F_c|^2)|)^2 / \sum w |F_o|^2}{\sum w |F_o|^2}^{1/2}$$

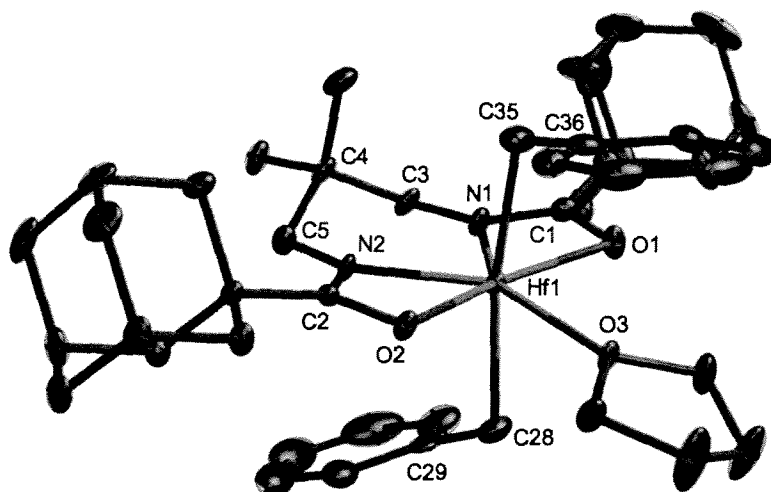


Figure A3 ORTEP depiction (ellipsoids at 30% probability) of solid-state molecular structure of $\text{Ad}[\text{O}_2\text{N}_2]\text{Hf}(\text{CH}_2\text{Ph})_2(\text{THF})$, **3.15** (hydrogens omitted)

Table A3.4 Selected Bond Distances (Å) and Angles (°) for $\text{Ad}[\text{O}_2\text{N}_2]\text{Hf}(\text{CH}_2\text{Ph})_2(\text{THF})$, **3.15**

Lengths		Angles		Angles	
Hf(1)-O(1)	2.193(2)	O(1)-Hf(1)-O(2)	160.35(8)	C(36)-C(35)-Hf(1)	114.2(2)
Hf(1)-O(2)	2.181(2)	O(1)-Hf(1)-O(3)	81.68(8)	O(1)-C(1)-N(1)	112.2(3)
Hf(1)-O(3)	2.256(2)	O(2)-Hf(1)-O(3)	81.14(8)	C(29)-C(28)-Hf(1)	115.1(2)
Hf(1)-N(1)	2.166(2)	O(2)-Hf(1)-N(2)	60.28(9)	O(2)-C(2)-N(2)	112.9(3)
Hf(1)-N(2)	2.174(2)	O(1)-Hf(1)-N(1)	60.00(9)		
Hf(1)-C(28)	2.341(4)	N(2)-Hf(1)-N(1)	78.13(9)		
Hf(1)-C(35)	2.357(4)	C(28)-Hf(1)-C(35)	168.71(12)		

Appendix A: X-Ray Crystallographic Data

Table A3.5 Crystallographic Data and Refinement Details for $^{Ad}[O_2N_2]Hf(CH_2Ph)_2(THF)$, **3.15**

Empirical Formula	$C_{45}H_{62}N_2O_3Hf_1$	Crystal system	Triclinic
Formula Weight	857.46	Space group	<i>P</i> -1 (#2)
<i>a</i> , <i>b</i> , <i>c</i> (Å); α , β , γ (°)	11.4687(12), 17.4135(18), 22.171(2); 103.5860(10), 94.322(2), 109.066(3)		
<i>V</i> , Å ³	4011.6(7)	Total reflections	35599
<i>Z</i>	4	Unique reflections	16302
<i>D</i> _{calc} , g cm ⁻³	1.420	Parameters	923
μ (Mo K α), cm ⁻¹	2.642	<i>R</i> ₁ ^a	0.0368
<i>T</i> , K	173±1	<i>R</i> _w ^a	0.0749
2 θ range (°)	55.8	Goodness-of-fit	1.068

$$^a R_1 = \frac{\sum ||F_o| - |F_c||}{\sum |F_o|}; R_w = \frac{\sum w((|F_o|^2 - |F_c|^2)|)^2 / \sum w |F_o|^2}{\sum w |F_o|^2}^{1/2}$$

Table A3.6 Crystallographic Data and Refinement Details for $[^{DMP}(NO)^{iBu}]_2Zr(\eta^2-2,6-Me_2C_6H_3N=CCH_2Ph)_2$, **3.16**

Empirical Formula	$C_{58}H_{68}N_4O_2Zr_1$	Crystal system	Monoclinic
Formula Weight	944.38	Space group	<i>P</i> 21/ <i>c</i>
<i>a</i> , <i>b</i> , <i>c</i> (Å); β (°)	19.475(5), 12.736(5), 20.838(5); 90.379(5)		
<i>V</i> , Å ³	5168(3)	Total reflections	48486
<i>Z</i>	4	Unique reflections	6785
<i>D</i> _{calc} , g cm ⁻³	1.214	Parameters	586
μ (Mo K α), cm ⁻¹	2.57	<i>R</i> ₁ ^a	0.1215
<i>T</i> , K	173±1	<i>R</i> _w ^a	0.2504
2 θ range (°)	45.3	Goodness-of-fit	1.055

$$^a R_1 = \frac{\sum ||F_o| - |F_c||}{\sum |F_o|}; R_w = \frac{\sum w((|F_o|^2 - |F_c|^2)|)^2 / \sum w |F_o|^2}{\sum w |F_o|^2}^{1/2}$$

Appendix A: X-Ray Crystallographic Data

Table A3.7 Crystallographic Data and Refinement Details for $[\text{DMP}(\text{NO})^{\text{tBu}}]_2\text{Zr}(\eta^4\text{-ArNC}(\text{CH}_2\text{Ph})=\text{C}(\text{CH}_2\text{Ph})\text{NAr})$, **3.17** (Ar = 2,6-Me₂C₆H₃)

Empirical Formula	C ₅₈ H ₆₈ N ₄ O ₂ Zr ₁	Crystal system	Monoclinic
Formula Weight	944.38	Space group	<i>P</i> 21/ <i>n</i>
<i>a</i> , <i>b</i> , <i>c</i> (Å); β (°)	13.036(4), 22.774(7), 16.957(5); 94.825(10)		
<i>V</i> , Å ³	5016(3)	Total reflections	64748
<i>Z</i>	4	Unique reflections	14747
<i>D</i> _{calc} , g cm ⁻³	1.250	Parameters	586
μ (Mo Kα), cm ⁻¹	2.65	R ₁ ^a	0.0888
<i>T</i> , K	173±1	R _w ^a	0.1549
2θ range (°)	60.5	Goodness-of-fit	1.033

$$^a R_1 = \frac{\sum ||F_o| - |F_c||}{\sum |F_o|}; R_w = \frac{\sum w((|F_o|^2 - |F_c|^2)^2 / \sum w |F_o|^2)^{1/2}}{\sum w |F_o|^2}$$

Table A3.8 Crystallographic Data and Refinement Details for $\{[\text{DMP}(\text{NO})^{\text{Ph}}]_2\text{Hf}(\mu\text{-O})\}_4$, **3.21**

Empirical Formula	C ₁₂₀ H ₁₃₆ N ₈ O ₁₂ Hf ₄ ·3C ₇ H ₈	Crystal system	Triclinic
Formula Weight	2848.54	Space group	<i>P</i> -1 (#2)
<i>a</i> , <i>b</i> , <i>c</i> (Å); α, β, γ (°)	14.7220(8), 20.1280(9), 22.2090(9); 92.02(1), 99.12(1), 109.55(1)		
<i>V</i> , Å ³	6095.6(5)	Total reflections	57074
<i>Z</i>	2	Unique reflections	24854
<i>D</i> _{calc} , g cm ⁻³	1.552	Parameters	1472
μ (Mo Kα), cm ⁻¹	3.46	R ₁ ^a	0.045
<i>T</i> , K	173±1	R _w ^a	0.086
2θ range (°)	55.8	Goodness-of-fit	1.13

$$^a R_1 = \frac{\sum ||F_o| - |F_c||}{\sum |F_o|}; R_w = \frac{\sum w((|F_o|^2 - |F_c|^2)^2 / \sum w |F_o|^2)^{1/2}}{\sum w |F_o|^2}$$

Appendix A: X-Ray Crystallographic Data

Table A4.1 Crystallographic Data and Refinement Details for
 $[\text{DIPP}(\text{NO})^{\text{Ph}}]_2\text{Zr}(\text{NH}-2,6\text{-Me}_2\text{C}_6\text{H}_3)(\text{NMe}_2)$, **4.17**

Empirical Formula	$\text{C}_{48}\text{H}_{60}\text{N}_4\text{O}_2\text{Zr}_1$	Crystal system	Triclinic
Formula Weight	816.22	Space group	<i>P</i> -1 (#2)
<i>a</i> , <i>b</i> , <i>c</i> (Å); α , β , γ (°)	13.2918(13), 14.7147(12), 15.3965(14); 84.176(5), 67.997(5), 63.409(4)		
<i>V</i> , Å ³	2488.7(4)	Total reflections	16396
<i>Z</i>	2	Unique reflections	9385
<i>D</i> _{calc} , g cm ⁻³	1.089	Parameters	524
μ (Mo K α), cm ⁻¹	2.57	<i>R</i> ₁ ^a	0.0688
<i>T</i> , K	173±1	<i>R</i> _w ^a	0.1799
2 θ range (°)	59.8	Goodness-of-fit	1.082

$$^a R_1 = \frac{\sum ||F_o| - |F_c||}{\sum |F_o|}; R_w = \frac{\sum w((|F_o|^2 - |F_c|^2)|)^2 / \sum w |F_o|^2}{\sum w |F_o|^2}^{1/2}$$

Table A4.2 Crystallographic Data and Refinement Details for
 $[\text{DIPP}(\text{NO})^{\text{Ph}}]_2\text{Zr}=\text{N}(2,6\text{-Me}_2\text{C}_6\text{H}_3)(\text{TPPO})$, **4.25**

Empirical Formula	$\text{C}_{64}\text{H}_{68}\text{N}_3\text{O}_3\text{P}_1\text{Zr}_1$	Crystal system	Monoclinic
Formula Weight	1049.44	Space group	<i>P</i> 21/ <i>n</i>
<i>a</i> , <i>b</i> , <i>c</i> (Å); β (°)	14.0824(4), 20.0887(6), 22.2465(5); 99.8050(10)		
<i>V</i> , Å ³	6201.5(3)	Total reflections	13318
<i>Z</i>	4	Unique reflections	10153
<i>D</i> _{calc} , g cm ⁻³	1.405	Parameters	703
μ (Mo K α), cm ⁻¹	3.08	<i>R</i> ₁ ^a	0.0574
<i>T</i> , K	173±1	<i>R</i> _w ^a	0.1252
2 θ range (°)	53.9	Goodness-of-fit	0.702

$$^a R_1 = \frac{\sum ||F_o| - |F_c||}{\sum |F_o|}; R_w = \frac{\sum w((|F_o|^2 - |F_c|^2)|)^2 / \sum w |F_o|^2}{\sum w |F_o|^2}^{1/2}$$

Appendix A: X-Ray Crystallographic Data

Table A4.3 Crystallographic Data and Refinement Details for
 $[\text{DMP}(\text{NO})^{\text{tBu}}]_2\text{Zr}=\text{N}(2,6\text{-Me}_2\text{C}_6\text{H}_3)(\text{TPPO})(\text{Py}), \mathbf{4.27}$

Empirical Formula	$\text{C}_{57}\text{H}_{65}\text{N}_4\text{O}_3\text{P}_1\text{Zr}_1\cdot\text{C}_7\text{H}_8$	Crystal system	Monoclinic
Formula Weight	994.87	Space group	$P21/c$
a, b, c (Å); β (°)	15.1106(9), 14.8531(9), 26.6101(14); 101.710(2)		
$V, \text{Å}^3$	5848.1(6)	Total reflections	95110
Z	4	Unique reflections	18713
$D_{\text{calc}}, \text{g cm}^{-3}$	1.130	Parameters	658
μ (Mo $K\alpha$), cm^{-1}	2.59	R_1^a	0.1119
T, K	173 ± 1	R_w^a	0.1514
2θ range (°)	66.1	Goodness-of-fit	1.025

$$^a R_1 = \frac{\sum ||F_o| - |F_c||}{\sum |F_o|}; R_w = \frac{\sum w((|F_o|^2 - |F_c|^2)|^2 / \sum w |F_o|^2)^{1/2}}$$

Table A4.4 Crystallographic Data and Refinement Details for
 $[\text{DIPP}(\text{NO})^{\text{Ph}}]_2\text{Zr}(\mu\text{-N}(2,6\text{-Me}_2\text{C}_6\text{H}_3))_2\text{Zr}[\text{DIPP}(\text{NO})^{\text{Ph}}]_2, \mathbf{4.31}$

Empirical Formula	$\text{C}_{92}\text{H}_{106}\text{N}_6\text{O}_4\text{Zr}_2$	Crystal system	Monoclinic
Formula Weight	1542.27	Space group	$C2/c$
a, b, c (Å); β (°)	40.697(3), 16.4151(11), 25.7332(15); 94.667(3)		
$V, \text{Å}^3$	17134.1(19)	Total reflections	111529
Z	9	Unique reflections	15093
$D_{\text{calc}}, \text{g cm}^{-3}$	1.345	Parameters	937
μ (Mo $K\alpha$), cm^{-1}	3.32	R_1^a	0.0958
T, K	173 ± 1	R_w^a	0.1919
2θ range (°)	50.2	Goodness-of-fit	1.090

$$^a R_1 = \frac{\sum ||F_o| - |F_c||}{\sum |F_o|}; R_w = \frac{\sum w((|F_o|^2 - |F_c|^2)|^2 / \sum w |F_o|^2)^{1/2}}$$

Appendix A: X-Ray Crystallographic Data

Table A4.5 Crystallographic Data and Refinement Details for $[\text{DMP}(\text{NO})^{\text{tBu}}]_2\text{Zr}(\mu\text{-N}(2,6\text{-Me}_2\text{C}_6\text{H}_3))_2\text{Zr}[\text{DMP}(\text{NO})^{\text{tBu}}]\text{NH}(2,6\text{-Me}_2\text{C}_6\text{H}_3)$, **4.33**

Empirical Formula	$\text{C}_{63}\text{H}_{82}\text{N}_6\text{O}_3\text{Zr}_2$	Crystal system	Monoclinic
Formula Weight	1153.79	Space group	$P1\ 21/c1$
a, b, c (Å); β (°)	14.882(3), 17.998(3), 22.014(4); 100.982(9)		
$V, \text{Å}^3$	5788.4(18)	Total reflections	109710
Z	4	Unique reflections	14210
$D_{\text{calc}}, \text{g cm}^{-3}$	1.314	Parameters	671
μ (Mo $K\alpha$), cm^{-1}	4.10	R_1^a	0.063
T, K	173±1	R_w^a	0.124
2 θ range (°)	56.6	Goodness-of-fit	1.073

$$^a R_1 = \frac{\sum ||F_o| - |F_c||}{\sum |F_o|}; R_w = \frac{\sum w((|F_o|^2 - |F_c|^2)|^2 / \sum w |F_o|^2)^{1/2}}{\sum w |F_o|^2}^{1/2}$$

Table A5.1 Crystallographic Data and Refinement Details for $\kappa^2\text{-}[\text{DIPP}(\text{NO})^{\text{tBu}}]\text{-}\kappa^1\text{-}[\text{DIPP}(\text{NO})^{\text{tBu}}]\text{Ti}=\text{NCH}_2\text{CPh}_2\text{CH}_2\text{CH}=\text{CH}_2(\text{NHMe}_2)$, **5.49·HNMe₂**

Empirical Formula	$\text{C}_{53}\text{H}_{76}\text{N}_4\text{O}_2\text{Ti}_1\cdot\text{C}_7\text{H}_8$	Crystal system	Triclinic
Formula Weight	941.21	Space group	$P\text{-}1$ (#2)
a, b, c (Å); α, β, γ (°)	10.4195(8), 15.7613(13), 18.6390(12); 67.019(2), 81.877(3), 85.825(3)		
$V, \text{Å}^3$	2789.3(4)	Total reflections	20790
Z	2	Unique reflections	8289
$D_{\text{calc}}, \text{g cm}^{-3}$	1.121	Parameters	604
μ (Mo $K\alpha$), cm^{-1}	1.97	R_1^a	0.0995
T, K	173±1	R_w^a	0.2099
2 θ range (°)	47.66	Goodness-of-fit	1.066

$$^a R_1 = \frac{\sum ||F_o| - |F_c||}{\sum |F_o|}; R_w = \frac{\sum w((|F_o|^2 - |F_c|^2)|^2 / \sum w |F_o|^2)^{1/2}}{\sum w |F_o|^2}^{1/2}$$

Appendix B

Computational Details

B1 Bis(amidate) bis(amido) DFT calculations

The density functional theory (DFT) calculations in Chapter 2 were performed by Federico Zahariev in the Wang research group at UBC. The calculations were carried out on a Linux cluster of IBM machines with Intel Xeon processors¹ using the Gaussian'03 package.² The initial guesses for some geometric isomers were generated from available crystallographic structures. The other isomers were generated with PyMol,³ a flexible open-source visualization tool that allows for easy repositioning of large groups of atoms.

The geometry optimization of the different geometric isomers of these Ti complexes was facilitated by first optimizing with the UFF molecular mechanics method,⁴ followed by an optimization by the Hartree-Fock-Slater α -method density-functional method⁵ with the minimal basis STO-3G. After this stage of pre-optimization, a subsequent optimization was performed using a hybrid density-functional/Hartree-Fock method, i.e. B3LYP.^{6, 7} All structure determinations were carried out with full geometry optimization using analytical energy gradients.⁸ For the Ti atoms an effective core potential basis was employed together with a Dauning-Huzinaga double-set basis for C,N,O, and H atoms, a combination abbreviated as LANL2DZ. The B3LYP/LANL2DZ quantum-chemical level of theory is known to provide accurate results for transition-metal complexes.^{9, 10}

The results were analyzed based on B3LYP/LANL2DZ energies of different geometric isomers and the visualization of molecular orbitals. The graphical representations of the orbitals were produced by gOpenMol, another versatile open-source visualization tool.¹¹

Appendix B: Computational Details

Table B2.1: Experimental and Calculated Bond Lengths (Å) and Angles (°) for **2.16**

BondLength(Å)/ Angle (°)	Experimental	Theoretical
Ti(1)-N(1)	2.234(5)	2.201
Ti(1)-O(1)	2.035(4)	1.983
Ti(1)-N(2)	1.907(6)	1.945
C(1)-O(1)	1.329(8)	1.384
C(1)-N(1)	1.283(8)	1.371
O(1)-C(1)-N(1)	113.9(6)	110.9
C(12)-N(2)-C(14)	113.5(6)	111.6
O(1)-Ti(1)-O(2)	157.59(19)	158.12
N(1)-Ti(1)-N(3)	85.5(2)	83.2
N(1)-Ti(1)-N(2)	95.4(2)	92.2
N(1)-Ti(1)-N(4)	149.9(2)	157.4
N(2)-Ti(1)-N(4)	98.6(3)	100.0
O(1)-Ti(1)-N(3)	100.52(19)	98.2
O(1)-Ti(1)-N(2)	105.9(2)	102.1
O(1)-Ti(1)-N(1)	61.50(19)	65.48
C(7)-C(2)-C(1)-O(1)	-93.6(8)	-84.8

Appendix B: Computational Details

Table B2.2: Experimental and Calculated Bond Lengths (Å) and Angles (°) for **2.23**

Bond Length(Å)/ Angle (°)	Experimental	Theoretical
Ti(1)-N(1)	2.211(1)	2.147
Ti(1)-N(2)	1.894(1)	1.944
Ti(1)-N(3)	2.375(1)	2.204
Ti(1)-N(4)	1.901(1)	1.943
Ti(1)-O(1)	2.076(1)	2.054
Ti(1)-O(2)	2.004(1)	1.978
C(1)-O(1)	1.293(2)	1.368
C(1)-N(1)	1.310(2)	1.392
C(20)-O(2)	1.318(2)	1.383
C(20)-N(3)	1.296(2)	1.379
O(1)-C(1)-N(1)	113.9(1)	110.8
C(18)-N(2)-C(16)	113.9(1)	111.1
O(1)-Ti(1)-O(2)	95.37(5)	95.63
N(1)-Ti(1)-N(3)	94.94(5)	93.56
N(1)-Ti(1)-N(2)	105.06(6)	102.30
N(1)-Ti(1)-N(4)	97.15(6)	97.96
N(2)-Ti(1)-N(4)	99.79(6)	102.11
N(3)-Ti(1)-N(4)	95.83(6)	95.45
N(3)-Ti(1)-N(2)	152.73(6)	154.31
O(1)-Ti(1)-N(3)	81.63(5)	79.91
O(1)-Ti(1)-N(2)	91.86(5)	88.40
O(1)-Ti(1)-N(1)	61.09(5)	65.41
O(1)-Ti(1)-N(4)	157.55(5)	162.15
O(2)-Ti(1)-N(1)	148.94	154.61
O(2)-Ti(1)-N(3)	59.62(4)	65.40
O(2)-Ti(1)-N(4)	102.58(5)	98.07
O(2)-Ti(1)-N(2)	95.02(5)	93.42
C(7)-C(2)-C(1)-O(1)	170.7(1)	165.5
C(9)-C(8)-N(1)-C(1)	89.1(2)	78.7

Appendix B: Computational Details

Table B2.3: Experimental and Calculated Bond Lengths (Å) and Angles (°) for **2.24**

Bond Length(Å)/ Angle (°)	Experimental	Theoretical
Ti(1)-N(1)	2.156(1)	2.120
Ti(1)-O(1)	2.146(1)	2.050
Ti(1)-N(2)	1.899(2)	1.948
C(1)-O(1)	1.283(2)	1.360
C(1)-N(1)	1.320(2)	1.403
O(1)-C(1)-N(1)	114.5(2)	110.4
C(20)-N(2)-C(22)	112.9(2)	110.5
O(1)-Ti(1)-O(1*)	81.92(7)	83.24
N(1)-Ti(1)-N(1*)	140.42(8)	141.48
N(1)-Ti(1)-N(2)	99.21(6)	102.30
N(1)-Ti(1)-N(2*)	105.68(6)	104.45
N(2)-Ti(1)-N(2*)	101.1(1)	100.9
O(1)-Ti(1)-N(1*)	88.30(5)	84.70
O(1)-Ti(1)-N(2)	159.30(5)	166.09
O(1)-Ti(1)-N(1)	61.21(5)	65.91
C(7)-C(2)-C(1)-O(1)	157.2(2)	166.6

Appendix B: Computational Details

Table B2.4: Energetic Ordering of Geometric Isomers:

Complex	Absolute Energy (Hartrees)	Absolute Energy (eV)	Relative Energy (eV)	Ordering	Symmetry
2.16	-1599.55151351	-43526.35597	0.111744971	2	C ₁
	-1599.55561987	-43526.46771	0.000000000	1	O-Trans C ₂
	-1599.51770137	-43525.43588	1.031827400	5	C _{2v}
	-1599.53645487	-43525.9462	0.521514660	4	C _{2h}
	-1599.54758735	-43526.24913	0.218582067	3	N-Trans C ₂
2.23	-1904.37830216	-51821.18061	0.035752943	2	C ₁
	-1904.37440731	-51821.07462	0.141738043	3	O-Trans C ₂
	-1904.35664829	-51820.59137	0.624989392	4	C _{2v}
	-1904.34609561	-51820.30422	0.912144699	5	C _{2h}
	-1904.37961619	-51821.21636	0.000000000	1	N-Trans C ₂
2.24	-2218.81489504	-60377.5034	0.095592130	2	C ₁
	-2218.80232288	-60377.16129	0.437700719	3	O-Trans C ₂
	-2218.76110419	-60376.03966	1.559327223	5	C _{2v}
	-2218.79609465	-60376.99181	0.607180822	4	C _{2h}
	-2218.81840814	-60377.59899	0.000000000	1	N-Trans C ₂

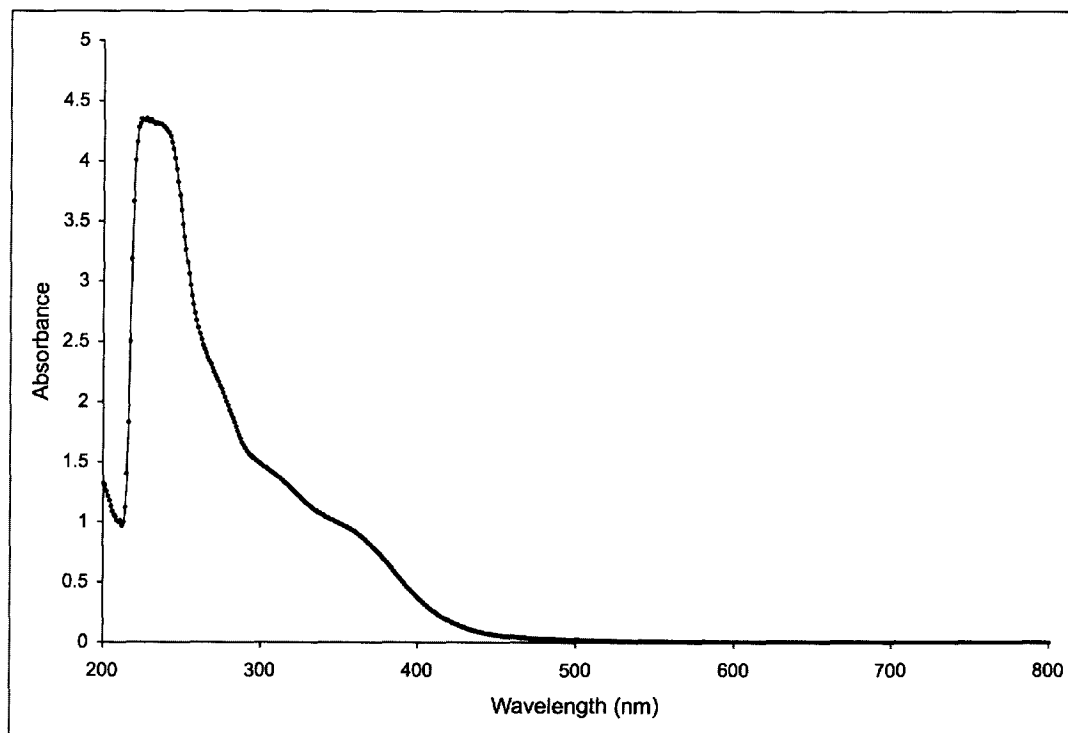


Figure B1 Experimental UV/vis spectrum of **2.23**

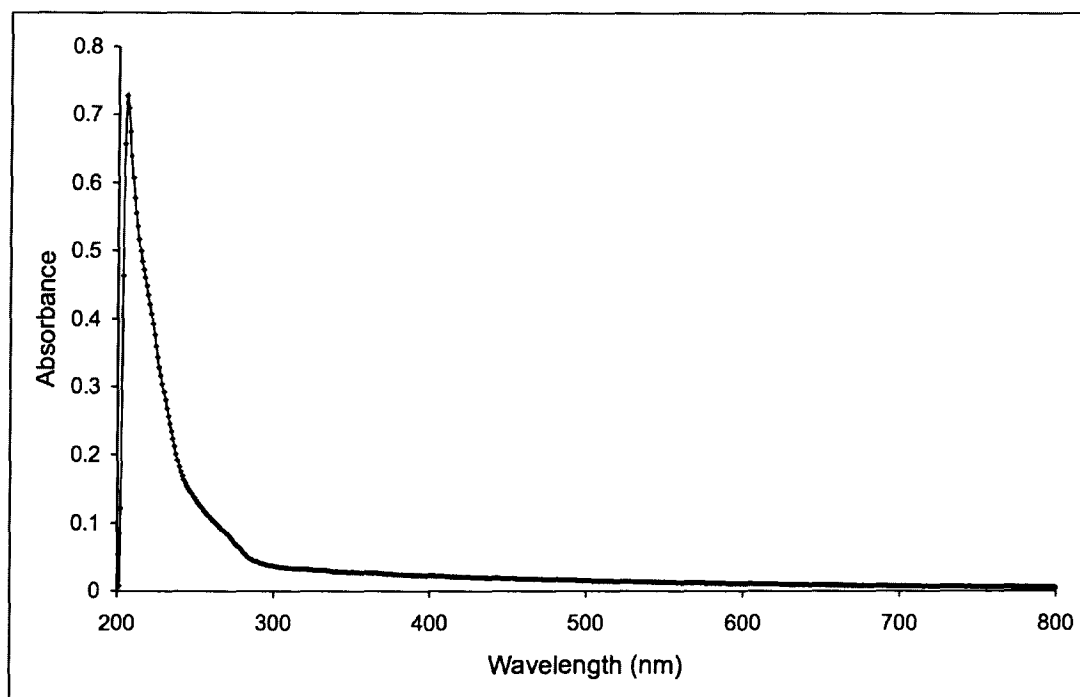


Figure B2 Experimental UV/vis spectrum of **2.24**

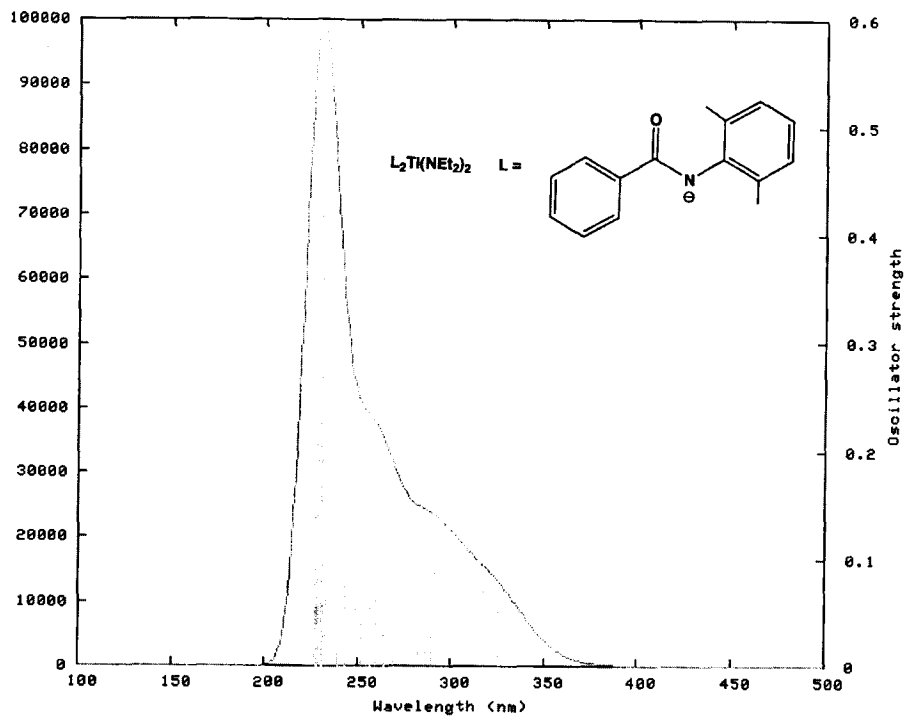


Figure B3 Calculated UV/vis spectrum for 2.23

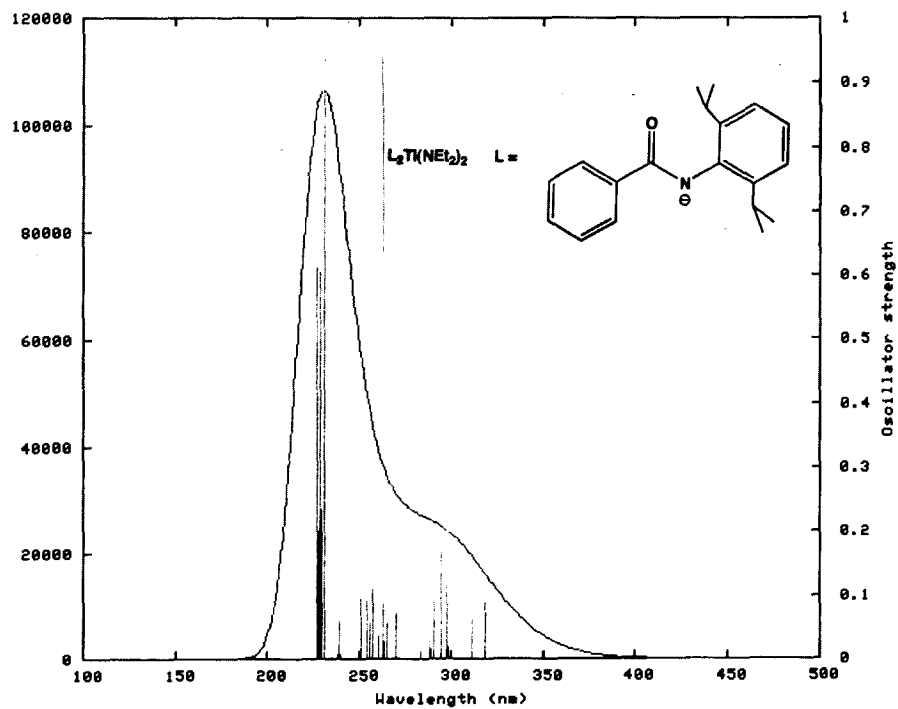


Figure B4 Calculated UV/vis spectrum of 2.24

Full eigenvalue tables and graphical representations of orbitals for **2.16**, **2.23**, and **2.24** are available as supporting information for Thomson, R. K.; Zahariev, F. E.; Zhang, Z.; Patrick, B. O.; Wang, Y. A.; and Schafer, L. L. *Inorg. Chem.* **2005**, *44*, 8680, which can be accessed via the world-wide-web at <http://pubs.acs.org>.

B2 Bis(amidate) imido DFT calculations

The density functional theory calculations performed on imido complex **4.25** were accomplished using the Amsterdam Density Functional (ADF2005.1)¹² suite of software, in collaboration with Pierre Kennepohl at UBC. The solid-state molecular structure of **4.25** was utilized as the starting point for these calculations, with geometry optimization accomplished with the PW91 XC functional, and default triple ζ basis sets with polarization for all non-Zr atoms, and a triple ζ basis set with polarization for Zr, where the core contains all orbitals up to and including the 3d orbitals. Single point calculations were performed to determine the electronic structure of **4.25**, where the orbitals were visualized with ADFview.¹² Ligand-metal bonding interactions were determined through calculation of ligand fragments and correlation to the overall molecular structure calculated for **4.25**.

B3 References

1. Westgrid, UBC Xeons.
2. Frisch, M. J.; et al. *Gaussian 03, Revision A.1*. Gaussian, Inc., Pittsburgh PA, **2003**.
3. Delano, W. L. The PyMOL Molecular Graphics System (2002), Delano Scientific, San Carlos, CA, USA.
4. Rapp, A. K.; Casewit, C. J.; Colwell, K. S.; Goddard III, W. A.; Skiff, W. M. *J. Am. Chem. Soc.* **1992**, *114*, 10024.
5. Slater, J. C. *Quantum Theory of Molecules and Solids Volume 4: The Self-Consistent Field for Molecules and Solids*. McGraw-Hill, New York, **1974**.
6. Becke, A. D. *Phys. Rev. A.* **1988**, *38*, 3098.
7. Lee, C.; Yang, W.; Parr, R. G. *Phys. Rev.* **1988**, *37*, 785.
8. Nasluzov, V. A.; Rsch, N. *Chem. Phys.* **1996**, *210*, 413.
9. Ziegler, T. *Chem. Rev.* **1991**, *91*, 651.
10. Rsch, N.; Krger, S.; Mayer, M.; Nasluzov, V.A. *Recent Developments and Applications of Modern Density Functional Theory*. Ed. Seminario, J.M. Elsevier, Amsterdam, **1996**, pp 497.
11. (a) Laaksonen, L. *J. Mol. Graph.* **1992**, *10*, 33. (b) Bergman, D. L.; Laaksonen, L.; Laaksonen, A. *J. Mol. Graph. Model.* **1997**, *15*, 301.
12. ADF2005.01, SCM, Theoretical Chemistry, Vrije Universiteit, Amsterdam, The Netherlands, <http://www.scm.com>.